THE UNIVERSITY OF CHICAGO

EXPERIMENTAL AND THEORETICAL EVIDENCE FOR DIVERSE THERMODYNAMIC INFLUENCES ON TRANSITION METAL-OXO MEDIATED C–H ACTIVATION

A DISSERTATION SUBMITTED TO

THE FACULTY OF THE DIVISION OF THE PHYSICAL SCIENCES

IN CANDIDACY FOR THE DEGREE OF

DOCTOR OF PHILOSPHY

DEPARTMENT OF CHEMISTRY

BY

JOSEPH EDWARD SCHNEIDER

CHICAGO, ILLINOIS

MARCH 2024

Table of Contents

List of Figures

Chapter 1

Chapter 2

Chapter 3

Chapter 4

Chapter 5

Appendix 1

Appendix 2

Appendix 3

Appendix 4

List of Schemes

Chapter 3

Chapter 4

Chapter 5

Appendix 2

List of Tables

Appendix 2

Appendix 3

Appendix 4

List of Regressions

Appendix 1

List of Calculations

Appendix 3

Acknowledgements

I would not have had any success in my PhD research without many mentors to support me along the way. My research advisor, Prof John Anderson, has been an immensely positive influence on my development as a scientist and as a scientific communicator. His relentless optimism was a source of constant motivation and inspiration throughout the last six years. I would also like to thank the rest of my committee, Prof. Mark Levin and Prof. David Mazziotti, whose instruction and guidance helped widen my view of chemistry. I am indebted to the entire Anderson group, Jordan Group, Hopkins Group, and Wuttig Group for their support, feedback, and suggestions over the years. Of note, Dr. Ethan Hill, Dr. McKenna Goetz, and Dr. Norman Zhao were excellent mentors in the oxo subgroup who put up with me as a first year and modelled what it is to be a successful researcher.

The instrumentation staff and facilities staff, including Dr. Josh Kurtz, Dr. Jin Qin, Laura Luburich, and Bentley Wall, have also been incredibly helpful and were always quick to respond to a question, be it a hung-up instrument or yet another broken key. The research here relied on crystallography done by Sophie Anferov and Dr. Alex Filatov, who were able to solve some truly horrendous structures. When the diffractometer at UChicago was down, Dr. Charlotte Stern and Dr. Christos Malliakas kindly helped Sophie and Alex collect data at Northwestern University.

I have had the pleasure of mentoring several great younger students throughout my time here. Undergraduate students Joel Gardner and Eyob Tewelde had an invaluable role in the design and synthesis of the original Forever Ligand. Younger graduate students Joseph Scott and Shilin Zeng and undergraduate student Ashley Zhu have been fantastic coworkers in the past years and

months as we have developed new perfluorinated ligand scaffolds, and I am excited to leave that project in their hands.

This research would not have been possible without a National Defense Science and Engineering Fellowship from the Department of Defense, an Eckhart Fellowship from the University of Chicago, and further support from the National Science Foundation and the National Institutes of Health. This funding is only available because of the administrative staff who assist in the writing and management of grant funds. I especially thank Karen Waters who helped me with my National Defense Science and Engineering Fellowship application.

I also need to thank everybody outside the UChicago whose mentorship got me to UChicago in the first place. I was incredibly fortunate to have Dr. Carson Matier as a mentor for much of my undergraduate research and Dr. Dylan Freas and Dr. Josef Schwann for the remainer of it. I learned an incredible amount under them and under my research advisers, Prof. Greg Fu, Prof. Harry Gray, and Prof. Jonas Peters, as well as other group members and professors too numerous to name here.

My friends and family have been incredible throughout not just the past six years but throughout the past twenty-eight. I do not have the words to express just how much their encouragement and support have meant to me. Through thick and thin, they have brought the best out of me, borne the worst, and I could not have done it without them.

Abstract

The selective activation and functionalization of C–H bonds is a major challenge in synthetic chemistry. Transition metal-oxo complexes are particularly adept at accomplishing such transformations. This has motived many studies into what factors control and predict the concerted proton electron transfer (CPET) reactivity between transition metal-oxo complexes and C–H bonds. Recently, there has been a much interest in, and no little controversy over, whether and how such C–H activation is influenced by the stepwise free energies of proton transfer and electron transfer, $\Delta G°_{PT}$ and $\Delta G°_{ET}$. At the time this research commenced, there was no clear framework for how these free energies affect CPET in general nor an understanding of whether their effect is distinct from their contribution to the overall driving force of the reaction $\Delta G°_{CPET}$.

This dissertation begins in Chapter 2 with the broadest study of transition metal-oxo mediated C–H activation to date. Reported rates of reactivity between transition metal-oxo complexes and DHA are found to only be predicted by the stepwise thermodynamic parameters $\Delta G°_{CPET}$, $\Delta G°_{PT}$, and $\Delta G°_{ET}$. Long-held beliefs regarding the reactivity of transition metal-oxo complexes towards C–H bonds, most notably the importance of high spin states, are not predictive of reaction rates. Our analysis demonstrates that $\Delta G°_{PT}$ and $\Delta G°_{ET}$ have an influence on reaction rates independent of their contribution to $\Delta G°_{CPET}$, and that this influence is not easily explained as a textbook linear free energy relationship.

Despite the mounting evidence for the role of stepwise thermodynamics in CPET reactions, there has been controversy over whether their effect is compatible with proton tunneling. Chapter 3 addresses this controversy by investigating the role of quantum tunneling in the $\Delta G°_{PT}$-dependent

CPET reactions between a cobalt(III)-oxo complex and C–H bonds. Variable temperature kinetic isotope effects support extensive proton tunneling in this reaction. Chapter 4 presents a computational study which demonstrates how this tunneling is enhanced by a lower $\Delta G°_{PT}$. There is a link between the C–H bond acidity, the anharmonicity of the proton potential energy well, and the overall rate of the reaction. This means that structure-reactivity relationships can be invoked even with a quantum mechanical treatment of protons. Model calculations parameterized with these computations demonstrate that experimentally observed trends with $\Delta G°_{PT}$ and $\Delta G°_{ET}$ can be explained primarily through the influence of stepwise thermodynamic on the proton potential energy wells.

Extending these studies of thermodynamic effects on C–H activation to strong C–H bonds required developing a new strategy for stabilizing highly reactive transition metal-oxo species capable of activating such bonds. Chapter 5 presents the development of a new ligand scaffold which is resistant to oxidation and preliminary studies on using this scaffold to generate high-valent transition metal-oxo complexes. The combination of a mesoionic scorpionate scaffold with trifluoromethyl groups yields a ligand which similar electron properties to established tris(imidazol-2-ylidene)borate scorpionate ligands, but with oxidatively robust trifluoromethyl flanking groups. This ligand supports the first ever isolation of a stable dicobalt(IV) complex, demonstrating the ability of this ligand to stabilize highly reactive species.

Chapter 1: Introduction

1. Diversity and Reactivity of Transition Metal-Oxo Complexes

Transition metal-oxo complexes are privileged intermediates in wide variety of chemical processes (Figure 1.1A).[1–11] Their ubiquity can be understood by viewing them as modular oxygen atom sources which can be tuned to have a wide variety of properties and reactivities. This allows their optimization for reactions as diverse as C–H activation,[11] oxygen atom transfer,[5,9] and O–O coupling (Figure 1.1B).[6,10]

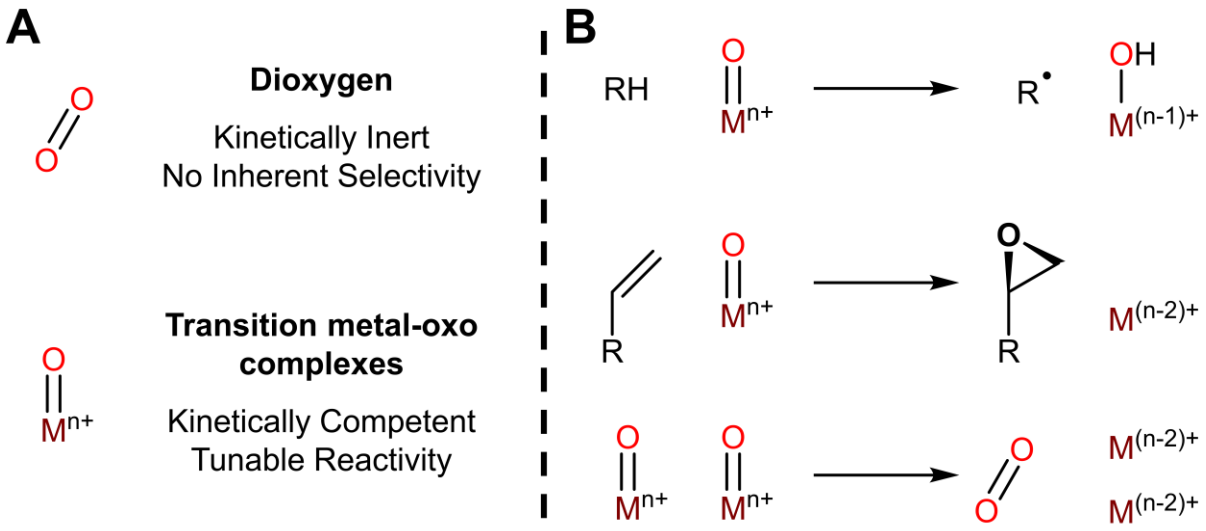

Figure 1.1 Overview of transition metal-oxo complex reactivity. (A) Transition metal-oxo compounds as a versatile tool for controlling oxygen chemistry. (B) Examples of reactions mediated by transition metal-oxo complexes.

The properties of a metal-oxo unit are strongly influenced by the number and configuration of *d*-electrons and by the supporting ligand scaffold, as this determines the nature of metal-oxygen bonding.[2,12] For instance, nonheme iron-oxo complexes are often tetragonal and d^4. This results in two electrons being placed in M–O π^* orbitals, weaking the M–O interaction and enhancing reactivity (Figure 1.2A). Later transition metals have more *d*-electrons and therefore form even

weaker M–O bonds. This creates an "oxo wall" at between groups VII and IV beyond which terminal metal-oxo complexes have not been observed in tetragonal geometries, as it is too difficult to oxidize these metals to *d*-electron counts low enough for a sufficiently strong M–O bond.[12,13] However, scorpionate ligands which enforce pseudotetrahedral geometries effect a different *d*-orbital splitting which can support up to six electrons without occupying the π* orbitals (Figure 1.2B), effectively circumventing this wall.[14,15] Lower coordinate geometries can also encourage high-spin states, which affects the nature of all metal-ligand bonds, including the M–O bond (Figure 1.2C).[16,17] Thus, by judicious choice of transition metal and coordination geometry, a variety of metal-oxo properties can be generated, all with unique properties and reactivity.

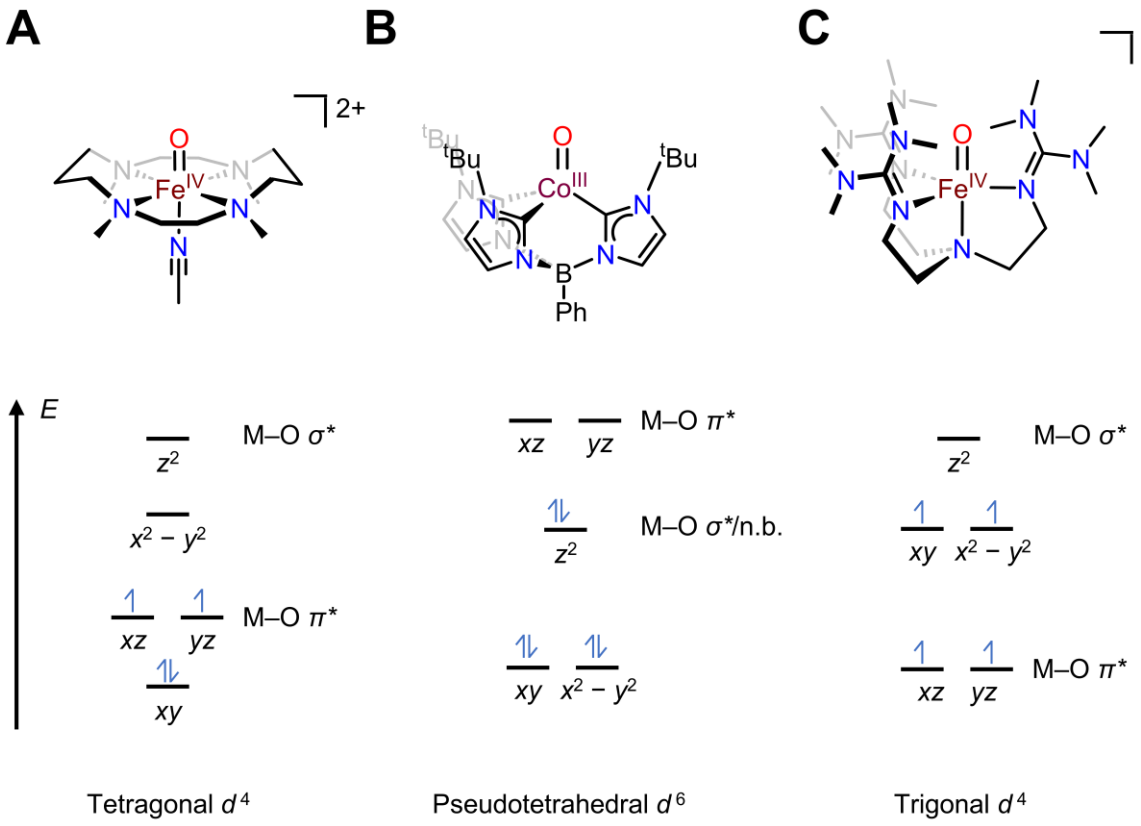

Figure 1.2 Selected examples of how coordination geometry and ligand field strength affect electronic structure of a transition metal and the nature of an M–O bond. (A) Tetragonal d^4 Fe(IV)-oxo.[18] (B) Pseudotetrahedral d^6 Co(III)-oxo.[14] (C) Trigonal d^4 Fe(IV)-oxo.[17]

This chemical diversity of transition metal-oxo complexes has in turn lead to a diversity of hypotheses for what properties of transition metal-oxo complexes lead to increased reactivity with C–H bonds. This dissertation builds on these studies by using linear free energy relationships to understand which of these hypotheses can broadly explain experimental observations. Thermodynamic variables are found to be particularly important predictors of reactivity. This result, and their traditional interpretation as LFERs, are evaluated within the context of modern theoretical treatments of concerted proton electron transfer reactions. Finally, work is made towards the stabilization and characterization of oxygenated transition metal complexes capable of controlled activation of particularly strong C–H bonds.

2. Models for the C–H activation reactivity of Transition Metal-oxo Complexes

The generally accepted mechanism for transition metal-oxo mediated C–H activation and functionalization is shown in Figure 1.3A.[19–22] A transition metal-oxo complex abstracts a hydrogen atom from an organic substrate, generating an organic radical and a transition metal-hydroxide. The organic radical can be subsequently functionalized in a variety of ways, commonly by rebound onto either the transition metal-hydroxide or another X-type ligand. Because the abstraction of the hydrogen atom consists of a proton transfer and an electron transfer, the C–H activation process can be viewed as a subset of concerted proton electron transfer (CPET) reactions more broadly.[23,24]

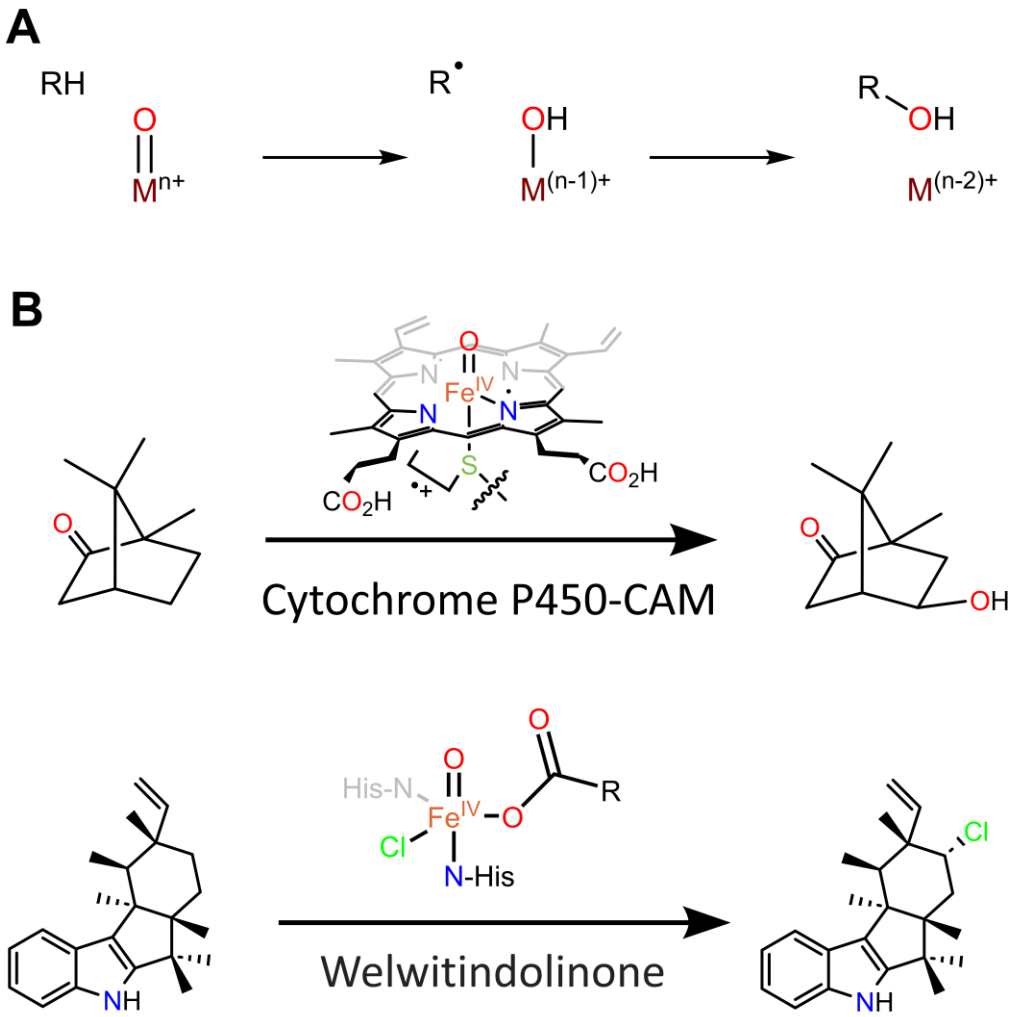

Figure 1.3 Mechanisms and examples of transition metal-oxo mediated C–H activation. (A) The general mechanism of C–H bond activation followed by radical rebound on an X-type ligand. (B) Examples of this mechanism being used by nature to functionalize C–H bonds.[25–27]

This is a common mode of C–H functionalization in biology (Figure 1.3B).[25–27] For instance, the oxygenation of C–H bonds by cytochrome P450s, which plays an important role in biosynthesis and drug metabolism, proceeds through the iron(IV)-oxo complex Compound I.[28] Nonheme iron(IV)-oxo complexes in halogenase enzymes similarly convert C–H bonds into C–halogen bonds.[27,29–31] These transformations have been successfully mimicked for C–H activation in synthetic systems.[1,32–34] This ubiquity has motivated many studies on what enables and controls the C–H activation reactivity of transition metal-oxo complexes.

It is widely acknowledged that the dominant influence on the CPET reactivity of a transition metal-oxo complex with C–H bonds is the free energy of reaction, $\Delta G°_{CPET}$.[35–38] For a given transition metal-oxo complex, there is typically a correlation between the logarithm of the rate constant of C–H activation (ln k_{CPET}) and the strength of the C–H bond being broken, as measured by its bond dissociation free energy (BDFE). Because the logarithm of the rate constant gives the activation free energy for the CPET process ($\Delta G^{‡}_{CPET}$), and the free energy of the reaction is in part determined by the strength of the C–H bond being broken, this is equivalent to there being, in general, a correlation between $\Delta G^{‡}_{CPET}$ and $\Delta G°_{CPET}$.

$$\ln k_{CPET} = m\, BDFE(C-H) + b \quad (1.1)$$

$$\Delta G^{‡}_{CPET} = \alpha\, \Delta G^{\circ}_{CPET} + C \quad (1.2)$$

The unitless slope α can inform on the nature of the transition state (see below). The intercept, *C*, gives all contributions to the barrier which are unrelated to the driving force for this reaction. Many theories have been stated for what contributes to *C*, but there is little consensus on this matter.

There is a rich literature tradition which links the reactivity of transition metal-oxo complexes to their spin state.[39–41] When different spin states are possible for a transition metal-oxo complex, DFT calculations have usually found that higher spin states have lower reaction barriers. This has been rationalized by the argument that higher spin states typically have more exchange energy with the transferring electron, which stabilizes the reaction.[41] By this line of reasoning a more energetically accessible high-spin state will lead to enhanced reactivity.[35,42] Thus, the intrinsic barrier may be quantitatively linked to the excitation energy needed to assess a high-spin

state. However, it has been argued that, as transition metal-hydroxide products are typically high-spin, this may simply be a reflection of the greater driving force for reactivity in a high-spin state.[43] Experimental attempts to demonstrate the higher reactivity of high spin states using model complexes are nontrivial to interpret because stabilizing a high-spin state necessarily entails complicated changes to the electronic, geometric, and steric profile of the transition metal-oxo complex.[17,44,45]

As the abstraction of an H-atom looks like an inherently radical reaction, there has been discussion on whether spin-density on the oxo ligand accelerates CPET reactivity.[46,47] However, as singlet transition metal-oxo complexes can cleave C–H bonds, spin-density is clearly not a requisite for reactivity.[48–50]

Recently, there has been much interest in how thermodynamic factors other than $\Delta G°_{CPET}$ affect CPET reactions. An increasing number of studies implicate the free energies needed to form stepwise intermediates, i.e. the free energy of solely proton transfer or of solely electron transfer, $\Delta G°_{PT}$ and $\Delta G°_{ET}$, respectively, as being important in understanding the rates of C–H bond activation and in CPET more broadly (Figure 1.4).[50–65] However, there is no common model for how these stepwise free energies are purported to affect reactivity.

It is well-understood how $\Delta G°_{PT}$ and $\Delta G°_{ET}$ can be viewed as components of $\Delta G°_{CPET}$.[23,52,66,67] Thus, even if a transition metal-oxo complex is not very oxidizing, it can still oxidatively cleave C–H bonds if it is sufficiently basic. Because this basicity does not enhance other oxidative reactions, this could lead to a higher thermodynamic preference for C–H activation.[68] Following this line of logic, many studies have expressed the outsized influence of

either $\Delta G°_{PT}$ or $\Delta G°_{ET}$ on reaction rates as being an uneven, or imbalanced, expression of the role of $\Delta G°_{CPET}$. In other words, $\Delta G°_{PT}$ and $\Delta G°_{ET}$ do not influence CPET reactivity independently from $\Delta G°_{CPET}$. Studies of multi-site CPET, in which the base and proton-transfer energetics are varied independently of the oxidant and electron-transfer energetics,[56,57,69] as well as the model of Barman et al.,[63] stand out as examples of this treatment of stepwise free energies.

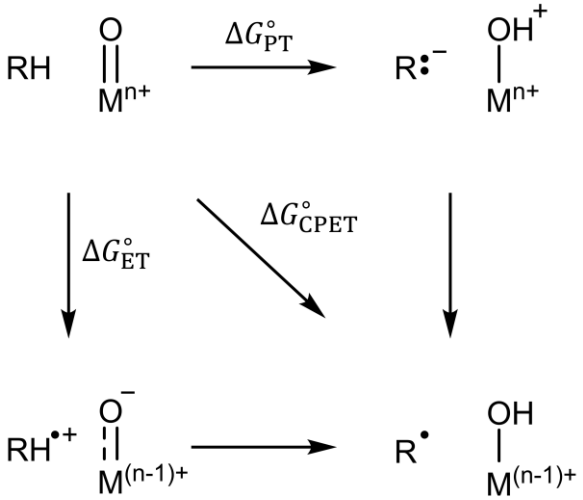

Figure 1.4 A generic square scheme for reactivity between transition metal-oxo complexes and C–H bonds.

However, there have also been indications that these free energies may dominate over the role of $\Delta G°_{CPET}$ in some cases. For instance, Nocera and coworkers have noted the sluggish or nonexistent reactivity with acetonitrile is incompatible with the traditional view that rates of transition metal-oxo C–H activation are determined by $\Delta G°_{CPET}$, but treating these reactions as responding to $\Delta G°_{ET}$ can explain this.[51] Additionally, there are now several reports of transition metal complexes that activate C–H bonds though a concerted process with rates which are better predicted by either C–H bond pK_a or $E°$ than they are by C–H bond BDFE.[50,54,58,59,61,65]

Furthermore, there is the view that stepwise thermodynamics affect the intrinsic barrier of a reaction more generally, but not so far as to replace the typical role of $\Delta G°_{CPET}$. Of note is the

work of Srnec and coworkers, who have expressed non-$\Delta G°_{CPET}$ parameters based on C–H and O–H bond acidities and reduction potentials and suggested they explain deviations from a dominant trend between the reaction barrier and the reaction driving force.[55,64] The view that $\Delta G°_{PT}$ and $\Delta G°_{ET}$ are merely reflecting the well-known polarity effect of organic hydrogen-atom transfer reactions, of which transition metal-oxo mediated C–H activation is at least similar to if not a subset of, could also fall in this third category.[70–72]

The big picture is that there is mounting evidence for the importance of $\Delta G°_{PT}$ and $\Delta G°_{ET}$ on CPET reactions, but the nature of their influence is unclear. Are they merely contributors of $\Delta G°_{CPET,}$ or important parameters in their own right? Do they only manifest in unusual instances, or are their effects more general? What formula can express their quantitative affect reaction rates? These questions call for an evaluation of both the experimental evidence as a whole and also of the theoretical foundation for these so-called "imbalanced" or "asynchronous" reactivity trends. As all the models for their influence on reactivity are built on linear free energy relationships, the textbook meaning of these relationships must be the starting point for any evaluation.

3. Brief Introduction to Linear Free Energy Relationships

Linear free energy relationships (LFERs) are simply linear models relating free energy changes to each other.[73,74] Most commonly this will be correlating a change in the activation free energy of a reaction ($\Delta G^{‡}_{Rxn}$) to either the free energy of the same reaction ($\Delta G°_{Rxn}$) or to the free energies of activation or reaction of reference chemical processes. These free energies are often given as the logarithm of rate constants ($RT \ln k_{Rxn} = \Delta G^{‡}_{Rxn}$) or the logarithm of equilibrium constants ($RT \ln K_{Rxn} = \Delta G°_{Rxn}$).

The simplest LFER is Brønsted's empirical power law which describes how the rate of an acid catalyzed reaction, k_{cat}, varies as the acid catalyst's equilibrium dissociation constant K_a is varied:[75,76]

$$\textbf{Equation 1.1} \qquad k_{cat} = GK_a^{-\alpha}$$

$$\textbf{Equation 1.2} \qquad \ln k_{cat} = -\alpha \ln K_a + \ln G$$

In these equations α and G are empirical constants specific to the reaction under study. Evans, and Polanyi,[77,78] building on work of Ogg and Polanyi,[79] and independently Bell,[80] justified this relationship from first principles. They modelled the potential energy surface of a reaction as the interaction between a reactant and product potential and demonstrated how shifting the relative energies of these potentials shifted the energy of the intersection. This predicts, in a general way, that the activation free energy of a reaction will be related to the same reaction's free energy of reaction:

$$\textbf{Equation 1.3} \qquad \Delta G_{Rxn}^{\ddagger} = \alpha \Delta G_{Rxn}^{\circ} + C$$

$$\textbf{Equation 1.4} \qquad \ln K_{Rxn} = -\alpha \ln k_{Rxn} + \mathrm{C}$$

This expected relationship between the driving force of a reaction and its kinetics is known as the Bell-Evans-Polanyi (BEP) principle, and it is what underlies the dominant trend of $\Delta G°_{\mathrm{CPET}}$ on C–H activation rates (C is an arbitrary constant which is not identical in both formulations). The Brønsted catalysis law can be seen to come from applying this principle to a rate-limiting step which involves proton-transfer.

More generally, identical substituent and structural changes often have similar effects on a variety of chemical reactions, and these changes are often tabulated with standard parameters determined from a reference reaction.[74,81] The slope of correlations between reaction rates and equilibrium constants with these standard parameters is used to inform on transition state structure, such as the importance of steric effects or the buildup of charge at the transition state.

The Brønsted coefficient α was eventually understood to reflect whether the transition state was more reactant-like ("early") or product-like ("late"), as formulated by Hammond and Leffler.[82,83] Hammond postulated that if two states are formed consecutively in a reaction and have similar energy, then they will have similar structure. Thus, a downhill reaction would have an "early" transition state resembling the reactants. Such reactions will have rates that are less dependent on $\Delta G^{\circ}_{\mathrm{Rxn}}$ and have selectivity which can be understood based on the reactant (electronic) structure. Similarly, uphill reaction rates will be more dependent on $\Delta G^{\circ}_{\mathrm{Rxn}}$ and have selectivity which reflects the product (electronic) structure. Leffler independently made a similar formulation, concluding that the Brønsted coefficient α would be smaller for a downhill reaction with an early transition state and larger for an uphill reaction with a late transition state. A corollary of Leffler's formulation is that α can function as an experimental measure of the reaction coordinate, and both α and the transition state structure are expected to change if $\Delta G^{\circ}_{\mathrm{Rxn}}$ changes.

Similar ideas were expressed by Marcus in his theory of electron transfer. Marcus modeled a reactant and a product electronic configuration as having a quadratic dependence on collective solvent coordinates, or on changes in the reaction environment more generally.[84,85] The transition state in this theory is where the resulting parabolic energy surfaces intersect. The key contribution here was recognizing that the reaction coordinate consisted of environmental factors, such as

collective solvent coordinates and distortions in bond lengths, which needed to fluctuate to a point where the reactant and product electronic states have the same energy. The electron then can tunnel directly from reactant to product. Thus, in Marcus theory, the coefficient α represents not the progress of the electron, but how reactant-like or product-like the environment is at the moment of tunneling. This is a significant difference between how LFERs are interpreted in electron transfer and how they are interpreted in other reactions.

In 1970 More O'Ferrall formulated a more generalized Hammond principle which accounts for multiple bond-making and bond-forming events utilizing a 2-dimentional reaction coordinate.[86] While he was far from the first to invoke such multidimensional reaction coordinates, he synthesized previous notions of transition state structure motion along a 2D surface with the Hammond postulate.[87–90] His model used ground state structures to anchor the transition state energy surface and thereby linked transition state structure and stabilization to ground state thermodynamics more broadly. Jencks expanded on this model, and in particular noted how the coefficients of different LFERs could be used to estimate the 2-dimensional coordinate of a transition state.[73,91]

Even in the earliest applications of such More O'Ferrall Jencks plots to understand reactions with multiple bond breaking and bond forming events, it was observed that different transition state structures would be inferred from different LFERs. For instance, in acid-catalyzed alcohol eliminations, the extent of O–C bond cleavage at the transition state would appear to change with varied acid strength if interrogated *via* a LFER with alkoxide leaving group basicity, but remain constant if interrogated *via* a LFER with organic substrate stability.[92–94] Such effects

were referred to as imbalances in the LFERs, with "imbalance" in this context referring to inconsistencies between different LFERs.

Using these textbook interpretations of LFER, the influences of $\Delta G°_{PT}$ and $\Delta G°_{ET}$ on CPET reactions can simply be understood as informing on the extent of proton transfer and electron transfer in the transition state, in the same way as Brønsted coefficients inform on the extent of proton transfer in general acid-catalyzed reactions. A role for stepwise thermodynamics which is distinct from $\Delta G°_{CPET}$ could simply be the anti-Hammond effect, in which stabilization of a stepwise intermediate can be transferred to a transition state if the transition state distorts to resemble said intermediate. Alternatively, changes in $\Delta G°_{PT}$ and $\Delta G°_{ET}$ could be viewed as two different measures for changes in $\Delta G°_{CPET}$, and therefore two different ways to determine how early or late the transition state is on a one-dimensional reactivity plot.

This textbook interpretation for the effect of $\Delta G°_{PT}$ and $\Delta G°_{ET}$ on reactivity has come into criticism for not properly taking proton tunneling into account.[67,95,96] Even in his earliest paper on the effect that partly bears his name, Bell noted that tunneling could be important to proton transfers.[80] However, the effects of tunneling were rarely viewed as an impediment to discussing the structure of a transition state with well-defined bond lengths, and thereby a localized proton position; often the only quantum effect considered would be zero-point vibrational energy. Modern computational studies which use DFT-optimized transition states to study the reactivity of transition metal-oxo complexes with C–H bonds is built on a similar semiclassical foundation. In contrast, the most advanced theoretical models of CPET treat it more similarly to an electron transfer, in that tunneling for both the proton and the electron is the foundation of the model.[97–99]

Overall, the recent interest in how C–H activation is affected by $\Delta G°_{PT}$ and $\Delta G°_{ET}$ clearly has roots in classic studies in physical organic chemistry, and their effect has largely been understood in this context. There is the view, however, that this interpretation is not physically justified.

4. A Note on Terminology

The field of concerted proton electron transfer has a dizzying array of acronyms, which can confuse new scholars in the field. These confused scholars may then use one acronym in early studies, but with the benefit of experience realize a different acronym is more ideal and use it in later papers. We speak of this from personal experience. This can be a vicious cycle, as such inconsistent usage does not help to clarify the terminology used in the literature.

In this work, we will use proton-coupled electron transfer (PCET) to refer to the overall process, agnostic to mechanism. Because we are only interested in concerted reactions we will rarely, if ever, use this acronym. We refer to concerted proton electron transfer (CPET) to denote a concerted mechanism. We never use CPET in the sense of the "C" standing for coupled, nor do we flirt with novel acronyms such as the concomitant transfer of electrons and protons (CTEP). We discuss CPET reactions as being inclusive of hydrogen atom transfer (HAT) reactions, because transition metal-oxo mediated C–H activation reactions often fall in the blurry boundary that is sometimes set between CPET and HAT reactions.

There are also several overlapping terms which specifically relate to the influences of $\Delta G°_{PT}$ and $\Delta G°_{ET}$ in CPET. Different papers have called an outsized influence for one of these thermodynamic free energies either asynchronous, imbalanced, or asymmetric. None of these terms are perfectly satisfactory. Early papers in physical organic chemistry rarely directly called

reactions asynchronous, even when contrasting against a perfectly synchronous transition state. Furthermore, this word implies that the transfers occur at different times, which strictly speaking would only apply to stepwise reactions. In the early literature, imbalance is typically restricted to apply to reactions for which different LFERs give facially inconsistent results. This would cover some formulations for $\Delta G°_{PT}$ and $\Delta G°_{ET}$ affect a CPET reaction, such as if they are viewed as disagreeing measures for the development of the reaction along a single reaction coordinate, but it does not apply if $\Delta G°_{PT}$ and $\Delta G°_{ET}$ are viewed as probing two separate transition state coordinates. Generically referring to these reactions as asymmetric, as used initially by Mayer, would avoid having any specific, technical meaning.[57] However, as Mayer later noted this comes at the risk of being confused as invoking chirality.[72] We will use refer to cases with an outsized influence of one stepwise free energy or another as imbalanced. The limitations of this descriptor are less severe, as it is a perhaps inevitable linguistic generalization which was already taking place within a decade of More O'Ferrall's and Jenck's seminal papers.

As a final note on terminology, while we have in the past discussed $\Delta G°_{PT}$ and $\Delta G°_{ET}$ as being off-diagonal elements in a square scheme, in that they deviate from the $\Delta G°_{CPET}$ diagonal, we found that this was too easily confused with the off-diagonal coupling element in a two-state Hamiltonian. Herein and hereafter we will only refer to $\Delta G°_{PT}$ and $\Delta G°_{ET}$ as being "stepwise thermodynamic parameters" to avoid this confusion.

Chapter 2: Statistical analysis supports multiple thermodynamic influences on the kinetics of C–H activation by transition metal-oxo complexes

Reproduced from Schneider, J. E.; Goetz, M. K.; Anderson, J. S. *Chem. Sci.* **2021**, *12*, 4173-4183 with permission from the Royal Society of Chemistry.

1. Introduction

In the past few decades, chemists have synthesized and experimentally characterized a wide diversity of transition metal-oxo complexes. Comparisons are often made between the C–H activation reactivity of these complexes, with the rate constant of reactivity with C–H substrates being a common quantitative metric. These studies have resulted various hypotheses for what factors enhance concerted proton electron transfer (CPET) reactivity between C–H bonds and transition metal-oxo complexes (Figure 2.1).

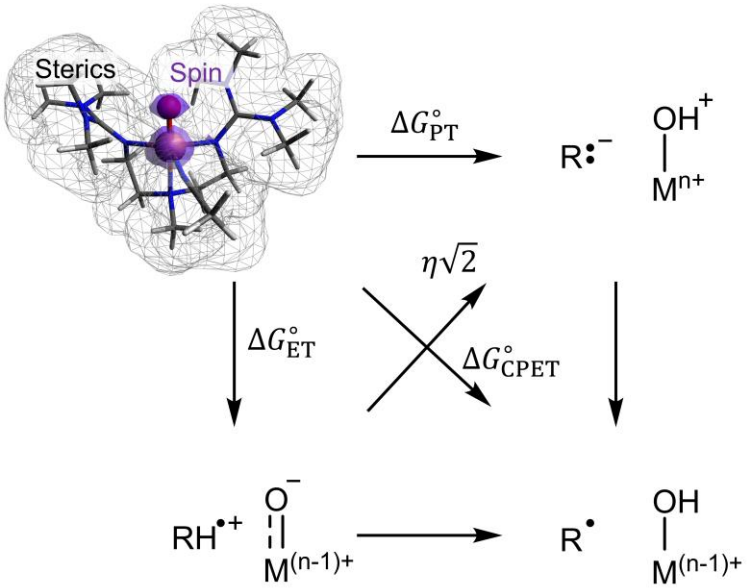

Figure 2.1 Parameters proposed to affect the reactivity of transition metal-oxo complexes.

As Chapter 1 elaborated on in detail, the free energy of reaction ($\Delta G°_{CPET}$) is central to transition metal-oxo mediated C–H activation and also offers a great deal of explanatory and predictive power;[35–38] additional properties have been cited as important although it is not clear if any have a widespread effect on reactivity. Individual cases support the influence of O-centered spin density,[46] spin state,[40–42] steric environment,[17,44,45] the free energies of proton and electron transfer ($\Delta G°_{PT}$ and $\Delta G°_{ET}$),[50,52,54,68,100,101] or the asynchronicity (η) of the reaction.[55,62,102,103] There is a lack of consensus regarding their generality and relative importance.[43,46,67,96] Very few studies have explored these parameters outside of a narrow range of complexes,[35,37,42,54,55,104] and none have statistically examined the significance of parameters other than $\Delta G°_{CPET}$ on the reactivity of a broad set of metal oxo complexes.

Previous research in the Anderson group found an atypical dependence on $\Delta G°_{PT}$ in the concerted C–H activation reactivity of a terminal cobalt-oxo complex which contrasts with the expected rate dependence on $\Delta G°_{CPET}$.[50] Given the disparity of this result with the literature, we sought to understand the interplay of characteristics affecting a broad range of transition metal oxo mediated CPET reactions using multivariable linear free energy relationships (LFERs). Our analysis enables a statistical examination of several hypotheses regarding what parameters of metal oxo species effect their CPET reactivity. Unsurprisingly, we observe that $\Delta G°_{CPET}$ is the most important factor. However, we also observe a significant role for $\Delta G°_{PT}$ and $\Delta G°_{ET}$ beyond and independent of their contribution to $\Delta G°_{CPET}$. Furthermore, the other parameters investigated do not have broad significance. These results suggest that thermodynamic factors are generally the dominant contributors to transition metal oxo C–H activation reactivity, but also demonstrate that thermodynamic parameters beyond the commonly invoked $\Delta G°_{CPET}$ are influential.

2. Introduction to Predictive Data Modelling

Linear free energy Relationships (LFERs) have historically been used to probe the structure and properties of transition states by relating the rate of a reaction to the reaction free energies or to parameters derived from reference reaction free energies.[73,74] The advent of density functional theory (DFT) as a cheap *ab initio* means to calculate the structure and properties of chemical species has made non-thermodynamic parameters such as calculated partial charges or estimates of steric bulk more available, and they are now commonly used as predictor variables in LFERs. Moreover, LFERs are increasingly used to predict figures of merit such as yield and enantioselectivity.[105–108] This allows them to be used as predictive models for what reaction conditions will have a more desirable outcome.

This increased interest in using quantitative models to predict chemical reactivity has led to the use of increasingly complex models. The simplest of these models are multivariable linear fits, i.e. the incorporation of more than one *x*-variable in a linear free energy relationship. These models are more powerful for predicting reaction properties and can inform on the relative importance of, and possible interaction between, different parameters.[109–111] However, they also come with increased risk of over-fitting and *p*-hacking in their construction. Thus, the evaluation of such models requires more care than simple correlation against a single free energy parameter.

Multivariable LFERs can be evaluated using R^2, leave-one-out R^2 (LOO R^2, sometimes referred to as Q^2), and a statistical *F*-test.[112–115] The R^2 value is a goodness of fit measure which quantifies the amount of variation explained by a model; it is identical to the r^2 used to evaluate LFERs against a single parameter. The predictive ability of a model is gauged with LOO R^2, in which each data point is left out and predicted by the remaining data points and the goodness of

fit is then reevaluated. For each R^2, a value close to 1 indicates a good fit and a value close to 0 indicates a poor fit. Critically, LOO R^2 can either increase or decrease with additional parameters. Overfitted models with too many parameters will display an increase in R^2, but a decrease in LOO R^2. Additionally, the significance of incorporating an *x*-variable can be evaluated with an *F*-test on each model. This gives a *p*-value which shows the probability the observed correlation arises from statistical noise. The lower this *p*-value is, the more significant a given parameter is. The calculation of *p*-values considers the number of parameters added to a model, so, as with LOO R^2, an *F*-test is not biased in favor of adding more parameters.

3. Results and Discussion of Multivariable LFER fits

We began our analysis by compiling an extensive data set of second order rate constants (k_2) for the oxidation of 9,10-dihydroanthracene (DHA) by thirty well-characterized metal oxo complexes.[17,44,49,50,52,116–132] This diverse data set comprises complexes of five different transition metals, tetragonal and trigonal geometries, spin multiplicities from 1 to 5, charges from −1 to +3, and d-electron counts from 0 to 6. We manually divided the data set into a training set of seventeen metal oxo complexes and a test set of thirteen metal oxo complexes such that each set had a diverse mix of species and converted the k_2 values into an effective free energy of reaction $\Delta G^{\ddagger}_{\mathrm{CPET}}$.

For our analysis, we calculated the values of parameters that have been hypothesized as important transition metal-oxo mediated CPET reactivity for each metal oxo complex. The investigated parameters include the steric environment (quantified by percent buried volume, %BV),[133] the spin density on the oxygen atom (via intrinsic bond order (IBO) analysis),[134,135] the energetic cost of accessing a higher spin state if one lies closer to the product spin multiplicity than the reactant ground spin state (spin excitation), the thermodynamic free energies $\Delta G^{\circ}_{\mathrm{CPET}}$, $\Delta G^{\circ}_{\mathrm{PT}}$,

and $\Delta G°_{ET}$, and the magnitude of the asynchronicity parameter ($|\eta|$).[55] The detailed approaches used to determine the values for these parameters are provided in the methods section. Importantly, none of these parameters require transition state optimizations which are relatively difficult and less reliable than ground state calculations.[136,137] While this precludes a direct estimation of transition state effects, we expect to indirectly capture some of them. For instance, parameters such as $\Delta G°_{CPET}$ and $|\eta|$ have been shown to correlate with tunneling.[103,138]

We examined the effect of each of these parameters on experimental reaction with multivariable LFERs. These models were constructed with ordinary least squares regression of the barrier heights against each set of parameters. Each model consists of a set of coefficients (with variable units such that the product with the respective parameter gives units of kcal/mol) and an intercept (with units kcal/mol). These models were evaluated with the above described R^2, LOO R^2, and the *p*-value from a statistical *F*-test. Because $\Delta G°_{CPET}$ has strong theoretical and experimental support for affecting reaction barrier heights,[35–37] we analyzed each parameter in combination with $\Delta G°_{CPET}$ and compared the resulting models to a model with only $\Delta G°_{CPET}$.

A summary of our findings is presented in Table 2.1. In line with previous reports, we find a strong correlation between the experimental reaction barriers $\Delta G°_{CPET}$. This parameter alone explains 70% of the variation in reaction barriers within the training set ($R^2 = 0.70$) and has high predictive ability (LOO $R^2 = 0.60$). Interestingly, most other parameters do not significantly improve the model. While we do observe a small correlation with %BV steric metrics, the magnitude of the effect is too small to be statistically significant. Compared to the $\Delta G°_{CPET}$ only model, spin-based parameters and $|\eta|$ barely improve R^2 and perform similarly or worse by LOO R^2 cross-validation. While it is difficult to rule out the importance of these parameters in individual

cases, an *F*-test indicates they do not have a statistically significant effect across our entire data set.

Table 2.1 Statistical Results of Various Models.

Parameter(s) Regressed with $\Delta G°_{CPET}$	Training Set on DHA[a]			All Data for Multiple Substrates[b]	
	R^2	LOO[c] R^2	*p*-value[d]	R^2	LOO[e] R^2
$\Delta G°_{CPET}$ only	0.70	0.60	< 0.001[f]	0.45	0.36
%BV Steric Metrics	0.77	0.64	0.15	0.48	0.28
Oxo Spin Density	0.70	0.55	0.78	0.53	0.37
Spin Excitation	0.71	0.50	0.49	0.50	0.39
$\lvert\eta\rvert$	0.73	0.53	0.22	0.50	0.30
$\Delta G°_{PT}$, $\Delta G°_{ET}$	0.86	0.71	0.0082 0.023[g] 0.0038[h]	0.64	0.50

[a]A subset of the reactions between DHA and 17 transition metal-oxo complexes. [b]Excluding outlier transition metal-oxo complexes (ruthenium-oxo complexes and oxo complexes supported by 13-TMC); substrates are DHA, 1,4-cyclohexadiene, xanthene, and fluorene. [c]Leave-One-Out. [d]From an *F*-test where the null hypothesis is that only $\Delta G°_{CPET}$ has an effect. [e]Leave-One-Out, slightly modified such that all reactions for a given metal oxo are left out together. [f]From an *F*-test where the null hypothesis is that $\Delta G°_{CPET}$ has no effect. [g]From an *F*-test where the null hypothesis is that $\Delta G°_{PT}$ has no effect. [h]From an *F*-test where the null hypothesis is that $\Delta G°_{ET}$ has no effect.

In contrast, addition of $\Delta G°_{PT}$ and $\Delta G°_{ET}$ does significantly improve the fit. Compared to the $\Delta G°_{CPET}$ only model, the $\{\Delta G°_{CPET},\Delta G°_{PT},\Delta G°_{ET}\}$ model has R^2 increase from 0.70 to 0.86 and LOO R^2 increases from 0.60 to 0.71, indicating both better explanation of the available data and better predictive ability. An *F*-test on the significance of $\Delta G°_{PT}$ and $\Delta G°_{ET}$ gives $p < 0.01$ which suggests the observed effect is statistically significant.

Equation 2.1 $$\Delta G^{\ddagger}_{CPET} = 0.31\,\Delta G^{\circ}_{CPET} + 0.07\Delta G^{\circ}_{PT} + 0.12\,\Delta G^{\circ}_{ET} - 0.26$$

The equation from the $\{\Delta G°_{CPET},\Delta G°_{PT},\Delta G°_{ET}\}$ fit is given in Equation 2.1. All coefficients are unitless; free energies and intercept in kcal/mol. Typically, $\Delta G°_{CPET}$ is a negative value while $\Delta G°_{PT}$ and $\Delta G°_{ET}$ are positive values. Thus, the positive sign of the $\Delta G°_{CPET}$ coefficient indicates that a more exergonic reaction will have a lower barrier while an increase in either $\Delta G°_{PT}$ or $\Delta G°_{ET}$

will raise the barrier. The larger coefficient of $\Delta G°_{CPET}$ indicates the reaction barrier is most sensitive to this free energy. The intercept of −0.26 contains contributions to the average barrier not accounted for by the three free energies.

The significance of $\Delta G°_{PT}$ and $\Delta G°_{ET}$ is intriguing because the literature discussion of these values has often been framed in terms of how they contribute to $\Delta G°_{CPET}$ rather than in terms of their intrinsic contribution to reaction barrier heights.[52,67,68,100,101] However, $\Delta G°_{PT}$ and $\Delta G°_{ET}$ as defined here are the energies to form the intermediates involved in stepwise reactivity – the protonated metal oxo with the deprotonated substrate, or the reduced metal oxo with the oxidized substrate (Figure 2.1). Critically, $\Delta G°_{PT}$ and $\Delta G°_{ET}$ do not form a full thermodynamic cycle with $\Delta G°_{CPET}$ and thus are fundamentally distinct. This fact is statistically supported by poor correlations between $\Delta G°_{CPET}$ and $(\Delta G°_{PT} + \Delta G°_{ET})$ (Figure 2.2A). The improved LOO R^2 and the *F*-test clearly demonstrate that $\Delta G°_{PT}$ and $\Delta G°_{ET}$ have importance independent of a contribution to $\Delta G°_{CPET}$. All of our analyses therefore suggest that the combination of $\Delta G°_{PT}$ and $\Delta G°_{ET}$ is an independent and significant contributor to C–H activation barrier heights.

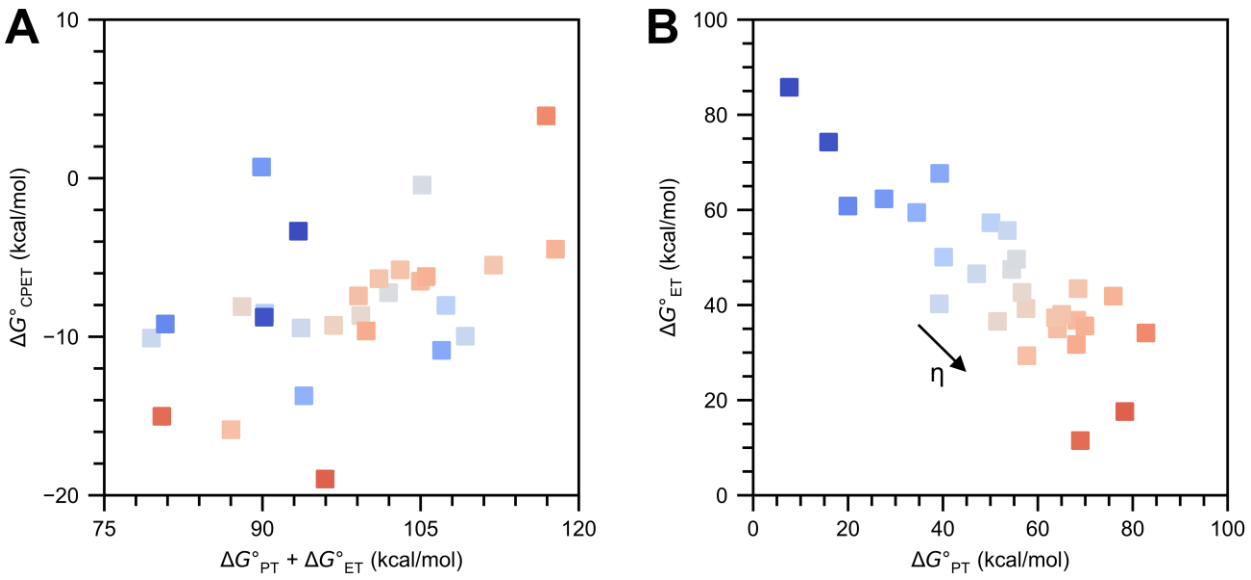

Figure 2.2 Scatterplots of thermodynamic free energies for the reactivity between DHA and all transition metal-oxo complexes in our dataset. Reactions which are proton-transfer biased and have a negative value of η are shown in a bluer shade; reactions which are electron-transfer biased and have a positive value of η are shown in a redder shade. (A) $\Delta G°_{CPET}$ against ($\Delta G°_{PT} + \Delta G°_{ET}$) and (B) $\Delta G°_{ET}$ against $\Delta G°_{PT}$.

Assigning a direct role for $\Delta G°_{PT}$ and $\Delta G°_{ET}$ is in line with recent computational studies of CPET transition states which invoke non-$\Delta G°_{CPET}$ thermodynamic terms in the form of asynchronicity (η), as key contributors to DFT derived reaction barriers.[55,62,102,103] Asynchronicity is derived not from the sum of $\Delta G°_{PT}$ and $\Delta G°_{ET}$, but rather their difference:

Equation 2.2 $$\eta = \frac{\sqrt{2}}{2}(\Delta G^{\circ}_{PT} - \Delta G^{\circ}_{ET})$$

These previous studies found lower reaction barriers for larger magnitudes of this asynchronicithyh parameter ($|\eta|$). Conversely, we do not observe an effect on $|\eta|$. Moreover, in our model the positive sign for both $\Delta G°_{PT}$ and $\Delta G°_{ET}$ indicates that the sum of $\Delta G°_{PT}$ and $\Delta G°_{ET}$ has a more significant effect than η. This distinction is noteworthy, because there is a strong negative correlation between $\Delta G°_{PT}$ and $\Delta G°_{ET}$ such that our data set sees a much larger variation in η than it does with ($\Delta G°_{PT} + \Delta G°_{ET}$) (Figure 2.2B). Thus, the trend with ($\Delta G°_{PT} + \Delta G°_{ET}$), while significant, may have less overall impact on reaction rates than any trend with $|\eta|$ would have.

The reason for this discrepancy between our results and earlier DFT studies is unclear, but possibly related to a more general inability to resolve second-order effects in our dataset. As η changes sign if the reaction order is reversed, a direct role for η is, in general, disallowed by microscopic reversibility. However, a second order effect from η^2, or similarly $|\eta|$, is allowed. Thus, the absence of an effect from $|\eta|$ is no more meaningful than is an absence from the effect of $\Delta G°_{CPET}{}^2$ (Regression A1.7). These more subtle second order effects could be obscured by experimental noise or by unexplained variation between the diverse transition metal-oxo complexes in our data. Furthermore, the well-controlled nature of the series of complexes previously investigated for asynchronicity may have too little variation in ($\Delta G°_{PT}$ + $\Delta G°_{ET}$) to observe an effect similar to what we observe.

4. Evaluation of Individual Cases with our Thermodynamic Model

The $\{\Delta G°_{CPET},\Delta G°_{PT},\Delta G°_{ET}\}$ model is depicted graphically in Figure 2.3. This graph depicts the predicted barrier height (from Equation 2.1) on the *y*-axis against the experimentally determined barrier height on the *x*-axis, with the grey line giving where predicted equals experimental. The tight clustering around this grey line indicates that the training data and the test data are well predicted. Nonetheless, several metal oxo complexes are clearly outliers (given unique symbols in Figure 2.3) and deserve further discussion.

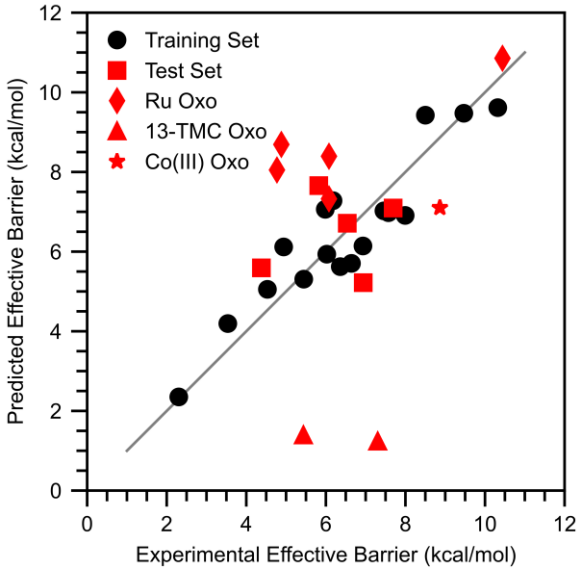

Figure 2.3. Regression analysis of the experimental reaction barrier vs. $\Delta G°_{CPET}$, $\Delta G°_{PT}$, and $\Delta G°_{ET}$ for various transition metal-oxo complexes reacting with DHA. Specific outlier cases discussed in the main text are given unique symbols. The grey line marks where predicted equals experimental. Predicted values are computed using Equation 2.1.

The $\{\Delta G°_{CPET},\Delta G°_{PT},\Delta G°_{ET}\}$ model behaves the most poorly in predicting reaction barriers for the iron(IV)-oxo and cobalt(IV)-oxo complexes supported by the ligand 13-TMC.[130,139] Essentially no barrier is predicted for these reactions, which is not observed experimentally. This is due to a large negative calculated $\Delta G°_{CPET}$ in both cases; in fact, these complexes are outliers even in the $\Delta G°_{CPET}$ only fit (Regression A1.1). In our original published report of this study, we suggested that this discrepancy could arise from ambiguity in the primary coordination sphere of these complexes. No structural characterization is reported for the iron(IV)-oxo complex, and while a short Co–O bond is identified by EXAFS for the cobalt(IV)-oxo complex, it is difficult to conclusively determine the primary coordination sphere and protonation state by EXAFS. Shortly after we made this prediction, the Nam group published a revised structure of the 13-TMC supported cobalt(IV)-oxo complex.[140] Thus, our prediction was correct, and the thermodynamic

parameters were calculated for the incorrect structures, which explains the poor prediction for these complexes.

Another class of outliers are ruthenium-oxo complexes. The reaction barrier is overestimated for all ruthenium-oxo complexes, and for three of them by more than two kcal/mol. As ruthenium is the only second row transition metal in our data set, we suspect this overestimation is due to a consistent difference between first and second row transition metals rather than ruthenium-oxo complexes not following the same general trends. For instance, it is possible that the ruthenium-oxo complexes have relatively low structural reorganization energy or that relativistic effects influence the coefficients. It may also simply be a change in the systemic DFT error upon going to the second row. Regardless, regression of barriers from the kinetics of an individual ruthenium-oxo complex reacting with several different substrates reveals there is a trend with $\Delta G°_{CPET}$, $\Delta G°_{PT}$, and $\Delta G°_{ET}$ with similar coefficients to those obtained from the more general model with multiple different oxo complexes (Table A1.24). The coefficients of $\Delta G°_{PT}$ and $\Delta G°_{ET}$ are similar to those of Equation 2.1. This supports that the same trends in free energies are at play in the ruthenium-oxo complexes.

The $\{\Delta G°_{CPET},\Delta G°_{PT},\Delta G°_{ET}\}$ model also moderately underestimates the reaction barrier for a terminal cobalt(III)-oxo complex which has unusual trends in its reactivity with various substrates.[50] Unlike most metal oxo complexes, the reactivity of this complex does not have a clear trend with $\Delta G°_{CPET}$; its kinetics are instead dominated by $\Delta G°_{PT}$. Therefore, this complex may be expected to display slightly different trends than transition metal-oxo complexes in a multivariable fit as well. We regressed the experimental reaction barriers for the reactivity of this complex with several substrates against only $\Delta G°_{PT}$ as well as against $\{\Delta G°_{PT},\Delta G°_{CPET}\}$ (Figure 2.4). We find

that the inclusion of $\Delta G°_{CPET}$ significantly improves the model, increasing R^2 from 0.94 to 0.97 and LOO R^2 from 0.93 to 0.94 and having an *F*-test *p*-value of 0.02 (Table A1.26). However, the relative weighting of the contribution from $\Delta G°_{CPET}$ is quite different than for the broader set of complexes. In the broader set we observe that $\Delta G°_{CPET}$ has a larger effect on the reaction barriers than either $\Delta G°_{CPET}$ or $\Delta G°_{CPET}$, which is reflected in the larger coefficient for the $\Delta G°_{CPET}$ term than for the $\Delta G°_{PT}$ and $\Delta G°_{ET}$ terms in the fit equation (Equation 2.1). In contrast, $\Delta G°_{PT}$ has a greater effect than $\Delta G°_{CPET}$ on the reaction barriers for the cobalt(III)-oxo complex, again reflected in the magnitude of their coefficients:

Equation 2.3 $$\Delta G^{\ddagger}_{CPET} = 0.22\ \Delta G^{\circ}_{PT} + 0.12\Delta G^{\circ}_{CPET} - 2.1$$

Furthermore, the inclusion of $\Delta G°_{ET}$ significantly improves the model for the broader set of metal oxo complexes, but its significance is unclear for the series of substrates reacting with the cobalt(III)-oxo complex (R^2 increases to 0.95, *p*-value = 0.07, Regression A1.48). Overall, this cobalt(III)-oxo complex is not so dissimilar from the broader set of metal oxo complexes in that the same thermodynamic free energies explain the reactivity of both. However, this individual case demonstrates a different weighting of parameters than that observed in the broad set.

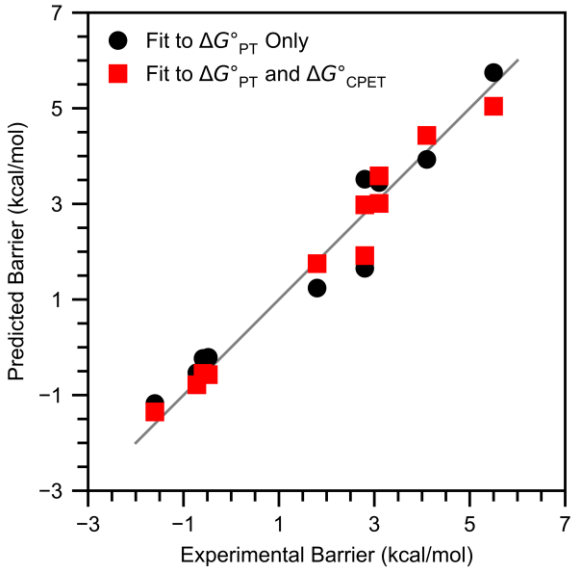

Figure 2.4 Regression analysis for a cobalt(III)-oxo complex against only $\Delta G°_{PT}$ and against both $\Delta G°_{PT}$ and $\Delta G°_{CPET}$. The negative barriers are due to overestimation of the entropy of association. The gray line marks where the predicted barrier matches the experimentally determined barrier.

The all-thermodynamic model we present here provides insights and possible alternative explanations for previously reported trends in CPET reactivity. In one study,[44] steric and spin state effects were invoked to explain the comparatively high reactivity of the $S = 2$ complex $[Fe^{IV}(O)(TMG_2dien)(CH_3CN)]^{2+}$. A higher rate of C–H activation as compared to $S = 2$ $[Fe^{IV}(O)(TMG_3tren)]^{2+}$ was ascribed to reduced steric hinderance in the TMG_2dien complex,[17] and the higher rate of C–H activation as compared to the $S = 1$ complexes $[Fe^{IV}(O)(N4Py)]^{2+}$ and $[Fe^{IV}(O)(TMC)(CH_3CN)]^{2+}$ was ascribed to the $S = 2$ spin state in the TMG_2dien complex.[118,125] However, it was noted that the even faster reactivity of $[Fe^{IV}(O)(Me_3NTB,CH_3CN)]^{2+}$, which is $S = 1$ and has a similar %BV profile to $[Fe^{IV}(O)(TMG_2dien)(CH_3CN)]^{2+}$,[116] is not easily explained by either hypothesis. Our analysis suggests that the thermodynamic properties of these complexes may provide an alternative explanation in these comparisons (Table A1.12). The Me_3NTB complex has by far the most exergonic reaction with DHA ($\Delta G°_{CPET} = -16$ kcal/mol), followed by the

TMG_2dien complex ($\Delta G°_{CPET}$ = −9 kcal/mol), followed by the complexes of TMG_3tren, TMC, and N4Py ($\Delta G°_{CPET}$ = −7, −6, and −6 kcal/mol, respectively). Thus, thermodynamic parameters would predict the Me_3NTB complex to have the lowest reaction barrier and fastest rate of reaction, with the TMG_2dien complex being the next most reactive, and the remaining complexes the least reactive as is observed experimentally.

In another study, it was observed that the rates of CPET reactions performed by $[Fe^{IV}(O)(TMC)(X)]^{n+}$ decrease with more strongly donating axial X-ligands.[118] This report ruled out variation in $\Delta G°_{CPET}$ as the cause of this trend, as it was calculated to be similar for all complexes investigated. It was suggested that changes in the accessibility of a high-spin state may explain this variation in the rates, as the relative energy of the quintet excited state decreased with stronger axial X-ligands. However, our calculations indicate that while stronger axial donors increase $\Delta G°_{ET}$, $\Delta G°_{PT}$ decreases more substantially (Table A1.12). In our model, these changes result in a net decrease in the reaction barrier, suggesting that despite a similar $\Delta G°_{CPET}$, the reactivity trend could be explained by thermodynamic effects. These analyses do not rule out that spin state or steric effects may be important in the previous studies, but they suggest that thermodynamics may also play an important role.

5. Evaluation with Multiple Substrates

Thus far, our analysis has been primarily limited to explaining how variations in the transition metal-oxo complex affect reaction rates, with variations in substrate only evaluated in select cases. To broaden the scope of this analysis, we extended our data set to include reactivity with 1,4-cyclohexadiene (CHD), fluorene, and xanthene in addition to DHA. We refit the model with reported data for the reactions between each substrate and all metal oxo complexes (excluding

the previously discussed ruthenium-oxo and 13-TMC-metal-oxo complexes). As with our regressions for DHA alone, the inclusion of $\Delta G°_{PT}$ and $\Delta G°_{ET}$ notably improves the fit (Table 2.1, Figure 2.5). Other parameters offer comparably little improvement to the fit and do not perform well by LOO cross validation. The equation for this model is given by Equation 2.4, which is satisfyingly similar to the equation of the fit to DHA data alone:

Equation 2.4 $$\Delta G^{\ddagger}_{CPET} = 0.23\,\Delta G^{\circ}_{CPET} + 0.04\Delta G^{\circ}_{PT} + 0.10\,\Delta G^{\circ}_{ET} - 2.10$$

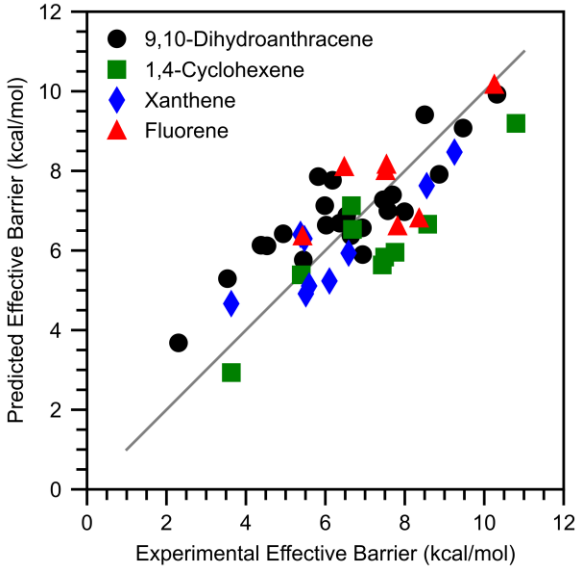

Figure 2.5 Regression analysis of the experimental reaction barrier to CPET reactivity between various C–H bonds and transition metal-oxo complexes vs. $\Delta G°_{CPET}$, $\Delta G°_{PT}$, and $\Delta G°_{ET}$. Available data was used for all non-outlier transition metal-oxo complexes reacting with DHA, CHD, xanthene, and fluorene. The gray line marks where predicted equals experimental. Predicted values are computed using Equation 2.4.

6. Implications of the {$\Delta G°_{PT}$,$\Delta G°_{PT}$,$\Delta G°_{CPET}$} Model

The independence of ($\Delta G°_{PT}$ + $\Delta G°_{ET}$) from $\Delta G°_{CPET}$ can be understood by splitting $\Delta G°_{CPET}$ into either of the two thermodynamic cycles shown in Figure 2.6: ($\Delta G°_{PT}$ + $\Delta G°_{ET}$') and ($\Delta G°_{ET}$ and $\Delta G°_{PT}$'). Because these must both sum to $\Delta G°_{CPET}$, the energetic difference between

both sides of the square scheme must be the same – that is, $\Delta G°_{PT}$ and $\Delta G°_{PT}$' differ the same amount as $\Delta G°_{ET}$ and $\Delta G°_{ET}$' differ. Let us denote this difference as the free energy of charge coupling $\Delta G°_{CC}$, i.e. the energetic benefit obtained by coupling the electron transfer and proton transfer. This allows us to break the overall free energy of reaction down into three terms:

Equation 2.5 $$\Delta G^{\circ}_{CPET} = \Delta G^{\circ}_{PT} + \Delta G^{\circ}_{ET} + \Delta G^{\circ}_{CC}$$

This breakdown illustrates that the distinction between $\Delta G°_{CPET}$ and ($\Delta G°_{PT}$ + $\Delta G°_{ET}$) is this electron-proton coupling energy $\Delta G°_{CC}$. Intriguingly, this coupling energy is identical for the forward and backwards reaction: substitution of $-\Delta G°_{CPET}$ for $\Delta G°_{CPET}$, substitution of $-(\Delta G°_{ET/PT}$ + $\Delta G°_{CC})$ for $\Delta G°_{PT/ET}$, and application of Equation 2.5 reveals that upon reversal of the direction of the reaction, ($\Delta G°_{CPET}$ − $\Delta G°_{ET}$ − $\Delta G°_{PT}$) does not change. Thus, $\Delta G°_{CC}$ represents a thermodynamic parameter which is independent of the reaction's driving force.

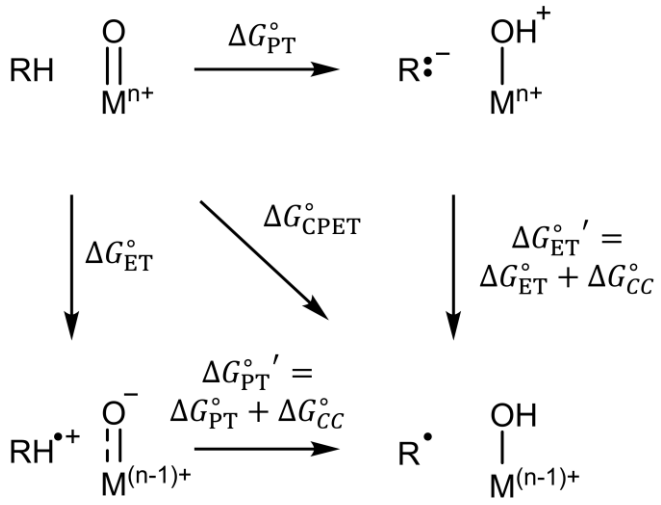

Figure 2.6 A generic square scheme for transition metal-oxo C–H activation.

This microscopic reversibility of $\Delta G°_{CC}$ motivates reformulation Equation 2.1 in terms of $\Delta G°_{CPET}$, $\Delta G°_{CC}$, and η. Substitution of Equation 2.2 and Equation 2.5 into Equation 2.1 gives:

Equation 2.6 $$\Delta G^{\ddagger}_{CPET} = 0.41\ \Delta G^{\circ}_{CPET} - 0.10\ \Delta G^{\circ}_{CC} + 0.04\ \eta - 0.26$$

This coefficient of $\Delta G°_{CPET}$ is now slightly larger and nearly identical to the value in the $\Delta G°_{CPET}$-only model (Regression A1.1). The negative sign of $\Delta G°_{CC}$ means that there is a kinetic penalty for reactions with more thermodynamic coupling between electron transfer and proton transfer. That is, faster reactivity is expected for reactions whose driving force is less reliant on the proton and electron transfers being concerted.

The unequal coefficients of $\Delta G°_{PT}$ and $\Delta G°_{ET}$, in Equation 2.1, which leads to the inclusion of η in Equation 2.6, implies that a different barrier is expected for the forwards and backwards direction because η changes sign when the reaction changes direction. On the surface, this violates microscopic reversibility and invalidates our model. However, two important points resolve this dilemma. First, we are primarily interested in the exchange of a C–H for an O–H bond reactivity, and there is no reason why the same model needs to apply to the reverse sort of exchange. Separately, the empirical nature of Equation 2.1 means that any systemic differences between oxidizing transition metal-oxo complexes and basic transition metal-oxo complexes could be compensated for by a dependence on η. Upon examination of our data set, such a systemic difference does stand out: basic transition metal-oxo complexes are more likely to have been studied in hydrogen-bond donating solvents. Hydrogen-bonding solvents are known to decrease rates of hydrogen-atom transfer reactions, as a hydrogen-bond to the solvent must be broken prior to forming the encounter complex with the substrate.[104,141] Thus, the effect of a low $G°_{PT}$ may partially masked by solvent hydrogen-bonding, leading to $\Delta G°_{PT}$ having a smaller apparent effect

than does $\Delta G°_{ET}$. Indeed, approximately correcting for hydrogen-bonding interactions leads to equal coefficients of $\Delta G°_{PT}$ and $\Delta G°_{ET}$ and an insignificant contribution from η (Regression A1.18 and Regression A1.23).

The use of $\Delta G°_{CC}$ and η to express the effect of stepwise thermodynamic elements is useful because it demonstrates how, even if a reaction is strongly dominated by a stepwise thermodynamic element, such as the reactions between C–H bonds and the cobalt(III)-oxo complex discussed above are, then this can still be understood as an effect on top of the effect of $\Delta G°_{CPET}$; it does not need to be interpreted as an instance where $\Delta G°_{CPET}$ is empirically less important. This view also interprets the reaction as having a strong kinetic dependence on η. This kinetic dependence on η has a textbook interpretation as giving the position of the transition state in the direction perpendicular to the reaction coordinate, i.e. the coefficient of η measures the transition state's similarity to one stepwise intermediate or another. By contrast, it is not immediately clear what meaning $\Delta G°_{CC}$ has in a textbook, physical organic context.

Our conclusion that stepwise thermodynamic parameters influence a reaction *via* a change in $\Delta G°_{CC}$ is a unique interpretation for the influence of stepwise thermodynamic parameters in CPET reactivity. Most studies which can systemically vary $\Delta G°_{PT}$ and $\Delta G°_{ET}$ do so by using a separate base and a separate oxidant.[57,67,69,95] This results in a fixed value of $\Delta G°_{CC}$, as the strength of the base does not depend on if the oxidant has been reduced or not, and *vice versa*. Thus, changes in $\Delta G°_{PT}$ or $\Delta G°_{ET}$ must affect $\Delta G°_{CPET}$ as they cannot be "absorbed" by $\Delta G°_{CC}$ (Equation 2.5). Classical studies in physical organic chemistry often had the same limitation. For example, many textbook concepts were drawn from studies on how the rate of general acid catalysis varied with the nucleophile's nucleophilicity and the acid catalyst's acidity.[73,74] These variations will not affect

these reactions' coupling energy, as they will not change how substrate electrophilicity changes upon protonation. That energetic interaction between different reaction steps can only be varied by varying the substrate.

Indeed, physical organic studies which varied all three reaction components often found that the LFERs were inconsistent or imbalanced. Acid-catalyzed alcohol eliminations from organic substrates are notable examples.[91–94] These studies found that the effects of varying either the strength of the acid catalyst or the relative stability of the product did not match the effect of varying the basicity of the alkoxide leaving group. Explanations for this included electrostatic effects, the tightening or loosening of the transition state, or incomplete formation of resonance effects. That is, imbalances in LFERs were explained as being due to the transition state having a more complicated structure than could be modelled by two LFERs. However, these explanations were not linked to ground state thermodynamics. Our results suggest this link could be the energetic coupling between C^+–O^- bond cleavage and O^-–H^+ bond formation. Changes in acid strength or product stability will not affect the stability of a protonated product or free alkoxide separately from the overall energy of alcohol elimination, but a change in the alkoxide leaving group can.

7. Conclusions

Overall, this thorough analysis of the reported C–H activation reactivity of transition metal oxo complexes demonstrates that $\Delta G°_{CPET}$, $\Delta G°_{PT}$, and $\Delta G°_{ET}$ all have a statistically significant correlation with the reaction barrier. Interestingly, no other parameters examined here, including steric environment and spin-based parameters, provide a significant improvement to a $\Delta G°_{CPET}$ only model. This is in contrast to previous literature reports which implicate such factors in

explaining metal oxo mediated C–H activation. The $\{\Delta G°_{CPET},\Delta G°_{PT},\Delta G°_{ET}\}$ model predicts all but five of the reaction barrier heights for reactivity with DHA within 2 kcal/mol, and predicts most of these barrier heights within 1 kcal/mol. We find that the same model can explain the reactivity of a cobalt(III)-oxo complex whose CPET reactivity anonymously trends with C–H bond $p\mathrm{K_a}$ instead of with C–H bond BDFE, although re-fitting the model to this cobalt(III)-oxo complex specifically reveals a higher weighting of $\Delta G°_{PT}$ and negligible contribution of $\Delta G°_{ET}$.

While the relative importance of these thermodynamic parameters can vary between specific cases, this study on a broad set of metal oxo complexes suggests that thermodynamic parameters provide the most general contribution to reaction barriers. Furthermore, while a strong dependence on $\Delta G°_{CPET}$ is observed, as is expected based on literature precedent, significant and independent contributions from $\Delta G°_{PT}$ and $\Delta G°_{ET}$ are observed. The independent contribution of stepwise thermodynamics, as opposed to them being contributors to the overall reaction energy, can be reformulated as being a penalty for electronic coupling between electron-transfer and proton-transfer driving forces, expressed by the intrinsic free energy $\Delta G°_{CC}$. This coupling energy has been underappreciated in previous application of LFERs, both in studies of CPET but also in the classical canon of physical organic chemistry. Our identification that $\Delta G°_{CC}$ is the key thermodynamic contributor to a reaction's intrinsic barrier is perhaps the most broadly relevant contribution in this whole dissertation.

Ultimately, these conclusions add to the growing body of literature supporting the importance of stepwise thermodynamic parameters in CPET reactivity. However, the structural and electronic bases for these effects was not fully established at the time of this research. Modern theoretical treatments of CPET reactions treats electron-proton transfer as nonadiabatic and

suggest that proton tunnelling is too extensive for semiclassical models of reactivity. Thus it is not clear if the textbook structure-reactivity based interpretation of LFERs with stepwise thermodynamics is appropriate for C–H activation reactions, even in the case of the cobalt(III)-oxo complex which whose LFERs display clear signs of a proton-transfer like transition state. Experimentally evaluating the importance of proton tunneling, and thereby the suitability of a semiclassical transition state, in explaining the reactivity of this cobalt-oxo complex will be the focus of Chapter 3. Theoretical reconciliation between traditional interpretations of LFERs and nonadiabatic reactivity models will be the focus of Chapter 4.

8. Methods

Tabulation of Experimental Kinetics

In this study we used thirty reported k_2 values of metal oxo species reacting with DHA.[17,44,49,50,52,116–132] We excluded a few metal oxo species from our analysis despite having reported kinetic data for reactivity with DHA. The reasons for these exclusions were varied: several did not have a well-defined primary coordination sphere,[31,142–144] we were unable to calculate the reduced form of Mn^{III} oxo complexes without deprotonation of the hydrogen-bonding ligands,[52,54] one vanadium(V)-oxo has too much experimental uncertainty in its k_2 value,[145] corrolazine complexes were too large to calculate their vibrational frequencies using our methods,[100,146] vibrational frequencies did not converge for the reduced form of two ruthenium(VI)-dioxo complexes,[131] we did not include third row complexes or complexes with ligand radicals,[119,147–149] and in one case saturation was reported at higher concentrations of DHA.[150] We also found several reports of metal oxo mediated C–H activation of substrates besides DHA,[40,45,48,121,139,151–162] and this literature search was aided by useful reviews.[11,163]

All rate constants utilized here were reported as k_2 values with the exception of several rate constants used in the cobalt(III)-oxo reactivity analysis.[50] In this case, for substrates which did not have a reported k_2, the pseudo-first order rate constant k_{obs} at 0.0125 M of substrate was divided by 0.0125 M to obtain an approximate k_2. We used all substrates with reported kinetic data in this analysis except for 1,1,3,3-tetraphenylpropene. This substrate reacts unusually slowly, which we believe to be due to large steric hindrance of the reacting C–H bond. The remaining substrates were sterically similar enough that there is no steric effect on their kinetics (Regression A1.46).

Determination of Experimental Barrier Heights

Before determining barrier heights from experimental k_2 values, we first multiplied each k_2 by any reported stochiometric and statistical adjustments so as to start from consistently unadjusted k_2 rate constants (experimental k_2 rate constants are often reported with statistical corrections to facilitate comparisons between substrates, either for the stoichiometry of the substrate's reactivity or for the number of benzylic C–H bonds). We assume that where no adjustment is noted in a paper, none has been made. The barriers of CPET reactivity were then determined from the unadjusted experimental k_2 values by solving the Eyring equation[164] and subtracting approximate expressions for the free energy of metal oxo-substrate association:

Equation 2.7 $$\Delta G^{\ddagger}_{PCET} = RT \ln\left(\frac{k_2 h}{n_{CH} n_O RT}\right) - RT\left[\ln\left(\left(\frac{2\pi\,\mu\,RT}{h^2}\right)^{\frac{3}{2}}\frac{1}{C^\circ}\right) + \frac{5}{2}\right]$$

where h is Planck's constant, n_{CH} is 2 for DHA and CHD and 1 for fluorene and xanthene, n_O is the number of oxo ligands in the metal oxo complex, RT is the thermal energy, μ is the reduced mass of the metal oxo and the substrate, and C° is 1 M. Our n_{CH} adjusts for the typical stoichiometry of each substrate's oxidation (DHA and CHD tend to lose two H-atoms, fluorene

and xanthene one H-atom). We do not adjust for the number of reactive H-atoms, as ring puckering of the substrates means that not all reactive C–H bonds are equivalent. For instance, DHA has four benzylic C–H bonds, with two lying equatorial to the central ring and two lying axial. It is unlikely that the equatorial and axial positions are equally reactive, and it is entirely possible that reactivity predominantly occurs at only one of the positions. It is therefore not necessarily true that DHA is four times as reactive as an otherwise similar substrate with only one benzylic C–H bond.

The second and third terms in Equation 2.7 are an approximation for the free energy of association of the metal oxo and the substrate.[164] This adjustment allows us to compare kinetic data collected at different temperatures. As C–H bonds are poor hydrogen-bond donors, we assume that the cost of association is purely entropic (or at least that enthalpic components vary minimally between different metal oxo complexes and substrates) and further assume this entropy cost is solely the loss of translational entropy. This neglects the loss of rotational entropy and the gain of low frequency metal oxo-substrate vibrational modes, but these effects will partially cancel. Regression with $\Delta G°_{CPET}$ and RT does not fit DHA reaction barrier heights significantly better than a fit to $\Delta G°_{CPET}$ alone (Regression A1.12), indicating that this adjustment satisfactorily accounts for the temperature dependence of the reaction barrier.

Calculation of Parameters

For each of these oxo complexes we calculated the values of parameters that have been proposed to influence metal oxo mediated CPET reactivity. Specifically, the parameters investigated were %BV steric metrics, spin density on the oxygen atom, available spin states, thermodynamic free energies $\Delta G°_{CPET}$, $\Delta G°_{PT}$, and $\Delta G°_{ET}$, and the magnitude of the asynchronicity parameter ($|\eta|$). Geometry optimization and frequency calculations were performed in ORCA using

the def2 basis sets of Weigend and Ahlrichs and the O3LYP functional.[165–170] For the wider set of metal oxo complexes, all transition metals were given the def2-TZVPP basis set, all metal-bonded atoms and the transferring hydrogen atom the def2-TZVP basis set, and the remaining atoms the def2-SV(P) basis set. Substrates were calculated entirely with the def2-TZVP basis set. For calculations regarding the cobalt(III)-oxo and various substrates, Co, N, O, the carbene carbons of the ligand, and the carbon undergoing C–H activation was given def2-TZVPP; all other atoms were given def2-SVP. For both sets of calculations solvent effects were included as a polarizable continuum (CPCM with the dielectric constant of acetonitrile for the broader set of metal oxo complexes; COSMO with the dielectric constant of THF for the cobalt(III)-oxo with substrates). This is primarily to mitigate the effect of self-interaction error;[171] we assume that the solvent dielectric has little effect on the rate of CPET, as reported solvent effects on similar reactions are typically limited to hydrogen bonding.[104,141,172] The def2 ECP was used for ruthenium.[173] The resolution of identity approximation was used for coulomb integrals and the chain of spheres approximation for exchange integrals (with def2/J as the auxiliary basis). No change was made to ORCA's default grid settings. Free energies were derived from the electronic energies and vibrational calculations using the quasi-harmonic oscillator formulation of Grimme and coworkers.[174]

Unfortunately, several of our optimized structures have small imaginary frequencies. Occasionally these frequencies lie below −100 cm^{-1} but in each of these cases the mode is isolated to a soft dihedral motion, e.g. methyl rotation on an acetonitrile ligand. We used the absolute value of these frequencies when calculating the thermodynamic enthalpy and entropy values, believing

that to be a better approximation for these modes than either nonexistence or a frequency of 0 cm^{-1}. We were unable to reoptimize these structures to remove the imaginary frequencies.

In many cases, the correct ground state multiplicity of a species was not immediately clear. In such cases we confirmed our initial assignment by running ten geometry optimization cycles on alternate spin states and confirming these alternate assignments were several kcal/mol uphill of the assigned spin state. In a few cases where the energy was within 5 kcal/mol and the optimization was not close to convergence, we fully optimized the alternate spin state. Whenever two spin states had nearly the same energy, we chose the higher spin state as the ground state due to the typically higher entropy of high spin states.

To quantify the steric environment around each metal oxo center or substrate reactive C–H bond, we calculated percent buried volume (%BV) steric metrics using the online SambVCA web application.[133] We centered the calculation on the oxygen atom (for oxo complexes) or the transferring hydrogen (for substrates), defined the negative *z*-axis as going through the metal center (for oxos) or the reacting carbon center (for substrates), and defined the *xz*-plane as containing another atom bonded to the metal or carbon. We had the center oxygen or hydrogen atom deleted from the calculation, included hydrogen atoms in the calculation, and left all other settings to their default value (using Bondi radii scaled by 1.17, a sphere radius of 3.5 Angstroms, and a mesh setting of 0.10 Angstroms). The application returns a total percent buried volume, as well as that for individual quadrants of the sphere. For metal oxo complexes, we used the total percent buried volume (%BV Tot) and the standard deviation of these four quadrants (%BV Dev) in our regressions in order to capture both overall steric bulk and how evenly distributed this bulk is

around the metal oxo moiety. For substrates, we solely used %BV Tot. See Appendix 1 for a further discussion of steric parameters and their effect on reaction barrier heights.

To evaluate the effect of spin and spin state on reactivity, we used two parameters that have been discussed in the literature: spin density on the oxo ligand and the energy to excite to a higher spin state.[42,46] Atomic spin populations were determined via IBO analysis using the freely available IBOView software.[134,135] We recorded the spin density on the metal and on oxygen for each metal oxo complex as well as how much spin both atoms gain upon CPET reduction; we also tabulated similar values for the IBO charges. In the regression analysis we solely used the spin density on the oxo ligand. The "Spin Excitation Energy" is the vertical energy from the ground spin state of the initial oxo complex to the lowest lying excited spin state that is within one spin multiplicity of the resulting metal hydroxide ground spin state. If the ground spin state is already one spin multiplicity greater or lower than the product hydroxide spin state, then the spin excitation energy is taken to be zero. For instance, in the case of a triplet cobalt(IV)-oxo reacting to give a sextet iron(III)-hydroxide the spin excitation energy is the energy of the quintet iron(IV)-oxo relative to the triplet iron(IV)-oxo at the ground state optimized geometry. This is the scenario for most iron(IV)-oxos in the data set. But in the case of the two non-heme iron(IV)-quintet oxos,[17,44] the spin excitation energy is zero because the ground spin state is already within one spin multiplicity of the sextet hydroxide product. Essentially, the spin excitation energy is the energy needed to reach a spin surface on which reduction to the metal hydroxide's ground spin state is spin allowed. While this simple metric ignores the nuances of two state reactivity theory (such as the spin inversion probability) it is relatively simple to compute and has precedent as a quantitative measure of CPET reactivity.[42,118]

For each metal oxo-substrate combination assessed here, we tabulated the free energies of proton coupled electron transfer ($\Delta G°_{CPET}$, Equation 2), proton transfer ($\Delta G°_{PT}$, Equation 3), electron transfer (ΔG_{ET}, Equation 4), and the asynchronicity as defined by Srnec and coworkers (η, Equation 5):[55]

Equation 2.8 $$\Delta G_{PCET} = G_{M-OH} + G_{C\cdot} - G_{M=O} - G_{C-H}$$

Equation 2.9 $$\Delta G_{PT} = G_{M-OH^+} + G_{C:^-} - G_{M=O} - G_{C-H}$$

Equation 2.10 $$\Delta G_{ET} = G_{M-O^-} + G_{C-H^+} - G_{M=O} - G_{C-H}$$

Equation 2.11 $$\eta = {G_{M-OH^+} + G_{C:^-} - G_{M-O^-} - G_{C-H^+}}\Big/{\sqrt{2}}$$

where $G_{M=O}$ is the calculated free energy of the oxo species, G_{C-H} is the calculated free energy of the substrate, and all other free energies are defined analogously. We also tabulated the analogous electronic energies (same notation, with *G* replaced with *E*).

Statistical Analysis

All statistical analysis was performed in Python using the Numpy, Scipy, Pandas, Sklearn, and Matplotlib packages.[175–179] A script ran a prescribed set of regression models and reported statistics on each model. All regressions were performed with ordinary least squares. Prior to fitting any regression, we separated the data into a test set and a training set of metal oxo species. While we show both test and training sets for each regression in the Regressions of Appendix 1, we initially did not plot the test set or calculate statistics with it. We solely used the training set in the earlier stages of our analysis, where we determined which parameters improved a fit to $\Delta G°_{CPET}$ only and which did not. We then examined if the good fits to the training set extrapolated well to the test set. We had to make a few changes to the initial division of the training and test sets,

however. Initially, the cobalt(IV)-oxo was included in the training set,[130] but that was interfering with the fit to $\Delta G°_{CPET}$. We moved it to the test set, and to provide insight into this poor fit we calculated the iron(IV)-oxo complex of 13-TMC and added it to the test set.[139] We also saw, visually, that the inclusion of a ruthenium(IV)-oxo in the training set was interfering with the addition of other parameters and moved all ruthenium-oxo complexes to the test set.[120,124,126,131,132]

The simplest metrics reported from these models are the mean square error (MSE) and the goodness of fit R^2.[112–115] These both give an indication of how well a model fits the available data but are prone to overfitting; more complicated models can only improve these metrics, regardless of whether or not the model is actually better.

We also evaluated each model with cross validation (CV) metrics, which can become worse upon overfitting. In K-fold cross validation, the training data is further subdivided into K subsets, and each subset is predicted by the $K-1$ remaining subsets.[113,115] When K is the number of data points, i.e. each data point being predicted by the rest of the data points, this is known as leave-one-out (LOO) cross validation. These predicted data points can be used to calculate the MSE and R^2 as above. The MSE from LOO cross validation is an approximately unbiased estimate of the expected error of a test set; however, it has high variability from training set to training set because each prediction uses nearly every point in a given training set. By repeatedly subdividing into larger groups and averaging the resultant K-fold MSEs, one obtains a pessimistic but less variable estimate of the expected test error. As we see similar trends for both LOO and 5-fold CV, we only report LOO R^2 in this chapter but show all metrics in Appendix 1.

Another way to determine the significance of the model is to use a statistical *F*-test.[112,114] This allows one to compare an unrestricted model with a more restricted one (fewer parameters used as regressors, or no parameters regressed, or restrictions placed on the relationship between coefficients, etc.). In the language of hypothesis testing, the null hypothesis is that the unrestricted model offers no improvement on the restricted model and the alternate hypothesis is that there is an improvement. When both models are fit to the data, the unrestricted model will have less total squared error than the restricted model. Assuming said error of each data point is normally distributed (or that there is enough data such that the error is approximately normally distributed), that the average error is zero, and that the model is properly formulated, it is possible to determine the probability that this reduction in total squared error is spurious. This probability is known as the *p*-value. The test relies on a well-defined number of degrees of freedom in both the restricted and unrestricted model to draw out what the statistical distribution of total squared error ought to be.

For regressions on multiple substrates at once, the unequal weighting of different metal oxo complexes (depending on how many substrates are reported for them) renders these statistical metrics unreliable.[115] We ameliorate this issue for LOO cross validation by leaving out all reaction barriers for a given metal oxo complex together rather than one at a time. That is, we leave one metal oxo complex out and predict its reaction barrier heights based on all other metal oxos' reaction barrier heights rather than leave one reaction barrier height out and predict this barrier based off all other barriers. We accordingly only report LOO CV metrics for this set of regressions.

Further details regarding the individual models examined and the nature of the parameters which went into them can be found in Appendix 1.

Chapter 3: Variable temperature kinetic isotope effects demonstrate extensive tunnelling in the C–H activation reactivity of a transition metal-oxo complex

Reproduced from Schneider, J. E.; Goetz, M. K.; Anderson, J. S.; *Chem. Commun.*, **2023**, *59*, 8584-8587 with permission from the Royal Society of Chemistry.

Adapted with permission from Schneider, J. E.; Anderson J. S.; *J. Phys. Chem. Lett.*, **2023**, *14*(43), 9548-9555. Copyright 2023 American Chemical Society.

1. Introduction

A wide array of chemical processes proceed through the concerted transfer of both a proton and an electron (concerted proton electron transfer, CPET).[180–184] This has motivated a large body of research into what factors control this reactivity.[23,35,37,44,55,66–68,118,125,185–189] Typically, reactions with a more favorable free energy of reaction (ΔG°_{CPET}) have a lower free energy of activation ($\Delta G^{\ddagger}_{CPET}$).[23,35–37,66,78,190] However, there has recently been evidence that this well-established reactivity trend is not omnipotent. As detailed in Chapter 1, there is strong evidence that the activation of C–H bonds *via* CPET to transition metal-oxo complexes is separately influenced by the thermodynamic energies of stepwise elements in a classical CPET square scheme, namely individual proton transfer and electron transfer energies (ΔG°_{PT} and ΔG°_{ET}, the energies to form distinct charge-separated intermediates along stepwise net CPET pathways, Figure 3.1). In some cases, trends with these stepwise thermodynamics dominate the trend with ΔG°_{CPET}, as if the reactions are following a mechanism intermediate that of a stepwise and concerted process (e.g. the curved arrow in Figure 3.1).[50,51,53–55,57–59,61,63,191] The influence of stepwise states is well

precedented in organic hydrogen atom transfer reactions,[70,71,192] but their relevance in the broader class of CPET reactions has implications for the mechanism and selectivity of many biological and synthetic systems.[193–198]

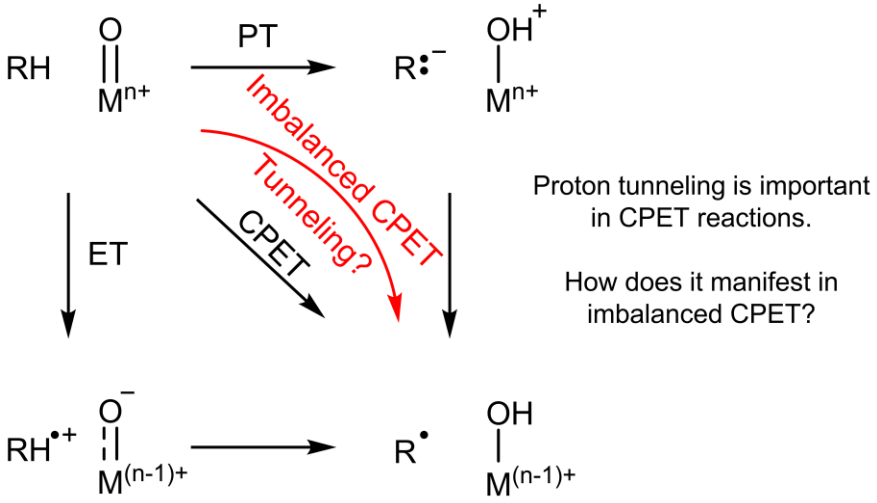

Figure 3.1 Square scheme depicting imbalanced CPET.

A central paradox that has recently emerged is how the semiclassical models used to explain the outsized influence of stepwise thermodynamic elements can be reconciled with CPET reactions which are widely acknowledged to be nonclassical or nonadiabatic.[67,95,96,199,200] The specific formulations for how ΔG°_{PT} and ΔG°_{ET} can affect CPET reactivity vary, but are commonly supported by DFT optimized transition states[53,55,57,59] and invoke textbook physical organic concepts such as nonperfect synchronization, imbalanced and asynchronous transition states, reaction disparity, and More O'Ferrall–Jencks diagrams.[73,74,86,201–204] These structure-reactivity models all assume semiclassical transition states. However, the light mass of protons means that quantum effects such as tunneling are often important, and even dominant, in CPET reactivity.[103,138,187,205–213]

While semiclassical transition states can be corrected for a moderate amount of tunneling,[138] extensive tunneling requires a dedicated quantum mechanical treatment which invokes nonadiabatic proton/electron transfer.[97,205,206,214,215] In these theories, the entire H-atom directly tunnels from a vibronic state localized on the reactant to a vibronic state localized on the product. The proton is treated with a quantum mechanical wavefunction that is never localized halfway across the reaction coordinate, as is assumed in semiclassical transition state theory. It is unclear if semiclassical structure-activity relationships are compatible with the significant quantum effects which can occur in proton transfer,[67,95,96,199] or if other phenomena are solely responsible for the observed imbalanced reactivity.[60,200,216] While this dilemma has been explicitly raised in the context of CPET reactions, it may apply to any imbalanced transition state or asynchronous reactivity with a proton transfer component.

To better understand the intersection of proton tunneling, nonadiabaticity, and asynchronous CPET reactivity, we used variable temperature kinetic isotope effect (VT-KIE) studies to evaluate the nature of proton tunneling in the reactivity of a terminal cobalt-oxo complex which displays basic-imbalanced reactivity with C–H bonds, as was examined in Chapter 1 (Figure 3.2).[50] We find significant tunneling with 9,10-dihydroanthracene (DHA) and even more so with fluorene. These observations demonstrate that proton tunneling must be treated as an inherent feature in, and not a correction to, physical models of imbalanced CPET reactivity. They further motivate theoretical studies aimed at reconciling quantum mechanical tunneling with more classical free energy relationships.

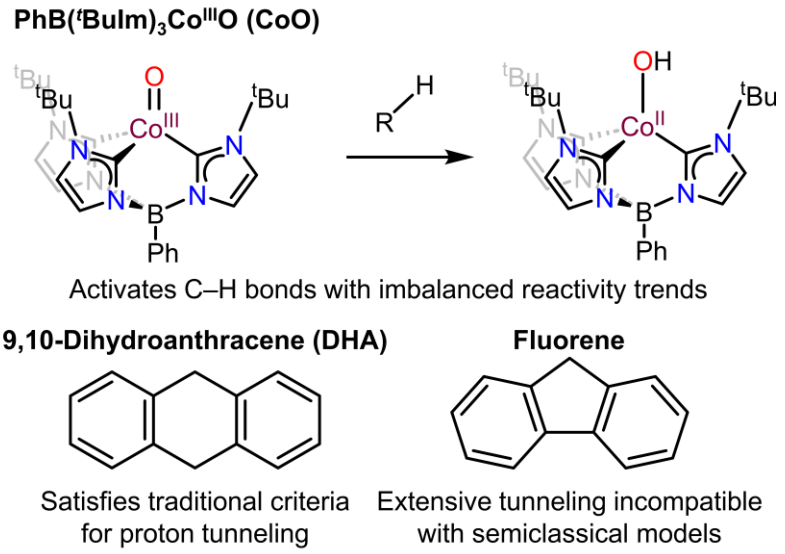

Figure 3.2 The compounds and reaction discussed in this chapter.

2. Interpretation of Variable Temperature Kinetic Isotope Effects

Variable temperature kinetic isotope effect (VT-KIE) experiments are the most rigorous way to experimentally evaluate proton tunneling, as they break the KIE down into effects on the activation energy (E_a) and the Arrhenius prefactor (A).[138,205,217] Analogous to rate constants, a plot of lnKIE against $1/RT$ is expected to be linear. The slope, $E_a(D) - E_a(H)$, gives the isotope effect on E_a. The intercept, $\ln(A_H/A_D)$, gives the isotope effect on A. These values can be compared with theoretical predictions to understand the nature of proton tunneling. In particular, semiclassical theory places reliable limits on the values of $E_a(D) - E_a(H)$ and $\ln(A_H/A_D)$ without tunneling (Figure 3.3). While nonadiabatic theory is less restrictive in the parameters it can predict, VT-KIE data can still be inform on the nature of tunneling in a nonadiabatic context. For instance, VT-KIEs have revealed that tunneling is highly optimized in enzymes.[205,217] However, there have been comparably few studies on the temperature dependence of kinetic isotope effects

in molecular systems, particularly with transition metal-oxo complexes. Furthermore, molecular studies typically restrict the interpretation of KIEs to a semiclassical context.

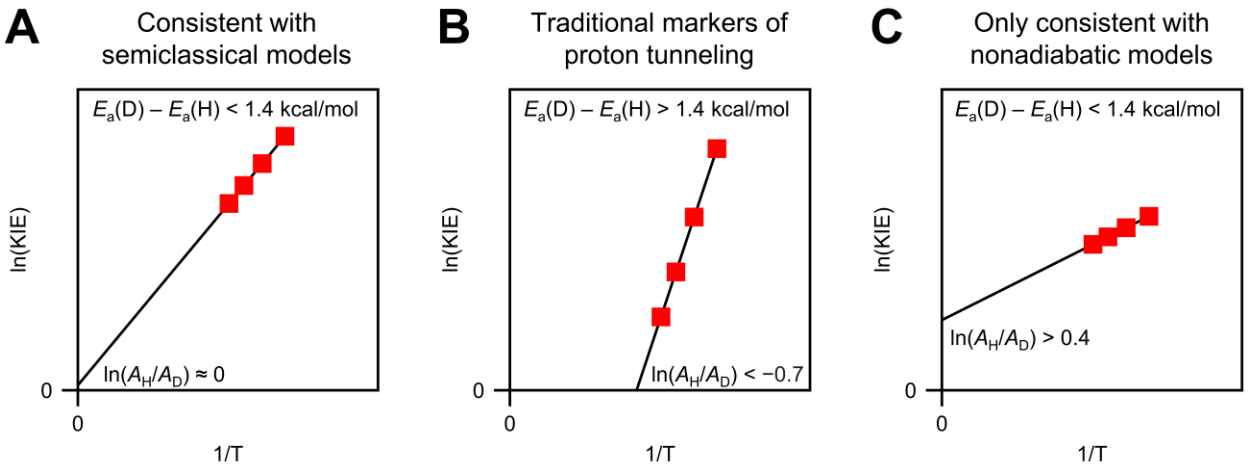

Figure 3.3 Generic plots of ln(KIE) vs. 1/*RT* for systems displaying (A) trends consistent with semiclassical theory, (B) trends which require a proton-tunneling correction, and (C) trends which can only be explained using a nonadiabatic reactivity model.

In semiclassical treatments KIEs are interpreted as the loss of zero-point energy in the transition state. This creates an isotope effect on E_a with minimal effect on A (Figure 3.3A). Based on the frequencies of typical C–H and C–D bonds, this loss of zero-point energy can explain a value of $E_a(D) - E_a(H)$ as high as ~1.4 kcal/mol, which corresponds to a KIE of ~10 at room temperature. Semiclassical rates can be corrected for proton tunneling through the barrier, which increases the magnitude of k_H and decrease its temperature dependence. However, realistic barriers are too wide to allow substantial deuterium tunneling. This results in tunneling-corrected semiclassical theory predicting larger KIEs, larger $E_a(H) - E_a(D)$, and an extrapolated intercept of $\ln(A_H/A_D)$ much less than 0. Therefore, the traditional markers of substantial tunneling effects assayed via variable temperature KIE measurements have been observation of a KIE greater than

10, of a slope $E_a(D) - E_a(H)$ greater than 1.4 kcal/mol, or of an intercept $\ln(A_H/A_D)$ less than −0.7 (Figure 3.3B).[138]

The above scenario considers significant tunneling effects, but still relies on a semiclassical framework. However, if the transferring proton is treated as a quantum mechanical particle positioned in discrete vibrational energy states, then both H and D can tunnel extensively during a reaction. Without complicating factors such as variations in tunneling distance, this leads to a largely temperature independent KIE, and thus a small isotope effect on the slope, $E_a(D) - E_a(H)$.[218] Instead, the isotope effect will primarily manifest as a positive intercept, $\ln(A_H/A_D)$. This results in the counter-intuitive scenario where more extensive tunneling manifests in a smaller slope, generally smaller KIEs, and the above-mentioned positive intercept (Figure 3.3C). A significantly positive intercept, above 0.4 as a conservative value, indicates this most extensive tunneling regime, even with traditionally small KIE values (<10). This limiting regime of extensive tunneling is a clear signal that semiclassical theory is an inappropriate model for the reaction under study, and it can only be observed through variable temperature KIE measurements.

3. Results and Discussion

We measured the temperature dependent KIEs of $PhB(^tBuIm)_3Co^{III}O$ (**CoO**) reacting with both fluorene and DHA (Figure 3.2, Figure 3.3, Table 3.1). We measured KIEs for fluorene oxidation by competition, analyzing the deuteration of the dimerized radical product (bifluorenyl) from reactions with d_1-fluorene (intramolecular KIEs) and with 50% d_0-fluorene/50% d_2-fluorene (intermolecular KIEs). This allowed us to determine both the primary and secondary KIEs for this reaction. In contrast, the KIEs for the reaction of **CoO** with DHA were too large for analysis via product composition; instead, we measured the KIEs by separately measuring k_H and k_D for d_0-

DHA and d_4-DHA, respectively. Data analysis accounted for the true isotopic composition of the starting substrates (see Methods). For completeness, we also performed kinetic measurements for reactivity of **CoO** with fluorene. Similar magnitudes were found for most of the KIE values; however, slight curvature in the variable temperature data arising from experimental artifacts made it difficult to confidently estimate the slope $\ln(A_H/A_D)$ (see Table A2.3 and accompanying discussion). Thus, we limit our discussion here to the values obtained from the competition experiments.

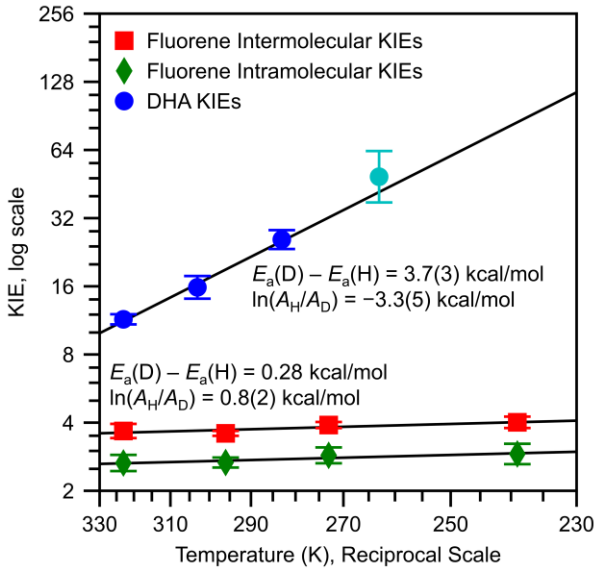

Figure 3.4 Plots of ln(KIE) vs 1/*RT* for the reactions of **CoO** with fluorene and DHA and the corresponding linear fits. The cyan colored data point at 263 K for DHA had k_D determined via initial rates. This data point is graphed to demonstrate consistency with the other data points, but not included in the linear fits to variable temperature. The activation parameters shown for fluorene are the primary KIE; the secondary isotope effect has $E_a(D) - E_a(H) = 0.01(6)$ and $\ln(A_H/A_D) = 0.1(1)$. For graphical purposes, the observed and predicted proton proportions (p_H) and deuterium proportions (p_D) from the competition data are displayed as KIE = p_H/p_D for intermolecular competition between 1:1 d_0-fluorene:d_2-fluorene and as KIE = p_D/p_H for intramolecular competition within d_1-fluorene.

KIEs for the oxidation of DHA are larger than 10 and have a temperature dependence significantly steeper than 1.4 kcal/mol (Figure 3.4). This importantly suggests significant tunneling

contributions in this reaction. It is consistent with either semiclassical theories with a tunneling correction, or with non-adiabatic rate theories with extensive tunneling. For instance, the reactivity of impaired enzymes often displays this behavior, and it is explained by invoking deuterium being more sensitive to tunneling distance.[217] In any case, the KIE data for DHA clearly indicates there is significant proton tunnelling in the C–H activation reactions of **CoO**.

For fluorene, we instead observe a shallow slope and a significantly positive intercept of 0.8(2) in the plot of ln(KIE) vs. 1/RT. This indicates extensive tunnelling in this reaction, with proton and deuterium tunnelling being similarly efficient (Figure 3.4). This observation supports that tunnelling is so extensive that semiclassical transition states are not sufficient – trying to reproduce this data by utilizing tunneling corrections to semiclassical transition state theory would require an unreasonably thin barrier (Figure A2.7 and Figure A2.9). Much like in enzymatic systems, this behavior can only be understood if the transferring proton is treated fundamentally as a quantum mechanical particle. This means that factors more typically thought of in the context of electron transfers, such as the effect of tunnelling distance and the reorganization energy, are central in understanding this reactivity.

The temperature insensitive KIEs for reactions between **CoO** and fluorene and the resulting positive value of ln(A_H/A_D) are uncommon in small molecule reactions; however, it is the norm in enzymatic systems (see Table 3.1 for a representative sample of other systems).[38,63,117,219–228] Within the more specific context of metal complex mediated C–H activation, the paucity of data makes it difficult to draw general conclusions regarding the temperature dependence of KIEs and the importance of tunneling. Most reported data have negative intercept ln(A_H/A_D) values which suggest tunneling, but are technically still compatible with semiclassical theory.

Table 3.1 Isotope dependence of Arrhenius parameters for various reactions.

Reaction	Ref.	$E_a(D) - E_a(H)$ (kcal/mol)	$\ln(A_H/A_D)$
CoO + DHA	*g*	3.7(3)	−3.3(5)
CoO + Fluorene	*g*	0.28(8)	0.8(2)
TAMLFe^{V}O + EtPh	117	3.3(8)	−4(2)
(TMP)$^{+\bullet}$Fe^{IV}(O) + BnOH	219	7.0(6)	-8(1)
L^{NHC}Fe^{IV}(MeCN)(O)$^{2+}$ + DHA	220	4.5(5)	-5(1)
^{pipMe}LCu^{III}OH + DHA	38	2.9(4)	−3(2)
LCu^{III}OH + DHA	38	0.4(2)	3(3)
^{NO2}LCu^{III}OH + DHA	38	3.6(3)	−5.0(7)
(L^{iPr_3}Cu^{III})$_2$(μ-O)$_2^{2+}$[a,b]	221	0.5(7)	2.0(7)
	222	1.9(7)	−0.7(1)
(L^{Bn_3}Cu^{III})$_2$(μ-O)$_2^{2+}$[a]	222	2.5(7)	−1.6(1)
(Tp''Co^{II})$_2$(μ-O$_2$) [a]	223	2.8(7)	−2.0(7)
Ru^{III}(bpy)$_3^{3+}$/H$_2$O + PhOH	224	1.68(4)	−1.40(7)
4-*oxo*-TEMPO$^{\bullet}$ + TEMPOH[c]	225	0.3(6)	1.1(6)
9a*H*-Quinolozine[d]	226	−0.01(2)	1.64(3)
SLO[e]	227	0.9(2)	2.9(3)
PHM[f]	228	0.4(3)	1.8(5)

[a]Activation of a ligand C–H bond. [b]Two distinct sets of parameters are reported for this compound. [c]Values reported in dichloromethane; similar results were also reported in acetonitrile. [d]Sigmatropic rearrangement to 4*H*-Quinozoline. [e]Soybean Lipogenase-1. [f]Peptidylglycine α-hydroxylating monooxygenase. [g]This work. Where necessary, reported changes in entropy of activation in e.u. were converted to unitless $\ln(A_H/A_D)$ by multiplication of both value and error by 0.503; changes in enthalpy of activation were used as reported for activation energy differences.

In comparing **CoO** with other model complexes, our results are most reminiscent of a series of three copper hydroxide complexes' reactivity with DHA.[38] Two of these complexes display negative intercepts ($\ln(A_H/A_D) = -3(2)$ and $-5.0(7)$) but one displays a positive intercept ($\ln(A_H/A_D) = 3(3)$). Similar results have been reported for bis-μ-oxo complexes of copper.[221,222,229] It is not immediately apparent why reactivity between **CoO** and fluorene and some of these copper reactions are more "enzyme-like" with a positive intercept $\ln(A_H/A_D)$ whereas reactivity between **CoO** and DHA and most small molecule CPET reactions are not; however, these studies suggest

that evidence for tunneling is perhaps best evaluated in a series of reactions rather than with just one substrate. As one general conclusion from our study, we note the need for additional variable temperature KIE data for molecular model complexes. Notably, many experimental studies use room temperature KIE values to determine whether tunneling is important. While room temperature KIE values >10 do mandate that tunneling is important, our study illustrates that values <10 can still indicate extensive tunneling.

Our experimental conclusion that proton tunneling is essential in the C–H activation reactions of transition metal-oxo complexes is not without precedent in transition metal-oxo studies. Combined experimental and theoretical studies have implicated proton tunneling in the counter-electrophilicity trends and selectivity observed in C–H activation.[209,230,231] Tunneling has also been observed to play a role in reported kinetic trends with $\Delta G°_{CPET}$ and η.[103,208] However, these studies have all utilized a semiclassical framework and have not examined transition metal-oxo reactivity with nonadiabatic rate theory. The need to properly address quantum mechanical tunneling with a nonadiabatic framework for transition metal-oxo mediated C–H activation raises broader implications. For example, a nonadiabatic reaction pathway could blur the distinction between σ and π reaction pathways for metal-oxo mediated C–H activation, as the electron does not need to transfer into the orbital approached by the C–H bond.[232] Nonadiabatic reactions could also proceed through a spin-forbidden transitions, complicating consideration of spin states in transition metal-oxo reactivity.

The experimental evidence for extensive tunneling that we find in the reactivity of **CoO** with C–H bonds highlights the need to consider the quantum mechanical nature of the proton and nonadiabatic effects when explaining imbalanced reactivity trends in CPET; the use of

semiclassical structure-reactivity relationships is not sufficient. Experimental demonstrations of imbalanced CPET must be explained using factors more commonly used to understand electron transfers, such as the tunneling distance, reorganization energy, and vibronic coupling. As an example, two recent studies found that lower proton-transfer energies correlate with shorter distances between the proton donor and the proton acceptor.[60,200] Furthermore, the experimental data we present in this chapter bolsters recent questions about whether the influence of stepwise thermodynamic parameters beyond their contribution to $\Delta G°_{CPET}$, as was found in the last chapter, is compatible with tunneling in CPET reactions.[67,95,96] The focus of Chapter 4 will be on addressing these questions.

4. Conclusions

Based on the variable temperature KIEs reported herein, we find evidence of extensive tunneling in CPET reactions between **CoO** and C–H bonds. For the reactivity with fluorene, temperature insensitive KIEs indicate tunneling which is so extensive that reactivity must proceed through a nonadiabatic process and cannot be explained with semiclassical theories of proton transfer. This is a clear demonstration that semiclassical structure-activity relationships are not sufficient to explain the CPET reactions of metal-oxygen complexes in general. Specifically, this result calls for a quantum mechanism for how stepwise free energies can affect nonadiabatic CPET reactions.

Furthermore, our results underscore the need for additional variable temperature KIE data and analysis on synthetic CPET reactions. We have a detailed understanding of how proton tunneling and nonadiabatic reaction pathways influence enzymatic reactivity, in large part due to thorough studies of variable temperature KIE data which have guided further theoretical analysis.

Similar research is lacking for synthetic reactions with small molecules. More work is needed, both from theoretical and experimental chemists, to fully understand the role of tunneling and nonadiabatic pathways in the C–H activation reactivity of transition metal-oxo complexes.

5. Methods

Unless stated otherwise, all manipulations were performed under an inert atmosphere in mBraun Unilab Pro gloveboxes or using standard Schlenk techniques. $PhB(^{t}BuIm)_3Co^{III}O$ (**CoO**), d_1-fluorene, d_2-fluorene, and d_4-DHA were synthesized according to literature procedures;[14,233–235] all other chemicals were obtained from commercial sources. We found that to selectively obtain d_1-fluorene and not d_2-fluorene it was critical to use exactly one equivalent of n-butyllithium and to rapidly quench with D_2O. For d_2-fluorene and d_4-DHA, we found using enough d_6-DMSO to fully dissolve the starting substrate allowed us to achieve higher isotopic purity but suspect heating the reaction only resulted in decreased yield. All substrates were recrystallized from hot hexanes prior to use. All data analysis was performed in python 3.7 utilizing Numy, Scipy, and Matplotlib packages.[175,177,179]

Measurement of KIEs by Competition Experiments

Competition experiments were run with 1.25 mM of **CoO** and 20 equivalents of substrate in 2.0 mL of toluene. In a typical experiment, the substrate was dissolved in 1.9 mL of solvent and equilibrated to the desired temperature (a sealed vial in the glovebox freezer for 239 K data, a Unisoku USP-203-B cryostat for 263 K data, a taped vial in a cold bath outside of the glovebox for 273 K data, a sealed vial set on the glovebox floor for 296 K data, and a sealed vial set in a glovebox heat block for 323 K data), then 100 μL of **CoO** stock solution (25 mM) was added via syringe. The reaction was run to > 99% completion, as determined by five time constants (inverse

rate constant) of the expected rate for the 10 equivalents of reactive C–H bonds based on an Arrhenius analysis of the fluorene d_0-kinetic data (Table 3.3). After the reaction, it was passed through either alumina or silica to remove Co containing products, dried, redissolved in DCM, and analyzed by GC-MS. See SI p. 7 for yield measurements and a discussion of their significance.

GC-MS analysis was performed with an Agilent 7890B GC system and Agilent 4977A MSD. Chemical ionization was used to avoid fractionation. The amount of each isotopomer was determined by measuring a reference spectrum with no deuterium and fitting the partially deuterated spectra to a sum of the reference spectra shifted by each possible amount of deuterium; i.e. intensity at m/z was modeled as $inten_m = \sum ref_{m-n} p_n$; with ref_{m-n} being the intensity of the reference spectra at m/z-n and p_n giving the amount of d_n-compound in the mixture; these p_n were fit with least squares and then normalized to add to 1. A weighted sum of the amount of deuterium in each isotopomer could be used for a total amount proportion of deuterium p_D in each sample ($p_D = \sum p_n n$). Fluorene was fit for m/z = 195–199, DHA was fit to m/z = 209–215, and bifluoreneyl fit to m/z = 331–335. The Fluorene and DHA peaks correspond to ionization with $C_2H_5^+$, which were used to avoid complications with hydride/deuteride loss which complicated the features for ionization with H^+. No M–1 peak was observed for bifluorenyl, so the more intense peak with H^+ ionization was used. The experimental data was modeled with the formula:

Equation 3.1
$$\frac{p_{PH}}{p_{PD}} = \frac{2k_{SH_2}p_{SH_2} + k_{SDH}p_{SHD}}{k_{SHD}p_{SD_2} + 2k_{SD_2}p_{SHD}} = \frac{2KIE^{1^\circ}KIE^{2^\circ}p_{SH_2} + KIE^{2^\circ}p_{SHD}}{KIE^{1^\circ}p_{SHD} + 2p_{SD_2}}$$

where the p_p values indicate the proportions of protons/deuterons in the product, the p_S values indicate the proportion of the indicated isotopomer in the substrate, and the k_S values indicate the rate of reaction with the indicated isotopomer (k_{SHD} refers to abstraction of an H–atom with a secondary D–atom, and vice-versa for k_{SDH}). See Scheme 3.1 for an illustration of Equation 3.1 in

the ideal case of pure d_1-fluorene and 1:1 d_0-fluorene:d_2-fluorene. The KIEs were in turn modeled as

$$\textbf{Equation 3.2} \qquad \mathrm{KIE} = \frac{A_\mathrm{H}}{A_\mathrm{D}} e^{\frac{E_\mathrm{a}(\mathrm{D}) - E_\mathrm{a}(\mathrm{H})}{RT}}$$

with the primary and secondary KIE having separate differences in activation energy $E_a(D) - E_a(A)$ and prefactor ratios A_H/A_D. Individual KIE values at a given temperature were determined by a nonlinear least squares fit of Equation 3.1 with p_p values from both intramolecular and intermolecular competition (Table 3.2). Substituting Equation 3.2 into Equation 3.1 and performing a nonlinear least squares fit to all competition data yielded the reported values and errors of $E_a(D) - E_a(A)$ and A_H/A_D. We used mean values of the p_S from three measurements to prevent complicated correlations in error from biasing our best fit parameters; however, if we use any individual measurement of p_s the results do not change within error. We see no evidence for scrambling between product radicals and the substrate in the GCMS peak of unreacted substrate and reported rate constants of C–H scrambling are much smaller than reported dimerization rate constants (Figure A2.6).[104,236]

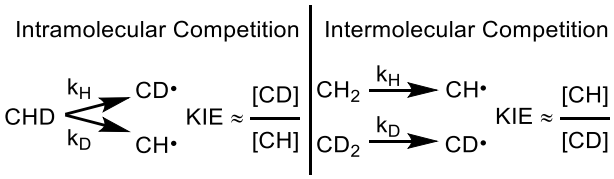

Scheme 3.1 An illustration of how KIEs are determined by product isotope distribution in competition experiments.

Table 3.2. Competition measurements of the oxidation of fluorene and the resulting KIE values.

T (K)	Intramolecular Product p_H[a]	Intramolecular Product p_H[i]	Primary KIE	Secondary KIE
323	27.4(9)%	78.6(7)%	3.6(1)	1.18(4)
296	27.3(6)%	78.2(2)%	3.57(8)	1.16(2)
273	25.9(9)%	79.6(3)%	3.9(1)	1.17(3)
263	25.2(7)%	80.2(2)	4.1(1)	1.17(2)
239	26(1)%	80.0(5)%	4.0(2)	1.18(4)

All proportions were measured in triplicate. Reported errors are the standard errors of the mean. [a]Proportion of d_0-fluorenyl in the bifluorenyl product from oxidation of d_1-fluorene. [b]Proportion of d_0-fluorenyl in the bifluorenyl product from the oxidation of 1:1 d_0-fluorene:d_2-fluorene.

Measurement of KIEs by Kinetic Experiments

UV-vis data were collected with a Thermo Fisher EVO300 LS spectrometer and a Unisoku USP-203-B cryostat. All experiments were run with 1.25 mM of **CoO** with 10 equivalents of substrate in 2 mL of toluene. In a typical experiment, a cuvette was prepared in an N_2 glovebox with 1.8 mL toluene and 100 μL of a stock solution of 250 mM substrate, and then sealed with a screwtop cap with a puncturable septum. The cuvette was allowed to equilibrate to the desired temperature and then 100 μL of 25 mM **CoO** was injected via syringe. The absorbance at 470 nm was followed to ~85% completion, and the rate constant k_{obs} was obtained via a nonlinear least squares fit of the absorbance at 470 nm to the exponential form:

$$\textbf{Equation 3.3} \qquad A(t) = A_\Delta e^{-k_{obs}t} + A_\infty.$$

For undeuterated substrates, k_H was estimated as the mean of three k_{obs} measurements; the reported error is the standard error of the mean. Three k_{obs} for deuterated substrate were similarly averaged to obtain $k_{D,obs}$ and these were corrected with Equation 3.4 for the actual extent of deuteration in the sample (p_D) to obtain $k_{D,corr}$ values, which is what k_D refers to unless otherwise stated (Table 3.4, Table 3.3).

Equation 3.4 $$k_{D,corr} = \frac{1}{p_D}\left(k_{D,obs} - k_H(1 - p_D)\right)$$

The p_D were determined both by ^{1}H NMR spectroscopy and GC-MS analysis, which closely agreed: For d_2-fluorene, ^{1}H NMR spectrum analysis gave 98% and GC-MS gave 96%; 97% was used. For d_4-DHA, ^{1}H-NMR spectrum analysis gave >99% and GC-MS gave 95-97% (depending on how much of the M+29 peak is assigned to a d_2-anthracene impurity); 98% was used. Error in the estimate of p_D was not propagated because it would lead to complicated correlations between temperature data points which would confound later analysis (assuming this error is in the measurement and not in the sampling of the substrate). Instead, we confirmed that our conclusions are consistent within the whole range of possible p_D values indicated above.

KIEs were then calculated as the ratio of k_H and $k_{D,corr}$, with error propagated from k_H and $k_{D,obs}$. Arrhenius parameters $E_a(D)$-$E_a(H)$ and $\ln(A_H/A_D)$ were calculated by a least squares linear fit of ln(KIE) estimates to $1/RT$. We also performed a nonlinear least squares fit of values of $E_a(D) - E_a(H)$ and $\ln(A_H/A_D)$ to the experimental k_H and $k_{D,obs}$ and found identical mean estimates and similar error bars.

For d_4-DHA at 263 K, the rate was too slow to follow to completion; instead, we measured initial rates to ~9% completion, with the average fit value of A_Δ from other temperatures used to convert the rate from of absorbance per second to a rate constant in per second ($k_{D,obs} = k_{Init}/A_\Delta$, with k_{Init} the slope of the absorbance at 470 nm with time). For error propagation, the standard error of A_Δ was used (not the standard error of the mean). This data point is graphed to demonstrate consistency with the other data points, but not included in the linear fits to variable temperature.

See Appendix 2 for a discussion of fluorene kinetic KIEs and a comparison with the competition KIEs.

Table 3.3. Kinetic measurements of the oxidation of Fluorene and the resulting KIE values.

T (K)	k_H (1/s)	$k_{D,obs}$ (1/s)	$k_{D,corr}$ (1/s)	KIE	ln(KIE)
323	$2.72(2) \cdot 10^{-2}$	$7.7(3) \cdot 10^{-3}$	$7.1(3) \cdot 10^{-3}$	3.8(2)	1.34(5)
303	$7.47(5) \cdot 10^{-3}$	$2.10(3) \cdot 10^{-3}$	$1.94(3) \cdot 10^{-3}$	3.86(6)	1.35(2)
283	$1.78(2) \cdot 10^{-3}$	$4.60(7) \cdot 10^{-4}$	$4.19(7) \cdot 10^{-4}$	4.24(9)	1.44(2)
263	$3.44(6) \cdot 10^{-4}$	$7.3(2) \cdot 10^{-5}$	$6.5(3) \cdot 10^{-5}$	5.3(2)	1.67(4)

All rates were measured in triplicate. Reported errors are the standard errors of the mean.

Table 3.4. Kinetic measurements of the oxidation of DHA and the resulting KIE values.

T (K)	k_H (1/s)	$k_{D,obs}$ (1/s)	$k_{D,corr}$ (1/s)	KIE	ln(KIE)
323	$1.19(1) \cdot 10^{-2}$	$1.26(3) \cdot 10^{-3}$	$1.04(3) \cdot 10^{-3}$	11.4(3)	2.44(3)
303	$3.34(8) \cdot 10^{-3}$	$2.7(1) \cdot 10^{-4}$	$2.1(1) \cdot 10^{-4}$	16(1)	2.76(7)
283	$7.9(1) \cdot 10^{-4}$	$4.6(2) \cdot 10^{-5}$	$3.1(2) \cdot 10^{-5}$	26(1)	3.25(6)
263[a]	$1.49(3) \cdot 10^{-4}$	$6.0(8) \cdot 10^{-6}$	$3.0(8) \cdot 10^{-6}$	50(10)	3.9(3)

All rates were measured in triplicate. Reported errors are the standard errors of the mean. [a]Collected with initial rates.

Chapter 4: Reconciling Imbalanced and Nonadiabatic Reactivity in Transition Metal–Oxo-Mediated Concerted Proton Electron Transfer

Adapted with permission from Schneider, J. E.; Anderson J. S.; *J. Phys. Chem. Lett.*, **2023**, *14*(43), 9548-9555.

1. Introduction

Concerted proton electron transfer (CPET) is a broadly relevant class of reactions important in a variety of processes, such as C–H activation and energy transport.[23,32,66,67,237–239] Recently, there has been much interest in how the free energies needed to form stepwise intermediates, $\Delta G°_{PT}$ and $\Delta G°_{ET}$, can influence the rates of concerted reactions independently of their contribution to $\Delta G°_{CPET}$ (Figure 4.1, left). Chapter 2 of this dissertation discussed how these stepwise thermodynamic parameters have a broad effect on CPET reactions between transition-metal oxo complexes and C–H bonds in general. However, the traditional basis for interpreting such linear free energy relationships (LFERs) with stepwise thermodynamic parameters, and for many theories regarding transition metal-oxo C–H activation reactions more generally, are built on a semiclassical understanding of a transition state.[73,74] Questions have been raised about whether such models are adequate for CPET reactivity. Chapter 3 of this dissertation laid out evidence for extensive tunneling in a Co-oxo complex $PhB(^{t}BuIm)_3Co^{III}O$ (**CoO**) for which the rate of concerted C–H activation trends with $\Delta G°_{PT}$ instead of $\Delta G°_{CPET}$.[50] These results can only be explained with a nonadiabatic model of CPET reactivity.

In contrast to the semiclassical view of the proton being localized midway across the reaction coordinate at the transition state, nonadiabatic theory views the proton transfer

fundamentally as a tunneling event. Thus, the transition state is better described as resonance between reactant and product than as localized at an intermediate position (Figure 4.1, right). The absence of a localized transition state structure is the crux of the argument that semiclassical structure-reactivity relations are not appropriate for nonadiabatic reactions.

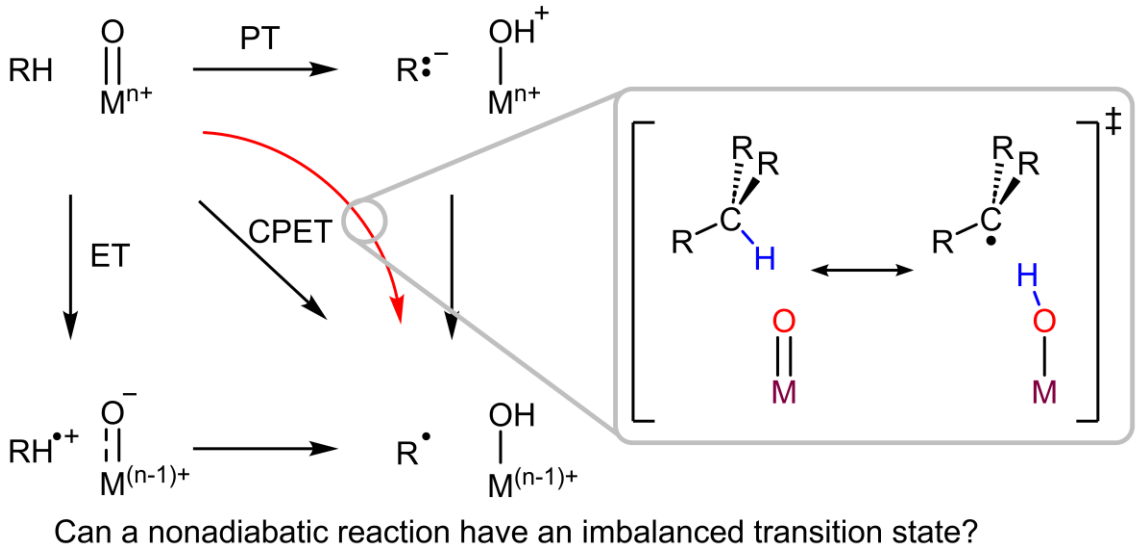

Figure 4.1 A generic square-scheme for CPET from an organic substrate to a metal-oxo complex. The imbalanced reaction mechanism, shown in red, is traditionally viewed as an alternate reaction pathway. Questions remain about whether this picture is compatible with proton tunneling, as depicted on the right.

To better understand these seemingly semiclassical reactivity trends in a system with established extensive tunneling, we computationally examined the reactivity of **CoO** with C–H bonds (Scheme 4.1). Our calculations demonstrate that the experimentally observed reactivity trend stems from a lower $\Delta G°_{PT}$ leading to a more anharmonic energy well for the reactant. This in turn makes the reactant proton probability distribution more diffuse and thereby enhances tunneling. We use these calculations to anchor a model system wherein the reactant and product energy wells are influenced by $\Delta G°_{PT}$ and $\Delta G°_{ET}$. This model organically predicts trends with stepwise thermodynamic parameters that have been observed from both statistical and

computational analyses of metal-oxo mediated CPET reactions and also makes further predictions of how stepwise thermodynamics can affect reaction rates. Our results show how imbalanced transition states can manifest in nonadiabatic CPET reactions and demonstrate that semiclassical structure-activity relationships are compatible with quantum mechanical treatments of reactivity.

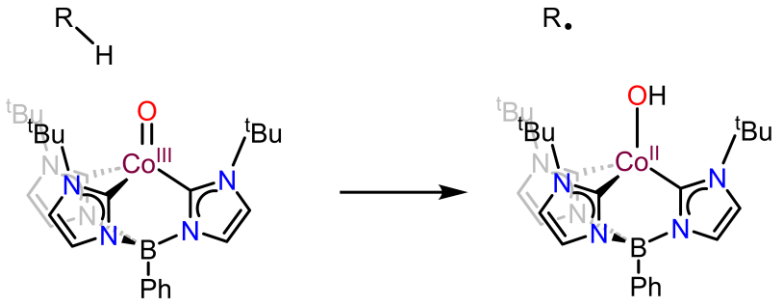

Scheme 4.1 The cobalt(III)-oxo complex **CoO** (left) and the C–H activation reaction studied in this work.

2. Basics of Nonadiabatic Rate Theory

Nonadiabatic CPET can be conceptualized as occurring in two steps: (1) The reactants and the solvent reorganize to a configuration where the reactant and product have the same energy (Figure 4.2A), and (2) the electron and proton transfer from a discrete reactant vibronic state to a discrete product vibronic state nonadiabatically (Figure 4.2B; the electron and proton are theoretically treated as two separate particles, even for concerted reactivity).[84,85,183] The first step places the reactant and product vibronic wavefunctions at an equal energy, ensuring that energy is conserved when the transfer occurs. The activation energy needed to reach this reorganized state depends on the driving force of the reaction ($\Delta G°_{CPET}$) and the reorganization energy of the reaction (λ). The second step, the actual electron and proton transfer, can then occur with a probability dependent on the coupling between the reactant and product vibronic states. In the limit where the transferring electron responds slowly to the movement of the proton, this coupling is the product

of an electronic coupling (V_{el}) and the Franck-Condon overlap between proton wavefunctions ($S_{\mu\nu}$, where μ and ν index the vibrational states).[215,240]

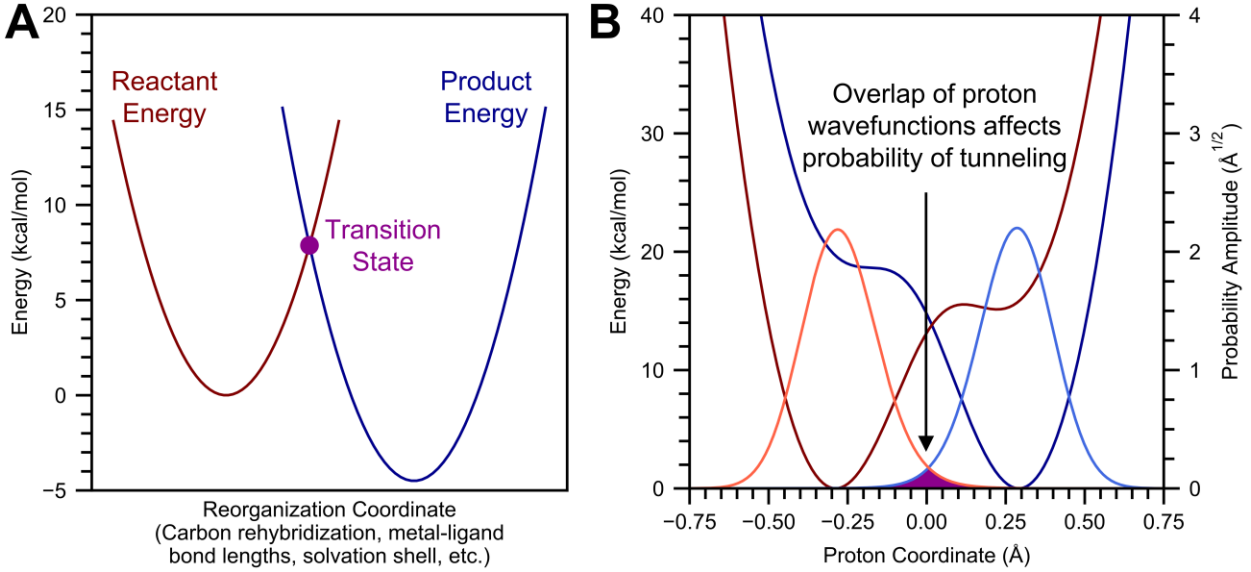

Figure 4.2 General overview of a nonadiabatic transition states. (A) Energy along the reorganization coordinate of CPET. (B) Energy along the proton coordinate at the reorganized transition state (the purple dot in panel (A)). The darker red and blue lines are the proton potential energy surfaces (left y-axis) and the lighter red and blue represent the corresponding ground state vibronic wavefunctions of the proton (right y-axis) and their overlap in purple. While it is vibronic energy levels which must be equalized at a reorganized complex, for graphical purposes we show the reactant and product potential energy surfaces as having the same minimum energy.

These two steps can occur with a distribution of proton tunneling distances (R). A shorter tunneling distance requires a more compressed transition state, which increases the activation energy needed to achieve the reorganized complex. This "compression energy" is designated as $U(R)$. Shorter tunneling distances also lead to larger overlap integrals between the proton's vibrational wavefunctions, so the optimal tunneling distance is formed from a balance between increasing $U(R)$ and an increasing $S_{\mu\nu}$ with shorter tunneling distances.

Thus, instead of representing CPET as having a single potential energy surface characterized by an activation barrier to climb, nonadiabatic models of CPET involve separate

reactant and product potential energy surfaces and three separate reaction coordinates. Along the proton transfer coordinates, these potential energy surfaces are potential energy wells which represent the restoring force holding the proton on either the reactant or the product. The overlap of the proton's wavefunctions in these two wells, the electronic coupling between them, and the energy needed to reach a reorganized geometry with a sufficiently short tunneling distance take the place of the barrier height in determining the rate of transfer. Greater overlap leads to faster reactivity in a manner analogous to greater orbital overlap leading to stronger bonding.

We hypothesized that the stepwise thermodynamic elements $\Delta G°_{PT}$ and $\Delta G°_{ET}$ can create an imbalanced transition state even with a nonadiabatic proton transfer through their influence on the reactant/product proton energy wells, as defined in the four-state model of Hammes-Schiffer and Soudackov.[98,99] This model includes electronic states for each of the four corners of the square scheme (Figure 4.3A,B). Calculating rate constants requires solving for proton vibrational states at the reorganized complex and then calculating the transition rate between vibronic states. However, states which differ by only proton transfer are expected to have a large electronic coupling, so it is typically best to mix these states first (Figure 4.2C). This creates a reactant energy well (shown in red) from the reactant state, R–H with metal-oxo, and the proton transfer state, $R:^-$ anion with oxidized metal-hydroxide. It creates a product energy well (shown in black) from the product state, R· radical with reduced metal-hydroxide, and the electron transfer state, $R\text{--}H^+$ cation with reduced metal-oxo. The vibrational wavefunctions are then solved within these new energy wells. Because the proton transfer and electron transfer electronic states affect the construction of these wells, they can also affect the vibrational wavefunctions, their Franck-Condon overlap, and thus the overall CPET rate constant.

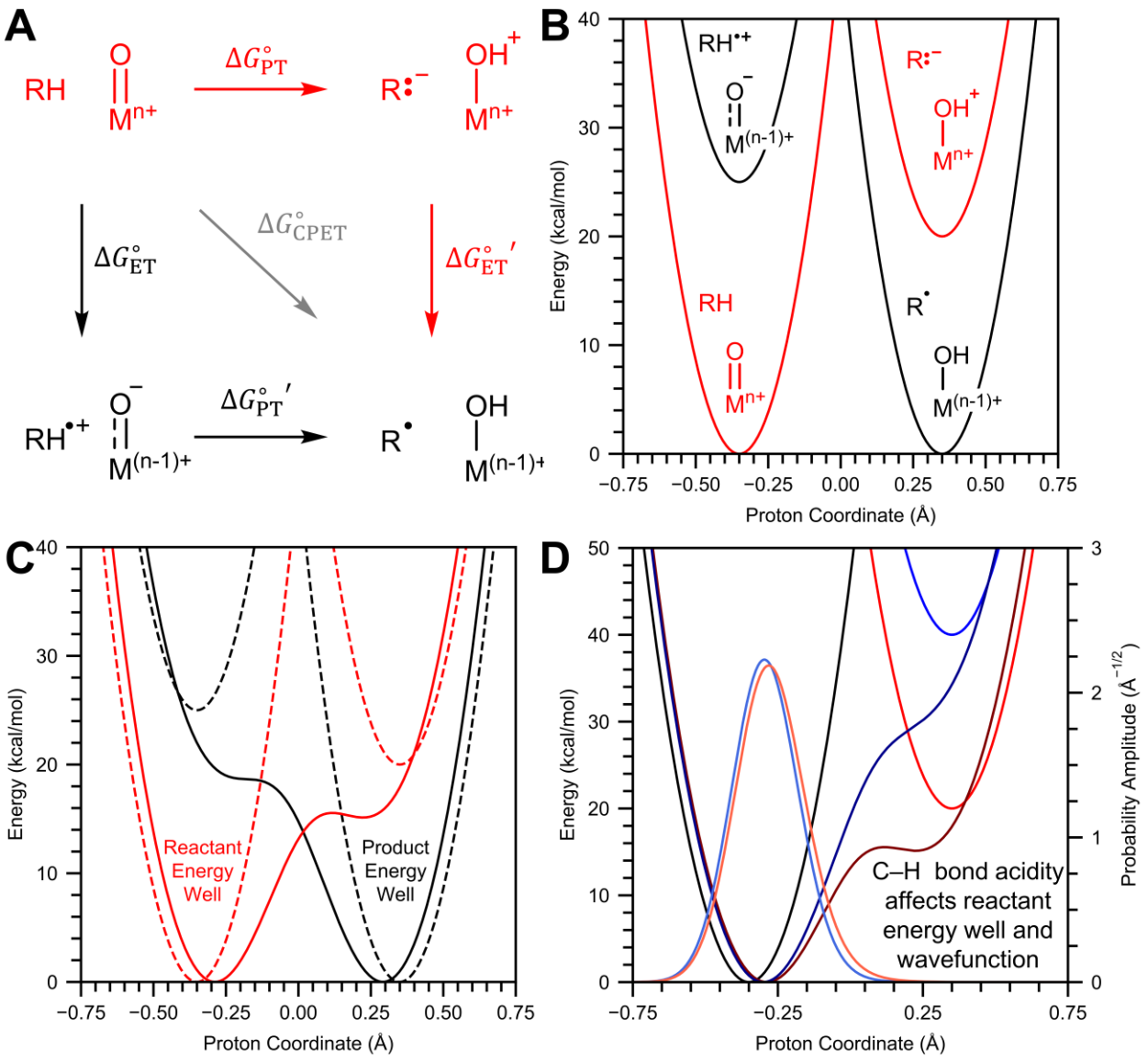

Figure 4.3 Overview of how all four states of the square scheme influence a nonadiabatic transition state. (A) A typical square scheme for CPET reactivity, with the thermodynamic energies $\Delta G°_{PT}$, $\Delta G°_{ET}$, and $\Delta G°_{CPET}$ as referred to in this work. (B) The energy of the four states of the square scheme as a function of proton position, with heavy atoms frozen at the reorganized complex. (C) The reactant and proton transfer electronic states (red) and the product and electron transfer electronic states (black) will have large electronic coupling which needs to be accounted for before vibrational states relevant to CPET reactivity are calculated. (D) A more acidic C–H bond will lower the energy of the proton transfer electronic state (blue to red). This will create a more anharmonic energy well for the reactant and affect the vibrational states of the transferring proton (light blue to pink).

This fundamentally nonadiabatic model, and similar models by Shaik, Borovik, Cukier, and Nocera,[53,97] clearly demonstrates that the energies of proton transfer and electron transfer have a role in CPET reactions beyond their intrinsic contribution to $\Delta G°_{CPET}$. They influence the reactant and product energy wells, and thereby the proton vibrational wavefunctions. For instance, a more acidic C–H bond, with a lower $\Delta G°_{PT}$, is expected to have a proton transfer electronic state that is lower in energy. This will make the reactant energy well more anharmonic and influence the vibrational wavefunctions of the proton in the reactant state (Figure 4.2D). We propose this is a major mechanism by which CPET reaction rates can be affected by changes in $\Delta G°_{PT}$ and $\Delta G°_{ET}$, and moreover it provides an avenue to explain observed semiclassical structure-reactivity effects that is still rooted in nonadiabatic rate theory.

3. DFT-Calculation of CPET Reaction Rates

We used DFT to optimize minimum energy crossing points for electron-proton tunneling and then calculated potential energy wells at these geometries to examine if the reactant energy wells could be the cause of **CoO**'s kinetic trend with $\Delta G°_{PT}$. The relative rate constants from these calculations give a satisfyingly good agreement to experimental kinetic trends with pK_a (Figure 4.4A) and kinetic isotope effects (KIEs, Figure 4.4B).[50] This good correspondence validates using these calculations to better understand the asynchronous CPET reactivity of **CoO**.

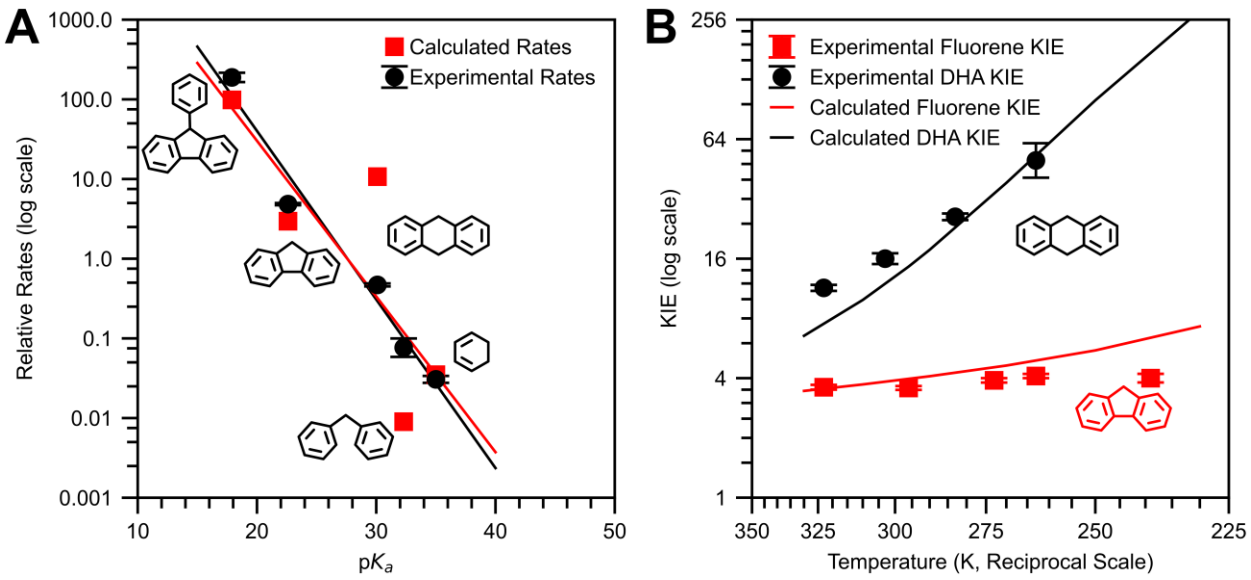

Figure 4.4 Comparison of experimental and calculated trends in the C–H activation reactions of a cobalt(III)-oxo complex.

As expected, we observe that more acidic C–H bonds, with lower pK_a and $\Delta G°_{PT}$, have more anharmonic reactant energy wells (Figure 4.5A). Within these more anharmonic energy wells the proton density distribution is more diffuse, with the proton being more likely to be found further across the reaction coordinate at the reorganized geometry (Figure 4.5B). The effect on the average proton position is subtle, but it substantially increases the vibronic coupling of the reaction (Figure 4.5C). This increased diffusivity and vibronic coupling is largely, but not solely, due to increased access to higher vibrational energy states in the reactant (Table A3.1). Overlap integrals between reactant and product vibrational states generally increase, including between the ground states. Additionally, the increased potential well anharmonicity lowers the energy of vibrationally excited states. Because excited vibrational states are more diffuse and have larger overlap integrals with product wavefunctions, this increased energetic accessibility results in an accelerated reaction rate.

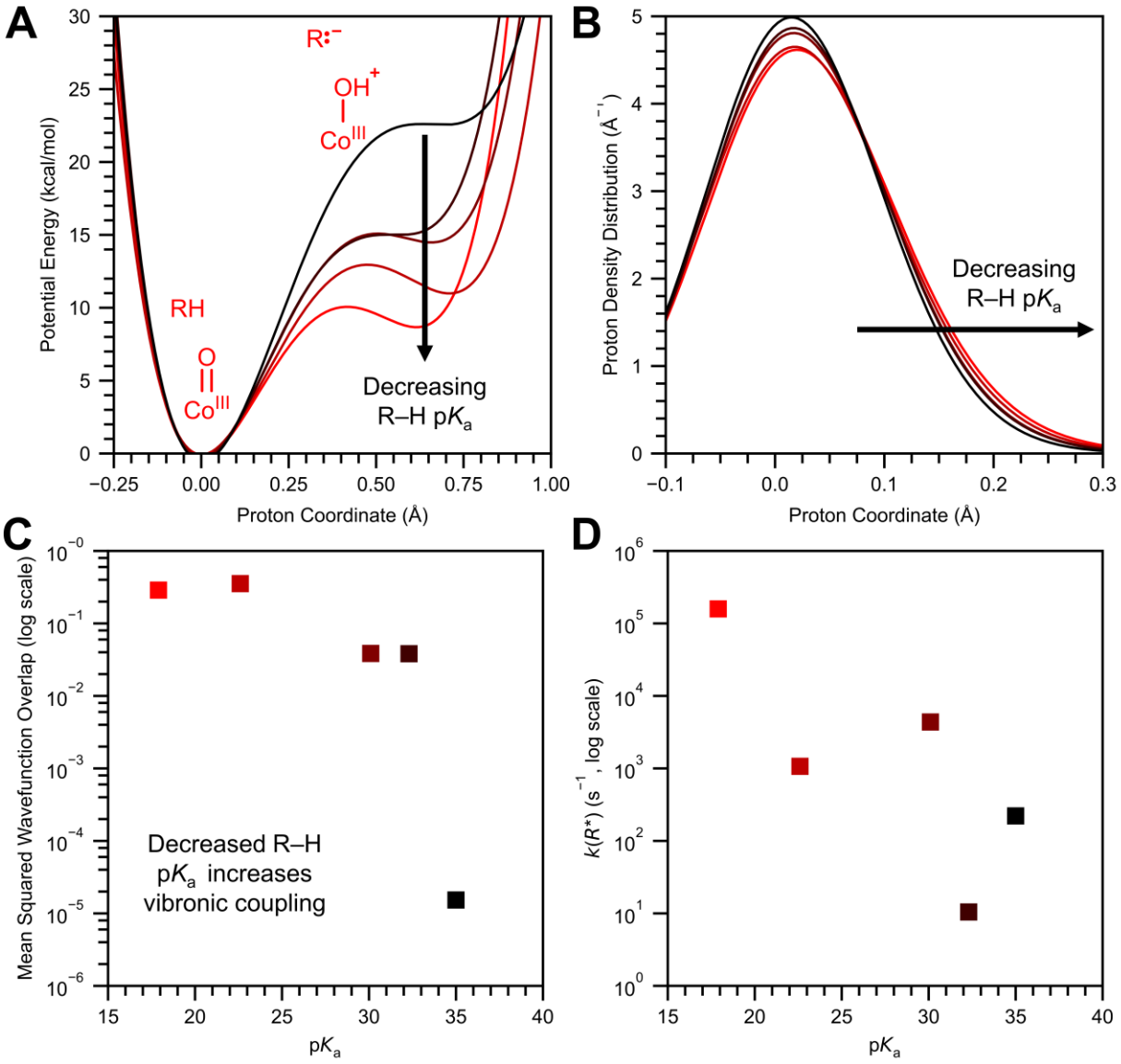

Figure 4.5 Effect of lowering pK_a on reactant proton potential energy wells, vibronic coupling, and reaction rates. (A) The reactant energy well for each substrate near the optimal tunnelling distance, with more acidic substrates being shown in lighter shades of red. (B) The effect of increased anharmonicity of the energy well on the probability density of the reactant proton. (C) The average Franck-Condon factor as a function of pK_a, weighted by a given pair of vibronic state's contribution to the calculated rate constant. (D) Calculated rate constants specifically at the optimal tunneling distance R^*. Substrates are, from pink to black and increasing in pK_a, 9-phenylfluorene, fluorene, 9,10-dihydroanthracene, diphenylmethane, and 1,3-cyclohexadiene.

This picture aligns well with parallel models in semiclassical transition state theory.[73,74,86]

In particular, it is reminiscent of an anti-Hammond effect: the lowering of $\Delta G°_{PT}$ results in a

transition state with increased probability of the proton being closer to the product. Ultimately, it is this greater probability of being found further along the reaction coordinate which leads to an accelerated reaction rate with a more acidic C–H bond.

The shape of potential energy well shapes has been noted before to have influence reaction well energies. Model calculations for CPET reactions commonly use parabolic or Morse potentials for the proton potential energy surface;[185,205,241,242] however, the extreme anharmonicity induced by hydrogen bonding has been noted to render these models indadequate.[242–244] Furthermore, anharmonicity induced by homolytic bond strengths has been noted to be important in rates of hydrogen atom transfer reactions.[245–249] Our findings can be understood as indicating that in certain reactions, it is most appropriate to model the proton's potential energy well using heterolytic bond strengths, as opposed to the homolytic bond strengths which are more commonly employed.

Other studies have found that more favorable stepwise thermodynamics will increase the rate by facilitating a short proton tunneling distance.[60,200] For instance, in the oxidation of fluorenyl benzoates a more basic benzoate was calculated to result in stronger hydrogen bonding between the fluorenyl C–H proton donor and the carboxylate proton acceptor. This in turn lead to lead to a decreased value of $U(R^*)$ at the optimal tunneling distance R^*. Thus, the outsized influence of ΔG°_{PT} on the reaction rate could be explained by a decrease in $U(R^*)$. However, our calculations with **CoO** do not find a strong trend between ΔG°_{PT} and $U(R^*)$, as would be predicted in this model, nor do they demonstrate a strong trend between ΔG°_{PT} and R^* (Figure 4.6). A better trend is observed between the optimal tunneling distance, $k(R^*)$, and ΔG°_{PT}, indicating that the increased reactivity is attributable to factors other than tunneling distance (Figure 4.5D). Nonetheless, the

poorer trend with U(R*) does have the expected slope, so we cannot rule it out as having a supporting contribution.

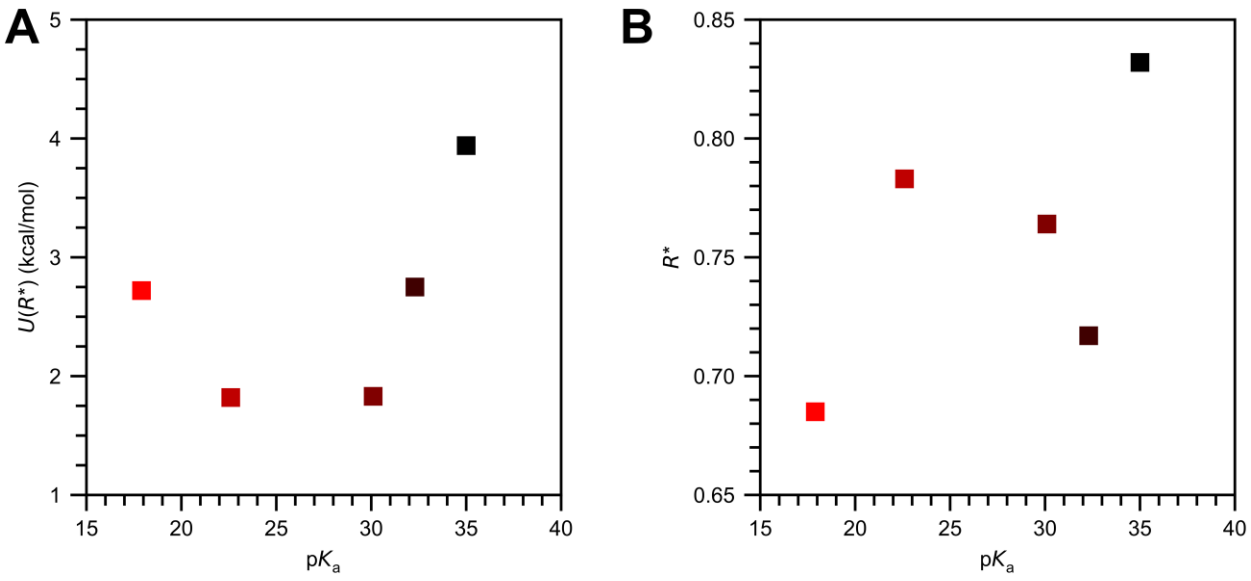

Figure 4.6 The effect of substrate pK_a on compression energy and tunneling distance. (A) Variation in the compression energy $U(R)$ at the optimal tunneling distance R* with pK_a. (B) Variation in the optimal tunneling distance R* with pK_a. Substrates are, from pink to black and increasing in pK_a, 9-phenylfluorene, fluorene, 9,10-dihydroanthracene, diphenylmethane, and 1,3-cyclohexadiene.

The upshot of this analysis it that in the activation of C–H bonds by **CoO**, there is a direct connection between the acidity of the C–H substrate and the anharmonicity of the reactant proton's potential energy well. Increased anharmonicity increases the reorganized complex's vibrational wavefunction overlap and enhances proton tunnelling. This conclusion provides a plausible explanation for how substrate acidity affects the rate of C–H activation by **CoO** even with extensive tunneling, and it suggests a more general mechanism by which $\Delta G°_{PT}$ can affect the rates of CPET reactions.

4. Building a Generalized Theoretical Model

The connection between $\Delta G°_{PT}$ and the reactant well anharmonicity provides a mechanism by which a decrease in $\Delta G°_{PT}$ can influence the rate of CPET independent of a concomitant decrease in $\Delta G°_{CPET}$. To test the general effect of this mechanism, we fit the DFT-calculated potential energy wells as a function of $\Delta G°_{PT} - \frac{1}{2}\Delta G°_{CPET}$ and tunneling distance. First, we rearranged the quartic fits to DFT-calculated data into a form that was normalized with respect to the tunnelling distance *R*.

Equation 4.1 $$V_S(r,R) = A_S(R) + B_S(R)\frac{r}{R} + C_S(R)\frac{r^2}{R^2} + D_S(R)\frac{r^3}{R^3} + E_S(R)\frac{r^4}{R^4}$$

The coefficients of this polynomial differed based on the tunneling distance *R* and the substrate *S*. We found these differences could be quantitatively modeled with a polynomial quadratic in *R* linear in $\Delta G°_{PT} - \frac{1}{2}\Delta G°_{CPET}$ (see Appendix 3 for a discussion of the $\frac{1}{2}\Delta G°_{CPET}$ term).

Equation 4.2 $$A_S(R) = 2.21R - 1.30R^2 - 0.02(\Delta G^\circ_{PT} - 0.5\Delta G^\circ_{CPET}) - 0.79$$

Equation 4.3 $$B_S(R) = 40.24R - 32.14R^2 - 0.03(\Delta G^\circ_{PT} - 0.5\Delta G^\circ_{CPET}) - 11.37$$

Equation 4.4 $$C_S(R) = -97.31R + 376.05R^2 + 1.62(\Delta G^\circ_{PT} - 0.5\Delta G^\circ_{CPET}) - 12.28$$

Equation 4.5 $$D_S(R) = -113.21R - 508.83R^2 - 1.28(\Delta G^\circ_{PT} - 0.5\Delta G^\circ_{CPET}) + 106.31$$

Equation 4.6 $$E_S(R) = 166.39R + 176.50R^2 + 0.22(\Delta G^\circ_{PT} - 0.5\Delta G^\circ_{CPET}) - 81.84$$

The reactant energy wells obtained from these equations closely resemble those directly fit to DFT-calculations (Figure A3.16). While the specific coefficients of this fit are unique to the studied system, it is important to note that a general CPET reaction will still have reactant energy wells that are influenced by $\Delta G°_{PT}$. These equations give a chemically reasonable estimate for the

magnitude of this influence. Similarly, by substituting in $\Delta G°_{ET}$ in place of $\Delta G°_{PT}$, we can use the same equations to obtain a chemically reasonable estimate for how product energy wells will change due to variation in $\Delta G°_{ET}$. This motivates the use of Equation 4.1 through Equation 4.6 to qualitatively evaluate what general effects stepwise thermodynamic parameters are expected to have on the rate of CPET reactions.

We used equations 1 and 2 to simulate CPET rate constants over a range of $\Delta G°_{PT}$ and $\Delta G°_{ET}$ values with all other features of the reaction held constant. The reactant energy wells were varied with $\Delta G°_{PT}$ using this DFT-regressed fit, and product energy wells could be varied by substituting $\Delta G°_{ET}$ in place of $\Delta G°_{PT}$. We fixed the tunneling compression energy, $U(R)$, to that calculated for fluorene, ΔG°_{CPET} to −6 kcal/mol, the reorganization energy to 40 kcal/mol, and the temperature to 296 K.

The predominant effect that we observe from these simulations is a marked dependency on the sum ($\Delta G°_{PT} + \Delta G°_{ET}$) (Figure 4.7). Because our definitions of $\Delta G°_{PT}$ and $\Delta G°_{ET}$ do not sum to $\Delta G°_{CPET}$, i.e. they are along separate stepwise pathways, this trend with ($\Delta G°_{PT} + \Delta G°_{ET}$) is not redundant with a trend with ΔG°_{CPET}. Instead, it demonstrates how CPET reaction rates are expected to trend with $\Delta G°_{PT}$ and $\Delta G°_{ET}$ even with fixed $\Delta G°_{CPET}$. This overall observation is satisfyingly consistent with the analysis discussed in Chapter 1. The slope of RT times the log of the simulated rate constants plotted against ($\Delta G°_{PT} + \Delta G°_{ET}$) for our simulated rate constants is ~0.2, quite close to the experimental coefficient of ~0.1 from the statistical analysis. The slightly higher value for the simulated slope is likely due to the use of a system with relatively strong stepwise thermodynamic effects to parameterize the energy wells.

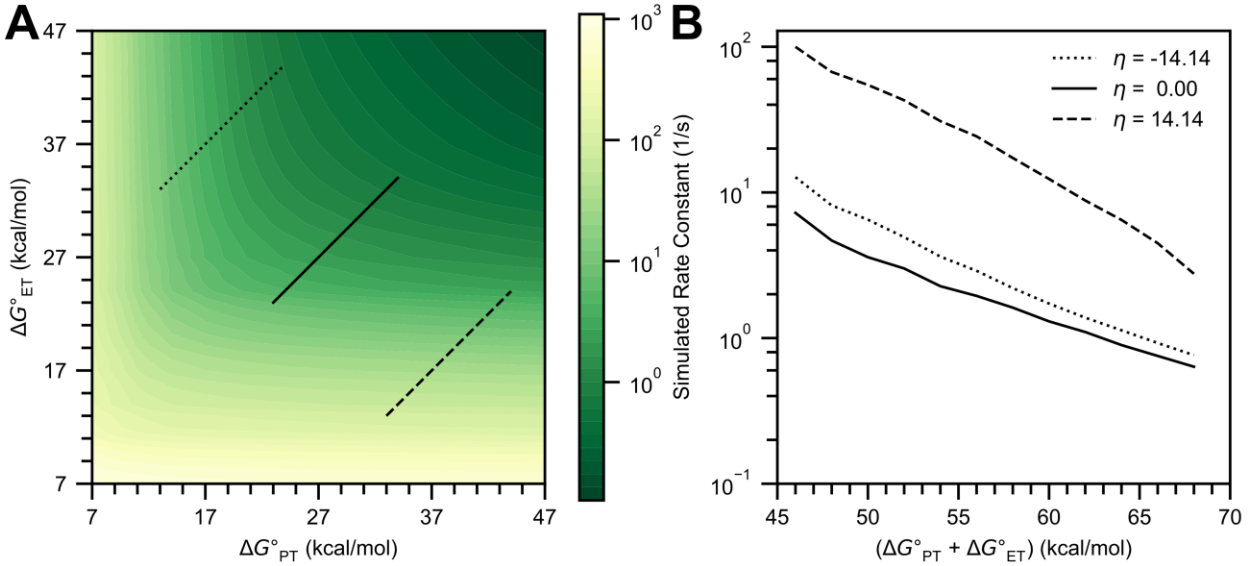

Figure 4.7 Simulated rate constants for exergonic CPET as a function of proton and electron transfer energetics. $\Delta G°_{CPET}$ is fixed at −6 kcal/mol. (A) The effect of both $\Delta G°_{PT}$ and $\Delta G°_{ET}$ on the simulated rate constant (1/s) which is shown from green to yellow according to the sidebar. The lines illustrate cross-sections which are plotted in (B). (B) Plot of simulated rate constants versus $\Delta G°_{PT} + \Delta G°_{ET}$ for $\Delta G°_{PT} > \Delta G°_{ET}$ (dashed line), $\Delta G°_{PT} = \Delta G°_{ET}$ (solid line), and $\Delta G°_{PT} < \Delta G°_{ET}$ (dotted line). The same lines in (A) show the *x*-axis for each cross section. Simulated rate constants are plotted on a logarithmic scale.

Interestingly, the simulated rate constants provide a more nuanced picture of kinetic trends with $(\Delta G°_{PT} + \Delta G°_{ET})$ than our previous linear regression analysis did. When either $\Delta G°_{PT}$ or $\Delta G°_{ET}$ becomes small, the reaction becomes more sensitive to this lower depth. This is seen in the curvature of contour lines in Figure 4.7A near the bottom or left edges of the plot. This more subtle trend goes further than our previous statistical analysis in that it explains the apparent insensitivity of the reactivity of **CoO** to $\Delta G°_{ET}$ as being due to the particularly low values of $\Delta G°_{PT}$ and comparatively high values of $\Delta G°_{ET}$ in this system. This curvature also leads to a slight dependence on the asynchronicity parameter η as previously presented by Srnec and coworkers (η is proportional to $\Delta G°_{PT} - \Delta G°_{ET}$).[55] Namely, our model predicts that as the magnitude of η becomes larger rates should accelerate independent of changes in $(\Delta G°_{PT} + \Delta G°_{ET})$, in agreement with the previous analysis by Srnec and coworkers.

While the terms "asynchronous" or "imbalanced" often refer to specific cases with a large value of $|\eta|$ (equivalently a large difference between $\Delta G°_{PT}$ and $\Delta G°_{ET}$),[50,53,54,58,59] our model clearly shows that the influence of stepwise free energies is broader than just these extremes. Even in cases with very small $|\eta|$, $\Delta G°_{PT}$ and $\Delta G°_{ET}$ have significant influences on reactivity. Furthermore, while the influence of $\Delta G°_{CPET}$ on rate constants can be sensitive to the individual contributions of $\Delta G°_{PT}$ and $\Delta G°'_{ET}$ (or alternatively $\Delta G°_{ET}$ and $\Delta G°'_{PT}$, Figure 4.5A),[57,199] our results demonstrate that the stepwise free energies $\Delta G°_{PT}$ and $\Delta G°_{ET}$ influence rate constants independent of their contributions to $\Delta G°_{CPET}$. This clearly demonstrates that the kinetics of CPET reactions is highly influenced by their energetic coupling, $\Delta G°_{CC}$. However, we acknowledge that experimentally disentangling these effects is challenging.

Intriguingly, there is also asymmetry in the dependence on η (Figure 4.7B). For a given value of $(\Delta G°_{PT} + \Delta G°_{ET})$, the slowest rate occurs with slightly negative η. This means that systems with relatively favorable electron transfer (positive η) are expected to be faster than systems with a similar preference for proton transfer (positive η). This preference for low $\Delta G°_{ET}$ over low $\Delta G°_{PT}$ increases as the reaction becomes more exergonic (Figure A3.17). However, if the reaction is made to be endergonic, the preference is reversed: a lower $\Delta G°_{PT}$ (negative η) is more effective than a lower $\Delta G°_{ET}$ (positive η) for increased rates (Figure 4.8). This asymmetric dependence on η is due to the involvement of excited states in the reaction. Exergonic reactions commonly occur through excited product vibrational states.[216] A lower $\Delta G°_{ET}$ will make the product energy well more anharmonic, this synergistically increases access to and Franck-Condon overlap with these same excited product vibrational states. However, a lower $\Delta G°_{PT}$ only affects the reactant energy well and vibrational states. Therefore, an exergonic reaction will get a greater boost from low $\Delta G°_{ET}$

than from low $\Delta G°_{PT}$. Conversely, endergonic reactions tend to occur more from excited reactant states and are therefore more sensitive to $\Delta G°_{PT}$. If we consider only the reactant ground state to product ground state reactivity, we observe that while reactions with $|\eta| > 0$ are still favorable, there is no longer an asymmetry between positive and negative η (Figure A3.18).

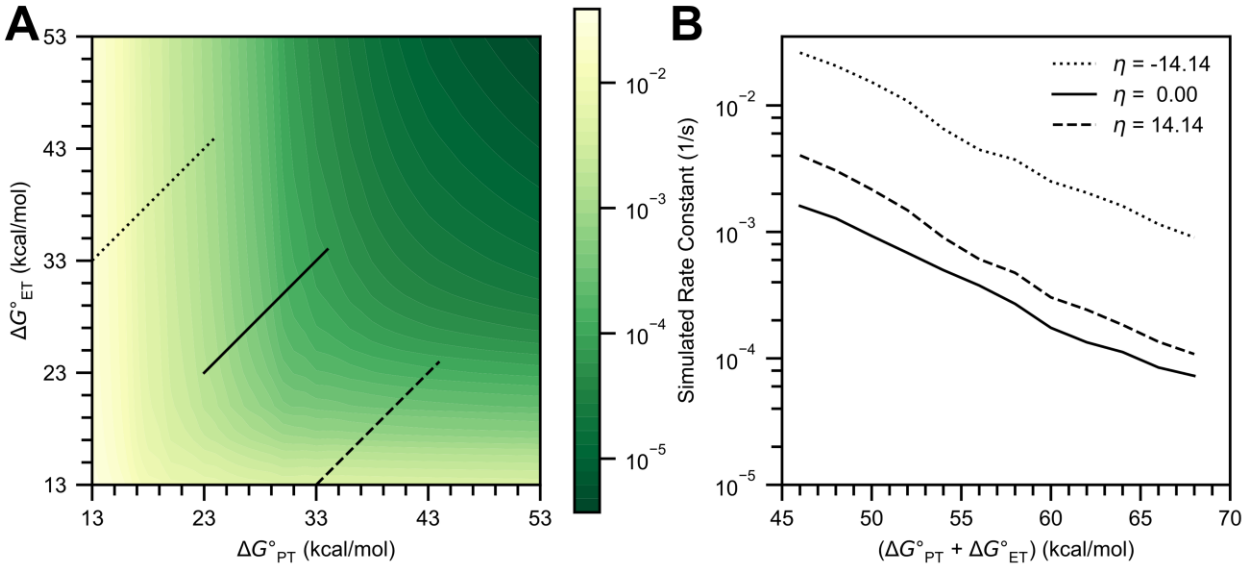

Figure 4.8 Simulated rate constants for endergonic CPET as a function of proton and electron transfer energetics. $\Delta G°_{CPET}$ is fixed at +6 kcal/mol. (A) The effect of both $\Delta G°_{PT}$ and $\Delta G°_{ET}$ on the simulated rate constant (1/s) which is shown from green to yellow according to the sidebar. The lines illustrate cross-sections which are plotted in (B). (B) Plot of simulated rate constants versus $\Delta G°_{PT} + \Delta G°_{ET}$ for $\Delta G°_{PT} > \Delta G°_{ET}$ (dashed line), $\Delta G°_{PT} = \Delta G°_{ET}$ (solid line), and $\Delta G°_{PT} < \Delta G°_{ET}$ (dotted line). The same lines in (A) show the *x*-axis for each cross section. Simulated rate constants are plotted on a logarithmic scale.

This asymmetry in the dependence on η may be of broad relevance to selectivity and optimal reactivity in C–H activation. For instance, compound I in cytochrome P450 performs uphill reactivity and has been found to be quite basic.[28,68,250] It is possible that a lower $\Delta G°_{PT}$ is beneficial for high rates in this system outside of its contribution to $\Delta G°_{CPET}$. Important roles for the high basicity of P450 enzymes have been invoked previously, but primarily as a thermodynamic component of $\Delta G°_{CPET}$ which prevents deleterious oxidation reactivity.[68,250] Our results indicate there is a distinct kinetic benefit to utilizing a highly basic oxo complex in uphill C–H activation.

5. Conclusions

The hypothesis which prompted this study was that imbalanced transition states can manifest in a nonadiabatic reaction through the effect that stepwise thermodynamic energies have on the anharmonicity of proton energy wells. A more anharmonic energy well will lead to increased delocalization of the proton across the reaction coordinate. Our DFT calculations support that this is the predominant mechanism by which ΔG°_{PT} affects the C–H activation of **CoO**; we do not observe a strong effect of $\Delta G°_{PT}$ on the optimal compression energy $U(R^*)$. We use these DFT studies to parameterize energy wells as a function of $\Delta G°_{PT}$ and $\Delta G°_{ET}$ for a general CPET reaction, and then simulate how CPET reaction rates vary with $\Delta G°_{PT}$ and $\Delta G°_{ET}$ when all other facets of the reaction are fixed. These simulations demonstrate that stepwise free energies can have a substantial effect on the rate constants of nonadiabatic reactions. Simulated rates reproduce experimental rate dependencies on the sum of $\Delta G°_{PT}$ and $\Delta G°_{ET}$ as well as previously reported dependencies on η, all within a nonadiabatic framework. Furthermore, this model not only supports previous studies, but it also makes new predictions about how spontaneity of the reaction affects the relative influences of $\Delta G°_{PT}$ and $\Delta G°_{ET}$. These results reconcile the semiclassical predictions and explanations of imbalanced transition states within a nonadiabatic context and motivate a deeper inspection of the importance of stepwise thermodynamic effects as a design principle.

6. Methodology

We calculated CPET rate constants for the oxidation of C–H bonds by **CoO** using a method modified from that of Hammes-Schiffer and coworkers.[60,216] We optimized minimum energy crossing points (MECPs) for electron-proton tunneling under the assumption that all reactivity occurs on the singlet spin surface.[251] Restricted Kohn-Sham DFT was used to estimate the energy

of reactants (singlet **CoO** and C–H substrate) and broken symmetry DFT was used to estimate the energy of the products (doublet **CoOH** antiferromagnetically coupled to carbon radicals).[170,174,252,253] To vary the tunneling distance, a force was applied between the carbon donor and oxo acceptor in the direction of proton tunneling. We then used the energies at the optimized geometries to calculate the energy of compressing to a given tunneling distance $U(R)$, to estimate the reorganization energy, and to scan the proton coordinate for reactant and product energy wells. Reactant energy wells were fit to quartic polynomials. Because the broken symmetry solution could not be converged across the entire reaction coordinate, we used a Morse potential to extrapolate product energy wells. We used these energy wells to determine 1D approximations to the transferring proton's reactant and product vibrational wavefunctions and calculated CPET rate constants.[216,218] An adiabatic tunneling penalty was applied to the population of any reactant vibrational states found localized on the reactant to avoid assuming rapid equilibrium with localized proton transfer states, as is consistent with the concerted reactivity observed experimentally. Model system rate constants were determined similarly, with the energy wells determined from regressing quartic coefficients of the fits to DFT-calculated energy wells to $\Delta G°_{PT}$ $-½\ \Delta G°_{CPET}$ and the tunneling distance.

Optimization of Minimum Energy Crossing Points

Minimum energy crossing points (MECPs) were calculated using the scheme of Harvey *et al.*,[251] implemented in python and using ORCA 4.2 as an external geometry optimizer.[170,252] Each geometry optimization cycle the external optimizer passes new atomic coordinates to the python script. These consist of a shared set of coordinates for heavy atoms and non-transferring protons, coordinates for the reactant proton, and coordinates for the product proton. The script then runs

ORCA 5.0.0 to calculate single point energies (E) and gradients (J) for both the reactant and the product at the given atomic coordinates. The python script uses these energies and gradients to derive an overall energy and gradient to pass back to the geometry optimizer. First, sum (Σ) and differences (Δ) of the reactant state (Rxt) and product state (Prd) are constructed:

Equation 4.7 $$E_{\Sigma} = \frac{1}{2}(E_{Rxt} + E_{Prd})$$

Equation 4.8 $$E_{\Delta} = \frac{1}{2}(E_{Rxt} - E_{Prd})$$

Equation 4.9 $$J_{\Sigma} = \frac{1}{2}(J_{Rxt} + J_{Prd})$$

Equation 4.10 $$J_{\Delta} = \frac{1}{2}(J_{Rxt} - J_{Prd})$$

The difference gradient J_{Δ} is then set to zero for indices corresponding to the reactant proton or reactant hydrogen, and the total energy and gradient are determined as follows:

Equation 4.11 $$\sigma = \frac{J_{\Sigma} \cdot J_{\Delta}}{J_{\Delta} \cdot J_{\Delta}} - \frac{E_{\Delta}}{C}$$

Equation 4.12 $$\sigma_J \approx -\frac{J_{\Delta}}{C}$$

Equation 4.13 $$E_{Tot} = E_{\Sigma} - \sigma E_{\Delta}$$

Equation 4.14 $$J_{Tot} = J_{\Sigma} - \sigma J_{\Delta} - \sigma_J E_{\Delta}$$

In these formula σ is a modified Lagrange multiplier; if $E_{\Delta} = 0$ then the first term of Equation 4.11 will project out any force on the atoms which would cause the reactant energy and product energy to differ. However, if E_{Δ} is nonzero then the other term in Equation 4.11 acts as a

penalty which reintroduces J_{Δ} into J_{Tot} such that the energies of the reactant and product state are brought nearer to each other. C is a scaling factor needed because σ is unitless; we found that $C = 0.1$ Hartree works well.

This procedure allowed us to optimize geometries under the constraint of two vibronic states having the same energy (assuming similar vibrational energies), but CPET reactions typically occur at a distribution of compressed tunneling distances. This means reorganized geometries must also be optimized at a range of constrained tunneling distances. We did this by adding to both J_{Rxt} and J_{Prd} an external force pushing the proton donor and proton acceptor closer to each other. This force was applied in a direction parallel to the vector between the transferring proton's positions in the reactant and in the product, i.e. the tunneling direction. This is equivalent to constraining the relative positions of the donor and acceptor atoms, but because the force is parallel to the tunneling direction and not the vector from donor atom to acceptor atoms it is not the equivalent of constraining a specific distance between the donor and acceptor. By applying forces of differing magnitudes, we were able to calculate reorganized geometries at different tunneling distances.

7. Estimation of Reorganization and Reaction Free Energies

Free energies of reactants, products, and reorganized complexes were determined in ORCA 5.0.0 using TPSS0, the D3BJ dispersion correction, and the quasi-QRRHO method of Grimme with a standard concentration of 1 M.[174,252,253] For MECPs, this was done using the total hessian:

Equation 4.15 $$H_{Tot} = \frac{1}{2}\left(H_{rxt} + H_{prd} - 350 * (J_{Prd} - J_{Rxt})(J_{Prd} - J_{Rxt})^{T}\right)$$

Where Hs are hessians and Js are gradients. This formulation is based on an arbitrarily small coupling of ½ cm^{-1} between a reactant energy product energy, leading to a saddle point in the direction of $(J_{Prd} - J_{Rxt})$. This allowed an estimation of the reorganization energy by inverting Marcus's formula for the activation energy based on a reorganization energy and reaction free energy:

Equation 4.16 $$\Delta G^{\ddagger}_{\mathrm{Reorg}} = G_{\mathrm{MECP}} - G_{\mathrm{Rxt}}$$

Equation 4.17 $$\Delta G^{\mathrm{Calc}}_{\mathrm{Rxn}} = G_{\mathrm{Prd}} - G_{\mathrm{Rxt}}$$

Equation 4.18 $$\lambda = -\Delta \mathrm{G}^{\mathrm{Calc}}_{\mathrm{Rxn}} + 2\Delta G^{\ddagger}_{\mathrm{Reorg}} + \sqrt{4\Delta \mathrm{G}^{\ddagger}_{\mathrm{Reorg}}{}^{2} - 4 * \Delta \mathrm{G}^{\mathrm{Calc}}_{\mathrm{Rxn}} \Delta G^{\ddagger}_{\mathrm{Reorg}}}$$

The estimates of *G* for reorganized complexes could not include the transferring hydrogen atom, so for consistency this atom was excluded for all ΔG in Equation 4.18. Estimates of the reaction free energy in other contexts included this atom.

It was necessary to use a functional with high amounts of Hartree-Fock exchange in order to stabilize the broken symmetry surfaces used to represent the products. However, a side effect of this large amount of Hartree-Fock exchange is an overstabilization of higher spin cobalt centers in the products as compared to the reactants. Because this biases the reaction free energy to more negative values, it needs to be corrected for in the calculation of CPET rate constants.

The thermodynamic (free) energies relevant to the reaction between **CoO** and fluorene are given in Table 4.1. It is found that the functional used for our calculations, TPSS0, underestimates the value of $\Delta G°_{\mathrm{CPET}}$ by about 15.7 kcal/mol. Appling this correction to the electronic energy

ΔE_{CPET} gives an estimated electronic energy of -3.7 kcal/mol for the reaction. This value applies for the energy from the product's singlet ground state to reactant's quartet ground state. However, by calculating the reaction entirely as a singlet we also need to find a correction to the lower spin doublet state for the reactant. A comparison between the electronic energy differences determined with TPSS0 and those determined with either O3LYP or M06L suggests that TPSS0 overstabilizes doublet products half as much as it overstabilizes quartet products. We therefore used a correction factor of 7.9 kcal/mol for the free energies used to calculate singlet manifold CPET rate constants.

Equation 4.19 $$\Delta G^{\circ}_{\text{Rxn}} = G_{\text{Rxt}} - G_{\text{Prd}} + 7.9\,\frac{kcal}{mol}$$

Table 4.1 Thermodynamic Parameters for Reactivity between **CoO** and fluorene.

	$\Delta G^{\circ}_{\text{CPET}}{}^{a}$	$\Delta E_{\text{CPET}}{}^{b}$	$\Delta^{1}E_{\text{CPET}}{}^{c}$
TPSS0	−23.7	−19.4	−4.1
O3LYP		+2.0	+5.6
M06L		−0.1	+5.4
Experiment	−8.0[d]		
Best Estimate	−8.0	−3.7	+3.8

All energies in kcal/mol and all geometries optimized with TPSS0. [a]Free energy difference between reactants and products. [b]Electronic energy difference between reactants and product ground states (singlet to quartet). [c]Electronic energy difference restrained to a singlet manifold, i.e. of the reactant singlet to the product singlet. [d]Experimental difference in the BDFEs of **CoOH** and fluorene.[23,50,66]

8. Calculation of Rate Constants

Our calculated rate constants are based on a procedure from Sayfutyarova and coworkers.[60,216] At a given tunneling distance R, a rate is calculated as:

Equation 4.20 $$k_R = \frac{1}{\sum_{\mu} P_{\mu}} \sqrt{\frac{\pi}{\lambda k_B T}} \sum_{\mu,\nu} P_{\mu} \frac{\left|S_{\mu\nu} V_{el}\right|^2}{\hbar} \exp\left(-\frac{\left(\Delta G^{\circ}_{\text{Rxn}} + E_{\mu} - E_{\nu} + \lambda\right)^2}{4\lambda k_B T}\right)$$

P_μ is the (unnormalized) population of the reactant state μ, $S_{\mu\nu}$ is the overlap integral between reactant state μ and product state ν, $\Delta G^\circ_{\mathrm{Rxn}}$ is reaction free energy on the singlet surface calculated as described above, $E_\mu - E_\nu$ is and adjustment to the reaction energy based on the vibrational energy of the reactant and product states, and λ is the reorganization energy calculated as described above. The electronic coupling V_{el} is difficult to calculate, but under the standard assumption that it does not vary then only causes a level shift. Therefore, its value does not affect relative rates or KIE estimates. We implicitly set it to 1 kcal/mol, or 350 cm^{-1}. In our theoretical model calculations, we subtracted the reactant zero-point energy from E_μ and the product zero-point energy from E_ν in order to maintain a fixed $\Delta G^\circ_{\mathrm{CPET}}$ (the contribution of higher vibrational states on the overall enthalpy and entropy is negligible).

The weighting factor P_μ is typically the thermal Boltzmann population of the vibrational energy level. However, the double well feature of reactant energy wells at longer tunneling distances means this formulation implicitly assumes fast establishment of PT equilibria. This led to a substantial amount of calculated reactivity occurring through a stepwise mechanism, evidenced by reactivity at long tunneling distances and inverse KIEs. This is inconsistent with experiment, and to avoid this stepwise reactivity we had to suppress the extent of PT equilibria at reorganized complexes. We used the WKB approximation to estimate an adiabatic tunneling correction to the Boltzmann population:

Equation 4.21 $$P_\mu = \exp\left(-\frac{E_\mu}{k_B T}\right) * \exp\left(-\frac{2}{\hbar}\int_{x_1}^{x_2}\sqrt{4(V_{rxt}(x) - E_\mu)}dx\right)$$

with $V_{rxt}(x)$ being the value of the reactant energy surface at the x-value, and the integration being carried out for the classically forbidden region with $E_\mu < V_{rxt}(X)$. This correction was only applied to vibrational states for which (1) the proton is most likely located past a maximum in the reactant energy well and (2) the vibrational energy is less than this maximum energy. When no correction was necessary, then P_μ was taken just as the Boltzmann population $\exp\left(-\frac{E_\mu}{k_B T}\right)$. While heuristic, this is an automated, objective measure by which we can limit the formation of a proton-transfer equilibria and thereby calculate the experimentally determined mechanism.

For the total rate constant, these k_R need to be averaged across different tunnelling distances, with each tunneling distance weighted by its thermal population based. This thermal population is determined by the "compression energy" $U(R)$, the electronic energy difference between the reorganized geometry constrained to a tunneling distance R and the MECP without the tunneling distance constraint. To ensure the same similar integration range for all substrates, we first regressed both $U(R)$ and $\ln k(R)$ as a function of R:

Equation 4.22 $$U(R) = \frac{A_U}{R^2} + \frac{B_U}{R} + C_U$$

Equation 4.23 $$\ln k(R) = A_k R^2 + B_k R + C_k$$

We then performed the weighted averaging of $k(R)$ to get a total rate constant:

Equation 4.24 $$k_{Tot} = \frac{\int_{0.5}^{1.2} \exp\left(-\frac{U(R)}{kT} + \ln\, k(R)\right) dR}{\int_{0.5}^{1.5} \exp\left(-\frac{U(R)}{kT}\right) dR}$$

The integration bounds were chosen based off inspection of where $\exp\left(-\frac{U(R)}{kT}+\ln\ k(R)\right)$ became insignificant for all substrates. While this normalization ignores the probability of long tunneling distances with no reactivity, we assume the odds of such a configuration to be similar for all substrates and therefore this neglect is only a level shift in calculated rates.

Chapter 5: Design of a New Ligand Scaffold Capable of Supporting Highly Oxidizing Transition Metal Complexes

Adapted with permission from Scott, J. S.; Schneider, J. E.; Tewelde, E. G.; Gardner, J. G.; Anferov, S. W.; Filatov, A. S.; Anderson, J. S. *Inorg Chem.*, **2023**, *62*(51), 21224-21232.

1. Introduction

A hallmark of enzymatic C–H activation is functionalization of strong aliphatic C–H bonds, including those in simple alkanes and even methane.[29,254–257] Synthetic systems have provided detailed insight into the nuances of transition metal mediated C–H oxygenation, but isolable complexes are rarely capable of oxidizing substrates with strong C–H bonds. Cases where such bond functionalization is possible typically involve oxidizing intermediates which are often identified indirectly, such as through calculations or stereoselectivity patterns,[33,34,161,239] or are limited to oxidation of C–H bonds on the ligand scaffold.[221,223,258,259]

The tetravalent cobalt(IV)-oxo complex shown in Scheme 5.1A is one of the better characterized examples of a synthetic transition metal-oxo complexes which is capable of cleaving unactivated C–H bonds.[259] This complex is capable of functionalizing an unactivated sp^3 bond on the flanking adamantyl group. It has a comparably low oxidation potential, so the driving force for this C–H activation is dependent on the basicity of the reduced cobalt(III)-oxo complex. Additionally, the C–H bond activation is slightly uphill – subsequent rebound of the cobalt(III)-hydroxide onto the organic radical is necessary for overall downhill reactivity. Despite the mild thermodynamic driving force for C–H activation, it occurs rapidly, even at low temperatures. As a

result, this cobalt(IV)-complex cannot be used to study model aliphatic C–H bond oxidation in general.

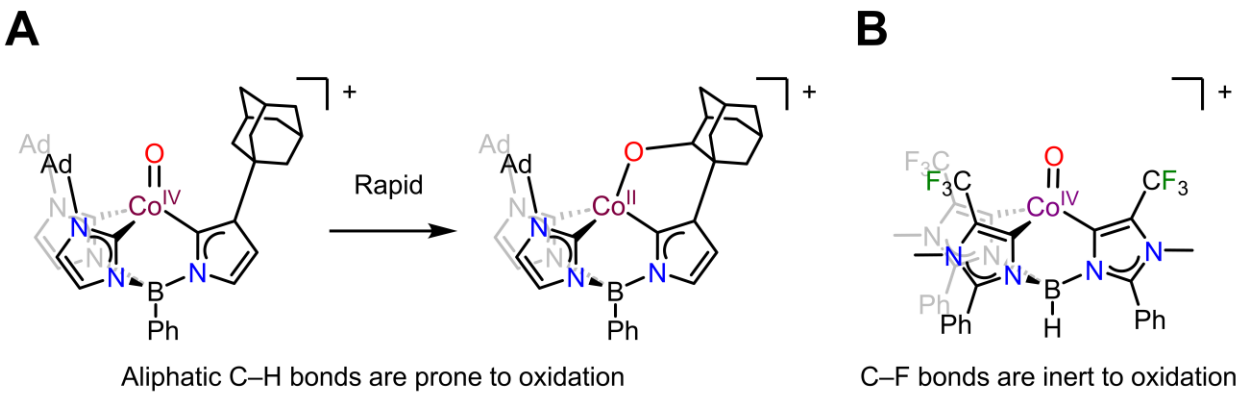

Scheme 5.1 The problem of ligand degradation and our design to address it. (A) Known decay of a cobalt(IV)-oxo *via* the activation of a strong C–H bond on a flanking adamantyl group. (B) The ligand scaffold introduced in this chapter. The trifluoromethyl groups are resistant to oxidation and the imiadol-5-ylidene donor arms ensures ligand strength.

Such ligand oxidation is a common decay pathway for highly oxidizing species – most of the ligand platforms used in synthetic inorganic chemistry are not stable to oxidation.[221,223,258,259] The isolation and direct comparison of highly oxidizing complexes will require new ligand scaffolds which are stable to the compounds they are meant to support.[260] In particular, the cobalt(IV) oxo complex shown in Scheme 5.1A has thermodynamic parameters are similar to those for compound I in cytochrome P450 enzymes, the workhorses of enzymatic C–H oxygenation.[28,68,261] It would be desirable to retain these thermodynamic parameters while modifying the ligand to be more oxidatively robust.

A known strategy for increasing the oxidative stability of ligand platforms is to replace C–H bonds with C–F bonds. Ligands with perfluorinated alkyl groups are known to support oxidatively robust coordination complexes.[262–268] The same ligands are also relatively weak

donors because perfluoroalkyl groups are potent electron withdrawing groups. For this reason, substitution of perfluoroalkyl groups is not an "innocent" means of increasing a transition metal complex's oxidative stability; it will also profoundly influence the electronic structure of complex.

We wished to generate a ligand with flanking perfluoroalkyl groups that retained the electronic properties of the tris(imidazol-2-ylidene)borate ligands which are known to stabilize cobalt-oxo complexes.[14,259] We sought to offset the electron-withdrawing nature of a perfluoroalkyl flanking group by using a framework consisting of mesoionic carbene ligands, as such ligands are known to be powerful sigma donors.[269,270] To this end, we synthesized a new scorpionate ligand with imidazol-5-ylidene donor arms (Scheme 5.1B). Formation of a $\{NiNO\}^{10}$ complex and measurement of the ν_{NO} stretching frequency confirms that this ligand retains strong donor properties. This new ligand supports a cobalt(II)-chloride complex which forms a stable adduct with dioxygen, a rare side-on cobalt(III)-superoxide complex. Dimerization of this dioxygen adduct with another equivalent of cobalt(II)-chloride forms an unprecedented dicobalt(IV)-bis-μ-oxo diamond core with exceptional stability.

2. Synthesis and Metalation of a new perfluorinated ligand

Synthesis of our new ligand is given in Scheme 5.2A. The trifluoromethylated ligand arm is synthesized using an *in situ* generated trifluoromethylated iodoxy reagent following a modified literature procedure.[271] The proligand $[HB(^{CF3,Ph}m\text{ImH})_3](OTf)_2$ is then assembled using standard substitution chemistry with $HBBr_2{\bullet}SMe_2$ and TMSOTf, employing conditions similar to those previously used to synthesize imidazolyl scorpionate proligands.[272] Assembly was verified by multinuclear NMR spectroscopy and elemental analysis. NMR spectroscopy highlights the compound's trigonal symmetry, and its ^{1}H NMR spectrum features a downfield resonance at δ 7.88

ppm which can be assigned to the comparatively acidic imidazolium protons. The $^{1}J_{CH}$ of this proton is 205 Hz, suggesting that its corresponding tris(carbene)borate should be similarly donating to PhB(^{Ad}Im)$_3^-$ ($^{1}J_{CH}$ = 217 Hz).[270,273]

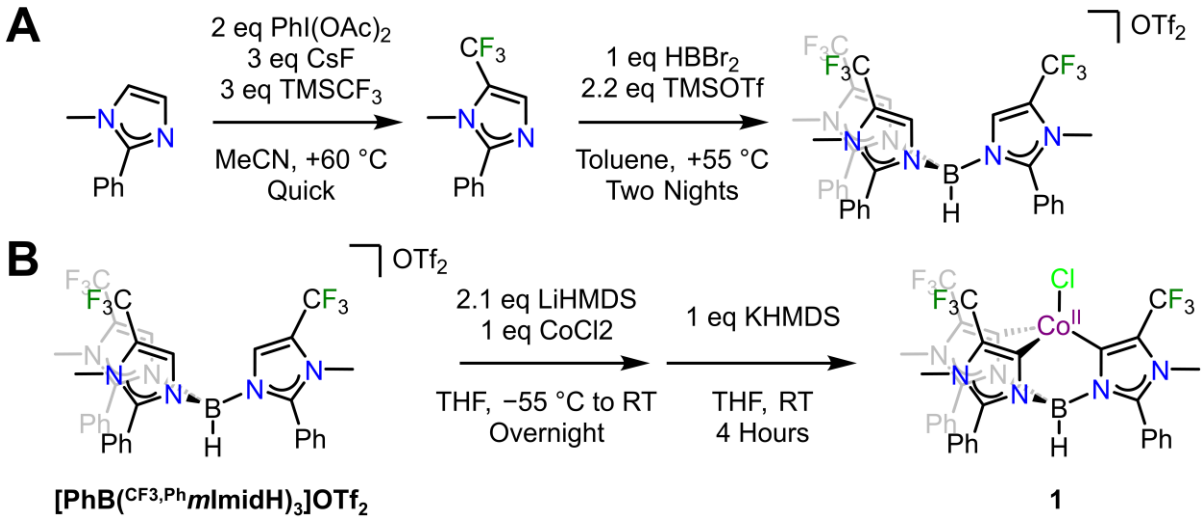

Scheme 5.2 Overview of the synthesis and metalation of HB(^{CF3,Ph}*m*ImH)$_3$](OTf)$_2$ (A) Synthesis of the proligand. (B) Two-step metalation with cobalt dichloride.

Addition of LiHMDS (HMDS = hexamethyldisilazide) to a chilled slurry of [HB(^{CF3,Ph}*m*ImH)$_3$](OTf)$_2$ in THF results in an orange-red solution. This deprotonated intermediate is temperature sensitive; solutions warmed above −35 °C turn dark reddish-brown. Similarly intense colors are observed with alternative bases such as KHMDS or lithium diisopropylamide (LDA), even at lower temperatures. The use of NaH also leads to mixtures of products (i.e. with free imidazole arm). The instability of this proposed deprotonated intermediate contrasts with previously reported tris(carbene)borates, many of which are deprotonated with LDA and can be observed by NMR at room temperature.[269,272,274]

Despite this instability, [HB(^{CF3,Ph}*m*ImH)$_3$](OTf)$_2$ can be effectively deprotonated and metalated *via* a two-step procedure (Scheme 5.2B). A slurry of the proligand and 2.1 equivalents

of LiHMDS in THF is stirred at −55 °C for fifteen minutes, then 1.0 equivalents of cobalt dichloride is added and the reaction is allowed to stir at room temperature overnight. A blue precipitate is collected from this reaction by filtration; this precipitate has not been fully characterized but is believed to be [Co^{II}(κ^2- HB(^{CF3,Ph}*m*Im)$_3$H)Cl_2], with two-arms bound to the cobalt center and one-arm protonated. This initial product is formed even in the presence of three or more equivalents of LiHMDS. Stirring a slurry of this blue precipitate with one equivalent KHMDS in THF at room temperature yields, after four hours, a blue precipitate with a distinct ^{1}H and ^{19}F NMR signals. This compound is identified as the tripodal complex [Co^{II}(HB(^{CF3,Ph}*m*Im)$_3$)Cl] (**1**) on the basis of multinuclear NMR spectroscopy, IR spectroscopy, elemental analysis, and SXRD.

A similar procedure was followed to metalate a {NiNO}^{10} complex. {NiNO}^{10} complexes are common vibrational reporters for the ligand strength of scorpionate ligands, so this complex enables an evaluation of our new ligand's donor strength compared to those of established ligand scaffolds.[269,272,275,276] We found that the ν_{NO} of [Ni(HB(^{CF3,Ph}*m*ImH)$_3$)(NO)] is 1,700 cm^{-1}. This places the donor strength of [HB(^{CF3,Ph}*m*Im)$_3$]$^-$ squarely within the range of typical tris(imidazol-2-ylide)borate ligands (1690-1725 cm^{-1}).[276] Thus, the extra donation gained *via* coordination at the 5-imidazoyl position perfectly balances out the electron withdrawing nature of the trifluoromethyl groups.

Our attempts to substitute the chloride ligand in **1** with a hydroxide ligand have been unsuccessful. This has prevented us from performing studies analogous to those with the ligand shown in Scheme 5.1A, as cobalt(II)-hydroxide complexes are the entry point into cobalt-oxygen chemistry with of tris(imidazol-2-ylidene) scorpionates.[14,259,274] However, we hoped that the low

steric bulk of the trifluoromethyl groups would enable us to instead contrast the chemistry of **1** to that of similar cobalt(I) complexes of tris(pyrazolyl)borate scorpionate ligands.[223,277] These complexes, and analogous copper(I) complexes,[221,222,229] are known to bind dioxygen and subsequently dimerize into bis-μ-oxo complexes. However, these dimers quickly degrade *via* ligand oxidation. As such, we targeted the analogous oxygen activation and dimerization chemistry with **1**.

We find that **1** forms a highly stable dioxygen adduct, the first crystallographically characterized side-on cobalt(III)-superoxide complex. Addition of a second equivalent of **1** and concomitant removal of the chloride ligands forms a remarkably stable dicobalt(IV)-bis-μ-oxo core. This is, to our knowledge, the first report of a isolable dicobalt(IV) complex. Its isolation is a potent demonstration of the oxidative stability of $[HB(^{CF3,Ph}m\text{Im})_3]^-$ and its ability to support highly oxidized transition metal complexes.

3. Formation and Characterization of a Dioxygen Adduct

Upon overnight exposure to dry O_2 **1** slowly turns from blue to brown (Scheme 5.3). The product of this reaction was identified as the side-on cobalt-superoxide complex $[Co^{III}(HB(^{CF3,Ph}m\text{Im})_3)Cl(\eta^2\text{-}O_2\cdot)]$ (**1-O₂**) by EPR spectroscopy, ^{1}H NMR spectroscopy, IR spectroscopy, elemental analysis, and SXRD. While **1-O₂** is silent by ^{19}F NMR spectroscopy, its ^{1}H NMR spectrum resolves a set of slightly broadened peaks indicative of a single major product. Solution X-band EPR spectroscopy at room temperature reveals an isotropic signal with $g = 2.03$ and 8-line hyperfine coupling of 32 MHz, consistent with an $S = ½$ species with a single cobalt center.

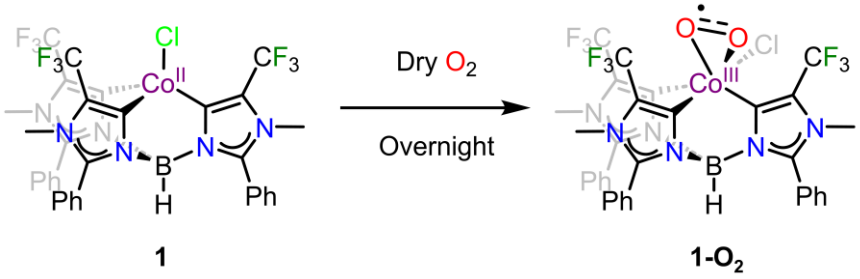

Scheme 5.3 Formation of a dioxygen adduct.

The side-on binding mode of the dioxygen moiety was confirmed by SXRD (Figure 5.1A). The observed O–O bond length of 1.38(1) Å seen in the structure of **1-O₂** is rather long for a superoxide complex, suggesting that a cobalt(IV)-peroxide may be a significant resonance contributor for this complex.[278] However, DFT-calculations clearly place 99% of the spin density on dioxygen unit, (as measured by Löwdin population analysis and visually shown in Figure 5.1B), which is more consistent with an entirely diamagnetic cobalt(III) center with a superoxide ligand. EPR spectroscopy also suggests that spin is localized onto the dioxygen unit. At room temperature the isotropic cobalt hyperfine coupling is 32 MHz (Figure A4.8A), which is similar to those seen for end-on cobalt(III)-superoxide complexes (Table 5.1).[259,278–281] The largest directional hyperfine component from a frozen solution measurement is 65 MHz (Figure A4.8B); this measure of hyperfine anisotropy, when compared to the spin-dipolar coupling of cobalt(II) complexes, indicates that there is at most 30% cobalt(IV) character.[280] Contraction of the *d*-orbitals upon oxidation from cobalt(II) to cobalt(IV) would be expected to increase the dipolar coupling, so this is likely a generous upper estimate.

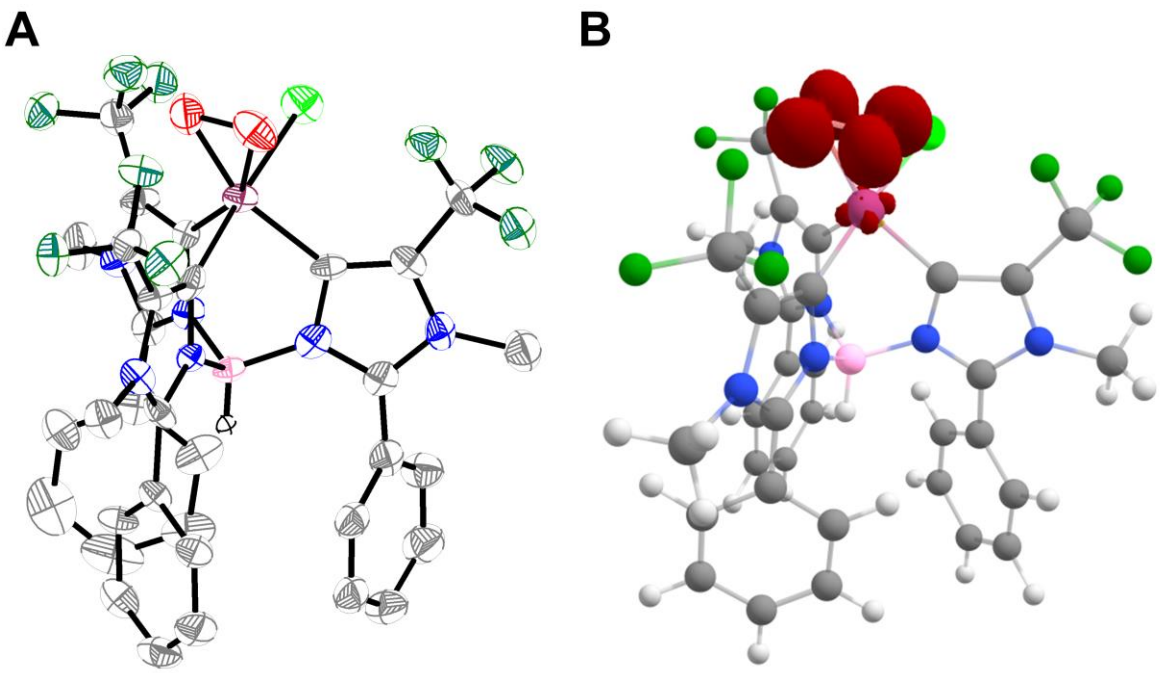

Figure 5.1 (A) ORTEP diagram of the structure of **1-O₂** as determined by SXRD. Selected bond lengths: O1–O2 = 1.38(1), Co1–O1 = 1.961(8), Co1–O2 = 1.922(8), Co1–Cl1 = 2.85(3); Co1–C1 = 1.955(1); Co1–C12 = 1.942(1), Co1–C23 1.962(1). (B) DFT-optimized structure with the SCF spin density shown at an isovalue of 0.01.

To further assess the strength of the O–O bond in **1-O₂** we turned to IR spectroscopy. The IR spectrum of **1-O₂** is highly congested in the region of interest due to the trifluoromethyl groups (Figure 5.2). However, upon isotopic labelling with $^{18}O_2$ there a peak at 1103 cm^{-1} disappears and a new peak appears ~40 cm^{-1} lower in frequency. This is within the range expected for the O–O vibrational frequency of a superoxide ligand.[278] Furthermore, we also observe a peak at 416 cm^{-1} which clearly redshifts ~5 cm^{-1} upon isotopic labelling with $^{18}O_2$; we assign these features to a Co–(O_2) stretch. The $^{16}O_2$–$^{18}O_2$ difference spectrum can be qualitatively reproduced by DFT calculations (Figure A4.9). The observed isotopic shifts are of a similar magnitude but slightly smaller than the ideal harmonic oscillator predictions of 60 cm^{-1} and 15 cm^{-1}, respectively, suggesting some degree of coupling to other vibrational features.

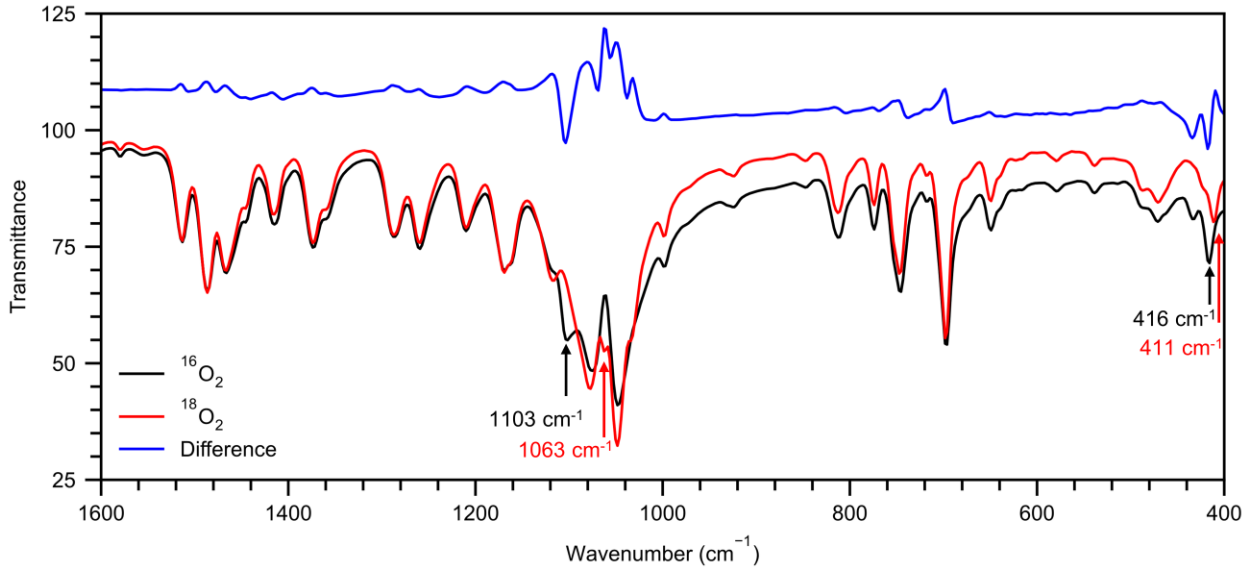

Figure 5.2 IR spectra of **1-$^{16}O_2$** and **1-$^{18}O_2$** (red) along with their difference (blue). Clear instances of peaks sensitive to the oxygen isotope are labeled.

Figure 5.3 graphically compares the O–O vibrational energy and bond length of **1-O_2** with other known transition metal-dioxygen adducts.[277,279,280,282–293] **1-O_2** has an O–O vibrational frequency much greater than that typical for peroxide complexes; this difference is more than can be reasonably attributed to coupling to other modes in the molecule. This clearly indicates an O–O bond order greater than 1 for **1-O_2**. Additionally, the O–O bond length, while long for a superoxide, is still shorter all but two cobalt(III)-peroxides O–O bond lengths. For both of these two exceptions, previous reports have suggested that the O–O bond length is artificially short due to librational motion.[284,294] Overall, the balance of evidence strongly supports the assignment of **1-O_2** as a side-on cobalt(III)-superoxide complex.

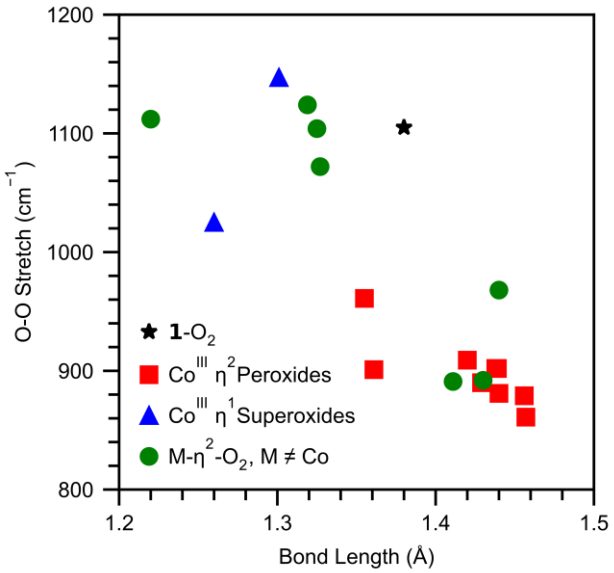

Figure 5.3 A comparison of O–O stretching frequencies and bond lengths for known cobalt-dioxygen adducts.

A side-on binding mode is unusual for a cobalt(III)-superoxide complex (see Table 5.1 for a representative list of similar cobalt-dioxygen adducts).[277,279,280,282–293] Previous reports of cobalt(III)-superoxide complexes are typically end-on. Conversely, there are several reports of side-on cobalt(III)-peroxides. This may partly be a function of coordination number – all but two complexes shown are 6-coordinate, with the two exceptions being 5-coordinate side-on cobalt(III)-peroxide complexes (the two with relatively short bond lengths for a peroxide). Thus, previous instances of cobalt(III)-superoxides may have simply lacked the extra coordination geometry needed to bind in a side-on fashion. Nonetheless, the absence of side-bound superoxide complexes represents an interesting gap in cobalt-dioxygen coordination chemistry which this work helps to fill.

Table 5.1 Comparison of selected cobalt(III)-superoxide and cobalt(III)-peroxide complexes.

	$\nu_{O\text{-}O}$	$L_{o\text{-}o}$	$a_{iso,Co}$	$A_{1,Co}$	Ref
$[Co^{III}(HB(^{CF3,Ph}m\text{Im})_3)Cl(\eta^2\text{-}O_2\cdot)]$ (**1**-O_2)	1105	1.38(1)	32	65	
$[Co^{III}(Tp^{iPr,Me})(\eta^2\text{-}O_2)]$	961	1.355(3)	N.A.	N.A.	277,294
$[Co^{III}(tmen)_2(\eta^2\text{-}O_2)]^+$	861[a]	1.457(3)	N.A.	N.A.	288
$[Co^{III}_2(CN)_4(PMe_2Ph)_5(\eta^2\text{-}O_2)]$	881[a]	1.44	N.A.	N.A.	286
$[Co^{III}(TBDAP)(\eta^2\text{-}O_2)]^+$	879	1.456(3)	N.A.	N.A.	283
$[Co^{III}(TIMEN^{xyl})Co(\eta^2\text{-}O_2)]^+$	890	1.429(3)	N.A.	N.A.	282
$[Co^{III}(2{=}phos)_2(\eta^2\text{-}O_2)]^+$	909[a]	1.42(1)	N.A.	N.A.	285
$[Co^{III}(NAcNAc^{Dipp,tBu})(\eta^2\text{-}O_2)]$	901	1.361(5)	N.A.	N.A.	284
$[Co^{III}(12\text{-}TMC)(\eta^2\text{-}O_2)]^+$	902	1.439(2)	N.A.	N.A.	287
$[Co^{III}(13\text{-}TMC)(\eta^2\text{-}O_2)]^+$	902	1.438(4)	N.A.	N.A.	287
$[Co^{III}(Tp^{me2})(L^{Ph})(\eta^1\text{-}O_2\cdot)]$	1147	1.301(5)	N.R.	49	290
$[Co^{III}(acacen)(py)(\eta^1\text{-}O_2\cdot)]$	1025	1.26(4)[b]	39	57	280,291,293
$[Co^{III}(acacen)(\eta^1\text{-}O_2\cdot)]$	1146	N.R.	38	N.R.	280,291
$[Co^{III}(BDPP)(\eta^1\text{-}O_2\cdot)]$	1135	N.R.	N.R.	54	289
$[Co^{III}(salen)(\eta^1\text{-}O_2\cdot)]$	1144	N.R.	37	52	279,292

Headers are, respectively, the O–O stretching frequency $\nu_{O\text{-}O}$ (cm^{-1}), the O–O bond length $L_{O\text{-}O}$ (Å), the isotropic hyperfine coupling to cobalt (MHz), the maximum component of the anisotropic hyperfine coupling to cobalt (MHz), and the reference. N.A. = Not Appropriate, N.R. = Not Reported. [a]Not confirmed by isotopic labelling. [b]Determined for the bzacen in place of acacen.

Superoxide complexes are known to react with H-atom donors, including stronger O–H and C–H donors such as phenols and 9,10-dihydroanthracene.[289,290,295–297] However, **1-O_2** has distinctly muted reactivity in this context. It shows signs of reactivity with TEMPOH, an H-atom donor with a low O–H bond strength; however, this reaction does not go to completion (**Figure 5.4**). This supports a BDE of approximately 70 kcal/mol for the O–H bond in a putative **1-O_2H** hydroperoxide complex.[298] For contrast, hydrogen peroxide has a BDE of ~ 90 kcal/mol.

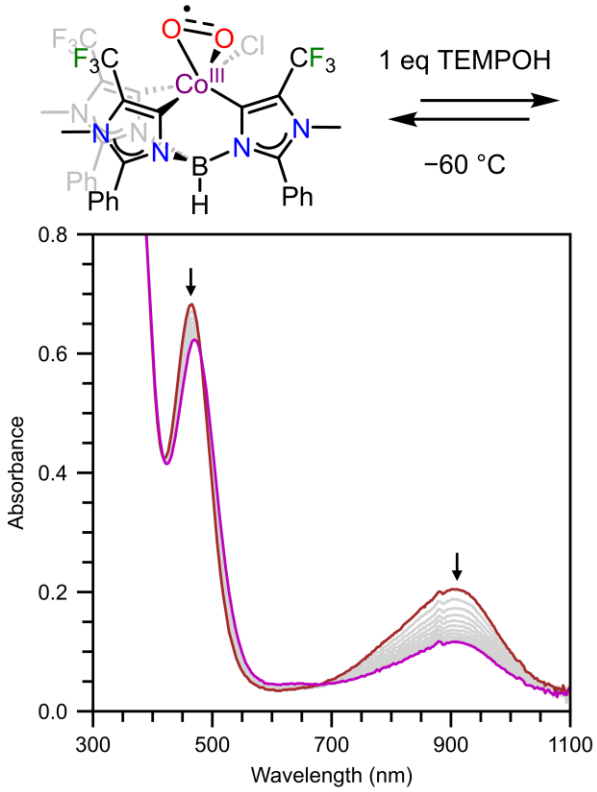

Figure 5.4 Incomplete reactivity between **1-O2** and TEMPOH.

4. Dimerization Studies

Slow addition of **1** co-solubilized in d_2-DCM with 2 equivalents of $NaBAr^F$ ($NaBAr^F{}_4$ = sodium tetrakis(3,5-bistrifluoromethylphenyl)borate) to a chilled solution of **1-O2** in d_2-DCM generates a deep green solution (Scheme 5.4). We have identified this product as an unprecedented dicobalt(IV)-bis-μ-oxo diamond core through SXRD structure determination and XAS spectroscopy.

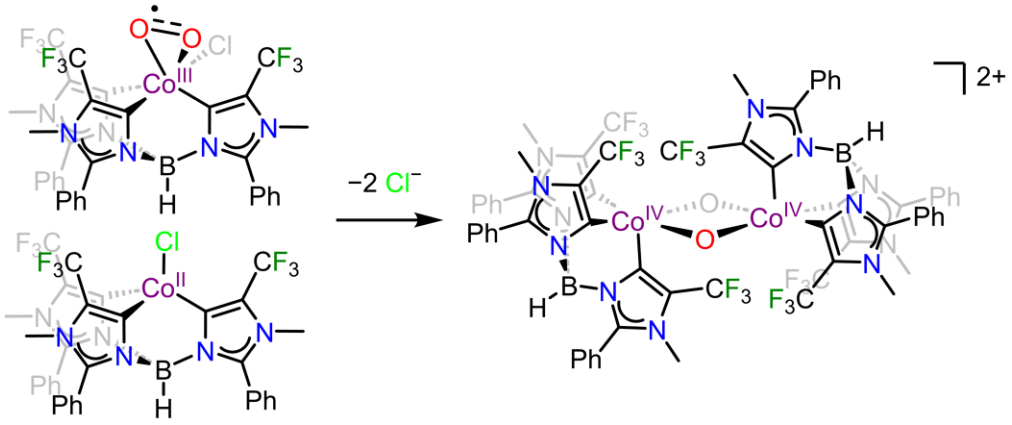

1-O₂ + 1 **2**

Scheme 5.4 Dimerization of **1** and **1-O₂** to generate the bis-μ-oxo complex **2**.

The reaction between **2** and four equivalents of 2,4-bis(*tert*-butyl)phenol, as monitored by NMR spectroscopy, cleanly generates the dicobalt(III)-bis-hydroxo complex **2-H₂** as the sole diamagnetic product (Scheme 5.5). Integration of both ^{1}H and ^{19}F{^{1}H} spectroscopic signals indicates that this product is formed in ~50% yield relative to the [BAr^{F}]$^{-}$ counteranion; while this may represent a low initial yield of **2**, the lack of any other identifiable products by NMR spectroscopy indicates it may optimistically be interpreted as a lower bound.

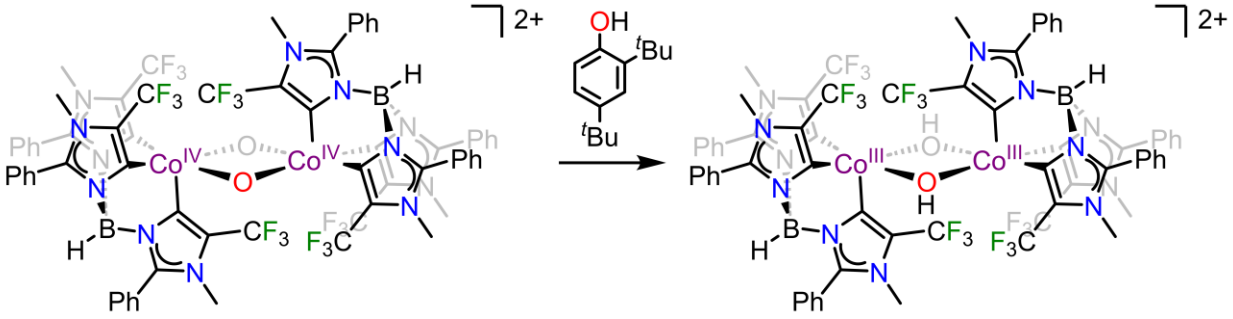

2 **2-H₂**

Scheme 5.5 Reduction of dicobalt(IV) complex **2** to the dicobalt(III) complex **2-H₂**.

The structures of **2** and **2-H₂** were elucidated by ^{1}H NMR spectroscopy. Both complexes consist of two square-pyramidal cobalt centers, with a crystallographic inversion center in the

center of the diamond core. The dicobalt(III) complex has an average Co–O bond lengths of 1.884(3) A and a Co–Co distance of 2.980(1) A. These are significantly longer than the analogous distances in the dicobalt(IV) complex, which has an average Co–O length of 1.84(2) A and a Co–Co distance of 2.6801(8) A, indicative of a more highly oxidized core. The presence of one $[BAr^F]^-$ counteranion per cobalt indicates both dimers are dicationic.

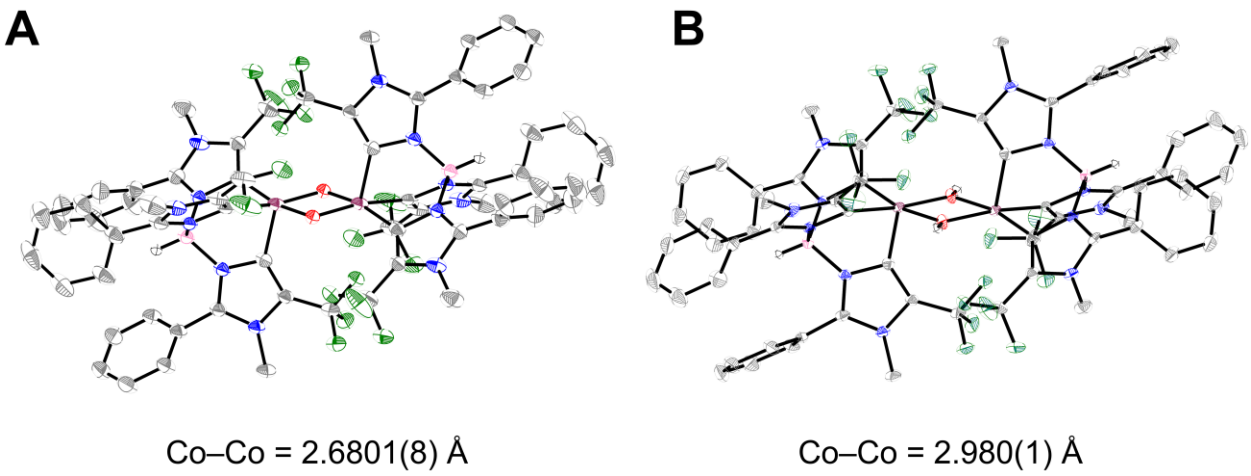

Figure 5.5 Structures of the diamond core complexes. Hydrogens bound to carbon, cocrystallized solvent, and $[BAr^F]^-$ counteranions are omitted for clarity. (A) Dicobalt(IV)-bis-μ-oxo. Co1–Co1 = 2.6801(8), Co1–O1 = 1.832(2), Co1–O1 = 1.836(2), Co1–C1 = 1.926(3); Co1–C12 = 1.976(3) 1.974(3); Co1–C23 = 1.974(3). The cobalt centers are equivalent by inversion symmetry and C1 is located on the axial carbene. (B) Dicobalt(III)-bis-μ-hydroxo. Co1–Co1 = 2.980(1), Co1–O1 = 1.885(3), Co1–O1 = 1.892(3), Co1–C1 = 1.920(4); Co1–C12 = 1.888(4); Co1–C23 = 1.948(4). The cobalt centers are equivalent by inversion symmetry and C12 is located on the axial carbene.

The reactivity between **2** and 2,4-bis(*tert*-butyl)phenol demonstrates that **2** is capable of H-atom abstraction reactions. However, reactivity with dihydroanthracene (DHA) is more sluggish than what may be expected of an oxygenated dicobalt(IV) complex. Similar dicobalt and diiron diamond core complexes are known to open and become much more reactive in the presence of additional ligands,[299,300] and while **2** degrades appreciably quickly in the presence of excess chloride there is no evidence for anthracene formation under these conditions. While further studies on the C–H reactivity of **2** are needed, a viable hypothesis from available data is that

without the diamond core is too shielded by trifluoromethyl groups to rapidly react with substrates in solution. Upon being opened by excess chloride ligands, the subsequent complex rapidly reacts with solvent in favor of the less available dihydroanthracene.

This assignment of **2** as an unprecedented dicobalt(IV)-bis-μ-oxo is supported by recently collected X-ray absorption spectroscopy (XAS). There is a clear ~1 eV shift in the edge energy upon the formation of the dioxygen adduct **1-O$_2$**, and another ~1 eV shift in the edge energy upon dimerization to form **2** (Figure 5.6). This clearly supports further oxidation of the cobalt center beyond the cobalt(III) oxidation state found in **1-O$_2$**.

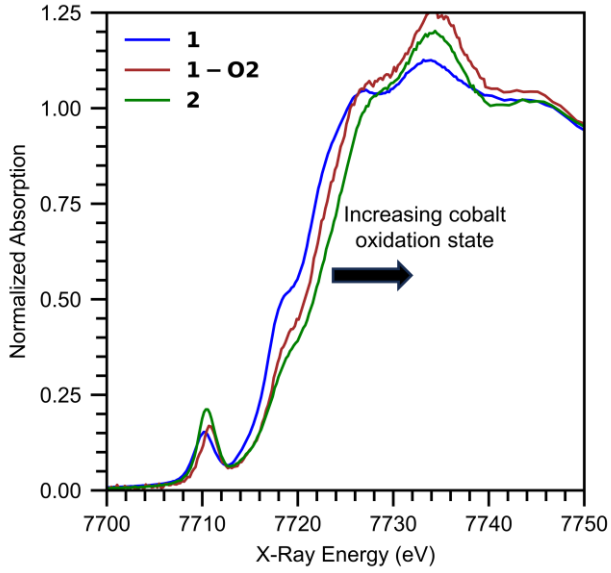

Figure 5.6 Cobalt K-edge spectra of **1**, **1-O$_2$**, and **2**.

Additionally, preliminary fitting of the extended X-ray absorption fine structure (EXAFS) spectrum of **2** supports the formation of a diamond core complex with a short Co–Co bond distance (Figure 5.7). We can fit the inner shell as five Co–C/O scatters at an average distance of 1.91 Å, three second sphere Co–C scatters to 2.84 Å, and one Co–Co scatter at 2.60 Å. This fit is satisfyingly close to the initial Co–Co distance observed crystallographically. Furthermore, it is

consistent with Co–Co distances seen in other reports of dicobalt complexes.[301,302] Overall, the XAS data strongly supports that dimerization forms a dicobalt species with a higher oxidation state than cobalt(III), consistent with our formulation of **2** as a dicobalt(IV)-bis-μ-oxo complex.

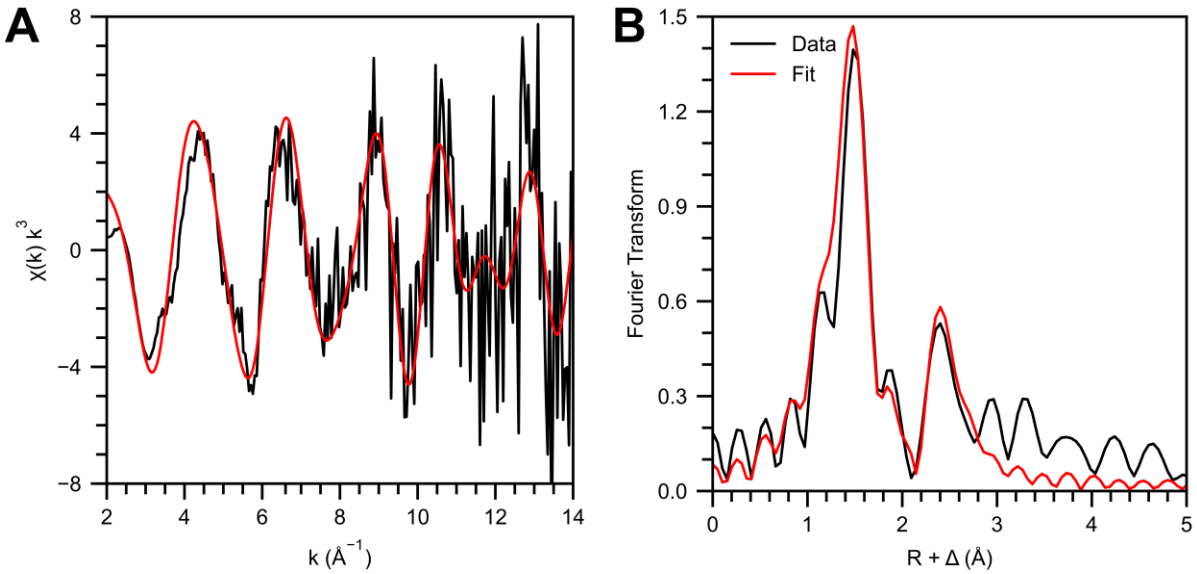

Figure 5.7 EXAFS Spectrum of **2**. (A) *k*-space data weighted by k^3 with fit (B) Fourier transform with fit.

The apparent stability of **2** stands out in marked contrast to the dicobalt(III)-bis-μ-oxo complexes formed from the analogous activation of oxygen by cobalt(I) tris(pyrazolyl)borate complexes.[223] More generally, there only a handful of cobalt-μ-oxo clusters which contain a single cobalt(IV) ion, and no precedent for isolated dicobalt(IV) clusters.[301,303] Our ability to form **2** and spectroscopically characterize it is a potent demonstration of the oxidative stability of $[HB(^{CF3,Ph}m\text{Im})_3]^-$.

5. Conclusions

We have designed and synthesized a new scorpionate ligand with mesoionic imidazol-5-ylidene arms and trifluoromethyl flanking groups. The $\{NiNO\}^{10}$ complex of this ligand has a ν_{NO} stretching frequency similar to those of known tris(imidazole-2-ylidene) scorpionate ligands,

which indicates that the electron-withdrawing flanking groups are balanced out by the strongly donating arms. Our new ligand is therefore expected to be able to support complexes with similar electronic structure and stabilization as those supported by common triscarbene ligands, while still utilizing a perfluorinated flanking group to enhance its oxidative stability.

We successfully metalated this ligand with cobalt(II)-chloride, and found that this cobalt synthon can form a stable adduct with dioxygen. The side-on binding of dioxygen is unusual for cobalt(III)-superoxide complexes, but comparison with known cobalt(III)-peroxide complexes clearly indicates that a superoxide formulation is most appropriate. Dimerization of this dioxygen adduct with the cobalt(II)-chloride complex generates a dicobalt(IV)-bis-μ-oxo complex. Our ability to isolate and characterize such a species is a powerful demonstration of the oxidative stability of our new ligand and its capability to enable the study of highly oxidized transition metal-complexes.

6. Methodology

All manipulations were performed under a dry nitrogen atmosphere using either standard Schlenk techniques or in an mBraun Unilab Pro glovebox unless otherwise stated. All chemicals were obtained from commercial sources and used as received unless otherwise stated. All solvents except for 1,2-difluorobenzene were dried on a solvent purification system from Pure Process Technologies before storing over 4 Å molecular sieves under N_2. Tetrahydrofuran (THF) and diethyl ether (Et_2O) were stirred over NaK alloy and passed through a plug of activated alumina prior to storing over 4 Å sieves under N_2. 1,2-difluorobenzene was purified with acidified potassium permanganate (CAUTION: exothermic reaction), washed with water, dried with anhydrous magnesium sulfate, distilled from calcium hydride, and stored over 4 Å molecular

sieves under N_2. All solvent used in the synthesis and manipulation of **2** was passed through a submicron filter before use.

^{1}H, $^{11}B\{^{1}H\}$, $^{13}C\{1H\}$, and $^{19}F\{^{1}H\}$ NMR spectra were collected on either a 400 MHz Bruker DRX spectrometer equipped with a BBO probe or a 500 MHz Bruker Avance-III-HD spectrometer equipped with a BBFO SmartProbe. ^{1}H and $^{13}C\{^{1}H\}$ spectra were referenced to residual proteo-solvent peaks. CW-EPR spectra were collected on a Bruker Elexsys 500 3500 spectrometer with an X-band SHQE resonator. IR spectra were collected as solids on a Bruker Alpha II using a Platinum Diamond ATR module. UV-vis spectra were recorded on a Thermo Scientific Evolution 300 spectrometer equipped with a Unisoku USP-203-B cryostat. Combustion analysis was performed by Midwest Microlabs.

Synthesis of 1-methyl-2-phenyl-1H-imidazole

A 1 L round bottom flask was charged with 2-phenylimidazole (30 g, 210 mmol) and 600 mL of acetonitrile. The mixture was cooled in an ice bath to 0 °C and stirred. NaH, as a 60% dispersion in mineral oil (9.2 g, 230 mmol), was washed with hexanes and then carefully added to the reaction mixture. After all the hydride was incorporated and bubbling had ceased then a solution of methyl iodide (14.3 mL, 230 mmol) in 150 mL acetonitrile was added dropwise. The reaction was stirred for 3 h and then concentrated via rotary evaporation. The resulting crude product was washed with aqueous NaOH (~1 M) and extracted three times with diethyl ether. The combined organic layers were passed through an alumina plug, washed with brine, dried with a copious amount of anhydrous magnesium sulfate, and filtered through alumina. The solution was dried to a yellow solid (23 g, 70% yield) which was used without further purification. The spectral

data for this compound matches a previous literature report.[304] ^{1}H NMR ($CDCl_3$, 400 MHz): δ 7.63 (2H, Ph-*H*), 7.44 (3H, Ph-*H*), 7.13 (1H, Imid-*H*), 6.97 (Imid-*H*), 3.75 (3H, Me-*H*).

Synthesis of 5-trifluoromethyl-1-methyl-2-phenyl-1H-imidazole

This procedure was modified from a literature procedure.[271] A 1 L Schlenk flask was charged with 1-methyl-2-phenyl-1H-imidazole (12 g, 76 mmol), (diacetoxyiodo)benzene (49 g, 150 mmol), cesium fluoride (35 g, 230 mmol), and 600 mL acetonitrile. The mixture was heated to 70 °C and stirred. A solution of (trimethylsilyl)trifluoromethane (32 g, 230 mmol) in 100 mL acetonitrile was added dropwise. The reaction was allowed to cool to room temperature and stirred overnight. Acetonitrile was removed by rotary evaporation and the resulting crude product was washed with saturated sodium bicarbonate and extracted three times with dichloromethane. The combined organic layers were washed with water, dried with anhydrous magnesium sulfate, and filtered through alumina. Dichloromethane was removed by rotary evaporation and the crude material was purified by column chromatography (500 mL of alumina, 15% ethyl acetate in hexanes). Fractions with large amounts of impurities were discarded and the remaining eluent was removed by rotary evaporation. The resulting crude product was recrystallized from 15% ethyl acetate in hexanes to obtain off-white crystals (5.1 g, 30% yield). The spectral data for this compound matches a previous literature report.[305] ^{1}H NMR ($CDCl_3$, 400 MHz): δ 7.62 (2H, Ph-*H*), 7.52 (4H, Ph-*H* and Imid-*H*), 3.78 (3H, Me-*H*).

Synthesis of $[HB(^{CF3}mImH)_3](OTf)_2$

This procedure was based on literature procedures.[272] A 1 L Schlenk flask was charged with 5-trifluoromethyl-1-methyl-2-phenyl-1*H*-imidazole (8.1 g, 36 mmol) and 200 mL of toluene. While stirring, dibromoborane dimethylsulfide as a 1.0 M solution in dichloromethane (11 mL, 11 mmol) was added, resulting in a cloudy solution. This solution was heated to 100 °C, which

clarified the solution, and trimethylsilyl trifluoromethanesulfonate (5.5 mL, 25 mmol) was added. The reaction was stirred for two nights at 100 °C. The precipitate was filtered off and washed with diethyl ether, then hot 1,2-dichloroethane, and then diethyl ether again. The resulting white powder (8 g, 60% yield) was dried on a high vacuum line until no dichloroethane was visible by ^{1}H NMR spectroscopy and characterized and used without further purification. ^{1}H NMR (CD_3CN, 400 MHz): δ 7.86 (3H, Imid–*H*), δ 7.60 (3H, Ph-*H*), 7.42 (6H, Ph-*H*), 6.86 (6H, Ph-*H*), 3.62 (9H, Me-*H*). We do not observe a signal from the B–*H* proton by ^{1}H NMR spectroscopy. ^{13}C{^{1}H} NMR (CD_3CN, 500 MHz): δ 151.7, 132.6, 129.7, 129.3, 125.1 (q, J = 4.2 Hz), 124.4 (q, J = 42.1 Hz), 121.5 (q, J = 268 Hz), 34.4 (q, J = 1.8 Hz). ^{11}B{^{1}H} NMR (CD_3CN, 400 MHz): δ −5.0 ^{19}F{^{1}H} NMR (CD_3CN, 400 MHz): δ −61.9, −79.3. IR (solid, cm^{-1}): 2610, 2550 (w, B–H). Anal. calcd for $C_{35}H_{28}BF_{15}N_6O_6S_2$: C 42.53, H 2.86, N 8.50. Found: C 42.29, H 2.88, N 8.43.

Synthesis of 1

A suspension of [HB(^{CF3}mImH)$_3$](OTf)$_2$ (0.75 g, 0.76 mmol) in 15 mL THF was chilled to −55 °C. LiHMDS (0.27 g, 1.6 mmol) was added as a solid, and the reaction was stirred cold until homogenous, approximately 15 minutes. Anhydrous cobalt dichloride (0.10 g, 0.76 mmol) was added, and the reaction was stirred at room temperature overnight. The resulting blue powder was filtered out from the solution, washed with THF, and dried under vacuum (520 mg, 0.64 mmol, 86% yield). ^{1}H NMR (CD_2Cl_2, 400 MHz): δ 12.1 (6H, Me-*H*), δ 9.9 (2H, Ph-*H*), δ 9.4 (2H, Ph-*H*), δ 9.3 (2H, Ph-*H*), δ 9.6 (2H, Ph-*H*), 7.6 (2H, Ph-*H*), 7.5 (1H, Imid-*H*), 7.4 (1H, Ph-*H*), 7.1 (2H, Ph-*H*), 6.7 (2H, Ph-*H*), 3.1 (3H, Me-*H*). ^{19}F{^{1}H} NMR (CD_2Cl_2, 400 MHz): δ 31.2 (6F), −52.8 (3F). We do not observe a signal from the B–*H* proton by ^{1}H NMR spectroscopy. Without any further characterization of purification, this blue powder was suspended in 15 mL of THF and

KHMDS (0.13 g, 0.64 mmol) was added as a solid. The mixture was stirred at room temperature for 4 hours. The resulting blue powder was filtered onto celite, washed with THF, and extracted with acetonitrile. The green acetonitrile solution was concentrated under vacuum and layered under diethyl ether. After diffusion at room temperate a blue powder was collected (340 mg, 58% yield over two steps). ^{1}H NMR (CD_2Cl_2, 400 MHz): δ 10.6 (9H, Me-*H*), δ 6.2 (6H, Ph-*H*), 4.4 (3H, Ph-*H*), 1.8 (6H, Ph-*H*). We do not observe a signal from the B–*H* proton by ^{1}H NMR spectroscopy. ^{19}F{^{1}H} NMR (CD_2Cl_2, 400 MHz): δ −1.2. IR (solid, cm^{-1}): 2573 (w, B–H). Anal. calcd for $C_{33}H_{25}BClCoF_9N_6$: C 50.70, H 3.22, N 10.75. Found: C 47.87, H 3.19, N 10.27. As the same material passed EA as the dioxygen adduct **1-O₂**, the low value obtained for C is attributed to incomplete combustion of trifluoromethyl groups.

Synthesis and reactivity of 1-O₂

10 mg of **1** was sealed in a septum-capped vial and the vial was sparged with dry O_2 and allowed to react overnight. The excess dioxygen was removed by vacuum and the material was thereafter handled under an inert atmosphere. $^{18}O_2$ enriched material was synthesized by injection of six equivalents of enriched oxygen gas instead of sparging. Crystals suitable for SXRD were grown by layering a DCM solution under pentanes and diffusing at −35 °C. ^{1}H NMR (CD_2Cl_2, 400 MHz): δ 7.46 (3H, Ph-*H*), δ 7.18 (4H, Ph-*H*), δ 7.07 (2H, Ph-*H*), δ 6.96 (4H, Ph-*H*), δ 6.82 (2H, Ph-*H*), δ 3.60 (Me-*H*). We do not observe a signal from the B–*H* proton by ^{1}H NMR spectroscopy, and no signals are observed by ^{19}F{^{1}H} NMR spectroscopy. CW-EPR (CH_2Cl_2, 9.43 GHz): *g* 2.03, a_{iso}(Co) 32 MHz. IR (solid, cm^{-1}): 2570 (w, B–H), 1103 (O–O), 416 (Co–O_2). Anal. calcd for $C_{33}H_{25}BClCoF_9N_6$: C 48.71, H 3.10, N 10.33. Found: C 48.07, H 3.16, N 10.07.

For the reaction between **1-O₂** and TEMPOH, A solution of **1** in DCM (2 mL, 1.25 mM) was sealed in a screwtop cuvette and chilled in a Unisoku cryostat to −60 °C. One equivalent of TEMPOH was added as a DCM solution, and the reaction was monitored by UV-vis spectroscopy.

Synthesis of 2

A solution of **1-O₂** (1.0 mL, 2.5 mM) and of **1** cosolubilized with 2 equivalents of $NaBAr^F$ (1.0 mL, 2.5 mM in Co**, 1** and 2 $NaBAr^F$ were mixed as solids prior to dissolution), each in d_2-dichloromethane, were chilled to −100 °C and the solution of **1** was slowly added to the solution of **1-O₂** while stirring vigorously. The reaction was allowed to warm to room temperature, stirred for 10 minutes, and filtered through celite. Crystals suitable for SXRD were grown by layering a d_2-DCM solution under pentanes and diffusing at −35 °C.

For the reaction between **2** and DHA, a solution of **2** (2 mL, 0.5 mM) was sealed in a screwtop cuvette. Ten equivalents of DHA was added as a DCM solution, and the reaction was monitored for 15 minutes by UV-vis spectroscopy. After no reactivity was observed over 15 minutes, 10 equivalents of bis(triphenylphosphine)iminium chloride was added as a DCM solution and the reaction was monitored by UV-vis spectroscopy.

Synthesis of 2-H₂

A solution of freshly-generated **2** (2.5 mM, 0.4 mL) was cooled to −100 °C and 4 equivalents of 2,4-bis(*tert*-butyl)phenol were added (100 µL, 40 mM). The mixture is stirred while warming to room temperature and analyzed by NMR to assay the overall yield of **2-H₂** relative to $[BAr^F]^-$. Sufficient quantities of **2-H₂** for characterization were obtained by scaling up this reaction to 8 mL of the stock solution of **2** (generated in proteo-DCM), using only 1 equivalent of 2,4-

bis(*tert*-butyl)phenol, layering the solution under pentane, and allowing diffusion at −35 °C yielded. Crystals suitable for SXRD were grown by vapor diffusion of hexanes into a 0.625 mM solution of **2-H₂** in 1,3-difluorobenzene at room temperature under air. ^{1}H NMR (CD_2Cl_2, 400 MHz): δ 7.65 (8H, $[BAr^F]^-$ Ar-*H*), δ 7.53 (3H, Ph-*H*), 7.48 (4H, $[BAr^F]^-$ Ar-*H*), 7.24 (6H, Ph-*H*), 6.91 (6H, Ph-*H*), 3.67 (3H, Me-*H*), 0.25 (1H, O-*H*). We do not observe a signal from the B–*H* proton by ^{1}H NMR spectroscopy. ^{19}F{^{1}H} NMR (CD_3CN, 400 MHz): δ −56.4, −62.9. IR (solid, cm^{-1}): 3735 (O–H), 2601 (w, B–H).

X-Ray Crystallography

The diffraction data for **2** and **2-H₂** were measured at 100 K on a Bruker D8 VENTURE with PHOTON 100 CMOS detector system equipped with a Mo-target micro-focus X-ray tube (λ = 0.71073 Å. Data reduction and integration were performed with the Bruker APEX3 software package (Bruker AXS, version 2015.5-2, 2015). Data were scaled and corrected for absorption effects using the multi-scan procedure as implemented in SADABS (Bruker AXS, version 2014/5, 2015, part of Bruker APEX3 software package). The structure was solved by the dual method implemented in SHELXT and refined by a full-matrix least-squares procedure using OLEX23 software package (XL refinement program version 2014/7).[306–308] Suitable crystals were mounted on a cryo-loop and transferred into the cold nitrogen stream of the Bruker D8 Venture diffractometer. C-H hydrogen atoms were generated by geometrical considerations, constrained to idealized geometries, and allowed to ride on their carrier atoms with an isotropic displacement parameter related to the equivalent displacement parameter of their carrier atoms. We note a couple B-level alerts for **2** resulting from the presence of a twin from overlapping plates of crystals, the

propensity of the phenyl rings to disorder, and the general insolubility of this family of complexes which leads to small crystals of poor quality.

The diffraction data for **1-O$_2$** was measured at 100 K on an XtalAB Synergy-S dual-source single-crystal X-ray diffractometer using a PhotonJet-S Cu 50W Microfocus X-ray source (λ = 1.54184 Å) and a HyPix-6000HE Hybrid Photon Counting detector. Data reduction and integration for 2 was performed with the CrysAlisPro 1.171.43.75a (Rigaku Oxford Diffraction, 2023) software package, with numerical absorption correction based on Gaussian integration over a multifaceted crystal model and empirical absorption correction using spherical harmonics, implemented in the SCALE3 ABSPACK scaling algorithm. The structures were solved by SHELXT (Version 2018/2) and refined by a full-matrix least-squares procedure using OLEX2 (XL refinement program version 2018/3).[306–308] We note a couple B-level alerts resulting from the propensity of the phenyl rings of complex **1-O$_2$** to disorder, and the general insolubility of this family of complexes which leads to small crystals of poor quality.

XAS Data Collection

XAS data collection was performed at the Stanford Synchrotron Radiation Lightsource on beam line 7-3 using a oxford Helium cryostat at 10 K and collected in fluorescence mode using 30-element solid-state Canberra germanium detectors. Incoming X-rays were de-tuned to 50% to remove harmonic overtones. Photoreduction was monitored by varying the sample position irradiated for each scan. Data was referenced to cobalt foil with an edge energy of 7709.3 eV and normalized at 8000 eV. Data was analyzed using EXAFSPAK.

The XAS spectra of **2** was taken on a 1.25 mM solution in 1,2-difluorobernzene which was prepared freshly from **1** and **1-O$_2$** following the above procedure, with thawing 1,2-benzene −100 °C substituted for d_2-dichloromethane and at a lower concentration due to limited solubility of **1-O$_2$** in 1,2-difluorobenzene. XAS data was similarly collected at 1.25 mM in frozen 1,2-difluorobenzene for **1-O$_2$** and on solid dispersed in potassium carbonate for **1**.

DFT Calculations

The geometry of **1** was optimized by DFT in the ORCA 5.0.2 software suite using the TPSSh functional with the resolution of identity and chain of spheres approximations and the D3 dispersion correction with Becke-Johnson damping.[253,309,310] The cobalt center was given the def-TZVPP basis set, all atoms bound to the cobalt center were given the def2-TZVP basis set, and all other atoms were given the def2-SV(P) basis set.[165,166] Numerical frequency calculations were used to predict IR spectra and confirm convergence to a stable minimum.

Concluding Remarks

The central aim of this dissertation has been to understand the nature of thermodynamic influences on CPET reactions, with a focus on the C–H bond activation by transition metal-oxo complexes. In particular, we have focused on untangling various models for how the stepwise thermodynamics $\Delta G°_{PT}$ and $\Delta G°_{ET}$ affect concerted reactivity. This has led to a broad and general evaluation of the experimental support for the effect of these free energies on C–H activation rates, as well as an analysis of the theoretical foundation for their influences.

We performed a through statistical analysis of C–H activation rates by transition metal-oxo complexes. This analysis (1) revealed the broad relevance of $\Delta G°_{PT}$ and $\Delta G°_{ET}$ on C–H activation reaction rates, and (2) found that a myriad of other factors, such as spin state based influences, are not predictive of reaction rates in general. Our model provides a unified picture for transition metal-oxo mediated C–H activation and it explains and predicts the kinetics of wide variety of transition-metal oxo complexes with several substrates. Moreover, even in cases for which the model is comparably insufficient, the same thermodynamic trends are present – the specific parameters of the model merely need to be tuned separately for certain cases.

This statistical analysis demonstrated how $\Delta G°_{PT}$ and $\Delta G°_{ET}$ have an influence independent of that of $\Delta G°_{CPET}$. There is a penalty for energetic coupling between proton transfer and electron transfer which can be expressed as the free energy $\Delta G°_{CC}$. This free energy is completely independent of the driving force for the reaction, and it goes beyond the traditional interpretation of $\Delta G°_{PT}$ and $\Delta G°_{ET}$ as merely contributors to $\Delta G°_{CPET}$. A linear free energy relationship (LFER) with $\Delta G°_{CC}$ does not have a clear connection to a specific reaction coordinate along a More

O'Ferrall-Jencks diagram, and similar coupling energies may partially explain imbalances in the relationships between different free energy parameters for canonical reactions in physical organic chemistry.

We have also reevaluated the role that proton tunneling plays in imbalanced CPET reactions. Variable temperature isotope effect data indicate that proton tunneling is extensive in the C–H activation reaction of a cobalt(III)-oxo complex which displays basic imbalanced kinetic trends. This imbalanced CPET reactivity must be explained with a nonadiabatic reaction model, and not with a semiclassical structure-reactivity relationship.

By applying algorithms used to optimize the crossing points between electronic energy surfaces we were able to optimize the transition states of this cobalt(III)-oxo complex reacting with a variety of C–H bonds and apply modern nonadiabatic theories of CPET to this reaction. Our calculations reproduce the experimentally observed trend between reaction rates and C–H pK_a and are able to provide an explanation for this imbalanced reactivity trend. Decreased $\Delta G°_{PT}$ renders the reactant proton potential energy well more anharmonic, which leads to increased diffusivity of the proton across the proton transfer coordinates. This results in higher vibronic coupling and faster reaction rates. In other words, more energetically accessible proton transfer leads to the proton being found, on average, further across the reaction coordinate and thereby accelerates the reaction. This demonstrates that textbook structure-reactivity relationships can also be based in nonadiabatic models for reactivity, and do not require a localized proton position at the transition state to be applicable.

These calculations also allowed us to parameterize a model complex and test the hypothesis that the dependence of CPET reaction rates trend with stepwise thermodynamics can be explained, in general, by $\Delta G°_{PT}$ affecting the anharmonicity of the reactant proton potential energy well and $\Delta G°_{ET}$ affecting the anharmonicity of the product proton potential energy well. We are able to reproduce the trend with $\Delta G°_{PT}$ and $\Delta G°_{ET}$ seen in the statistical analysis, supporting our hypothesis that potential energy wells, and the resulting electronic coupling, underly the effects of these stepwise thermodynamic parameters. Our model also makes new productions, namely that downhill reactions will have a slight tendency towards oxidatively imbalanced CPET reactions and that uphill reactions will have a slight tendency towards basic imbalanced CPET reactions.

Our finding that uphill CPET is expected to tend towards basic imbalanced CPET motivated a study of difficult, uphill CPET reactions; unfortunately, systems known to be capable of this reaction are unstable with respect to ligand oxidation. We therefore designed a new ligand scaffold which is stable to oxidation using perfluoroalkyl groups. Unlike preexisting perfluorinated ligand platforms, our ligand retains strong donor properties and is therefore capable of supporting high-valent, highly oxidizing transition metal complexes.

While studies with this new ligand platform are ongoing, we have found that a cobalt(II)-chloride complex of this ligand binds dioxygen to generate the first crystallographically characterized side-on cobalt(III)-superoxide complex. Dimerization of this complex with another equivalent of cobalt(II) and removal of chloride ligands results in a dicobalt(IV)-bis-μ-oxo complex, the first stable dicobalt(IV) complex, demonstrating how this ligand platform and design strategy will enable new studies in oxidative chemistry.

Several major ideas stand out as being notable results from these studies. First, the coupling between different components of a reaction does not neatly map to a specific direction on a More O'Ferrall-Jencks diagram, but it can be a very important mode by with stepwise thermodynamics affect reaction rates.

Secondly, much more research is needed to elucidate the nature of proton tunneling in transition metal-oxo mediated C–H activation. It is important to consider how nonadiabatic effects may intersect with current models of this reaction. This will require going beyond semiclassical and DFT-based models for theoretically investigating these reactions, and more frequently measuring variable temperature KIEs to fingerprint the tunneling in specific reactions.

Thirdly, while this study has been limited the effects of $\Delta G°_{PT}$ and $\Delta G°_{ET}$, the theoretical explanation for these effects would apply to any process with high electronic coupling to the reactant or the product states. For instance, the reactant potential energy well need not be proton transfer but could be a hydride transfer from a C–H bond – this might be expected for an electrophilic transition metal-oxo complex. Indeed, many instances of oxidatively imbalanced CPET reactions may actually be hydridic. Additionally, excited electronic states could be relevant to proton potential energy surfaces if they have higher electronic coupling than the ground state.

Finally, the application of the kinetic effect of $\Delta G°_{PT}$ and $\Delta G°_{ET}$ to affect the selectivity of organic transformations is an exciting area of future research. Our prediction that uphill reactivity may encourage basic asynchronous processes suggests that these effects could be useful in accomplishing selectivity in the functionalization of strong C–H bonds, and we are optimistic that our new perfluorinated ligand may enable this hypothesis to be tested in the near future.

Appendix A1: Summary of Data and Regressions for Chapter 2

1. Summary of Experimental Data

In Table A1.1 we list each metal oxo species considered, their references, their reported k_2 values for reactivity with 9,10-dihydroanthracene (DHA), any reported statistical or stochiometric corrections to these k_2 values (the k_2 values were multiplied by these numbers prior to determining barrier heights), the temperature these k_2 values were collected at, and the resultant experimental reaction barriers (calculated as described in the main text methods). Where multiple temperatures or multiple experimental conditions are reported, only one set of those conditions was chosen to represent the metal oxo complex's reaction rate with DHA. We also list the experimental slope of RT log k_2 vs. experimental substrate BDFE for cases with enough data to determine it (at least three different substrates with k_2 reported, counting DHA and xanthene as only one substrate due to their similar experimental BDFEs, and excepting the Co^{III} oxo complex whose kinetics trend not with BDFE but with pK_a). Chemdraws for each metal oxo complex are provided in Figure A1.1 (training set) and Figure A1.2 (test set).

Table A1.1 Metal oxo species analyzed with their experimental kinetics and barriers.

Oxo	Refs	k_2[a] (s^{-1})	Literature Correction	T (°C)	CPET Barrier[a] (kcal/mol)	BDFE Slope[b]
$[Fe^{IV}(O)(Me_3NTB)(MeCN)]^{2+}$	116	780	4	−40	2.30	−0.18
$[Fe^{IV}(O)(TMG_2dien)(MeCN)]^{2+}$	44	5		−30	4.38	
$[Fe^{IV}(O)(TMG_3tren)]^{2+}$	17	0.09		−30	7.46	
$[Fe^{V}(O)(TAML)]^{-}$	117,311	263	1	−37	3.54	−0.22
$[Fe^{IV}(O)(TMC)(MeCN)]^{2+}$	18,118	0.2		0	7.99	
$[Fe^{IV}(O)(TMC)(N_3)]^{+}$	118	2.4		0	6.64	−0.28
$[Fe^{IV}(O)(TMC)(OCOCF_3)]^{+}$	118	1.3		0	6.93	−0.35
$[Fe^{IV}(O)(TMCS)]^{+}$	118,312	7.5		0	6.02	
$[Mn^{IV}(O)(H_3buea)]^{-}$	52,313	0.038	8	30	8.50	
$[Fe^{IV}(O)(TMP)]$	119	2.2		−15	6.18	
$[Co^{III}(O)(PhB^{tBu}Im_3)]$	14,50	0.058	2	23	8.87	
$[Ru^{IV}(O)(H^{+}TPA)(bpy)]^{3+}$	120	105		25	4.88	
$[Fe^{IV}(O)(tpfpp)]$	121	13	1	15	5.82	−0.15
$[Mn^{VII}(O)_4]^{-}$	49,314	0.12	4	25	9.47	−0.67
$[Mn^{V}(O)_2(tf_4tmap)]^{3+}$	122	240	1	15	4.53	−0.25
$[Mn^{IV}(O)(OH)(tf_4tmap)]^{3+}$	122	4.9	1	15	6.36	−0.35
$[Cr^{IV}(O)(TMC)(Cl)]^{+}$	123,315	0.21	1	−10	7.69	
$[Ru^{VI}(O)_2(TMC)]^{2+}$	23,124	0.036	1	35	10.4	
$[Fe^{IV}(O)(N4Py)]^{2+}$	125,316	18		25	5.99	
$[Fe^{IV}(O)(BnTPEN)]^{2+}$	125	100		25	4.94	
$[Fe^{IV}(O)(^{Me2}TACN\text{-}Py_2)]^{2+}$	125	7.4		25	6.54	
$[Fe^{IV}(O)(BP1)]^{2+}$	125	1.1		25	7.57	
$[Fe^{IV}(O)(BP2)]^{2+}$	125	40		25	5.44	
$[Ru^{IV}(O)(bpy)_2(py)]^{2+}$	23,126	125	1	23	4.77	−0.54
$[Mn^{IV}(O)_2(Me_2EBC)]$	127	0.015		15	10.3	−0.09
$[Mn^{IV}(O)(N4Py)]^{2+}$	129	3.6	1	25	6.94	
$[Co^{IV}(O)(13\text{-}TMC)]^{2+}$	130	0.083	1	−40	7.30	−0.20
$[Fe^{IV}(O)(13\text{-}TMC)]^{2+}$	128	4.7	1	−40	5.44	−0.51
$[Ru^{VI}(O)_2(L)]^{2+}$	132,317	7.45	4	25	6.08	−0.60
$[Ru^{VI}(O)_2(F_{28}\text{-}tpp)]$	131	22.5	1	25	6.08	−0.43

[a]For reactivity with 9,10-dihydroanthracene. [b]Experimental slope of RT log k_2 vs. substrate BDFE.

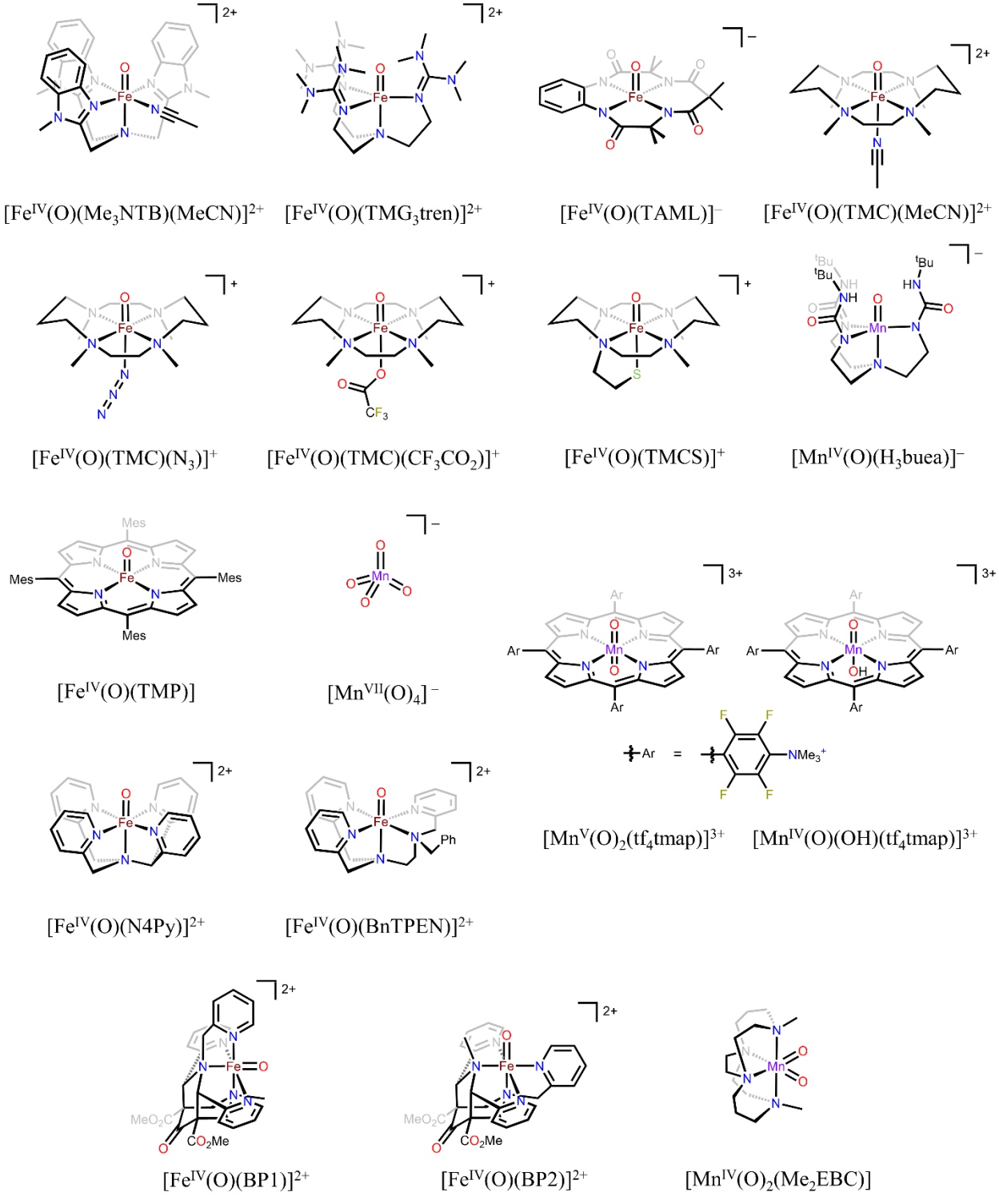

Figure A1.1 Metal oxo complexes in the training set. See Table A1.1 for references.

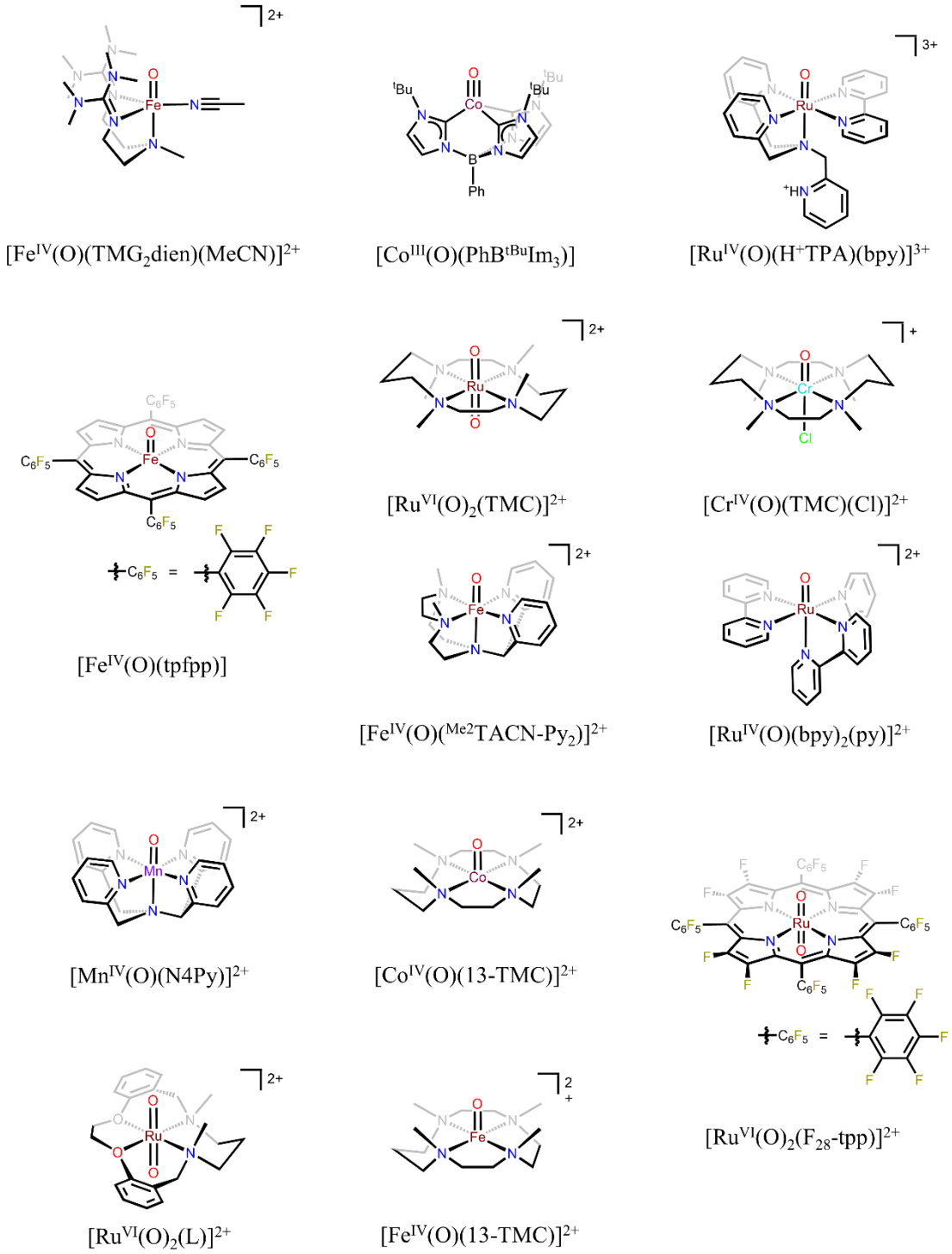

Figure A1.2 Metal oxo complexes in the test set. See Table A1.1 for references.

Table A1.2 Spin based parameters of each metal oxo complex

Oxo	Mult.[a] M–O	Mult.[a] M–OH	Mult.[a] P M–OH$^+$	Mult.[a] M–O$^-$	Spin Excit.[b]	IBO Spin Density
$[Fe^{IV}(O)(Me_3NTB)(MeCN)]^{2+}$	3	6	3	6	16.0	0.852
$[Fe^{IV}(O)(TMG_2dien)(MeCN)]^{2+}$	5	6	5	6	0	0.697
$[Fe^{IV}(O)(TMG_3tren)]^{2+}$	5	6	5	6	0	0.662
$[Fe^{V}(O)(TAML)]^{-}$	2	3	2	3	0	0.261
$[Fe^{IV}(O)(TMC)(MeCN)]^{2+}$	3	6	3	6	10.6	0.760
$[Fe^{IV}(O)(TMC)(N_3)]^{+}$	3	6	3	6	7.2	0.691
$[Fe^{IV}(O)(TMC)(OCOCF_3)]^{+}$	3	6	3	6	8.3	0.699
$[Fe^{IV}(O)(TMCS)]^{+}$	3	6	3	6	4.7	0.708
$[Mn^{IV}(O)(H_3buea)]^{-}$	4	5	4	5	0	0.229
$[Fe^{IV}(O)(TMP)]$	3	6	3	4	43.7	0.673
$[Co^{III}(O)(PhB^{tBu}Im_3)]$	1	4	1	4	11.9	0.000
$[Ru^{IV}(O)(H^+TPA)(bpy)]^{3+}$	3	2	3	2	0	0.929
$[Fe^{IV}(O)(tpfpp)]$	3	4	3	4	0	0.695
$[Mn^{VII}(O)_4]^{-}$	1	2	1	2	0	0.000
$[Mn^{V}(O)_2(tf_4tmap)]^{3+}$	1	4	1	2	24.5	0.000
$[Mn^{IV}(O)(OH)(tf_4tmap)]^{3+}$	4	5	4	5	0	0.546
$[Cr^{IV}(O)(TMC)(Cl)]^{+}$	3	4	3	4	0	−0.133
$[Ru^{VI}(O)_2(TMC)]^{2+}$	1	2	1	2	0	0.000
$[Fe^{IV}(O)(N4Py)]^{2+}$	3	6	3	6	75.5	0.814
$[Fe^{IV}(O)(BnTPEN)]^{2+}$	3	6	3	6	18.0	0.813
$[Fe^{IV}(O)(^{Me2}TACN\text{-}Py_2)]^{2+}$	3	6	3	6	73.6	0.795
$[Fe^{IV}(O)(BP1)]^{2+}$	3	6	3	6	19.6	0.821
$[Fe^{IV}(O)(BP2)]^{2+}$	3	6	3	6	19.8	0.830
$[Ru^{IV}(O)(bpy)_2(py)]^{2+}$	3	2	3	2	0	0.924
$[Mn^{IV}(O)_2(Me_2EBC)]$	4	5	4	5	0	0.162
$[Mn^{IV}(O)(N4Py)]^{2+}$	4	5	4	5	0	0.589
$[Co^{IV}(O)(13\text{-}TMC)]^{2+}$	4	5	4	5	0	1.238
$[Fe^{IV}(O)(13\text{-}TMC)]^{2+}$	3	6	3	6	17.7	0.691
$[Ru^{VI}(O)_2(L)]^{2+}$	1	2	1	2	0	0.000
$[Ru^{VI}(O)_2(F_{28}\text{-}tpp)]$	1	2	1	2	0	0.000

[a]Multiplicity. [b]Energy in kcal/mol needed to access the lowest spin state of the oxo complex that is one multiplicity away from the multiplicity of the hydroxide; calculated at the ground spin state's optimized geometry.

Table A1.3 Kinetics and barrier heights for reactivity with 9,10-dihydroanthracene

Oxo	k_2 (s^{-1})	CPET Barrier (kcal/mol)
$[Fe^{IV}(O)(Me_3NTB)(MeCN)]^{2+}$	780	2.3
$[Fe^{IV}(O)(TMG_2dien)(MeCN)]^{2+}$	57	4.4
$[Fe^{IV}(O)(TMG_3tren)]^{2+}$	0.09	7.5
$[Fe^{V}(O)(TAML)]^{-}$	263	3.5
$[Fe^{IV}(O)(TMC)(MeCN)]^{2+}$	0.2	8.0
$[Fe^{IV}(O)(TMC)(N_3)]^{+}$	2.4	6.6
$[Fe^{IV}(O)(TMC)(OCOCF_3)]^{+}$	1.3	6.9
$[Fe^{IV}(O)(TMCS)]^{+}$	7.5	6.0
$[Mn^{IV}(O)(H_3buea)]^{-}$	0.038	8.5
$[Fe^{IV}(O)(TMP)]$	2.2	6.2
$[Co^{III}(O)(PhB^{tBu}Im_3)]$	0.0584	8.9
$[Ru^{IV}(O)(H^{+}TPA)(bpy)]^{3+}$	105	4.9
$[Fe^{IV}(O)(tpfpp)]$	13	5.8
$[Mn^{VII}(O)_4]^{-}$	0.12	9.5
$[Mn^{V}(O)_2(tf_4tmap)]^{3+}$	240	4.5
$[Mn^{IV}(O)(OH)(tf_4tmap)]^{3+}$	4.9	6.4
$[Cr^{IV}(O)(TMC)(Cl)]^{+}$	0.21	7.7
$[Ru^{VI}(O)_2(TMC)]^{2+}$	0.036	10.4
$[Fe^{IV}(O)(N4Py)]^{2+}$	18	6.0
$[Fe^{IV}(O)(BnTPEN)]^{2+}$	100	4.9
$[Fe^{IV}(O)(^{Me2}TACN\text{-}Py_2)]^{2+}$	7.4	6.5
$[Fe^{IV}(O)(BP1)]^{2+}$	1.1	7.6
$[Fe^{IV}(O)(BP2)]^{2+}$	40	5.4
$[Ru^{IV}(O)(bpy)_2(py)]^{2+}$	125	4.8
$[Mn^{IV}(O)_2(Me_2EBC)]$	0.01496	10.3
$[Mn^{IV}(O)(N4Py)]^{2+}$	3.6	6.9
$[Co^{IV}(O)(13\text{-}TMC)]^{2+}$	0.083	7.3
$[Fe^{IV}(O)(13\text{-}TMC)]^{2+}$	4.7	5.4
$[Ru^{VI}(O)_2(L)]^{2+}$	7.45	6.1
$[Ru^{VI}(O)_2(F_{28}\text{-}tpp)]$	22.5	6.1

See Table A1.1 for references and experimental conditions.

Table A1.4 Thermodynamic parameters of reactivity with 9,10-dihydroanthracene

Oxo	$\Delta G°_{CPET}$	$\Delta G°_{PT}$	$\Delta G°_{ET}$	$\Delta E°_{CPET}$	$\Delta E°_{PT}$	$\Delta E°_{ET}$
$[Fe^{IV}(O)(Me_3NTB)(MeCN)]^{2+}$	−15.9	57.7	29.3	−8.9	61.4	37.8
$[Fe^{IV}(O)(TMG_2dien)(MeCN)]^{2+}$	−9.3	57.5	39.2	−5	61.5	46
$[Fe^{IV}(O)(TMG_3tren)]^{2+}$	−7.2	54.5	47.5	−3.1	57.6	54.4
$[Fe^{V}(O)(TAML)]^{-}$	−10.1	39.2	40.2	−6.9	43.2	44.8
$[Fe^{IV}(O)(TMC)(MeCN)]^{2+}$	−6.5	68.2	36.8	1.5	71.9	46.8
$[Fe^{IV}(O)(TMC)(N_3)]^{+}$	−9.4	47.1	46.6	−2.1	50.5	56.0
$[Fe^{IV}(O)(TMC)(OCOCF_3)]^{+}$	−8.7	56.7	42.7	−1.3	60.1	52.7
$[Fe^{IV}(O)(TMCS)]^{+}$	−8.5	40.1	50.1	−2.1	42.7	59.3
$[Mn^{IV}(O)(H_3buea)]^{-}$	0.71	27.6	62.3	5.3	29.5	69.3
$[Fe^{IV}(O)(TMP)]$	−10.9	39.3	67.7	−6.2	44.3	73.5
$[Co^{III}(O)(PhB^{tBu}Im_3)]$	−8.8	15.9	74.3	−3.2	19.6	82.7
$[Ru^{IV}(O)(H^{+}TPA)(bpy)]^{3+}$	−4.5	75.9	41.9	−2.6	78.8	45.7
$[Fe^{IV}(O)(tpfpp)]$	−8.0	50.1	57.3	−3.8	53.5	63.6
$[Mn^{VII}(O)_4]^{-}$	−0.4	55.5	49.6	3.5	58.7	54.4
$[Mn^{V}(O)_2(tf_4tmap)]^{3+}$	−13.7	34.5	59.5	−9.0	36.7	66.2
$[Mn^{IV}(O)(OH)(tf_4tmap)]^{3+}$	−9.2	20.0	60.8	−4.6	21.3	65.7
$[Cr^{IV}(O)(TMC)(Cl)]^{+}$	−10.0	53.6	55.7	−7.5	56.9	61.5
$[Ru^{VI}(O)_2(TMC)]^{2+}$	3.9	82.8	34.1	7.2	86.8	38.4
$[Fe^{IV}(O)(N4Py)]^{2+}$	−5.8	65.0	38.0	1.5	69.0	46.4
$[Fe^{IV}(O)(BnTPEN)]^{2+}$	−7.4	64.1	35.0	−1.2	66.7	43.0
$[Fe^{IV}(O)(^{Me2}TACN\text{-}Py_2)]^{2+}$	−6.3	63.7	37.3	1.4	67.5	46.6
$[Fe^{IV}(O)(BP1)]^{2+}$	−6.2	69.9	35.6	0.4	74.0	43.5
$[Fe^{IV}(O)(BP2)]^{2+}$	−9.6	68.1	31.7	−3.2	71.5	40.0
$[Ru^{IV}(O)(bpy)_2(py)]^{2+}$	−5.5	68.5	43.4	−3.8	71.8	47.5
$[Mn^{IV}(O)_2(Me_2EBC)]$	−3.3	7.6	85.8	0.8	7.2	93.7
$[Mn^{IV}(O)(N4Py)]^{2+}$	−8.1	51.5	36.6	−3.0	55.1	43.7
$[Co^{IV}(O)(13\text{-}TMC)]^{2+}$	−15.0	69.0	11.5	−11.0	74.1	16.7
$[Fe^{IV}(O)(13\text{-}TMC)]^{2+}$	−19.0	78.3	17.6	−13.8	83.4	24.1
$[Ru^{VI}(O)_2(L)]^{2+}$	0.11	85.5	22.1	2.8	89.4	26.5
$[Ru^{VI}(O)_2(F_{28}\text{-}tpp)]$	−4.6	64.9	37.2	−1.0	66.2	42.7

All energies in kcal/mol.

Table A1.5 Kinetics and barrier heights for reactivity with 1,4-cyclohexadiene

Oxo	k_2 (s^{-1})	CPET Barrier (kcal/mol)
$[Fe^{IV}(O)(Me_3NTB)(MeCN)]^{2+}$	240	3.6
$[Fe^{IV}(O)(TMG_2dien)(MeCN)]^{2+}$	18	5.4
$[Fe^{IV}(O)(TMG_3tren)]^{2+}$	1.2	6.7
$[Fe^{V}(O)(TAML)]^{-}$		
$[Fe^{IV}(O)(TMC)(MeCN)]^{2+}$		
$[Fe^{IV}(O)(TMC)(N_3)]^{+}$	1.4	7.4
$[Fe^{IV}(O)(TMC)(OCOCF_3)]^{+}$	1.2	7.5
$[Fe^{IV}(O)(TMCS)]^{+}$		
$[Mn^{IV}(O)(H_3buea)]^{-}$		
$[Fe^{IV}(O)(TMP)]$		
$[Co^{III}(O)(PhB^{tBu}Im_3)]$		
$[Ru^{IV}(O)(H^{+}TPA)(bpy)]^{3+}$		
$[Fe^{IV}(O)(tpfpp)]$	9	6.7
$[Mn^{VII}(O)_4]^{-}$		
$[Mn^{V}(O)_2(tf_4tmap)]^{3+}$		
$[Mn^{IV}(O)(OH)(tf_4tmap)]^{3+}$	1.3	7.8
$[Cr^{IV}(O)(TMC)(Cl)]^{+}$	0.096	8.6
$[Ru^{VI}(O)_2(TMC)]^{2+}$	0.015	11.5
$[Fe^{IV}(O)(N4Py)]^{2+}$		
$[Fe^{IV}(O)(BnTPEN)]^{2+}$		
$[Fe^{IV}(O)(^{Me2}TACN\text{-}Py_2)]^{2+}$		
$[Fe^{IV}(O)(BP1)]^{2+}$		
$[Fe^{IV}(O)(BP2)]^{2+}$		
$[Ru^{IV}(O)(bpy)_2(py)]^{2+}$		
$[Mn^{IV}(O)_2(Me_2EBC)]$	0.0159	10.8
$[Mn^{IV}(O)(N4Py)]^{2+}$		
$[Co^{IV}(O)(13\text{-}TMC)]^{2+}$	0.037	8.1
$[Fe^{IV}(O)(13\text{-}TMC)]^{2+}$	5.4	5.8
$[Ru^{VI}(O)_2(L)]^{2+}$		
$[Ru^{VI}(O)_2(F_{28}\text{-}tpp)]$	240	

See Table A1.1 for references and experimental conditions.

Table A1.6 Thermodynamic parameters of reactivity with 1,4-cyclohexadiene

Oxo	$\Delta G°_{CPET}$	$\Delta G°_{PT}$	$\Delta G°_{ET}$	$\Delta E°_{CPET}$	$\Delta E°_{PT}$	$\Delta E°_{ET}$
$[Fe^{IV}(O)(Me_3NTB)(MeCN)]^{2+}$	−19.2	64.8	26.5	−12.4	68.5	34.8
$[Fe^{IV}(O)(TMG_2dien)(MeCN)]^{2+}$	−12.6	64.6	36.4	−8.5	68.5	42.9
$[Fe^{IV}(O)(TMG_3tren)]^{2+}$	−10.6	61.6	44.7	−6.6	64.7	51.4
$[Fe^{V}(O)(TAML)]^{-}$	−13.4	46.3	37.4	−10.4	50.3	41.8
$[Fe^{IV}(O)(TMC)(MeCN)]^{2+}$	−9.8	75.3	34.0	−2.0	79.0	43.8
$[Fe^{IV}(O)(TMC)(N_3)]^{+}$	−12.8	54.2	43.8	−5.6	57.5	53.0
$[Fe^{IV}(O)(TMC)(OCOCF_3)]^{+}$	−12.0	63.8	39.9	−4.8	67.2	49.7
$[Fe^{IV}(O)(TMCS)]^{+}$	−11.8	47.3	47.3	−5.6	49.8	56.2
$[Mn^{IV}(O)(H_3buea)]^{-}$	−2.6	34.7	59.6	1.8	36.6	66.3
$[Fe^{IV}(O)(TMP)]$	−14.2	46.4	64.9	−9.7	51.3	70.5
$[Co^{III}(O)(PhB^{tBu}Im_3)]$	−12.1	23.0	71.5	−6.7	26.7	79.7
$[Ru^{IV}(O)(H^{+}TPA)(bpy)]^{3+}$	−7.8	83.0	39.1	−6.1	85.9	42.7
$[Fe^{IV}(O)(tpfpp)]$	−11.3	57.2	54.5	−7.3	60.6	60.6
$[Mn^{VII}(O)_4]^{-}$	−3.7	62.6	46.9	0.029	65.8	51.3
$[Mn^{V}(O)_2(tf_4tmap)]^{3+}$	−17	41.6	56.7	−12.5	43.8	63.2
$[Mn^{IV}(O)(OH)(tf_4tmap)]^{3+}$	−12.5	27.1	58.1	−8.1	28.4	62.6
$[Cr^{IV}(O)(TMC)(Cl)]^{+}$	−13.3	60.7	52.9	−11	64.0	58.5
$[Ru^{VI}(O)_2(TMC)]^{2+}$	0.63	89.9	31.4	3.7	93.9	35.4
$[Fe^{IV}(O)(N4Py)]^{2+}$	−9.1	72.1	35.3	−2.0	76.0	43.4
$[Fe^{IV}(O)(BnTPEN)]^{2+}$	−10.7	71.2	32.2	−4.7	73.8	40.0
$[Fe^{IV}(O)(^{Me2}TACN\text{-}Py_2)]^{2+}$	−9.7	70.8	34.6	−2.1	74.6	43.6
$[Fe^{IV}(O)(BP1)]^{2+}$	−9.5	77.0	32.9	−3.1	81.1	40.5
$[Fe^{IV}(O)(BP2)]^{2+}$	−12.9	75.2	29.0	−6.7	78.5	37.0
$[Ru^{IV}(O)(bpy)_2(py)]^{2+}$	−8.8	75.6	40.7	−7.3	78.9	44.5
$[Mn^{IV}(O)_2(Me_2EBC)]$	−6.7	14.7	83.0	−2.7	14.3	90.7
$[Mn^{IV}(O)(N4Py)]^{2+}$	−11.4	58.6	33.8	−6.5	62.2	40.7
$[Co^{IV}(O)(13\text{-}TMC)]^{2+}$	−18.4	76.1	8.7	−14.5	81.1	13.7
$[Fe^{IV}(O)(13\text{-}TMC)]^{2+}$	−22.3	85.4	14.8	−17.3	90.5	21.1
$[Ru^{VI}(O)_2(L)]^{2+}$	−3.2	92.7	19.3	−0.72	96.5	23.5
$[Ru^{VI}(O)_2(F_{28}\text{-}tpp)]$	−7.9	72.0	34.5	−4.5	73.3	39.7

All energies in kcal/mol.

Table A1.7 Kinetics and barrier heights for reactivity with xanthene

Oxo	k_2 (s^{-1})	CPET Barrier (kcal/mol)
$[Fe^{IV}(O)(Me_3NTB)(MeCN)]^{2+}$		
$[Fe^{IV}(O)(TMG_2dien)(MeCN)]^{2+}$		
$[Fe^{IV}(O)(TMG_3tren)]^{2+}$		
$[Fe^{V}(O)(TAML)]^{-}$		
$[Fe^{IV}(O)(TMC)(MeCN)]^{2+}$		
$[Fe^{IV}(O)(TMC)(N_3)]^{+}$	9.6	5.5
$[Fe^{IV}(O)(TMC)(OCOCF_3)]^{+}$	7.6	5.6
$[Fe^{IV}(O)(TMCS)]^{+}$		
$[Mn^{IV}(O)(H_3buea)]^{-}$		
$[Fe^{IV}(O)(TMP)]$	4.3	5.5
$[Co^{III}(O)(PhB^{tBu}Im_3)]$		
$[Ru^{IV}(O)(H^{+}TPA)(bpy)]^{3+}$		
$[Fe^{IV}(O)(tpfpp)]$	14	5.4
$[Mn^{VII}(O)_4]^{-}$	0.56	8.6
$[Mn^{V}(O)_2(tf_4tmap)]^{3+}$	570	3.6
$[Mn^{IV}(O)(OH)(tf_4tmap)]^{3+}$	3.8	6.1
$[Cr^{IV}(O)(TMC)(Cl)]^{+}$	0.86	6.6
$[Ru^{VI}(O)_2(TMC)]^{2+}$	0.057	9.7
$[Fe^{IV}(O)(N4Py)]^{2+}$		
$[Fe^{IV}(O)(BnTPEN)]^{2+}$		
$[Fe^{IV}(O)(^{Me2}TACN\text{-}Py_2)]^{2+}$		
$[Fe^{IV}(O)(BP1)]^{2+}$		
$[Fe^{IV}(O)(BP2)]^{2+}$		
$[Ru^{IV}(O)(bpy)_2(py)]^{2+}$	577	3.5
$[Mn^{IV}(O)_2(Me_2EBC)]$	0.048	9.3
$[Mn^{IV}(O)(N4Py)]^{2+}$		
$[Co^{IV}(O)(13\text{-}TMC)]^{2+}$	0.15	6.7
$[Fe^{IV}(O)(13\text{-}TMC)]^{2+}$		4.5
$[Ru^{VI}(O)_2(L)]^{2+}$	49.7	4.9
$[Ru^{VI}(O)_2(F_{28}\text{-}tpp)]$	59	5.1

See Table A1.1 for references and experimental conditions.

Table A1.8 Thermodynamic parameters of reactivity with xanthene

Oxo	$\Delta G°_{CPET}$	$\Delta G°_{PT}$	$\Delta G°_{ET}$	$\Delta E°_{CPET}$	$\Delta E°_{PT}$	$\Delta E°_{ET}$
$[Fe^{IV}(O)(Me_3NTB)(MeCN)]^{2+}$	−18.7	57.0	21.0	−12.3	61.3	27.1
$[Fe^{IV}(O)(TMG_2dien)(MeCN)]^{2+}$	−12.1	56.8	31.0	−8.4	61.3	35.3
$[Fe^{IV}(O)(TMG_3tren)]^{2+}$	−10.1	53.8	39.2	−6.5	57.5	43.8
$[Fe^{V}(O)(TAML)]^{-}$	−12.9	38.5	32.0	−10.3	43.1	34.2
$[Fe^{IV}(O)(TMC)(MeCN)]^{2+}$	−9.3	67.4	28.6	−1.9	71.8	36.1
$[Fe^{IV}(O)(TMC)(N_3)]^{+}$	−12.2	46.4	38.4	−5.5	50.3	45.4
$[Fe^{IV}(O)(TMC)(OCOCF_3)]^{+}$	−11.5	55.9	34.4	−4.7	60.0	42.1
$[Fe^{IV}(O)(TMCS)]^{+}$	−11.3	39.4	41.9	−5.5	42.5	48.6
$[Mn^{IV}(O)(H_3buea)]^{-}$	−2	26.8	54.2	1.8	29.3	58.6
$[Fe^{IV}(O)(TMP)]$	−13.7	38.6	59.4	−9.6	44.1	62.8
$[Co^{III}(O)(PhB^{tBu}Im_3)]$	−11.5	15.1	66.1	−6.6	19.4	72.1
$[Ru^{IV}(O)(H^{+}TPA)(bpy)]^{3+}$	−7.2	75.2	33.7	-6.0	78.6	35.1
$[Fe^{IV}(O)(tpfpp)]$	−10.8	49.4	49.1	−7.3	53.3	53.0
$[Mn^{VII}(O)_4]^{-}$	−3.2	54.7	41.5	0.092	58.6	43.7
$[Mn^{V}(O)_2(tf_4tmap)]^{3+}$	−16.5	33.7	51.3	−12.5	36.5	55.5
$[Mn^{IV}(O)(OH)(tf_4tmap)]^{3+}$	−12	19.2	52.6	-8.0	21.1	55.0
$[Cr^{IV}(O)(TMC)(Cl)]^{+}$	−12.8	52.8	47.4	−10.9	56.7	50.9
$[Ru^{VI}(O)_2(TMC)]^{2+}$	1.2	82.0	26.0	3.8	86.7	27.8
$[Fe^{IV}(O)(N4Py)]^{2+}$	−8.5	64.3	29.9	−1.9	68.8	35.8
$[Fe^{IV}(O)(BnTPEN)]^{2+}$	−10.2	63.4	26.8	−4.6	66.6	32.4
$[Fe^{IV}(O)(^{Me2}TACN\text{-}Py_2)]^{2+}$	−9.1	63.0	29.2	−2.0	67.4	35.9
$[Fe^{IV}(O)(BP1)]^{2+}$	−9	69.2	27.5	−3.0	73.8	32.8
$[Fe^{IV}(O)(BP2)]^{2+}$	−12.4	67.4	23.6	−6.7	71.3	29.3
$[Ru^{IV}(O)(bpy)_2(py)]^{2+}$	−8.2	67.7	35.3	−7.2	71.6	36.9
$[Mn^{IV}(O)_2(Me_2EBC)]$	−6.1	6.9	77.6	−2.6	7.0	83.1
$[Mn^{IV}(O)(N4Py)]^{2+}$	−10.9	50.7	28.4	−6.4	54.9	33.1
$[Co^{IV}(O)(13\text{-}TMC)]^{2+}$	−17.9	68.3	3.2.0	−14.4	73.9	6.1
$[Fe^{IV}(O)(13\text{-}TMC)]^{2+}$	−21.8	77.6	9.3.0	−17.3	83.3	13.5
$[Ru^{VI}(O)_2(L)]^{2+}$	−2.6	84.8	13.9	−0.65	89.2	15.9
$[Ru^{VI}(O)_2(F_{28}\text{-}tpp)]$	−7.4	64.2	29.1	−4.5	66.1	32.1

All energies in kcal/mol.

Table A1.9 Kinetics and barrier heights for reactivity with fluorene

Oxo	k_2 (s^{-1})	CPET Barrier (kcal/mol)
$[Fe^{IV}(O)(Me_3NTB)(MeCN)]^{2+}$		
$[Fe^{IV}(O)(TMG_2dien)(MeCN)]^{2+}$		
$[Fe^{IV}(O)(TMG_3tren)]^{2+}$		
$[Fe^{V}(O)(TAML)]^{-}$		
$[Fe^{IV}(O)(TMC)(MeCN)]^{2+}$		
$[Fe^{IV}(O)(TMC)(N_3)]^{+}$	0.15	7.8
$[Fe^{IV}(O)(TMC)(OCOCF_3)]^{+}$	0.051	8.4
$[Fe^{IV}(O)(TMCS)]^{+}$		
$[Mn^{IV}(O)(H_3buea)]^{-}$		
$[Fe^{IV}(O)(TMP)]$	0.09	7.5
$[Co^{III}(O)(PhB^{tBu}Im_3)]$	0.61	7.5
$[Ru^{IV}(O)(H^{+}TPA)(bpy)]^{3+}$		
$[Fe^{IV}(O)(tpfpp)]$	2.3	6.5
$[Mn^{VII}(O)_4]^{-}$		
$[Mn^{V}(O)_2(tf_4tmap)]^{3+}$	28	5.4
$[Mn^{IV}(O)(OH)(tf_4tmap)]^{3+}$		
$[Cr^{IV}(O)(TMC)(Cl)]^{+}$		
$[Ru^{VI}(O)_2(TMC)]^{2+}$		
$[Fe^{IV}(O)(N4Py)]^{2+}$		
$[Fe^{IV}(O)(BnTPEN)]^{2+}$		
$[Fe^{IV}(O)(^{Me2}TACN\text{-}Py_2)]^{2+}$		
$[Fe^{IV}(O)(BP1)]^{2+}$		
$[Fe^{IV}(O)(BP2)]^{2+}$		
$[Ru^{IV}(O)(bpy)_2(py)]^{2+}$	21.9	5.4
$[Mn^{IV}(O)_2(Me_2EBC)]$	0.00912	10.3
$[Mn^{IV}(O)(N4Py)]^{2+}$		
$[Co^{IV}(O)(13\text{-}TMC)]^{2+}$	0.0064	8.2
$[Fe^{IV}(O)(13\text{-}TMC)]^{2+}$		
$[Ru^{VI}(O)_2(L)]^{2+}$	1.58	7
$[Ru^{VI}(O)_2(F_{28}\text{-}tpp)]$	1.32	7.4

See Table A1.1 for references and experimental conditions.

Table A1.10 Thermodynamic parameters of reactivity with fluorene

Oxo	$\Delta G°_{CPET}$	$\Delta G°_{PT}$	$\Delta G°_{ET}$	$\Delta E°_{CPET}$	$\Delta E°_{PT}$	$\Delta E°_{ET}$
$[Fe^{IV}(O)(Me_3NTB)(MeCN)]^{2+}$	−11.6	47.8	25.9	−5.1	51.1	32.0
$[Fe^{IV}(O)(TMG_2dien)(MeCN)]^{2+}$	−5.0	47.7	35.8	−1.2	51.1	40.2
$[Fe^{IV}(O)(TMG_3tren)]^{2+}$	−3.0	44.6	44.1	0.74	47.3	48.6
$[Fe^{V}(O)(TAML)]^{-}$	−5.8	29.4	36.8	−3.1	32.9	39.0
$[Fe^{IV}(O)(TMC)(MeCN)]^{2+}$	−2.2	58.3	33.4	5.3	61.6	41.0
$[Fe^{IV}(O)(TMC)(N_3)]^{+}$	−5.2	37.2	43.2	1.7	40.1	50.2
$[Fe^{IV}(O)(TMC)(OCOCF_3)]^{+}$	−4.4	46.8	39.3	2.5	49.8	46.9
$[Fe^{IV}(O)(TMCS)]^{+}$	−4.3	30.3	46.7	1.7	32.4	53.5
$[Mn^{IV}(O)(H_3buea)]^{-}$	5.0	17.7	59.0	9.1	19.2	63.5
$[Fe^{IV}(O)(TMP)]$	−6.6	29.5	64.3	−2.4	33.9	67.7
$[Co^{III}(O)(PhB^{tBu}Im_3)]$	−4.5	6.1	70.9	0.64	9.3	76.9
$[Ru^{IV}(O)(H^{+}TPA)(bpy)]^{3+}$	−0.2	66.1	38.5	1.2	68.5	39.9
$[Fe^{IV}(O)(tpfpp)]$	−3.8	40.3	53.9	−0.023	43.2	57.8
$[Mn^{VII}(O)_4]^{-}$	3.8	45.7	46.3	7.3	48.4	48.6
$[Mn^{V}(O)_2(tf_4tmap)]^{3+}$	−9.5	24.6	56.1	−5.2	26.4	60.4
$[Mn^{IV}(O)(OH)(tf_4tmap)]^{3+}$	−4.9	10.1	57.5	−0.8	11.0	59.9
$[Cr^{IV}(O)(TMC)(Cl)]^{+}$	−5.7	43.7	52.3	−3.7	46.6	55.7
$[Ru^{VI}(O)_2(TMC)]^{2+}$	8.2	72.9	30.8	11.0	76.5	32.6
$[Fe^{IV}(O)(N4Py)]^{2+}$	−1.5	55.2	34.7	5.3	58.6	40.6
$[Fe^{IV}(O)(BnTPEN)]^{2+}$	−3.1	54.3	31.6	2.6	56.4	37.2
$[Fe^{IV}(O)(^{Me2}TACN\text{-}Py_2)]^{2+}$	−2.1	53.9	34.0	5.2	57.2	40.8
$[Fe^{IV}(O)(BP1)]^{2+}$	−1.9	60.1	32.3	4.2	63.7	37.7
$[Fe^{IV}(O)(BP2)]^{2+}$	−5.4	58.3	28.4	0.57	61.1	34.2
$[Ru^{IV}(O)(bpy)_2(py)]^{2+}$	−1.2	58.6	40.1	−0.0089	61.5	41.7
$[Mn^{IV}(O)_2(Me_2EBC)]$	0.93	−2.2	82.4	4.6	−3.1	87.9
$[Mn^{IV}(O)(N4Py)]^{2+}$	−3.8	41.6	33.2	0.81	44.8	37.9
$[Co^{IV}(O)(13\text{-}TMC)]^{2+}$	−10.8	59.1	8.1	−7.2	63.7	10.9
$[Fe^{IV}(O)(13\text{-}TMC)]^{2+}$	−14.7	68.5	14.2	−10.0	73.1	18.3
$[Ru^{VI}(O)_2(L)]^{2+}$	4.4	75.7	18.7	6.6	79.1	20.7
$[Ru^{VI}(O)_2(F_{28}\text{-}tpp)]$	−0.34	55.1	33.9	2.8	55.9	36.9

All (free) energies in kcal/mol.

2. Detailed Statistics on DHA Regressions

In Table A1.1 we report statistics on the regressions with DHA reaction barriers from Table 1. We also give regressions with $\Delta G°_{CPET}$[2] and with electronic energies instead of free energies. While the regression against $\{\Delta E°_{CPET}, \Delta E°_{PT}, \Delta E°_{ET}\}$ fits the data better than the regression against $\{\Delta G°_{CPET}, \Delta G°_{PT}, \Delta G°_{ET}\}$, there are good theoretical reasons to use free energies rather than electronic energies for LFER analyses and we therefore limit our discussion to free energies.[23] The table is followed by a detailed summary of each regression and a breakdown of the $\{\Delta G°_{CPET},\Delta G°_{PT},\Delta G°_{ET}\}$ model for each data point.

We report all the overall metrics as discussed in the methods section of the main text with more details specific to the parameters in each model and their corresponding coefficients. We report the correlation matrix of the parameters included in the model, their averages, and their standard deviations (all calculated with the training set). Within a linear regression, high correlation between two x-variables makes it difficult to untangle their effects on the y-variable, although the joint effect is unaffected.[114]

For the coefficients, we report their values, their standard errors, 95% t-confidence intervals, and weighted coefficients. The coefficients' units are kcal/mol divided by the associated parameters' units. The standard errors do not directly inform on how reliable the coefficients are and are therefore scaled to give 95% *t*-confidence intervals. These rely on similar assumptions as the F-tests, and therefore have similar weaknesses.[112,114] If the same analysis was performed on many different training sets – assuming the model is correctly formulated – one would expect to find the coefficients within the indicated interval 95% of the time (technically, this is the confidence in the method used to obtain the estimate of the coefficient, not in the estimate of the

coefficient itself). If the interval contains zero, then there is no significant effect from the associated parameter and the coefficient and even its sign cannot be reliably interpreted. The weighted coefficients are the coefficients multiplied by the standard deviation of the associated parameter (within the training set). These can be used to compare the magnitude of disparate parameters' effects.[105]

Table A 1.11 Summary of statistics of regressions with DHA data

Parameter(s) Regressed with $\Delta G°_{CPET}$	R^2	MSE[a]	LOO[b] R^2	LOO[b] MSE[a]	5-Fold CV[c] MSE[a]	p-value[d]
$\Delta G°_{CPET}$ only	0.70	1.18	0.60	1.57	1.49	< 0.001[f]
%BV Steric Metrics	0.77	0.88	0.64	1.39	1.46	0.15
Oxo Spin Density	0.70	1.18	0.55	1.77	1.73	0.78
Spin Excitation	0.71	1.14	0.50	1.95	1.97	0.49
$\lvert\eta\rvert$	0.73	1.06	0.53	1.82	1.76	0.22
$\Delta G°_{PT}$, $\Delta G°_{ET}$	0.86	0.57	0.71	1.14	1.34	0.0082 0.023[g] 0.0038[h]
$\Delta G°_{CPET}{}^2$	0.71	1.11	0.59	1.59	1.51	0.36
$\Delta E°_{CPET}$ only[e]	0.62	1.47	0.52	1.89	1.90	< 0.001[i]
$\Delta E°_{CPET}$, $\Delta E°_{PT}$, $\Delta E°_{ET}$[e]	0.86	0.53	0.75	0.96	1.16	0.0013[j]
ΔG_{CC}	0.73	1.04	0.60	1.56	1.62	0.19
ΔG_{CC}, η	0.86	0.57	0.71	1.14	1.34	0.006[k]

[a]Mean Squared Error, kcal^2 mol^{-2}. [b]Leave-One-Out. [c]Cross Validation. [d]From an F-test where the null hypothesis is that only $\Delta G°_{CPET}$ has an effect. [e] $\Delta G°_{CPET}$ not included in the regression. [f]From an F-test where the null hypothesis is that $\Delta G°_{CPET}$ has no effect. [g]From an F-test where the null hypothesis is that $\Delta G°_{PT}$ has no effect. [h]From an F-test where the null hypothesis is that $\Delta G°_{ET}$ has no effect. [i]From an *F*-test where the null hypothesis is that $\Delta E°_{CPET}$ has no effect. [j]From an *F*-test where the null hypothesis is that only $\Delta E°_{CPET}$ has an effect. [k]From an *F*-test where the null hypothesis is that only η has no effect.

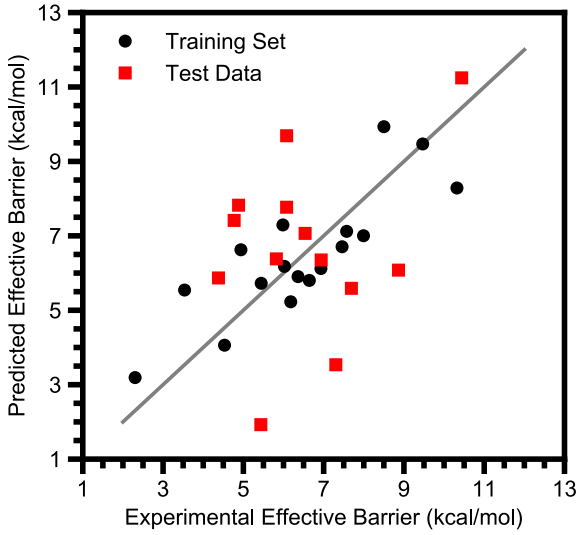

Regression A1.1 DHA barriers against $\Delta G°_{CPET}$ only.

```
['DHA ΔG_CPET'] Metrics:

Score on Training Data:                 0.6967248832007887
MSE of Training Data:                   1.1837466708175275
Score of LOO Cross Validation:          0.5971855224924804
MSE of LOO Cross Validation:            1.5722697652848394
MSE of 5-Fold Cross Validation:         1.49405736960365(0.04323619491372769)
F-Test p-value of final 1 variables:    3.078601862627206e-05

Correlation Matrix of x-values:
             DHA ΔG_ CPET'
DHA ΔG_CPET          1.0

['DHA ΔG_CPET'] Training Average:
[-7.77619718]

 ['DHA ΔG_CPET'] Training Deviation:
[4.05326542]

 ['DHA ΔG_CPET'] Coefficients:
[0.40685215]

 ['DHA ΔG_CPET'] Standard Error:
 [0.06930726]

 ['DHA ΔG_CPET'] t-Test "Error":
 [0.14772492]

 ['DHA ΔG_CPET'] Weighted Coefficients:
[1.64907974]

 ['DHA ΔG_CPET'] Intercept:
 9.645819215174036
```

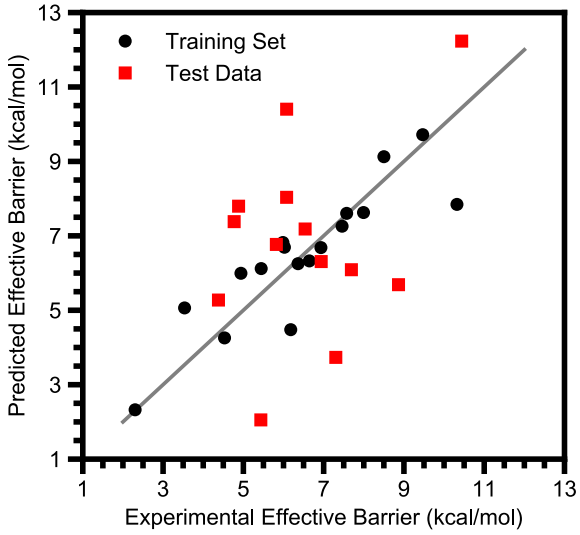

Regression A1.2 DHA barriers against $\Delta G°_{CPET}$ and percent buried volume sterics.

```
['DHA ΔG_CPET', '%BV Tot', '%BV Dev'] Metrics:

Score on Training Data:                  0.7746125436672053
MSE of Training Data:                    0.8797347236852846
Score of LOO Cross Validation:           0.644354460933599
MSE of LOO Cross Validation:             1.3881594616273243
MSE of 5-Fold Cross Validation:          1.46372512865656(0.059310929316259454)
F-Test p-value of final 2 variables:     0.14524602753892502

Correlation Matrix of x-values:
             DHA ΔG_CPET   %BV Tot   %BV Dev
DHA ΔG_CPET     1.000000 -0.107404  0.230500
%BV Tot        -0.107404  1.000000  0.134191
%BV Dev         0.230500  0.134191  1.000000

['DHA ΔG_CPET', '%BV Tot', '%BV Dev'] Training Average:
[-7.77619718 64.39411765  5.35367331]

 ['DHA ΔG_CPET', '%BV Tot', '%BV Dev'] Training Deviation:
[ 4.05326542 10.53891783  4.76681449]

 ['DHA ΔG_CPET', '%BV Tot', '%BV Dev'] Coefficients:
[ 0.44406794  0.01827786 -0.11845869]

 ['DHA ΔG_CPET', '%BV Tot', '%BV Dev'] Standard Error:
 [0.06664533 0.02516922 0.05685555]

 ['DHA ΔG_CPET', '%BV Tot', '%BV Dev'] t-Test "Error":
 [0.14397848 0.0543748  0.12282896]

 ['DHA ΔG_CPET', '%BV Tot', '%BV Dev'] Weighted Coefficients:
[ 1.79992522  0.19262889 -0.5646706 ]

 ['DHA ΔG_CPET', '%BV Tot', '%BV Dev'] Intercept:
 9.392418865022623
```

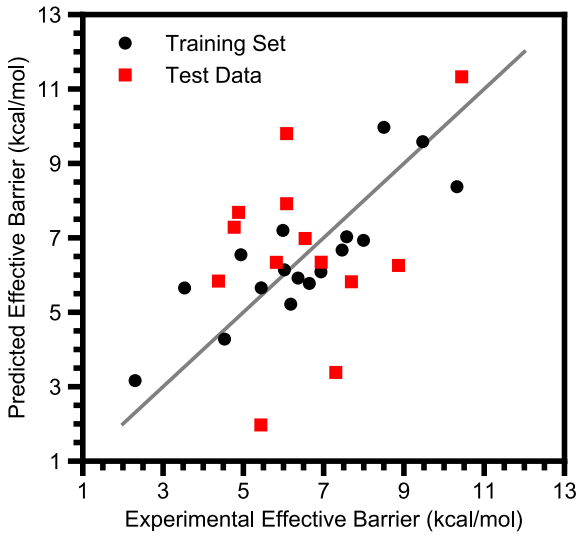

Regression A1.3 DHA barriers against $\Delta G°_{CPET}$ and the IBO spin density on the oxo ligand.

```
['DHA ΔG_CPET', 'IBO Spin O'] Metrics:

Score on Training Data:                 0.698551220951851
MSE of Training Data:                   1.176618089826692
Score of LOO Cross Validation:          0.546795585374296
MSE of LOO Cross Validation:            1.7689523053359144
MSE of 5-Fold Cross Validation:         1.7301047476523321(0.03545602037697516)
F-Test p-value of final 1 variables:    0.775139773791961

Correlation Matrix of x-values:
             DHA ΔG_CPET  IBO Spin O
DHA ΔG_CPET     1.000000   -0.346171
IBO Spin O     -0.346171    1.000000

['DHA ΔG_CPET', 'IBO Spin O'] Training Average:
[-7.77619718  0.55994471]

 ['DHA ΔG_CPET', 'IBO Spin O'] Training Deviation:
[4.05326542 0.29315117]

 ['DHA ΔG_CPET', 'IBO Spin O'] Coefficients:
[ 0.39916608 -0.30699241]

 ['DHA ΔG_CPET', 'IBO Spin O'] Standard Error:
 [0.07623711 1.05409519]

 ['DHA ΔG_CPET', 'IBO Spin O'] t-Test "Error":
 [0.16351234 2.26080932]

 ['DHA ΔG_CPET', 'IBO Spin O'] Weighted Coefficients:
[ 1.61792606 -0.08999518]

 ['DHA ΔG_CPET', 'IBO Spin O'] Intercept:
 9.757949587592675
```

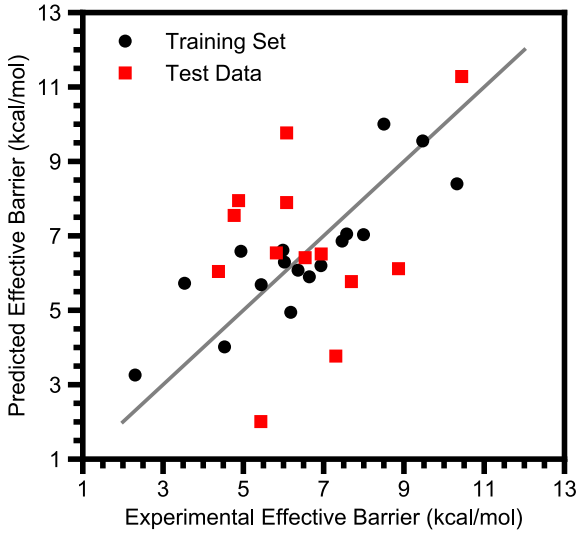

Regression A1.4 DHA barriers against $\Delta G°_{CPET}$ and the Spin Excitation Energy.

```
['DHA ΔG_CPET', 'Spin Excitation'] Metrics:

Score on Training Data:                 0.7072135314484478
MSE of Training Data:                   1.1428072670986176
Score of LOO Cross Validation:          0.5009984749798582
MSE of LOO Cross Validation:            1.9477080751288274
MSE of 5-Fold Cross Validation:         1.970364948730487(0.0559990030724594)
F-Test p-value of final 1 variables:    0.49045257892652216

Correlation Matrix of x-values:
                 DHA ΔG_CPET  Spin Excitation
DHA ΔG_CPET          1.00000         -0.20409
Spin Excitation     -0.20409          1.00000

['DHA ΔG_CPET', 'Spin Excitation'] Training Average:
[-7.77619718 14.58587927]

 ['DHA ΔG_CPET', 'Spin Excitation'] Training Deviation:
[ 4.05326542 19.10348113]

 ['DHA ΔG_CPET', 'Spin Excitation'] Coefficients:
[ 0.39644513 -0.01081924]

 ['DHA ΔG_CPET', 'Spin Excitation'] Standard Error:
 [0.0720039  0.01527737]

 ['DHA ΔG_CPET', 'Spin Excitation'] t-Test "Error":
 [0.154433   0.03276669]

 ['DHA ΔG_CPET', 'Spin Excitation'] Weighted Coefficients:
[ 1.60689734 -0.20668517]

 ['DHA ΔG_CPET', 'Spin Excitation'] Intercept:
 9.722700343793177
```

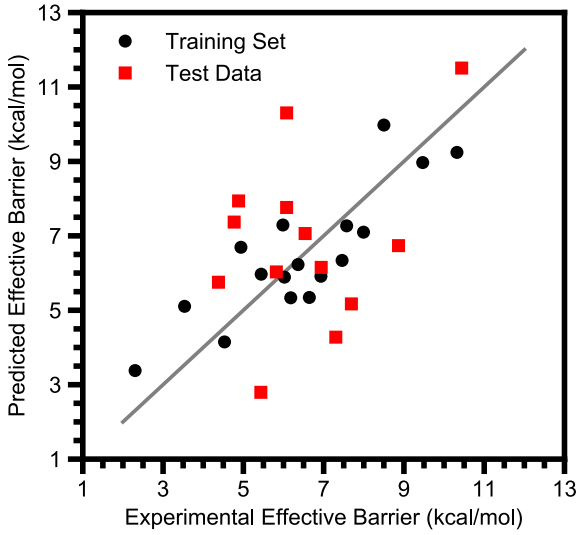

Regression A1.5 DHA barriers against $\Delta G°_{CPET}$ and the magnitude of the asynchronicity.

```
['DHA ΔG_CPET', 'DHA |η| (G)'] Metrics:

Score on Training Data:                 0.7281325727412633
MSE of Training Data:                   1.0611558419885931
Score of LOO Cross Validation:          0.5349640252644873
MSE of LOO Cross Validation:            1.815133376959526
MSE of 5-Fold Cross Validation:         1.7554887437479856(0.08293293544608828)
F-Test p-value of final 1 variables:    0.2241810808486162

Correlation Matrix of x-values:
             DHA ΔG_CPET  DHA |η| (G)
DHA ΔG_CPET     1.000000     0.184231
DHA |η| (G)     0.184231     1.000000

['DHA ΔG_CPET', 'DHA |η| (G)'] Training Average:
[-7.77619718 17.96727543]

 ['DHA ΔG_CPET', 'DHA |η| (G)'] Training Deviation:
[ 4.05326542 12.92730813]

 ['DHA ΔG_CPET', 'DHA |η| (G)'] Coefficients:
[0.39066077 0.02755618]

 ['DHA ΔG_CPET', 'DHA |η| (G)'] Standard Error:
 [0.06910646 0.02166784]

 ['DHA ΔG_CPET', 'DHA |η| (G)'] t-Test "Error":
 [0.14821863 0.04647289]

 ['DHA ΔG_CPET', 'DHA |η| (G)'] Weighted Coefficients:
[1.58345179 0.35622725]

 ['DHA ΔG_CPET', 'DHA |η| (G)'] Intercept:
 9.024802368188036
```

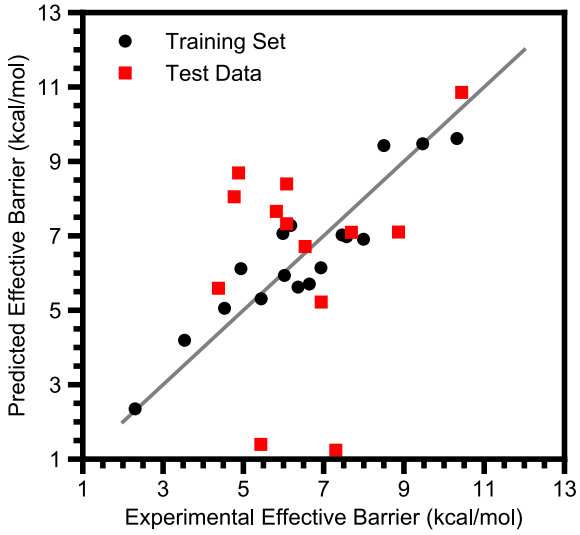

Regression A1.6 DHA barriers against $\Delta G°_{CPET}$, $\Delta G°_{PT}$, and $\Delta G°_{ET}$.

```
['DHA ΔG_CPET', 'DHA ΔG_PT', 'DHA ΔG_ET'] Metrics:

Score on Training Data:                 0.8550607749306552
MSE of Training Data:                   0.5657283293053714
Score of LOO Cross Validation:          0.708584021837019
MSE of LOO Cross Validation:            1.137457954395417
MSE of 5-Fold Cross Validation:         1.3430227389100244(0.09649120302575805)
F-Test p-value of final 2 variables:    0.008237008538600432
F-Test p-value of 2nd to last variable (DHA ΔG_PT):    0.023223177281245677
F-Test p-value of final variable (DHA ΔG_ET):    0.00377509573731305

Correlation Matrix of x-values:
             DHA ΔG_CPET  DHA ΔG_PT  DHA ΔG_ET
DHA ΔG_CPET     1.000000  -0.116636   0.300610
DHA ΔG_PT      -0.116636   1.000000  -0.886456
DHA ΔG_ET       0.300610  -0.886456   1.000000

['DHA ΔG_CPET', 'DHA ΔG_PT', 'DHA ΔG_ET'] Training Average:
[-7.77619718 47.94811989 48.18969167]

 ['DHA ΔG_CPET', 'DHA ΔG_PT', 'DHA ΔG_ET'] Training Deviation:
[ 4.05326542 17.72475347 14.50071323]

 ['DHA ΔG_CPET', 'DHA ΔG_PT', 'DHA ΔG_ET'] Coefficients:
[0.3120842  0.06952437 0.12109262]

 ['DHA ΔG_CPET', 'DHA ΔG_PT', 'DHA ΔG_ET'] Standard Error:
 [0.05736941 0.02703542 0.03441251]

 ['DHA ΔG_CPET', 'DHA ΔG_PT', 'DHA ΔG_ET'] t-Test "Error":
 [0.12393907 0.05840647 0.07434371]

 ['DHA ΔG_CPET', 'DHA ΔG_PT', 'DHA ΔG_ET'] Weighted Coefficients:
[1.26496011 1.23230225 1.75592936]

 ['DHA ΔG_CPET', 'DHA ΔG_PT', 'DHA ΔG_ET'] Intercept:
 -0.2600936876032849
```

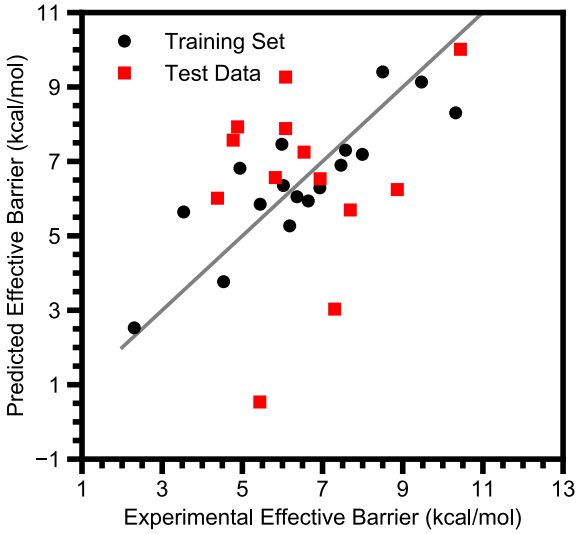

Regression A1.7 DHA barriers against $\Delta G°_{CPET}$ and $\Delta G°_{CPET}{}^2$.

```
['DHA ΔG_CPET', 'DHA ΔG_CPET^2'] Metrics:

Score on Training Data:                 0.7149873903247832
MSE of Training Data:                   1.112464258211542
Score of LOO Cross Validation:          0.5915803011130514
MSE of LOO Cross Validation:            1.5941481251619116
MSE of 5-Fold Cross Validation:         1.5101598742890083(0.056935040823286265)
F-Test p-value of final 1 variables:    0.3596321487917926

Correlation Matrix of x-values:
               DHA ΔG_CPET  DHA ΔG_CPET^2
DHA ΔG_CPET       1.000000      -0.929028
DHA ΔG_CPET^2    -0.929028       1.000000

['DHA ΔG_CPET', 'DHA ΔG_CPET^2'] Training Average:
[-7.77619718 76.89820308]

 ['DHA ΔG_CPET', 'DHA ΔG_CPET^2'] Training Deviation:
[ 4.05326542 62.99805804]

 ['DHA ΔG_CPET', 'DHA ΔG_CPET^2'] Coefficients:
[ 0.24146465 -0.01145385]

 ['DHA ΔG_CPET', 'DHA ΔG_CPET^2'] Standard Error:
 [0.18795835 0.01209315]

 ['DHA ΔG_CPET', 'DHA ΔG_CPET^2'] t-Test "Error":
 [0.40313056 0.02593723]

 ['DHA ΔG_CPET', 'DHA ΔG_CPET^2'] Weighted Coefficients:
[ 0.97872033 -0.72157062]

 ['DHA ΔG_CPET', 'DHA ΔG_CPET^2'] Intercept:
 9.240514307521131
```

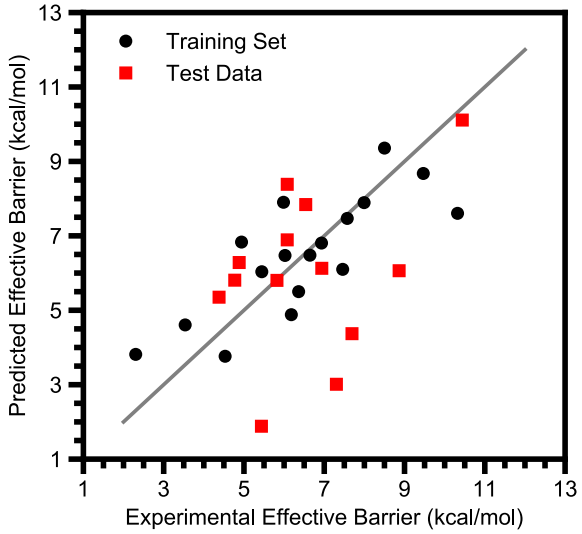

Regression A1.8 DHA barriers against $\Delta E°_{CPET}$.

```
['DHA ΔE_CPET'] Metrics:

Score on Training Data:                 0.6246046731001371
MSE of Training Data:                   1.4652470441627932
Score of LOO Cross Validation:          0.5157469389983269
MSE of LOO Cross Validation:            1.8901417130553664
MSE of 5-Fold Cross Validation:         1.9017782503654304(0.04647736834316938)
F-Test p-value of final 1 variables:    0.00015966818653256887

Correlation Matrix of x-values:
             DHA ΔE_CPET
DHA ΔE_CPET          1.0

['DHA ΔE_CPET'] Training Average:
[-2.08594867]

 ['DHA ΔE_CPET'] Training Deviation:
[3.99325888]

 ['DHA ΔE_CPET'] Coefficients:
[0.39100845]

 ['DHA ΔE_CPET'] Standard Error:
 [0.07826766]

 ['DHA ΔE_CPET'] t-Test "Error":
 [0.16682356]

 ['DHA ΔE_CPET'] Weighted Coefficients:
[1.56139797]

 ['DHA ΔE_CPET'] Intercept:
 7.297680247312937
```

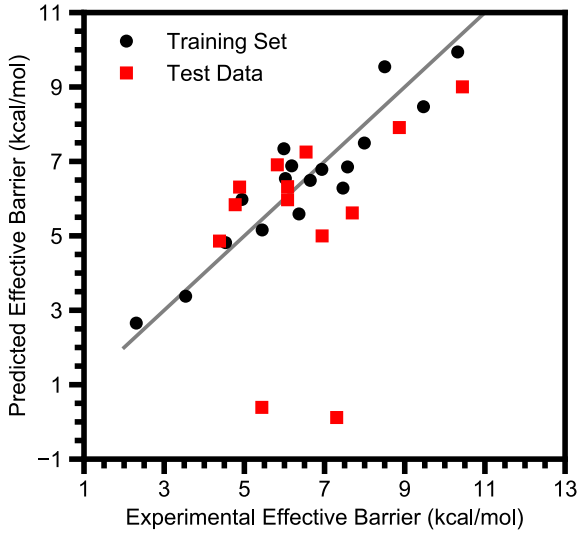

Regression A1.9 DHA barriers against $\Delta E°_{CPET}$, $\Delta E°_{PT}$, and $\Delta E°_{ET}$.

```
['DHA ΔE_CPET', 'DHA ΔE_PT', 'DHA ΔE_ET'] Metrics:

Score on Training Data:                 0.8642292420790744
MSE of Training Data:                   0.5299418705349127
Score of LOO Cross Validation:          0.7546196643252872
MSE of LOO Cross Validation:            0.9577711435895295
MSE of 5-Fold Cross Validation:         1.162034462523503(0.0776391752517394)
F-Test p-value of final 2 variables:    0.0013460555172805089

Correlation Matrix of x-values:
             DHA ΔE_CPET  DHA ΔE_PT  DHA ΔE_ET
DHA ΔE_CPET     1.000000   0.093539   0.119751
DHA ΔE_PT       0.093539   1.000000  -0.868929
DHA ΔE_ET       0.119751  -0.868929   1.000000

['DHA ΔE_CPET', 'DHA ΔE_PT', 'DHA ΔE_ET'] Training Average:
[-2.08594867 50.96221826 55.73635424]

 ['DHA ΔE_CPET', 'DHA ΔE_PT', 'DHA ΔE_ET'] Training Deviation:
[ 3.99325888 18.62129223 14.02559969]

 ['DHA ΔE_CPET', 'DHA ΔE_PT', 'DHA ΔE_ET'] Coefficients:
[0.32595791 0.04033659 0.11282918]

 ['DHA ΔE_CPET', 'DHA ΔE_PT', 'DHA ΔE_ET'] Standard Error:
 [0.05562276 0.02392676 0.03185668]

 ['DHA ΔE_CPET', 'DHA ΔE_PT', 'DHA ΔE_ET'] t-Test "Error":
 [0.12016567 0.05169063 0.06882218]

 ['DHA ΔE_CPET', 'DHA ΔE_PT', 'DHA ΔE_ET'] Weighted Coefficients:
[1.30163433 0.75111934 1.58249696]

 ['DHA ΔE_CPET', 'DHA ΔE_PT', 'DHA ΔE_ET'] Intercept:
 -1.1823410363409037
```

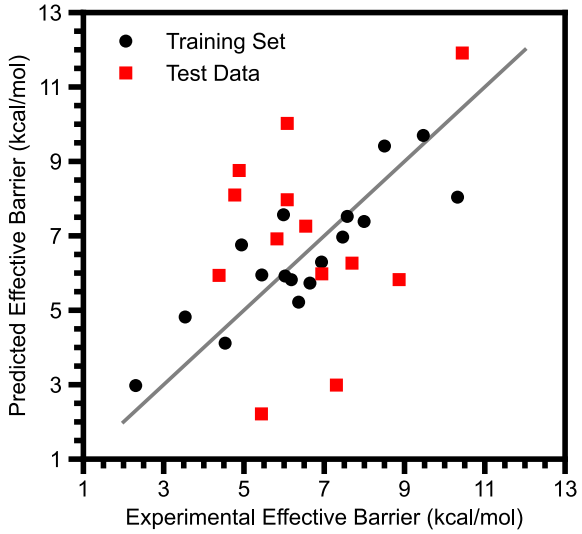

Regression A1.10 DHA barriers against $\Delta G°_{CPET}$ and $\Delta G°_{CC}$.

```
['DHA ΔG_CPET', 'DHA ΔG_CC'] Metrics:

Score on Training Data:                 0.7328944232795918
MSE of Training Data:                   1.0425693361744381
Score of LOO Cross Validation:          0.5997603617332107
MSE of LOO Cross Validation:            1.5622196252955347
MSE of 5-Fold Cross Validation:         1.6235818400869788(0.08443072754350571)
F-Test p-value of final 1 variables:    0.19017088212970568

Correlation Matrix of x-values:
             DHA ΔG_CPET  DHA ΔG_CC
DHA ΔG_CPET     1.000000   0.215833
DHA ΔG_CC       0.215833   1.000000

['DHA ΔG_CPET', 'DHA ΔG_CC'] Training Average:
[  -7.77619718 -103.91400874]

 ['DHA ΔG_CPET', 'DHA ΔG_CC'] Training Deviation:
[4.05326542 8.16161558]

 ['DHA ΔG_CPET', 'DHA ΔG_CC'] Coefficients:
[ 0.42734269 -0.0471482 ]

 ['DHA ΔG_CPET', 'DHA ΔG_CC'] Standard Error:
 [0.06895125 0.03424294]

 ['DHA ΔG_CPET', 'DHA ΔG_CC'] t-Test "Error":
 [0.14788572 0.0734438 ]

 ['DHA ΔG_CPET', 'DHA ΔG_CC'] Weighted Coefficients:
[ 1.73213335 -0.38480545]

 ['DHA ΔG_CPET', 'DHA ΔG_CC'] Intercept:
 4.9057996396298345
```

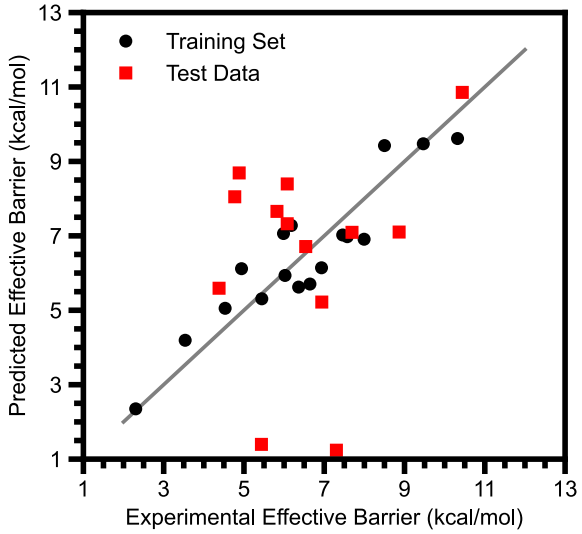

Regression A1.11 DHA barriers against $\Delta G°_{CPET}$, $\Delta G°_{CC}$, and η.

```
['DHA ΔG_CPET', 'DHA ΔG_CC', 'DHA η'] Metrics:

Score on Training Data:                  0.8550607749306552
MSE of Training Data:                    0.5657283293053715
Score of LOO Cross Validation:           0.7085840218370183
MSE of LOO Cross Validation:             1.1374579543954197
MSE of 5-Fold Cross Validation:          1.343022738910026(0.09649120302575828)
F-Test p-value of final 1 variables:     0.0056360075993103775

Correlation Matrix of x-values:
             DHA ΔG_CPET  DHA ΔG_CC     DHA η
DHA ΔG_CPET     1.000000   0.215833 -0.205272
DHA ΔG_CC       0.215833   1.000000 -0.508560
DHA η          -0.205272  -0.508560  1.000000

['DHA ΔG_CPET', 'DHA ΔG_CC', 'DHA η'] Training Average:
[  -7.77619718 -103.91400874   -0.17079124]

 ['DHA ΔG_CPET', 'DHA ΔG_CC', 'DHA η'] Training Deviation:
[ 4.05326542  8.16161558 22.13389058]

 ['DHA ΔG_CPET', 'DHA ΔG_CC', 'DHA η'] Coefficients:
[ 0.4073927  -0.09530849 -0.03646977]

 ['DHA ΔG_CPET', 'DHA ΔG_CC', 'DHA η'] Standard Error:
 [0.05305258 0.0299482  0.01101738]

 ['DHA ΔG_CPET', 'DHA ΔG_CC', 'DHA η'] t-Test "Error":
 [0.11461314 0.06469914 0.02380161]

 ['DHA ΔG_CPET', 'DHA ΔG_CC', 'DHA η'] Weighted Coefficients:
[ 1.65127073 -0.77787128 -0.80721789]

 ['DHA ΔG_CPET', 'DHA ΔG_CC', 'DHA η'] Intercept:
 -0.26009368760328133
```

Table A1.12 Barrier heights predicted by the {$\Delta G°_{CPET}$, $\Delta G°_{PT}$, $\Delta G°_{ET}$} model and the contribution of each thermodynamic parameter

Oxo	Ref	0.31 × $\Delta G°_{CPET}$	0.070 × $\Delta G°_{PT}$	0.12 × $\Delta G°_{ET}$	Pred Barrier[a]	Exp[b] Barrier
$[Fe^{IV}(O)(Me_3NTB)(MeCN)]^{2+}$	116	-5.0	4.0	3.6	2.4	2.3
$[Fe^{IV}(O)(TMG_2dien)(MeCN)]^{2+}$	44	-2.9	4.0	4.8	5.6	4.4
$[Fe^{IV}(O)(TMG_3tren)]^{2+}$	17	-2.3	3.8	5.7	7.0	7.5
$[Fe^{V}(O)(TAML)]^{-}$	117	-3.1	2.7	4.9	4.2	3.5
$[Fe^{IV}(O)(TMC)(MeCN)]^{2+}$	118	-2.0	4.7	4.5	6.9	8.0
$[Fe^{IV}(O)(TMC)(N_3)]^{+}$	118	-2.9	3.3	5.6	5.7	6.6
$[Fe^{IV}(O)(TMC)(OCOCF_3)]^{+}$	118	-2.7	3.9	5.2	6.1	6.9
$[Fe^{IV}(O)(TMCS)]^{+}$	118	-2.7	2.8	6.0	5.9	6.0
$[Mn^{IV}(O)(H_3buea)]^{-}$	52	0.2	1.9	7.5	9.4	8.5
$[Fe^{IV}(O)(TMP)]$	119	-3.4	2.7	8.2	7.3	6.2
$[Co^{III}(O)(PhB^{tBu}Im_3)]$	50	-2.7	1.1	9.0	7.1	8.9
$[Ru^{IV}(O)(H^{+}TPA)(bpy)]^{3+}$	120	-1.4	5.3	5.0	8.7	4.9
$[Fe^{IV}(O)(tpfpp)]$	121	-2.5	3.5	6.9	7.7	5.8
$[Mn^{VII}(O)_4]^{-}$	49	-0.14	3.9	6.0	9.5	9.5
$[Mn^{V}(O)_2(tf_4tmap)]^{3+}$	122	-4.3	2.4	7.2	5.1	4.5
$[Mn^{IV}(O)(OH)(tf_4tmap)]^{3+}$	122	-2.9	1.4	7.4	5.6	6.4
$[Cr^{IV}(O)(TMC)(Cl)]^{+}$	123	-3.1	3.7	6.7	7.1	7.7
$[Ru^{VI}(O)_2(TMC)]^{2+}$	124	1.2	5.8	4.1	10.9	10.4
$[Fe^{IV}(O)(N4Py)]^{2+}$	125	-1.8	4.5	4.6	7.1	6.0
$[Fe^{IV}(O)(BnTPEN)]^{2+}$	125	-2.3	4.5	4.2	6.1	4.9
$[Fe^{IV}(O)(^{Me2}TACN\text{-}Py_2)]^{2+}$	125	-2.0	4.4	4.5	6.7	6.5
$[Fe^{IV}(O)(BP1)]^{2+}$	125	-1.9	4.9	4.3	7.0	7.6
$[Fe^{IV}(O)(BP2)]^{2+}$	125	-3.0	4.7	3.8	5.3	5.4
$[Ru^{IV}(O)(bpy)_2(py)]^{2+}$	126	-1.7	4.8	5.3	8.0	4.8
$[Mn^{IV}(O)_2(Me_2EBC)]$	127	-1.0	0.5	10.4	9.6	10.3
$[Mn^{IV}(O)(N4Py)]^{2+}$	129	-2.5	3.6	4.4	5.2	6.9
$[Co^{IV}(O)(13\text{-}TMC)]^{2+}$	130	-4.7	4.8	1.4	1.2	7.3
$[Fe^{IV}(O)(13\text{-}TMC)]^{2+}$	128	-5.9	5.4	2.1	1.4	5.4
$[Ru^{VI}(O)_2(L)]^{2+}$	132	0.03	6.0	2.6	8.4	6.1
$[Ru^{VI}(O)_2(F_{28}tpp)]$	131	-1.4	4.5	4.5	7.3	6.1

[a] $0.31\Delta G_{CPET} + 0.070\ \Delta G°_{PT} + 0.12\ \Delta G°_{ET} - 0.26$. [b] Experimental. All energies in kcal/mol.

3. Entropy Adjustment to Reaction Barriers

We subtracted from the experimental reaction barrier the loss of translational entropy upon metal oxo and substrate association. This correction is derived from the expression of the translational entropy of a chemical species of mass m and concentration C:[164]

Equation A1.1 $$TS_t = RT \ln\left(\left(\frac{2\pi mRT}{h^2}\right)^{\frac{3}{2}} C^{-1}\right) + \frac{5}{2}RT$$

where RT is the thermal energy in kcal/mol and h is Plank's constant. With all species in the standard state of $C^\circ = 1\ M$, the standard change in translational entropy upon association is:

$$(T\Delta S_t^\circ)_{assoc} = \mathrm{TS_{t,MO+CH}} - \left(TS_{t,MO} - TS_{t,CH}\right) = RT \ln\left(\left(\frac{2\pi(m_{MO}+m_{CH})RT}{h^2}\right)^{\frac{3}{2}} C^{\circ -1}\right) + \frac{5}{2}RT -$$

$$\left(RT \ln\left(\left(\frac{2\pi m_{MO}RT}{h^2}\right)^{\frac{3}{2}} C^{\circ -1}\right) + \frac{5}{2}RT + RT \ln\left(\left(\frac{2\pi m_{CH}RT}{h^2}\right)^{\frac{3}{2}} C^{\circ\ -1}\right) + \frac{5}{2}RT\right)$$

Equation A1.2

in which the metal oxo is denoted as MO, the substrate as CH, and the associated complex as MO+CH. Simplifying this by combining the log terms via the identity $\ln a - \ln b - \ln c = -\ln\frac{bc}{a}$, canceling two of the $\frac{5}{2}RT$ terms, and factoring out RT gives:

Equation A1.3 $$(T\Delta S_t)_{assoc} = -RT\left[\ln\left(\left(\frac{2\pi(\frac{m_{Oxo}m_{Sub}}{m_{Oxo}+m_{Sub}})RT}{h^2}\right)^{\frac{3}{2}} C^{\circ -1}\right) + \frac{5}{2}\right]$$

Combining the masses into $\mu = \frac{m_{Oxo}m_{Sub}}{m_{Oxo}+m_{Sub}}$ finishes the derivation of Equation 2.7. We find this correction adequately accounts for the temperature dependence of the barriers; in Regression A1.12 we show that RT does not improve a fit to $\Delta G^\circ_{\mathrm{CPET}}$ alone the fit.

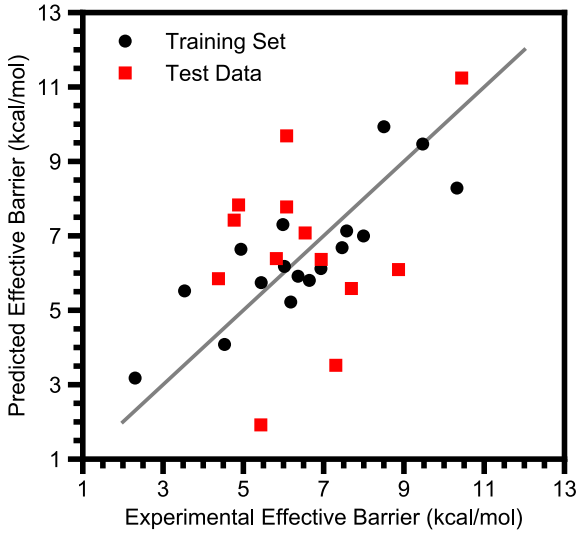

Regression A1.12 DHA barriers against $\Delta G°_{CPET}$ and RT.

```
['DHA ΔG_CPET', 'kT'] Metrics:

Score on Training Data:                 0.6967643666901857
MSE of Training Data:                   1.1835925584405569
Score of LOO Cross Validation:          0.5227899514128529
MSE of LOO Cross Validation:            1.8626513518737027
MSE of 5-Fold Cross Validation:         1.868642947451995(0.09296746191926707)
F-Test p-value of final 1 variables:    0.9665472615379543

Correlation Matrix of x-values:
             DHA ΔG_CPET        kT
DHA ΔG_CPET     1.000000  0.575834
kT              0.575834  1.000000

['DHA ΔG_CPET', 'kT'] Training Average:
[-7.77619718  0.55186587]

 ['DHA ΔG_CPET', 'kT'] Training Deviation:
[4.05326542 0.04426339]

 ['DHA ΔG_CPET', 'kT'] Coefficients:
[0.40469496 0.34304495]

 ['DHA ΔG_CPET', 'kT'] Standard Error:
 [0.08774231 8.03469455]

 ['DHA ΔG_CPET', 'kT'] t-Test "Error":
 [ 0.18818853 17.23270591]

 ['DHA ΔG_CPET', 'kT'] Weighted Coefficients:
[1.64033608 0.01518433]

 ['DHA ΔG_CPET', 'kT'] Intercept:
 9.439729679880315
```

4. Effect of Solvent – Oxo Hydrogen Bonding on Regressions

Hydrogen bonding between protic solvents and the oxo ligand of metal oxo complexes likely results in raising the apparent barrier of CPET reactions,[104,141] but we were unable to derive a reliable adjustment for this effect. Direct calculation of the equilibria between metal oxo complexes and solvent molecules was not feasible: DFT calculations of weak intermolecular interactions are unreliable,[137,318,319] and even if largely electrostatic hydrogen bonds are an exception it would be difficult to determine the free energy of unbound solvent molecules in the variety of solvent mixtures which protic solvents appear in. We were, however, able to make a crude attempt at quantifying hydrogen bonding to demonstrate that our neglect of this effect does not affect our overall conclusions. Snelgrove et al.[141] have shown that for hydrogen atom transfer reactions of O–H and N–H bonds the effect of hydrogen bonding to the solvent can be accounted for by means of Abraham's hydrogen bonding parameters:[320,321]

Equation A1.4 $$\log k^S = \log k^\circ + 8.3\,\alpha \cdot \beta$$

where k^S is the rate in the presence of solvent hydrogen bonding, k° is the rate in the absence of solvent hydrogen bonding, α is Abraham's hydrogen bond acidity of the substrate O–H or N–H bond, β is Abraham's hydrogen bond basicity of the solvent, and all logarithms are base 10. This is very similar to a formula from Abraham for the equilibrium constant K of the formation of a hydrogen bond dimer between a donor with hydrogen bond acidity α and an acceptor with hydrogen bond basicity β (again with a common logarithm):[321]

Equation A1.5 $$\log K = 7.354\,\alpha \cdot \beta - 1.094$$

The similarity indicates that Snelgrove et al.'s expression is fundamentally related to the free energy of forming a hydrogen bonded dimer, and that it may be a good approximation for a more

general situation than an O–H or N–H substrate donating a hydrogen bond to the solvent. However, the ability of protic solvents to form hydrogen bonds with each other renders it unclear if a simple application of the energy of dimer formation will apply as well to the case of hydrogen bonding to a protic solvent. It is further unclear how this formula's applicability is affected by temperature changes, use of solvent mixtures, or the presence of electrolytes. The biggest hindrance to applying this formula, however, is that the Abraham hydrogen bond basicities of metal oxo complexes are not known. For all these reasons we are not confident that the use of this formula to adjust k_2 values for solvent hydrogen bonding will result in more accurate reaction barriers than neglect of this effect entirely. Nonetheless, we apply this formula as best we can to demonstrate that our results hold as well with or without and adjustment for hydrogen bonding.

We utilized the known β values of various carbon, nitrogen, phosphorus, and sulfur oxides to correlate the value of β with the DFT electronic energy of forming a dimer with water (calculated with the same level of theory as described in the Chapter 2, with the def2-TZVP basis on all atoms).[166,321] The resulting correlation is:

Equation A1.6 $$\beta = 0.0909x + 0.279$$

with x benig the calculated dimerization energy with water. This fit is shown in Figure A1.3 and the numerical data is given in Table A1.13. While the correlation is not spectacular ($r^2 = 0.61$), it allows us to come up with a reasonable estimate of β for each metal oxo complex with reported kinetics in a protic solvent via DFT calculations of the corresponding dimer between the metal oxo complex and water (calculated with the same level of theory as described in the main text, with the def2-TZVP basis on the water molecule).

Table A1.13 Reference data used to construct the correlation between hydrogen bond basicity and electronic energy of dimerization and the resulting estimates of the hydrogen bond basicities of metal oxo complexes

Main Group Y=O or Transition Metal M=O	Calculated Electronic Energy of Dimerization with Water	Hydrogen Bond Basicity (Abraham Scale)
Acetone	1.91	0.40[a]
Methyl Isopropyl Ketone	3.40	0.46[a]
Benzophenone	3.04	0.46[a]
Benzaldehyde	1.86	0.42[a]
Acetophenone	4.44	0.51[a]
Nitrobenzene	1.90	0.34[a]
N,N-Dimethyl-^{t}Butylamide	2.98	0.70[a]
Triethyl Phosphine	8.78	1.02[a]
Dimethyl Sulfoxide	4.67	0.78[a]
N,N-Dimethyl-Methanesulfinamide	4.25	0.52[a]
N,N-Dimethyl-Methanesulfonamide	3.65	0.74[a]
Triphenyl Phosphite	2.81	0.62[a]
Triphenyl Phosphine	4.37	0.92[a]
$[Fe^{IV}(O)(TMC, MeCN)]^{2+}$	1.76	0.43[d]
$[Fe^{IV}(O)(TMC,N_3)]^{+}$	3.54[b]	0.59[d]
$[Fe^{IV}(O)(TMCS)]^{+}$	4.33	0.66[d]
$[Mn^{V}(O)(tf_4tmap,O)]^{3+}$	4.57	0.69[d]
$[Mn^{IV}(O)(tf_4tmap,OH)]^{3+}$	6.40	0.85[d]
$[Mn^{IV}(O)(Me_2EBC,O)]$	4.41[c]	0.67[d]
$[Mn^{IV}(O)(N4Py)]^{2+}$	3.59	0.60[d]

All energies in kcal/mol. [a]Reference [321]. [b]The conditions used in our analysis do not include a protic solvent, but an additional k_2 value is reported which was measured in a protic solvent mixture. [c]This complex formed two hydrogen bonds upon dimerization, one for each of its oxo ligands and the water molecule's O–H bonds; the value given here is accordingly half the dimerization energy. [d]Estimated from the electronic dimerization energy.

With these estimates of hydrogen bond basicities in hand we were able to apply the formula of Snelgrove et al.[141] to correct reaction barriers for solvent hydrogen bonding, giving as the overall formula for the reaction barrier:

Equation A1.7 $$\Delta G^{\ddagger}_{PCET} = RT \ln\left(\frac{k_2 h}{n_{CH} n_O RT}\right) + (T\Delta S_t)_{assoc} - (1.4 \cdot 8.3)\, \alpha \cdot \beta \quad \text{(S4)}$$

where α is the hydrogen bond acidity of the solvent (0 for aprotic solvents), β is this derived hydrogen bond basicity of the metal oxo complex, and 1.4 is the conversion from common logarithm units to kcal/mol at room temperature (we assume there is no temperature dependence of the hydrogen bonding correction). This amounts to a reduction of ~2–3 kcal/mol in the reaction barrier for metal oxo complexes with $\alpha \neq 0$. Using these barriers we repeated the regressions summarized in Table A 1.11, summarizing the new results in Table A1.14 with a detailed summary of each regression following. These regressions should be viewed as examining how our results are affected by an adjustment for hydrogen bonding, not as tests of distinct hypotheses. While the overall fits are slightly worse, our main result – that only $\Delta G°_{PT}$ and $\Delta G°_{ET}$ offer a significant improvement to the $\Delta G°_{CPET}$ only fit – is unchanged upon this hydrogen bonding adjustment of the reaction barriers. The only notable differences are: (a) cross validation no longer gives evidence for a small, statistically insignificant steric effect, (b) that the ruthenium(IV)-oxo is not predicted as accurately,[124] although its prediction is still off by less than 2 kcal/mol, (c) that the cobalt(III)-oxo is now an outlier,[50] but not grossly so, and (d) there is no significant difference between the coefficients of $\Delta G°_{PT}$ and $\Delta G°_{ET}$, i.e. no effect from η. Our finding that the same free energies explain the kinetics of the broader set of metal oxo complexes and this cobalt(III)-oxo complex remains valid.

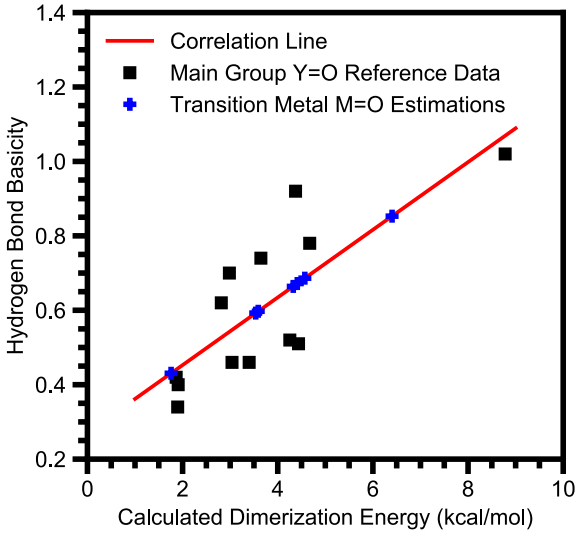

Figure A1.3 Correlation of main group oxides' hydrogen bond basicities and their calculated electronic energies of dimerization with water and the placement of relevant metal oxo complexes on the correlation line.

Table A1.14 Summary of statistics of regressions with hydrogen bonding corrected DHA data

Parameter(s) Regressed with $\Delta G°_{CPET}$	R^2	MSE[a]	LOO[b] R^2	LOO[b] MSE[a]	5-Fold CV[c] MSE[a]	p-value[d]
$\Delta G°_{CPET}$ only	0.66	1.65	0.59	2.00	2.02	< 0.001[f]
%BV Steric Metrics	0.68	1.56	0.36	3.11	3.10	0.68
Oxo Spin Density	0.69	1.51	0.59	1.96	1.98	0.27
Spin Excitation	0.66	1.63	0.39	2.93	3.00	0.70
$\|\eta\|$	0.67	1.60	0.55	2.18	2.15	0.53
$\Delta G°_{PT}$, $\Delta G°_{ET}$	0.80	0.94	0.71	1.40	1.54	0.027 0.0092[g] 0.028[h]
$\Delta G°_{CPET}{}^2$	0.66	1.63	0.53	2.25	2.23	0.69
$\Delta E°_{CPET}$ only[e]	0.65	1.71	0.57	2.10	2.08	< 0.001[i]
$\Delta E°_{CPET}$, $\Delta E°_{PT}$, $\Delta E°_{ET}$[e]	0.74	1.26	0.59	1.98	2.09	0.13[j]
$\Delta G°_{CC}$	0.80	0.95	0.74	1.24	1.28	0.0060
$\Delta G°_{CC}$, η	0.80	0.94	0.71	1.40	1.54	0.87[k]

[a]Mean Squared Error, kcal^2 mol^{-2}. [b]Leave-One-Out. [c]Cross Validation. [d]From an F-test where the null hypothesis is that only $\Delta G°_{CPET}$ has an effect. [e]$\Delta G°_{CPET}$ not included in the regression. [f]From an F-test where the null hypothesis is that $\Delta G°_{CPET}$ has no effect. [g]From an F-test where the null hypothesis is that $\Delta G°_{PT}$ has no effect. [h]From an F-test where the null hypothesis is that $\Delta G°_{ET}$ has no effect. [i]From an F-test where the null hypothesis is that $\Delta E°_{CPET}$ has no effect. [j]From an F-test where the null hypothesis is that only $\Delta E°_{CPET}$ has an effect. [k]From an F-test where the null hypothesis is that η has no effect.

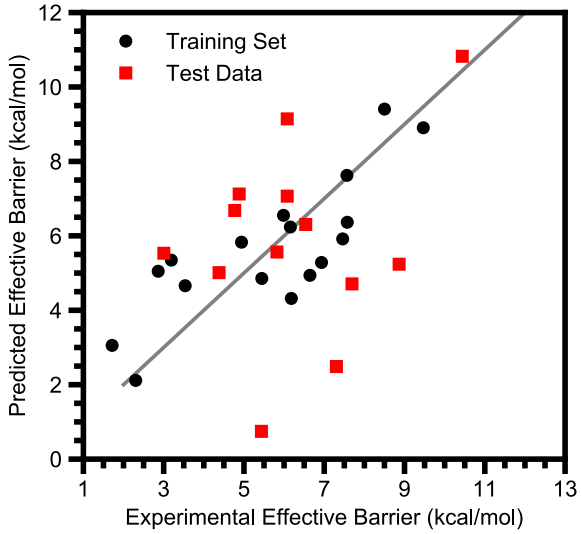

Regression A1.13 H-Bond corrected DHA barriers against $\Delta G°_{CPET}$.

```
['DHA ΔG_CPET'] Metrics:

Score on Training Data:                 0.6583716699943287
MSE of Training Data:                   1.6502710857317893
Score of LOO Cross Validation:          0.5855573288938136
MSE of LOO Cross Validation:            2.0020083135629743
MSE of 5-Fold Cross Validation:         2.0163090946670144(0.05795110828250081)
F-Test p-value of final 1 variables:    7.702231253337022e-05

Correlation Matrix of x-values:
             DHA ΔG_CPET
DHA ΔG_CPET          1.0

['DHA ΔG_CPET'] Training Average:
[-7.77619718]

 ['DHA ΔG_CPET'] Training Deviation:
[4.05326542]

 ['DHA ΔG_CPET'] Coefficients:
[0.43997827]

 ['DHA ΔG_CPET'] Standard Error:
 [0.08183272]

 ['DHA ΔG_CPET'] t-Test "Error":
 [0.17442231]

 ['DHA ΔG_CPET'] Weighted Coefficients:
[1.78334872]

 ['DHA ΔG_CPET'] Intercept:
 9.095284617394316
```

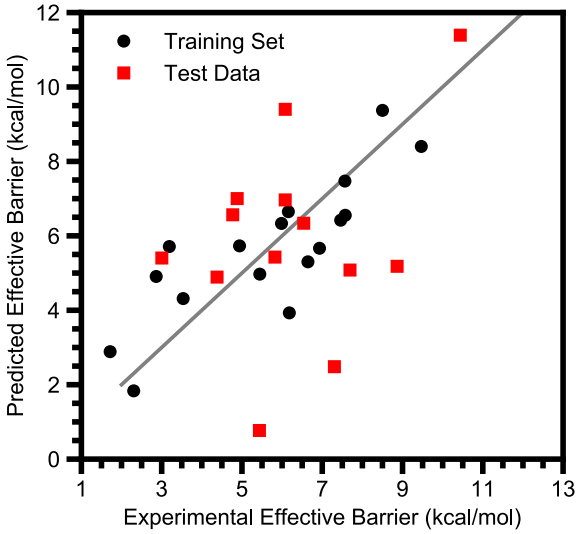

Regression A1.14 H-Bond adjusted DHA barriers against $\Delta G°_{CPET}$ and percent buried volume sterics.

```
['DHA ΔG_CPET', '%BV Tot', '%BV Dev'] Metrics:

Score on Training Data:                 0.6780065083153538
MSE of Training Data:                   1.555422962469681
Score of LOO Cross Validation:          0.3568563395708818
MSE of LOO Cross Validation:            3.106772165997647
MSE of 5-Fold Cross Validation:         3.0971664143020705(0.07200841580974428)
F-Test p-value of final 2 variables:    0.6806218722701031

Correlation Matrix of x-values:
             DHA ΔG_CPET   %BV Tot   %BV Dev
DHA ΔG_CPET     1.000000 -0.107404  0.230500
%BV Tot        -0.107404  1.000000  0.134191
%BV Dev         0.230500  0.134191  1.000000

['DHA ΔG_CPET', '%BV Tot', '%BV Dev'] Training Average:
[-7.77619718 64.39411765  5.35367331]

 ['DHA ΔG_CPET', '%BV Tot', '%BV Dev'] Training Deviation:
[ 4.05326542 10.53891783  4.76681449]

 ['DHA ΔG_CPET', '%BV Tot', '%BV Dev'] Coefficients:
[ 0.45769236  0.02716673 -0.03736001]

 ['DHA ΔG_CPET', '%BV Tot', '%BV Dev'] Standard Error:
 [0.08861722 0.03346711 0.07559991]

 ['DHA ΔG_CPET', '%BV Tot', '%BV Dev'] t-Test "Error":
 [0.19144586 0.07230129 0.16332368]

 ['DHA ΔG_CPET', '%BV Tot', '%BV Dev'] Weighted Coefficients:
[ 1.85514862  0.28630793 -0.17808825]

 ['DHA ΔG_CPET', '%BV Tot', '%BV Dev'] Intercept:
 7.683668572672475
```

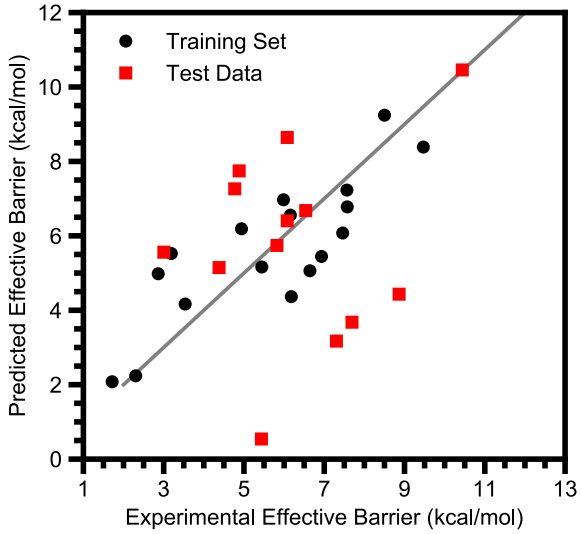

Regression A1.15 H-Bond adjusted DHA barriers against $\Delta G°_{CPET}$ and IBO spin density on the oxo ligand.

```
['DHA ΔG_CPET', 'IBO Spin O'] Metrics:

Score on Training Data:                 0.6880892431477332
MSE of Training Data:                   1.5067172659640655
Score of LOO Cross Validation:          0.5948329610682959
MSE of LOO Cross Validation:            1.9572014101683484
MSE of 5-Fold Cross Validation:         1.9794617560199796(0.05727008301927087)
F-Test p-value of final 1 variables:    0.26745197027806

Correlation Matrix of x-values:
              DHA ΔG_CPET  IBO Spin O
DHA ΔG_CPET      1.000000   -0.346171
IBO Spin O      -0.346171    1.000000

['DHA ΔG_CPET', 'IBO Spin O'] Training Average:
[-7.77619718  0.55994471]

 ['DHA ΔG_CPET', 'IBO Spin O'] Training Deviation:
[4.05326542 0.29315117]

 ['DHA ΔG_CPET', 'IBO Spin O'] Coefficients:
[0.47446962 1.37763277]

 ['DHA ΔG_CPET', 'IBO Spin O'] Standard Error:
 [0.08627094 1.19282835]

 ['DHA ΔG_CPET', 'IBO Spin O'] t-Test "Error":
 [0.18503277 2.55836236]

 ['DHA ΔG_CPET', 'IBO Spin O'] Weighted Coefficients:
[1.92315131 0.40385466]

 ['DHA ΔG_CPET', 'IBO Spin O'] Intercept:
 8.592097982909333
```

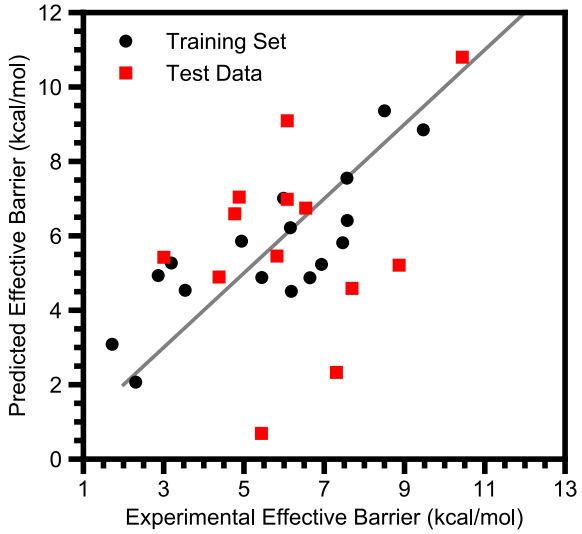

Regression A1.16 H-Bond adjusted DHA barriers correction against $\Delta G°_{CPET}$ and the spin excitation energy.

```
['DHA ΔG_CPET', 'Spin Excitation'] Metrics:

Score on Training Data:                 0.6622103027351723
MSE of Training Data:                   1.6317281720897845
Score of LOO Cross Validation:          0.3927294822859495
MSE of LOO Cross Validation:            2.9334832289354793
MSE of 5-Fold Cross Validation:         3.0032229238497066(0.09884773576992516)
F-Test p-value of final 1 variables:    0.6960080190817327

Correlation Matrix of x-values:
                 DHA ΔG_CPET  Spin Excitation
DHA ΔG_CPET          1.00000         -0.20409
Spin Excitation     -0.20409          1.00000

['DHA ΔG_CPET', 'Spin Excitation'] Training Average:
[-7.77619718 14.58587927]

 ['DHA ΔG_CPET', 'Spin Excitation'] Training Deviation:
[ 4.05326542 19.10348113]

 ['DHA ΔG_CPET', 'Spin Excitation'] Coefficients:
[0.44698225 0.0072814 ]

 ['DHA ΔG_CPET', 'Spin Excitation'] Standard Error:
 [0.08603861 0.01825517]

 ['DHA ΔG_CPET', 'Spin Excitation'] t-Test "Error":
 [0.18453447 0.03915345]

 ['DHA ΔG_CPET', 'Spin Excitation'] Weighted Coefficients:
[1.81173768 0.13910013]

 ['DHA ΔG_CPET', 'Spin Excitation'] Intercept:
 9.043543240499048
```

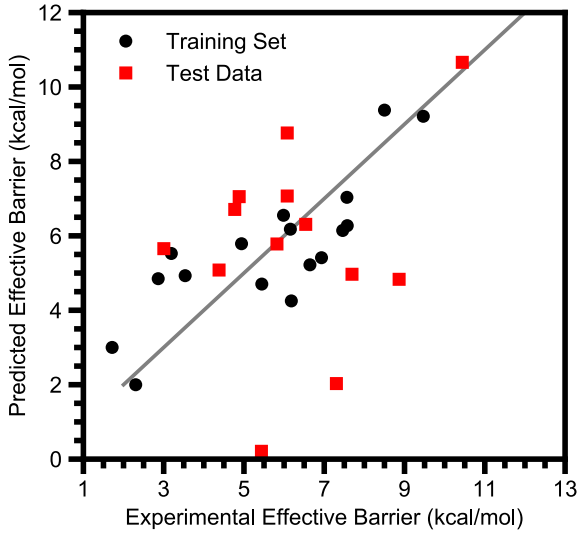

Regression A1.17 H-Bond adjusted DHA barriers against $\Delta G°_{CPET}$ and the magnitude of the asynchronicity.

```
['DHA ΔG_CPET', 'DHA |η| (G)'] Metrics:

Score on Training Data:                 0.6680402250602184
MSE of Training Data:                   1.6035661275517157
Score of LOO Cross Validation:          0.5492930546538306
MSE of LOO Cross Validation:            2.1771866520289285
MSE of 5-Fold Cross Validation:         2.149580788555342(0.0830651883177897)
F-Test p-value of final 1 variables:    0.5334165382839267

Correlation Matrix of x-values:
              DHA ΔG_CPET  DHA |η| (G)
DHA ΔG_CPET      1.000000     0.184231
DHA |η| (G)      0.184231     1.000000

['DHA ΔG_CPET', 'DHA |η| (G)'] Training Average:
[-7.77619718 17.96727543]

 ['DHA ΔG_CPET', 'DHA |η| (G)'] Training Deviation:
[ 4.05326542 12.92730813]

 ['DHA ΔG_CPET', 'DHA |η| (G)'] Coefficients:
[ 0.4499722  -0.01700872]

 ['DHA ΔG_CPET', 'DHA |η| (G)'] Standard Error:
 [0.08495179 0.02663603]

 ['DHA ΔG_CPET', 'DHA |η| (G)'] t-Test "Error":
 [0.18220347 0.0571286 ]

 ['DHA ΔG_CPET', 'DHA |η| (G)'] Weighted Coefficients:
[ 1.82385677 -0.21987692]

 ['DHA ΔG_CPET', 'DHA |η| (G)'] Intercept:
 9.478599679619604
```

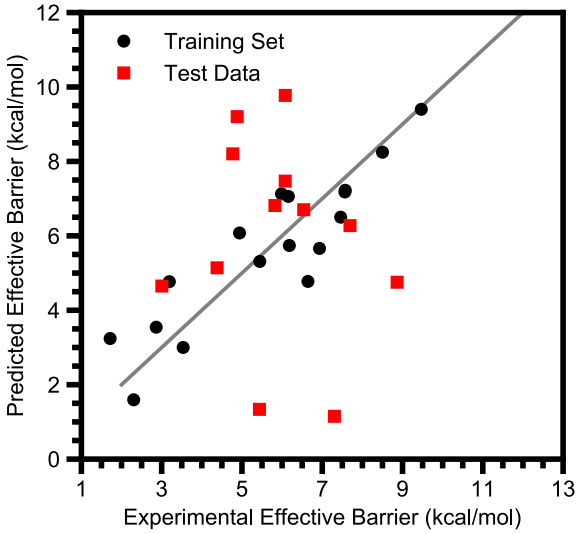

Regression A1.18 H-Bond adjusted DHA barriers against $\Delta G°_{CPET}$, $\Delta G°_{PT}$, and $\Delta G°_{ET}$.

```
['DHA ΔG_CPET', 'DHA ΔG_PT', 'DHA ΔG_ET'] Metrics:

Score on Training Data:                  0.8044848580527584
MSE of Training Data:                    0.9444561742667039
Score of LOO Cross Validation:           0.7106357878785099
MSE of LOO Cross Validation:             1.397803842853806
MSE of 5-Fold Cross Validation:          1.5386337886747041(0.08094085043482879)
F-Test p-value of final 2 variables:     0.026581064997124648
F-Test p-value of 2nd to last variable (DHA ΔG_PT):    0.009188466064706025
F-Test p-value of final variable (DHA ΔG_ET):    0.027671643184978723

Correlation Matrix of x-values:
             DHA ΔG_CPET  DHA ΔG_PT  DHA ΔG_ET
DHA ΔG_CPET     1.000000  -0.116636   0.300610
DHA ΔG_PT      -0.116636   1.000000  -0.886456
DHA ΔG_ET       0.300610  -0.886456   1.000000

['DHA ΔG_CPET', 'DHA ΔG_PT', 'DHA ΔG_ET'] Training Average:
[-7.77619718 47.94811989 48.18969167]

 ['DHA ΔG_CPET', 'DHA ΔG_PT', 'DHA ΔG_ET'] Training Deviation:
[ 4.05326542 17.72475347 14.50071323]

 ['DHA ΔG_CPET', 'DHA ΔG_PT', 'DHA ΔG_ET'] Coefficients:
[0.37589886 0.10676076 0.11021676]

 ['DHA ΔG_CPET', 'DHA ΔG_PT', 'DHA ΔG_ET'] Standard Error:
 [0.07412544 0.03493173 0.04446347]

 ['DHA ΔG_CPET', 'DHA ΔG_PT', 'DHA ΔG_ET'] t-Test "Error":
 [0.16013829 0.07546541 0.09605748]

 ['DHA ΔG_CPET', 'DHA ΔG_PT', 'DHA ΔG_ET'] Weighted Coefficients:
[1.52361784 1.89230808 1.59822164]

 ['DHA ΔG_CPET', 'DHA ΔG_PT', 'DHA ΔG_ET'] Intercept:
 -1.8332987921810613
```

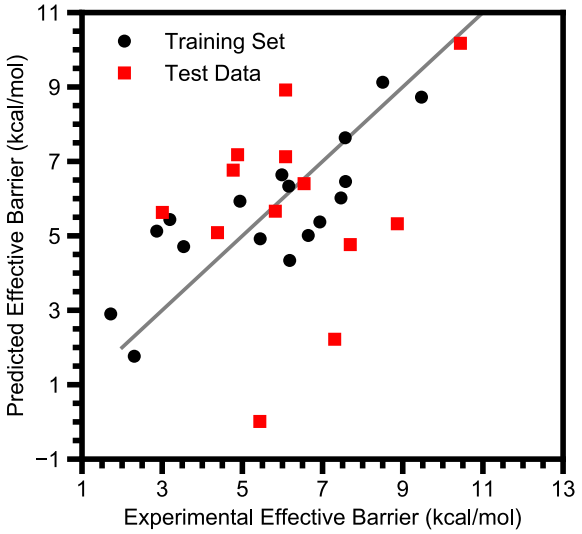

Regression A1.19 H-Bond adjusted DHA barriers against $\Delta G°_{CPET}$ and $\Delta G°_{CPET}{}^2$.

```
['DHA ΔG_CPET', 'DHA ΔG_CPET^2'] Metrics:

Score on Training Data:                 0.6624878412462136
MSE of Training Data:                   1.6303874935226972
Score of LOO Cross Validation:          0.5335369455694108
MSE of LOO Cross Validation:            2.2532981713669833
MSE of 5-Fold Cross Validation:         2.232966896805831(0.07882751337208369)
F-Test p-value of final 1 variables:    0.685715324703223

Correlation Matrix of x-values:
               DHA ΔG_CPET  DHA ΔG_CPET^2
DHA ΔG_CPET       1.000000      -0.929028
DHA ΔG_CPET^2    -0.929028       1.000000

['DHA ΔG_CPET', 'DHA ΔG_CPET^2'] Training Average:
[-7.77619718 76.89820308]

 ['DHA ΔG_CPET', 'DHA ΔG_CPET^2'] Training Deviation:
[ 4.05326542 62.99805804]

 ['DHA ΔG_CPET', 'DHA ΔG_CPET^2'] Coefficients:
[ 0.35262908 -0.00604934]

 ['DHA ΔG_CPET', 'DHA ΔG_CPET^2'] Standard Error:
 [0.22754327 0.01464003]

 ['DHA ΔG_CPET', 'DHA ΔG_CPET^2'] t-Test "Error":
 [0.48803178 0.03139974]

 ['DHA ΔG_CPET', 'DHA ΔG_CPET^2'] Weighted Coefficients:
[ 1.42929925 -0.38109659]

 ['DHA ΔG_CPET', 'DHA ΔG_CPET^2'] Intercept:
 8.881223350642781
```

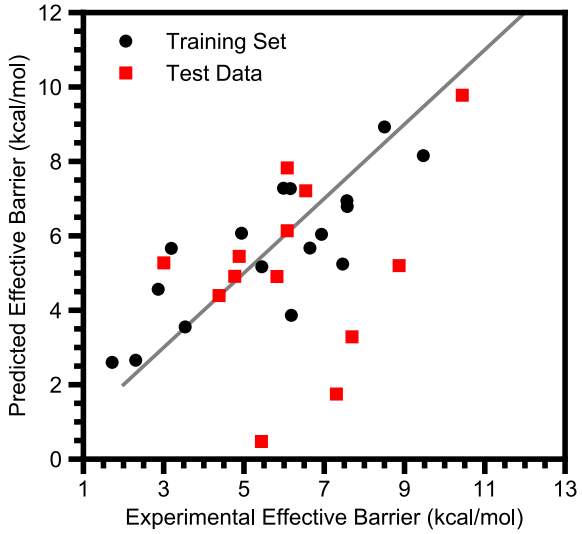

Regression A1.20 H-Bond adjusted DHA barriers against $\Delta E°_{CPET}$.

```
['DHA ΔE_CPET'] Metrics:

Score on Training Data:                 0.6454910010142754
MSE of Training Data:                   1.7124924933718166
Score of LOO Cross Validation:          0.565956327438351
MSE of LOO Cross Validation:            2.0966929843360327
MSE of 5-Fold Cross Validation:         2.0816331006068287(0.05733164762040685)
F-Test p-value of final 1 variables:    0.00010251166252062127

Correlation Matrix of x-values:
             DHA ΔE_CPET
DHA ΔE_CPET          1.0

['DHA ΔE_CPET'] Training Average:
[-2.08594867]

 ['DHA ΔE_CPET'] Training Deviation:
[3.99325888]

 ['DHA ΔE_CPET'] Coefficients:
[0.44219959]

 ['DHA ΔE_CPET'] Standard Error:
 [0.08461381]

 ['DHA ΔE_CPET'] t-Test "Error":
 [0.18035006]

 ['DHA ΔE_CPET'] Weighted Coefficients:
[1.76581744]

 ['DHA ΔE_CPET'] Intercept:
 6.596332462651391
```

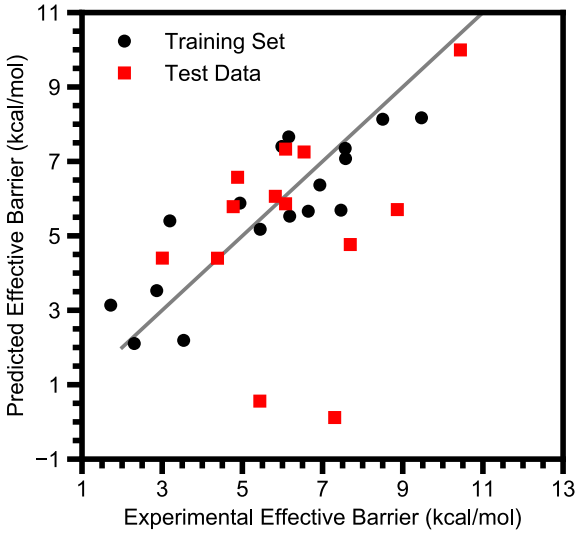

Regression A1.21 H-Bond adjusted DHA barriers $\Delta E°_{CPET}$, $\Delta E°_{T}$, and $\Delta E°_{ET}$.

```
['DHA ΔE_CPET', 'DHA ΔE_PT', 'DHA ΔE_ET'] Metrics:

Score on Training Data:                 0.7398301329358178
MSE of Training Data:                   1.2567775306795423
Score of LOO Cross Validation:          0.5909484679893019
MSE of LOO Cross Validation:            1.975965856930953
MSE of 5-Fold Cross Validation:         2.089103798214306(0.09558230895231092)
F-Test p-value of final 2 variables:    0.133842257174152

Correlation Matrix of x-values:
             DHA ΔE_CPET  DHA ΔE_PT  DHA ΔE_ET
DHA ΔE_CPET     1.000000   0.093539   0.119751
DHA ΔE_PT       0.093539   1.000000  -0.868929
DHA ΔE_ET       0.119751  -0.868929   1.000000

['DHA ΔE_CPET', 'DHA ΔE_PT', 'DHA ΔE_ET'] Training Average:
[-2.08594867 50.96221826 55.73635424]

 ['DHA ΔE_CPET', 'DHA ΔE_PT', 'DHA ΔE_ET'] Training Deviation:
[ 3.99325888 18.62129223 14.02559969]

 ['DHA ΔE_CPET', 'DHA ΔE_PT', 'DHA ΔE_ET'] Coefficients:
[0.36471025 0.07661204 0.10478331]

 ['DHA ΔE_CPET', 'DHA ΔE_PT', 'DHA ΔE_ET'] Standard Error:
 [0.08565794 0.03684674 0.04905865]

 ['DHA ΔE_CPET', 'DHA ΔE_PT', 'DHA ΔE_ET'] t-Test "Error":
 [0.18505273 0.07960254 0.10598478]

 ['DHA ΔE_CPET', 'DHA ΔE_PT', 'DHA ΔE_ET'] Weighted Coefficients:
[1.45638243 1.42661521 1.46964876]

 ['DHA ΔE_CPET', 'DHA ΔE_PT', 'DHA ΔE_ET'] Intercept:
 -3.309865589515569
```

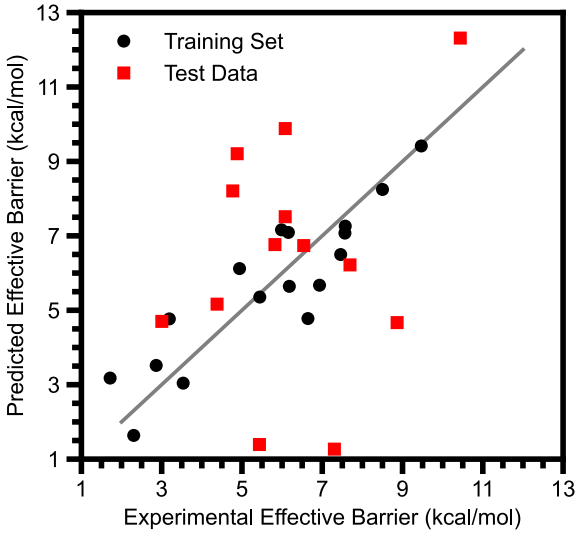

Regression A1.22 H-Bond adjusted DHA barriers against $\Delta G°_{CPET}$, $\Delta G°_{CC}$.

```
['DHA ΔG_CPET', 'DHA ΔG_CC'] Metrics:

Score on Training Data:                 0.8040414986255869
MSE of Training Data:                   0.9465978679700207
Score of LOO Cross Validation:          0.7431092648007716
MSE of LOO Cross Validation:            1.2409373440564213
MSE of 5-Fold Cross Validation:         1.279085369418012(0.047752173629508135)
F-Test p-value of final 1 variables:    0.006096735426386779

Correlation Matrix of x-values:
             DHA ΔG_CPET  DHA ΔG_CC
DHA ΔG_CPET     1.000000   0.215833
DHA ΔG_CC       0.215833   1.000000

['DHA ΔG_CPET', 'DHA ΔG_CC'] Training Average:
[  -7.77619718 -103.91400874]

 ['DHA ΔG_CPET', 'DHA ΔG_CC'] Training Deviation:
[4.05326542 8.16161558]

 ['DHA ΔG_CPET', 'DHA ΔG_CC'] Coefficients:
[ 0.48572463 -0.10526115]

 ['DHA ΔG_CPET', 'DHA ΔG_CC'] Standard Error:
 [0.06570107 0.03262882]

 ['DHA ΔG_CPET', 'DHA ΔG_CC'] t-Test "Error":
 [0.14091478 0.06998185]

 ['DHA ΔG_CPET', 'DHA ΔG_CC'] Weighted Coefficients:
[ 1.96877083 -0.85910103]

 ['DHA ΔG_CPET', 'DHA ΔG_CC'] Intercept:
 -1.4870906194890088
```

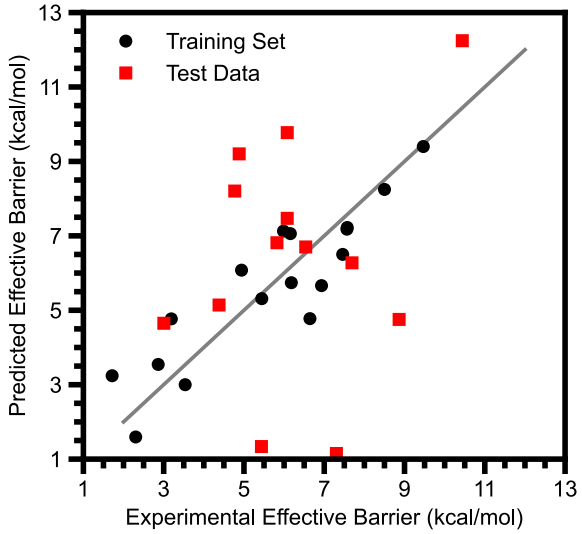

Regression A1.23 H-Bond adjusted DHA barriers $\Delta G°_{CPET}$, $\Delta G°_{CC}$, and η.

```
['DHA ΔG_CPET', 'DHA ΔG_CC', 'DHA η'] Metrics:

Score on Training Data:                 0.8044848580527585
MSE of Training Data:                   0.9444561742667036
Score of LOO Cross Validation:          0.7106357878785099
MSE of LOO Cross Validation:            1.3978038428538055
MSE of 5-Fold Cross Validation:         1.5386337886747048(0.08094085043482874)
F-Test p-value of final 1 variables:    0.866320640475112

Correlation Matrix of x-values:
             DHA ΔG_CPET  DHA ΔG_CC     DHA η
DHA ΔG_CPET     1.000000   0.215833 -0.205272
DHA ΔG_CC       0.215833   1.000000 -0.508560
DHA η          -0.205272  -0.508560  1.000000

['DHA ΔG_CPET', 'DHA ΔG_CC', 'DHA η'] Training Average:
[  -7.77619718 -103.91400874   -0.17079124]

 ['DHA ΔG_CPET', 'DHA ΔG_CC', 'DHA η'] Training Deviation:
[ 4.05326542  8.16161558 22.13389058]

 ['DHA ΔG_CPET', 'DHA ΔG_CC', 'DHA η'] Coefficients:
[ 0.48438762 -0.10848876 -0.00244413]

 ['DHA ΔG_CPET', 'DHA ΔG_CC', 'DHA η'] Standard Error:
 [0.06854779 0.03869525 0.01423526]

 ['DHA ΔG_CPET', 'DHA ΔG_CC', 'DHA η'] t-Test "Error":
 [0.1480885  0.083596   0.03075341]

 ['DHA ΔG_CPET', 'DHA ΔG_CC', 'DHA η'] Weighted Coefficients:
[ 1.96335158 -0.88544354 -0.05409818]

 ['DHA ΔG_CPET', 'DHA ΔG_CC', 'DHA η'] Intercept:
 -1.8332987921810453
```

5. Further Discussion of Steric Parameters

There is little discussion in the literature about quantitative steric metrics for metal oxo mediated CPET, but in other systems such as asymmetric catalysis the nature of steric parameters is important.[109] Therefore, in addition to the percent buried volume (%BV) metric discussed in the main text we also determined distance and angle metrics (see Figure A1.4). These metrics ultimately do not fit the data any better than the %BV metrics.

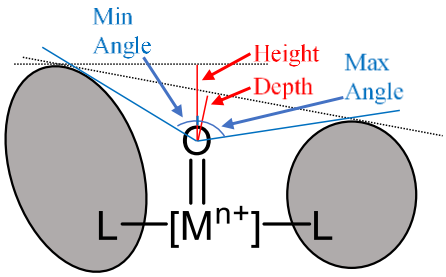

Figure A1.4 Illustration of distance and angle steric metrics.

Distance metrics were defined as how far from the oxo atom an infinitely wide flat substrate could approach without being encumbered by another atom in the complex. For this determination we used Bondi radii scaled by 1.17 with the Rowland-Taylor radii for hydrogen.[322,323] The "height" as we defined it is the distance if the substrate is restricted to approaching along the metal-oxygen axis; that is, how much higher than the oxygen atom is there no steric bulk in any direction. The "depth" does not have this directionality restriction; it is the closest a substrate can approach along any direction with no steric encumberment perpendicular to its approach.

Angle metrics were based on cones with a vertex on the oxo atom and an axis along the M–O bond. We recorded the minimum angle of a cone which touches at least one other atom in the complex (using the same radii as with distance metrics) as well as the maximum angle of a cone in which at least one segment of the surface does not go through another atom.

After collecting these parameters, we analyzed the correlations between them to determine which were statistically distinct (Table A1.15). There were high correlations among many of them, such that it only took two parameters to convey most of the statistical information contained within this set of parameters. We used %BV sterics as the pair within the main text, for which we observed a small, statistically insignificant improvement to the $\Delta G°_{CPET}$ fit (which disappears in the H-bonding correction discussed above). In **Regression A1.24** we demonstrate that height and max angle perform worse; unlike %BV sterics, these metrics even behave poorly under cross validation. Overall, while we cannot decisively rule out a small correlation with %BV sterics there is no clear and irrefutable evidence for the influence of steric bulk on the reaction rates. This is surprising and demonstrates that oxo ligands are in general very unencumbered. However, it is chemically unfathomable that steric bulk has absolutely no influence on the reaction barrier; thus, the question of whether we observe a small effect or no effect is immaterial. Regardless, within our data set steric bulk is not as important as free energies in explaining and predicting reaction barriers.

Table A1.15 Correlations between various steric metrics

	%BV Tot	%BV Dev	Height	Depth	Min Angle	Max Angle
%BV Tot	1	0.14236	0.33877	0.40745	− 0.78889	−0.68510
%BV Dev	0.14236	1	0.64977	0.47271	−0.61376	0.01750
Height	0.33877	0.64977	1	0.90480	−0.75467	−0.09366
Depth	0.40745	0.47271	0.90480	1	−0.69931	−0.25180
Min Angle	−0.78889	−0.61376	−0.75467	−0.69931	1	0.41571
Max Angle	−0.68510	0.01750	−0.09366	−0.25180	0.41571	1

Table A1.16 Steric parameters considered in this study

Oxo	Total %BV	%BV Dev	Height	Depth	Minimum Angle	Maximum Angle
$[Fe^{IV}(O)(Me_3NTB)(MeCN)]^{2+}$	66.3	10.4	3.43	2.57	31.0	81.3
$[Fe^{IV}(O)(TMG_2dien)(MeCN)]^{2+}$	68.0	10.5	3.42	2.84	31.1	86.3
$[Fe^{IV}(O)(TMG_3tren)]^{2+}$	79.6	3.2	3.40	3.4	29.5	52.1
$[Fe^{V}(O)(TAML)]^{-}$	56.0	7.4	1.80	1.17	49.2	98.7
$[Fe^{IV}(O)(TMC)(MeCN)]^{2+}$	74.1	2.0	1.70	1.70	44.8	61.0
$[Fe^{IV}(O)(TMC)(N_3)]^{+}$	74.1	1.9	1.70	1.70	44.7	61.0
$[Fe^{IV}(O)(TMC)(OCOCF_3)]^{+}$	74.2	1.8	1.73	1.73	44.1	61.4
$[Fe^{IV}(O)(TMCS)]^{+}$	74.1	2.3	1.75	1.74	42.5	59.2
$[Mn^{IV}(O)(H_3buea)]^{-}$	72.3	16.0	4.75	3.99	14.7	50.2
$[Fe^{IV}(O)(TMP)]$	58.2	9.8	3.74	3.62	42.3	92.9
$[Co^{III}(O)(PhB^{tBu}Im_3)]$	67.8	8.9	2.75	1.99	40.6	83.1
$[Ru^{IV}(O)(H^{+}TPA)(bpy)]^{3+}$	58.1	5.6	1.49	1.15	52.2	88.5
$[Fe^{IV}(O)(tpfpp)]$	52.4	0.15	2.16	2.14	65.3	91.6
$[Mn^{VII}(O)_4]^{-}$	35.2	1.1	0.00	0.00	101.3	101.3
$[Mn^{V}(O)_2(tf_4tmap)]^{3+}$	55.3	0.43	2.36	2.36	63.3	84.8
$[Mn^{IV}(O)(OH)(tf_4tmap)]^{3+}$	53.1	0.23	2.24	2.23	64.8	88.9
$[Cr^{IV}(O)(TMC)(Cl)]^{+}$	75.0	2.1	1.74	1.74	44.3	59.9
$[Ru^{VI}(O)_2(TMC)]^{2+}$	73.1	2.0	1.75	1.73	43.8	74.0
$[Fe^{IV}(O)(N4Py)]^{2+}$	60.6	9.4	1.40	1.32	55.3	63.5
$[Fe^{IV}(O)(BnTPEN)]^{2+}$	69.0	11.5	5.17	2.75	22.4	85.7
$[Fe^{IV}(O)(^{Me2}TACN\text{-}Py_2)]^{2+}$	63.8	4.7	1.26	1.26	61.5	65.9
$[Fe^{IV}(O)(BP1)]^{2+}$	65.6	2.0	1.57	1.57	48.5	57.5
$[Fe^{IV}(O)(BP2)]^{2+}$	64.5	1.5	1.58	1.51	48.0	70.5
$[Ru^{IV}(O)(bpy)_2(py)]^{2+}$	58.8	5.5	1.73	1.21	46.2	88.5
$[Mn^{IV}(O)_2(Me_2EBC)]$	62.5	10.2	1.72	1.38	46.6	106.2
$[Mn^{IV}(O)(N4Py)]^{2+}$	59.1	4.8	1.35	1.27	57.0	65.7
$[Co^{IV}(O)(13\text{-}TMC)]^{2+}$	63.3	1.2	1.42	1.35	55.7	94.9
$[Fe^{IV}(O)(13\text{-}TMC)]^{2+}$	66.7	1.1	1.57	1.49	52.4	92.2
$[Ru^{VI}(O)_2(L)]^{2+}$	63.7	1.7	1.56	1.54	52.2	86.4
$[Ru^{VI}(O)_2(F_{28}\text{-}tpp)]$	54.9	2.6	2.88	2.25	58.9	92.0

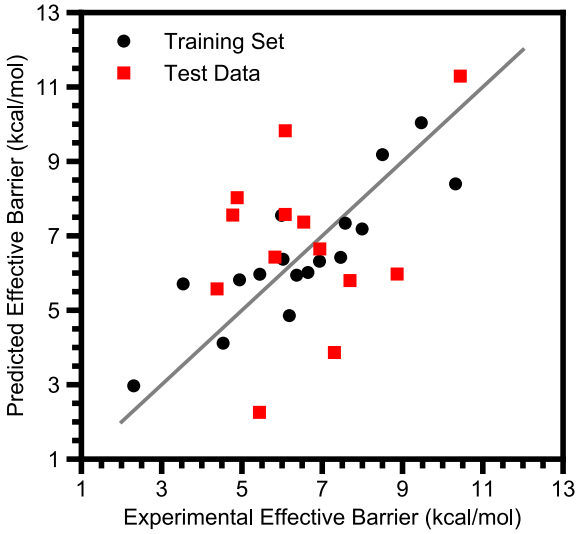

Regression A1.24 DHA barriers against $\Delta G°_{CPET}$ and the height, max angle steric metrics.

```
['DHA ΔG_CPET', 'Height', 'Max Angle'] Metrics:

Score on Training Data:                 0.7296160767550646
MSE of Training Data:                   1.0553654132979189
Score of LOO Cross Validation:          0.4869671105616551
MSE of LOO Cross Validation:            2.0024754463934866
MSE of 5-Fold Cross Validation:         2.343099781826322(0.09930972506610071)
F-Test p-value of final 2 variables:    0.47417271859314414

Correlation Matrix of x-values:
             DHA ΔG_CPET    Height  Max Angle
DHA ΔG_CPET     1.000000 -0.115239  -0.114024
Height         -0.115239  1.000000  -0.138121
Max Angle      -0.114024 -0.138121   1.000000

['DHA ΔG_CPET', 'Height', 'Max Angle'] Training Average:
[-7.77619718  2.35675364 75.05752356]

 ['DHA ΔG_CPET', 'Height', 'Max Angle'] Training Deviation:
[ 4.05326542  1.27930252 17.85106944]

 ['DHA ΔG_CPET', 'Height', 'Max Angle'] Coefficients:
[ 0.39618155 -0.28333271 -0.00072724]

 ['DHA ΔG_CPET', 'Height', 'Max Angle'] Standard Error:
 [0.07139195 0.22689345 0.0162581 ]

 ['DHA ΔG_CPET', 'Height', 'Max Angle'] t-Test "Error":
 [0.15423294 0.4901735  0.03512348]

 ['DHA ΔG_CPET', 'Height', 'Max Angle'] Weighted Coefficients:
[ 1.60582897 -0.36246825 -0.01298204]

 ['DHA ΔG_CPET', 'Height', 'Max Angle'] Intercept:
 10.28517288957433
```

6. Attempts to Determine Reorganization Parameters

A common theme in chemistry is that reaction barriers are in large part determined by the reorganization energy needed to deform to the transition state geometry without accounting for interaction between reactants; CPET chemistry is no exception to this. In one case, the deformation energy needed to reach a transition state geometry has been shown to correlate well with computed reaction barriers;[41] in another case, the reorganization energy was the primary factor differentiating the reactivity between a ruthenium(IV)-oxo and a vanadium(V)-oxo.[145] In light of both these studies, and our hypothesis that anomalously low reorganization energies could contribute to the overestimation of ruthenium(IV)-oxo reaction barriers,[120,126] we have made several attempts to quantify reorganization and fit it to the data. Ultimately, no parameter examined demonstrated a significant effect.

The classical definition of reorganization energy is the energy needed to deform the products into the reactant geometry, or vice-versa, without the reaction actually occurring.[85,324] We calculated a reorganization energy for the oxo complexes in just this manner, removing the hydroxide hydrogen from our optimized metal hydroxide structures and determining the energy of the metal oxo species at the resultant geometry (with the same level of theory as described in the main text). Wherever relevant, we checked multiple spin states at this geometry and used the lowest energy obtained, regardless of the ground spin state of the oxo. We performed a similar calculation for metal hydroxides by constraining the cartesian position of all oxo atoms and optimizing a hydrogen atom on top of this structure.

As alternative measurements of distortions, we used the predominant M–O stretching frequency in both the metal hydroxide and metal oxo complexes to determine the energies of

stretching or compressing this specific bond into the other structure. The result heavily correlated with the change in the M–O bond distance, indicating similar information could be obtained without incorporating the vibrational frequency. Therefore, because mixing with other ligand vibrational modes made finding "stretching energies" for the non-oxo M–L bonds infeasible we instead tabulated the total change in M–L bond lengths.

The results of regressions with these parameters are given in Table A1.17. While the stretching energies and change in bond lengths offer some improvement to the fit, cross validation indicates this is mere overfitting and none of these regressions are statistically significant. Similarly, regressions along with the magnitude of Srnec's asynchronicity parameter (which has been reported as being an effect on the reorganization energy) do not provide a significant improvement.[55]

Table A1.17 Summary of statistics on regressions with measures of deformation energy

Parameter(s) Regressed with $\Delta G°_{CPET}$	R^2	MSE[a]	LOO[b] R^2	LOO[b] MSE[a]	5-Fold CV[c] MSE[a]	p-value[d]
$\Delta G°_{CPET}$ only	0.70	1.18	0.60	1.57	1.49	< 0.001[e]
Reorganization Energies	0.70	1.18	0.44	2.18	2.20	0.96
Stretching Energies	0.74	1.00	0.46	2.09	2.27	0.34
Bond Length Changes	0.75	0.97	0.47	2.07	2.01	0.27
Reorganization Energies, $\lvert\eta\rvert$	0.75	0.97	0.48	2.03	2.12	0.48
Stretching Energies, $\lvert\eta\rvert$	0.78	0.87	0.43	2.21	2.50	0.27
Bond Length Changes, $\lvert\eta\rvert$	0.78	0.88	0.47	2.08	2.36	0.29

[a]Mean Squared Error, kcal^2 mol^{-2}. [b]Leave-One-Out. [c]Cross Validation. [d]From an F-test where the null hypothesis is that only $\Delta G°_{CPET}$ has an effect. [e]From an F-test where the null hypothesis is that $\Delta G°_{CPET}$ has no effect.

Table A1.18 Reorganization parameters considered in this study

Oxo	M–O Reorg.[a]	M–OH Reorg.[a]	M–O Stretch[b]	M–OH Stretch[b]	M–O ΔL[c]	ΣM–L ΔL[d]
$[Fe^{IV}(O)(Me_3NTB)(MeCN)]^{2+}$	23.1	35.5	42.5	21.4	0.19	0.92
$[Fe^{IV}(O)(TMG_2dien)(MeCN)]^{2+}$	17.8	17.1	45.5	22.3	0.20	0.33
$[Fe^{IV}(O)(TMG_3tren)]^{2+}$	18.5	16.1	50.8	23.3	0.21	0.33
$[Fe^{V}(O)(TAML)]^{-}$	13.6	15.7	48.2	21.4	0.20	0.0092
$[Fe^{IV}(O)(TMC)(MeCN)]^{2+}$	21.0	22.7	41.8	20.0	0.19	0.58
$[Fe^{IV}(O)(TMC)(N_3)]^{+}$	19.5	22.1	62.3	25.7	0.24	0.512
$[Fe^{IV}(O)(TMC)(OCOCF_3)]^{+}$	20.1	23.3	59.6	25.0	0.23	0.47
$[Fe^{IV}(O)(TMCS)]^{+}$	15.1	19.8	57.3	17.7	0.24	0.56
$[Mn^{IV}(O)(H_3buea)]^{-}$	20.8	21.2	37.1	16.0	0.21	0.20
$[Fe^{IV}(O)(TMP)]$	20.7	23.8	64.2	24.0	0.23	0.44
$[Co^{III}(O)(PhB^{tBu}Im_3)]$	20.9	19.6	43.1	17.7	0.22	0.38
$[Ru^{IV}(O)(H^{+}TPA)(bpy)]^{3+}$	8.5	8.6	24.5	13.7	0.16	-0.13
$[Fe^{IV}(O)(tpfpp)]$	21.0	19.5	87.5	28.8	0.27	0.045
$[Mn^{VII}(O)_4]^{-}$	14.7	13.0	43.4	21.0	0.18	0.025
$[Mn^{V}(O)_2(tf_4tmap)]^{3+}$	29.3	22.1	116.9	32.4	0.33	0.023
$[Mn^{IV}(O)(OH)(tf_4tmap)]^{3+}$	14.7	13.4	30.4	14.8	0.18	0.19
$[Cr^{IV}(O)(TMC)(Cl)]^{+}$	12.9	17.4	61.9	26.7	0.25	0.0060
$[Ru^{VI}(O)_2(TMC)]^{2+}$	14.6	13.9	43.9	20.5	0.19	-0.032
$[Fe^{IV}(O)(N4Py)]^{2+}$	34.7	28.4	37.0	20.0	0.18	0.93
$[Fe^{IV}(O)(BnTPEN)]^{2+}$	24.4	24.6	39.9	20.5	0.19	0.89
$[Fe^{IV}(O)(^{Me2}TACN\text{-}Py_2)]^{2+}$	23.6	28.5	30.3	16.8	0.16	0.89
$[Fe^{IV}(O)(BP1)]^{2+}$	26.2	28.7	33.8	18.6	0.17	0.89
$[Fe^{IV}(O)(BP2)]^{2+}$	24.1	31.9	42.0	21.5	0.19	0.86
$[Ru^{IV}(O)(bpy)_2(py)]^{2+}$	8.9	8.6	25.8	13.8	0.16	-0.13
$[Mn^{IV}(O)_2(Me_2EBC)]$	22.8	26.2	62.6	21.2	0.25	0.20
$[Mn^{IV}(O)(N4Py)]^{2+}$	22.9	21.5	22.6	11.9	0.14	0.63
$[Co^{IV}(O)(13\text{-}TMC)]^{2+}$	10.1	11.6	5.7	4.8	0.084	0.41
$[Fe^{IV}(O)(13\text{-}TMC)]^{2+}$	20.9	25.1	50.6	25.4	0.19	0.57
$[Ru^{VI}(O)_2(L)]^{2+}$	13.9	13.3	44.1	21.3	0.19	-0.033
$[Ru^{VI}(O)_2(F_{28}\text{-}tpp)]$	15.9	14.8	50.4	21.3	0.22	-0.032

[a]Reorganization; i.e. energy of the oxo at the hydroxide geometry or vice versa (kcal/mol). The position of the transferring H-atom was optimized for the hydroxide reorganization. [b]Energy needed to distort the metal–oxygen bond of the oxo complex to its length in the hydroxide, or vice versa (kcal/mol); determined from frequency calculations. [c]The change in the length of the metal–oxygen bond between the oxo complex and the hydroxide complex (Å). [d]The sum of the change in the lengths of all metal–ligand bonds besides the metal–oxygen bond between the oxo complex and the hydroxide complex (Å).

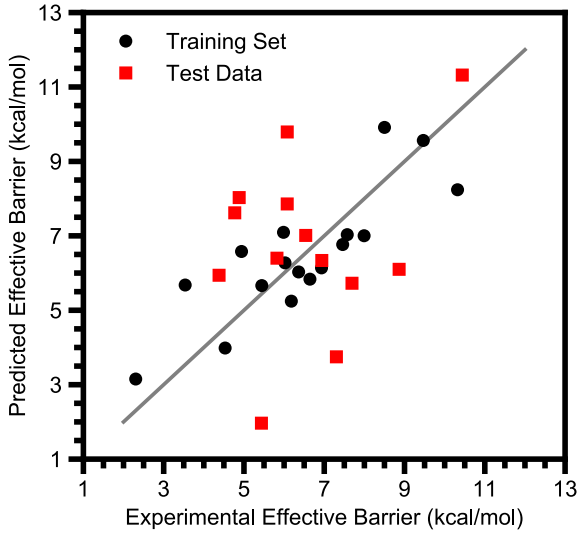

Regression A1.25 DHA barriers against $\Delta G°_{CPET}$ and the oxo reorganization energy.

```
['DHA ΔG_CPET', 'Oxo λ', 'Hydroxide λ'] Metrics:

Score on Training Data:                  0.6985337405659753
MSE of Training Data:                    1.1766863194552986
Score of LOO Cross Validation:           0.4413190508659992
MSE of LOO Cross Validation:             2.1806494399090437
MSE of 5-Fold Cross Validation:          2.1995049703717857(0.06742190086236298)
F-Test p-value of final 2 variables:     0.9618615594550874

Correlation Matrix of x-values:
              DHA ΔG_CPET     Oxo λ  Hydroxide λ
DHA ΔG_CPET     1.000000 -0.113949    -0.336879
Oxo λ          -0.113949  1.000000     0.685471
Hydroxide λ    -0.336879  0.685471     1.000000

['DHA ΔG_CPET', 'Oxo λ', 'Hydroxide λ'] Training Average:
[-7.77619718 21.37229441 22.86499201]

 ['DHA ΔG_CPET', 'Oxo λ', 'Hydroxide λ'] Training Deviation:
[4.05326542 5.37099513 6.03190216]

 ['DHA ΔG_CPET', 'Oxo λ', 'Hydroxide λ'] Coefficients:
[ 0.40306166 -0.0127441  -0.00372249]

 ['DHA ΔG_CPET', 'Oxo λ', 'Hydroxide λ'] Standard Error:
 [0.08000681 0.07807801 0.07335822]

 ['DHA ΔG_CPET', 'Oxo λ', 'Hydroxide λ'] t-Test "Error":
 [0.17284421 0.16867729 0.1584808 ]

 ['DHA ΔG_CPET', 'Oxo λ', 'Hydroxide λ'] Weighted Coefficients:
[ 1.6337159  -0.06844851 -0.0224537 ]

 ['DHA ΔG_CPET', 'Oxo λ', 'Hydroxide λ'] Intercept:
 9.973829077770457
```

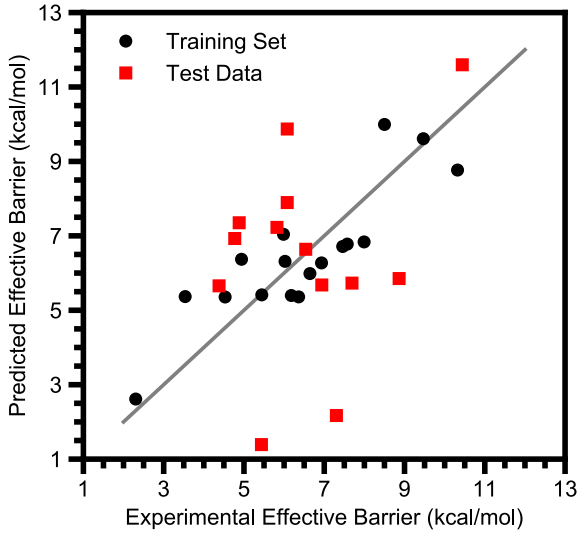

Regression A1.26 DHA barriers against $\Delta G°_{CPET}$ and stretching energies of M–O(H) bonds.

```
['DHA ΔG_CPET', 'Oxo Stretch', 'Hydroxide Stretch'] Metrics:

Score on Training Data:                 0.7429488443721649
MSE of Training Data:                   1.0033248125190048
Score of LOO Cross Validation:          0.46372208300228446
MSE of LOO Cross Validation:            2.09320568590959
MSE of 5-Fold Cross Validation:         2.266485644527874(0.09874421962655447)
F-Test p-value of final 2 variables:    0.34134070652340187

Correlation Matrix of x-values:
                   DHA ΔG_CPET  Oxo Stretch  Hydroxide Stretch
DHA ΔG_CPET           1.000000    -0.399234          -0.481905
Oxo Stretch          -0.399234     1.000000           0.865424
Hydroxide Stretch    -0.481905     0.865424           1.000000

['DHA ΔG_CPET', 'Oxo Stretch', 'Hydroxide Stretch'] Training Average:
[-7.77619718 51.16490969 21.37839275]

 ['DHA ΔG_CPET', 'Oxo Stretch', 'Hydroxide Stretch'] Training Deviation:
[ 4.05326542 19.44134649  3.86935373]

 ['DHA ΔG_CPET', 'Oxo Stretch', 'Hydroxide Stretch'] Coefficients:
[ 0.45176185  0.02455864 -0.00460389]

 ['DHA ΔG_CPET', 'Oxo Stretch', 'Hydroxide Stretch'] Standard Error:
 [0.07828656 0.02854359 0.15006501]

 ['DHA ΔG_CPET', 'Oxo Stretch', 'Hydroxide Stretch'] t-Test "Error":
 [0.16912782 0.06166468 0.32419574]

 ['DHA ΔG_CPET', 'Oxo Stretch', 'Hydroxide Stretch'] Weighted Coefficients:
[ 1.83111067  0.47745294 -0.01781408]

 ['DHA ΔG_CPET', 'Oxo Stretch', 'Hydroxide Stretch'] Intercept:
 8.836929319321026
```

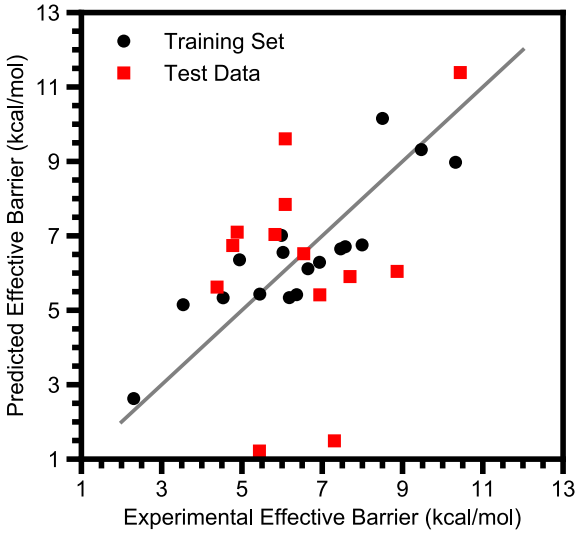

Regression A1.27 DHA barriers against $\Delta G°_{CPET}$ and change in metal–ligand bond lengths.

```
['DHA ΔG_CPET', 'ΔLength M-O', 'Total ΔLength M-L'] Metrics:

Score on Training Data:                 0.751448256020735
MSE of Training Data:                   0.9701498183121323
Score of LOO Cross Validation:          0.46889535893792444
MSE of LOO Cross Validation:            2.073013300096122
MSE of 5-Fold Cross Validation:         2.0136398644927245(0.07838159315728596)
F-Test p-value of final 2 variables:    0.27432806144440447

Correlation Matrix of x-values:
                   DHA ΔG_CPET  ΔLength M-O  Total ΔLength M-L
DHA ΔG_CPET           1.000000    -0.308863          -0.233562
ΔLength M-O          -0.308863     1.000000          -0.440362
Total ΔLength M-L    -0.233562    -0.440362           1.000000

['DHA ΔG_CPET', 'ΔLength M-O', 'Total ΔLength M-L'] Training Average:
[-7.77619718  0.2135339   0.47312783]

 ['DHA ΔG_CPET', 'ΔLength M-O', 'Total ΔLength M-L'] Training Deviation:
[4.05326542 0.03836354 0.32487374]

 ['DHA ΔG_CPET', 'ΔLength M-O', 'Total ΔLength M-L'] Coefficients:
[ 0.44882346 13.36221923  0.15539224]

 ['DHA ΔG_CPET', 'ΔLength M-O', 'Total ΔLength M-L'] Standard Error:
 [0.07860524 8.99430283 1.03891916]

 ['DHA ΔG_CPET', 'ΔLength M-O', 'Total ΔLength M-L'] t-Test "Error":
 [ 0.1698163  19.43100991  2.24444839]

 ['DHA ΔG_CPET', 'ΔLength M-O', 'Total ΔLength M-L'] Weighted Coefficients:
[1.8192006  0.51262207 0.05048286]

 ['DHA ΔG_CPET', 'ΔLength M-O', 'Total ΔLength M-L'] Intercept:
 7.045389227464227
```

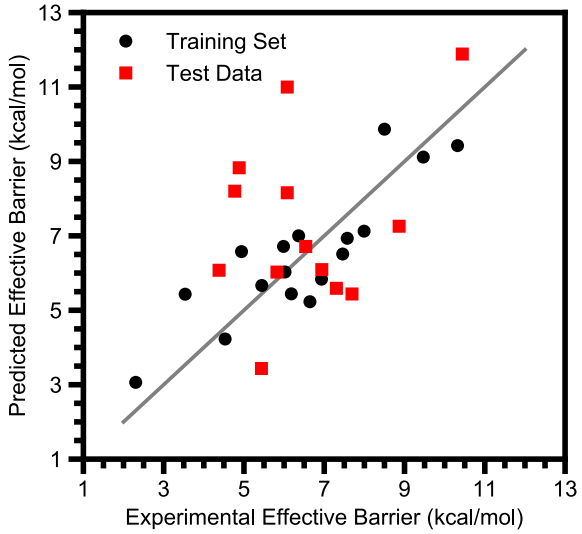

Regression A1.28 DHA barriers against $\Delta G°_{CPET}$, reorganization, and the magnitude of the asynchronicity.

```
['DHA ΔG_CPET', 'Oxo λ', 'Hydroxide λ', 'DHA |η| (G)'] Metrics:

Score on Training Data:                 0.7508389994578081
MSE of Training Data:                   0.9725278750272693
Score of LOO Cross Validation:          0.47878455120218033
MSE of LOO Cross Validation:            2.034413699365813
MSE of 5-Fold Cross Validation:         2.1242747875853207(0.07222199871900489)
F-Test p-value of final 3 variables:    0.48404896214361404

Correlation Matrix of x-values:
              DHA ΔG_CPET     Oxo λ  Hydroxide λ  DHA |η| (G)
DHA ΔG_CPET      1.000000 -0.113949    -0.336879     0.184231
Oxo λ           -0.113949  1.000000     0.685471     0.360767
Hydroxide λ     -0.336879  0.685471     1.000000     0.411410
DHA |η| (G)      0.184231  0.360767     0.411410     1.000000

['DHA ΔG_CPET', 'Oxo λ', 'Hydroxide λ', 'DHA |η| (G)'] Training Average:
[-7.77619718 21.37229441 22.86499201 17.96727543]

 ['DHA ΔG_CPET', 'Oxo λ', 'Hydroxide λ', 'DHA |η| (G)'] Training Deviation:
[ 4.05326542  5.37099513  6.03190216 12.92730813]

 ['DHA ΔG_CPET', 'Oxo λ', 'Hydroxide λ', 'DHA |η| (G)'] Coefficients:
[ 0.35613308 -0.01975543 -0.04662405  0.04146195]

 ['DHA ΔG_CPET', 'Oxo λ', 'Hydroxide λ', 'DHA |η| (G)'] Standard Error:
 [0.08127479 0.07401256 0.0744917  0.02612321]

 ['DHA ΔG_CPET', 'Oxo λ', 'Hydroxide λ', 'DHA |η| (G)'] t-Test "Error":
 [0.17708255 0.16125951 0.16230347 0.05691758]

 ['DHA ΔG_CPET', 'Oxo λ', 'Hydroxide λ', 'DHA |η| (G)'] Weighted Coefficients:
[ 1.44350191 -0.10610634 -0.28123169  0.53599146]

 ['DHA ΔG_CPET', 'Oxo λ', 'Hydroxide λ', 'DHA |η| (G)'] Intercept:
 9.994736811747302
```

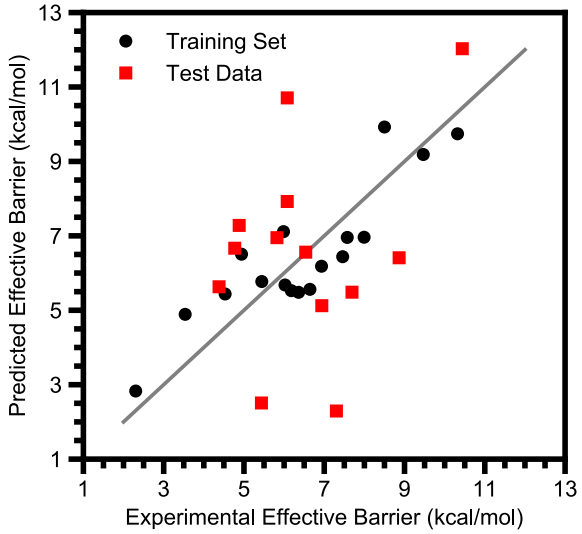

Regression A1.29 DHA barriers against $\Delta G°_{CPET}$, stretching energies, and the magnitude of the asynchronicity.

```
['DHA ΔG_CPET', 'Oxo Stretch', 'Hydroxide Stretch', 'DHA |η| (G)'] Metrics:

Score on Training Data:                 0.7778036840135025
MSE of Training Data:                   0.8672790306468683
Score of LOO Cross Validation:          0.4336095053173339
MSE of LOO Cross Validation:            2.2107414203295503
MSE of 5-Fold Cross Validation:         2.4951787280872217(0.09740659325306181)
F-Test p-value of final 3 variables:    0.27479651348982703

Correlation Matrix of x-values:
                   DHA ΔG_CPET  Oxo Stretch  Hydroxide Stretch  DHA |η| (G)
DHA ΔG_CPET           1.000000    -0.399234          -0.481905     0.184231
Oxo Stretch          -0.399234     1.000000           0.865424    -0.078940
Hydroxide Stretch    -0.481905     0.865424           1.000000    -0.241536
DHA |η| (G)           0.184231    -0.078940          -0.241536     1.000000

['DHA ΔG_CPET', 'Oxo Stretch', 'Hydroxide Stretch', 'DHA |η| (G)'] Training Average:
[-7.77619718 51.16490969 21.37839275 17.96727543]

 ['DHA ΔG_CPET', 'Oxo Stretch', 'Hydroxide Stretch', 'DHA |η| (G)'] Training
Deviation:
[ 4.05326542 19.44134649  3.86935373 12.92730813]

 ['DHA ΔG_CPET', 'Oxo Stretch', 'Hydroxide Stretch', 'DHA |η| (G)'] Coefficients:
[0.44430222 0.01412713 0.0616774  0.03059378]

 ['DHA ΔG_CPET', 'Oxo Stretch', 'Hydroxide Stretch', 'DHA |η| (G)'] Standard Error:
 [0.07595257 0.02864889 0.15304247 0.02229869]

 ['DHA ΔG_CPET', 'Oxo Stretch', 'Hydroxide Stretch', 'DHA |η| (G)'] t-Test "Error":
 [0.16548644 0.06242056 0.3334509  0.04858468]

 ['DHA ΔG_CPET', 'Oxo Stretch', 'Hydroxide Stretch', 'DHA |η| (G)'] Weighted
Coefficients:
[1.80087482 0.27465053 0.23865166 0.39549526]

 ['DHA ΔG_CPET', 'Oxo Stretch', 'Hydroxide Stretch', 'DHA |η| (G)'] Intercept:
 7.3459742258465806
```

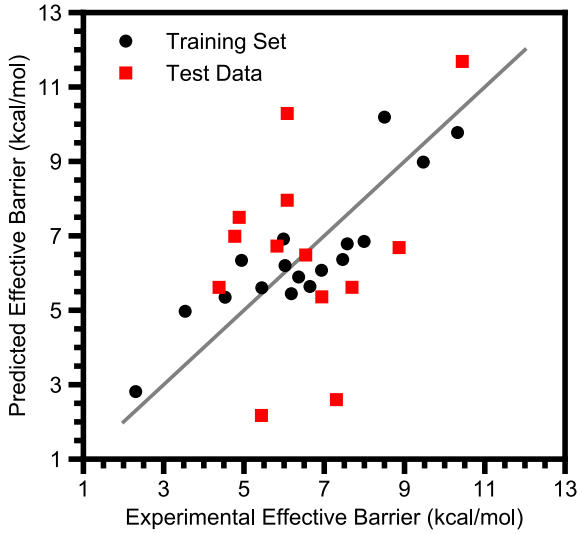

Regression A1.30 DHA barriers against $\Delta G°_{CPET}$, bond length changes, and the magnitude of the asynchronicity.

```
['DHA ΔG_CPET', 'ΔLength M-O', 'Total ΔLength M-L', 'DHA |η| (G)'] Metrics:

Score on Training Data:                 0.7754144322642288
MSE of Training Data:                   0.8766047835599248
Score of LOO Cross Validation:          0.4683307976976163
MSE of LOO Cross Validation:            2.075216901551265
MSE of 5-Fold Cross Validation:         2.361928941102483(0.0997562689075115)
F-Test p-value of final 3 variables:    0.29022403136241515

Correlation Matrix of x-values:
                   DHA ΔG_CPET  ΔLength M-O  Total ΔLength M-L  DHA |η| (G)
DHA ΔG_CPET           1.000000    -0.308863          -0.233562     0.184231
ΔLength M-O          -0.308863     1.000000          -0.440362     0.036738
Total ΔLength M-L    -0.233562    -0.440362           1.000000     0.117113
DHA |η| (G)           0.184231     0.036738           0.117113     1.000000

['DHA ΔG_CPET', 'ΔLength M-O', 'Total ΔLength M-L', 'DHA |η| (G)'] Training Average:
[-7.77619718  0.2135339   0.47312783 17.96727543]

 ['DHA ΔG_CPET', 'ΔLength M-O', 'Total ΔLength M-L', 'DHA |η| (G)'] Training
Deviation:
[ 4.05326542  0.03836354  0.32487374 12.92730813]

 ['DHA ΔG_CPET', 'ΔLength M-O', 'Total ΔLength M-L', 'DHA |η| (G)'] Coefficients:
[ 0.42084833 10.92517568 -0.16992622  0.02512143]

 ['DHA ΔG_CPET', 'ΔLength M-O', 'Total ΔLength M-L', 'DHA |η| (G)'] Standard Error:
 [0.08160516 9.15568025 1.0673317  0.0221996 ]

 ['DHA ΔG_CPET', 'ΔLength M-O', 'Total ΔLength M-L', 'DHA |η| (G)'] t-Test "Error":
 [ 0.17780238 19.94851359  2.325516    0.04836878]

 ['DHA ΔG_CPET', 'ΔLength M-O', 'Total ΔLength M-L', 'DHA |η| (G)'] Weighted
Coefficients:
[ 1.70581     0.41912845 -0.05520457  0.32475242]

 ['DHA ΔG_CPET', 'ΔLength M-O', 'Total ΔLength M-L', 'DHA |η| (G)'] Intercept:
 7.050794199068996
```

7. Robustness of Results to Computational Methodology

Calculated free energies of reactions for transition metal complexes can depend greatly on the DFT functional used. This is particularly true for reactions which involve a transition from low-spin reactants to high-spin products, as is the case here.[137,325] To confirm that our results are not an artifact of our computational methodology we recalculated the electronic energies with different computational methods at the O3LYP optimized geometries. These alternate methods were the B3LYP functional, the M06L functional, and O3LYP with the zeroth order regular approximation (ZORA) scalar relativistic correction. Importantly, the functionals tested incorporate varying amounts of Hartree Fock Exchange. Because M06L and ZORA are relatively sensitive to the integration grid used (per the ORCA manual),[170,326] we used a finer integration grid than in our other calculations (Grid7/FinalGrid7, the finest grid setting available) and recalculated the O3LYP energies at this finer grid for comparison. As shown in Table A1.19 and the following regressions, we find $\Delta E°_{PT}$ and $\Delta E°_{ET}$ have significant contributions to reaction barriers regardless of the computational method used to calculate them.

Table A1.19 Summary of statistics on regressions with different computational methodology

Method	Parameter(s)	R^2	MSE[a]	LOO[b] R^2	LOO[b] MSE[a]	5-Fold CV[c] MSE[a]	*p*-value
O3LYP	$\Delta E°_{CPET}$	0.62	1.46	0.52	1.89	1.90	< 0.001[d]
	$\Delta E°_{CPET}$, $\Delta E°_{PT}$, $\Delta E°_{ET}$	0.87	0.52	0.76	0.95	1.15	0.001[e]
B3LYP	$\Delta E°_{CPET}$	0.72	1.10	0.58	1.66	1.70	<0.001[d]
	$\Delta E°_{CPET}$, $\Delta E°_{PT}$, $\Delta E°_{ET}$	0.88	0.47	0.76	0.95	1.24	0.004[e]
M06L	$\Delta E°_{CPET}$	0.65	1.37	0.54	1.81	1.94	< 0.001[d]
	$\Delta E°_{CPET}$, $\Delta E°_{PT}$, $\Delta E°_{ET}$	0.85	0.58	0.71	1.14	1.46	0.004[e]
O3LYP-ZORA	$\Delta E°_{CPET}$	0.58	1.62	0.46	2.10	2.10	< 0.001[d]
	$\Delta E°_{CPET}$, $\Delta E°_{PT}$, $\Delta E°_{ET}$	0.85	0.59	0.75	0.99	1.21	0.001[e]

[a]Mean Squared Error, kcal^2 mol^{-2}. [b]Leave-One-Out. [c]Cross Validation. [d]From an *F*-test where the null hypothesis is that $\Delta E°_{CPET}$ has no effect. [e]From an F-test where the null hypothesis is that $\Delta E°_{PT}$ and $\Delta E°_{PT}$ have no effect.

Table A1.20 $\Delta E°_{CPET}$ computed with different computational methodologies

Oxo	O3LYP $\Delta E°_{CPET}$	B3LYP $\Delta E°_{CPET}$	M06L $\Delta E°_{CPET}$	O3LYP-ZORA $\Delta E°_{CPET}$
$[Fe^{IV}(O)(Me_3NTB)(MeCN)]^{2+}$	–9.0	–17.9	–15.7	–6.3
$[Fe^{IV}(O)(TMG_2dien)(MeCN)]^{2+}$	–5.0	–12.0	–7.9	–3.3
$[Fe^{IV}(O)(TMG_3tren)]^{2+}$	–3.0	–10.0	–5.7	–1.4
$[Fe^{V}(O)(TAML)]^{-}$	–6.9	–14.2	–6.6	–5.2
$[Fe^{IV}(O)(TMC)(MeCN)]^{2+}$	1.4	–6.9	–2.2	3.3
$[Fe^{IV}(O)(TMC)(N_3)]^{+}$	–2.1	–9.9	–5.2	–0.24
$[Fe^{IV}(O)(TMC)(OCOCF_3)]^{+}$	–1.3	–9.0	–4.3	0.18
$[Fe^{IV}(O)(TMCS)]^{+}$	–2.3	–10.2	–5.8	–0.67
$[Mn^{IV}(O)(H_3buea)]^{-}$	5.2	–1.6	1.8	6.9
$[Fe^{IV}(O)(TMP)]$	–6.3	–13.7	–14.1	–4.4
$[Co^{III}(O)(PhB^{tBu}Im_3)]$	–3.0	–17.6	–6.0	0.41
$[Ru^{IV}(O)(H^{+}TPA)(bpy)]^{3+}$	–2.6	–4.1	–1.7	–3.3
$[Fe^{IV}(O)(tpfpp)]$	–3.8	–10.6	–3.1	–2.3
$[Mn^{VII}(O)_4]^{-}$	3.5	–5.5	8.2	5.6
$[Mn^{V}(O)_2(tf_4tmap)]^{3+}$	–9.1	–19.6	–14.6	–7.0
$[Mn^{IV}(O)(OH)(tf_4tmap)]^{3+}$	–4.7	-9.6	–5.6	–1.8
$[Cr^{IV}(O)(TMC)(Cl)]^{+}$	–7.5	–14.0	–10.2	–5.9
$[Ru^{VI}(O)_2(TMC)]^{2+}$	7.1	0.88	7.4	5.6
$[Fe^{IV}(O)(N4Py)]^{2+}$	1.4	–9.2	–6.4	4.3
$[Fe^{IV}(O)(BnTPEN)]^{2+}$	–1.2	–10.9	–7.1	1.2
$[Fe^{IV}(O)(^{Me2}TACN\text{-}Py_2)]^{2+}$	1.3	–8.0	–4.9	3.7
$[Fe^{IV}(O)(BP1)]^{2+}$	0.26	–9.8	–7.2	2.9
$[Fe^{IV}(O)(BP2)]^{2+}$	–3.3	–12.5	–10.9	–0.71
$[Ru^{IV}(O)(bpy)_2(py)]^{2+}$	–3.8	–5.1	–2.7	–4.6
$[Mn^{IV}(O)_2(Me_2EBC)]$	0.70	–5.3	1.2	2.7
$[Mn^{IV}(O)(N4Py)]^{2+}$	–3.1	–10.1	–5.4	–0.84
$[Co^{IV}(O)(13\text{-}TMC)]^{2+}$	–11.0	–18.7	–10.7	–9.6
$[Fe^{IV}(O)(13\text{-}TMC)]^{2+}$	–13.8	–21.2	–19.5	–12.4
$[Ru^{VI}(O)_2(L)]^{2+}$	2.8	–3.6	4.3	1.2
$[Ru^{VI}(O)_2(F_{28}\text{-}tpp)]$	–1.1	–7.2	–0.20	–2.4

Table A1.21 $\Delta E°_{PT}$ computed with different computational methodologies

Oxo	O3LYP $\Delta E°_{PT}$	B3LYP $\Delta E°_{PT}$	M06L $\Delta E°_{PT}$	O3LYP-ZORA $\Delta E°_{PT}$
$[Fe^{IV}(O)(Me_3NTB)(MeCN)]^{2+}$	61.4	64.4	63.8	60.9
$[Fe^{IV}(O)(TMG_2dien)(MeCN)]^{2+}$	61.4	64.2	62.4	61.0
$[Fe^{IV}(O)(TMG_3tren)]^{2+}$	57.6	61.0	59.4	56.8
$[Fe^{V}(O)(TAML)]^{-}$	43.2	38.3	45.0	44.7
$[Fe^{IV}(O)(TMC)(MeCN)]^{2+}$	72.0	73.8	74.7	71.5
$[Fe^{IV}(O)(TMC)(N_3)]^{+}$	50.5	53.4	54.4	50.0
$[Fe^{IV}(O)(TMC)(OCOCF_3)]^{+}$	60.1	62.2	62.7	58.4
$[Fe^{IV}(O)(TMCS)]^{+}$	42.7	45.7	46.1	42.3
$[Mn^{IV}(O)(H_3buea)]^{-}$	29.5	31.4	27.9	28.8
$[Fe^{IV}(O)(TMP)]$	44.2	41.9	45.5	44.7
$[Co^{III}(O)(PhB^{tBu}Im_3)]$	19.5	21.2	22.1	21.7
$[Ru^{IV}(O)(H^{+}TPA)(bpy)]^{3+}$	78.8	79.4	80.3	78.8
$[Fe^{IV}(O)(tpfpp)]$	53.6	52.1	54.2	51.9
$[Mn^{VII}(O)_4]^{-}$	58.7	62.1	60.5	59.0
$[Mn^{V}(O)_2(tf_4tmap)]^{3+}$	36.6	38.6	40.1	35.8
$[Mn^{IV}(O)(OH)(tf_4tmap)]^{3+}$	21.3	24.4	23.2	20.1
$[Cr^{IV}(O)(TMC)(Cl)]^{+}$	56.9	60.4	59.4	56.2
$[Ru^{VI}(O)_2(TMC)]^{2+}$	86.9	89.5	88.6	86.8
$[Fe^{IV}(O)(N4Py)]^{2+}$	68.9	69.7	71.6	68.5
$[Fe^{IV}(O)(BnTPEN)]^{2+}$	66.7	68.1	69.3	66.1
$[Fe^{IV}(O)(^{Me2}TACN\text{-}Py_2)]^{2+}$	67.5	68.8	70.2	67.0
$[Fe^{IV}(O)(BP1)]^{2+}$	74.0	75.1	76.8	73.6
$[Fe^{IV}(O)(BP2)]^{2+}$	71.4	72.9	74.0	70.9
$[Ru^{IV}(O)(bpy)_2(py)]^{2+}$	71.8	72.7	74.1	71.9
$[Mn^{IV}(O)_2(Me_2EBC)]$	7.1	10.2	10.0	6.4.0
$[Mn^{IV}(O)(N4Py)]^{2+}$	55.1	57.3	56.7	54.4
$[Co^{IV}(O)(13\text{-}TMC)]^{2+}$	74.0	76.5	75.1	73.9
$[Fe^{IV}(O)(13\text{-}TMC)]^{2+}$	83.4	86.2	84.5	83.1
$[Ru^{VI}(O)_2(L)]^{2+}$	89.3	92.9	90.0	88.9
$[Ru^{VI}(O)_2(F_{28}\text{-}tpp)]$	66.3	69.9	67.3	61.9

Table A1.22 $\Delta E°_{ET}$ computed with different computational methodologies

Oxo	O3LYP $\Delta E°_{ET}$	B3LYP $\Delta E°_{ET}$	M06L $\Delta E°_{ET}$	O3LYP-ZORA $\Delta E°_{ET}$
$[Fe^{IV}(O)(Me_3NTB)(MeCN)]^{2+}$	37.8	29.3	27.1	41.1
$[Fe^{IV}(O)(TMG_2dien)(MeCN)]^{2+}$	45.9	39.4	39.7	48.4
$[Fe^{IV}(O)(TMG_3tren)]^{2+}$	54.4	47.9	48.9	56.8
$[Fe^{V}(O)(TAML)]^{-}$	44.8	37.4	42.2	46.6
$[Fe^{IV}(O)(TMC)(MeCN)]^{2+}$	46.7	40.3	41.4	49.2
$[Fe^{IV}(O)(TMC)(N_3)]^{+}$	56.0	49.9	50.1	58.4
$[Fe^{IV}(O)(TMC)(OCOCF_3)]^{+}$	52.7	47.2	48.0	55.7
$[Fe^{IV}(O)(TMCS)]^{+}$	59.2	52.5	52.9	61.3
$[Mn^{IV}(O)(H_3buea)]^{-}$	69.2	64.5	66.0	72.2
$[Fe^{IV}(O)(TMP)]$	73.5	75.1	69.7	73.6
$[Co^{III}(O)(PhB^{tBu}Im_3)]$	82.8	74.8	74.6	85.6
$[Ru^{IV}(O)(H^{+}TPA)(bpy)]^{3+}$	45.8	48.8	41.5	45.9
$[Fe^{IV}(O)(tpfpp)]$	63.6	65.2	59.6	66.0
$[Mn^{VII}(O)_4]^{-}$	54.4	44	55.4	56.3
$[Mn^{V}(O)_2(tf_4tmap)]^{3+}$	66.2	87.1	61.7	67.9
$[Mn^{IV}(O)(OH)(tf_4tmap)]^{3+}$	65.7	67.9	60.4	67.6
$[Cr^{IV}(O)(TMC)(Cl)]^{+}$	61.5	56.4	56.7	63.8
$[Ru^{VI}(O)_2(TMC)]^{2+}$	38.5	33.1	35.1	37.5
$[Fe^{IV}(O)(N4Py)]^{2+}$	46.4	36.4	34.9	49.9
$[Fe^{IV}(O)(BnTPEN)]^{2+}$	42.9	34.7	34.6	46.1
$[Fe^{IV}(O)(^{Me2}TACN\text{-}Py_2)]^{2+}$	46.5	37.9	36.7	49.4
$[Fe^{IV}(O)(BP1)]^{2+}$	43.3	33.9	32.2	46.5
$[Fe^{IV}(O)(BP2)]^{2+}$	40.0	31.6	28.9	43.3
$[Ru^{IV}(O)(bpy)_2(py)]^{2+}$	47.6	51.1	43.7	47.7
$[Mn^{IV}(O)_2(Me_2EBC)]$	93.7	87.4	89.3	95.6
$[Mn^{IV}(O)(N4Py)]^{2+}$	43.7	37.2	37.0	47.1
$[Co^{IV}(O)(13\text{-}TMC)]^{2+}$	16.8	9.3	13.9	18.8
$[Fe^{IV}(O)(13\text{-}TMC)]^{2+}$	24.2	17.5	16.2	26.3
$[Ru^{VI}(O)_2(L)]^{2+}$	26.5	20.8	24	25.4
$[Ru^{VI}(O)_2(F_{28}\text{-}tpp)]$	42.7	38.1	39	45.6

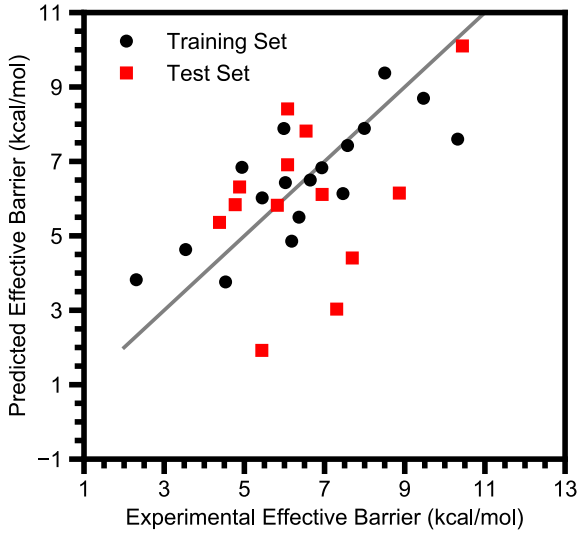

Regression A1.31 DHA barriers against O3LYP's $\Delta E°_{CPET}$.

```
['O3LYP ΔE_CPET'] Metrics:

Score on Training Data:                 0.6248135531191439
MSE of Training Data:                   1.4644317414445578
Score of LOO Cross Validation:          0.5155711219123456
MSE of LOO Cross Validation:            1.8908279641807464
MSE of 5-Fold Cross Validation:         1.9028770862454243(0.04693830813373367)
F-Test p-value of final 1 variables:    0.0001589808441718743

Correlation Matrix of x-values:
                O3LYP ΔE_CPET
O3LYP ΔE_CPET             1.0

['O3LYP ΔE_CPET'] Training Average:
[-2.1557534]

 ['O3LYP ΔE_CPET'] Training Deviation:
[3.99653951]

 ['O3LYP ΔE_CPET'] Coefficients:
[0.39075281]

 ['O3LYP ΔE_CPET'] Standard Error:
 [0.07818165]

 ['O3LYP ΔE_CPET'] t-Test "Error":
 [0.16664024]

 ['O3LYP ΔE_CPET'] Weighted Coefficients:
[1.56165903]

 ['O3LYP ΔE_CPET'] Intercept:
 7.3244233791333135
```

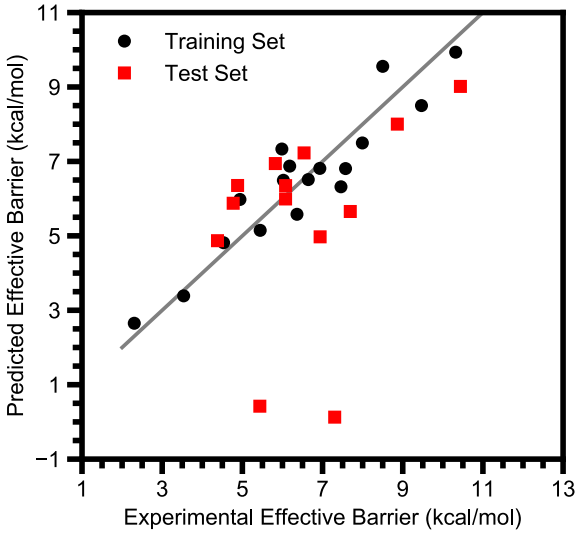

Regression A1.32 DHA barriers against O3LYP's $\Delta E°_{CPET}$, $\Delta E°_{PT}$, and $\Delta E°_{ET}$.

```
 ['O3LYP ΔE_CPET', 'O3LYP ΔE_PT', 'O3LYP ΔE_ET'] Metrics:

Score on Training Data:                 0.8661041977336073
MSE of Training Data:                   0.522623523624661
Score of LOO Cross Validation:          0.7561336561488596
MSE of LOO Cross Validation:            0.951861714554554
MSE of 5-Fold Cross Validation:         1.154890730587609(0.07663350650334944)
F-Test p-value of final 2 variables:    0.0012341809272257143

Correlation Matrix of x-values:
               O3LYP ΔE_CPET  O3LYP ΔE_PT  O3LYP ΔE_ET
O3LYP ΔE_CPET       1.000000     0.092458     0.118059
O3LYP ΔE_PT         0.092458     1.000000    -0.869440
O3LYP ΔE_ET         0.118059    -0.869440     1.000000

['O3LYP ΔE_CPET', 'O3LYP ΔE_PT', 'O3LYP ΔE_ET'] Training Average:
[-2.1557534  50.94173114 55.69690677]

 ['O3LYP ΔE_CPET', 'O3LYP ΔE_PT', 'O3LYP ΔE_ET'] Training Deviation:
[ 3.99653951 18.63116025 14.02743234]

 ['O3LYP ΔE_CPET', 'O3LYP ΔE_PT', 'O3LYP ΔE_ET'] Coefficients:
[0.32591958 0.04105499 0.11375599]

 ['O3LYP ΔE_CPET', 'O3LYP ΔE_PT', 'O3LYP ΔE_ET'] Standard Error:
 [0.05506456 0.02374144 0.03161931]

 ['O3LYP ΔE_CPET', 'O3LYP ΔE_PT', 'O3LYP ΔE_ET'] t-Test "Error":
 [0.11895975 0.05129026 0.06830937]

 ['O3LYP ΔE_CPET', 'O3LYP ΔE_PT', 'O3LYP ΔE_ET'] Weighted Coefficients:
[1.30255047 0.76490212 1.59570441]

 ['O3LYP ΔE_CPET', 'O3LYP ΔE_PT', 'O3LYP ΔE_ET'] Intercept:
 -1.2426099746813781
```

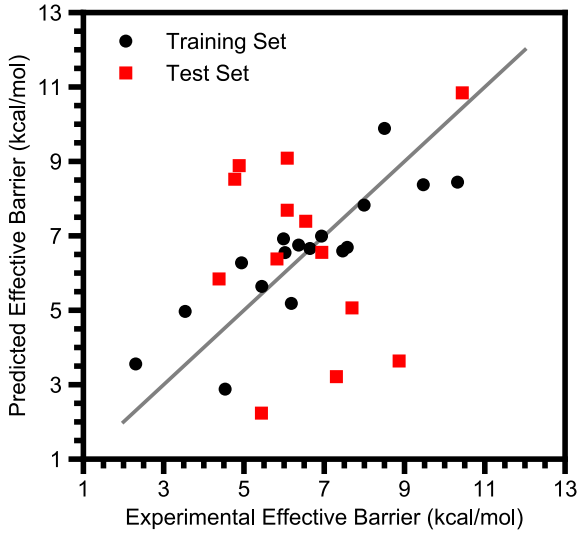

Regression A1.33 DHA barriers against B3LYP's $\Delta E°_{CPET}$.

```
 ['B3LYP ΔE_CPET'] Metrics:

Score on Training Data:                 0.7185873128148237
MSE of Training Data:                   1.0984130023493341
Score of LOO Cross Validation:          0.5752474491511528
MSE of LOO Cross Validation:            1.6578986871562655
MSE of 5-Fold Cross Validation:         1.7027161796546295(0.07407851365423393)
F-Test p-value of final 1 variables:    1.733634882372659e-05

Correlation Matrix of x-values:
                B3LYP ΔE_CPET
B3LYP ΔE_CPET             1.0

['B3LYP ΔE_CPET'] Training Average:
[-10.33181066]

 ['B3LYP ΔE_CPET'] Training Deviation:
[4.30591229]

 ['B3LYP ΔE_CPET'] Coefficients:
[0.38894267]

 ['B3LYP ΔE_CPET'] Standard Error:
 [0.06284519]

 ['B3LYP ΔE_CPET'] t-Test "Error":
 [0.13395135]

 ['B3LYP ΔE_CPET'] Weighted Coefficients:
[1.67475302]

 ['B3LYP ΔE_CPET'] Intercept:
 10.500538700135094
```

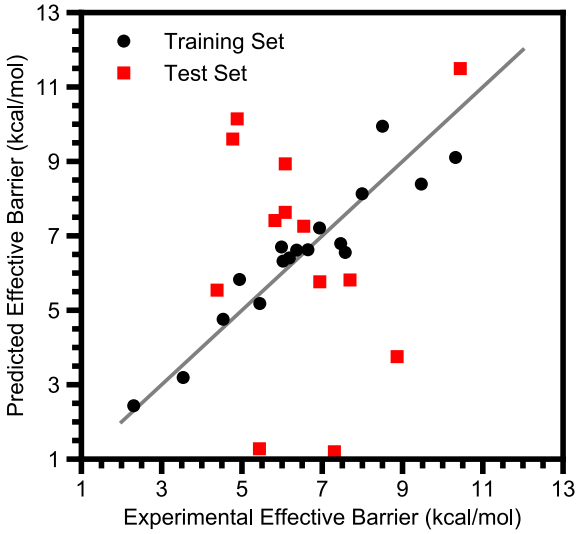

Regression A1.34 DHA barriers against B3LYP's $\Delta E°_{CPET}$, $\Delta E°_{PT}$, and $\Delta E°_{ET}$.

```
 ['B3LYP ΔE_CPET', 'B3LYP ΔE_PT', 'B3LYP ΔE_ET'] Metrics:

Score on Training Data:                 0.8784702014938369
MSE of Training Data:                   0.4743564058440075
Score of LOO Cross Validation:          0.7572853874456303
MSE of LOO Cross Validation:            0.947366264671894
MSE of 5-Fold Cross Validation:         1.2363937155719087(0.09772669492501583)
F-Test p-value of final 2 variables:    0.004262890528072938

Correlation Matrix of x-values:
               B3LYP ΔE_CPET  B3LYP ΔE_PT  B3LYP ΔE_ET
B3LYP ΔE_CPET       1.000000    -0.127181     0.046790
B3LYP ΔE_PT        -0.127181     1.000000    -0.826294
B3LYP ΔE_ET         0.046790    -0.826294     1.000000

['B3LYP ΔE_CPET', 'B3LYP ΔE_PT', 'B3LYP ΔE_ET'] Training Average:
[-10.33181066  52.5454078   50.98919915]

 ['B3LYP ΔE_CPET', 'B3LYP ΔE_PT', 'B3LYP ΔE_ET'] Training Deviation:
[ 4.30591229 18.62901372 18.26010309]

 ['B3LYP ΔE_CPET', 'B3LYP ΔE_PT', 'B3LYP ΔE_ET'] Coefficients:
[0.40163668 0.04998103 0.07462551]

 ['B3LYP ΔE_CPET', 'B3LYP ΔE_PT', 'B3LYP ΔE_ET'] Standard Error:
 [0.04497118 0.01843489 0.01867506]

 ['B3LYP ΔE_CPET', 'B3LYP ΔE_PT', 'B3LYP ΔE_ET'] t-Test "Error":
 [0.09715433 0.03982616 0.04034501]

 ['B3LYP ΔE_CPET', 'B3LYP ΔE_PT', 'B3LYP ΔE_ET'] Weighted Coefficients:
[1.72941233 0.93109722 1.36266952]

 ['B3LYP ΔE_CPET', 'B3LYP ΔE_PT', 'B3LYP ΔE_ET'] Intercept:
 4.200322441694215
```

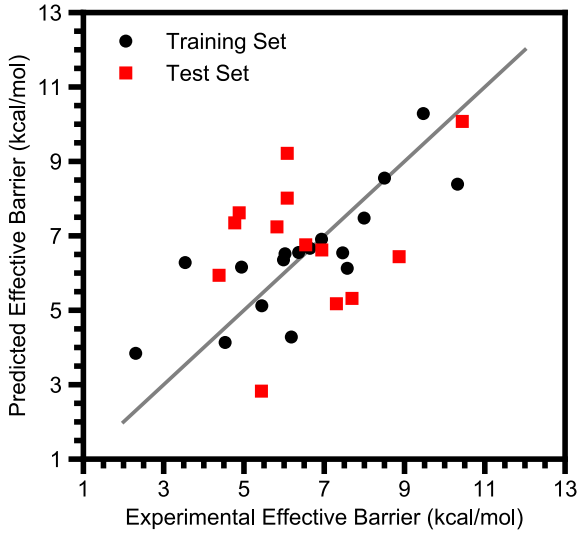

Regression A1.35 DHA barriers against M06L's $\Delta E°_{CPET}$.

```
 ['M06L ΔE_CPET'] Metrics:

Score on Training Data:                 0.6489813916645575
MSE of Training Data:                   1.3700995762444375
Score of LOO Cross Validation:          0.53623765519843
MSE of LOO Cross Validation:            1.810162131016007
MSE of 5-Fold Cross Validation:         1.943021323080626(0.07769574536680626)
F-Test p-value of final 1 variables:    9.496453767954272e-05

Correlation Matrix of x-values:
              M06L ΔE_CPET
M06L ΔE_CPET           1.0

['M06L ΔE_CPET'] Training Average:
[-5.8857926]

 ['M06L ΔE_CPET'] Training Deviation:
[5.90685145]

 ['M06L ΔE_CPET'] Coefficients:
[0.26944558]

 ['M06L ΔE_CPET'] Standard Error:
 [0.05116517]

 ['M06L ΔE_CPET'] t-Test "Error":
 [0.10905597]

 ['M06L ΔE_CPET'] Weighted Coefficients:
[1.59157503]

 ['M06L ΔE_CPET'] Intercept:
 8.067957508683563
```

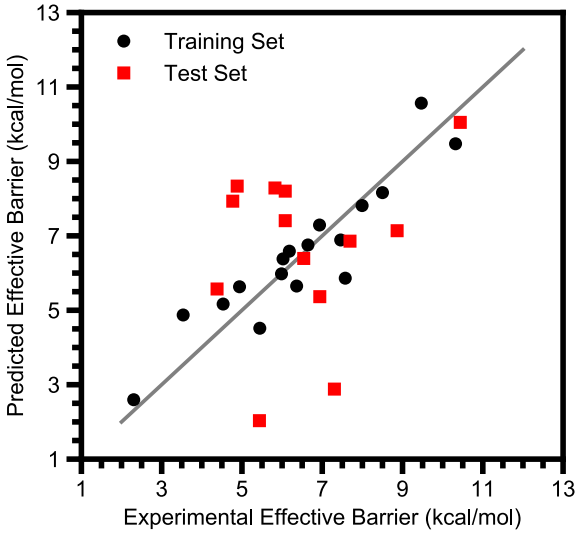

Regression A1.36 DHA barriers against M06L's $\Delta E°_{CPET}$, $\Delta E°_{PT}$, and $\Delta E°_{ET}$.

```
 ['M06L ΔE_CPET', 'M06L ΔE_PT', 'M06L ΔE_ET'] Metrics:

Score on Training Data:                 0.8510495458264639
MSE of Training Data:                   0.5813850015311927
Score of LOO Cross Validation:          0.7071919877823828
MSE of LOO Cross Validation:            1.1428913565658008
MSE of 5-Fold Cross Validation:         1.4555347084599448(0.09713878607647679)
F-Test p-value of final 2 variables:    0.0038029971170726595

Correlation Matrix of x-values:
              M06L ΔE_CPET  M06L ΔE_PT  M06L ΔE_ET
M06L ΔE_CPET      1.000000   -0.207271    0.353413
M06L ΔE_PT       -0.207271    1.000000   -0.867418
M06L ΔE_ET        0.353413   -0.867418    1.000000

['M06L ΔE_CPET', 'M06L ΔE_PT', 'M06L ΔE_ET'] Training Average:
[-5.8857926  53.24122039 49.62308161]

 ['M06L ΔE_CPET', 'M06L ΔE_PT', 'M06L ΔE_ET'] Training Deviation:
[ 5.90685145 18.94195623 16.00741272]

 ['M06L ΔE_CPET', 'M06L ΔE_PT', 'M06L ΔE_ET'] Coefficients:
[0.20521987 0.0711776  0.116457  ]

 ['M06L ΔE_CPET', 'M06L ΔE_PT', 'M06L ΔE_ET'] Standard Error:
 [0.03917302 0.02296595 0.02842   ]

 ['M06L ΔE_CPET', 'M06L ΔE_PT', 'M06L ΔE_ET'] t-Test "Error":
 [0.08462816 0.04961491 0.06139768]

 ['M06L ΔE_CPET', 'M06L ΔE_PT', 'M06L ΔE_ET'] Weighted Coefficients:
[1.21220329 1.34824305 1.86417519]

 ['M06L ΔE_CPET', 'M06L ΔE_PT', 'M06L ΔE_ET'] Intercept:
 -1.8785991938222475
```

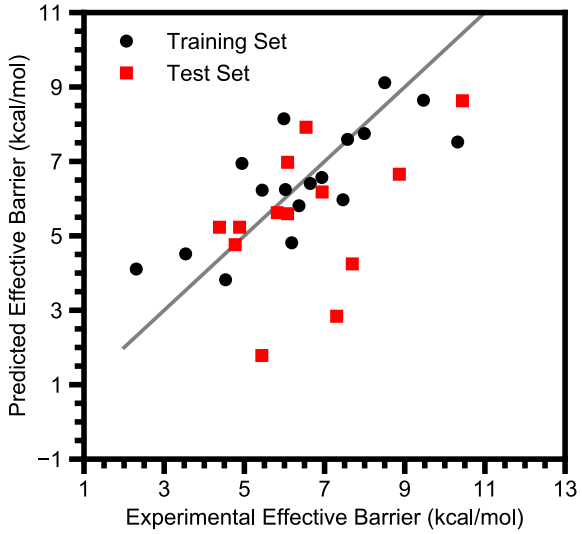

Regression A1.37 DHA barriers against O3LYP-ZORA's $\Delta E°_{CPET}$.

```
 ['ZORA ΔE_CPET'] Metrics:

Score on Training Data:                 0.5837879956450376
MSE of Training Data:                   1.6245631349823895
Score of LOO Cross Validation:          0.4632551558748629
MSE of LOO Cross Validation:            2.095028200853886
MSE of 5-Fold Cross Validation:         2.100418828317726(0.04913667840929494)
F-Test p-value of final 1 variables:    0.000356141781854169

Correlation Matrix of x-values:
               ZORA ΔE_CPET
ZORA ΔE_CPET            1.0

['ZORA ΔE_CPET'] Training Average:
[-0.04816983]

 ['ZORA ΔE_CPET'] Training Deviation:
[3.95594462]

 ['ZORA ΔE_CPET'] Coefficients:
[0.38158243]

 ['ZORA ΔE_CPET'] Standard Error:
 [0.08319026]

 ['ZORA ΔE_CPET'] t-Test "Error":
 [0.17731583]

 ['ZORA ΔE_CPET'] Weighted Coefficients:
[1.50951897]

 ['ZORA ΔE_CPET'] Intercept:
 6.500437449829684
```

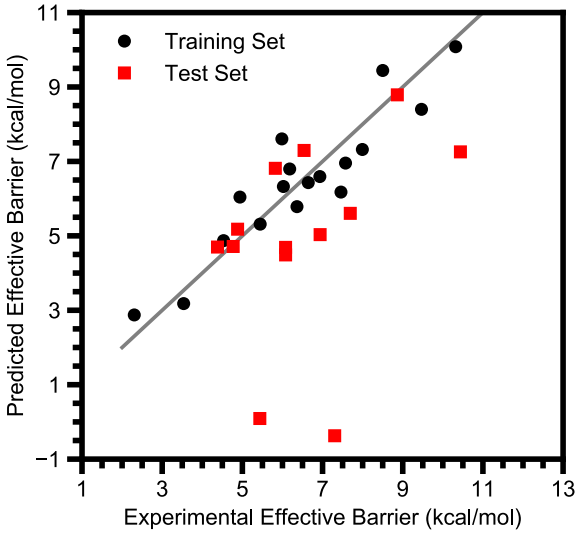

Regression A1.38 DHA barriers against O3LYP-ZORA's $\Delta E°_{CPET}$, $\Delta E°_{PT}$, and $\Delta E°_{ET}$.

```
 ['ZORA ΔE_CPET', 'ZORA ΔE_PT', 'ZORA ΔE_ET'] Metrics:

Score on Training Data:                 0.849900635628982
MSE of Training Data:                   0.585869440069017
Score of LOO Cross Validation:          0.7468405586771689
MSE of LOO Cross Validation:            0.9881346317321933
MSE of 5-Fold Cross Validation:         1.20988798980493(0.07486597934720962)
F-Test p-value of final 2 variables:    0.0013210450640702698

Correlation Matrix of x-values:
              ZORA ΔE_CPET  ZORA ΔE_PT  ZORA ΔE_ET
ZORA ΔE_CPET      1.000000    0.115023    0.106737
ZORA ΔE_PT        0.115023    1.000000   -0.872438
ZORA ΔE_ET        0.106737   -0.872438    1.000000

['ZORA ΔE_CPET', 'ZORA ΔE_PT', 'ZORA ΔE_ET'] Training Average:
[-4.81698302e-02  5.05000651e+01  5.81283061e+01]

 ['ZORA ΔE_CPET', 'ZORA ΔE_PT', 'ZORA ΔE_ET'] Training Deviation:
[ 3.95594462 18.67471947 13.55389964]

 ['ZORA ΔE_CPET', 'ZORA ΔE_PT', 'ZORA ΔE_ET'] Coefficients:
[0.31228114 0.04369815 0.12462006]

 ['ZORA ΔE_CPET', 'ZORA ΔE_PT', 'ZORA ΔE_ET'] Standard Error:
 [0.05972849 0.02574095 0.0354332 ]

 ['ZORA ΔE_CPET', 'ZORA ΔE_PT', 'ZORA ΔE_ET'] t-Test "Error":
 [0.12903556 0.05560993 0.07654877]

 ['ZORA ΔE_CPET', 'ZORA ΔE_PT', 'ZORA ΔE_ET'] Weighted Coefficients:
[1.23536689 0.81605065 1.68908777]

 ['ZORA ΔE_CPET', 'ZORA ΔE_PT', 'ZORA ΔE_ET'] Intercept: -2.9536129994751716
```

8. Analysis of Ru Oxo Kinetics with Several Substrates

Due to the overestimation reaction barriers for ruthenium-oxo complexes, we have investigated whether free energies other than $\Delta G°_{CPET}$ have an effect on the kinetics of $[Ru^{IV}(O)(bpy)_2(py)]^{2+}$ with several substrates. The experimental data is from two reports from Mayer and coworkers.[126,327] The determination of barrier heights and computational methodology were the same as for the data on multiple oxo complexes.

Table A1.23 Summary of data for regressions with the ruthenium-oxo data

Substrate	Corr.[a]	k_2 (mol s^{-1})	CPET Barrier	$\Delta G°_{CPET}$	$\Delta G°_{CPET}$	$\Delta G°_{CPET}$
9,10-Dihydroanthracene	2	125[e]	4.77	-5.48	68.5	43.4
Ethylbenzene	2	0.022[e]	10.22	2.90	82.8	51.7
Isopropylbenzene	2	0.033[e]	9.90	1.29	85.1	53.9
Toluene	1	0.0064[e]	10.65	8.69	83.5	53.8
Xanthene	1	577[e]	3.46	-8.24	67.7	35.3
Fluorene	1	21.9[e]	5.44	-1.21	58.6	40.1
$AcrH_2$[b]	1	5,700[f]	2.11	-11.4	70.5	19.5
BNAH[c]	1	70,000[f]	0.457	-12.1	88.1	19.3
Indene	1	10.8[e]	6.11	-2.61	54.5	40.0
Cyclohexene	1[c]	0.92[e]	7.81	-4.94	84.5	41.5

All energies in kcal/mol. [a]Stoichiometric correction to the rate. [b]10-Methyl9,10-dihydroacridine. [c]*N*-Benzyl-1,4-dihydronicatinamide. [c]Cyclohexenone is the only observed product, which we take to imply a 1:1 reaction stoichiometry. [e]Reference [126]. [f]Reference [327].

We find that $\Delta G°_{PT}$ and $\Delta G°_{ET}$ improve the fit to all substrates except *N*-benzyl-1,4-dihydronicotinamide (BNAH). It is unclear why BNAH does not fit the trend, as it is thought to react via the same CPET mechanism as the other substrates. Nonetheless there does not seem to be a broader issue with hydridic C–H bonds because 10-methyl-9,10-dihydroacridine ($AcrH_2$) fits well. The coefficients of the fits with ΔG_{PT} and ΔG_{ET} are similar to those seen in the fit with DHA ($\Delta G°_{CPET}$ has a coefficient ~0.3; $\Delta G°_{PT}$ and $\Delta G°_{ET}$ have a coefficients ~0.1), which reinforces the

conclusion that we are observing the same trends in both data sets. Similar to the hydrogen-bonding corrected DHA analysis, there is no significant effect of η, i.e $\Delta G°_{PT}$ and $\Delta G°_{ET}$ appear to have equal influence on the reactivity of this ruthenium-oxo complex.

Table A1.24 Summary of statistics on regressions with the ruthenium-oxo data

Parameter(s) Regressed with	R^2	MSE[a]	LOO[b] R^2	LOO[b] MSE[a]	5-Fold CV[c] MSE[a]	p-value
$\Delta G°_{CPET}$ only	0.81	1.58	0.69	2.61	2.77	<0.001[d]
$\Delta G°_{CPET}$, $\Delta G°_{PT}$, and $\Delta G°_{ET}$	0.94	0.48	0.79	1.79	2.18	0.051[e]
$\Delta G°_{CPET}$, $\Delta G°_{CC}$	0.94	0.49	0.86	1.23	1.37	0.010
$\Delta G°_{CPET}$, $\Delta G°_{ET}$, η	0.94	0.48	0.79	1.79	2.18	0.83[f]

[a]Mean Squared Error, kcal^2 mol^{-2}. [b]Leave-One-Out. [c]Cross Validation. [d]From an F-test where the null hypothesis is that $\Delta G°_{CPET}$ has no effect. [e]From an F-test where the null hypothesis is that ΔG_{PT} and ΔG_{ET} have no effect. [f]From an F-test where the null hypothesis is that η has no effect.

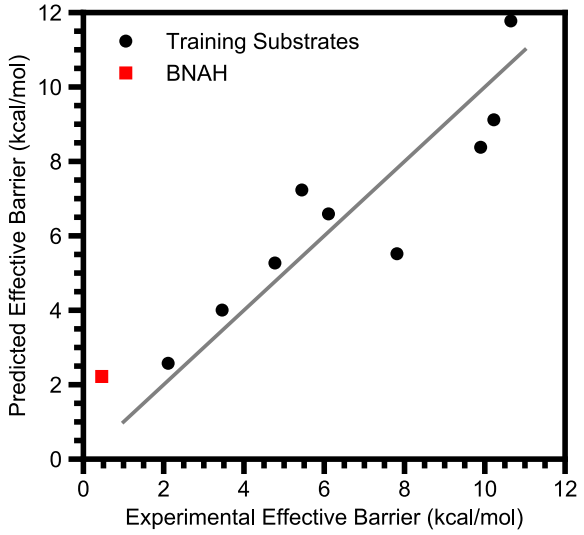

Regression A1.39 Ruthenium-oxo barriers against $\Delta G°_{CPET}$.

```
['ΔG_CPET'] Metrics:

Score on Training Data:                 0.8141313040751759
MSE of Training Data:                   1.5840108561567379
Score of LOO Cross Validation:          0.6935554692619883
MSE of LOO Cross Validation:            2.6115826609941655
MSE of 5-Fold Cross Validation:         2.769340429340532(0.09523255744448217)
F-Test p-value of final 1 variables:    0.0008715558586384065

Correlation Matrix of x-values:
          ΔG_CPET
ΔG_CPET       1.0

['ΔG_CPET'] Training Average:
[-2.32885283]

 ['ΔG_CPET'] Training Deviation:
[5.73889131]

 ['ΔG_CPET'] Coefficients:
[0.4589815]

 ['ΔG_CPET'] Standard Error:
 [0.08288998]

 ['ΔG_CPET'] t-Test "Error":
 [0.19600367]

 ['ΔG_CPET'] Weighted Coefficients:
[2.63404493]

 ['ΔG_CPET'] Intercept:
 7.787390135961275
```

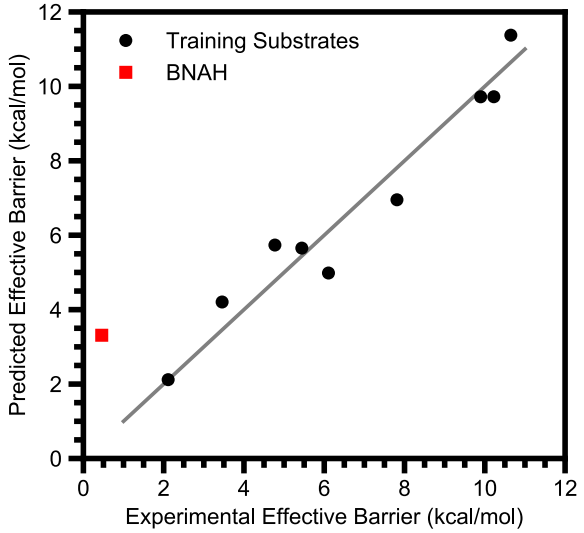

Regression A1.40 Ruthenium-oxo against $\Delta G°_{CPET}$, $\Delta G°_{PT}$, and $\Delta G°_{ET}$.

```
['ΔG_CPET', 'ΔG_PT', 'ΔG_ET'] Metrics:

Score on Training Data:                 0.9433272836504076
MSE of Training Data:                   0.48297642321627954
Score of LOO Cross Validation:          0.789763533352954
MSE of LOO Cross Validation:            1.7916779577753412
MSE of 5-Fold Cross Validation:         2.1772658070507824(0.09820218535610042)
F-Test p-value of final 2 variables:    0.0513356946380471

Correlation Matrix of x-values:
          ΔG_CPET     ΔG_PT     ΔG_ET
ΔG_CPET  1.000000  0.418868  0.876863
ΔG_PT    0.418868  1.000000  0.501120
ΔG_ET    0.876863  0.501120  1.000000

['ΔG_CPET', 'ΔG_PT', 'ΔG_ET'] Training Average:
[-2.32885283 72.85902939 42.13973614]

 ['ΔG_CPET', 'ΔG_PT', 'ΔG_ET'] Training Deviation:
[ 5.73889131 10.9865912  10.20429223]

 ['ΔG_CPET', 'ΔG_PT', 'ΔG_ET'] Coefficients:
[0.24144858 0.07967059 0.09854522]

 ['ΔG_CPET', 'ΔG_PT', 'ΔG_ET'] Standard Error:
 [0.11278959 0.0327295  0.06656052]

 ['ΔG_CPET', 'ΔG_PT', 'ΔG_ET'] t-Test "Error":
 [0.28993488 0.08413386 0.17109926]

 ['ΔG_CPET', 'ΔG_PT', 'ΔG_ET'] Weighted Coefficients:
[1.38564716 0.87530822 1.00558426]

 ['ΔG_CPET', 'ΔG_PT', 'ΔG_ET'] Intercept:
 -2.676603704473255
```

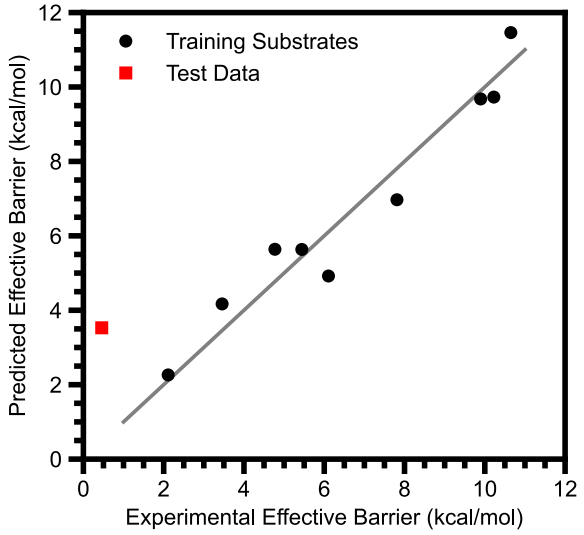

Regression A1.41 Ruthenium-oxo barriers against $\Delta G°_{CPET}$, $\Delta G°_{CC}$.

```
['ΔG_CPET', 'ΔG_CC'] Metrics:

Score on Training Data:                 0.9427367032442787
MSE of Training Data:                   0.488009469636963
Score of LOO Cross Validation:          0.8551716538682033
MSE of LOO Cross Validation:            1.2342566423599277
MSE of 5-Fold Cross Validation:         1.369958164234941(0.08381947525076561)
F-Test p-value of final 1 variables:    0.010443635304320797

Correlation Matrix of x-values:
          ΔG_CPET     ΔG_CC
ΔG_CPET  1.000000 -0.533178
ΔG_CC   -0.533178  1.000000

['ΔG_CPET', 'ΔG_CC'] Training Average:
[  -2.32885283 -117.32761837]

 ['ΔG_CPET', 'ΔG_CC'] Training Deviation:
[ 5.73889131 14.64952737]

 ['ΔG_CPET', 'ΔG_CC'] Coefficients:
[ 0.34401336 -0.08447144]

 ['ΔG_CPET', 'ΔG_CC'] Standard Error:
 [0.05874061 0.02301139]

 ['ΔG_CPET', 'ΔG_CC'] t-Test "Error":
 [0.1437331  0.05630684]

 ['ΔG_CPET', 'ΔG_CC'] Weighted Coefficients:
[ 1.97425528 -1.23746667]

 ['ΔG_CPET', 'ΔG_CC'] Intercept:
 -2.391186625530832
```

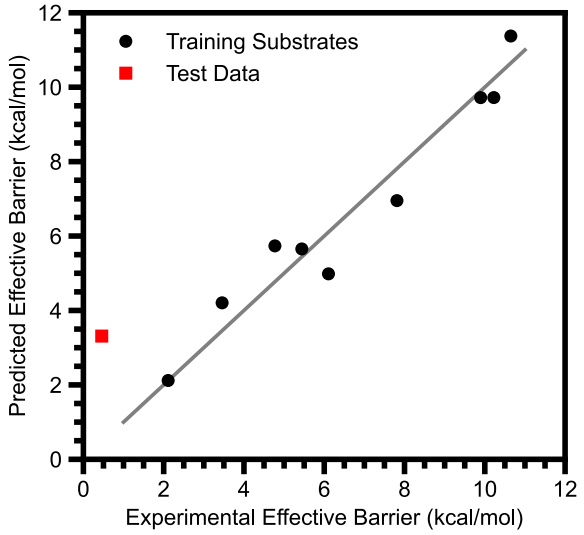

Regression A1.42 Ruthenium-oxo barriers against $\Delta G°_{CPET}$, $\Delta G°_{CC}$, η.

```
['ΔG_CPET', 'ΔG_CC', 'η'] Metrics:

Score on Training Data:                 0.9433272836504075
MSE of Training Data:                   0.48297642321627976
Score of LOO Cross Validation:          0.7897635333529542
MSE of LOO Cross Validation:            1.7916779577753397
MSE of 5-Fold Cross Validation:         2.177265807050784(0.09820218535610048)
F-Test p-value of final 1 variables:    0.8284825305556193

Correlation Matrix of x-values:
          ΔG_CPET     ΔG_CC         η
ΔG_CPET  1.000000 -0.533178 -0.409781
ΔG_CC   -0.533178  1.000000 -0.267233
η       -0.409781 -0.267233  1.000000

['ΔG_CPET', 'ΔG_CC', 'η'] Training Average:
[  -2.32885283 -117.32761837   21.71854033]

 ['ΔG_CPET', 'ΔG_CC', 'η'] Training Deviation:
[ 5.73889131 14.64952737  7.49791167]

 ['ΔG_CPET', 'ΔG_CC', 'η'] Coefficients:
[ 0.33055649 -0.08910791 -0.0133484 ]

 ['ΔG_CPET', 'ΔG_CC', 'η'] Standard Error:
 [0.08702479 0.03227146 0.05847787]

 ['ΔG_CPET', 'ΔG_CC', 'η'] t-Test "Error":
 [0.22370436 0.08295643 0.15032216]

 ['ΔG_CPET', 'ΔG_CC', 'η'] Weighted Coefficients:
[ 1.89702776 -1.30538873 -0.10008509]

 ['ΔG_CPET', 'ΔG_CC', 'η'] Intercept:
 -2.6766037044732247
```

9. Summary of statistics on regressions on the cobalt(III)-oxo data

Table A1.1 gives a summary of the regressions performed on the cobalt(III)-oxo complex. We reiterate the previously reported trend with $\Delta G°_{PT}$ and lack of a trend with $\Delta G°_{CPET}$.[50] We also detail how the addition of $\Delta G°_{CPET}$ to the regression with $\Delta G°_{PT}$ is significant and demonstrate that addition of neither the substrates' %BV sterics nor $\Delta G°_{ET}$ improve the fit further. The substrate 1,1,3,3-tetraphenylpropene was excluded from this analysis due to its relatively large steric hinderance.

Table A1.25 Summary of data for regressions with the cobalt(III)-oxo data

Substrate	k_2 (mol/s)[a]	CPET Barrier	$\Delta G°_{CPET}$	$\Delta G°_{PT}$	$\Delta G°_{ET}$	%BV[b]
9,10-Dihydroanthracene	0.0584[c]	3.1	–6.7	29.5	94.8	47.4
Fluorene	0.61	1.8	–3.3	19.3	90.5	43.2
1,3-Cyclohexadiene	0.0027[c]	5.5	–11.8	38.9	82.8	41.9
9-(*p*-CF_3Ph)Fluorene	112	–1.6	–9.9	8.8	91.9	57.6
9-(*p*-MeOPh)Fluorene	17.6	–0.48	–11.1	13.0	84.6	57.8
9-(*p*-MePh)Fluorene	22.4	–0.59	–10.7	12.9	88.8	57.7
3-Methylxanthene	0.088	2.8	–11.2	29.2	82.3	46.0
Diphenylmethane	0.012	4.1	–2.4	31.0	99.4	48.2
9-Phenylfluorene	29.6	–0.72	–10.3	11.6	90.0	57.7
9-*tert*-Butylfluorene	0.088	2.8	–5.2	21.1	89.0	61.5
1,1,3,3-Tetraphenylpropene	0.008	2.7	–12.5	18.0	88.1	73.5
Xanthene	0.1128	3.1	–10.4	28.9	85.3	45.8

All energies in kcal/mol. [a]Reference [50]. [b]Percent buried volume of a sphere around the reactive hydrogen atom. [c]Corrected by a stoichiometric factor of 2.

Table A1.26 Summary of statistics on regressions with the cobalt(III)-oxo data

Parameter(s) Regressed with	R^2	MSE[a]	LOO[b] R^2	LOO[b] MSE[a]	5-Fold CV[c] MSE[a]	p-value
$\Delta G°_{PT}$ only	0.94	0.28	0.93	0.36	0.39	< 0.001[d]
$\Delta G°_{CPET}$ only	0.09	4.39	-0.32	6.35	6.37	0.37[e]
$\Delta G°_{PT}$ and $\Delta G°_{CPET}$	0.97	0.13	0.94	0.27	0.29	0.017[e]
$\Delta G°_{PT}$, $\Delta G°_{CPET}$, and %BV Sterics	0.98	0.10	0.83	0.80	0.80	0.21[f]
$\Delta G°_{PT}$ and $\Delta G°_{ET}$	0.95	0.25	0.93	0.36	0.52	0.41[g]
$\Delta G°_{PT}$, $\Delta G°_{CPET}$, and $\Delta G°_{ET}$	0.98	0.08	0.95	0.23	0.29	0.072[g]
$\Delta G°_{CPET}$ and $\Delta G°_{CC}$	0.80	0.96	0.56	2.11	2.27	< 0.001
$\Delta G°_{CPET}$, $\Delta G°_{CC}$, and η	0.98	0.08	0.95	0.23	0.29	< 0.001[h]

[a]Mean Squared Error, kcal^2 mol^{-2}. [b]Leave-One-Out. [c]Cross Validation. [d]From an F-test where the null hypothesis is that $\Delta G°_{PT}$ has no effect. [e]From an F-test where the null hypothesis is that $\Delta G°_{CPET}$ has no effect. [f]From an F-test where the null hypothesis is that %BV Sterics has no effect. [g]From an F-test where the null hypothesis is that $\Delta G°_{ET}$ has no effect. [h]From an F-test where the null hypothesis is that η has no effect.

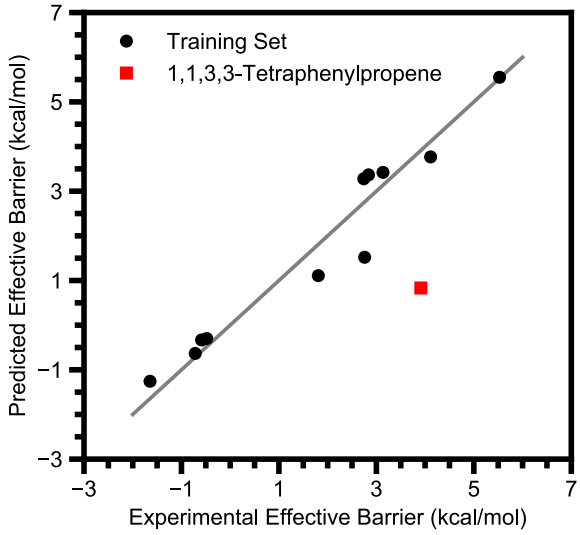

Regression A1.43 Cobalt(III)-oxo barriers against $\Delta G°_{PT}$.

```
['ΔG_PT'] Metrics:

Score on Training Data:                0.9424632998739368
MSE of Training Data:                  0.27729834873004827
Score of LOO Cross Validation:         0.9252474025325068
MSE of LOO Cross Validation:           0.36027043253438246
MSE of 5-Fold Cross Validation:        0.38974742022611514(0.011222596536024027)
F-Test p-value of final 1 variables:   6.966522436702149e-07

Correlation Matrix of x-values:
       ΔG_PT
ΔG_PT    1.0

['ΔG_PT'] Training Average:
[22.19752727]

 ['ΔG_PT'] Training Deviation:
[9.42668502]

 ['ΔG_PT'] Coefficients:
[0.22608638]

 ['ΔG_PT'] Standard Error:
 [0.01862059]

 ['ΔG_PT'] t-Test "Error":
 [0.0421227]

 ['ΔG_PT'] Weighted Coefficients:
[2.13124506]

 ['ΔG_PT'] Intercept:
 -3.246666603888153
```

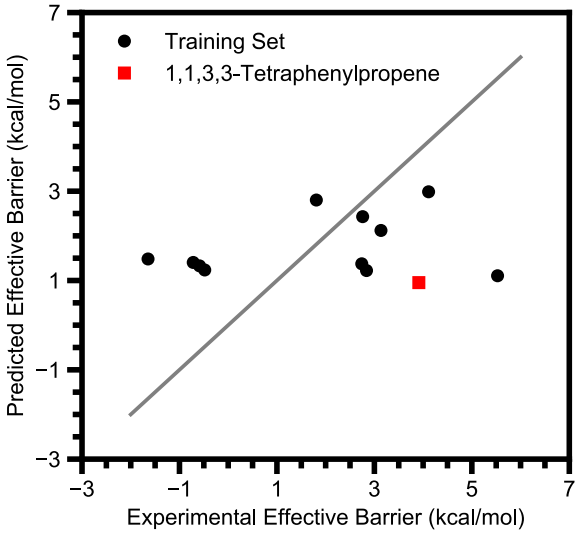

Regression A1.44 Cobalt(III)-oxo barriers against $\Delta G°_{CPET}$.

```
['ΔG_CPET'] Metrics:

Score on Training Data:                0.08862503668507471
MSE of Training Data:                  4.392375159635855
Score of LOO Cross Validation:         -0.31700265884710466
MSE of LOO Cross Validation:           6.34729940666087
MSE of 5-Fold Cross Validation:        6.37119453049353(0.09952217793998655)
F-Test p-value of final 1 variables:   0.3739434558155724

Correlation Matrix of x-values:
          ΔG_CPET
ΔG_CPET       1.0

['ΔG_CPET'] Training Average:
[-8.45470682]

 ['ΔG_CPET'] Training Deviation:
[3.26244406]

 ['ΔG_CPET'] Coefficients:
[0.20032553]

 ['ΔG_CPET'] Standard Error:
 [0.21413388]

 ['ΔG_CPET'] t-Test "Error":
 [0.48440449]

 ['ΔG_CPET'] Weighted Coefficients:
[0.65355084]

 ['ΔG_CPET'] Intercept:
 3.465585563988545
```

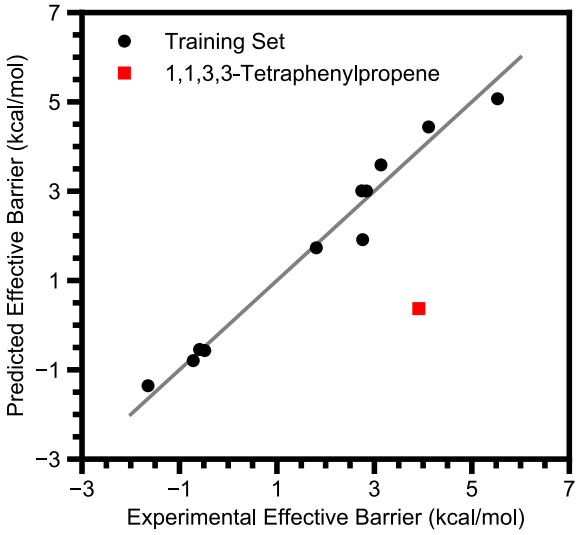

Regression A1.45 Cobalt(III)-oxo barriers against $\Delta G°_{PT}$ and $\Delta G°_{CPET}$.

```
['ΔG_PT', 'ΔG_CPET'] Metrics:

Score on Training Data:                0.9728720534806891
MSE of Training Data:                  0.13074324314324676
Score of LOO Cross Validation:         0.943560930601589
MSE of LOO Cross Validation:           0.2720083131940089
MSE of 5-Fold Cross Validation:        0.2929711051982866(0.01173660654476484)
F-Test p-value of final 1 variables:   0.01721332594582059

Correlation Matrix of x-values:
            ΔG_PT    ΔG_CPET
ΔG_PT    1.000000  0.128517
ΔG_CPET  0.128517  1.000000

['ΔG_PT', 'ΔG_CPET'] Training Average:
[22.19752727 -8.45470682]

 ['ΔG_PT', 'ΔG_CPET'] Training Deviation:
[9.42668502 3.26244406]

 ['ΔG_PT', 'ΔG_CPET'] Coefficients:
[0.22082357 0.11832428]

 ['ΔG_PT', 'ΔG_CPET'] Standard Error:
 [0.01367484 0.03951282]

 ['ΔG_PT', 'ΔG_CPET'] t-Test "Error":
 [0.03153423 0.09111673]

 ['ΔG_PT', 'ΔG_CPET'] Weighted Coefficients:
[2.08163428 0.38602634]

 ['ΔG_PT', 'ΔG_CPET'] Intercept:
 -2.129448313216325
```

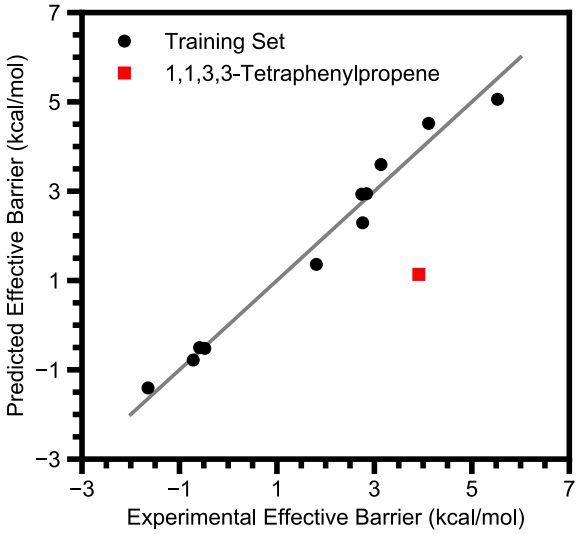

Regression A1.46 Cobalt(III)-oxo barriers against $\Delta G°_{PT}$, $\Delta G°_{CPET}$, and substrates' percent buried volume sterics.

```
['ΔG_PT', 'ΔG_CPET', '%BV'] Metrics:

Score on Training Data:                0.9785995318612503
MSE of Training Data:                  0.10313963894215689
Score of LOO Cross Validation:         0.8335055335504782
MSE of LOO Cross Validation:           0.8024207248241055
MSE of 5-Fold Cross Validation:        0.8002864721214152(0.03212409826687691)
F-Test p-value of final 1 variables:   0.21338614672251444

Correlation Matrix of x-values:
            ΔG_PT   ΔG_CPET       %BV
ΔG_PT    1.000000  0.128517 -0.777256
ΔG_CPET  0.128517  1.000000 -0.121393
%BV     -0.777256 -0.121393  1.000000

['ΔG_PT', 'ΔG_CPET', '%BV'] Training Average:
[22.19752727 -8.45470682 51.34545455]

 ['ΔG_PT', 'ΔG_CPET', '%BV'] Training Deviation:
[9.42668502 3.26244406 6.77567355]

 ['ΔG_PT', 'ΔG_CPET', '%BV'] Coefficients:
[0.24253036 0.120095   0.03899516]

 ['ΔG_PT', 'ΔG_CPET', '%BV'] Standard Error:
 [0.02049641 0.03754008 0.02848994]

 ['ΔG_PT', 'ΔG_CPET', '%BV'] t-Test "Error":
 [0.0484663  0.08876819 0.06736801]

 ['ΔG_PT', 'ΔG_CPET', '%BV'] Weighted Coefficients:
[2.2862573  0.39180322 0.26421845]

 ['ΔG_PT', 'ΔG_CPET', '%BV'] Intercept:
 -4.598538368410885
```

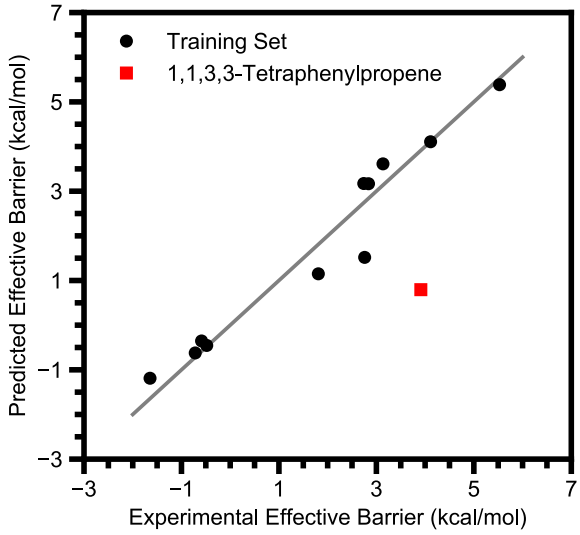

Regression A1.47 Cobalt(III)-oxo barriers against $\Delta G°_{PT}$ and $\Delta G°_{ET}$.

```
['ΔG_PT', 'ΔG_ET'] Metrics:

Score on Training Data:                 0.9473851700776209
MSE of Training Data:                   0.2535773762523971
Score of LOO Cross Validation:          0.9257014183495356
MSE of LOO Cross Validation:            0.35808230154870657
MSE of 5-Fold Cross Validation:         0.5218007751115226(0.09976949819374094)
F-Test p-value of final 1 variables:    0.4121834589527267

Correlation Matrix of x-values:
          ΔG_PT     ΔG_ET
ΔG_PT  1.000000 -0.106709
ΔG_ET -0.106709  1.000000

['ΔG_PT', 'ΔG_ET'] Training Average:
[22.19752727 89.03654545]

 ['ΔG_PT', 'ΔG_ET'] Training Deviation:
[9.42668502 4.97130331]

 ['ΔG_PT', 'ΔG_ET'] Coefficients:
[0.22783984 0.03115895]

 ['ΔG_PT', 'ΔG_ET'] Standard Error:
 [0.01899495 0.0360186 ]

 ['ΔG_PT', 'ΔG_ET'] t-Test "Error":
 [0.04380243 0.08305904]

 ['ΔG_PT', 'ΔG_ET'] Weighted Coefficients:
[2.14777439 0.15490058]

 ['ΔG_PT', 'ΔG_ET'] Intercept:
 -6.059874252255053
```

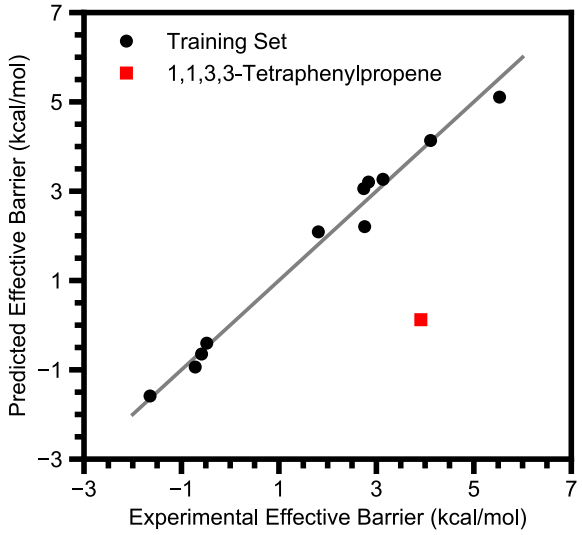

Regression A1.48 Cobalt(III)-oxo barriers against $\Delta G°_{PT}$, $\Delta G°_{CPET}$, and $\Delta G°_{ET}$.

```
['ΔG_PT', 'ΔG_CPET', 'ΔG_ET'] Metrics:

Score on Training Data:                 0.9834815349371753
MSE of Training Data:                   0.07961080624089117
Score of LOO Cross Validation:          0.9532389621068799
MSE of LOO Cross Validation:            0.2253650029330011
MSE of 5-Fold Cross Validation:         0.29298124182750607(0.036112502254110106)
F-Test p-value of final 1 variables:    0.0716825286335695

Correlation Matrix of x-values:
            ΔG_PT   ΔG_CPET     ΔG_ET
ΔG_PT    1.000000  0.128517 -0.106709
ΔG_CPET  0.128517  1.000000  0.750813
ΔG_ET   -0.106709  0.750813  1.000000

['ΔG_PT', 'ΔG_CPET', 'ΔG_ET'] Training Average:
[22.19752727 -8.45470682 89.03654545]

 ['ΔG_PT', 'ΔG_CPET', 'ΔG_ET'] Training Deviation:
[9.42668502 3.26244406 4.97130331]

 ['ΔG_PT', 'ΔG_CPET', 'ΔG_ET'] Coefficients:
[ 0.21293067  0.20413059 -0.07243803]

 ['ΔG_PT', 'ΔG_CPET', 'ΔG_ET'] Standard Error:
 [0.01199958 0.05219299 0.03416295]

 ['ΔG_PT', 'ΔG_CPET', 'ΔG_ET'] t-Test "Error":
 [0.02837449 0.12341681 0.08078254]

 ['ΔG_PT', 'ΔG_CPET', 'ΔG_ET'] Weighted Coefficients:
[ 2.00723035  0.66596465 -0.3601114 ]

 ['ΔG_PT', 'ΔG_CPET', 'ΔG_ET'] Intercept:
 5.2208535130795175
```

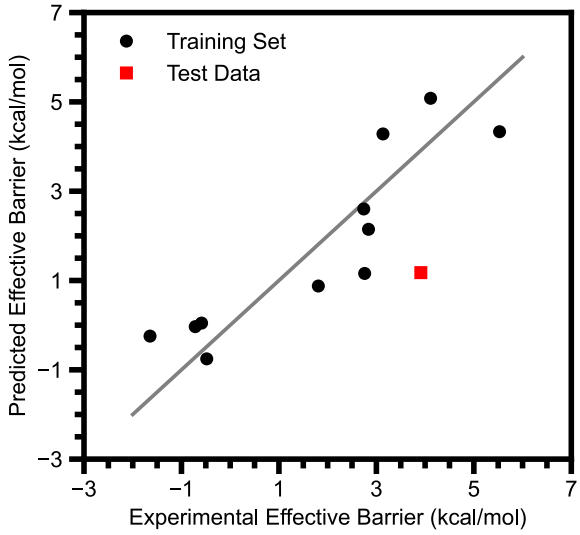

Regression A1.49 Cobalt(III)-oxo barriers against $\Delta G°_{CPET}$ and $\Delta G°_{CC}$.

```
['ΔG_CPET', 'ΔG_CC'] Metrics:

Score on Training Data:                 0.8016336292572781
MSE of Training Data:                   0.9560274908016876
Score of LOO Cross Validation:          0.5622569661430379
MSE of LOO Cross Validation:            2.1097042442590763
MSE of 5-Fold Cross Validation:         2.2696884676658153(0.09938569305545042)
F-Test p-value of final 1 variables:    0.0006757347967993876

Correlation Matrix of x-values:
          ΔG_CPET     ΔG_CC
ΔG_CPET  1.000000 -0.185743
ΔG_CC   -0.185743  1.000000

['ΔG_CPET', 'ΔG_CC'] Training Average:
[  -8.45470682 -119.68877955]

 ['ΔG_CPET', 'ΔG_CC'] Training Deviation:
[3.26244406 9.05313837]

 ['ΔG_CPET', 'ΔG_CC'] Coefficients:
[ 0.09291615 -0.20838832]

 ['ΔG_CPET', 'ΔG_CC'] Standard Error:
 [0.10783782 0.03886109]

 ['ΔG_CPET', 'ΔG_CC'] t-Test "Error":
 [0.24867446 0.08961384]

 ['ΔG_CPET', 'ΔG_CC'] Weighted Coefficients:
[ 0.30313375 -1.88656826]

 ['ΔG_CPET', 'ΔG_CC'] Intercept:
 -22.384272519087133
```

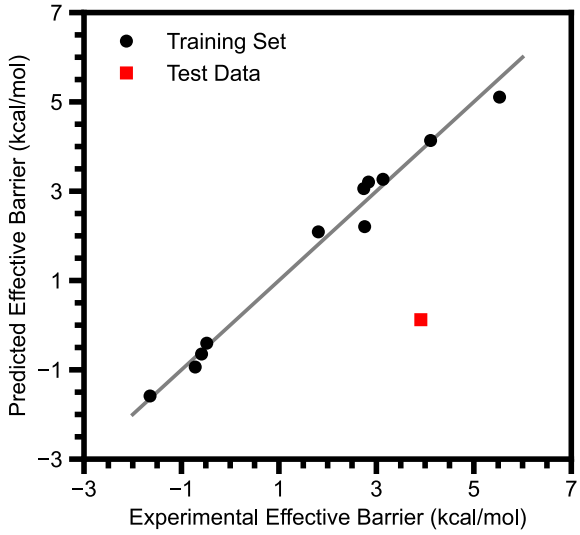

Regression A1.50 Cobalt(III)-oxo barriers against $\Delta G°_{CPET}$, $\Delta G°_{CC}$, and η

```
['ΔG_CPET', 'ΔG_CC', 'η'] Metrics:

Score on Training Data:                 0.9834815349382444
MSE of Training Data:                   0.07961080623573888
Score of LOO Cross Validation:          0.9532389621099332
MSE of LOO Cross Validation:            0.22536500291828565
MSE of 5-Fold Cross Validation:         0.2929812418306362(0.0361125022641722)
F-Test p-value of final 1 variables:    5.014967182892516e-05

Correlation Matrix of x-values:
          ΔG_CPET     ΔG_CC         η
ΔG_CPET  1.000000 -0.185743 -0.226782
ΔG_CC   -0.185743  1.000000 -0.719133
η       -0.226782 -0.719133  1.000000

['ΔG_CPET', 'ΔG_CC', 'η'] Training Average:
[  -8.45470682 -119.68877955  -47.25518585]

 ['ΔG_CPET', 'ΔG_CC', 'η'] Training Deviation:
[3.26244406 9.05313837 7.85940006]

 ['ΔG_CPET', 'ΔG_CC', 'η'] Coefficients:
[ 0.27437692 -0.07024632  0.20181662]

 ['ΔG_CPET', 'ΔG_CC', 'η'] Standard Error:
 [0.03916645 0.01978279 0.02298998]

 ['ΔG_CPET', 'ΔG_CC', 'η'] t-Test "Error":
 [0.09261394 0.04677886 0.05436266]

 ['ΔG_CPET', 'ΔG_CC', 'η'] Weighted Coefficients:
[ 0.89513934 -0.63594967  1.58615753]

 ['ΔG_CPET', 'ΔG_CC', 'η'] Intercept:
 5.220853513035006
```

10. Regressions of Metal Oxo Complexes with Multiple Substrates

Table A1.27 gives details on the regressions between multiple substrates' barriers for reactivity with several metal oxo species. Most of the parameters we analyze do not change between substrate to substrate (the exceptions being the free energies), so we were wary of giving too much weight to metal oxo complexes which had k_2 values reported for an unusually large number of substrates. For that reason we limited our analysis to the substrates which have the largest number of k_2 values reported with metal oxo complexes in our data set: 9,10-dihydroanthracene (DHA), 1,4-cyclohexadiene (CHD), xanthene (Xth), and fluorene (Fl). Due to the same concern with extra weight being given to specific metal oxo complexes we only report the overall R^2 and MSE of the fit along with a modified LOO R^2 and MSE. This modification is that we did not leave out one individual data point at a time to predict with all other data points; instead we left out all data for a given metal oxo complex and predicted them with the rest of the metal oxo complexes' data. Ultimately, the results from this analysis cohere with what is seen for that regressions to only DHA data: when compared to the fit to only $\Delta G°_{CPET}$, only $\Delta G°_{PT}$ and $\Delta G°_{ET}$ show a convincing effect.

Table A1.27 Summary of statistics on regressions with multiple substrates and multiple metal oxo complexes

Parameter(s) Regressed with $\Delta G°_{CPET}$	R^2	MSE[a]	LOO[b] R^2	LOO[b] MSE[a]
$\Delta G°_{CPET}$ only	0.45	1.79	0.36	2.10
%BV Sterics	0.48	1.71	0.28	2.37
Oxo Spin Density	0.53	1.55	0.37	2.08
Spin Excitation	0.50	1.66	0.39	2.01
$\lvert\eta\rvert$	0.50	1.63	0.30	2.30
$\Delta G°_{PT}$, $\Delta G°_{ET}$	0.64	1.18	0.50	1.64
$\Delta G°_{CC}$	0.49	1.68	0.33	2.24
$\Delta G°_{CC}$, η	0.64	1.20	0.46	1.79

[a]Mean Squared Error, $kcal^2\ mol^{-2}$. [b]Leave-One-Out.

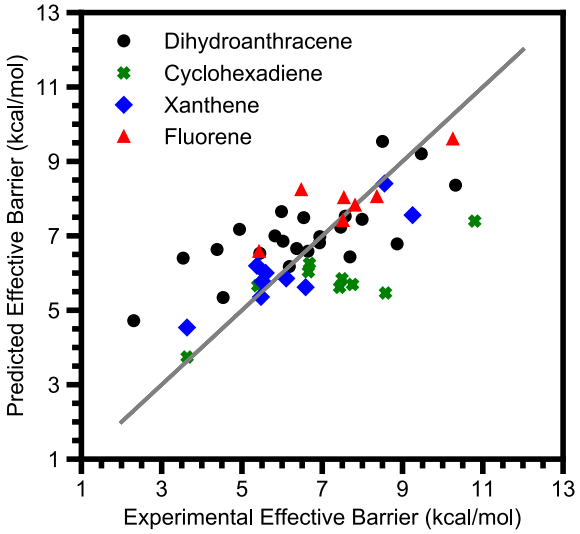

Regression A1.51 Multiple substrates' reaction barriers against $\Delta G°_{CPET}$.

```
['Sub ΔG_CPET'] Metrics:

Score on Training Data:                 0.45487429395449097
MSE of Training Data:                   1.7936813739581947
Score of LOO Cross Validation:          0.3623252595400116
MSE of LOO Cross Validation:            2.0982046744851544

Correlation Matrix of x-values:
              Sub ΔG_CPET
Sub ΔG_CPET           1.0

['Sub ΔG_CPET'] Training Average:
[-8.86079851]

 ['Sub ΔG_CPET'] Training Deviation:
[4.20784163]

 ['Sub ΔG_CPET'] Coefficients:
[0.29074391]

 ['Sub ΔG_CPET'] Standard Error:
 [0.04692825]

 ['Sub ΔG_CPET'] t-Test "Error":
 [0.09446167]

 ['Sub ΔG_CPET'] Weighted Coefficients:
[1.22340434]

 ['Sub ΔG_CPET'] Intercept:
 9.3326501024694
```

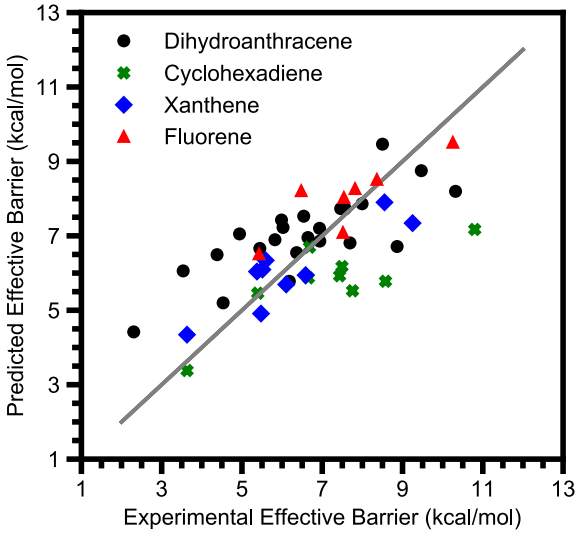

Regression A1.52 Multiple substrates' reaction barriers against $\Delta G°_{CPET}$ and percent buried volume sterics.

```
['Sub ΔG_CPET', '%BV Tot', '%BV Dev'] Metrics:

Score on Training Data:                 0.48027058057784117
MSE of Training Data:                   1.710117444063089
Score of LOO Cross Validation:          0.2785190099479361
MSE of LOO Cross Validation:            2.373960719829397

Correlation Matrix of x-values:
             Sub ΔG_CPET   %BV Tot   %BV Dev
Sub ΔG_CPET     1.000000 -0.155632  0.192876
%BV Tot        -0.155632  1.000000  0.155131
%BV Dev         0.192876  0.155131  1.000000

['Sub ΔG_CPET', '%BV Tot', '%BV Dev'] Training Average:
[-8.86079851 63.96875     4.65175846]

 ['Sub ΔG_CPET', '%BV Tot', '%BV Dev'] Training Deviation:
[ 4.20784163 10.24309028  4.35809801]

 ['Sub ΔG_CPET', '%BV Tot', '%BV Dev'] Coefficients:
[ 0.30887955  0.02627491 -0.04095496]

 ['Sub ΔG_CPET', '%BV Tot', '%BV Dev'] Standard Error:
 [0.04864807 0.01984959 0.04696706]

 ['Sub ΔG_CPET', '%BV Tot', '%BV Dev'] t-Test "Error":
 [0.09804374 0.04000422 0.09465589]

 ['Sub ΔG_CPET', '%BV Tot', '%BV Dev'] Weighted Coefficients:
[ 1.29971621  0.26913631 -0.17848572]

 ['Sub ΔG_CPET', '%BV Tot', '%BV Dev'] Intercept:
 8.003085518073675
```

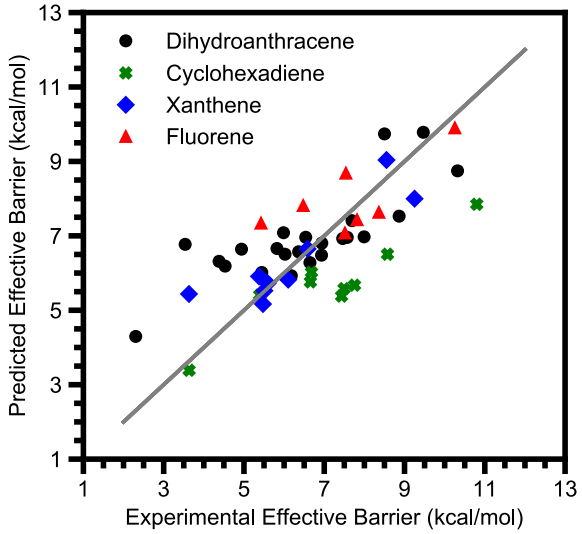

Regression A1.53 Multiple substrates' reaction barriers against $\Delta G°_{CPET}$ and IBO spin density on the oxo ligand.

```
['Sub ΔG_CPET', 'IBO Spin O'] Metrics:

Score on Training Data:                 0.5287385429894587
MSE of Training Data:                   1.5506384827018973
Score of LOO Cross Validation:          0.36879954216229527
MSE of LOO Cross Validation:            2.076901697904626

Correlation Matrix of x-values:
             Sub ΔG_CPET  IBO Spin O
Sub ΔG_CPET     1.000000   -0.170138
IBO Spin O     -0.170138    1.000000

['Sub ΔG_CPET', 'IBO Spin O'] Training Average:
[-8.86079851  0.48515917]

 ['Sub ΔG_CPET', 'IBO Spin O'] Training Deviation:
[4.20784163 0.32509068]

 ['Sub ΔG_CPET', 'IBO Spin O'] Coefficients:
[ 0.27051544 -1.53891806]

 ['Sub ΔG_CPET', 'IBO Spin O'] Standard Error:
 [0.04476805 0.57945946]

 ['Sub ΔG_CPET', 'IBO Spin O'] t-Test "Error":
 [0.09016748 1.16709126]

 ['Sub ΔG_CPET', 'IBO Spin O'] Weighted Coefficients:
[ 1.13828612 -0.50028792]

 ['Sub ΔG_CPET', 'IBO Spin O'] Intercept:
 9.900029869312357
```

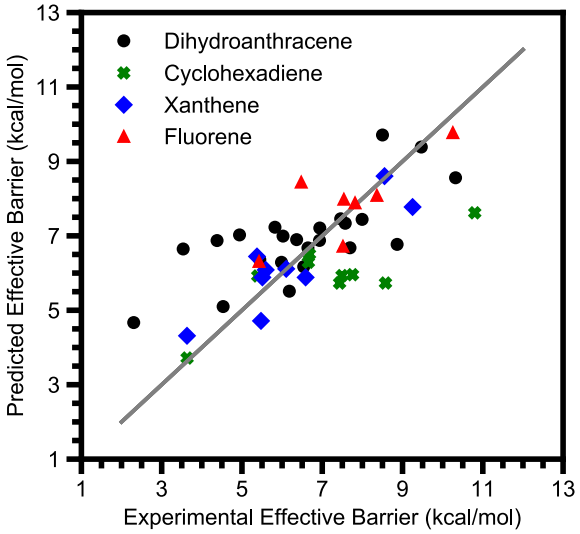

Regression A1.54 Multiple substrates' reaction barriers against $\Delta G°_{CPET}$ and the spin excitation energy.

```
['Sub ΔG_CPET', 'Spin Excitation'] Metrics:

Score on Training Data:                 0.49613389580124573
MSE of Training Data:                   1.6579207989041966
Score of LOO Cross Validation:          0.39044592960659175
MSE of LOO Cross Validation:            2.0056764345539455

Correlation Matrix of x-values:
                 Sub ΔG_CPET  Spin Excitation
Sub ΔG_CPET         1.000000        -0.077451
Spin Excitation    -0.077451         1.000000

['Sub ΔG_CPET', 'Spin Excitation'] Training Average:
[-8.86079851 11.34056619]

 ['Sub ΔG_CPET', 'Spin Excitation'] Training Deviation:
[ 4.20784163 17.66873331]

 ['Sub ΔG_CPET', 'Spin Excitation'] Coefficients:
[ 0.28394156 -0.02091645]

 ['Sub ΔG_CPET', 'Spin Excitation'] Standard Error:
 [0.04575333 0.01089624]

 ['Sub ΔG_CPET', 'Spin Excitation'] t-Test "Error":
 [0.09215195 0.02194616]

 ['Sub ΔG_CPET', 'Spin Excitation'] Weighted Coefficients:
[ 1.1947811  -0.36956713]

 ['Sub ΔG_CPET', 'Spin Excitation'] Intercept:
 9.509580161062551
```

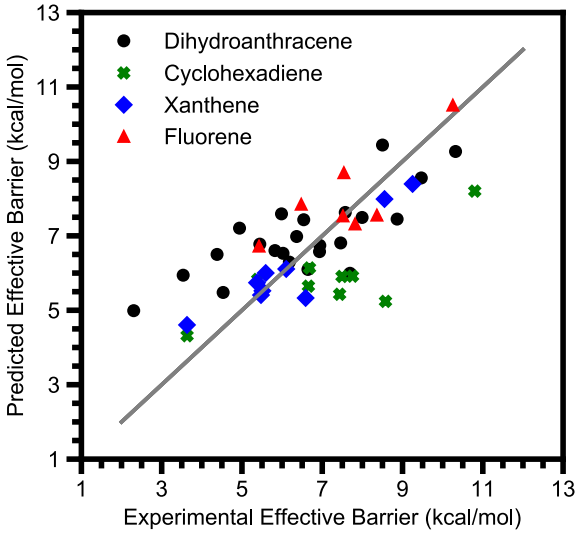

Regression A1.55 Multiple substrates' reaction barriers against $\Delta G°_{CPET}$ and the magnitude of the asynchronicity.

```
['Sub ΔG_CPET', 'Sub |η| (G)'] Metrics:

Score on Training Data:                 0.5041455584938033
MSE of Training Data:                   1.6315592276432798
Score of LOO Cross Validation:          0.2998360096801256
MSE of LOO Cross Validation:            2.3038192736560474

Correlation Matrix of x-values:
              Sub ΔG_CPET  Sub |η| (G)
Sub ΔG_CPET      1.000000     0.298842
Sub |η| (G)      0.298842     1.000000

['Sub ΔG_CPET', 'Sub |η| (G)'] Training Average:
[-8.86079851 17.97838265]

 ['Sub ΔG_CPET', 'Sub |η| (G)'] Training Deviation:
[ 4.20784163 14.68415922]

 ['Sub ΔG_CPET', 'Sub |η| (G)'] Coefficients:
[0.26077867 0.02873333]

 ['Sub ΔG_CPET', 'Sub |η| (G)'] Standard Error:
 [0.04741871 0.01358814]

 ['Sub ΔG_CPET', 'Sub |η| (G)'] t-Test "Error":
 [0.09550618 0.02736792]

 ['Sub ΔG_CPET', 'Sub |η| (G)'] Weighted Coefficients:
[1.09731536 0.42192485]

 ['Sub ΔG_CPET', 'Sub |η| (G)'] Intercept:
 8.550555292333174
```

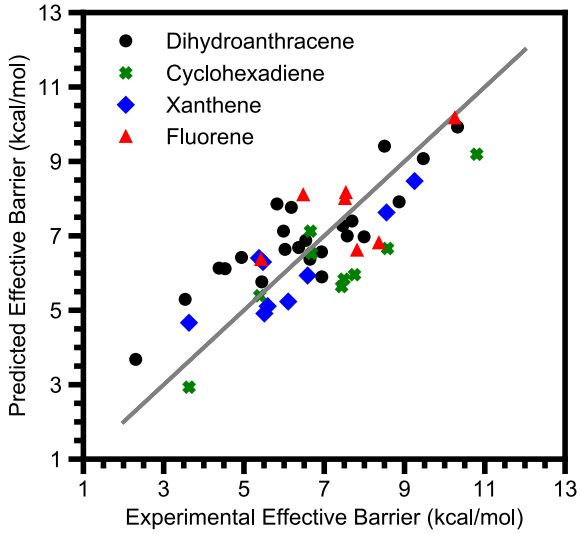

Regression A1.56 Multiple substrates' reaction barriers against $\Delta G°_{CPET}$, $\Delta G°_{PT}$, and $\Delta G°_{ET}$.

```
['Sub ΔG_CPET', 'Sub ΔG_PT', 'Sub ΔG_ET'] Metrics:

Score on Training Data:                 0.6424983850662855
MSE of Training Data:                   1.1763231503396485
Score of LOO Cross Validation:          0.5010163972835706
MSE of LOO Cross Validation:            1.6418554182588772

Correlation Matrix of x-values:
             Sub ΔG_CPET  Sub ΔG_PT  Sub ΔG_ET
Sub ΔG_CPET     1.000000  -0.308508   0.359117
Sub ΔG_PT      -0.308508   1.000000  -0.860287
Sub ΔG_ET       0.359117  -0.860287   1.000000

['Sub ΔG_CPET', 'Sub ΔG_PT', 'Sub ΔG_ET'] Training Average:
[-8.86079851 44.08376701 50.44489208]

 ['Sub ΔG_CPET', 'Sub ΔG_PT', 'Sub ΔG_ET'] Training Deviation:
[ 4.20784163 18.89575872 14.48110578]

 ['Sub ΔG_CPET', 'Sub ΔG_PT', 'Sub ΔG_ET'] Coefficients:
[0.2286421  0.04120077 0.09643366]

 ['Sub ΔG_CPET', 'Sub ΔG_PT', 'Sub ΔG_ET'] Standard Error:
 [0.04163513 0.01697321 0.02257307]

 ['Sub ΔG_CPET', 'Sub ΔG_PT', 'Sub ΔG_ET'] t-Test "Error":
 [0.08391008 0.03420727 0.04549303]

 ['Sub ΔG_CPET', 'Sub ΔG_PT', 'Sub ΔG_ET'] Weighted Coefficients:
[0.96208973 0.77851978 1.39646609]

 ['Sub ΔG_CPET', 'Sub ΔG_PT', 'Sub ΔG_ET'] Intercept:
 2.1015075758414623
```

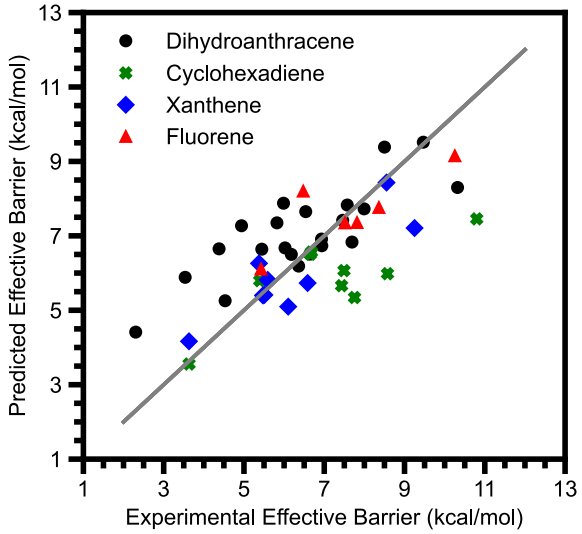

Regression A1.57 Multiple substrates' reaction barriers against $\Delta G°_{CPET}$ and $\Delta G°_{CC}$.

```
['Sub ΔG_CPET', 'Sub ΔG_CC'] Metrics:

Score on Training Data:                 0.4927894130286836
MSE of Training Data:                   1.683699914870677
Score of LOO Cross Validation:          0.32570237380024103
MSE of LOO Cross Validation:            2.2383500758714203

Correlation Matrix of x-values:
             Sub ΔG_CPET  Sub ΔG_CC
Sub ΔG_CPET     1.000000   0.422865
Sub ΔG_CC       0.422865   1.000000

['Sub ΔG_CPET', 'Sub ΔG_CC'] Training Average:
[  -8.95782599 -103.96306232]

 ['Sub ΔG_CPET', 'Sub ΔG_CC'] Training Deviation:
[ 4.24866355 10.62573614]

 ['Sub ΔG_CPET', 'Sub ΔG_CC'] Coefficients:
[ 0.3253448  -0.03068784]

 ['Sub ΔG_CPET', 'Sub ΔG_CC'] Standard Error:
 [0.0513955  0.02055031]

 ['Sub ΔG_CPET', 'Sub ΔG_CC'] t-Test "Error":
 [0.10364891 0.04144366]

 ['Sub ΔG_CPET', 'Sub ΔG_CC'] Weighted Coefficients:
[ 1.3822806  -0.32608085]

 ['Sub ΔG_CPET', 'Sub ΔG_CC'] Intercept:
 6.417557754825965
```

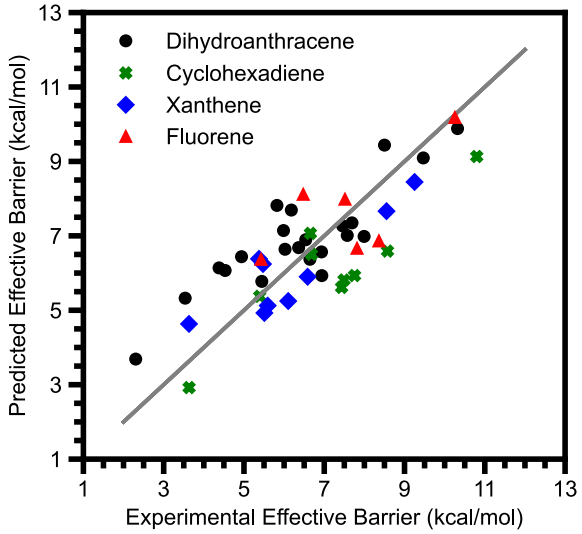

Regression A1.58 Multiple substrates' reaction barriers against $\Delta G°_{CPET}$, $\Delta G°_{CC}$, and η.

```
['Sub ΔG_CPET', 'Sub ΔG_CC', 'Sub η'] Metrics:

Score on Training Data:                 0.6390095777282225
MSE of Training Data:                   1.1983179351153677
Score of LOO Cross Validation:          0.46191603031320094
MSE of LOO Cross Validation:            1.7861849835681245

Correlation Matrix of x-values:
             Sub ΔG_CPET  Sub ΔG_CC     Sub η
Sub ΔG_CPET     1.000000   0.422865 -0.325886
Sub ΔG_CC       0.422865   1.000000 -0.514306
Sub η          -0.325886  -0.514306  1.000000

['Sub ΔG_CPET', 'Sub ΔG_CC', 'Sub η'] Training Average:
[  -8.95782599 -103.96306232   -2.7990005 ]

 ['Sub ΔG_CPET', 'Sub ΔG_CC', 'Sub η'] Training Deviation:
[ 4.24866355 10.62573614 21.7190691 ]

 ['Sub ΔG_CPET', 'Sub ΔG_CC', 'Sub η'] Coefficients:
[ 0.2998545  -0.06608632 -0.03777279]

 ['Sub ΔG_CPET', 'Sub ΔG_CC', 'Sub η'] Standard Error:
 [0.04430524 0.01952899 0.00915796]

 ['Sub ΔG_CPET', 'Sub ΔG_CC', 'Sub η'] t-Test "Error":
 [0.0894116 0.0394111 0.0184815]

 ['Sub ΔG_CPET', 'Sub ΔG_CC', 'Sub η'] Weighted Coefficients:
[ 1.27398089 -0.70221578 -0.82038974]

 ['Sub ΔG_CPET', 'Sub ΔG_CC', 'Sub η'] Intercept:
 2.4033595186725982
```

Appendix A2: Summary of Data and Supporting Analyses for Chapter 3

1. Analysis of the Yield of Competition Experiments

A yield of 17(3)% for five of the reactions at 263 K were determined by GC-MS, with 1.0 equivalents of *meta*-terphenyl as an internal standard include in the reactions (see Figure A2.1 and Table A1.1 and below). While this suggests caution must be taken in interpreting product isotope distributions, further considerations and experiments give us confidence in our conclusions based on the competition data.

By design our KIE determinations are resistant to being affected by side-reactions of fluorenyl radical. Because we measure the KIE with both (a) an intermolecular competition experiment between d_0-fluorene and d_2-fluorene and (b) an intramolecular competition C–H and C–D in d_1-fluorene, we can determine both the primary and secondary isotope effects separately. Promiscuous reactivity of fluorenyl radical may depend on the secondary isotope which is still present in the radical, but our results are based on the primary isotope effect which cannot have a direct influence on radical chemistry. In other words, in the intermolecular competition experiments, d_0-fluorenyl is produced by abstraction of an H-atom, so if there is selectively higher conversion of d_0-fluorenyl into bifluorenyl this will lead to an overestimation of k_H. However, in the intramolecular competition experiments d_0-fluorenyl is produced by abstraction of a D-atom, so the same overrepresentation of d_0-fluorenyl in the bifluorenyl product will instead result in an underestimation of k_H relative to k_D. The opposing effects on k_H manifests as a bias in the secondary isotope effect, not the primary isotope effect. For the primary isotope effect to be affected, the side

reactivity would require an interaction between the fluorene substrate and the fluorenyl radical, such as self-exchange or scrambling of between the two. However, the rate of self-exchange between C–H bonds and radicals is too low for this to affect our experiments, see blow.

Nonetheless, despite the robust experimental design, we sought to test the reliability of our KIEs by perturbing reaction conditions (Figure A2.2 and Table A2.2). Running the competition experiments at 296 K in THF, at a higher concentration, and in the presence 10 equivalents of TEMPO had no effect on the observed deutration of the bifluorenyl product. This is especially of note in the reactions run with TEMPO, because these reactions had higher yields as determined with an anthracene internal standard (we believe TEMPO is acting as a radical scavenger and thereby mitigating side reactivity). Overall then, it is clear that while side-reactivity of the radical is taking place, all available evidence and considerations suggest this is not affecting our KIE data nor our conclusions from this study.

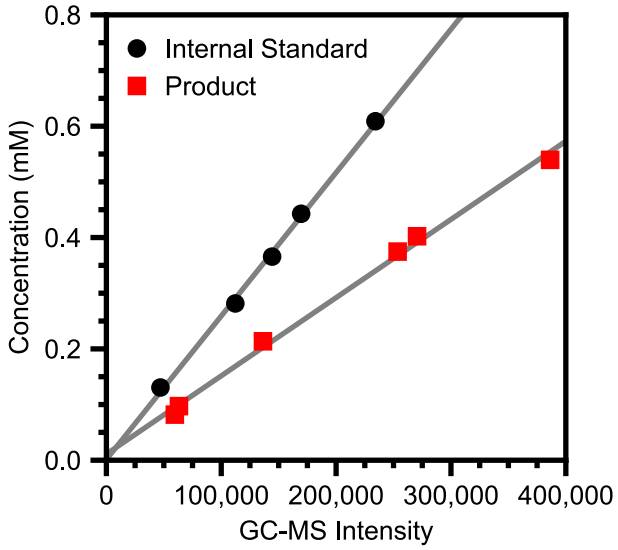

Figure A2.1 Calibration curves for GC-MS yields in DCM (toluene samples are dried and the GC-MS run with DCM, which is gentler on the instrument). The internal standard was meta-terphenyl, and the product bifluorenyl.

Table A2.1 Yields of reactions run at 263 K

Trial	Internal Standard	Product	
	Concentration (mM)	Concentration (mM)	Yield
1	0.556(6)	0.10(1)	17(2)%
2	0.441(5)	0.07(1)	16(2)%
3	0.452(5)	0.08(1)	18(2)%[b]

1 equivalent of *meta*-terphenyl was used as the internal standard. All errors propagated from the linear fits to calibration data.

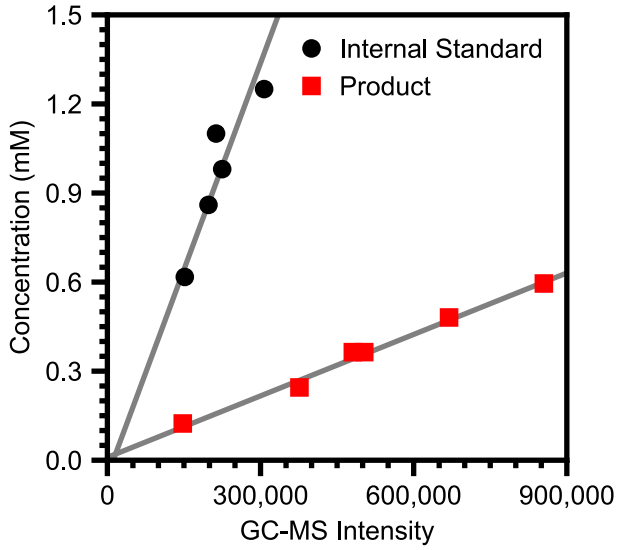

Figure A2.2 Calibration curves for GC-MS yields in THF. The internal standard was anthracene, and the product bifluorenyl. GC-maintenance and a change of solvent required new calibration curves. Due to perceived greater error in the intensity than in concentration, linear regression was done as intensity as a function of concentration to avoid attenuation bias in the calibration slope.

Table A2.2 Effect of Reaction Conditions on Yield and Product Deuteration

Change in Experimental Conditions	Yield[a]	p_D[b]	p-value[c]
1.25 mM in Toluene 20 equivalents d_1-fluorene[d]	N.D.[e]	72.7(6)%	N.D.[e]
1.25 mM in THF 20 equivalents d_1-fluorene	9.4%	73.5(1)%	0.29
2.27 mM in THF 100 equivalents d_1-fluorene	10.6%	73.80(6)%	0.29
25.0 mM in THF 40 equivalents d_1-fluorene	9.4%	73.5(4)%	0.29
1.25 mM in THF 20 equivalents d_1-fluorene 10 eq TEMPO additive	29%	73.47(7)%	0.29

Standard conditions are as described above, at 296 K. All reactions run as intramolecular competition with d_1-fluorene. 1 equivalent of anthracene was used as the internal standard. [a]Yield of bifluorenyl product. Propagated errors in the calibration curve are +/− 3–6%, but triplicate errors are +/- 2% or less. [b]Deuteration of bifluorenyl product. Errors are standard errors of the mean by a triplicate measurement. [c]Result from a two-tailed independent *t*-test of two populations assuming equal variances, with the null hypothesis that there is no change from standard conditions. [d]Standard conditions. [e]Not Determined.

2. Comparison of Competition and Kinetic KIE Data for Fluorene

Temperature dependent kinetic data for d_0-fluorene (k_H) and d_2-fluorene ($k_{D,obs}$) is shown in Figure A2.3. To check the consistency of this data with competition data, predicted $k_{D,obs}$ values were determined from k_H data and competition KIEs as measured by GC-MS with the formula:

Equation A2.1 $$k_{D,obs} = p_0 k_H + \frac{1}{2} p_1 \frac{k_H}{KIE^{1^\circ}} + \frac{1}{2} p_1 \frac{k_H}{KIE^{2^\circ}} + p_2 \frac{k_H}{KIE^{1^\circ} KIE^{2^\circ}}$$

with KIE^{1° the primary isotope effect and KIE^{2° the secondary isotope effect and $p_1 = 0.0284$, $p_2 = 0.0472$, and $p_3 = 0.9244$ being the proportions of d_n-fluorene as determined by GC-MS.

These data are also shown in Figure A2.3. A summary of the data is given in Table A2.3. While the experimental and predicted k_D values are close, the differences have a notable effect on the KIE trends. The kinetic data suggest a substantially more temperature sensitive KIE ($E_a(D) - E_a(H) = 0.9(2)$) which results in a negative estimate of $\ln(A_H/A_D) = -0.1(4)$. This raises the question of which data set, competition or kinetic, is correct. We strongly believe that the competition data is less prone to systemic error and more trustworthy because (a) the plot of ln(KIE) vs. $1/RT$ from kinetic data has unusual curvature and (b) competition experiments are less sensitive to background reactivity not accounted for in our modelling.

Figure A2.4 shows the KIE values obtained from both competition experiments and kinetic experiments along with linear fits to the data. There is apparent curvature in the KIEs from kinetic experiments but not the KIEs from competition experiments. An *F*-test indicates that including a quadratic term in the fit of ln(KIE) vs. $1/RT$ significantly improves the fit to KIEs from kinetic experiments, giving a *p*-value of 0.0097 (with the null hypothesis of no change in the error when a quadratic term is added to the regression and the alternative hypothesis that addition of a

quadratic term decreases the error). The same *F*-test with KIEs from competition experiments gives a *p*-value of 0.63. The positive curvature in ln(KIE) from kinetic data could be explained within semiclassical theory as the onset of tunneling across the temperature ranges studied. This onset would be expected to be caused by a reduction in the temperature sensitivity of k_H at lower temperature, i.e. positive curvature in ln(k_H) vs. 1/*RT*; less or no curvature would be expected in ln(k_D) vs. 1/*RT*.[138,328] However, this is not observed in our data; the same *F*-test for curvatures gives $p = 0.30$ for ln(k_H) and $p = 0.060$ for ln($k_{D,corr}$). The curvature is only significant at the $\alpha = 0.05$ level once k_H and k_D are compared, and if the curvature can be attributed to either of the data sets alone it would mostly likely be k_D, not k_H. This suggests the source of the curvature in KIEs from kinetic data is not the onset of tunneling within a semiclassical framework. We believe instead that the curvature is due to artifacts in the kinetic data, which leads us to conclude that the KIEs from competition experiments are more reliable.

A potential source for these artifacts is background reactivity which affect the UV-vis traces but the product ratios of the bifluorenyl product. That there is background reactivity in the kinetic reactions is demonstrated in Figure A2.5, a kinetic run of d_0-fluorene at 323 K run past completion. After the reaction is clearly completed, there is slight bleaching of the signal, as could be expected of a sensitive transition metal complex. However, this slight bleaching causes a monoexponential fit to underestimate the rate of reaction because the reaction appears to continue for longer than it really does (see the variation in the calculated k_{obs} value depending on which time point is used as the endpoint, Figure A2.5). Unless there is a coincidence, one would expect this bleaching to affect the rate differently at different temperatures and result in a slight bias to the measured activation energy and a larger bias to the extrapolated intercept. Further evidence for background reactivity

is in our moderate product yields (17(3)%, see Table A2.1) which indicate fluorenyl radicals are engaging in side reactivity other than dimerization. It is plausible this side reactivity affects the absorbance at 470 nm; this would bias the measured k_{obs}. The competition experiments, however, directly measure the relative amount of d_0-fluorenyl and d_1-fluorenyl as recorded in the bifluorenyl product. This selectively analyzes the relative formation of different isotopomers of fluorenyl. If side reactivity results in an isotope dependence on conversion of fluorenyl to bifluorenyl, this would affect the measured secondary kinetic isotope effect, not the primary isotope effect. By performing both intramolecular and intermolecular competition experiments we were able to distinguish between primary and secondary effects.

Ultimately, the deviations between the two sets of data points is slight. Differences between the predicted and experimental values of $k_{D,obs}$ is primarily found at lower temperatures. This difference is greater than the precision of the measurement, but plausibly less than the accuracy of a kinetic measurement that is nonspecific to the cobalt complexes being analyzed. The slight curvature in kinetically derived KIEs further suggests that the low-temperature kinetics are suspicious and cannot be trusted with the accuracy needed to confidently extrapolate to $1/RT = 0$. Therefore, we believe the competition experiments give an accurate estimate of $\ln(A_H/A_D)$, as presented in the main text.

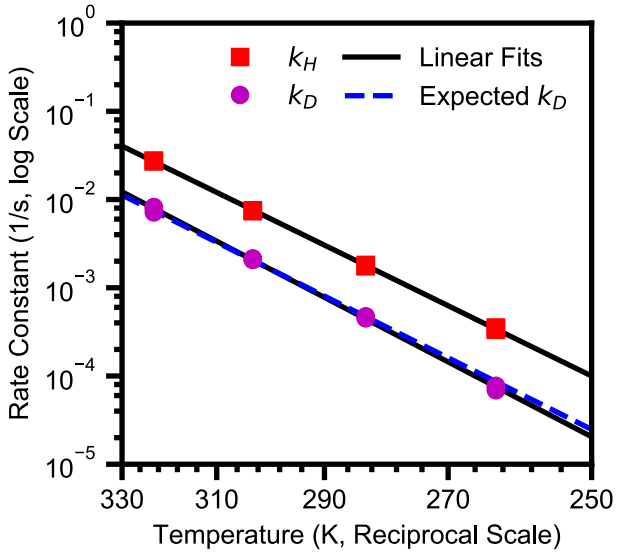

Figure A2.3 Plot of experimental k_H and $k_{D,obs}$ vs. $1/RT$ for the reaction of **CoO** with fluorene, with the corresponding linear fits shown in black. The predicted values of $k_{D,obs}$ determined from competition KIEs are shown in the blue dashed line (Table A2.3).

Table A2.3 Comparison of $k_{D,obs}$ measured by kinetics and expected from competition KIEs.

Temperature (K)	Expected $k_{D,obs}$ (s^{-1})	Experimental $k_{D,obs}$ (s^{-1})
323	$7.4 \cdot 10^{-3}$	$7.7(3) \cdot 10^{-3}$
303	$2.1 \cdot 10^{-3}$	$2.10(3) \cdot 10^{-3}$
283	$4.7 \cdot 10^{-4}$	$4.60(7) \cdot 10^{-4}$
263	$8.6 \cdot 10^{-5}$	$7.3(2) \cdot 10^{-5}$

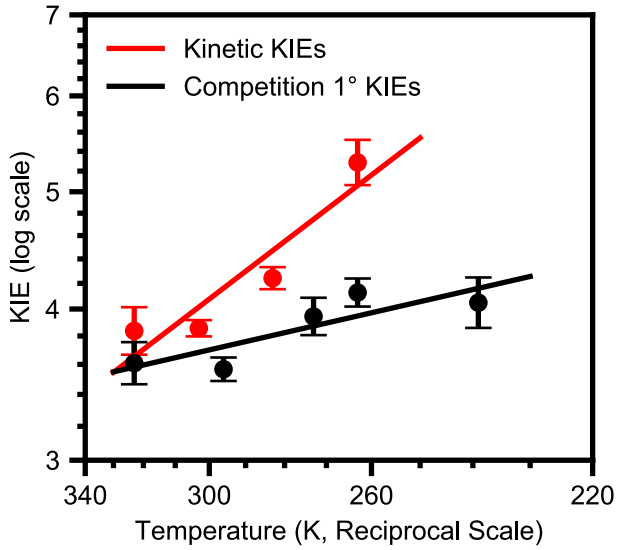

Figure A2.4 Plot of ln(KIE) vs. 1/*RT* for both KIEs from kinetic data and KIEs from competition data.

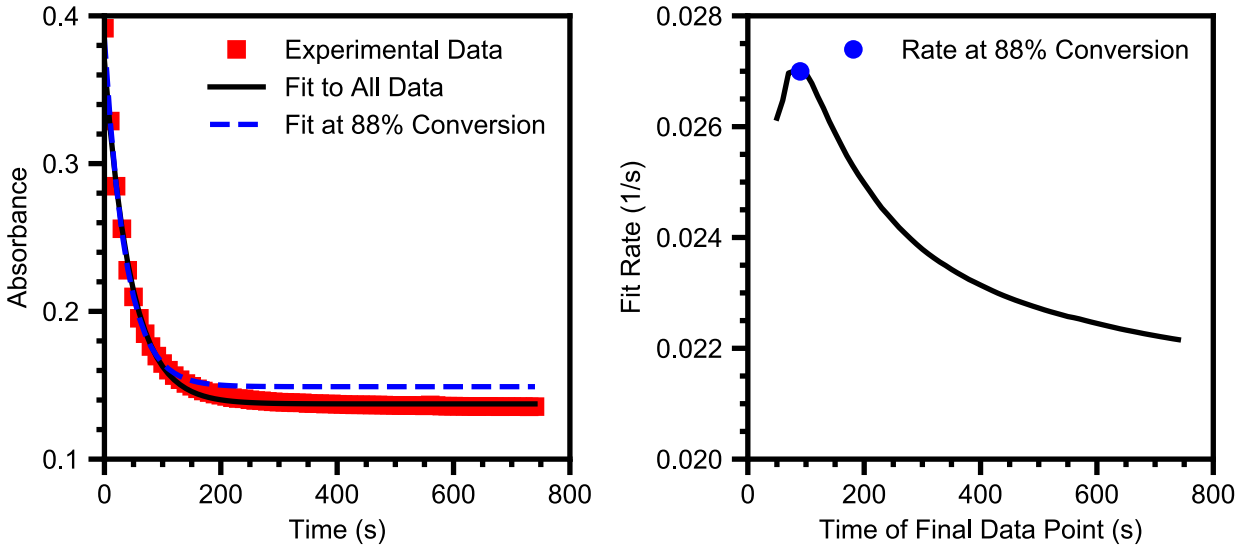

Figure A2.5 Absorbance at 470 nm for a reaction run past completion (left) and the dependency of k_{obs} on the reaction time (right).

3. Simulations of Scrambling in Competition Experiments

Our reliance on KIEs from competition data requires that any side reactivity of fluorenyl radical affects only the secondary KIE. However, it is possible for the primary KIE to be affected if self-exchange of H/D-atoms between fluorenyl and fluorene ("scrambling") is competitive with dimerization. For the intermolecular competition experiments with 1:1 d_0-fluorene:d_2-fluorene it would be expected that scrambling with d_0-fluorene is quicker than scrambling with d_2-fluorene, converting d_1-fluorenyl into d_0-fluorenyl. As d_0-fluorenyl is the product from C–H activation, this would result in a larger KIE (Scheme A2.1). For the intramolecular competition experiments with d_1-fluorenyl, the faster exchange of H-atoms than D-atoms would instead convert d_0-fluorene into d_1-fluorene, again converting C–D oxidation into apparent C–H oxidation with a higher corresponding KIE. However, the reported rate constants for self-exchange of organic radicals are orders of magnitude slower than the reported rate constants for dimerization.[104,236] Nonetheless, it is nontrivial to compare the rate constants of a reaction second order in radical (dimerization) with a rate constant first order in radical (scrambling), so we performed numerical simulations to confirm that this orders of magnitude difference is sufficient.

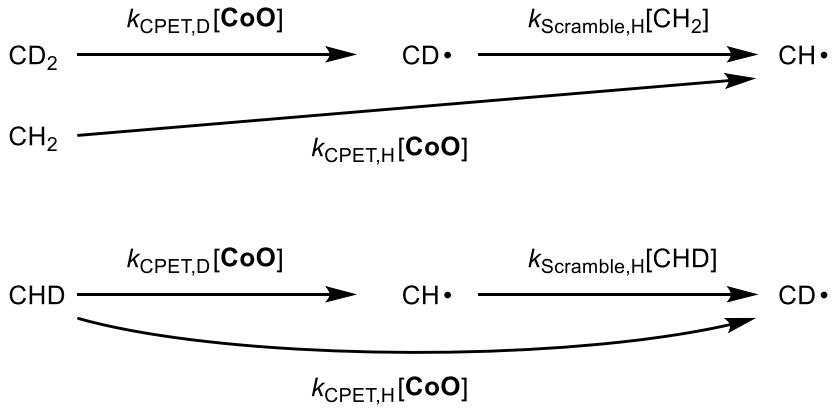

Scheme A2.1 How self-exchange could convert C–D oxidation into apparent C–H oxidation.

Kinetic modelling was done via numerical integration using python. For each reaction in Scheme A2.2, an instantaneous rate was determined for a given concentrations of each reagent. The contribution of all reactions on the individual reagents and products was summed to give an instantaneous rate of change in each species' concentration, which allows an estimate of the concentrations at a slightly later time. Concentrations were integrated from initial concentrations of 0.00125 M **CoO** and 0.0125 M each of CH_2 and CD_2 (as in our intermolecular competition experiments; all other initial concentrations 0) using the LSODA method implemented in scipy.[176,179] The values of k_{CPET} and KIE_{CPET} were set at 2.3 and 4, respectively, as determined by experiment. The value of $KIE_{scramble}$ was set to 100 to represent an extreme case.

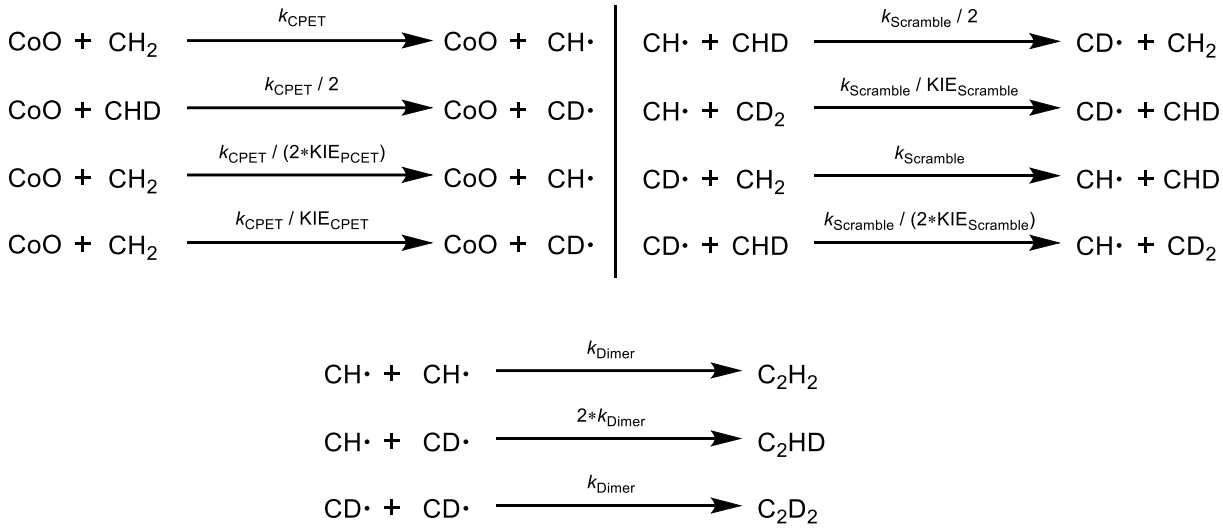

Scheme A2.2 Reactions and corresponding rate constants simulated to analyze the effect of scrambling.

Figure A2.6 shows the results of these simulations for both the expected low value of $k_{Scramble} = 10^{-10}$ $M^{-1}s^{-1}$ and the unrealistically large value of $k_{scramble} = 10^{-1}$ $M^{-1}s^{-1}$ (the self-exchange rate of toluene, ~10^{-4} $M^{-1}s^{-1}$, is a more realistic upper bound but is visually indistinguishable from the lower expected value).[104] Literature suggests that k_{Dimer} is expected to

be ~10^{10} $M^{-1}s^{-1}$, but we examined values as low as 1 $M^{-1}s^{-1}$.[236] Even with the unrealistically large rate of self-exchange, an unrealistically low rate of dimerization is necessary to have a noticeable impact in the measured KIE. Therefore, the ~20 orders of magnitude separating the dimerization rate constants and self-exchange rate constants are plenty to ensure our competition experiments are unaffected by scrambling.

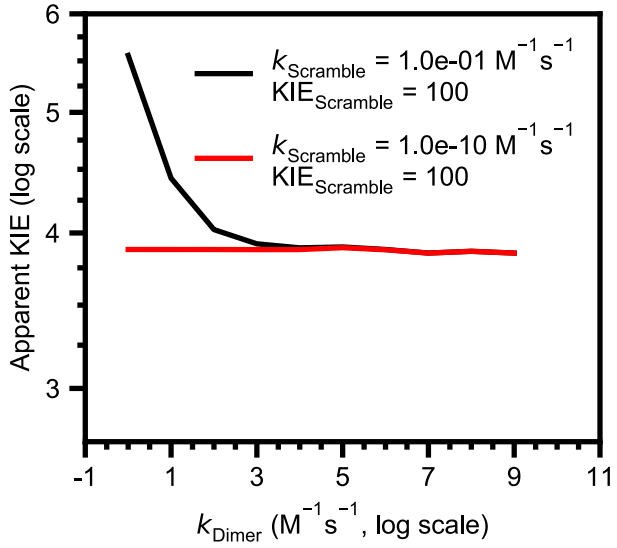

Figure A2.6 The apparent KIEs simulated for an actual KIE of 4 affected by the self-exchange of fluorenyl radical with fluorene.

4. Simulations of KIEs Within a Semiclassical Context

To demonstrate how the positive $\ln(A_H/A_D)$ is unexplainable within a semiclassical context, we fit the observed $E_a(D) - E_a(H)$ and $\ln(A_H/A_D)$ values to semiclassical Eckart barriers with a tunneling correction and show that the barriers needed to obtain a positive $\ln(A_H/A_D)$ are chemically implausible. Within a semiclassical framework the KIE can be modelled as:

Equation A2.2 $$KIE = \frac{Q_H(T)k_{H,S}}{Q_D(T)k_{D,s}} = \frac{Q_H(T)}{Q_D(T)}\left(\frac{A_H}{A_D}\right)_S e^{\frac{(E_a(D)-E_a(H))_S}{RT}}$$

with the subscript S indicating semiclassical values (no tunneling) for the rates k_H and k_D, the Arrhenius prefactor ratio A_H/A_D, and the difference in activation energies $E_a(E) - E_a(H)$. Q_H and Q_D are the tunneling corrections for the reactivity of H and D, respectively. These tunnelling corrections in turn are calculated from transmission coefficients of H and D integrated over various energies with each energy weighted according to temperature. See Bell for a more complete description of this framework for estimating semiclassical KIEs and their tunneling corrections, and Johnson and Heicklen for formula involving Eckart barriers in particular.[138,329] This then gives the temperature dependence in ln(KIE) as having a semiclassical slope and intercept modified by $\ln(Q_H(T)/Q_D(T))$:

Equation A2.3 $$\ln(KIE) = \ln\left(\frac{Q_H(T)}{Q_D(T)}\right) + \ln\left(\frac{A_H}{A_D}\right)_S + \frac{1}{RT}\left(E_a(D) - E_a(H)\right)_S$$

As the values of $\ln(Q_H(T)/Q_D(T))$ depend on the height and curvature of the barrier, the experimentally observed ln(KIE) can be used to determine a curvature and height, so long as assumptions can be made regarding the semiclassical values $\ln(A_H/A_D)_S$ and $(E_a(D) - E_a(H))_S$ and the barrier shape. Note that this "barrier height" does not need to equal the activation energy (or a hypothetical "no tunneling" activation energy), because some nuclear motions required for the reaction are not as susceptible to tunneling (e.g. rehybridization changes in bond lengths for the donor and acceptor). We use Eckart barriers, which is a typical choice in other studies.[103,187,208] Figure A2.7 shows the results of such simulations for fluorene competition KIEs, using Eckart barriers with a ΔE_{Rxn} of −3 kcal/mol and the mass of the proton/deuteron as the tunneling masses. Figure A2.8 show the same fit for DHA KIEs (ΔE_{Rxn} = −7 kcal/mol).

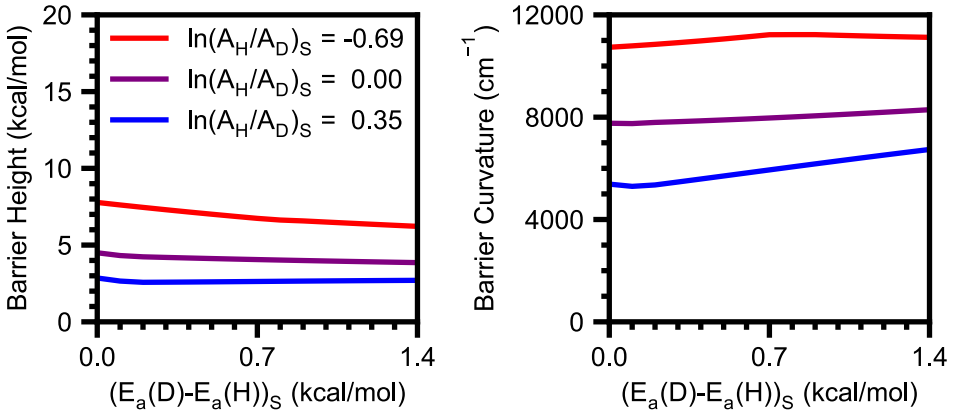

Figure A2.7 Simulated barrier heights (left) and curvature (right) for tunneling through an Eckart Barrier with ΔE_{rxn} = −3 kcal/mol resulting in the KIEs observed from fluorene competition experiments.

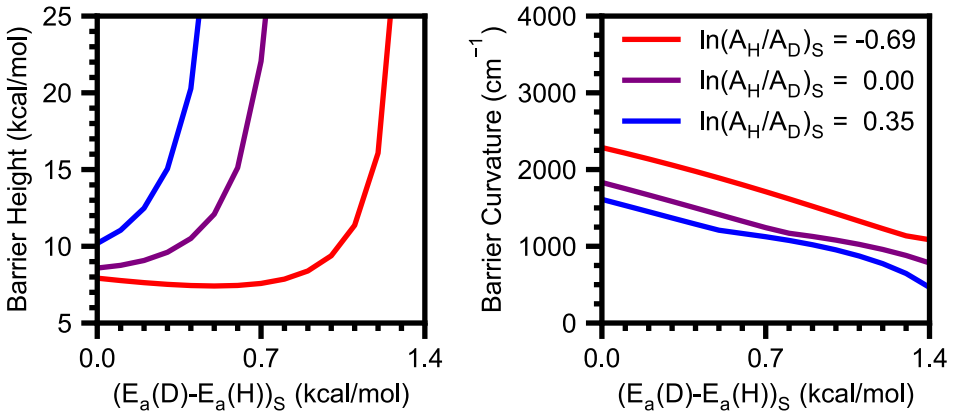

Figure A2.8 Simulated barrier heights (left) and curvature (right) for tunneling through an Eckart Barrier with ΔE_{rxn} = −7 kcal/mol resulting in the KIEs observed from DHA kinetic experiments. The y-axis is cut off at 25 kcal/mol to more clearly showcase the reasonable fits for certain values of $\ln(A_H/A_D)_S$.

These results are similar to those of Stern and Weston.[330] Essentially, to obtain an $\ln(A_H/A_D)$ as large as what is observed for fluorene, the transition state mode would need to have unreasonably sharp curvature, i.e. the barrier would need to be unreasonably thin. Transition states for metal-oxo mediated C–H activation typically lie within ~1,000-2,000 cm^{-1}, although slightly larger values are not unreasonable.[103,187,208] However, for the oxidation of fluorene by **CoO** the $\ln(A_H/A_D)$ observed from competition experiments would require transition state curvature

substantially sharper than the curvature of stable covalent hydrogen bond (around 3,000 cm^{-1} for a C–H bond and somewhat larger for O–H bonds) which is chemically implausible. The highly temperature-dependent KIEs observed for DHA, however, are consistent with reasonable barrier curvature. Certain assumptions for semiclassical temperature dependence give implausibly high barriers, but other values have perfectly reasonable results.

While we chose ΔE_{Rxn} to closely match ΔG°_{CPET}, there is no reason this has to be the case for the same reason that the barrier height does not need to match the activation energy (also spin state dynamics could change the apparent ΔG°_{CPET}), Figure A2.9 shows a fit to fluorene competition KIE with $\Delta E_{Rxn} = -7$ kcal/mol with qualitatively the same results.

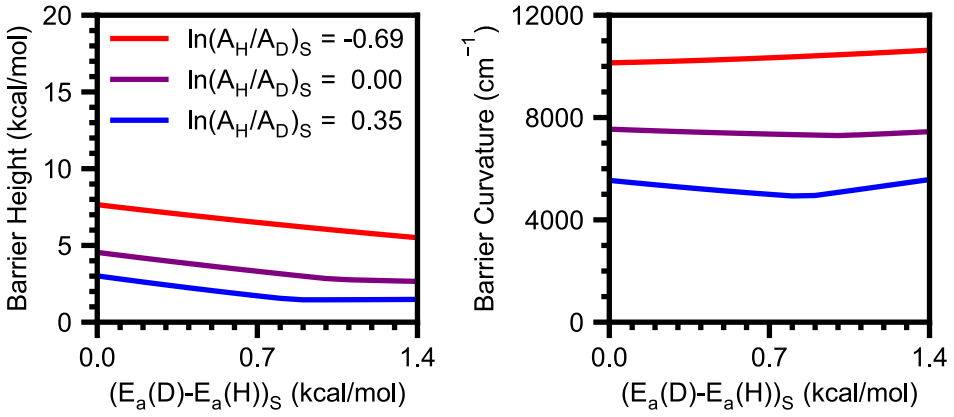

Figure A2.9 Simulated barrier heights (left) and curvature (right) for tunneling through an Eckart Barrier with $\Delta E_{rxn} = -7$ kcal/mol resulting in the KIEs observed from fluorene competition experiments.

5. Covariance Matrices of Arrhenius Parameters

Table A2.4, Table A2.5, and Table A2.6 give the covariance matrices of the fits to $E_a(D) - E_a(H)$ and $\ln(A_H/A_D)$. The diagonal entries are the variances of the fit, the off-diagonal entries are the covariances between different parameters.

Table A2.4 Variances and covariances for Arrhenius parameters of reactivity with fluorene fit to competition data.

	1° $E_a(D) - E_a(H)$ (kcal/mol)	1° $\ln(A_H/A_D)$	2° $E_a(D) - E_a(H)$ (kcal/mol)	2° $\ln(A_H/A_D)$
1° $E_a(D) - E_a(H)$ (kcal/mol)	0.0068026	-0.012325	0.0010725	-0.001938
1° $\ln(A_H/A_D)$	-0.012325	0.0225645	-0.001938	0.0035396
2° $E_a(D) - E_a(H)$ (kcal/mol)	0.0010725	-0.001938	0.0041682	-0.007565
2° $\ln(A_H/A_D)$	-0.001938	0.0035396	-0.007565	0.0138743

Table A2.5 Variances and covariances for Arrhenius parameters of reactivity with fluorene fit to kinetic data.

	$E_a(D) - E_a(H)$ (kcal/mol)	$\ln(A_H/A_D)$
$E_a(D) - E_a(H)$ (kcal/mol)	0.006174	−0.1066
$\ln(A_H/A_D)$	−0.1066	0.1852

Table A2.6 Variances and covariances for Arrhenius parameters of reactivity with DHA fit to kinetic data.

	$E_a(D) - E_a(H)$ (kcal/mol)	$\ln(A_H/A_D)$
$E_a(D) - E_a(H)$ (kcal/mol)	0.05836	−0.1008
$\ln(A_H/A_D)$	−0.1008	0.1751

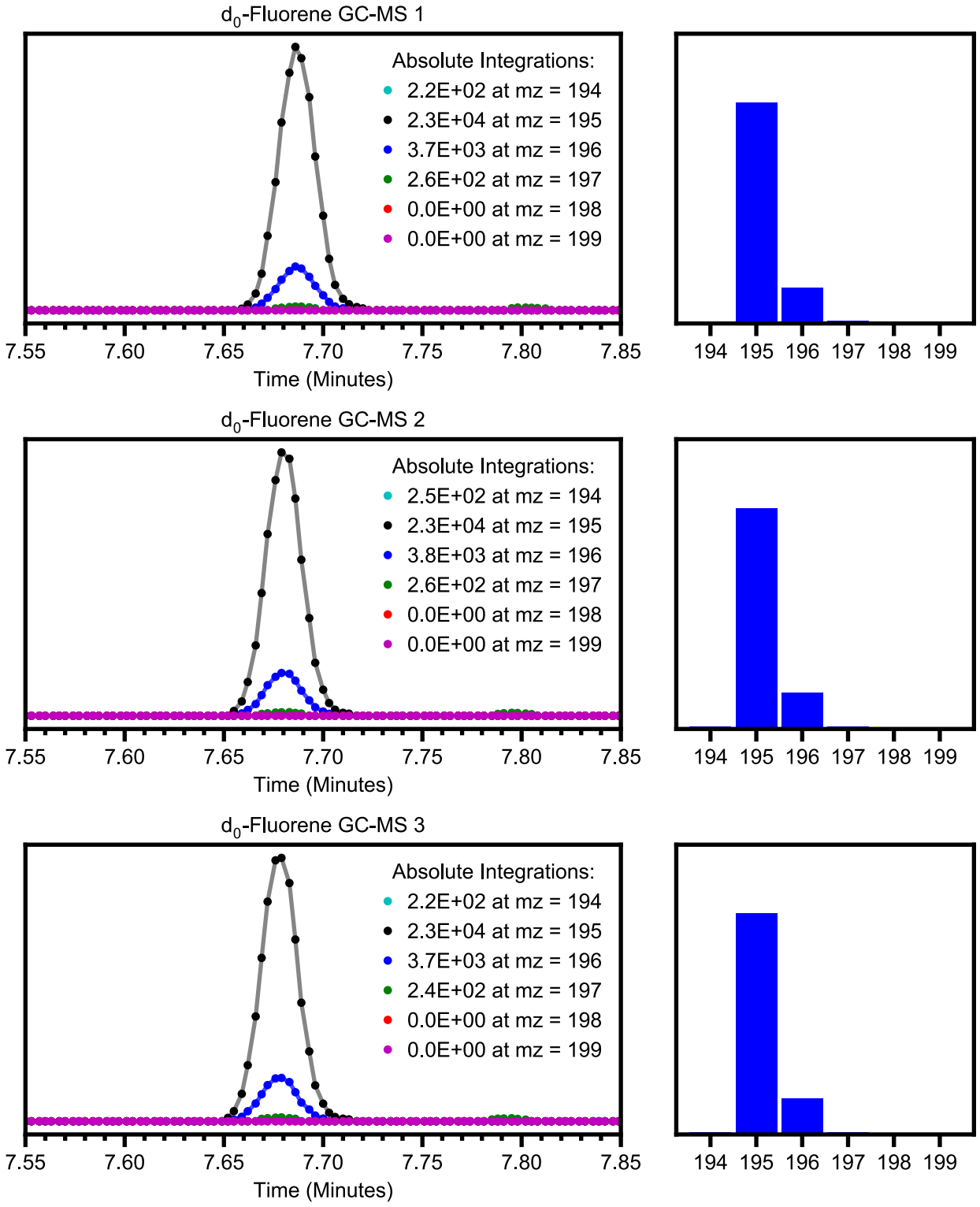

Figure A2.10 Reference GC-MS data for d_0-fluorene used for determining isotope composition of deuterated fluorene.

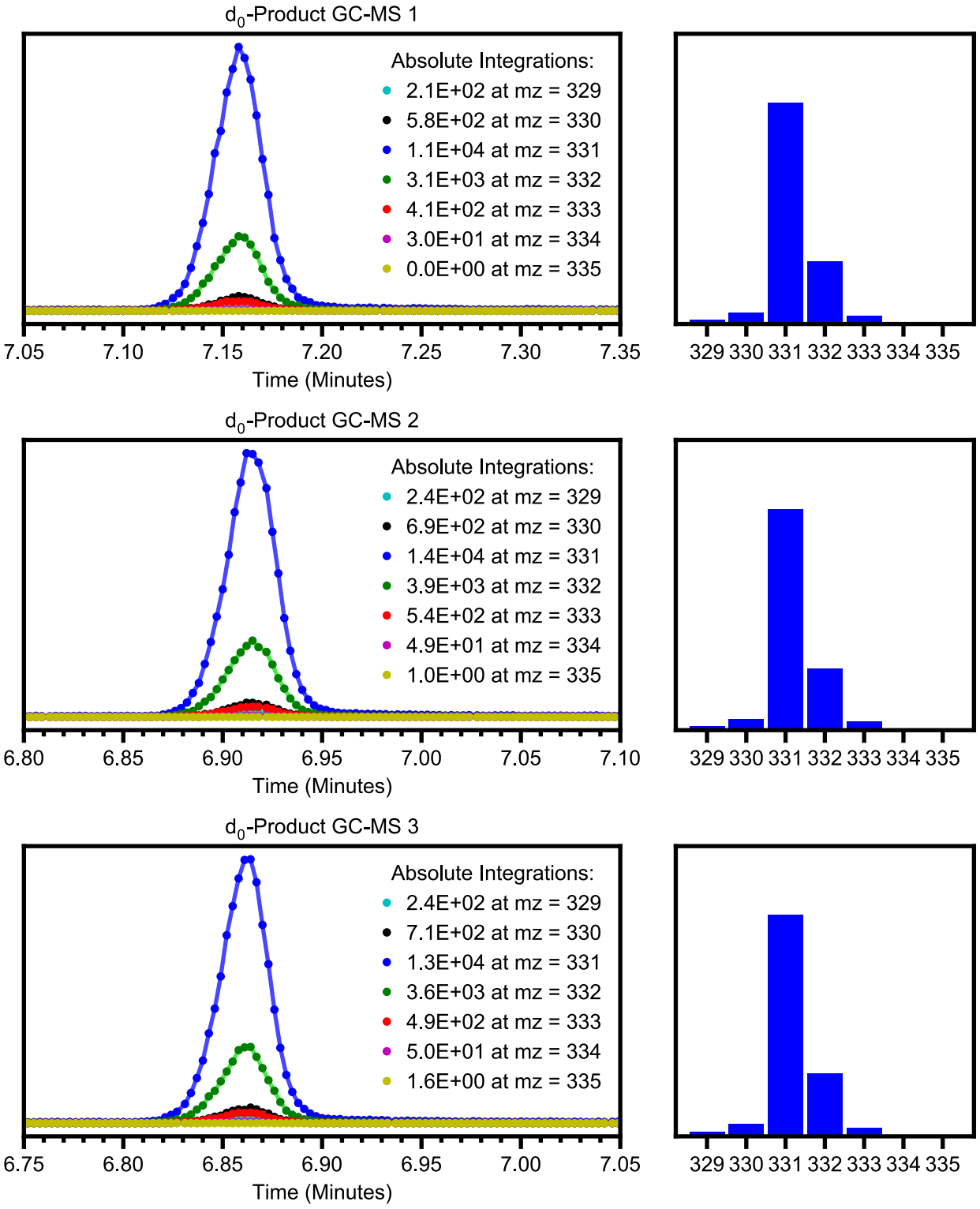

Figure A2.11 Reference GC-MS data for d_0-bifluorenyl used for determining isotope composition of deuterated bifluorenyl; sample prepared analogously to competition experiments but performed with d_0-fluorene.

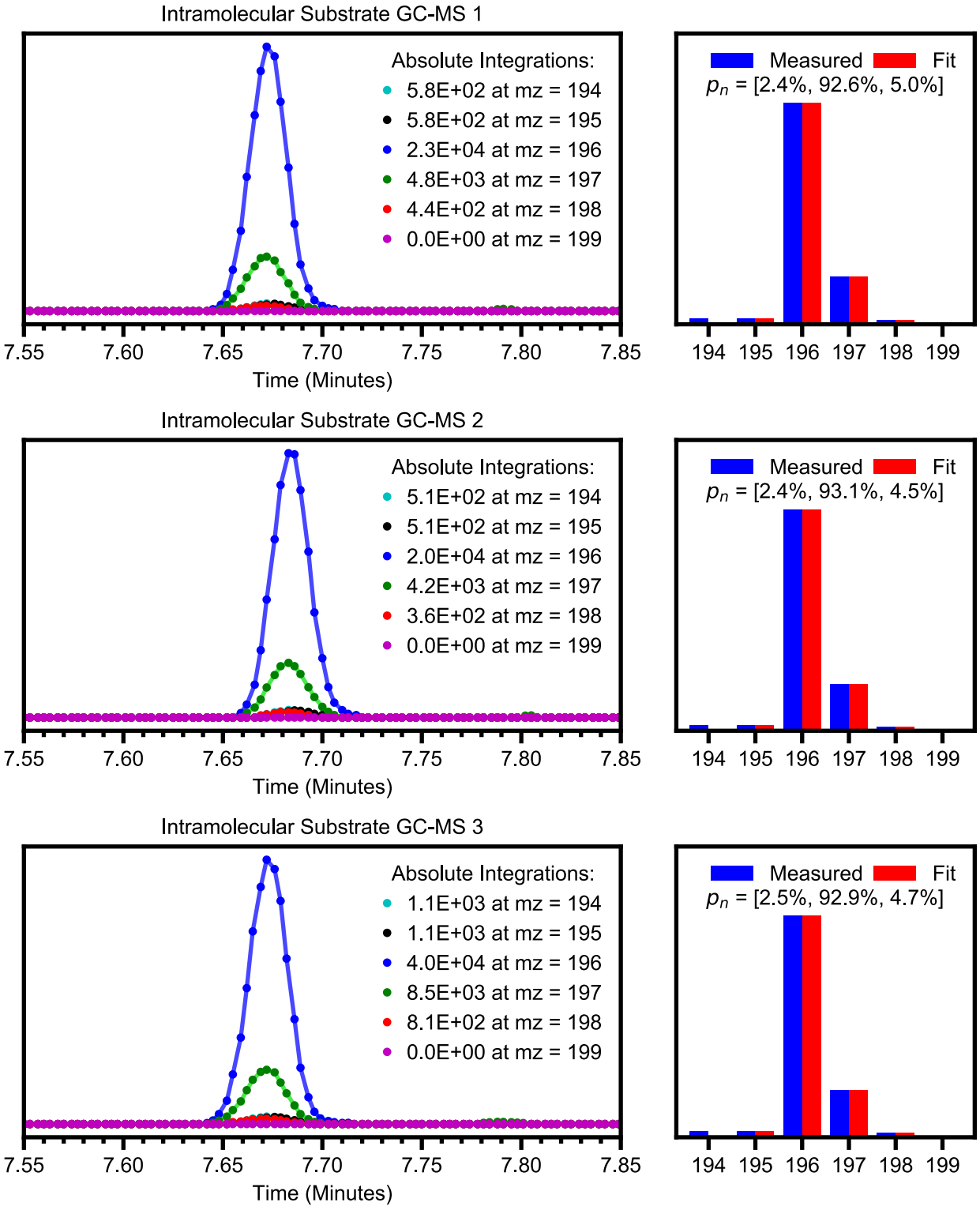

Figure A2.12 GC-MS data of mixture of d_1-fluorene used for intramolecular competition experiments.

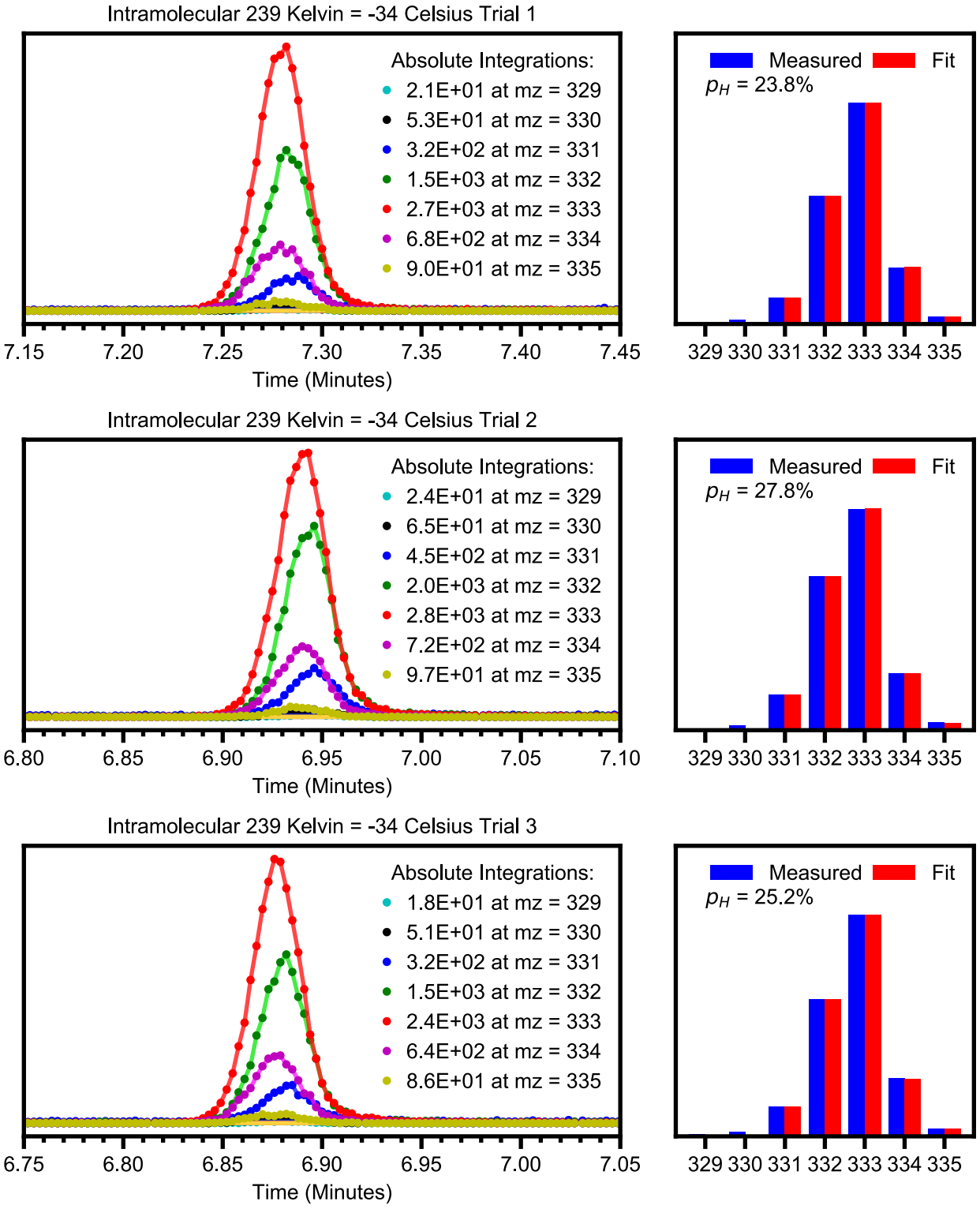

Figure A2.13 GC-MS data for the product analysis of the reaction of **CoO** and d_1-fluorene at 239 K.

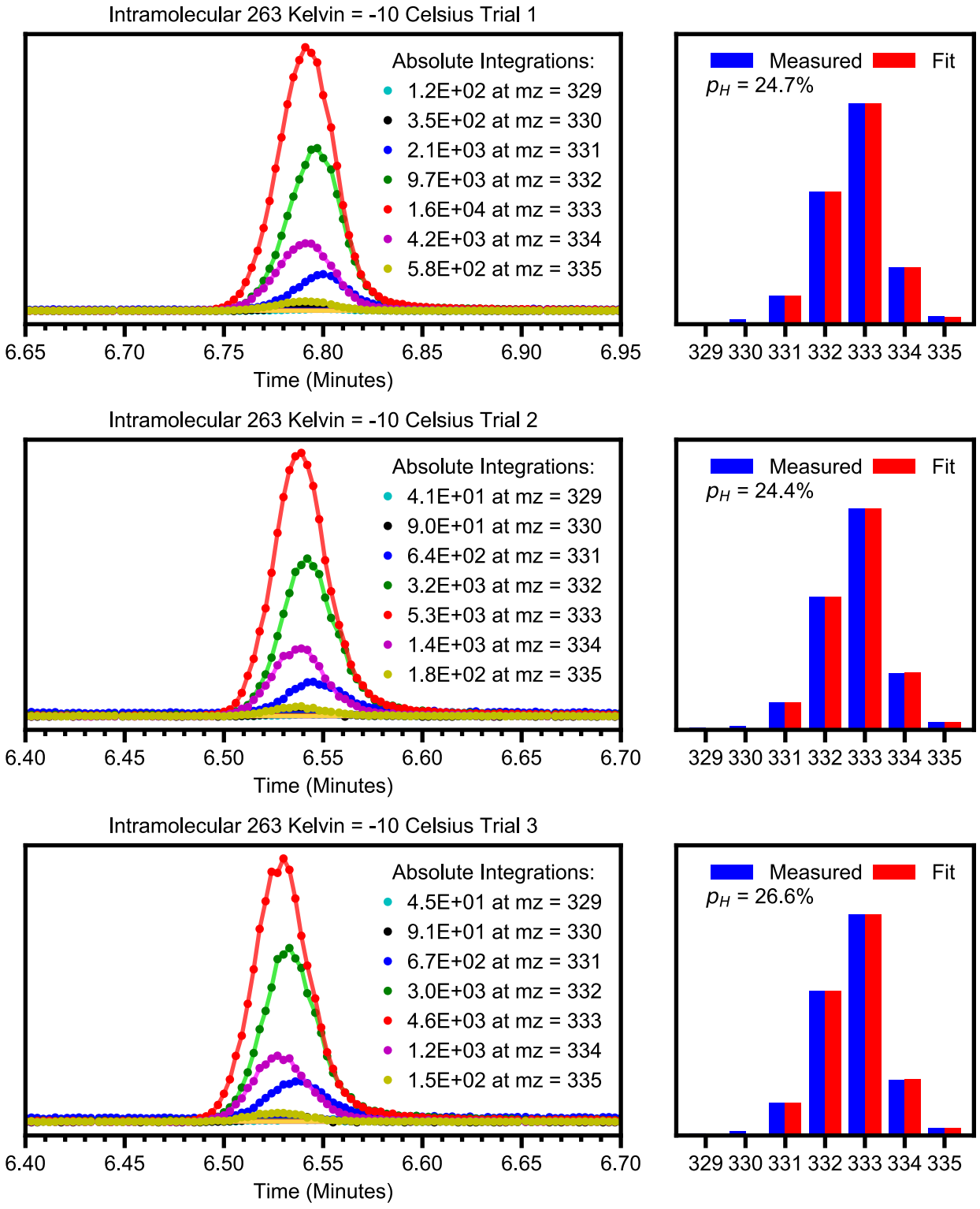

Figure A2.14 GC-MS data for the product analysis of the reaction of **CoO** and d_1-fluorene at 263 K.

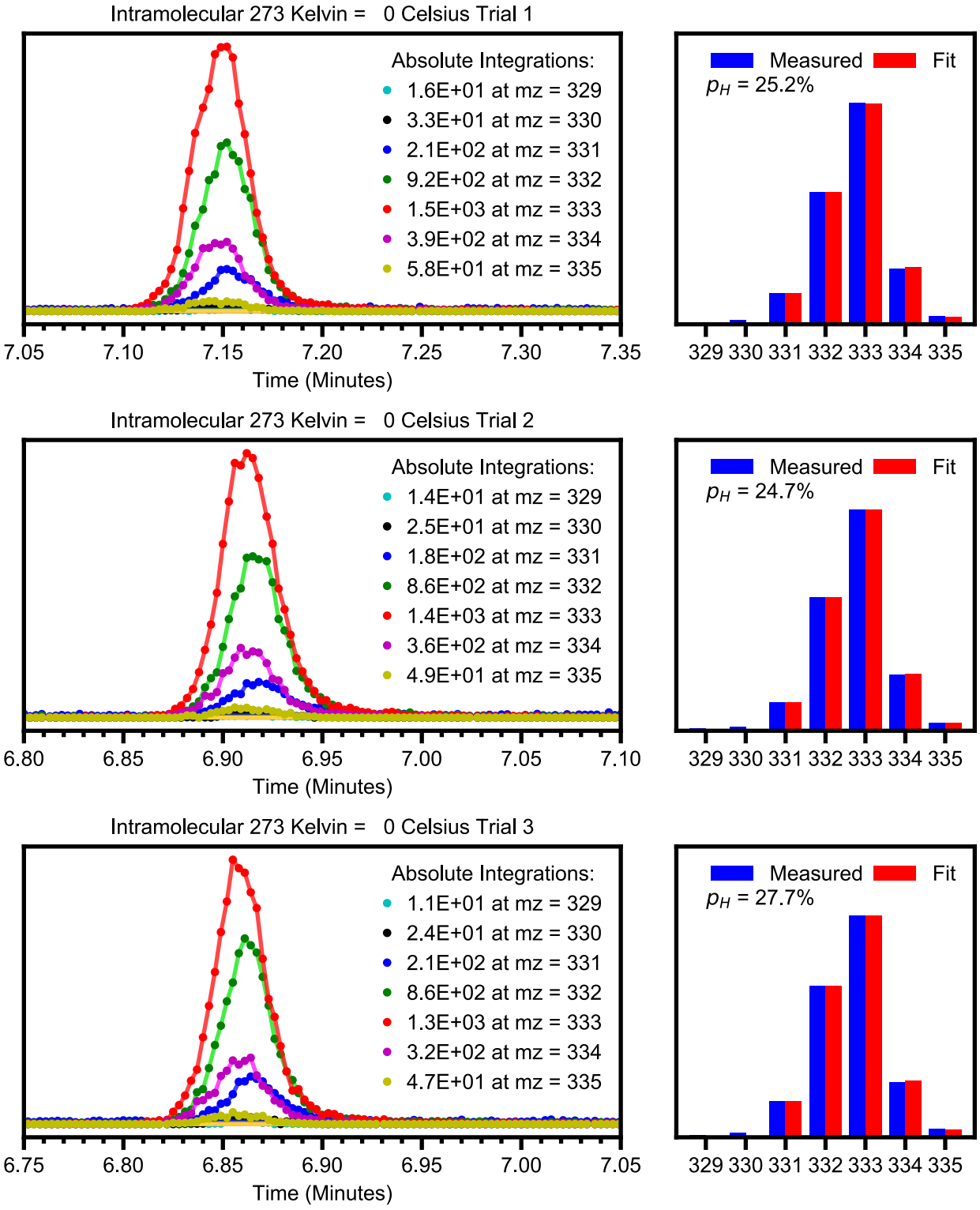

Figure A2.15 GC-MS data for the product analysis of the reaction of **CoO** and d_1-fluorene at 273 K.

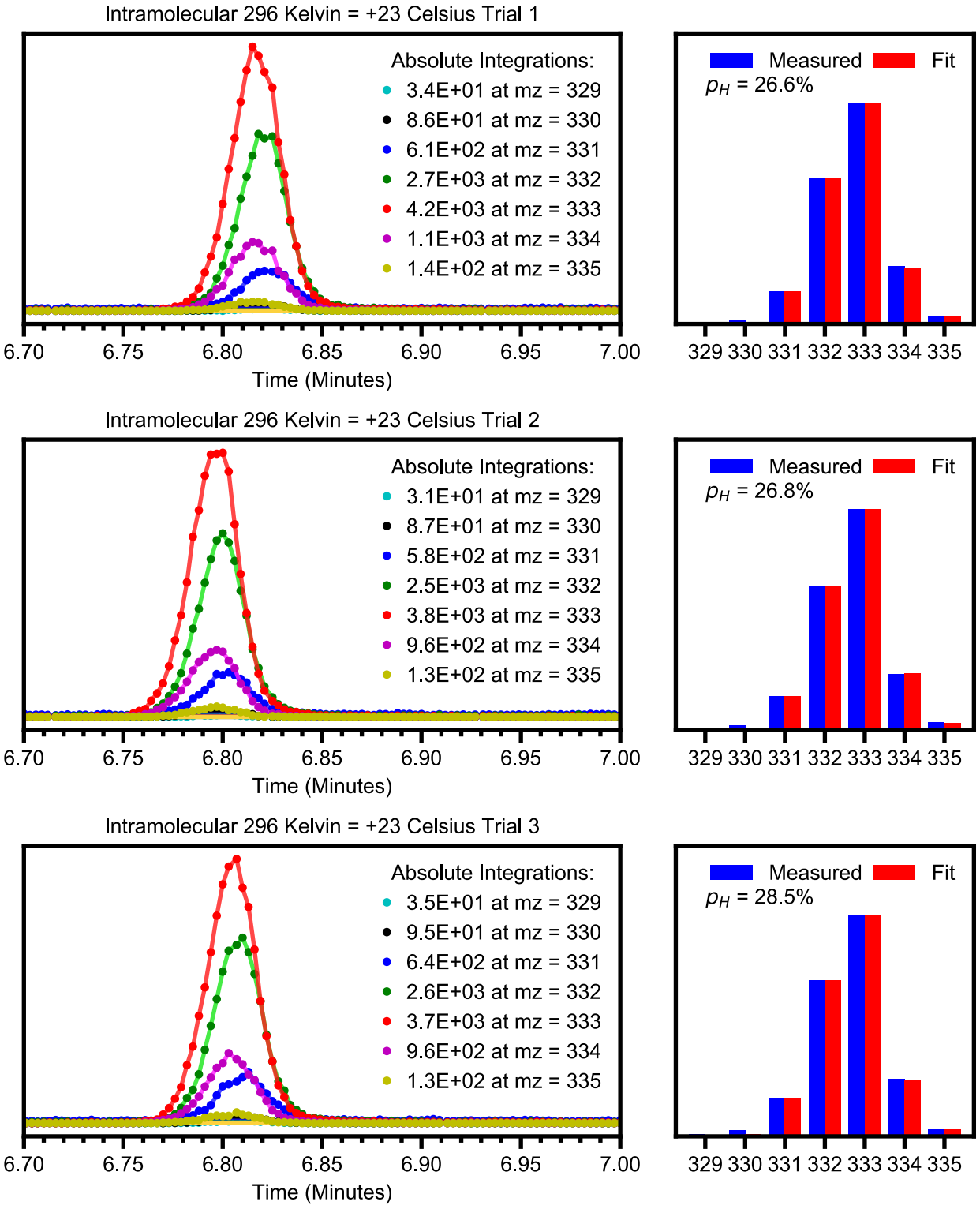

Figure A2.16 GC-MS data for the product analysis of the reaction of **CoO** and d_1-fluorene at 296 K.

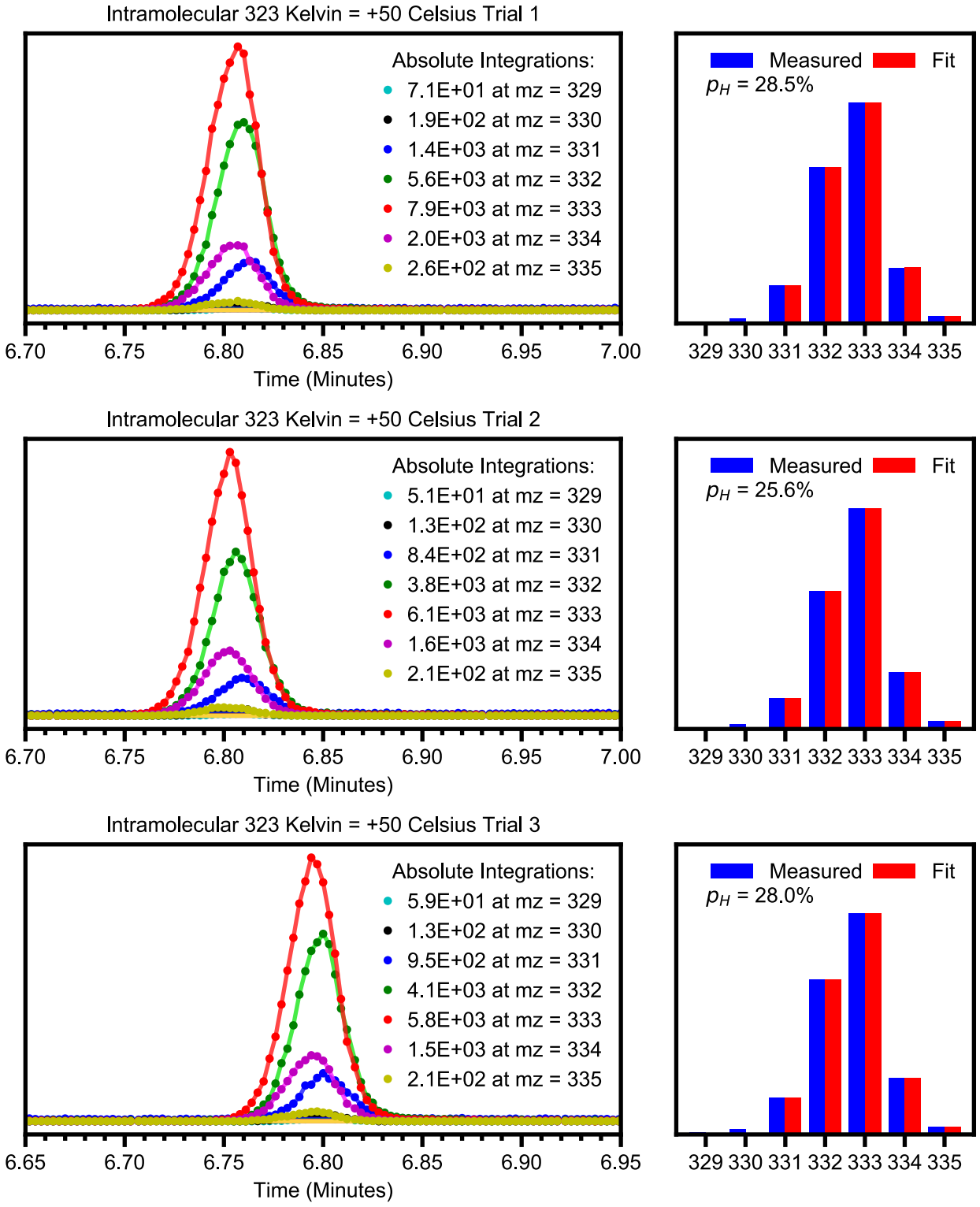

Figure A2.17 GC-MS data for the product analysis of the reaction of **CoO** and d_1-fluorene at 323 K.

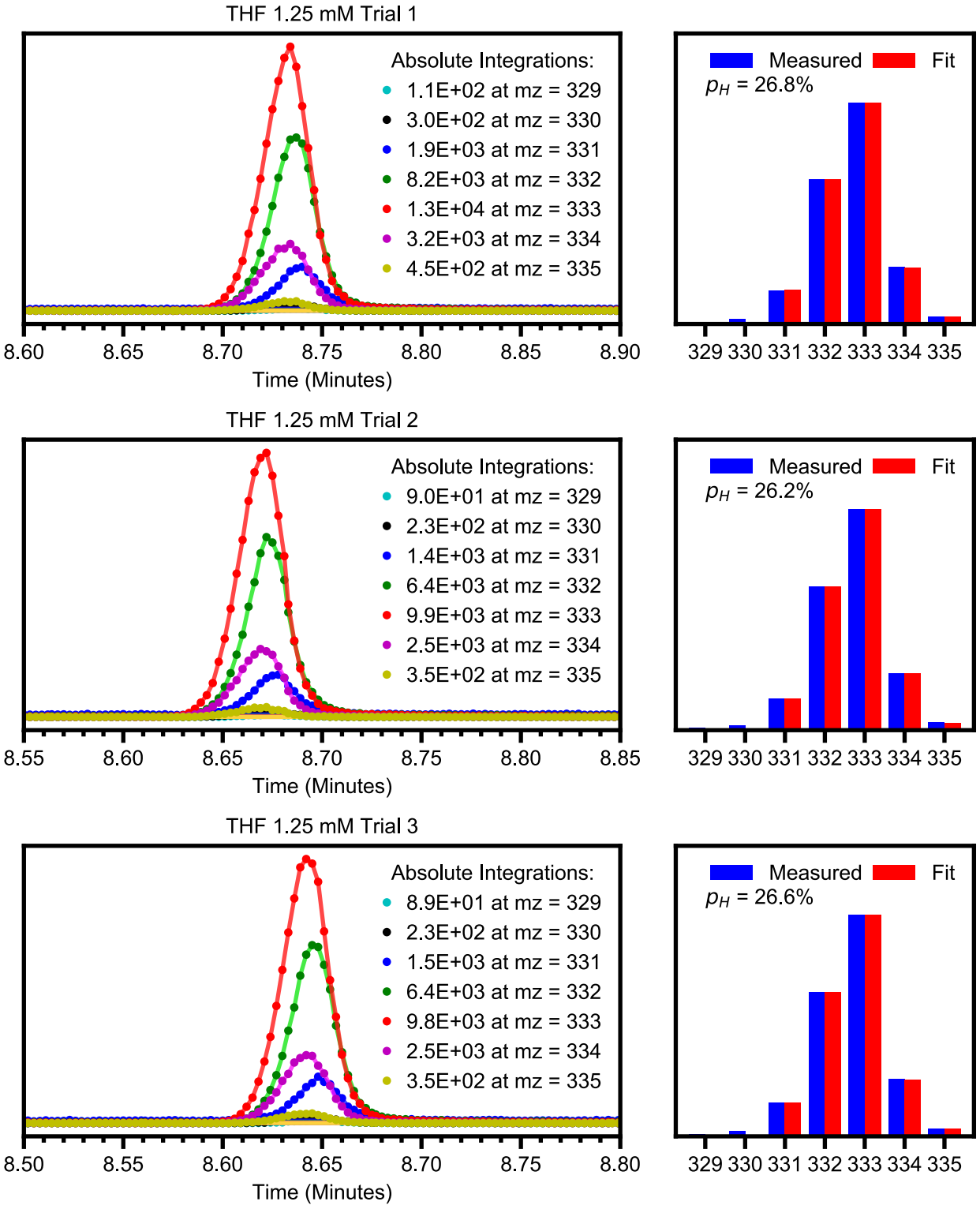

Figure A2.18 GC-MS data for the product analysis of the reaction of **CoO** and 20 equivalents d_1-fluorene at 296 K in THF at 1.25 mM **CoO**.

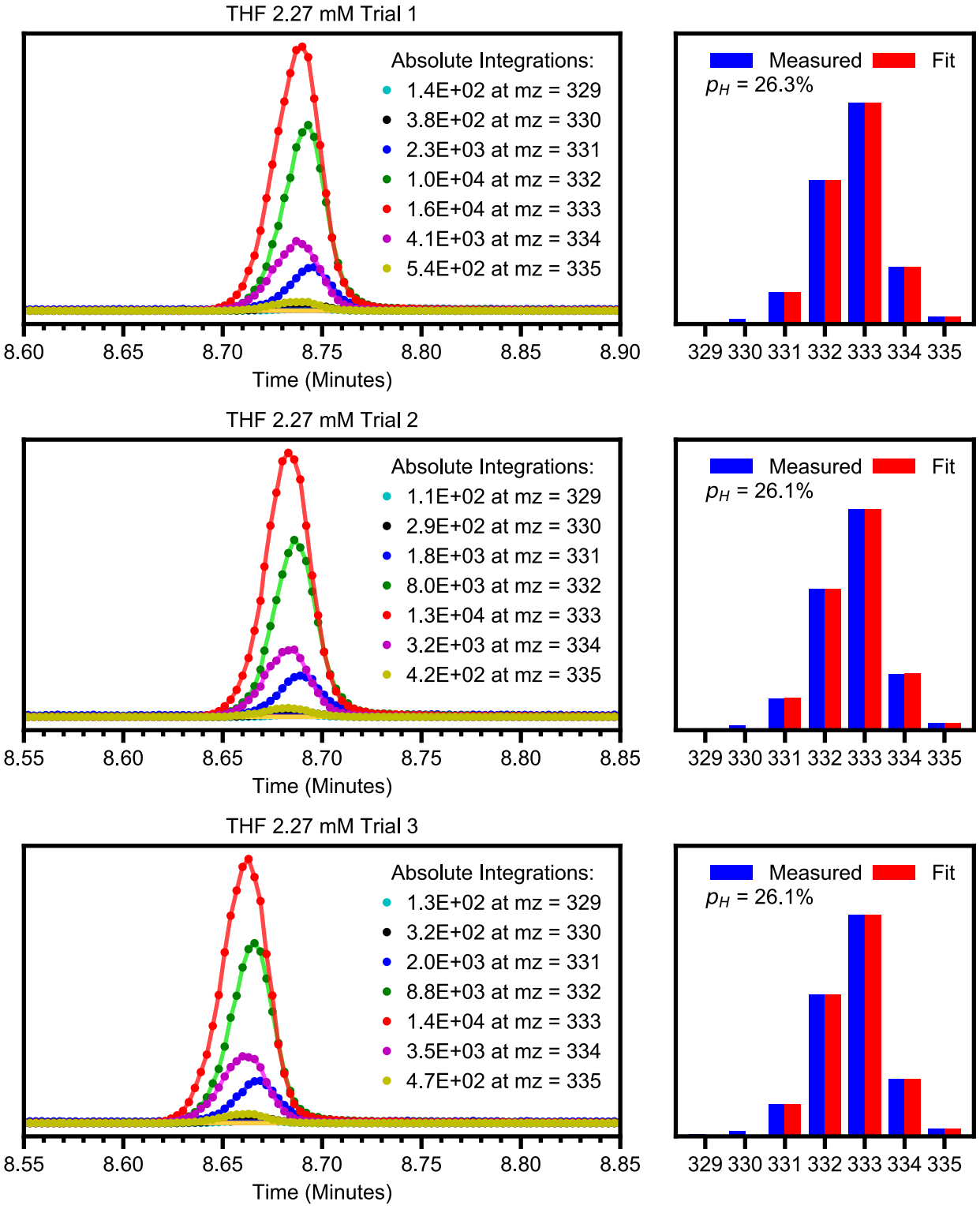

Figure A2.19 GC-MS data for the product analysis of the reaction of **CoO** and 100 equivalents d_1-fluorene at 296 K in THF at 2.27 mM **CoO**.

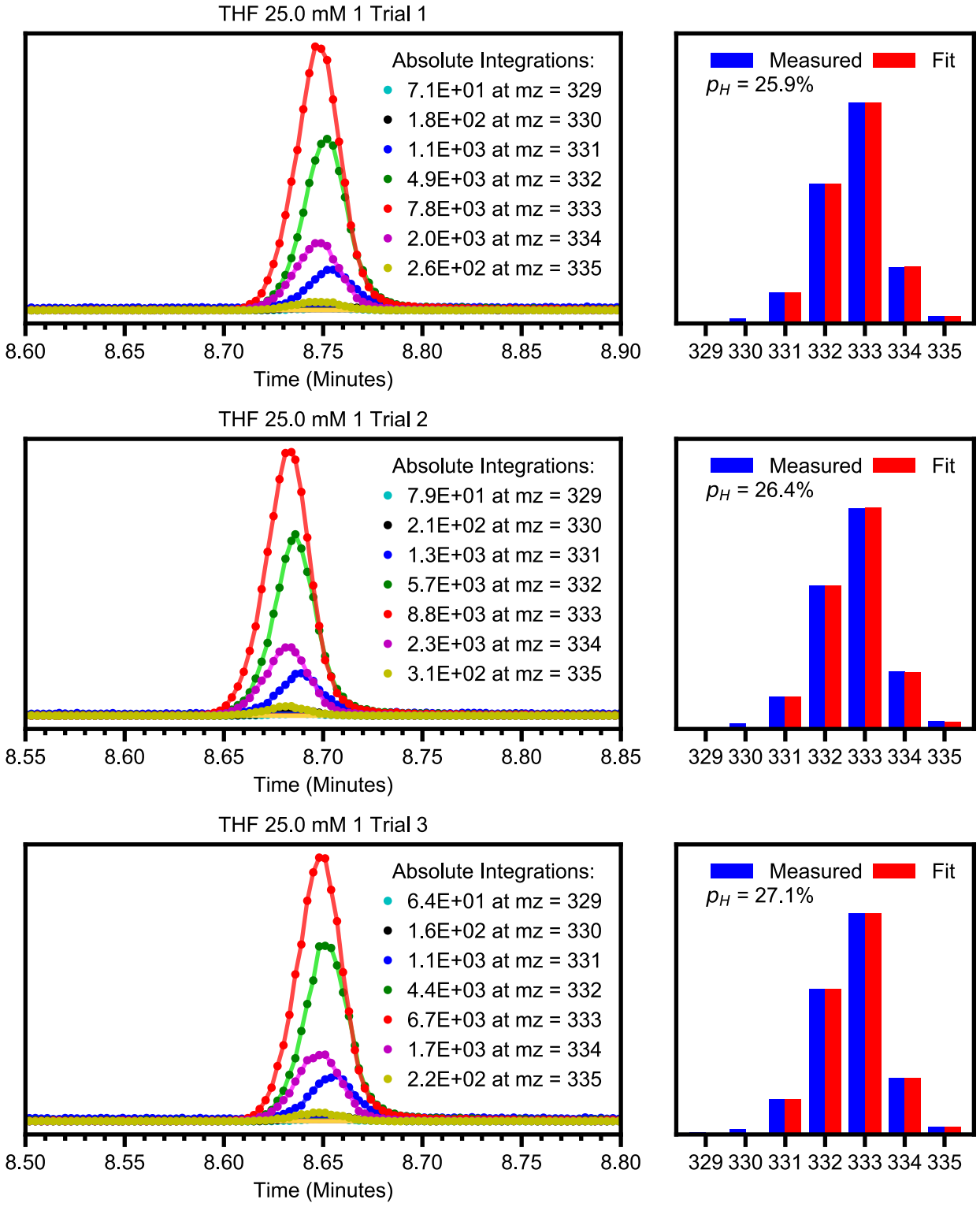

Figure A2.20 GC-MS data for the product analysis of the reaction of **CoO** and 40 equivalents d_1-fluorene at 296 K in THF at 25 mM **CoO**.

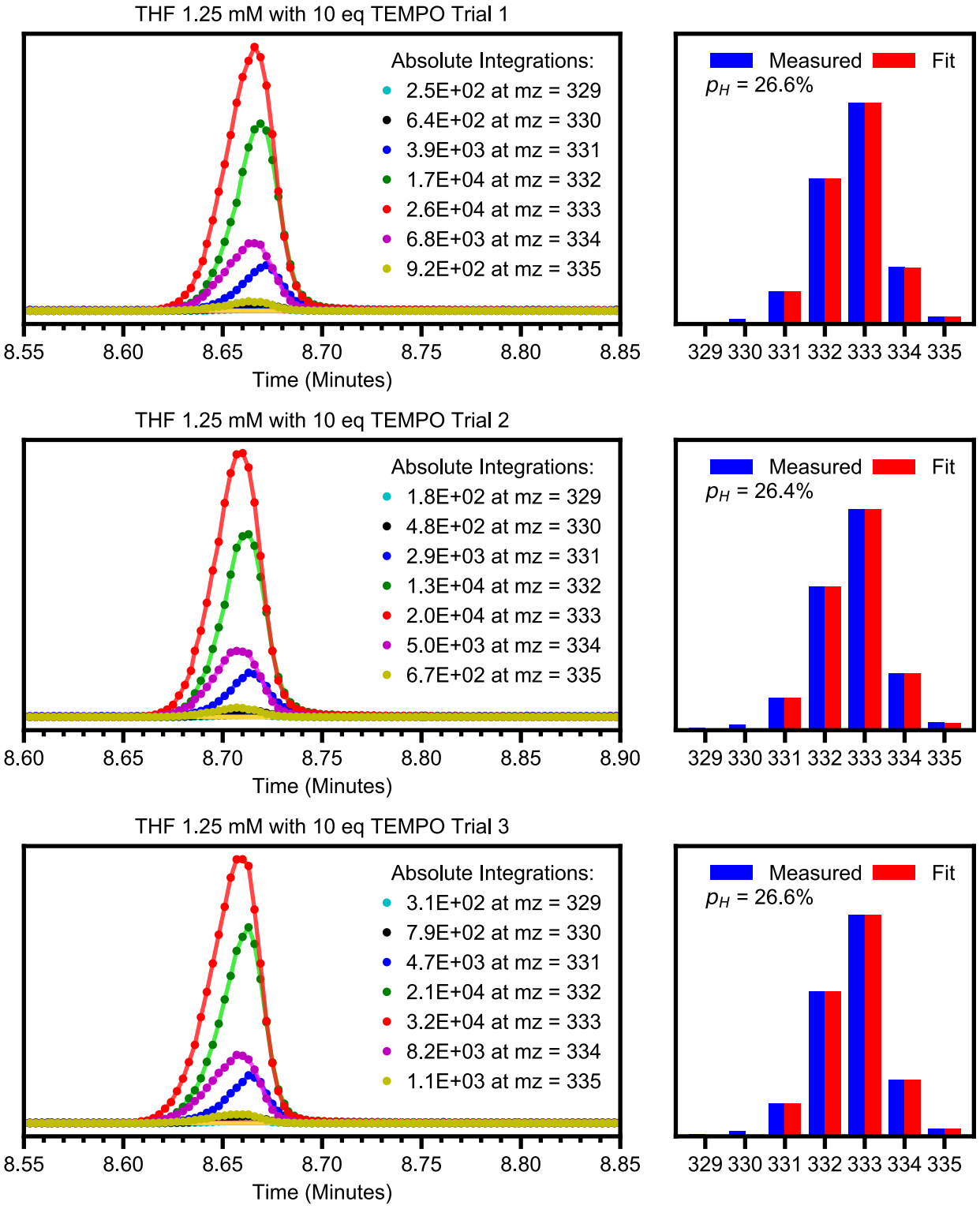

Figure A2.21 GC-MS data for the product analysis of the reaction of **CoO** and 20 equivalents d_1-fluorene at 296 K in THF at 1.25 mM **CoO** with an additive of 10 equivalents of TEMPO.

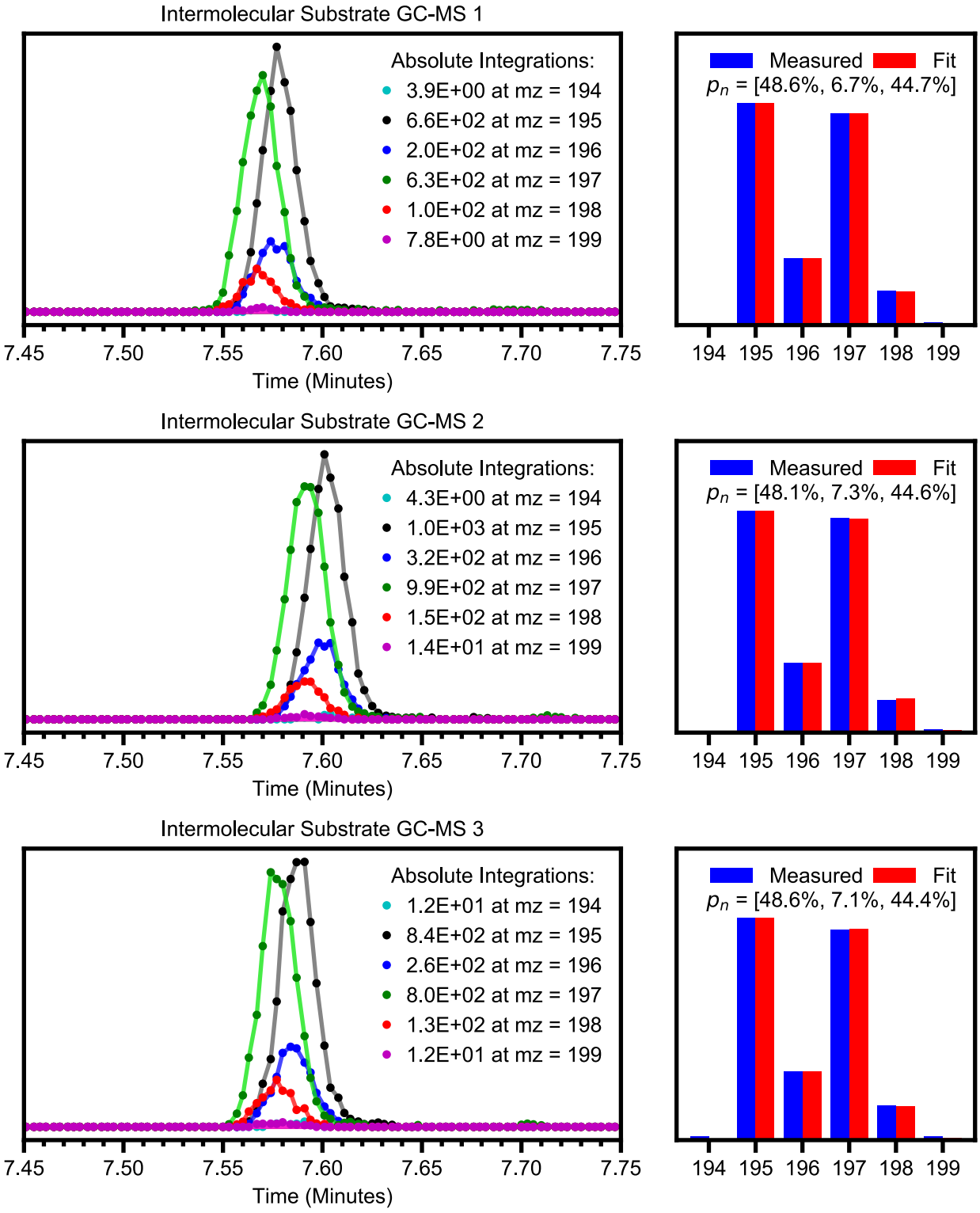

Figure A2.22 GC-MS data of mixture of d_0/d_2-fluorene used for intermolecular competition experiments.

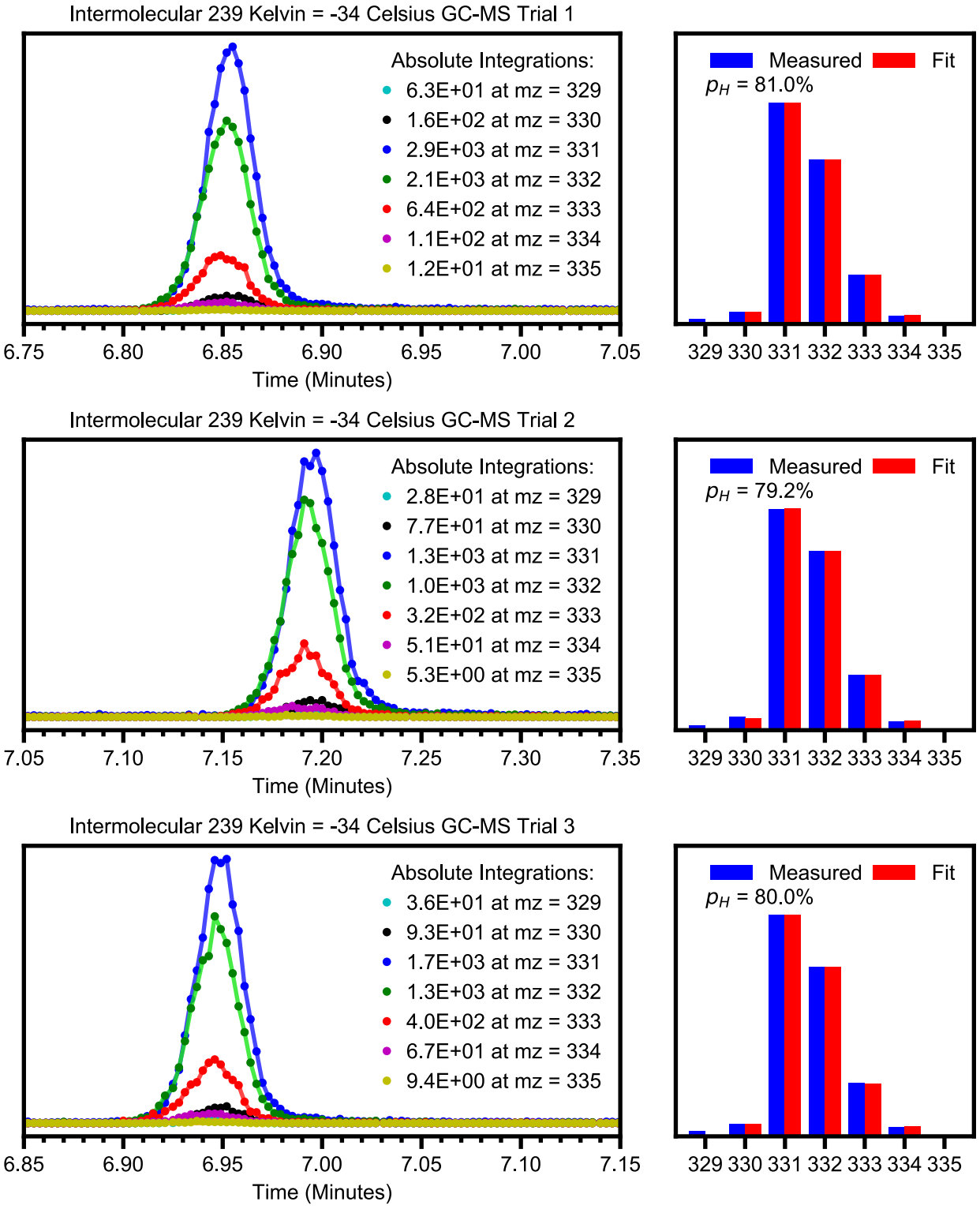

Figure A2.23 GC-MS data for the product analysis of the reaction of **CoO** and d_0/d_2-fluorene at 239 K.

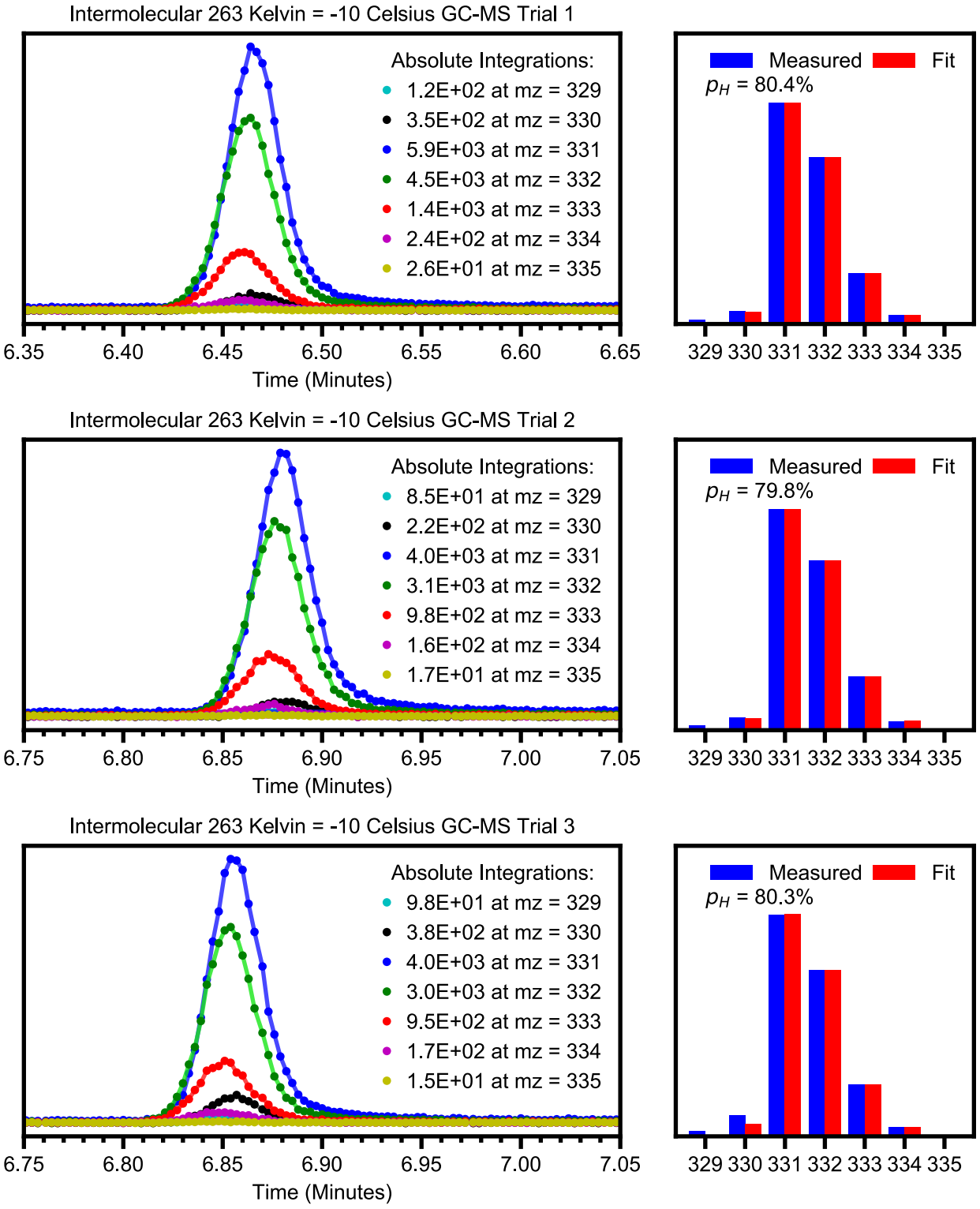

Figure A2.24 GC-MS data for the product analysis of the reaction of **CoO** and d_0/d_2-fluorene at 263 K.

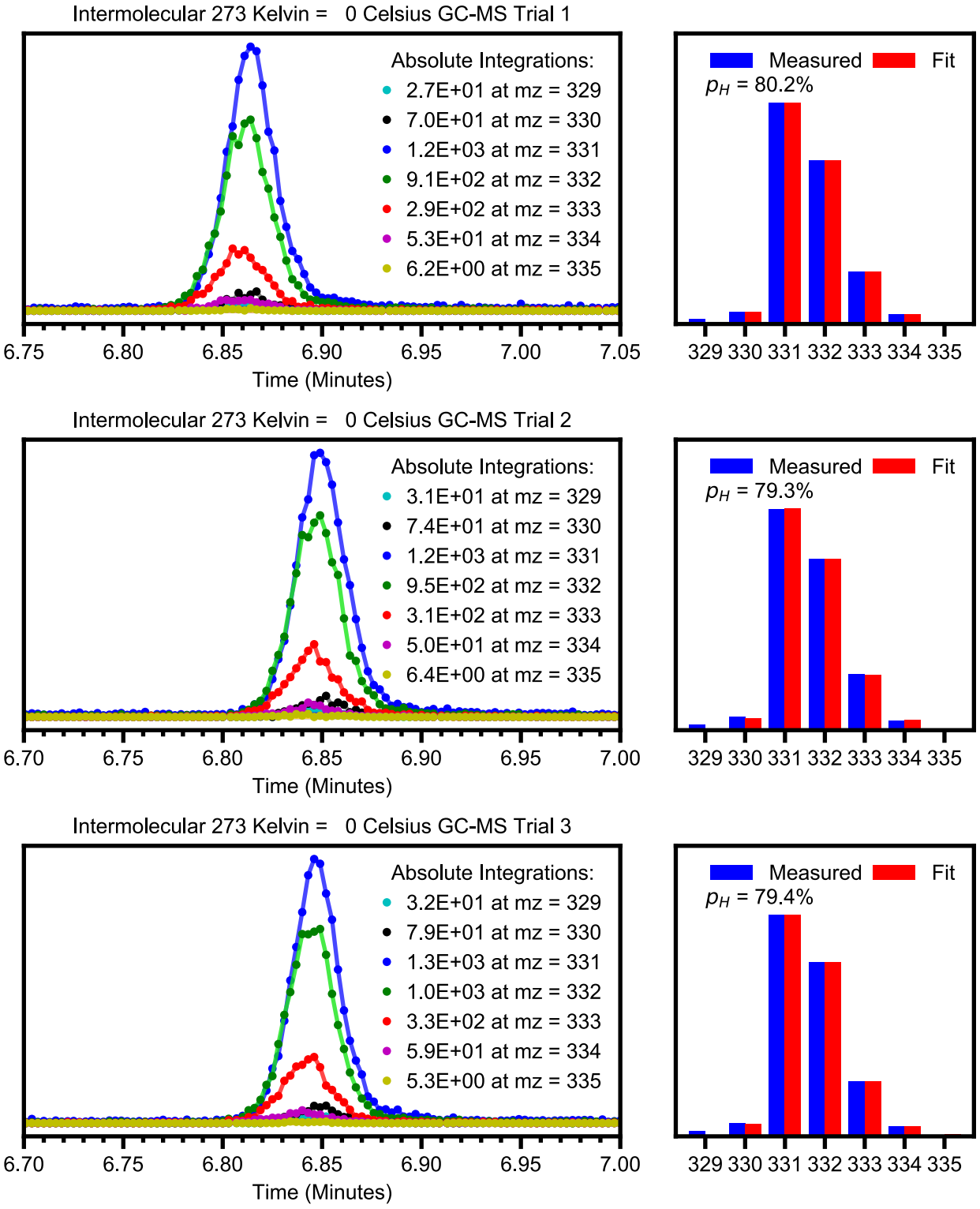

Figure A2.25 GC-MS data for the product analysis of the reaction of **CoO** and d_0/d_2-fluorene at 273 K.

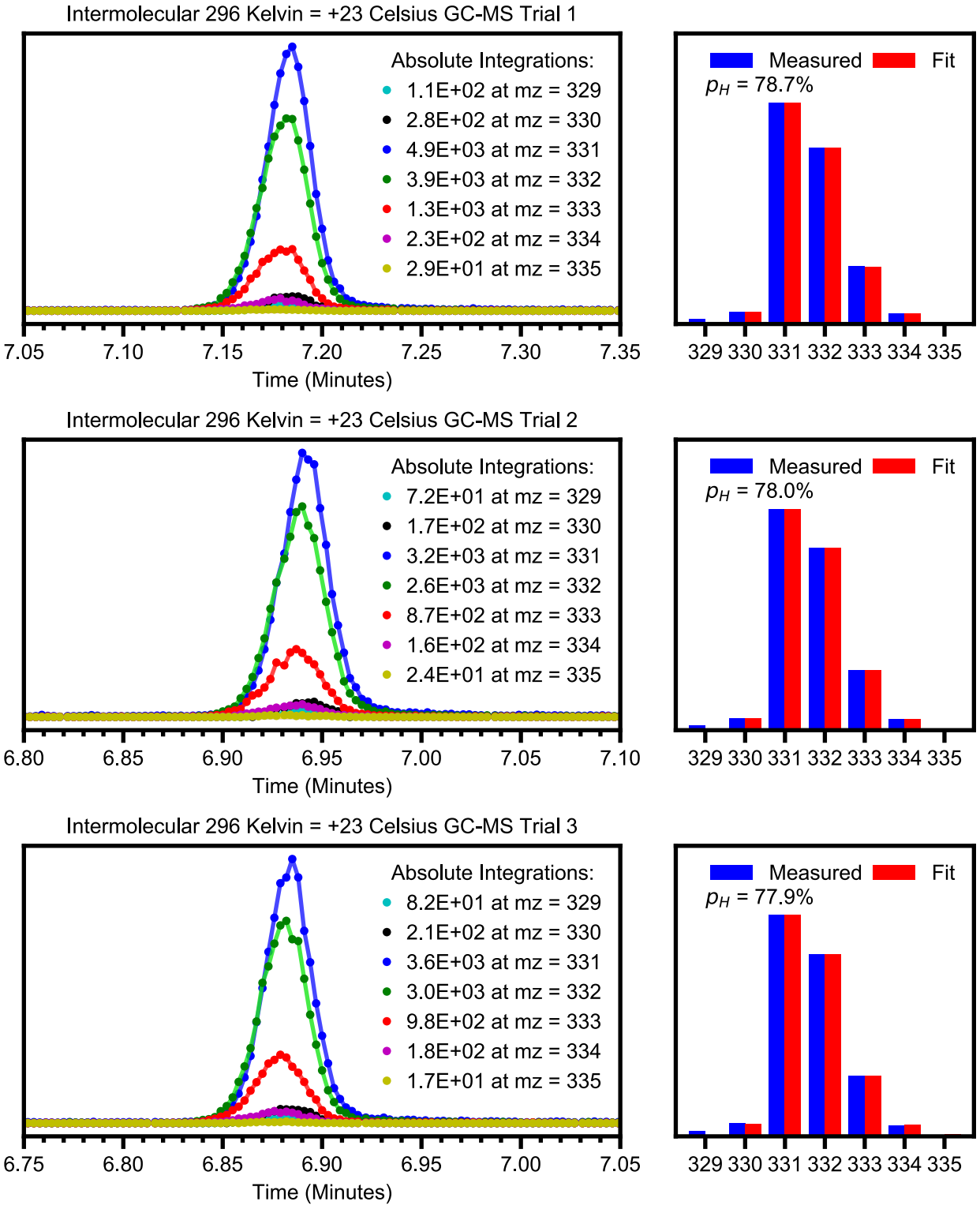

Figure A2.26 GC-MS data for the product analysis of the reaction of **CoO** and d_0/d_2-fluorene at 296 K.

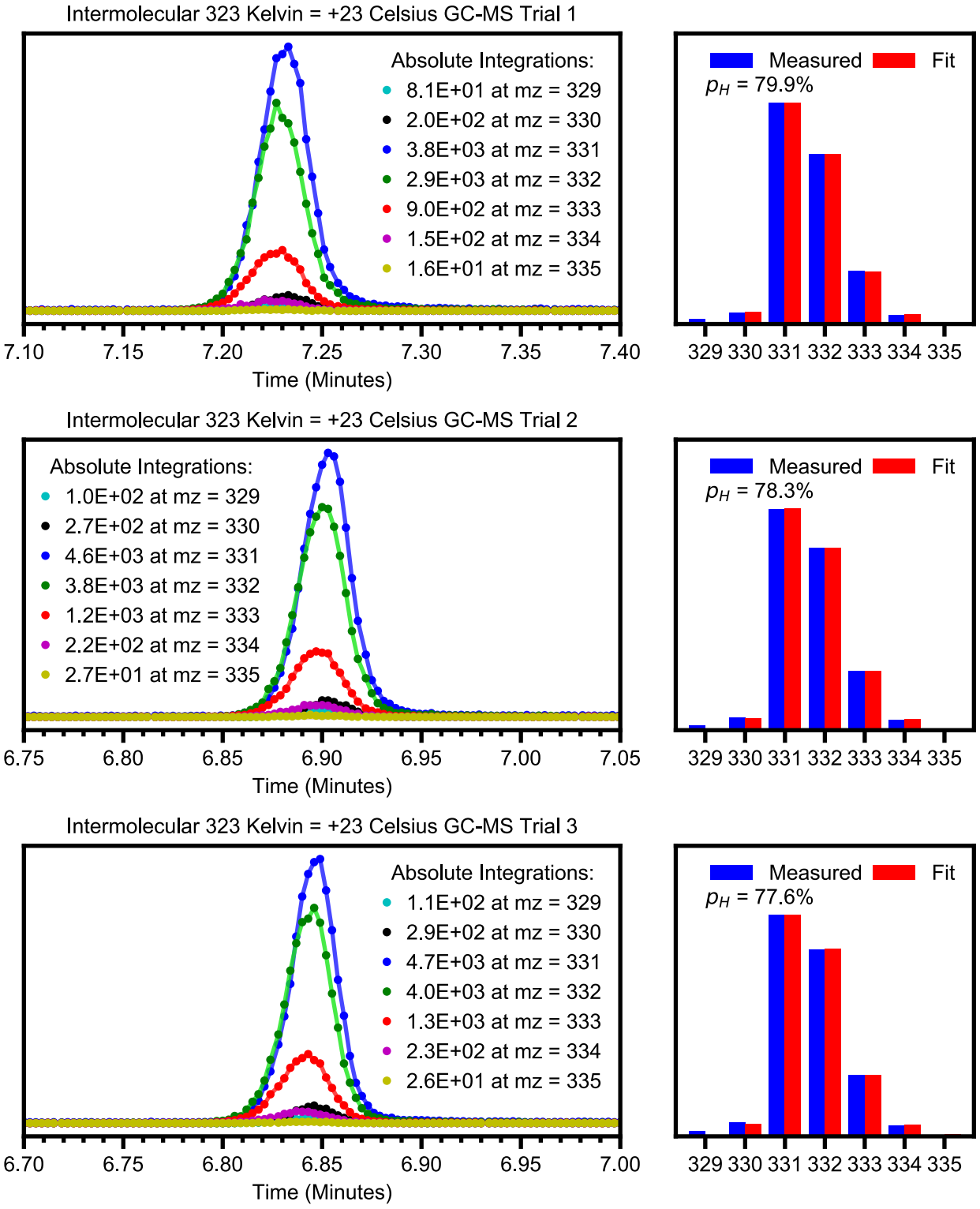

Figure A2.27 GC-MS data for the product analysis of the reaction of **CoO** and d_0/d_2-fluorene at 323 K.

6. **UV-Vis Data for Kinetic Experiments**

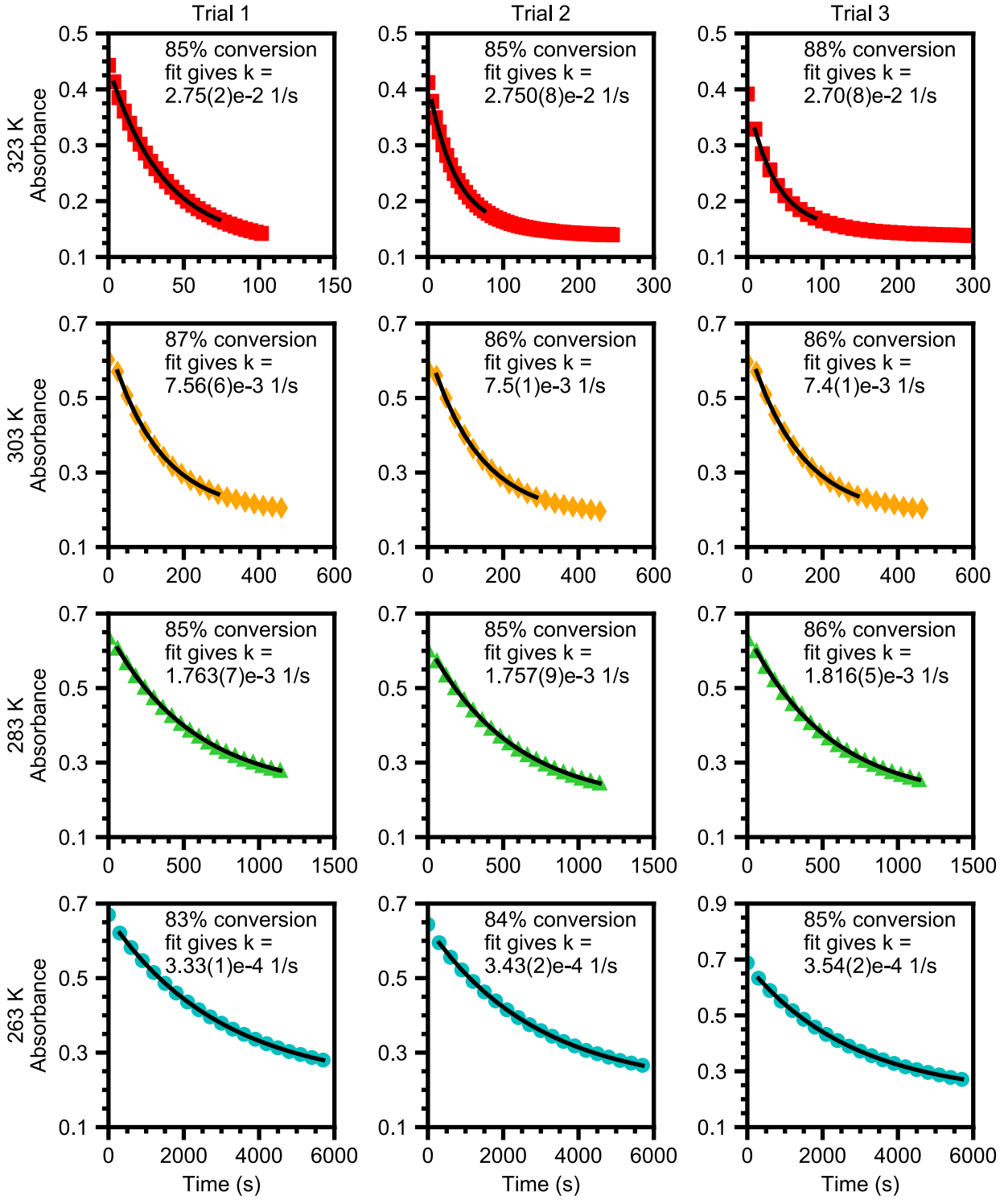

Figure A2.28 Plots of *A* vs. *t* for the reaction of **CoO** with d_0-Fluorene at various temperatures.

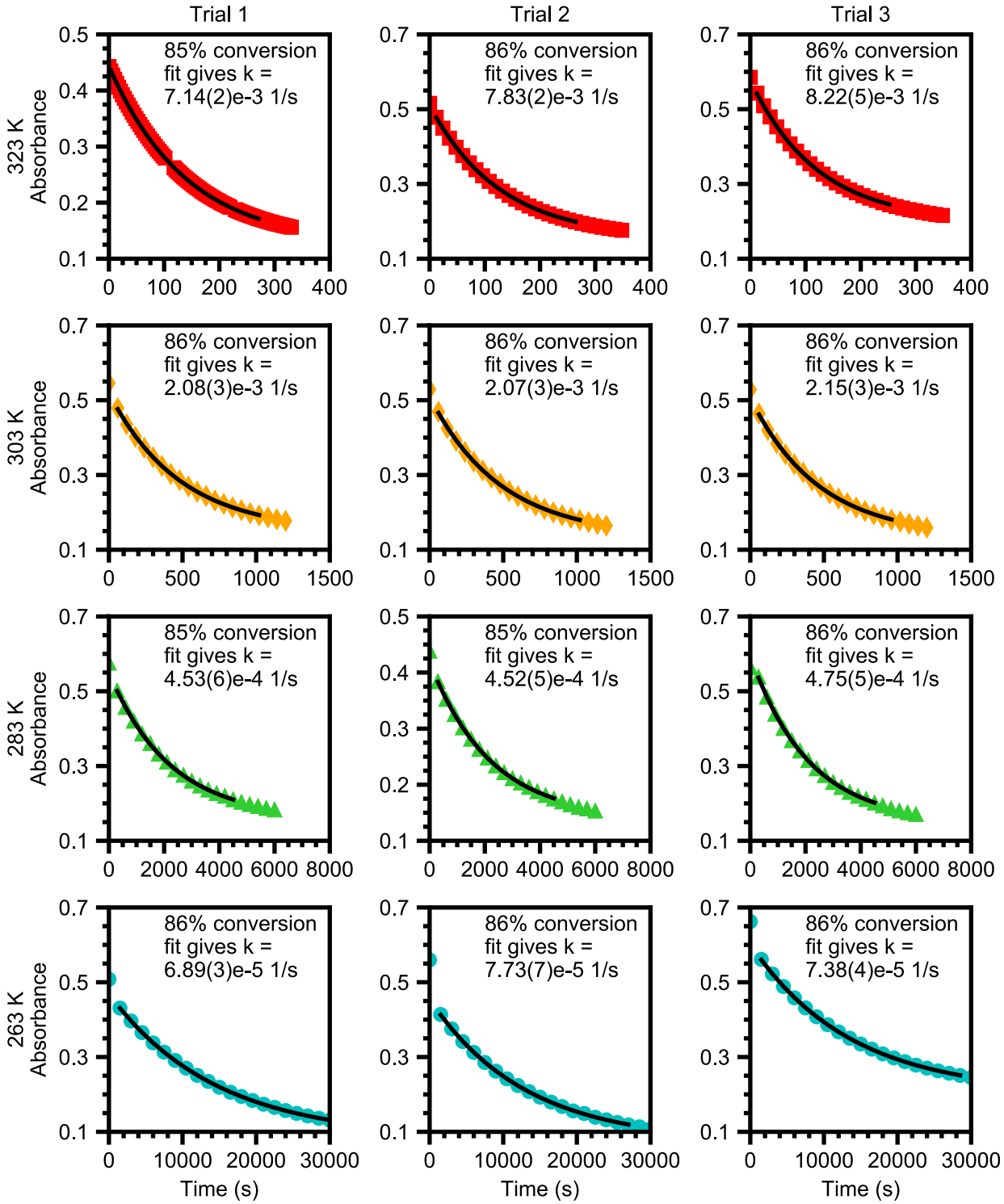

Figure A2.29 Plots of *A* vs. *t* for the reaction of **CoO** with d_2-Fluorene at various temperatures.

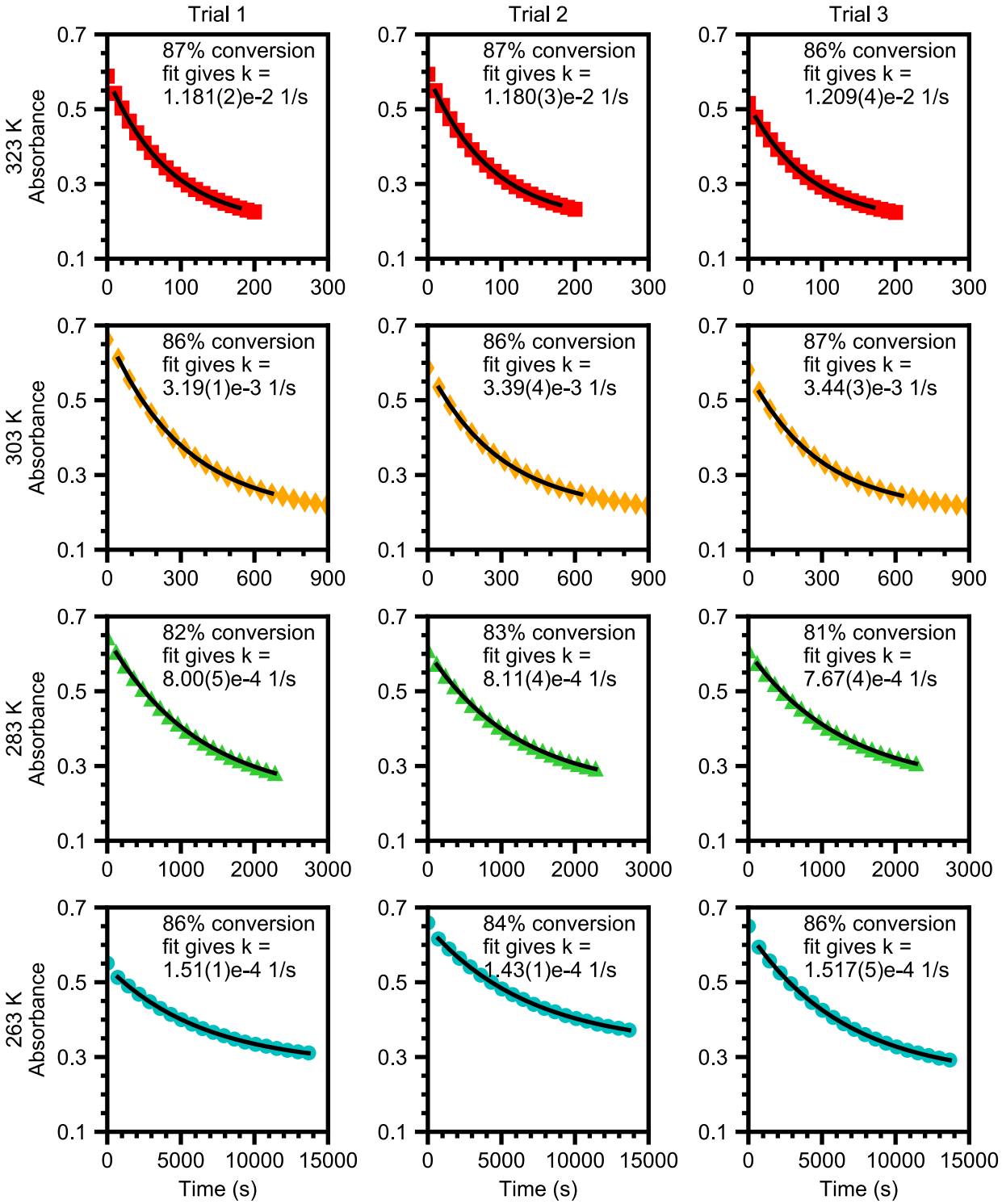

Figure A2.30 Plots of *A* vs. *t* for the reaction of **CoO** with d_0-DHA at various temperatures.

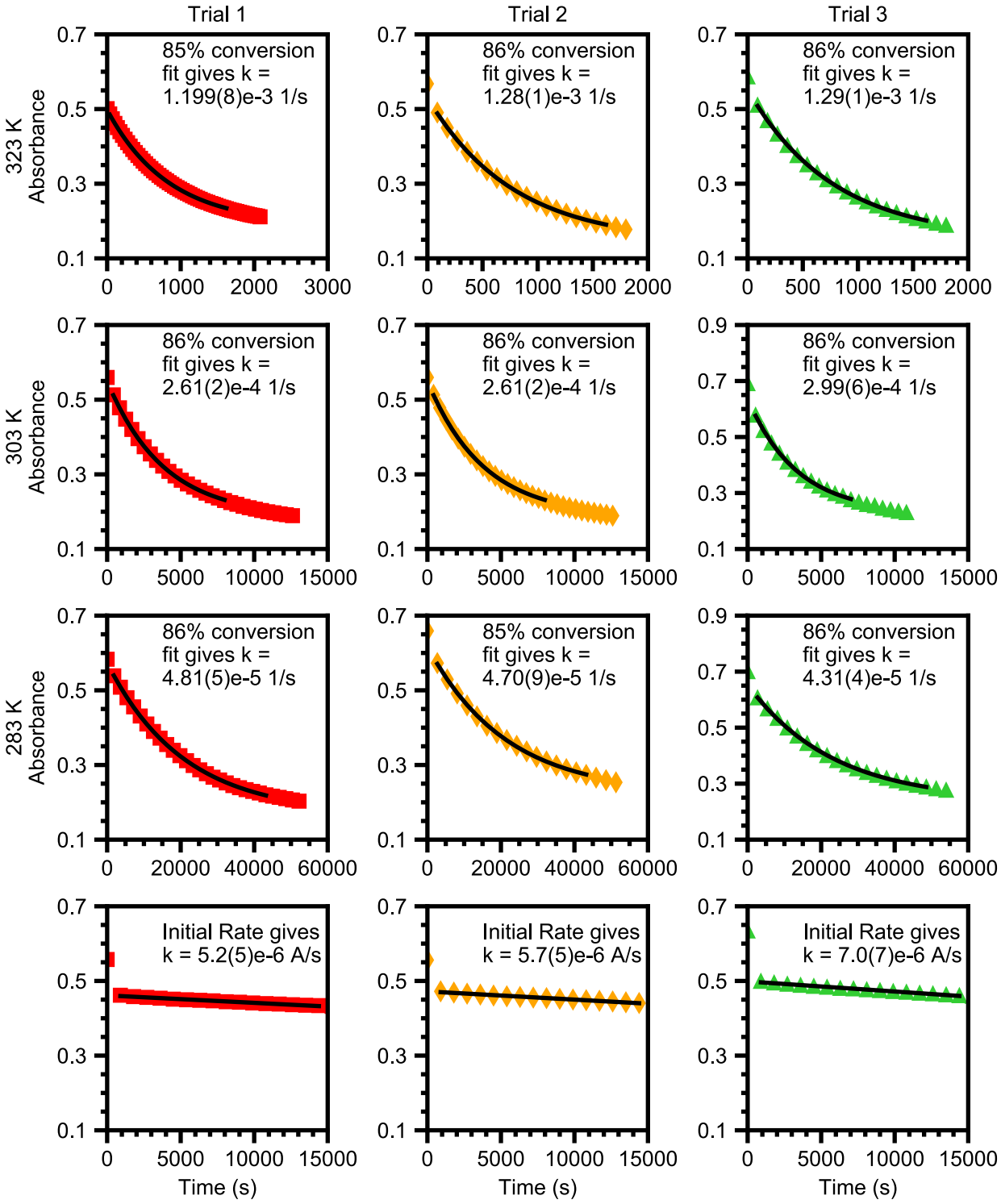

Figure A2.31 Plots of *A* vs. *t* for the reaction of **CoO** with d_4-DHA at various temperatures.

Appendix A3: Summary of Data for CPET Calculations in Chapter 4

Table A3.1 summarizes the calculated data for each substrate and breaks down the calculated rate near the optimal tunneling distance. It is clear that, in general, more acidic substrates both have more reactivity from excited vibration states of the product, but also that each vibrational state is more diffuse with greater Franck-Condon overlap for a given pair of reactant and product vibrational states.

Table A3.1 Comparison of vibronic contributions and overlap integrals near the optimal tunnelling distance.

	PhFluorene	Fluorene	DHA	DPM	CHD
Exp k_{rel}	190	4.8	0.47	0.076	0.031
Calc k_{rel}	98	3.0	10	0.009	0.035
BDE	74	82	76.3	84.5	74.3
pK_a	17.9	22.6	30.1	32.3	35
R	0.71	0.80	0.78	0.74	0.85
$U(R)$	2.4	1.5	1.5	2.4	3.3
λ	36	32	30	38	34
$\%k_{0,0}$	13%	2%	58%	49%	86%
$\%k_{1,0}$	30%	7%	18%	24%	4%
$\%k_{2,0}$	55%	79%	15%	19%	0%
$\%k_{3,0}$	1%	11%	6%	6%	0%
$S_{0,0}^2$	$3.7 \cdot 10^{-5}$	$1.0 \cdot 10^{-6}$	$7.3 \cdot 10^{-7}$	$2.5 \cdot 10^{-6}$	$5.5 \cdot 10^{-9}$
$S_{1,0}^2$	$2.9 \cdot 10^{-2}$	$8.3 \cdot 10^{-4}$	$2.3 \cdot 10^{-4}$	$5.1 \cdot 10^{-4}$	$1.1 \cdot 10^{-6}$
$S_{2,0}^2$	$5.0 \cdot 10^{-1}$	$4.1 \cdot 10^{-1}$	$7.2 \cdot 10^{-2}$	$6.6 \cdot 10^{-2}$	$1.8 \cdot 10^{-4}$
$S_{3,0}^2$	$2.6 \cdot 10^{-1}$	$2.7 \cdot 10^{-1}$	$4.3 \cdot 10^{-1}$	$3.8 \cdot 10^{-1}$	$3.0 \cdot 10^{-2}$

Substrates are 9-phenylfluorene (PhFluorene), fluorene, 9,10-dihydroanthracene (DHA), diphenylmethane (DPM), and 1,3-cyclohexadiene (CHD). Experimental (Exp) and calculated (Calc) relative rates k_{rel} are determined as the ratio of a substrates rate to the average rate. Experimental rates, BDEs, and pKas are taken from reference [50]. R (Å) is the tunneling distance for an optimized MECP which is nearest to but not less than the optimal tunneling distance. $U(R)$ (kcal/mol) is the energy needed to compress the reorganized complex to this tunneling distance. λ (kcal/mol) is the reorganization free energy. $\%k_{\mu,v}$ is the percentage of reactivity at this tunneling distance proceeding from reactant vibrational state μ to reactant vibrational state v. 10% of the rate for CHD is into the first excited product state. $S_{\mu,v}{}^2$ is the squared overlap Franck-Condon integral of reactant vibrational state μ with product vibrational state v; the vibronic coupling is $S_{\mu,v}^2$ multiplied by the square of the electronic coupling.

Figure A3.1 shows the reactant energy wells from main test Figure 4.5 along with their corresponding product energy wells. Aside from slightly different tunneling distances, there is no significant difference in the product energy wells. The tunneling distance, and the energy needed to compress to that tunneling distance, are plotted against pK_a in Figure 4.6; they demonstrate that tunneling distance dynamics cannot be solely responsible for the kinetic trend with pK_a and $\Delta G°_{PT}$.

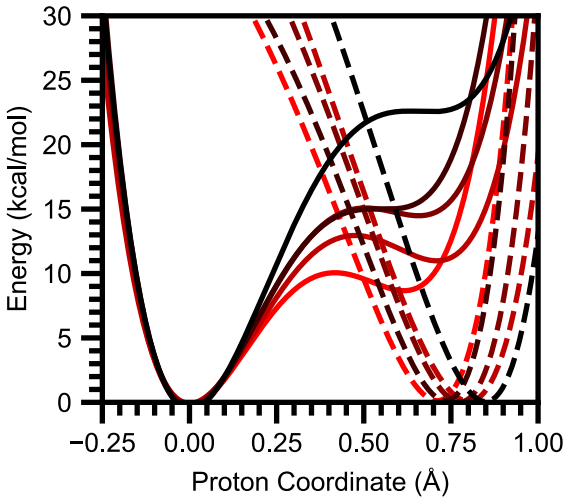

Figure A3.1 Reactant energy wells near the optimal tunneling distance (solid lines) and the corresponding product energy wells (dashed lines), with redder hues corresponding to more acidic substrates.

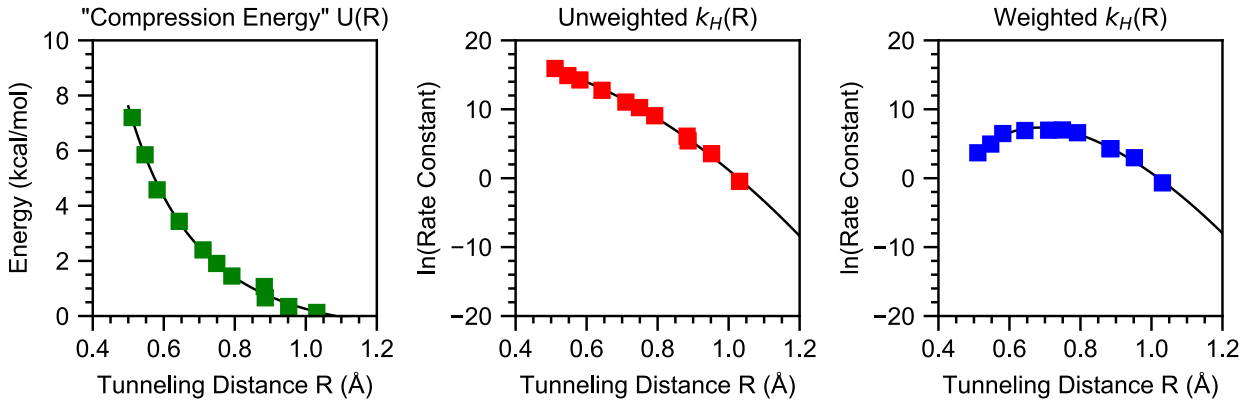

Calculation A3.1 $U(R)$, $k(R)$, and $(\ln k\text{-}U/k_BT)(R)$ and their fits at 296 K for 9-phenylfluorene.

```
Substrate is PhFluorene
At T = 296 K, kH = 1.00e+03
Reaction DG = -5.64 kcal/mol
Uncorrected DG = -13.54 kcal/mol
Uncorrected heavy DG = -10.20 kcal/mol
MECP/Reorganized DG = 4.61 kcal/mol
Reorganization Energy = 35.95 kcal/mol

  U(R) =   3.7454/R**2 +  -3.8876/R +   0.3999
lnk(R) = -26.5912*R**2 +  10.6374*R +  17.1381
  F    R (A)     U(R)       kH(R)      P*kH(R)
002    1.031     0.13   6.330e-01    5.079e-01
004    0.952     0.34   3.511e+01    1.956e+01
006    0.886     0.66   2.244e+02    7.302e+01
008    0.883     1.07   4.445e+02    7.220e+01
010    0.792     1.45   8.644e+03    7.339e+02
012    0.749     1.91   2.798e+04    1.095e+03
014    0.711     2.40   6.259e+04    1.062e+03
018    0.643     3.43   3.459e+05    1.009e+03
022    0.581     4.58   1.559e+06    6.521e+02
026    0.547     5.85   2.940e+06    1.417e+02
030    0.511     7.20   8.210e+06    3.985e+01
Opt H 0.684     2.72   1.585e+05    1.553e+03
Forces (F) are in atomic units, distances (R) are in Å, energies (U(R)) are in
kcal/mol, and rate constants (k(R) and P*k(R)) are in s**-1.

Fraction of kH from reactant state u to product state v near the optimal tunneling
distance
R = 0.711, force = 014, U(R) = 2.40
total rate = 6.26e+04, average overlap squared = 2.88e-01
  u\v     0       1       2       3
  0   0.134   0.003   0.000   0.000
  1   0.302   0.003   0.000   0.000
  2   0.547   0.002   0.000   0.000
  3   0.009   0.000   0.000   0.000
  4   0.000   0.000   0.000   0.000
  5   0.000   0.000   0.000   0.000
  6   0.000   0.000   0.000   0.000
```

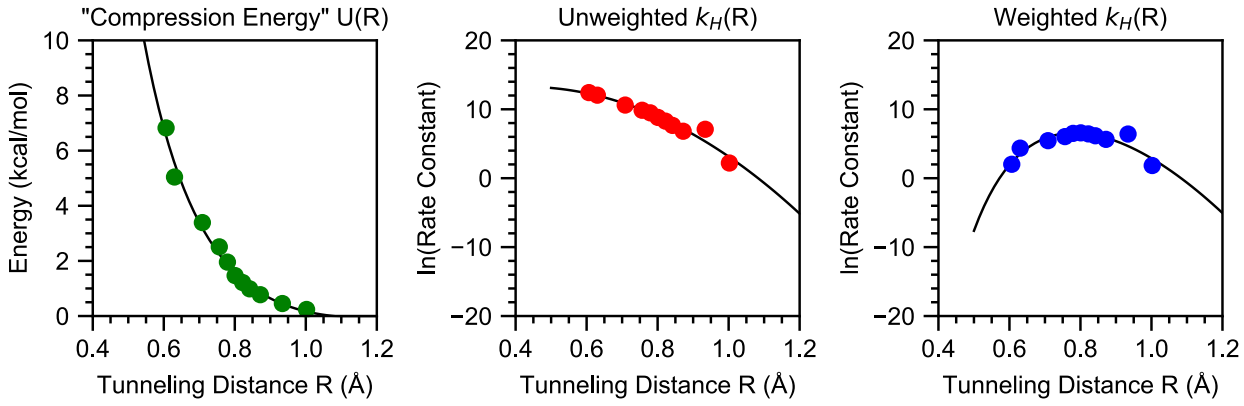

Calculation A3.2 $U(R)$, $k(R)$, and $(\ln k\text{-}U/k_BT)(R)$ and their fits at 330 K for fluorene.

```
Substrate is Fluorene
At T = 330 K, kH = 4.45e+02
Reaction DG = 0.35 kcal/mol
Uncorrected DG = -7.55 kcal/mol
Uncorrected heavy DG = -4.11 kcal/mol
MECP/Reorganized DG = 6.12 kcal/mol
Reorganization Energy = 32.17 kcal/mol

  U(R) =  10.3289/R**2 + -17.5557/R +   7.3962
lnk(R) = -30.7382*R**2 +  26.1949*R +   7.6839
  F    R (A)     U(R)       kH(R)      P*kH(R)
001    1.002     0.24    9.034e+00    6.286e+00
003    0.934     0.45    1.212e+03    6.075e+02
005    0.872     0.77    9.109e+02    2.801e+02
006    0.842     0.99    2.120e+03    4.719e+02
007    0.822     1.21    3.945e+03    6.196e+02
008    0.801     1.47    6.752e+03    7.215e+02
010    0.779     1.96    1.315e+04    6.676e+02
012    0.756     2.51    1.914e+04    4.174e+02
015    0.709     3.39    4.063e+04    2.316e+02
020    0.630     5.04    1.705e+05    7.827e+01
025    0.606     6.82    2.480e+05    7.536e+00
Opt H 0.783     1.82    1.149e+04    7.144e+02
Forces (F) are in atomic units, distances (R) are in Å, energies (U(R)) are in
kcal/mol, and rate constants (k(R) and P*k(R)) are in s**-1.

Fraction of kH from reactant state u to product state v near the optimal tunneling
distance
R = 0.801, force = 008, U(R) = 1.47
total rate = 6.75e+03, average overlap squared = 3.64e-01
  u\v     0       1       2       3
  0    0.009   0.000   0.000   0.000
  1    0.050   0.001   0.000   0.000
  2    0.796   0.004   0.000   0.000
  3    0.136   0.000   0.000   0.000
  4    0.004   0.000   0.000   0.000
  5    0.000   0.000   0.000   0.000
  6    0.000   0.000   0.000   0.000
```

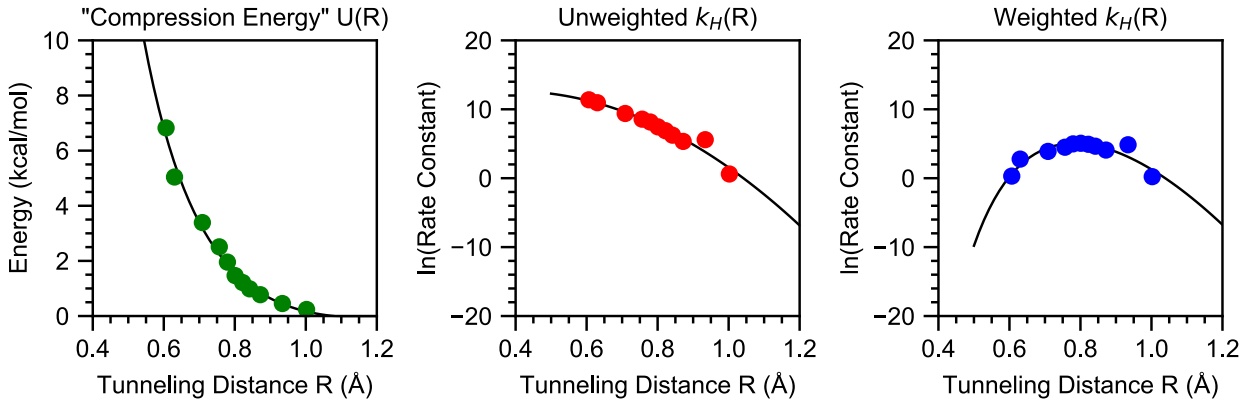

Calculation A3.3 $U(R)$, $k(R)$, and $(\ln k\text{-}U/k_BT)(R)$) and their fits at 310 K for fluorene.

```
Substrate is Fluorene
At T = 310 K, kH = 9.76e+01
Reaction DG = 0.44 kcal/mol
Uncorrected DG = -7.46 kcal/mol
Uncorrected heavy DG = -4.11 kcal/mol
MECP/Reorganized DG = 6.11 kcal/mol
Reorganization Energy = 32.14 kcal/mol

  U(R) =  10.3289/R**2 + -17.5557/R +   7.3962
lnk(R) = -29.4266*R**2 +  22.7097*R +   8.2702
  F    R (A)     U(R)       kH(R)      P*kH(R)
001    1.002     0.24   1.840e+00   1.250e+00
003    0.934     0.45   2.672e+02   1.281e+02
005    0.872     0.77   2.085e+02   5.941e+01
006    0.842     0.99   5.140e+02   1.038e+02
007    0.822     1.21   9.840e+02   1.372e+02
008    0.801     1.47   1.718e+03   1.589e+02
010    0.779     1.96   3.477e+03   1.456e+02
012    0.756     2.51   5.246e+03   8.940e+01
015    0.709     3.39   1.197e+04   4.891e+01
020    0.630     5.04   5.712e+04   1.597e+01
025    0.606     6.82   8.731e+04   1.356e+00
Opt H 0.783     1.82   3.013e+03   1.566e+02
Forces (F) are in atomic units, distances (R) are in Å, energies (U(R)) are in
kcal/mol, and rate constants (k(R) and P*k(R)) are in s**-1.

Fraction of kH from reactant state u to product state v near the optimal tunneling
distance
R = 0.801, force = 008, U(R) = 1.47
total rate = 1.72e+03, average overlap squared = 3.59e-01
  u\v     0       1       2       3
  0   0.014   0.000   0.000   0.000
  1   0.061   0.001   0.000   0.000
  2   0.795   0.003   0.000   0.000
  3   0.122   0.000   0.000   0.000
  4   0.003   0.000   0.000   0.000
  5   0.000   0.000   0.000   0.000
  6   0.000   0.000   0.000   0.000
```

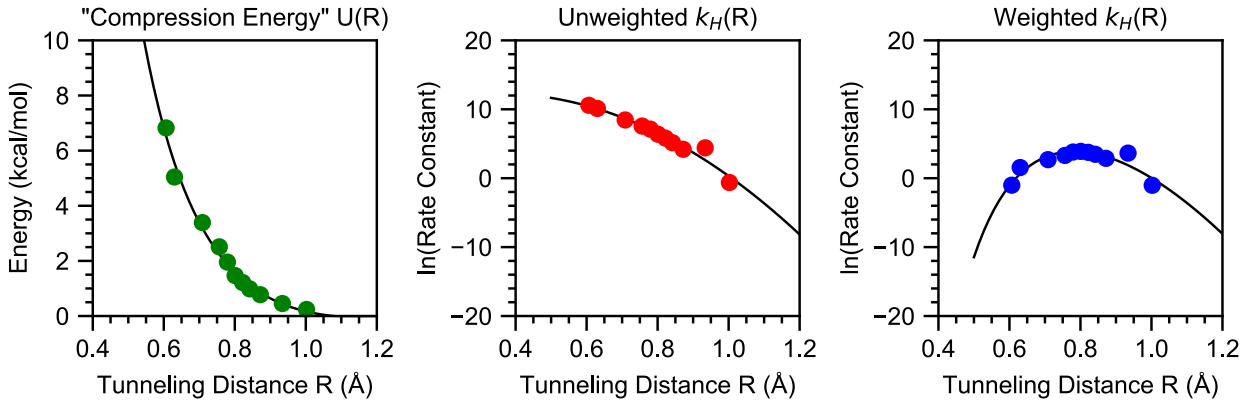

Calculation A3.4 $U(R)$, $k(R)$, and $(\ln k\text{-}U/k_BT)(R)$ their fits at 296 K for fluorene.

```
Substrate is Fluorene
At T = 296 K, kH = 3.01e+01
Reaction DG = 0.49 kcal/mol
Uncorrected DG = -7.41 kcal/mol
Uncorrected heavy DG = -4.11 kcal/mol
MECP/Reorganized DG = 6.11 kcal/mol
Reorganization Energy = 32.12 kcal/mol

  U(R) =  10.3289/R**2 + -17.5557/R +   7.3962
lnk(R) = -28.2675*R**2 +  19.7327*R +   8.8535
  F    R (A)     U(R)       kH(R)      P*kH(R)
001    1.002     0.24   5.347e-01    3.569e-01
003    0.934     0.45   8.219e+01    3.806e+01
005    0.872     0.77   6.623e+01    1.779e+01
006    0.842     0.99   1.710e+02    3.201e+01
007    0.822     1.21   3.349e+02    4.253e+01
008    0.801     1.47   5.938e+02    4.908e+01
010    0.779     1.96   1.240e+03    4.471e+01
012    0.756     2.51   1.930e+03    2.713e+01
015    0.709     3.39   4.685e+03    1.476e+01
020    0.630     5.04   2.475e+04    4.699e+00
025    0.606     6.82   3.936e+04    3.622e-01
Opt H 0.783     1.82   1.068e+03    4.826e+01
Forces (F) are in atomic units, distances (R) are in Å, energies (U(R)) are in
kcal/mol, and rate constants (k(R) and P*k(R)) are in s**-1.

Fraction of kH from reactant state u to product state v near the optimal tunneling
distance
R = 0.801, force = 008, U(R) = 1.47
total rate = 5.94e+02, average overlap squared = 3.54e-01
  u\v     0       1       2       3
  0   0.021   0.000   0.000   0.000
  1   0.071   0.001   0.000   0.000
  2   0.790   0.002   0.000   0.000
  3   0.112   0.000   0.000   0.000
  4   0.002   0.000   0.000   0.000
  5   0.000   0.000   0.000   0.000
  6   0.000   0.000   0.000   0.000
```

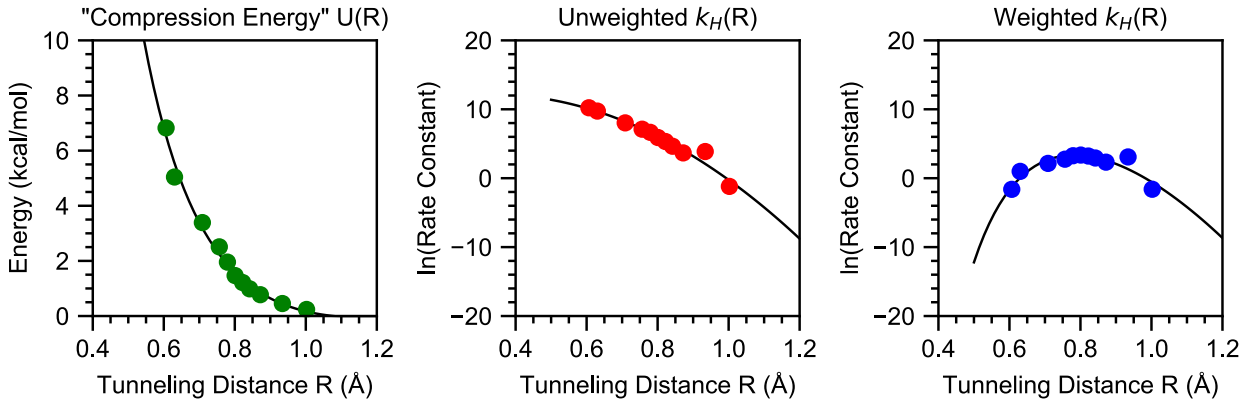

Calculation A3.5 $U(R)$, $k(R)$, and $(\ln k\text{-}U/k_BT)(R)$ and their fits at 290 K for fluorene.

```
Substrate is Fluorene
At T = 290 K, kH = 1.76e+01
Reaction DG = 0.52 kcal/mol
Uncorrected DG = -7.38 kcal/mol
Uncorrected heavy DG = -4.11 kcal/mol
MECP/Reorganized DG = 6.10 kcal/mol
Reorganization Energy = 32.11 kcal/mol

  U(R) =  10.3289/R**2 + -17.5557/R +   7.3962
lnk(R) = -27.7111*R**2 +  18.3156*R +   9.1493
  F    R (A)     U(R)       kH(R)      P*kH(R)
001    1.002     0.24   3.041e-01    2.013e-01
003    0.934     0.45   4.790e+01    2.183e+01
005    0.872     0.77   3.923e+01    1.025e+01
006    0.842     0.99   1.034e+02    1.871e+01
007    0.822     1.21   2.048e+02    2.492e+01
008    0.801     1.47   3.657e+02    2.871e+01
010    0.779     1.96   7.754e+02    2.609e+01
012    0.756     2.51   1.225e+03    1.576e+01
015    0.709     3.39   3.064e+03    8.565e+00
020    0.630     5.04   1.696e+04    2.697e+00
025    0.606     6.82   2.747e+04    1.988e-01
Opt H 0.783     1.82   6.659e+02    2.822e+01
Forces (F) are in atomic units, distances (R) are in Å, energies (U(R)) are in
kcal/mol, and rate constants (k(R) and P*k(R)) are in s**-1.

Fraction of kH from reactant state u to product state v near the optimal tunneling
distance
R = 0.801, force = 008, U(R) = 1.47
total rate = 3.66e+02, average overlap squared = 3.51e-01
  u\v     0       1       2       3
  0   0.025   0.000   0.000   0.000
  1   0.076   0.001   0.000   0.000
  2   0.786   0.002   0.000   0.000
  3   0.108   0.000   0.000   0.000
  4   0.002   0.000   0.000   0.000
  5   0.000   0.000   0.000   0.000
  6   0.000   0.000   0.000   0.000
```

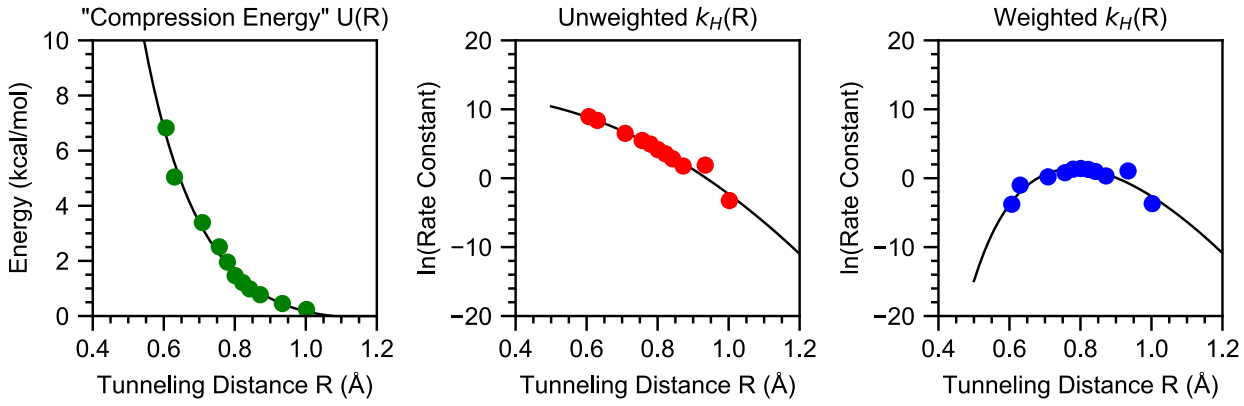

Calculation A3.6 $U(R)$, $k(R)$, and $(\ln k\text{-}U/k_BT)(R)$ and their fits at 270 K for fluorene.

```
Substrate is Fluorene
At T = 270 K, kH = 2.51e+00
Reaction DG = 0.60 kcal/mol
Uncorrected DG = -7.30 kcal/mol
Uncorrected heavy DG = -4.11 kcal/mol
MECP/Reorganized DG = 6.10 kcal/mol
Reorganization Energy = 32.07 kcal/mol

  U(R) =  10.3289/R**2 + -17.5557/R +   7.3962
lnk(R) = -25.6525*R**2 +  13.0301*R +  10.3163
  F    R (A)     U(R)       kH(R)      P*kH(R)
001    1.002     0.24   3.901e-02    2.504e-02
003    0.934     0.45   6.668e+00    2.867e+00
005    0.872     0.77   5.842e+00    1.382e+00
006    0.842     0.99   1.670e+01    2.662e+00
007    0.822     1.21   3.440e+01    3.581e+00
008    0.801     1.47   6.304e+01    4.098e+00
010    0.779     1.96   1.417e+02    3.708e+00
012    0.756     2.51   2.378e+02    2.216e+00
015    0.709     3.39   6.693e+02    1.211e+00
020    0.630     5.04   4.382e+03    3.645e-01
025    0.606     6.82   7.568e+03    2.280e-02
Opt H 0.782     1.84   1.238e+02    4.042e+00
Forces (F) are in atomic units, distances (R) are in Å, energies (U(R)) are in
kcal/mol, and rate constants (k(R) and P*k(R)) are in s**-1.

Fraction of kH from reactant state u to product state v near the optimal tunneling
distance
R = 0.801, force = 008, U(R) = 1.47
total rate = 6.30e+01, average overlap squared = 3.37e-01
  u\v     0       1       2       3
  0   0.048   0.000   0.000   0.000
  1   0.095   0.000   0.000   0.000
  2   0.763   0.001   0.000   0.000
  3   0.091   0.000   0.000   0.000
  4   0.001   0.000   0.000   0.000
  5   0.000   0.000   0.000   0.000
  6   0.000   0.000   0.000   0.000
```

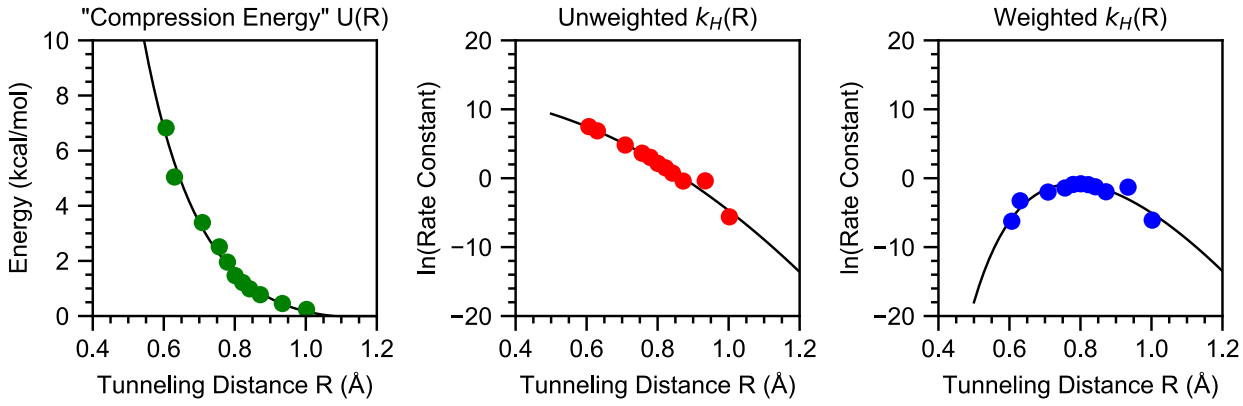

Calculation A3.7 $U(R)$, $k(R)$, and $(\ln k\text{-}U/k_BT)(R)$ and their fits at 250 K for fluorene.

```
Substrate is Fluorene
At T = 250 K, kH = 2.74e-01
Reaction DG = 0.67 kcal/mol
Uncorrected DG = -7.23 kcal/mol
Uncorrected heavy DG = -4.11 kcal/mol
MECP/Reorganized DG = 6.09 kcal/mol
Reorganization Energy = 32.04 kcal/mol

  U(R) =  10.3289/R**2 + -17.5557/R +   7.3962
lnk(R) = -23.5795*R**2 +   7.2794*R +  11.6098
  F    R (A)     U(R)       kH(R)      P*kH(R)
001    1.002     0.24   3.668e-03    2.273e-03
003    0.934     0.45   6.793e-01    2.730e-01
005    0.872     0.77   6.612e-01    1.394e-01
006    0.842     0.99   2.088e+00    2.872e-01
007    0.822     1.21   4.507e+00    3.915e-01
008    0.801     1.47   8.505e+00    4.444e-01
010    0.779     1.96   2.063e+01    4.035e-01
012    0.756     2.51   3.760e+01    2.411e-01
015    0.709     3.39   1.229e+02    1.341e-01
020    0.630     5.04   9.611e+02    3.770e-02
025    0.606     6.82   1.777e+03    1.935e-03
Opt H 0.780     1.87   1.895e+01    4.437e-01
Forces (F) are in atomic units, distances (R) are in Å, energies (U(R)) are in
kcal/mol, and rate constants (k(R) and P*k(R)) are in s**-1.

Fraction of kH from reactant state u to product state v near the optimal tunneling
distance
R = 0.801, force = 008, U(R) = 1.47
total rate = 8.51e+00, average overlap squared = 3.10e-01
  u\v     0       1       2       3
  0   0.095   0.000   0.000   0.000
  1   0.119   0.000   0.000   0.000
  2   0.710   0.001   0.000   0.000
  3   0.073   0.000   0.000   0.000
  4   0.001   0.000   0.000   0.000
  5   0.000   0.000   0.000   0.000
  6   0.000   0.000   0.000   0.000
```

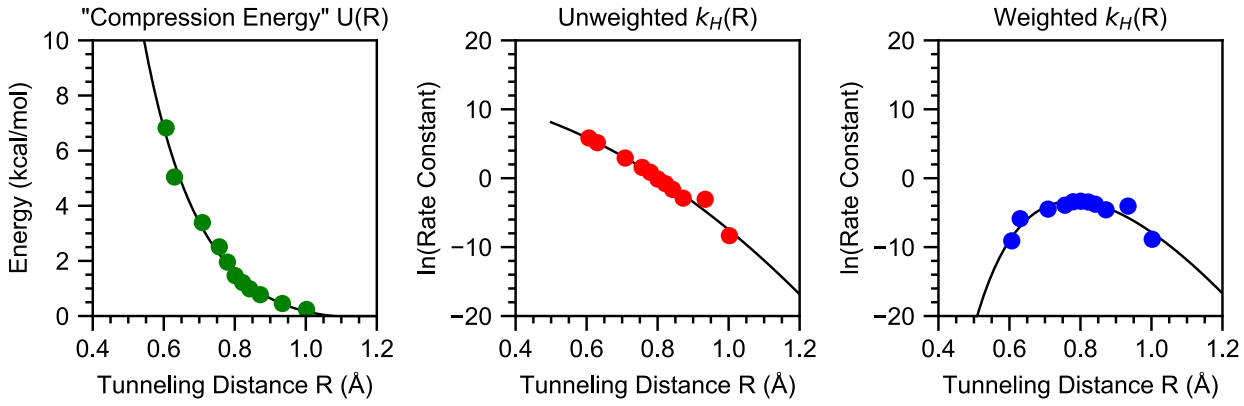

Calculation A3.8 $U(R)$, $k(R)$, and $(\ln k\text{-}U/k_BT)(R)$ and their fits at 230 K for fluorene.

```
Substrate is Fluorene
At T = 230 K, kH = 2.21e-02
Reaction DG = 0.74 kcal/mol
Uncorrected DG = -7.16 kcal/mol
Uncorrected heavy DG = -4.11 kcal/mol
MECP/Reorganized DG = 6.08 kcal/mol
Reorganization Energy = 32.00 kcal/mol

  U(R) =  10.3289/R**2 + -17.5557/R +   7.3962
lnk(R) = -22.4381*R**2 +   2.4886*R +  12.4760
  F    R (A)     U(R)       kH(R)      P*kH(R)
001    1.002     0.24   2.380e-04   1.414e-04
003    0.934     0.45   4.692e-02   1.742e-02
005    0.872     0.77   5.533e-02   1.019e-02
006    0.842     0.99   1.974e-01   2.285e-02
007    0.822     1.21   4.507e-01   3.166e-02
008    0.801     1.47   8.776e-01   3.547e-02
010    0.779     1.96   2.360e+00   3.279e-02
012    0.756     2.51   4.804e+00   1.986e-02
015    0.709     3.39   1.867e+01   1.126e-02
020    0.630     5.04   1.728e+02   2.805e-03
025    0.606     6.82   3.412e+02   1.126e-04
Opt H 0.778     1.90   2.295e+00   3.634e-02
Forces (F) are in atomic units, distances (R) are in Å, energies (U(R)) are in
kcal/mol, and rate constants (k(R) and P*k(R)) are in s**-1.

Fraction of kH from reactant state u to product state v near the optimal tunneling
distance
R = 0.779, force = 010, U(R) = 1.96
total rate = 2.36e+00, average overlap squared = 2.24e-01
  u\v     0       1       2       3
  0   0.267   0.000   0.000   0.000
  1   0.168   0.000   0.000   0.000
  2   0.535   0.000   0.000   0.000
  3   0.028   0.000   0.000   0.000
  4   0.000   0.000   0.000   0.000
  5   0.000   0.000   0.000   0.000
  6   0.000   0.000   0.000   0.000
```

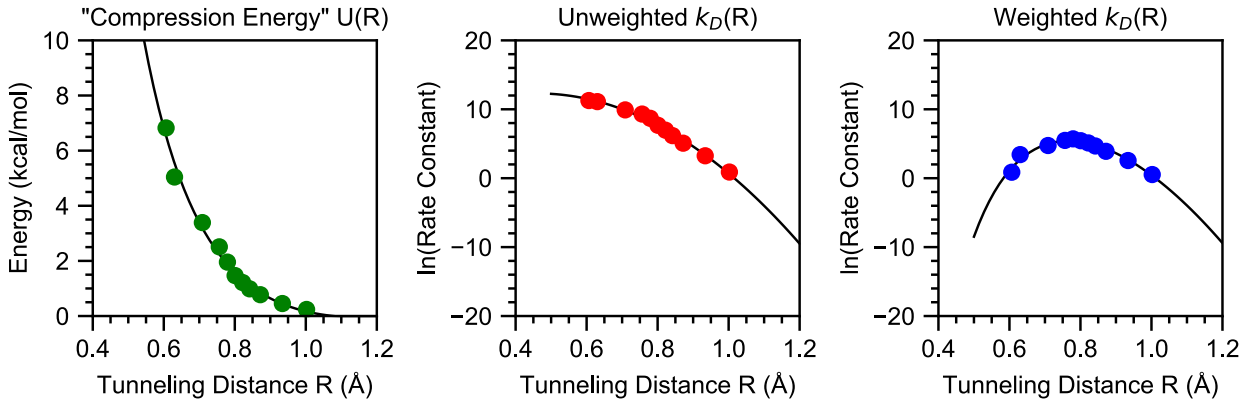

Calculation A3.9 $U(R)$, $k(R)$, and $(\ln k\text{-}U/k_BT)(R)$ and their fits at 330 K for deuterated fluorene.

```
Substrate is Fluorene
At T = 330 K, kD = 1.29e+02
Reaction DG = 0.35 kcal/mol
Uncorrected DG = -7.55 kcal/mol
Uncorrected heavy DG = -4.11 kcal/mol
MECP/Reorganized DG = 6.12 kcal/mol
Reorganization Energy = 32.17 kcal/mol

  U(R) =  10.3289/R**2 + -17.5557/R +   7.3962
lnk(R) = -39.8971*R**2 +  36.7608*R +   3.8351
  F    R (A)     U(R)       kD(R)      P*kD(R)
001    1.002     0.24    2.441e+00    1.698e+00
003    0.934     0.45    2.592e+01    1.299e+01
005    0.872     0.77    1.608e+02    4.943e+01
006    0.842     0.99    4.814e+02    1.071e+02
007    0.822     1.21    1.061e+03    1.666e+02
008    0.801     1.47    2.159e+03    2.307e+02
010    0.779     1.96    5.939e+03    3.015e+02
012    0.756     2.51    1.103e+04    2.406e+02
015    0.709     3.39    2.014e+04    1.148e+02
020    0.630     5.04    6.691e+04    3.071e+01
025    0.606     6.82    7.836e+04    2.381e+00
Opt D 0.766     2.08    5.346e+03    2.241e+02
Forces (F) are in atomic units, distances (R) are in Å, energies (U(R)) are in
kcal/mol, and rate constants (k(R) and P*k(R)) are in s**-1.

Fraction of kD from reactant state u to product state v near the optimal tunneling
distance
R = 0.779, force = 010, U(R) = 1.96
total rate = 5.94e+03, average overlap squared = 3.77e-01
  u\v     0       1       2       3
  0   0.000   0.000   0.000   0.000
  1   0.001   0.000   0.000   0.000
  2   0.037   0.003   0.000   0.000
  3   0.799   0.023   0.000   0.000
  4   0.119   0.000   0.000   0.000
  5   0.017   0.000   0.000   0.000
  6   0.001   0.000   0.000   0.000
```

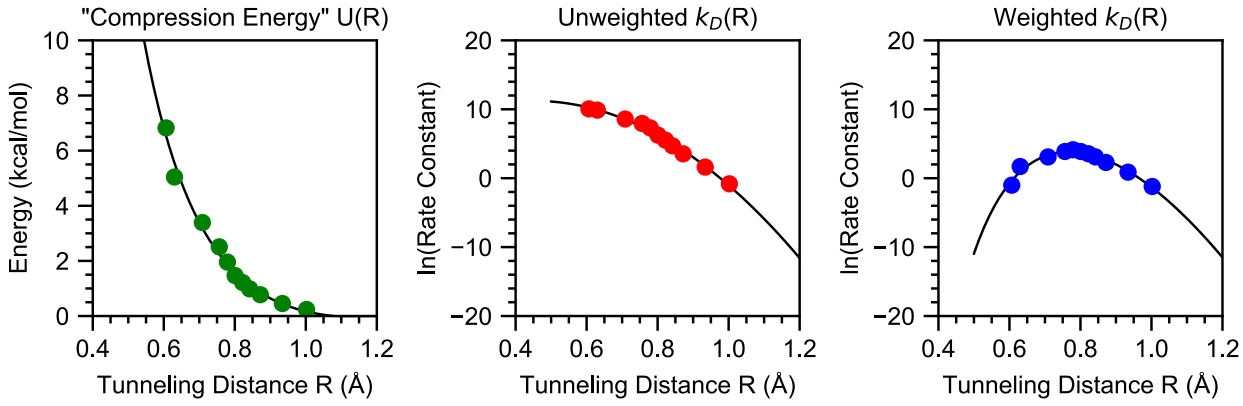

Calculation A3.10 $U(R)$, $k(R)$, and $(\ln k\text{-}U/k_BT)(R)$ and their fits at 310 K for deuterated fluorene.

```
Substrate is Fluorene
At T = 310 K, kD = 2.62e+01
Reaction DG = 0.44 kcal/mol
Uncorrected DG = -7.46 kcal/mol
Uncorrected heavy DG = -4.11 kcal/mol
MECP/Reorganized DG = 6.11 kcal/mol
Reorganization Energy = 32.14 kcal/mol

  U(R) =  10.3289/R**2 + -17.5557/R +   7.3962
lnk(R) = -40.7825*R**2 +  36.8766*R +   2.8814
  F    R (A)     U(R)       kD(R)      P*kD(R)
001    1.002     0.24   4.418e-01    3.003e-01
003    0.934     0.45   5.007e+00    2.401e+00
005    0.872     0.77   3.439e+01    9.799e+00
006    0.842     0.99   1.095e+02    2.212e+01
007    0.822     1.21   2.494e+02    3.476e+01
008    0.801     1.47   5.192e+02    4.803e+01
010    0.779     1.96   1.481e+03    6.201e+01
012    0.756     2.51   2.821e+03    4.806e+01
015    0.709     3.39   5.357e+03    2.188e+01
020    0.630     5.04   1.947e+04    5.443e+00
025    0.606     6.82   2.335e+04    3.627e-01
Opt D 0.768     2.05   1.272e+03    4.576e+01
Forces (F) are in atomic units, distances (R) are in Å, energies (U(R)) are in
kcal/mol, and rate constants (k(R) and P*k(R)) are in s**-1.

Fraction of kD from reactant state u to product state v near the optimal tunneling
distance
R = 0.779, force = 010, U(R) = 1.96
total rate = 1.48e+03, average overlap squared = 3.79e-01
  u\v     0       1       2       3
  0   0.000   0.000   0.000   0.000
  1   0.001   0.000   0.000   0.000
  2   0.041   0.002   0.000   0.000
  3   0.812   0.019   0.000   0.000
  4   0.110   0.000   0.000   0.000
  5   0.013   0.000   0.000   0.000
  6   0.001   0.000   0.000   0.000
```

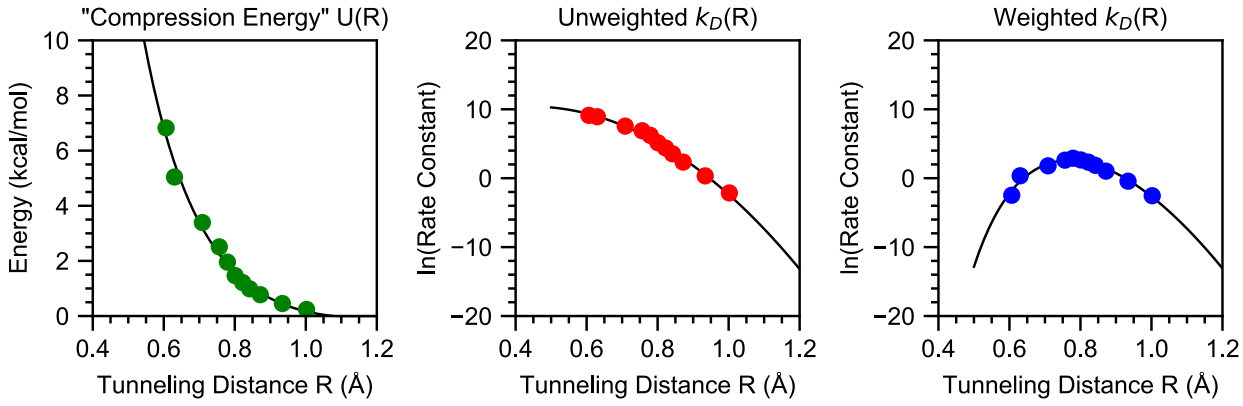

Calculation A3.11 $U(R)$, $k(R)$, and $(\ln k\text{-}U/k_BT)(R)$ and their fits at 296 K for deuterated fluorene.

```
Substrate is Fluorene
At T = 296 K, kD = 7.58e+00
Reaction DG = 0.49 kcal/mol
Uncorrected DG = -7.41 kcal/mol
Uncorrected heavy DG = -4.11 kcal/mol
MECP/Reorganized DG = 6.11 kcal/mol
Reorganization Energy = 32.12 kcal/mol

  U(R) =  10.3289/R**2 + -17.5557/R +   7.3962
lnk(R) = -41.2823*R**2 +  36.6685*R +   2.2562
  F    R (A)     U(R)       kD(R)      P*kD(R)
001    1.002     0.24   1.178e-01    7.861e-02
003    0.934     0.45   1.397e+00    6.470e-01
005    0.872     0.77   1.037e+01    2.784e+00
006    0.842     0.99   3.461e+01    6.481e+00
007    0.822     1.21   8.084e+01    1.027e+01
008    0.801     1.47   1.712e+02    1.415e+01
010    0.779     1.96   5.019e+02    1.809e+01
012    0.756     2.51   9.752e+02    1.371e+01
015    0.709     3.39   1.912e+03    6.021e+00
020    0.630     5.04   7.475e+03    1.419e+00
025    0.606     6.82   9.160e+03    8.428e-02
Opt D 0.769     2.03   4.206e+02    1.328e+01
Forces (F) are in atomic units, distances (R) are in Å, energies (U(R)) are in
kcal/mol, and rate constants (k(R) and P*k(R)) are in s**-1.

Fraction of kD from reactant state u to product state v near the optimal tunneling
distance
R = 0.779, force = 010, U(R) = 1.96
total rate = 5.02e+02, average overlap squared = 3.80e-01
  u\v     0       1       2       3
  0   0.000   0.000   0.000   0.000
  1   0.001   0.000   0.000   0.000
  2   0.044   0.002   0.000   0.000
  3   0.820   0.016   0.000   0.000
  4   0.103   0.000   0.000   0.000
  5   0.011   0.000   0.000   0.000
  6   0.000   0.000   0.000   0.000
```

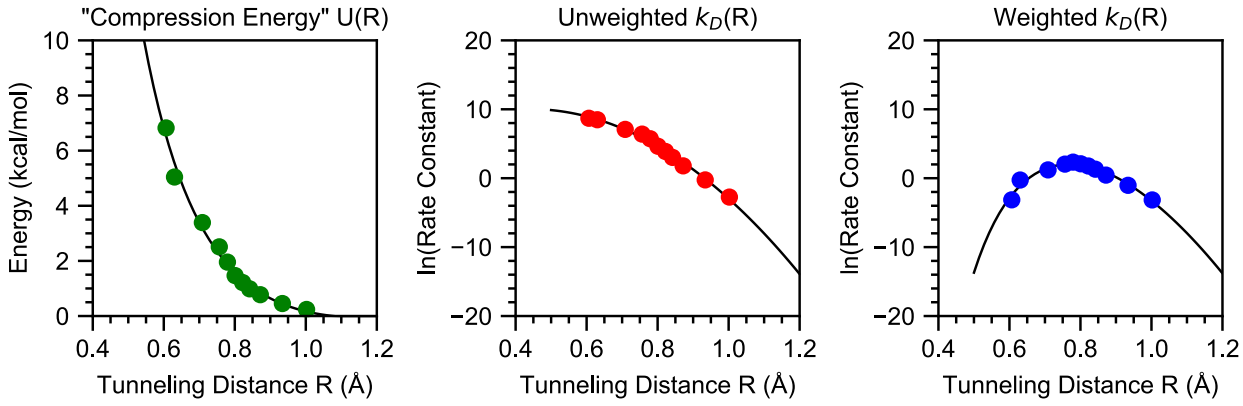

Calculation A3.12 $U(R)$, $k(R)$, and $(\ln k\text{-}U/k_BT)(R)$ and their fits at 290 K for deuterated fluorene.

```
Substrate is Fluorene
At T = 290 K, kD = 4.30e+00
Reaction DG = 0.52 kcal/mol
Uncorrected DG = -7.38 kcal/mol
Uncorrected heavy DG = -4.11 kcal/mol
MECP/Reorganized DG = 6.10 kcal/mol
Reorganization Energy = 32.11 kcal/mol

  U(R) =  10.3289/R**2 + -17.5557/R +   7.3962
lnk(R) = -41.4557*R**2 +  36.4857*R +   2.0049
  F    R (A)     U(R)       kD(R)      P*kD(R)
001    1.002     0.24   6.447e-02   4.267e-02
003    0.934     0.45   7.800e-01   3.555e-01
005    0.872     0.77   5.992e+00   1.566e+00
006    0.842     0.99   2.044e+01   3.698e+00
007    0.822     1.21   4.829e+01   5.877e+00
008    0.801     1.47   1.031e+02   8.090e+00
010    0.779     1.96   3.060e+02   1.030e+01
012    0.756     2.51   5.998e+02   7.719e+00
015    0.709     3.39   1.193e+03   3.337e+00
020    0.630     5.04   4.830e+03   7.679e-01
025    0.606     6.82   5.983e+03   4.331e-02
Opt D 0.769     2.03   2.565e+02   7.542e+00
Forces (F) are in atomic units, distances (R) are in Å, energies (U(R)) are in
kcal/mol, and rate constants (k(R) and P*k(R)) are in s**-1.

Fraction of kD from reactant state u to product state v near the optimal tunneling
distance
R = 0.779, force = 010, U(R) = 1.96
total rate = 3.06e+02, average overlap squared = 3.80e-01
  u\v     0       1       2       3
  0   0.000   0.000   0.000   0.000
  1   0.002   0.000   0.000   0.000
  2   0.046   0.002   0.000   0.000
  3   0.823   0.015   0.000   0.000
  4   0.100   0.000   0.000   0.000
  5   0.011   0.000   0.000   0.000
  6   0.000   0.000   0.000   0.000
```

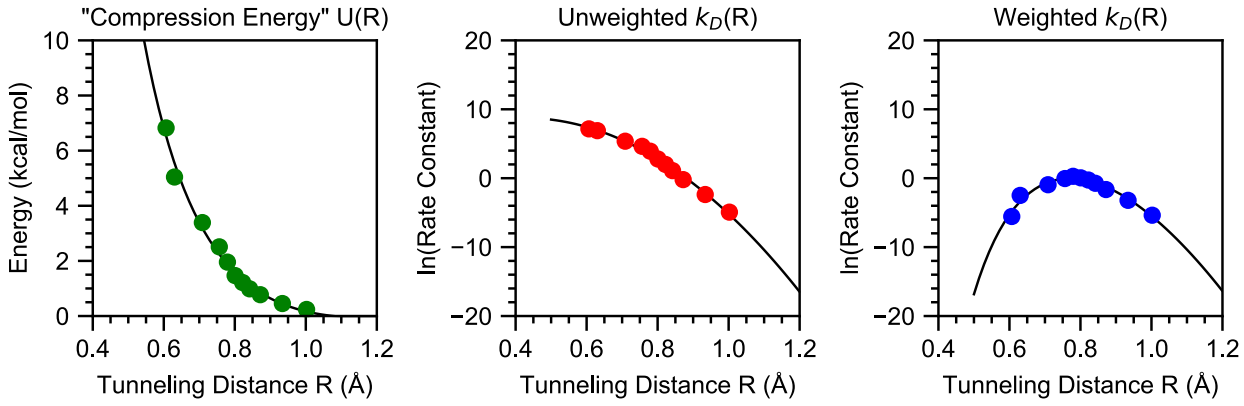

Calculation A3.13 $U(R)$, $k(R)$, and $(\ln k\text{-}U/k_BT)(R)$ and their fits at 270 K for deuterated fluorene.

```
Substrate is Fluorene
At T = 270 K, kD = 5.42e-01
Reaction DG = 0.60 kcal/mol
Uncorrected DG = -7.30 kcal/mol
Uncorrected heavy DG = -4.11 kcal/mol
MECP/Reorganized DG = 6.10 kcal/mol
Reorganization Energy = 32.07 kcal/mol

  U(R) =  10.3289/R**2 + -17.5557/R +   7.3962
lnk(R) = -41.7938*R**2 +  35.3461*R +   1.2784
  F    R (A)     U(R)       kD(R)      P*kD(R)
001    1.002     0.24   7.240e-03   4.647e-03
003    0.934     0.45   9.360e-02   4.025e-02
005    0.872     0.77   8.133e-01   1.924e-01
006    0.842     0.99   3.001e+00   4.782e-01
007    0.822     1.21   7.382e+00   7.686e-01
008    0.801     1.47   1.619e+01   1.052e+00
010    0.779     1.96   5.028e+01   1.316e+00
012    0.756     2.51   1.019e+02   9.498e-01
015    0.709     3.39   2.144e+02   3.878e-01
020    0.630     5.04   9.896e+02   8.231e-02
025    0.606     6.82   1.283e+03   3.865e-03
Opt D 0.770     2.02   4.107e+01   9.575e-01
Forces (F) are in atomic units, distances (R) are in Å, energies (U(R)) are in
kcal/mol, and rate constants (k(R) and P*k(R)) are in s**-1.

Fraction of kD from reactant state u to product state v near the optimal tunneling
distance
R = 0.779, force = 010, U(R) = 1.96
total rate = 5.03e+01, average overlap squared = 3.81e-01
  u\v     0       1       2       3
  0   0.000   0.000   0.000   0.000
  1   0.002   0.000   0.000   0.000
  2   0.052   0.002   0.000   0.000
  3   0.834   0.012   0.000   0.000
  4   0.089   0.000   0.000   0.000
  5   0.008   0.000   0.000   0.000
  6   0.000   0.000   0.000   0.000
```

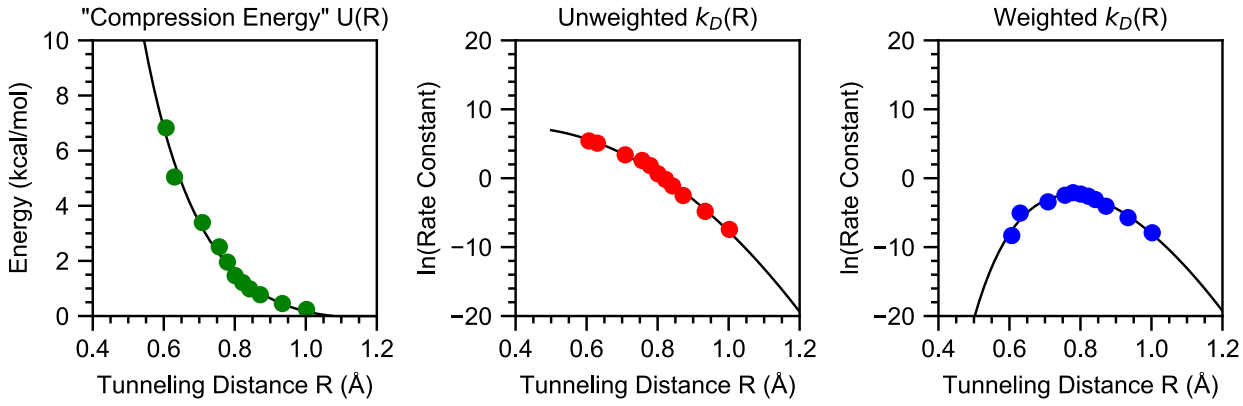

Calculation A3.14 $U(R)$, $k(R)$, and $(\ln k\text{-}U/k_BT)(R)$ and their fits at 250 K for deuterated fluorene.

```
Substrate is Fluorene
At T = 250 K, kD = 4.96e-02
Reaction DG = 0.67 kcal/mol
Uncorrected DG = -7.23 kcal/mol
Uncorrected heavy DG = -4.11 kcal/mol
MECP/Reorganized DG = 6.09 kcal/mol
Reorganization Energy = 32.04 kcal/mol

  U(R) =  10.3289/R**2 + -17.5557/R +   7.3962
lnk(R) = -41.6021*R**2 +  33.0770*R +   0.8263
  F    R (A)     U(R)       kD(R)      P*kD(R)
001    1.002     0.24   5.875e-04   3.640e-04
003    0.934     0.45   8.145e-03   3.274e-03
005    0.872     0.77   8.106e-02   1.709e-02
006    0.842     0.99   3.273e-01   4.503e-02
007    0.822     1.21   8.423e-01   7.317e-02
008    0.801     1.47   1.903e+00   9.945e-02
010    0.779     1.96   6.225e+00   1.217e-01
012    0.756     2.51   1.311e+01   8.409e-02
015    0.709     3.39   2.957e+01   3.227e-02
020    0.630     5.04   1.610e+02   6.316e-03
025    0.606     6.82   2.228e+02   2.427e-04
Opt D 0.772     1.99   4.795e+00   8.810e-02
Forces (F) are in atomic units, distances (R) are in Å, energies (U(R)) are in
kcal/mol, and rate constants (k(R) and P*k(R)) are in s**-1.

Fraction of kD from reactant state u to product state v near the optimal tunneling
distance
R = 0.779, force = 010, U(R) = 1.96
total rate = 6.22e+00, average overlap squared = 3.81e-01
  u\v     0       1       2       3
  0   0.001   0.000   0.000   0.000
  1   0.004   0.000   0.000   0.000
  2   0.060   0.001   0.000   0.000
  3   0.841   0.009   0.000   0.000
  4   0.078   0.000   0.000   0.000
  5   0.006   0.000   0.000   0.000
  6   0.000   0.000   0.000   0.000
```

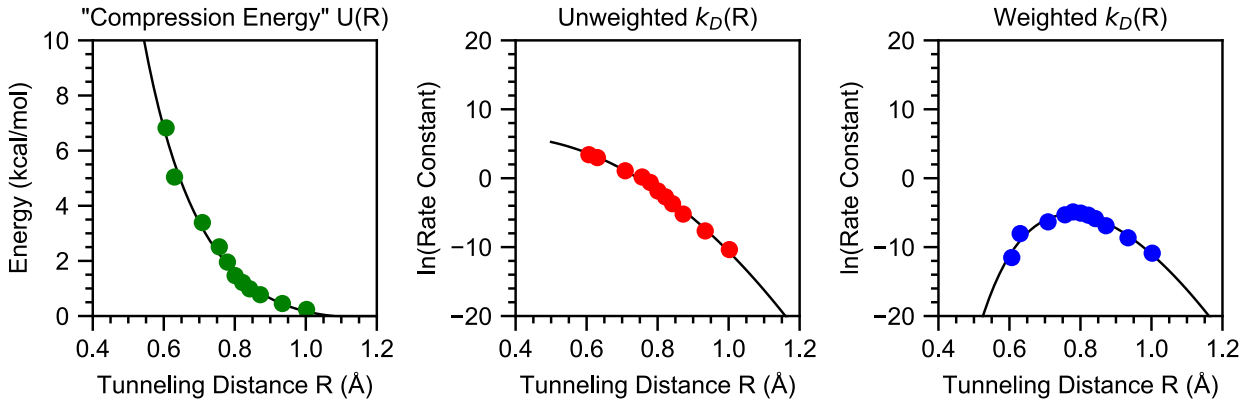

Calculation A3.15 $U(R)$, $k(R)$, and $(\ln k\text{-}U/k_BT)(R)$ and their fits at 230 K for deuterated fluorene.

```
Substrate is Fluorene
At T = 230 K, kD = 3.04e-03
Reaction DG = 0.74 kcal/mol
Uncorrected DG = -7.16 kcal/mol
Uncorrected heavy DG = -4.11 kcal/mol
MECP/Reorganized DG = 6.08 kcal/mol
Reorganization Energy = 32.00 kcal/mol

  U(R) =  10.3289/R**2 + -17.5557/R +   7.3962
lnk(R) = -40.5593*R**2 +  29.0528*R +   0.8697
  F    R (A)     U(R)       kD(R)      P*kD(R)
001    1.002     0.24   3.162e-05   1.879e-05
003    0.934     0.45   4.738e-04   1.759e-04
005    0.872     0.77   5.483e-03   1.010e-03
006    0.842     0.99   2.457e-02   2.845e-03
007    0.822     1.21   6.655e-02   4.675e-03
008    0.801     1.47   1.555e-01   6.286e-03
010    0.779     1.96   5.397e-01   7.498e-03
012    0.756     2.51   1.191e+00   4.924e-03
015    0.709     3.39   2.937e+00   1.771e-03
020    0.630     5.04   1.984e+01   3.221e-04
025    0.606     6.82   3.019e+01   9.966e-06
Opt D 0.773     1.97   4.034e-01   5.415e-03
Forces (F) are in atomic units, distances (R) are in Å, energies (U(R)) are in
kcal/mol, and rate constants (k(R) and P*k(R)) are in s**-1.

Fraction of kD from reactant state u to product state v near the optimal tunneling
distance
R = 0.779, force = 010, U(R) = 1.96
total rate = 5.40e-01, average overlap squared = 3.78e-01
  u\v     0       1       2       3
  0   0.002   0.000   0.000   0.000
  1   0.006   0.000   0.000   0.000
  2   0.071   0.001   0.000   0.000
  3   0.844   0.006   0.000   0.000
  4   0.066   0.000   0.000   0.000
  5   0.004   0.000   0.000   0.000
  6   0.000   0.000   0.000   0.000
```

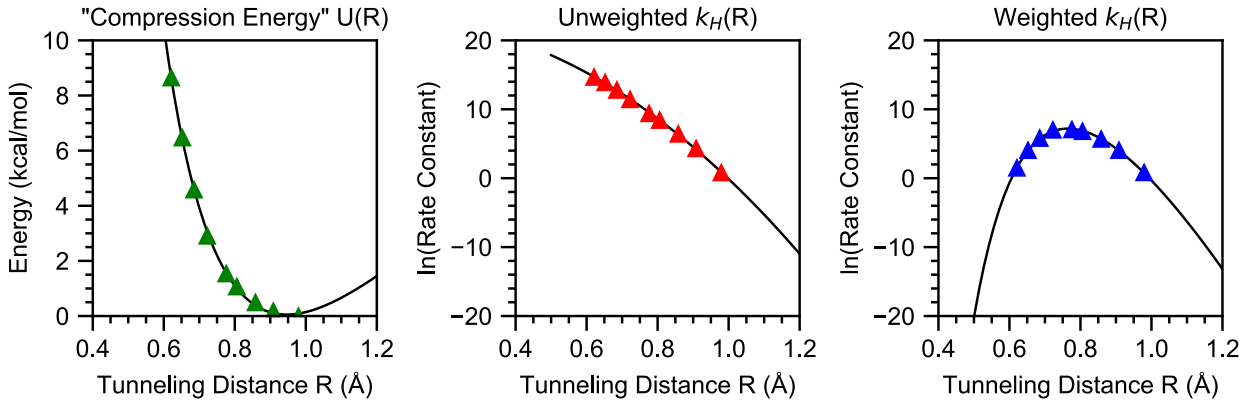

Calculation A3.16 $U(R)$, $k(R)$, and $(\ln k\text{-}U/k_BT)(R)$ and their fits at 330 K for 9,10-dihydroanthracene.

```
Substrate is DHA
At T = 330 K, kH = 7.56e+02
Reaction DG = -4.72 kcal/mol
Uncorrected DG = -12.62 kcal/mol
Uncorrected heavy DG = -9.10 kcal/mol
MECP/Reorganized DG = 3.58 kcal/mol
Reorganization Energy = 29.74 kcal/mol

  U(R) =  27.9964/R**2 + -59.1667/R +  31.3128
lnk(R) = -26.2053*R**2 +   3.3744*R +  22.7140
  F    R (A)     U(R)        kH(R)      P*kH(R)
001    0.979    -0.01    2.205e+00    2.238e+00
003    0.909     0.17    7.328e+01    5.649e+01
005    0.858     0.48    6.043e+02    2.890e+02
008    0.806     1.06    4.458e+03    8.860e+02
010    0.776     1.53    1.180e+04    1.140e+03
015    0.722     2.90    9.020e+04    1.081e+03
020    0.685     4.58    3.522e+05    3.285e+02
025    0.652     6.46    1.066e+06    5.601e+01
030    0.621     8.64    2.309e+06    4.384e+00
Opt H 0.765     1.81    2.115e+04    1.342e+03
Forces (F) are in atomic units, distances (R) are in Å, energies (U(R)) are in
kcal/mol, and rate constants (k(R) and P*k(R)) are in s**-1.

Fraction of kH from reactant state u to product state v near the optimal tunneling
distance
R = 0.776, force = 010, U(R) = 1.53
total rate = 1.18e+04, average overlap squared = 9.28e-02
  u\v     0        1        2        3
  0    0.312    0.017    0.000    0.000
  1    0.194    0.013    0.000    0.000
  2    0.284    0.011    0.000    0.000
  3    0.162    0.003    0.000    0.000
  4    0.002    0.000    0.000    0.000
  5    0.000    0.000    0.000    0.000
  6    0.000    0.000    0.000    0.000
```

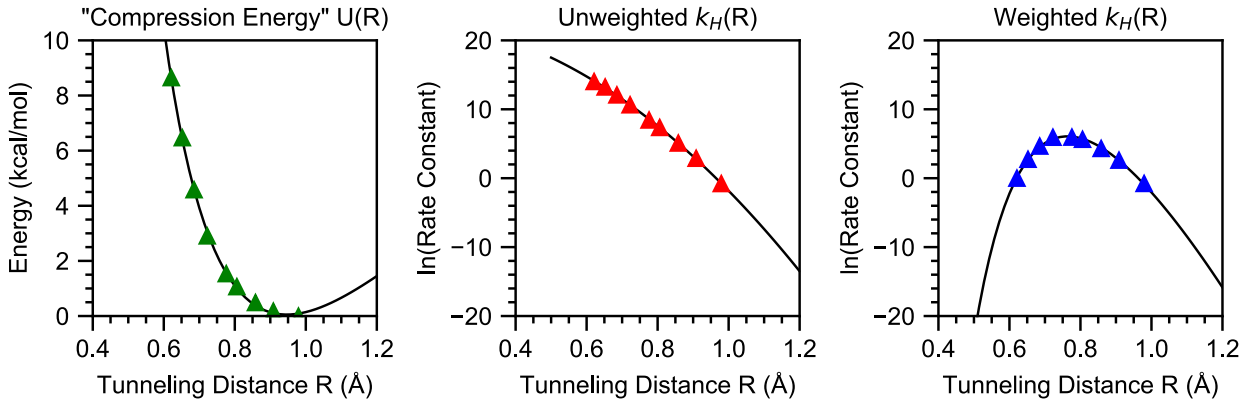

Calculation A3.17 $U(R)$, $k(R)$, and $(\ln k\text{-}U/k_BT)(R)$ and their fits at 310 K for 9,10-dihydroanthracene.

```
Substrate is DHA
At T = 310 K, kH = 2.44e+02
Reaction DG = -4.64 kcal/mol
Uncorrected DG = -12.54 kcal/mol
Uncorrected heavy DG = -9.10 kcal/mol
MECP/Reorganized DG = 3.57 kcal/mol
Reorganization Energy = 29.69 kcal/mol

  U(R) =  27.9964/R**2 + -59.1667/R +  31.3128
lnk(R) = -28.1396*R**2 +   3.5490*R +  22.7614
  F    R (A)     U(R)        kH(R)      P*kH(R)
001    0.979    -0.01    4.504e-01    4.576e-01
003    0.909     0.17    1.769e+01    1.341e+01
005    0.858     0.48    1.609e+02    7.339e+01
008    0.806     1.06    1.545e+03    2.766e+02
010    0.776     1.53    4.558e+03    3.789e+02
015    0.722     2.90    4.139e+04    3.728e+02
020    0.685     4.58    1.740e+05    1.035e+02
025    0.652     6.46    5.496e+05    1.529e+01
030    0.621     8.64    1.215e+06    9.855e-01
Opt H 0.764     1.83    8.501e+03    4.340e+02
Forces (F) are in atomic units, distances (R) are in Å, energies (U(R)) are in
kcal/mol, and rate constants (k(R) and P*k(R)) are in s**-1.

Fraction of kH from reactant state u to product state v near the optimal tunneling
distance
R = 0.776, force = 010, U(R) = 1.53
total rate = 4.56e+03, average overlap squared = 5.92e-02
  u\v     0        1        2        3
  0    0.465    0.017    0.000    0.000
  1    0.195    0.010    0.000    0.000
  2    0.204    0.006    0.000    0.000
  3    0.100    0.001    0.000    0.000
  4    0.001    0.000    0.000    0.000
  5    0.000    0.000    0.000    0.000
  6    0.000    0.000    0.000    0.000
```

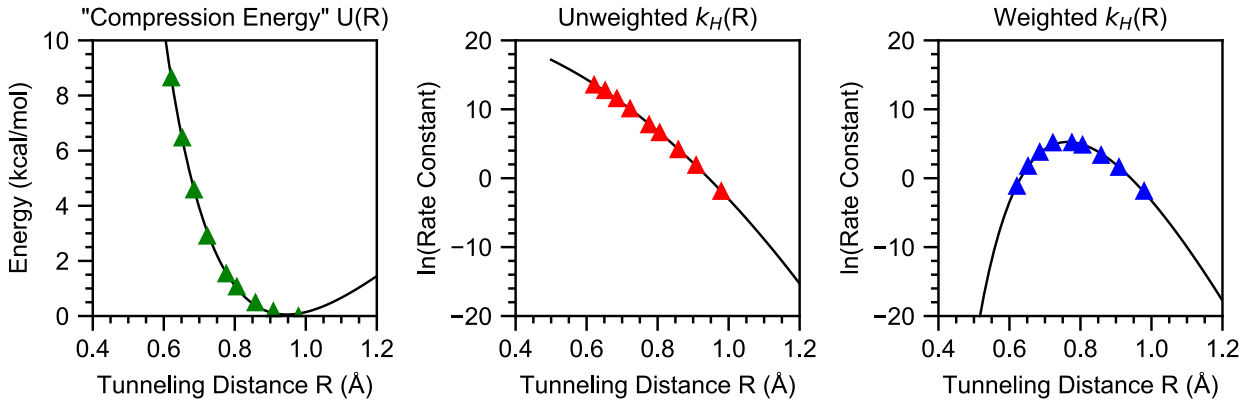

Calculation A3.18 $U(R)$, $k(R)$, and $(\ln k\text{-}U/k_BT)(R)$ and their fits at 296 K for 296 K for 9,10-dihydroanthracene.

```
Substrate is DHA
At T = 296 K, kH = 1.09e+02
Reaction DG = -4.59 kcal/mol
Uncorrected DG = -12.49 kcal/mol
Uncorrected heavy DG = -9.10 kcal/mol
MECP/Reorganized DG = 3.56 kcal/mol
Reorganization Energy = 29.65 kcal/mol

  U(R) =  27.9964/R**2 + -59.1667/R +  31.3128
lnk(R) = -29.9791*R**2 +   4.5570*R +  22.3990
  F   R (A)    U(R)       kH(R)     P*kH(R)
001   0.979   -0.01   1.500e-01   1.525e-01
003   0.909    0.17   6.537e+00   4.891e+00
005   0.858    0.48   6.350e+01   2.790e+01
008   0.806    1.06   7.469e+02   1.233e+02
010   0.776    1.53   2.359e+03   1.743e+02
015   0.722    2.90   2.373e+04   1.711e+02
020   0.685    4.58   1.040e+05   4.354e+01
025   0.652    6.46   3.366e+05   5.703e+00
030   0.621    8.64   7.508e+05   3.138e-01
Opt H 0.764    1.83   4.367e+03   1.937e+02
Forces (F) are in atomic units, distances (R) are in Å, energies (U(R)) are in
kcal/mol, and rate constants (k(R) and P*k(R)) are in s**-1.

Fraction of kH from reactant state u to product state v near the optimal tunneling
distance
R = 0.776, force = 010, U(R) = 1.53
total rate = 2.36e+03, average overlap squared = 3.85e-02
  u\v     0       1       2       3
  0   0.583   0.016   0.000   0.000
  1   0.181   0.007   0.000   0.000
  2   0.145   0.004   0.000   0.000
  3   0.063   0.001   0.000   0.000
  4   0.001   0.000   0.000   0.000
  5   0.000   0.000   0.000   0.000
  6   0.000   0.000   0.000   0.000
```

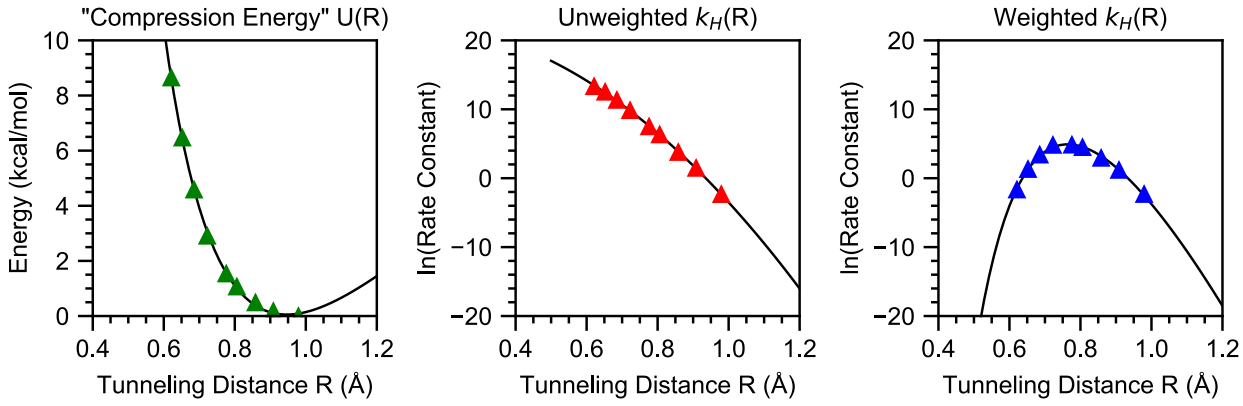

Calculation A3.19 $U(R)$, $k(R)$, and $(\ln k\text{-}U/k_BT)(R)$ and their fits at 290 K for 9,10-dihydroanthracene.

```
Substrate is DHA
At T = 290 K, kH = 7.70e+01
Reaction DG = -4.56 kcal/mol
Uncorrected DG = -12.46 kcal/mol
Uncorrected heavy DG = -9.10 kcal/mol
MECP/Reorganized DG = 3.56 kcal/mol
Reorganization Energy = 29.63 kcal/mol

  U(R) =  27.9964/R**2 + -59.1667/R +  31.3128
lnk(R) = -30.7014*R**2 +   4.9743*R +  22.2171
  F    R (A)    U(R)       kH(R)     P*kH(R)
001    0.979   -0.01   9.579e-02   9.741e-02
003    0.909    0.17   4.323e+00   3.215e+00
005    0.858    0.48   4.301e+01   1.858e+01
008    0.806    1.06   5.508e+02   8.758e+01
010    0.776    1.53   1.783e+03   1.249e+02
015    0.722    2.90   1.863e+04   1.213e+02
020    0.685    4.58   8.289e+04   2.953e+01
025    0.652    6.46   2.706e+05   3.652e+00
030    0.621    8.64   6.052e+05   1.867e-01
Opt H 0.764    1.83   3.285e+03   1.366e+02
Forces (F) are in atomic units, distances (R) are in Å, energies (U(R)) are in
kcal/mol, and rate constants (k(R) and P*k(R)) are in s**-1.

Fraction of kH from reactant state u to product state v near the optimal tunneling
distance
R = 0.776, force = 010, U(R) = 1.53
total rate = 1.78e+03, average overlap squared = 3.09e-02
  u\v     0       1       2       3
  0   0.634   0.015   0.000   0.000
  1   0.170   0.006   0.000   0.000
  2   0.121   0.003   0.000   0.000
  3   0.050   0.001   0.000   0.000
  4   0.000   0.000   0.000   0.000
  5   0.000   0.000   0.000   0.000
  6   0.000   0.000   0.000   0.000
```

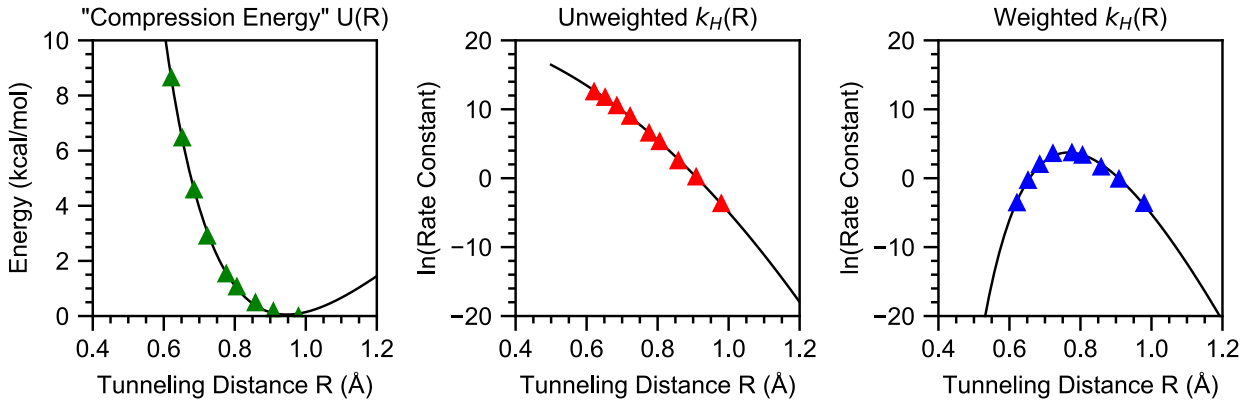

Calculation A3.20 $U(R)$, $k(R)$, and $(\ln k\text{-}U/k_BT)(R)$ and their fits at 270 K for 9,10-dihydroanthracene.

```
Substrate is DHA
At T = 270 K, kH = 2.40e+01
Reaction DG = -4.50 kcal/mol
Uncorrected DG = -12.40 kcal/mol
Uncorrected heavy DG = -9.10 kcal/mol
MECP/Reorganized DG = 3.55 kcal/mol
Reorganization Energy = 29.58 kcal/mol

  U(R) =  27.9964/R**2 + -59.1667/R +  31.3128
lnk(R) = -31.9974*R**2 +   5.2126*R +  21.8441
  F    R (A)    U(R)       kH(R)     P*kH(R)
001    0.979   -0.01   2.535e-02   2.582e-02
003    0.909    0.17   1.211e+00   8.815e-01
005    0.858    0.48   1.264e+01   5.131e+00
008    0.806    1.06   2.051e+02   2.846e+01
010    0.776    1.53   7.034e+02   4.045e+01
015    0.722    2.90   8.091e+03   3.627e+01
020    0.685    4.58   3.740e+04   7.400e+00
025    0.652    6.46   1.251e+05   7.357e-01
030    0.621    8.64   2.810e+05   2.855e-02
Opt H 0.767    1.76   1.117e+03   4.194e+01
Forces (F) are in atomic units, distances (R) are in Å, energies (U(R)) are in
kcal/mol, and rate constants (k(R) and P*k(R)) are in s**-1.

Fraction of kH from reactant state u to product state v near the optimal tunneling
distance
R = 0.776, force = 010, U(R) = 1.53
total rate = 7.03e+02, average overlap squared = 1.28e-02
  u\v     0       1       2       3
  0   0.782   0.011   0.000   0.000
  1   0.126   0.003   0.000   0.000
  2   0.057   0.001   0.000   0.000
  3   0.020   0.000   0.000   0.000
  4   0.000   0.000   0.000   0.000
  5   0.000   0.000   0.000   0.000
  6   0.000   0.000   0.000   0.000
```

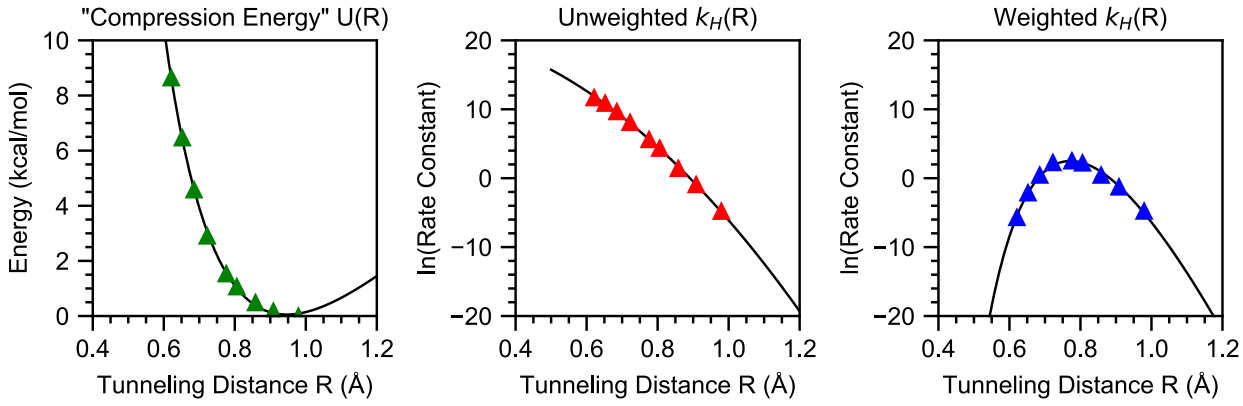

Calculation A3.21 $U(R)$, $k(R)$, and $(\ln k\text{-}U/k_BT)(R)$ and their fits at 250 K for 9,10-dihydroanthracene.

```
Substrate is DHA
At T = 250 K, kH = 7.22e+00
Reaction DG = -4.43 kcal/mol
Uncorrected DG = -12.33 kcal/mol
Uncorrected heavy DG = -9.10 kcal/mol
MECP/Reorganized DG = 3.53 kcal/mol
Reorganization Energy = 29.52 kcal/mol

  U(R) =  27.9964/R**2 + -59.1667/R +  31.3128
lnk(R) = -31.7834*R**2 +   3.9581*R +  21.7105
  F    R (A)    U(R)       kH(R)     P*kH(R)
001    0.979   -0.01   8.249e-03   8.412e-03
003    0.909    0.17   3.942e-01   2.796e-01
005    0.858    0.48   4.115e+00   1.554e+00
008    0.806    1.06   7.696e+01   9.118e+00
010    0.776    1.53   2.700e+02   1.236e+01
015    0.722    2.90   3.291e+03   9.572e+00
020    0.685    4.58   1.558e+04   1.558e+00
025    0.652    6.46   5.300e+04   1.190e-01
030    0.621    8.64   1.188e+05   3.327e-03
Opt H 0.772    1.65   3.382e+02   1.230e+01
Forces (F) are in atomic units, distances (R) are in Å, energies (U(R)) are in
kcal/mol, and rate constants (k(R) and P*k(R)) are in s**-1.

Fraction of kH from reactant state u to product state v near the optimal tunneling
distance
R = 0.776, force = 010, U(R) = 1.53
total rate = 2.70e+02, average overlap squared = 4.11e-03
  u\v     0       1       2       3
  0   0.886   0.007   0.000   0.000
  1   0.079   0.001   0.000   0.000
  2   0.021   0.000   0.000   0.000
  3   0.006   0.000   0.000   0.000
  4   0.000   0.000   0.000   0.000
  5   0.000   0.000   0.000   0.000
  6   0.000   0.000   0.000   0.000
```

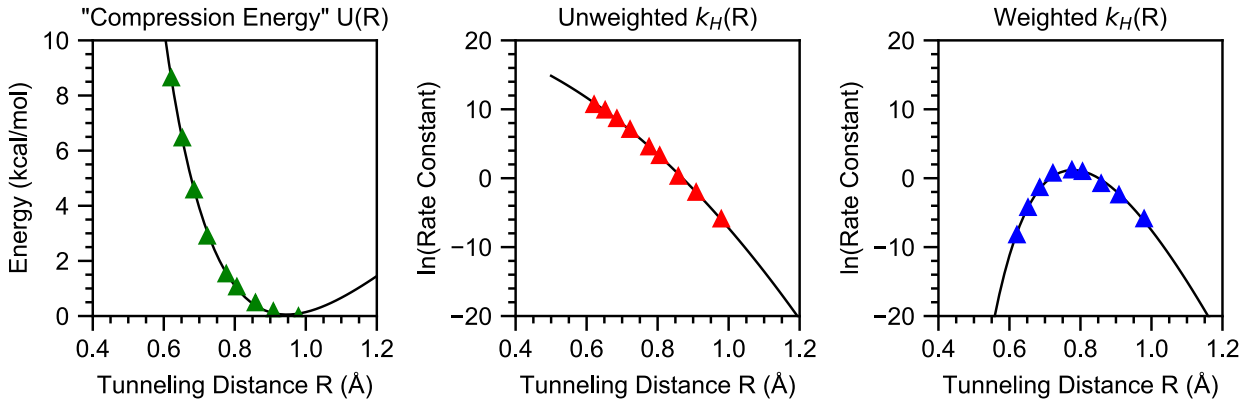

Calculation A3.22 $U(R)$, $k(R)$, and $(\ln k\text{-}U/k_BT)(R)$ and their fits at 230 K for 9,10-dihydroanthracene.

```
Substrate is DHA
At T = 230 K, kH = 1.99e+00
Reaction DG = -4.37 kcal/mol
Uncorrected DG = -12.27 kcal/mol
Uncorrected heavy DG = -9.10 kcal/mol
MECP/Reorganized DG = 3.52 kcal/mol
Reorganization Energy = 29.45 kcal/mol

  U(R) =  27.9964/R**2 + -59.1667/R +  31.3128
lnk(R) = -31.3352*R**2 +   2.8130*R +  21.2824
  F    R (A)     U(R)        kH(R)      P*kH(R)
001    0.979    -0.01    2.736e-03    2.794e-03
003    0.909     0.17    1.305e-01    8.988e-02
005    0.858     0.48    1.339e+00    4.645e-01
008    0.806     1.06    2.710e+01    2.668e+00
010    0.776     1.53    9.527e+01    3.334e+00
015    0.722     2.90    1.203e+03    2.106e+00
020    0.685     4.58    5.780e+03    2.595e-01
025    0.652     6.46    1.992e+04    1.443e-02
030    0.621     8.64    4.425e+04    2.733e-04
Opt H 0.779     1.50    8.633e+01    3.281e+00
Forces (F) are in atomic units, distances (R) are in Å, energies (U(R)) are in
kcal/mol, and rate constants (k(R) and P*k(R)) are in s**-1.

Fraction of kH from reactant state u to product state v near the optimal tunneling
distance
R = 0.806, force = 008, U(R) = 1.06
total rate = 2.71e+01, average overlap squared = 1.49e-03
  u\v     0        1        2        3
  0    0.944    0.003    0.000    0.000
  1    0.044    0.000    0.000    0.000
  2    0.006    0.000    0.000    0.000
  3    0.003    0.000    0.000    0.000
  4    0.000    0.000    0.000    0.000
  5    0.000    0.000    0.000    0.000
  6    0.000    0.000    0.000    0.000
```

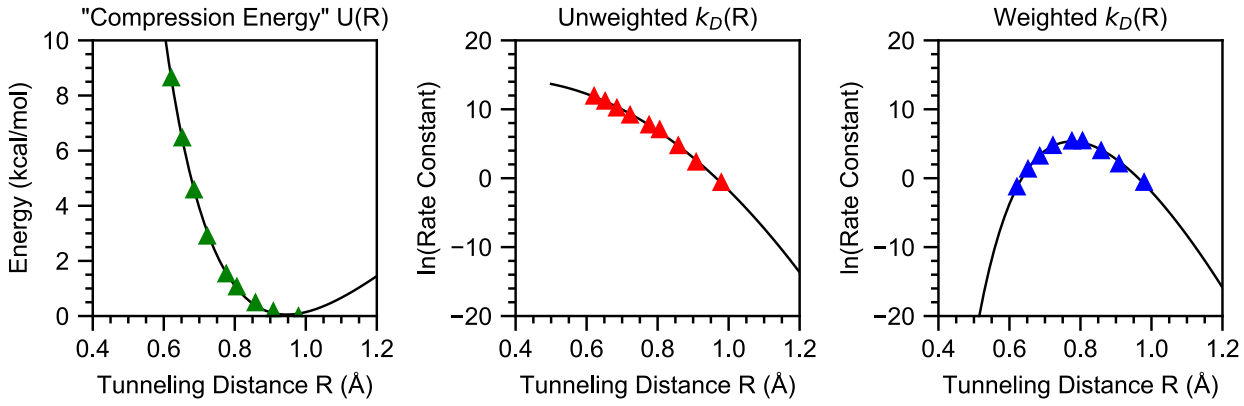

Calculation A3.23 $U(R)$, $k(R)$, and $(\ln k\text{-}U/k_BT)(R)$ and their fits at 330 K for deuterated 9,10-dihydroanthracene.

```
Substrate is DHA
At T = 330 K, kD = 1.16e+02
Reaction DG = -4.72 kcal/mol
Uncorrected DG = -12.62 kcal/mol
Uncorrected heavy DG = -9.10 kcal/mol
MECP/Reorganized DG = 3.58 kcal/mol
Reorganization Energy = 29.74 kcal/mol

  U(R) =  27.9964/R**2 + -59.1667/R +  31.3128
lnk(R) = -41.1139*R**2 +  30.8456*R +   8.5295
  F   R (A)    U(R)       kD(R)     P*kD(R)
001   0.979   -0.01   5.444e-01   5.525e-01
003   0.909    0.17   1.042e+01   8.034e+00
005   0.858    0.48   1.144e+02   5.471e+01
008   0.806    1.06   1.151e+03   2.288e+02
010   0.776    1.53   2.295e+03   2.218e+02
015   0.722    2.90   9.658e+03   1.157e+02
020   0.685    4.58   2.681e+04   2.501e+01
025   0.652    6.46   7.247e+04   3.808e+00
030   0.621    8.64   1.501e+05   2.849e-01
Opt D 0.776    1.56   2.226e+03   2.068e+02
Forces (F) are in atomic units, distances (R) are in Å, energies (U(R)) are in
kcal/mol, and rate constants (k(R) and P*k(R)) are in s**-1.

Fraction of kD from reactant state u to product state v near the optimal tunneling
distance
R = 0.806, force = 008, U(R) = 1.06
total rate = 1.15e+03, average overlap squared = 2.82e-01
  u\v     0       1       2       3
  0   0.000   0.000   0.000   0.000
  1   0.002   0.001   0.000   0.000
  2   0.008   0.003   0.000   0.000
  3   0.140   0.024   0.002   0.000
  4   0.699   0.065   0.002   0.000
  5   0.049   0.001   0.000   0.000
  6   0.003   0.000   0.000   0.000
```

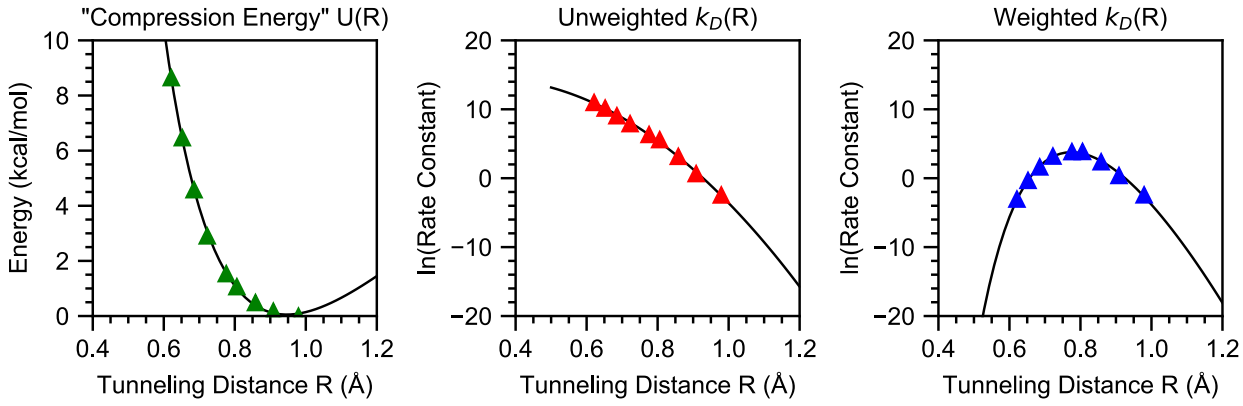

Calculation A3.24 $U(R)$, $k(R)$, and $(\ln k\text{-}U/k_BT)(R)$ and their fits at 310 K for deuterated 9,10-dihydroanthracene.

```
Substrate is DHA
At T = 310 K, kD = 2.46e+01
Reaction DG = -4.64 kcal/mol
Uncorrected DG = -12.54 kcal/mol
Uncorrected heavy DG = -9.10 kcal/mol
MECP/Reorganized DG = 3.57 kcal/mol
Reorganization Energy = 29.69 kcal/mol

  U(R) =  27.9964/R**2 + -59.1667/R +  31.3128
lnk(R) = -38.7784*R**2 +  24.6344*R +  10.5387
  F    R (A)     U(R)        kD(R)      P*kD(R)
001    0.979    -0.01    8.613e-02    8.750e-02
003    0.909     0.17    1.913e+00    1.450e+00
005    0.858     0.48    2.333e+01    1.064e+01
008    0.806     1.06    2.640e+02    4.727e+01
010    0.776     1.53    5.572e+02    4.632e+01
015    0.722     2.90    2.692e+03    2.425e+01
020    0.685     4.58    8.469e+03    5.036e+00
025    0.652     6.46    2.570e+04    7.151e-01
030    0.621     8.64    5.829e+04    4.730e-02
Opt D 0.775     1.58    5.663e+02    4.357e+01
Forces (F) are in atomic units, distances (R) are in Å, energies (U(R)) are in
kcal/mol, and rate constants (k(R) and P*k(R)) are in s**-1.

Fraction of kD from reactant state u to product state v near the optimal tunneling
distance
R = 0.776, force = 010, U(R) = 1.53
total rate = 5.57e+02, average overlap squared = 2.09e-01
  u\v     0       1       2       3
  0   0.003   0.001   0.000   0.000
  1   0.009   0.004   0.001   0.000
  2   0.028   0.008   0.001   0.000
  3   0.309   0.042   0.002   0.000
  4   0.521   0.039   0.001   0.000
  5   0.029   0.000   0.000   0.000
  6   0.001   0.000   0.000   0.000
```

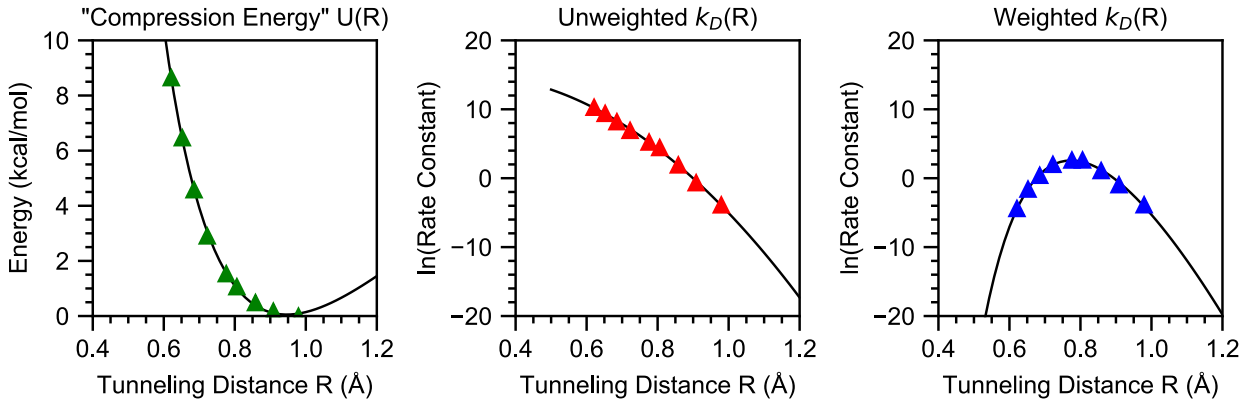

Calculation A3.25 $U(R)$, $k(R)$, and $(\ln k\text{-}U/k_BT)(R)$ and their fits at 296 K for deuterated 9,10-dihydroanthracene.

```
Substrate is DHA
At T = 296 K, kD = 7.47e+00
Reaction DG = -4.59 kcal/mol
Uncorrected DG = -12.49 kcal/mol
Uncorrected heavy DG = -9.10 kcal/mol
MECP/Reorganized DG = 3.56 kcal/mol
Reorganization Energy = 29.65 kcal/mol

  U(R) =  27.9964/R**2 + -59.1667/R +  31.3128
lnk(R) = -36.4370*R**2 +  18.8334*R +  12.5477
  F   R (A)    U(R)       kD(R)     P*kD(R)
001   0.979   -0.01   2.053e-02   2.087e-02
003   0.909    0.17   5.119e-01   3.831e-01
005   0.858    0.48   6.771e+00   2.975e+00
008   0.806    1.06   8.413e+01   1.389e+01
010   0.776    1.53   1.864e+02   1.377e+01
015   0.722    2.90   1.018e+03   7.338e+00
020   0.685    4.58   3.580e+03   1.498e+00
025   0.652    6.46   1.195e+04   2.024e-01
030   0.621    8.64   2.906e+04   1.215e-02
Opt D 0.774    1.60   1.996e+02   1.310e+01
Forces (F) are in atomic units, distances (R) are in Å, energies (U(R)) are in
kcal/mol, and rate constants (k(R) and P*k(R)) are in s**-1.

Fraction of kD from reactant state u to product state v near the optimal tunneling
distance
R = 0.776, force = 010, U(R) = 1.53
total rate = 1.86e+02, average overlap squared = 2.02e-01
  u\v     0       1       2       3
  0   0.006   0.002   0.000   0.000
  1   0.014   0.005   0.001   0.000
  2   0.035   0.009   0.001   0.000
  3   0.321   0.039   0.002   0.000
  4   0.504   0.034   0.001   0.000
  5   0.025   0.000   0.000   0.000
  6   0.001   0.000   0.000   0.000
```

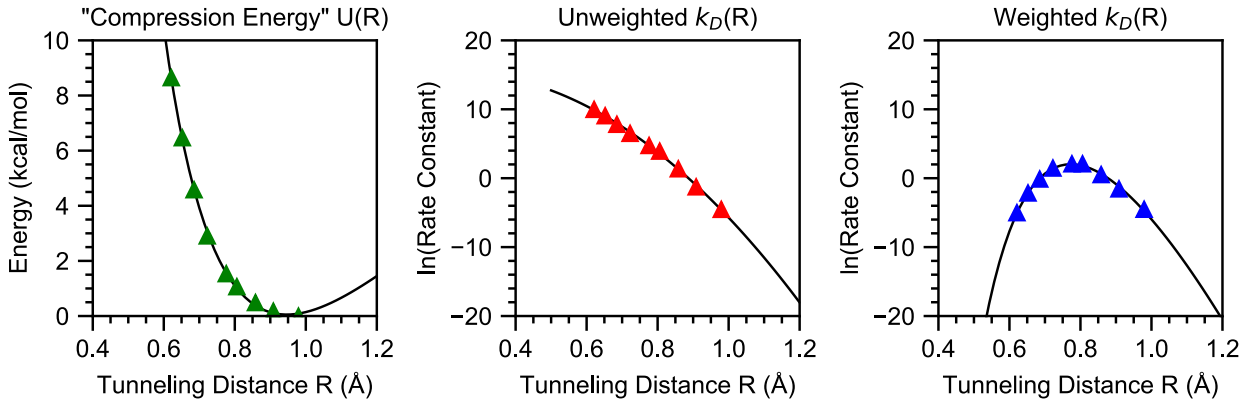

Calculation A3.26 $U(R)$, $k(R)$, and $(\ln k\text{-}U/k_BT)(R)$ and their fits at 290 K for deuterated 9,10-dihydroanthracene.

```
Substrate is DHA
At T = 290 K, kD = 4.35e+00
Reaction DG = -4.56 kcal/mol
Uncorrected DG = -12.46 kcal/mol
Uncorrected heavy DG = -9.10 kcal/mol
MECP/Reorganized DG = 3.56 kcal/mol
Reorganization Energy = 29.63 kcal/mol

  U(R) =  27.9964/R**2 + -59.1667/R +  31.3128
lnk(R) = -35.2369*R**2 +  15.9322*R +  13.5851
  F   R (A)    U(R)       kD(R)     P*kD(R)
001   0.979   -0.01   1.066e-02   1.084e-02
003   0.909    0.17   2.802e-01   2.084e-01
005   0.858    0.48   3.847e+00   1.662e+00
008   0.806    1.06   4.991e+01   7.937e+00
010   0.776    1.53   1.132e+02   7.929e+00
015   0.722    2.90   6.579e+02   4.283e+00
020   0.685    4.58   2.445e+03   8.712e-01
025   0.652    6.46   8.524e+03   1.151e-01
030   0.621    8.64   2.138e+04   6.596e-03
Opt D 0.773    1.62   1.272e+02   7.596e+00
Forces (F) are in atomic units, distances (R) are in Å, energies (U(R)) are in
kcal/mol, and rate constants (k(R) and P*k(R)) are in s**-1.

Fraction of kD from reactant state u to product state v near the optimal tunneling
distance
R = 0.776, force = 010, U(R) = 1.53
total rate = 1.13e+02, average overlap squared = 1.97e-01
  u\v     0       1       2       3
  0   0.008   0.002   0.000   0.000
  1   0.018   0.006   0.001   0.000
  2   0.039   0.009   0.001   0.000
  3   0.326   0.037   0.002   0.000
  4   0.495   0.031   0.000   0.000
  5   0.023   0.000   0.000   0.000
  6   0.001   0.000   0.000   0.000
```

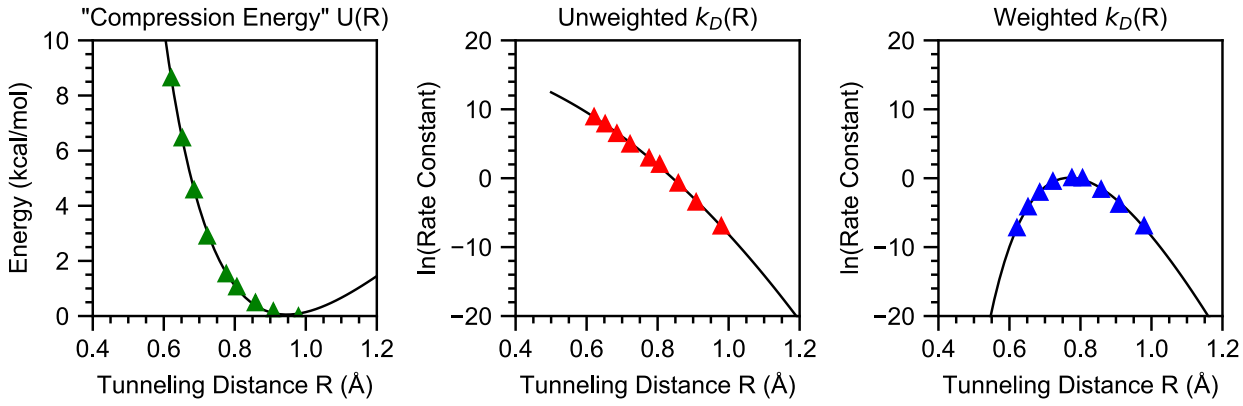

Calculation A3.27 $U(R)$, $k(R)$, and $(\ln k\text{-}U/k_BT)(R)$ their fits at 270 K for deuterated 9,10-dihydroanthracene.

```
Substrate is DHA
At T = 270 K, kD = 6.23e-01
Reaction DG = -4.50 kcal/mol
Uncorrected DG = -12.40 kcal/mol
Uncorrected heavy DG = -9.10 kcal/mol
MECP/Reorganized DG = 3.55 kcal/mol
Reorganization Energy = 29.58 kcal/mol

  U(R) =  27.9964/R**2 + -59.1667/R +  31.3128
lnk(R) = -30.4436*R**2 +   4.4519*R +  17.8459
  F    R (A)     U(R)        kD(R)      P*kD(R)
001    0.979    -0.01    9.764e-04    9.943e-04
003    0.909     0.17    3.125e-02    2.274e-02
005    0.858     0.48    4.912e-01    1.994e-01
008    0.806     1.06    7.517e+00    1.043e+00
010    0.776     1.53    1.881e+01    1.082e+00
015    0.722     2.90    1.423e+02    6.378e-01
020    0.685     4.58    6.571e+02    1.300e-01
025    0.652     6.46    2.674e+03    1.573e-02
030    0.621     8.64    7.420e+03    7.538e-04
Opt D 0.770     1.69    2.513e+01    1.074e+00
Forces (F) are in atomic units, distances (R) are in Å, energies (U(R)) are in
kcal/mol, and rate constants (k(R) and P*k(R)) are in s**-1.

Fraction of kD from reactant state u to product state v near the optimal tunneling
distance
R = 0.776, force = 010, U(R) = 1.53
total rate = 1.88e+01, average overlap squared = 1.79e-01
  u\v     0        1        2        3
  0    0.023    0.005    0.000    0.000
  1    0.036    0.008    0.001    0.000
  2    0.055    0.010    0.001    0.000
  3    0.335    0.031    0.001    0.000
  4    0.452    0.024    0.000    0.000
  5    0.017    0.000    0.000    0.000
  6    0.000    0.000    0.000    0.000
```

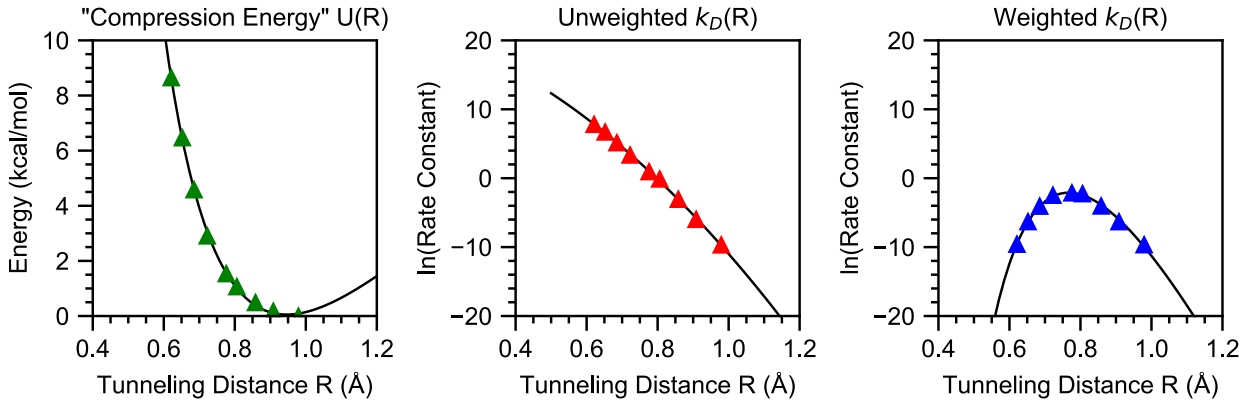

Calculation A3.28 $U(R)$, $k(R)$, and $(\ln k\text{-}U/k_BT)(R)$ and their fits at 250 K for deuterated 9,10-dihydroanthracene.

```
Substrate is DHA
At T = 250 K, kD = 7.19e-02
Reaction DG = -4.43 kcal/mol
Uncorrected DG = -12.33 kcal/mol
Uncorrected heavy DG = -9.10 kcal/mol
MECP/Reorganized DG = 3.53 kcal/mol
Reorganization Energy = 29.52 kcal/mol

  U(R) =  27.9964/R**2 + -59.1667/R +  31.3128
lnk(R) = -25.2223*R**2 +  -8.7667*R +  23.0092
  F   R (A)    U(R)       kD(R)     P*kD(R)
001   0.979   -0.01   6.181e-05   6.303e-05
003   0.909    0.17   2.515e-03   1.784e-03
005   0.858    0.48   4.632e-02   1.749e-02
008   0.806    1.06   8.787e-01   1.041e-01
010   0.776    1.53   2.559e+00   1.171e-01
015   0.722    2.90   2.847e+01   8.282e-02
020   0.685    4.58   1.696e+02   1.697e-02
025   0.652    6.46   8.019e+02   1.800e-03
030   0.621    8.64   2.425e+03   6.795e-05
Opt D 0.767    1.76   4.251e+00   1.227e-01
Forces (F) are in atomic units, distances (R) are in Å, energies (U(R)) are in
kcal/mol, and rate constants (k(R) and P*k(R)) are in s**-1.

Fraction of kD from reactant state u to product state v near the optimal tunneling
distance
R = 0.776, force = 010, U(R) = 1.53
total rate = 2.56e+00, average overlap squared = 1.47e-01
  u\v     0       1       2       3
  0   0.075   0.010   0.000   0.000
  1   0.075   0.012   0.001   0.000
  2   0.075   0.010   0.001   0.000
  3   0.317   0.023   0.001   0.000
  4   0.372   0.016   0.000   0.000
  5   0.011   0.000   0.000   0.000
  6   0.000   0.000   0.000   0.000
```

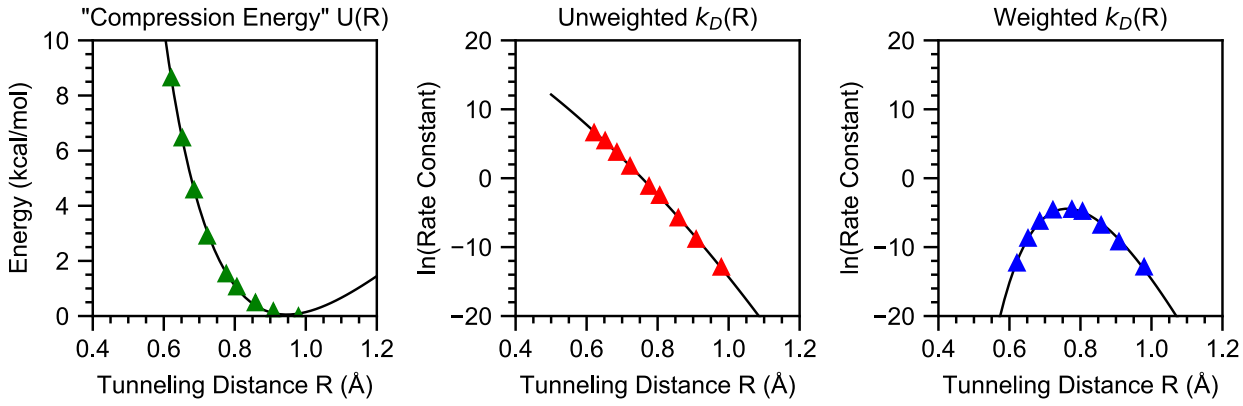

Calculation A3.29 $U(R)$, $k(R)$, and $(\ln k\text{-}U/k_BT)(R)$ and their fits at 230 K for deuterated 9,10-dihydroanthracene.

```
Substrate is DHA
At T = 230 K, kD = 7.02e-03
Reaction DG = -4.37 kcal/mol
Uncorrected DG = -12.27 kcal/mol
Uncorrected heavy DG = -9.10 kcal/mol
MECP/Reorganized DG = 3.52 kcal/mol
Reorganization Energy = 29.45 kcal/mol

  U(R) =  27.9964/R**2 + -59.1667/R +  31.3128
lnk(R) = -22.9411*R**2 + -18.5659*R +  27.1562
  F    R (A)    U(R)       kD(R)      P*kD(R)
001    0.979   -0.01   2.499e-06   2.553e-06
003    0.909    0.17   1.425e-04   9.810e-05
005    0.858    0.48   3.176e-03   1.102e-03
008    0.806    1.06   8.327e-02   8.196e-03
010    0.776    1.53   3.120e-01   1.092e-02
015    0.722    2.90   5.740e+00   1.005e-02
020    0.685    4.58   4.311e+01   1.936e-03
025    0.652    6.46   2.291e+02   1.659e-04
030    0.621    8.64   7.339e+02   4.532e-06
Opt D 0.763    1.86   6.941e-01   1.194e-02
Forces (F) are in atomic units, distances (R) are in Å, energies (U(R)) are in
kcal/mol, and rate constants (k(R) and P*k(R)) are in s**-1.

Fraction of kD from reactant state u to product state v near the optimal tunneling
distance
R = 0.776, force = 010, U(R) = 1.53
total rate = 3.12e-01, average overlap squared = 9.27e-02
  u\v     0       1       2       3
  0   0.234   0.019   0.000   0.000
  1   0.142   0.015   0.001   0.000
  2   0.085   0.008   0.000   0.000
  3   0.234   0.013   0.000   0.000
  4   0.233   0.008   0.000   0.000
  5   0.005   0.000   0.000   0.000
  6   0.000   0.000   0.000   0.000
```

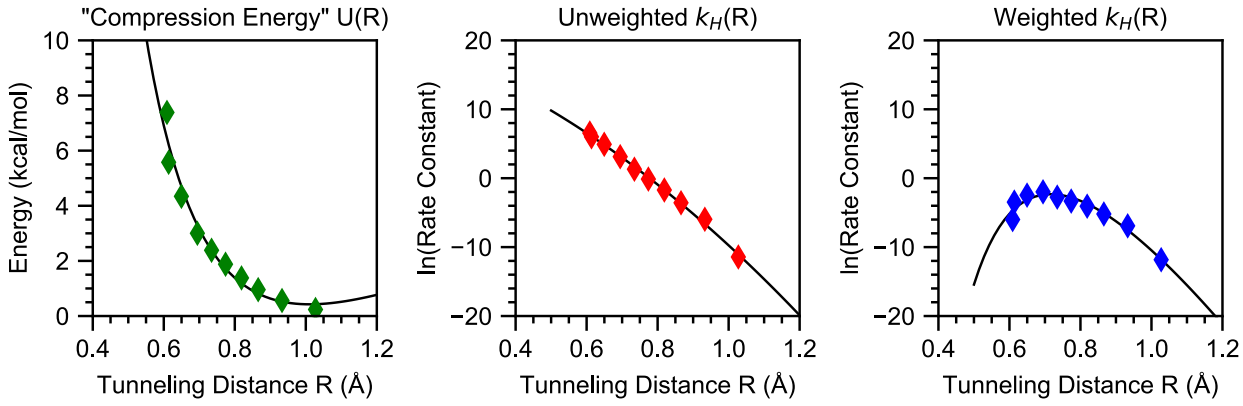

Calculation A3.30 $U(R)$, $k(R)$, and $(\ln k\text{-}U/k_BT)(R)$ and their fits at 296 K for diphenylmethane.

```
Substrate is DPM
At T = 296 K, kH = 9.26e-02
Reaction DG = 0.04 kcal/mol
Uncorrected DG = -7.86 kcal/mol
Uncorrected heavy DG = -5.36 kcal/mol
MECP/Reorganized DG = 7.07 kcal/mol
Reorganization Energy = 38.25 kcal/mol

  U(R) =  14.1312/R**2 + -27.9581/R +  14.2533
lnk(R) = -16.5836*R**2 + -14.2576*R +  21.0947
  F    R (A)     U(R)       kH(R)      P*kH(R)
002    1.027     0.24    1.084e-05    7.261e-06
004    0.933     0.56    2.578e-03    9.923e-04
006    0.866     0.96    2.820e-02    5.554e-03
008    0.819     1.38    1.802e-01    1.722e-02
010    0.774     1.88    8.791e-01    3.608e-02
012    0.735     2.38    3.682e+00    6.400e-02
014    0.695     3.00    2.264e+01    1.379e-01
018    0.650     4.34    1.367e+02    8.530e-02
022    0.614     5.58    4.070e+02    3.109e-02
024    0.609     7.39    7.010e+02    2.484e-03
Opt H 0.717     2.75    1.045e+01    9.796e-02
Forces (F) are in atomic units, distances (R) are in Å, energies (U(R)) are in
kcal/mol, and rate constants (k(R) and P*k(R)) are in s**-1.

Fraction of kH from reactant state u to product state v near the optimal tunneling
distance
R = 0.735, force = 012, U(R) = 2.38
total rate = 3.68e+00, average overlap squared = 3.82e-02
  u\v     0       1       2       3
  0    0.488   0.005   0.000   0.000
  1    0.244   0.003   0.000   0.000
  2    0.193   0.001   0.000   0.000
  3    0.065   0.000   0.000   0.000
  4    0.001   0.000   0.000   0.000
  5    0.000   0.000   0.000   0.000
  6    0.000   0.000   0.000   0.000
```

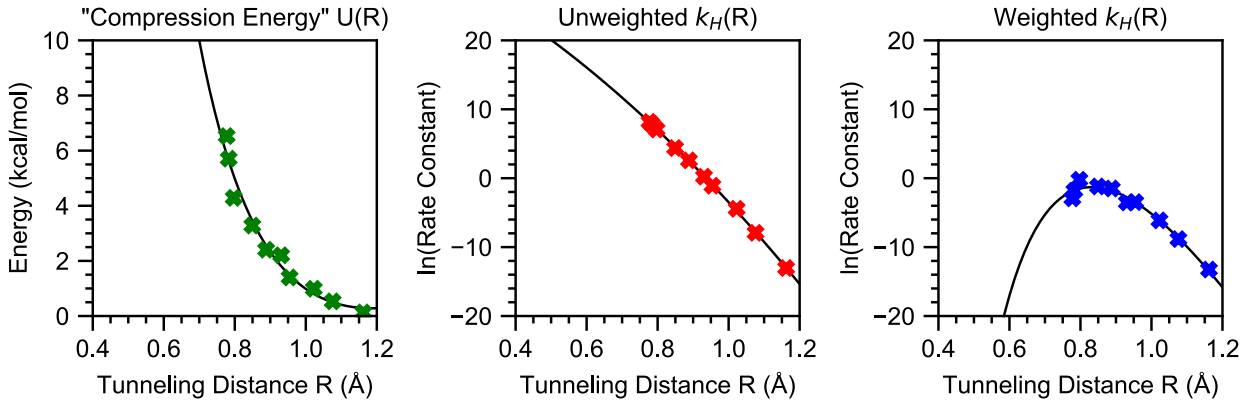

Calculation A3.31 $U(R)$, $k(R)$, and $(\ln k\text{-}U/k_BT)(R)$ and their fits at 296 K for 1,3-cyclohexadiene.

```
Substrate is CHD
At T = 296 K, kH = 3.59e-01
Reaction DG = -10.19 kcal/mol
Uncorrected DG = -18.09 kcal/mol
Uncorrected heavy DG = -14.41 kcal/mol
MECP/Reorganized DG = 2.78 kcal/mol
Reorganization Energy = 33.82 kcal/mol

  U(R) =  28.1998/R**2 + -47.4753/R +  20.2612
lnk(R) = -17.4387*R**2 + -20.9760*R +  34.9218
  F    R (A)    U(R)       kH(R)     P*kH(R)
002    1.162    0.13   2.189e-06   1.755e-06
004    1.076    0.53   3.589e-04   1.454e-04
006    1.023    0.99   1.178e-02   2.191e-03
008    0.954    1.40   3.359e-01   3.114e-02
010    0.931    2.20   1.252e+00   2.959e-02
012    0.888    2.41   1.337e+01   2.241e-01
014    0.849    3.28   7.952e+01   3.015e-01
018    0.797    4.29   1.166e+03   8.001e-01
022    0.783    5.71   2.640e+03   1.617e-01
024    0.777    6.53   3.530e+03   5.372e-02
Opt H 0.832    3.94   2.210e+02   2.745e-01
Forces (F) are in atomic units, distances (R) are in Å, energies (U(R)) are in
kcal/mol, and rate constants (k(R) and P*k(R)) are in s**-1.

Fraction of kH from reactant state u to product state v near the optimal tunneling
distance
R = 0.849, force = 014, U(R) = 3.28
total rate = 7.95e+01, average overlap squared = 1.53e-05
  u\v     0       1       2       3
  0   0.855   0.096   0.002   0.000
  1   0.036   0.009   0.000   0.000
  2   0.001   0.000   0.000   0.000
  3   0.000   0.000   0.000   0.000
  4   0.000   0.000   0.000   0.000
  5   0.000   0.000   0.000   0.000
  6   0.000   0.000   0.000   0.000
```

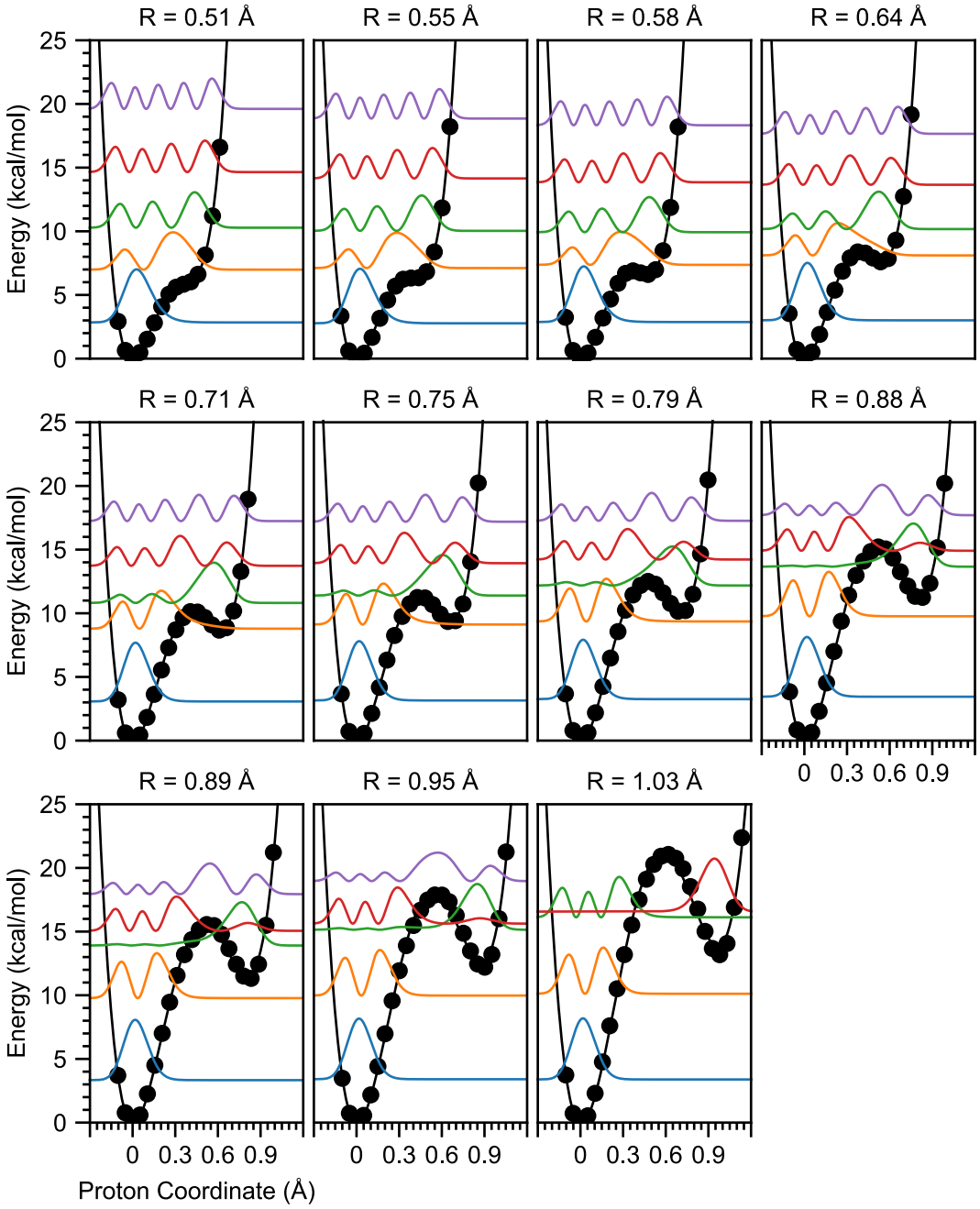

Figure A3.2 The calculated and fit reactant energy wells for 9-phenylfluorene, with vibrational wavefunctions up to 20 kcal/mol in vibrational energy and labeled with the tunneling distance.

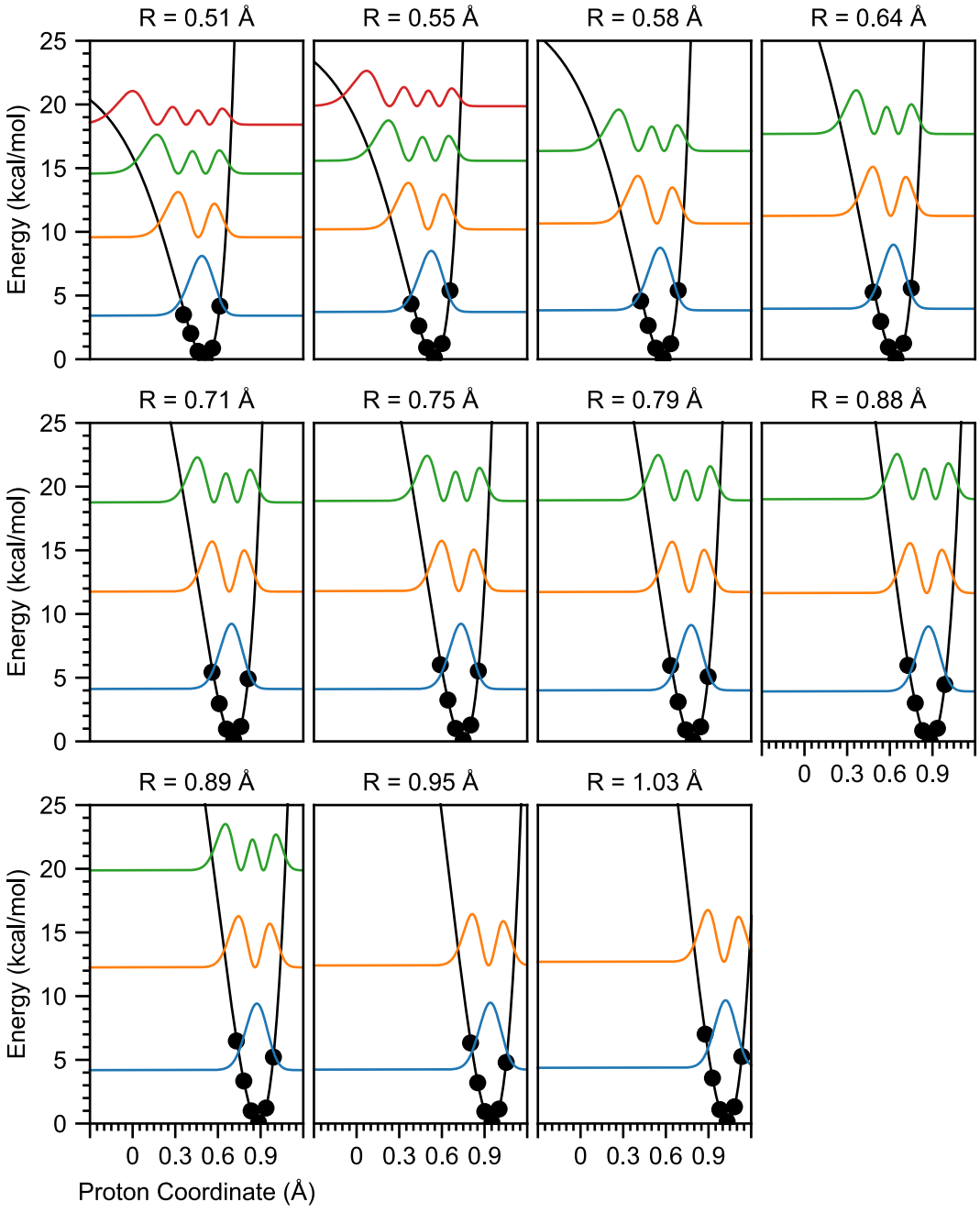

Figure A3.3 The calculated and fit product energy wells for 9-phenylfluorene, with vibrational wavefunctions up to 20 kcal/mol in vibrational energy and labeled with the tunneling distance.

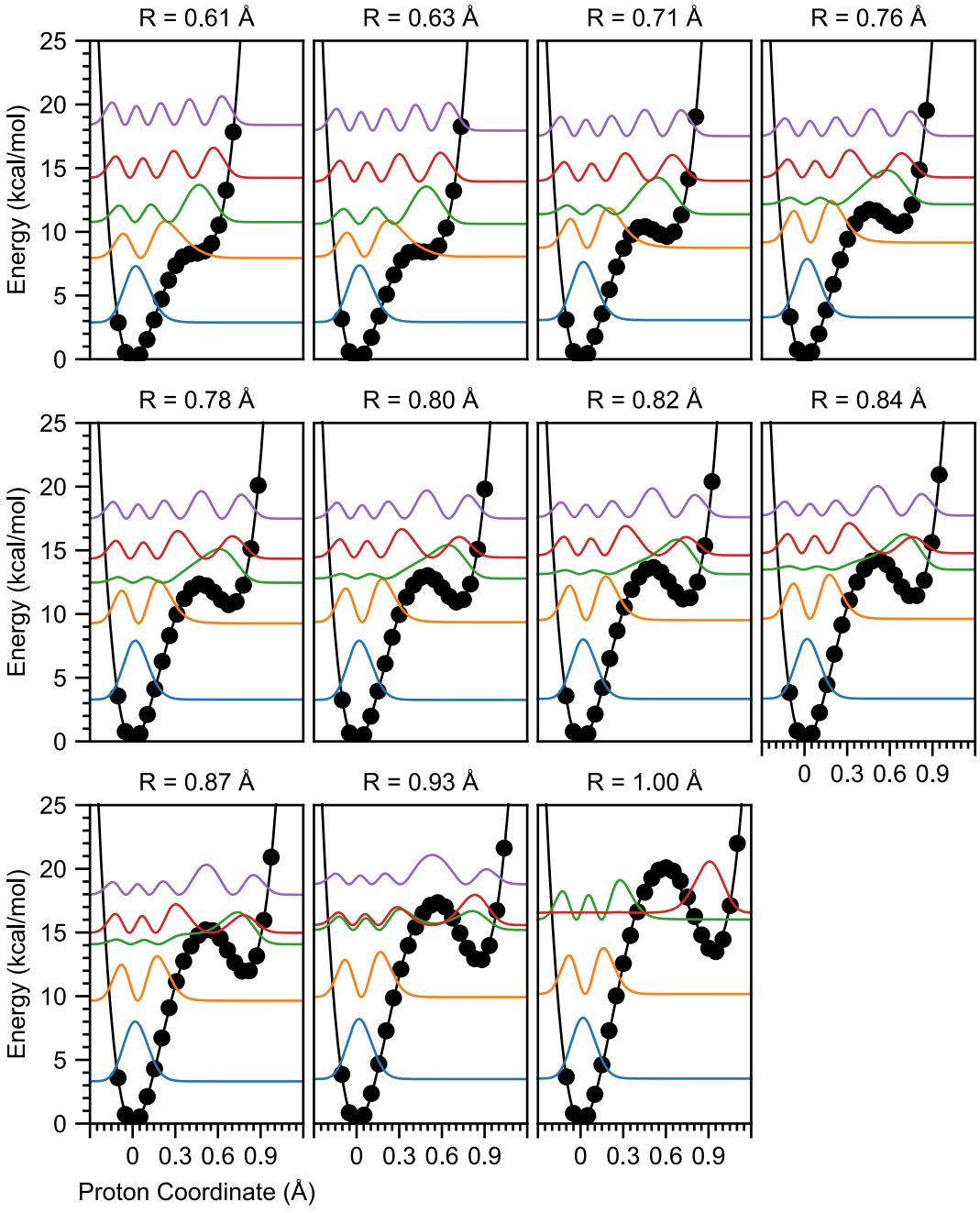

Figure A3.4 The calculated and fit reactant energy wells for fluorene, with vibrational wavefunctions up to 20 kcal/mol in vibrational energy and labeled with the tunneling distance.

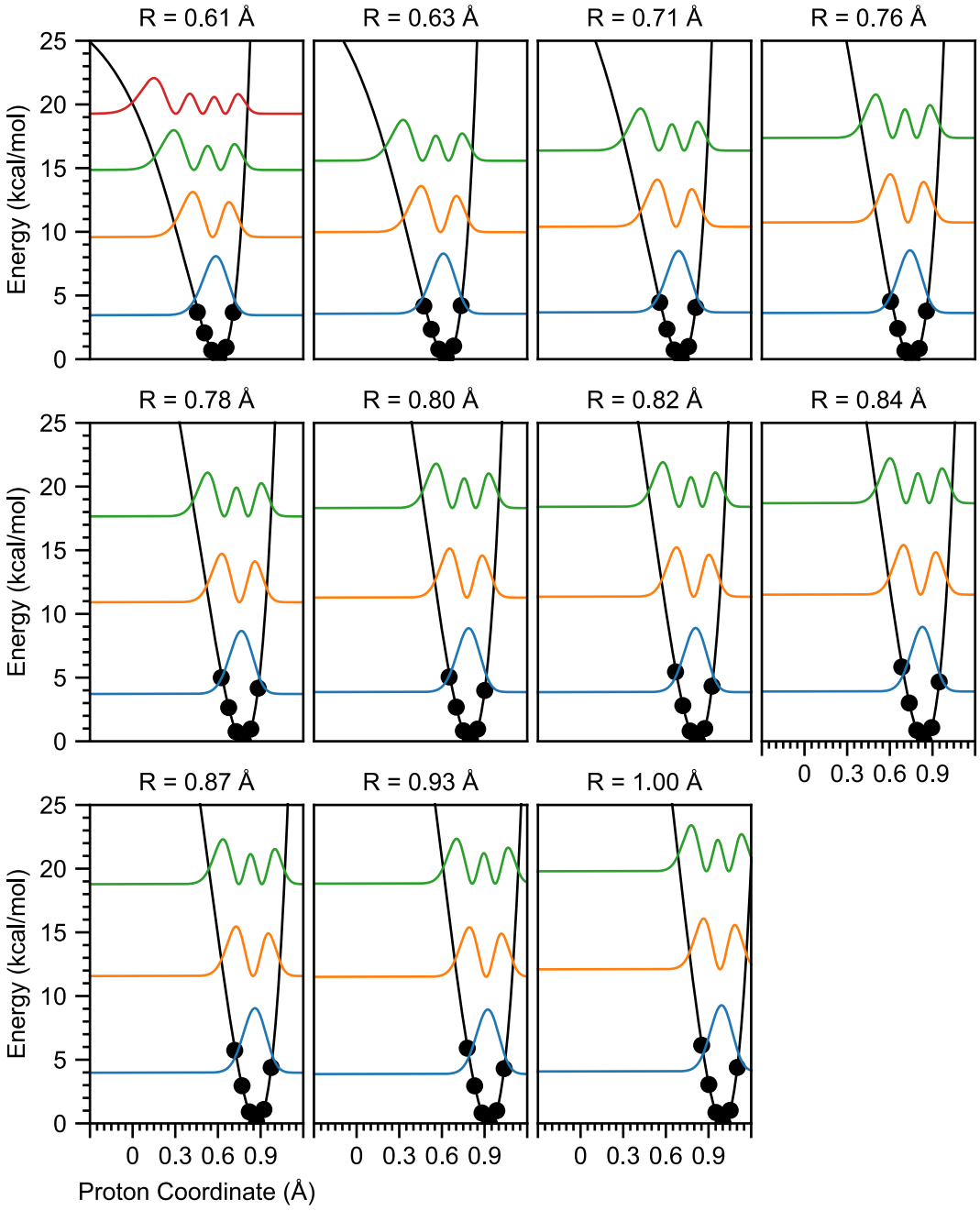

Figure A3.5 The calculated and fit product energy wells for fluorene, with vibrational wavefunctions up to 20 kcal/mol in vibrational energy and labeled with the tunneling distance.

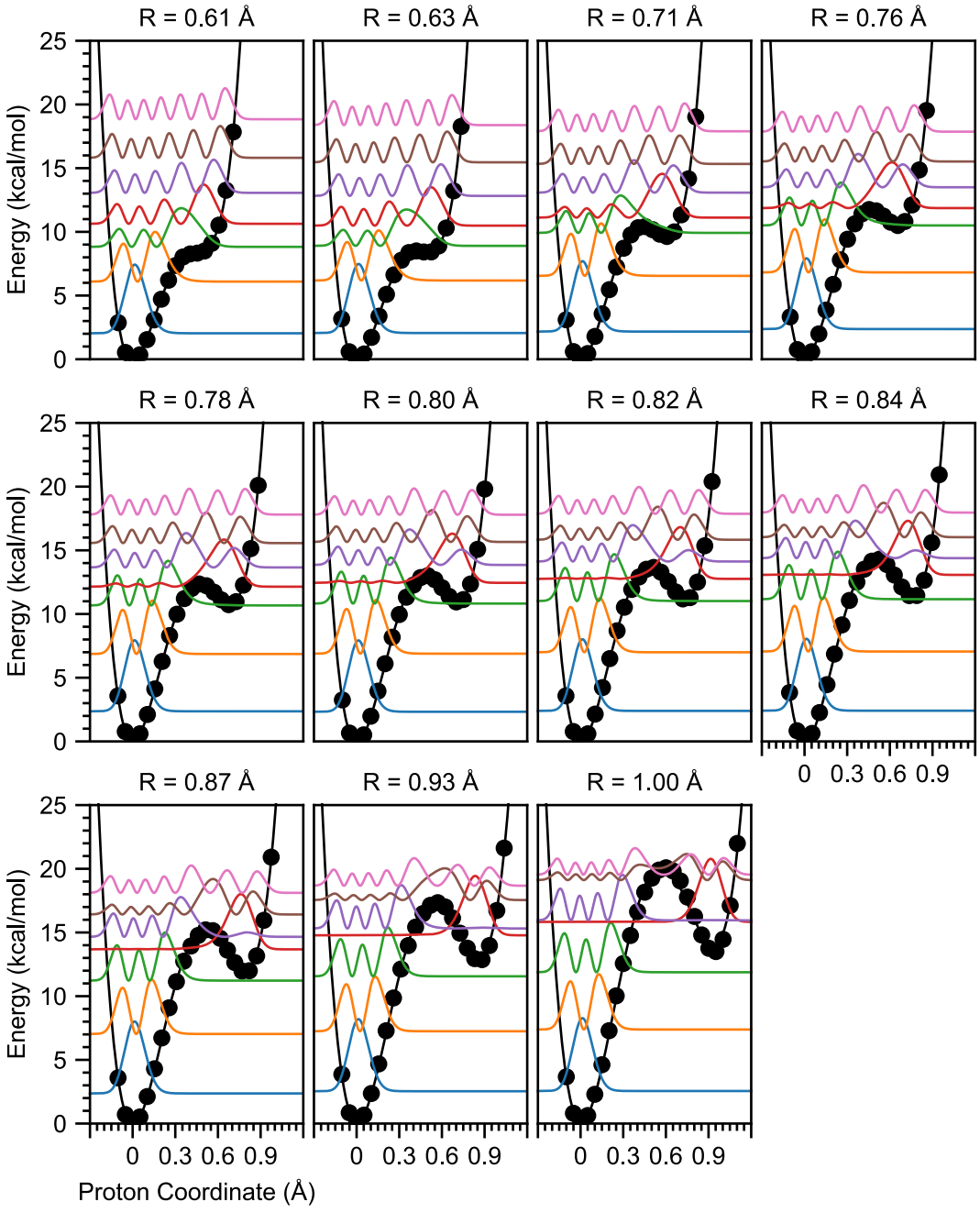

Figure A3.6 The calculated and fit reactant energy wells for deuterated fluorene, with vibrational wavefunctions up to 20 kcal/mol in vibrational energy and labeled with the tunneling distance.

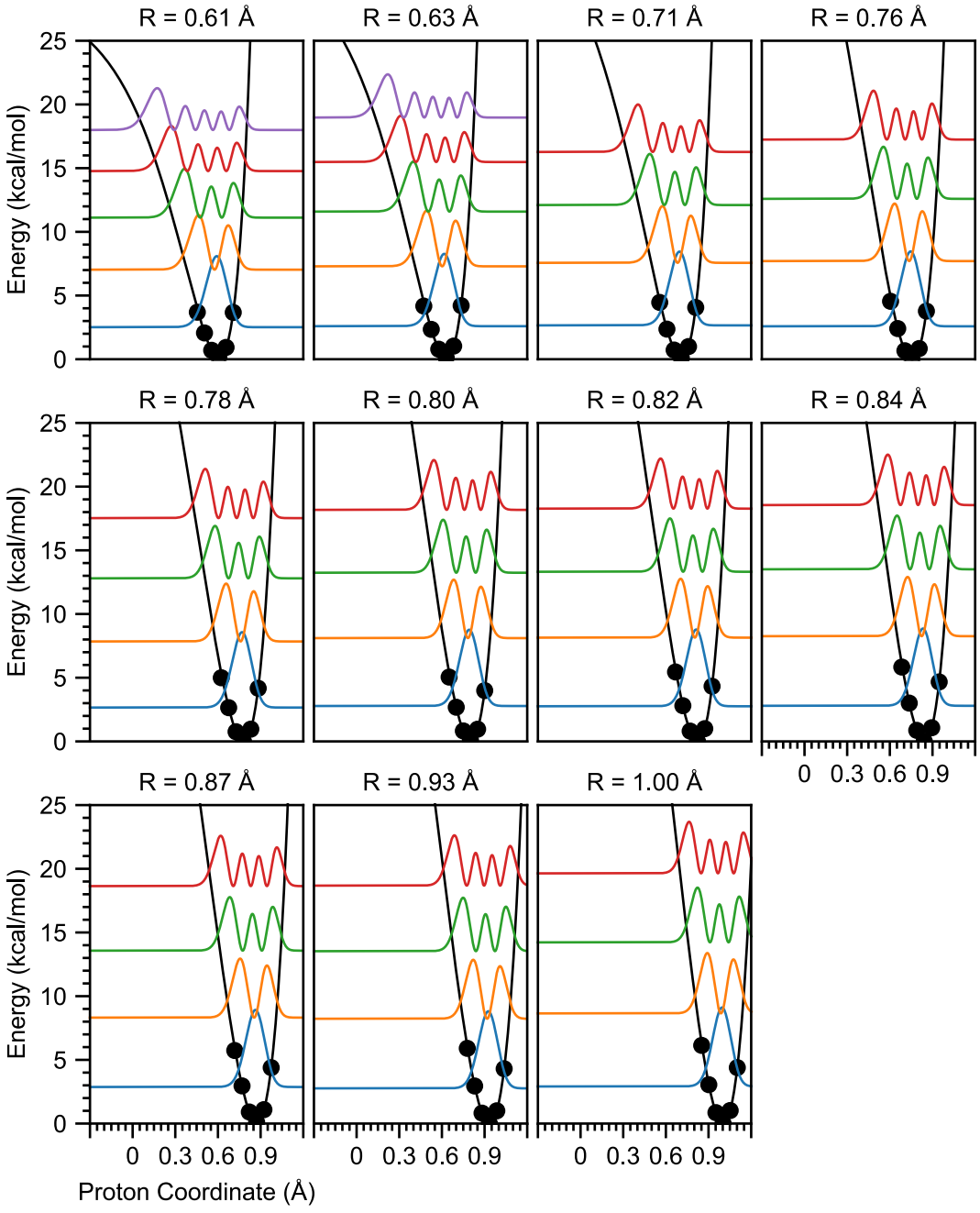

Figure A3.7 The calculated and fit product energy wells for deuterated fluorene, with vibrational wavefunctions up to 20 kcal/mol in vibrational energy and labeled with the tunneling distance.

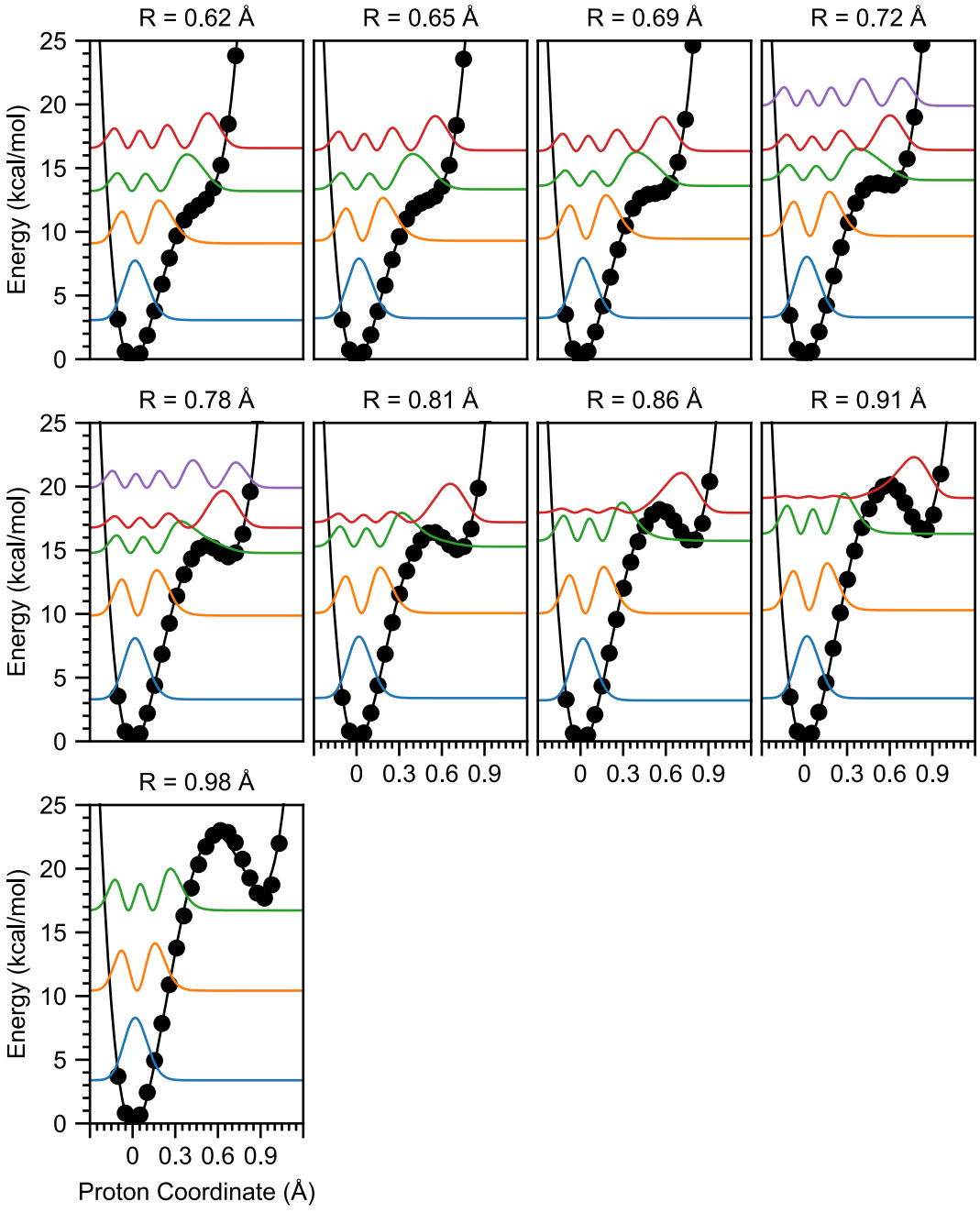

Figure A3.8 The calculated and fit reactant energy wells for 9,10-dihydroanthracene, with vibrational wavefunctions up to 20 kcal/mol in vibrational energy and labeled with the tunneling distance.

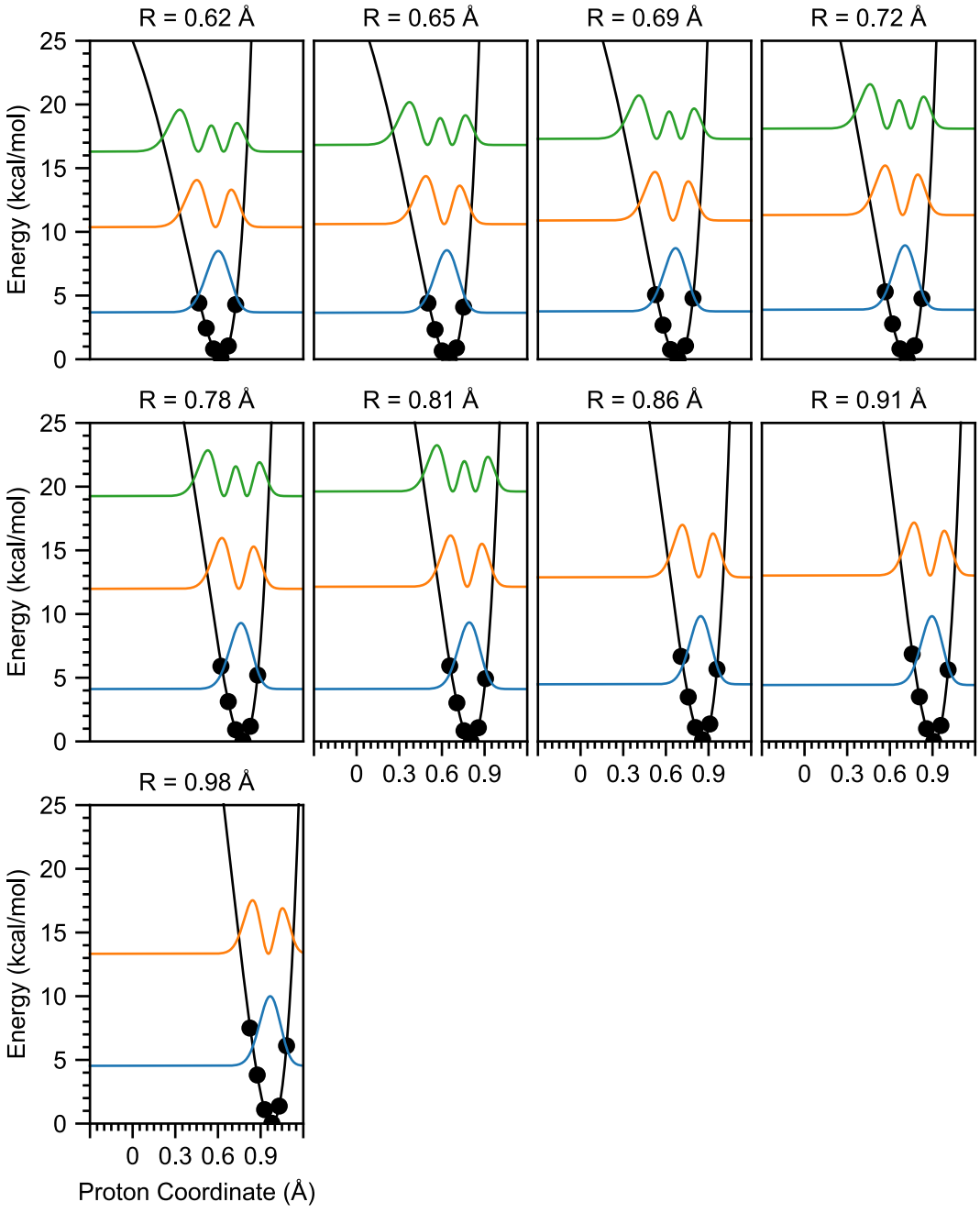

Figure A3.9 The calculated and fit product energy wells for 9,10-dihydroanthracene, with vibrational wavefunctions up to 20 kcal/mol in vibrational energy and labeled with the tunneling distance.

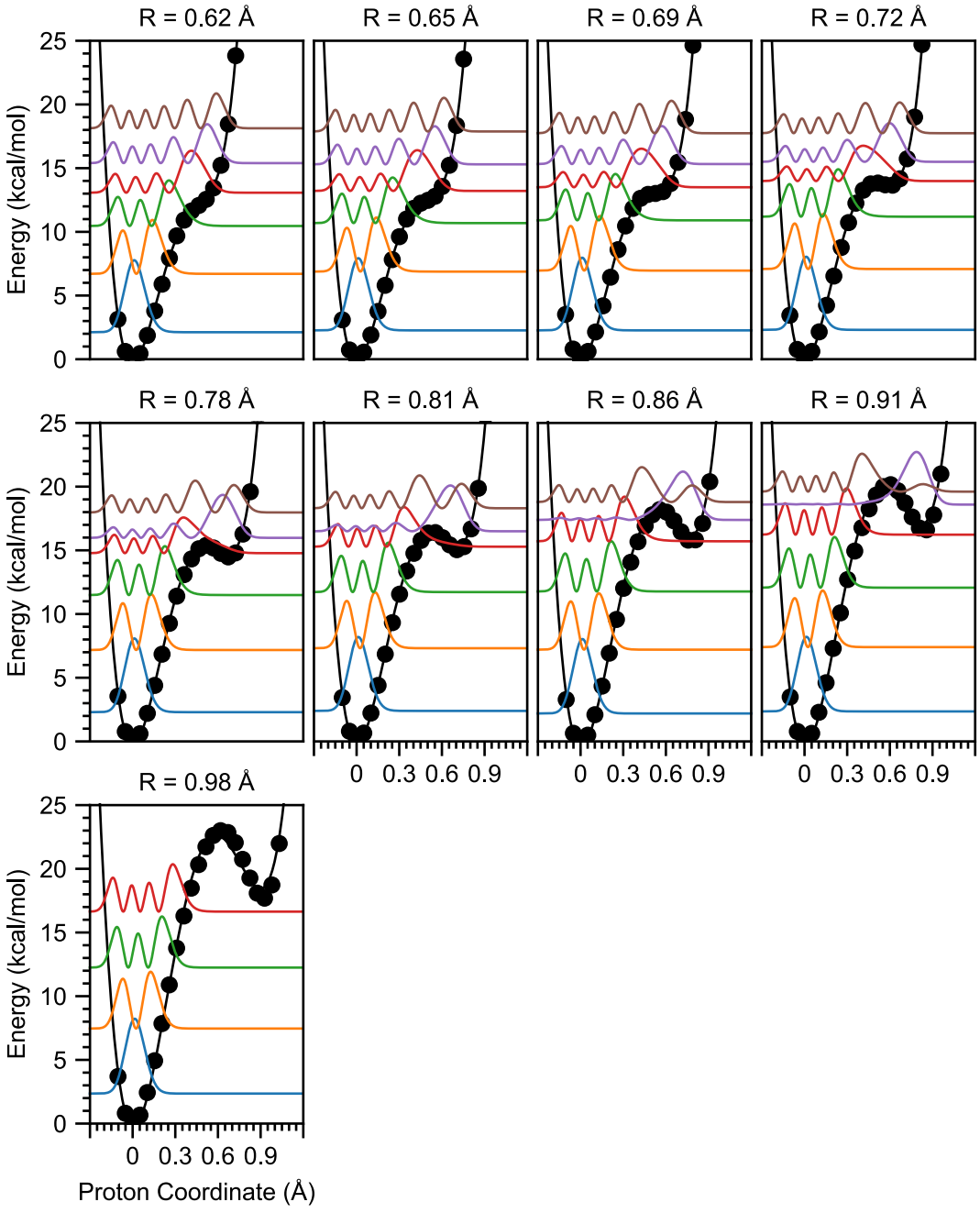

Figure A3.10 The calculated and fit reactant energy wells for deuterated 9,10-dihydroanthracene, with vibrational wavefunctions up to 20 kcal/mol in vibrational energy and labeled with the tunneling distance.

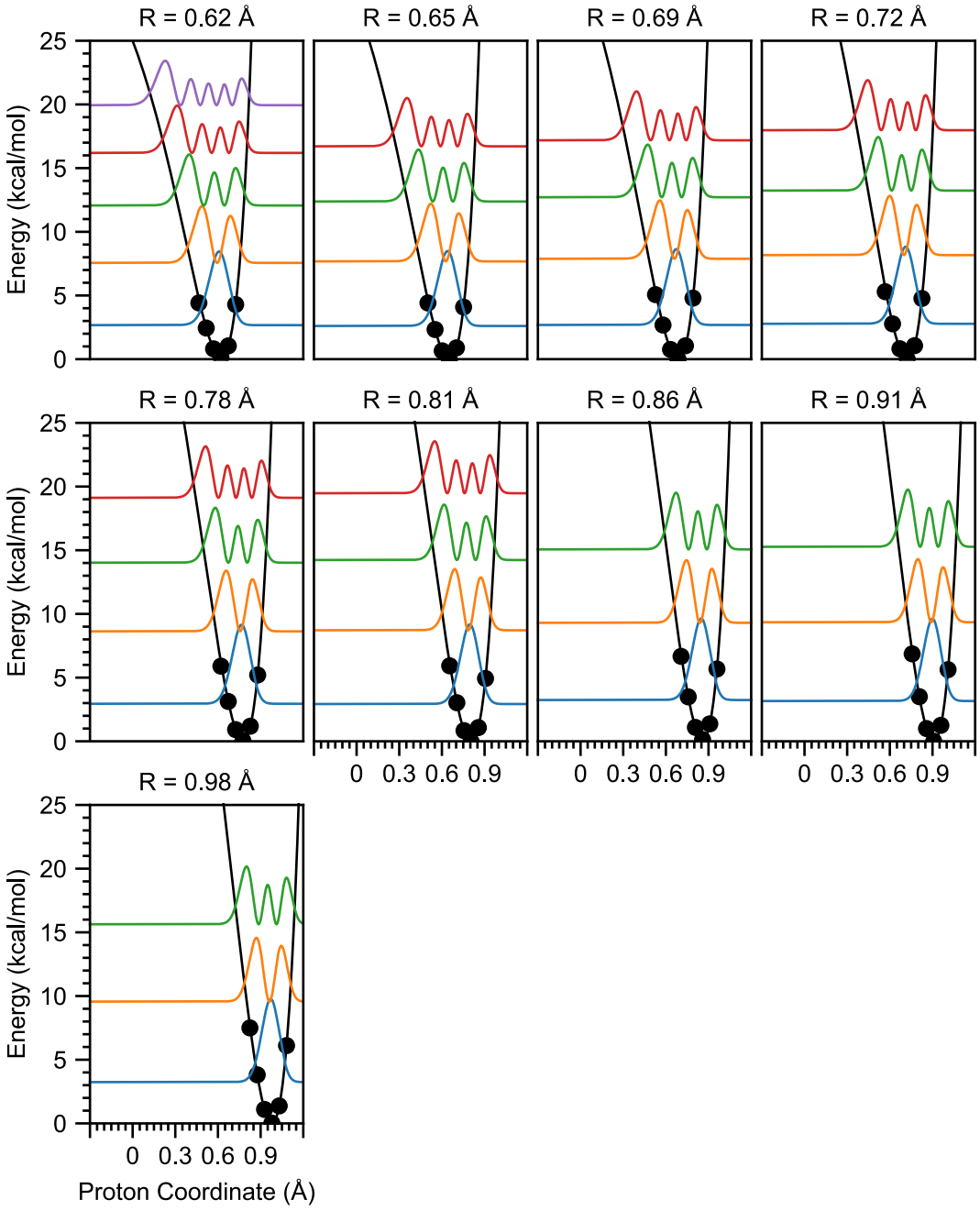

Figure A3.11 The calculated and fit product energy wells for deuterated 9,10-dihydroanthracene, with vibrational wavefunctions up to 20 kcal/mol in vibrational energy and labeled with the tunneling distance.

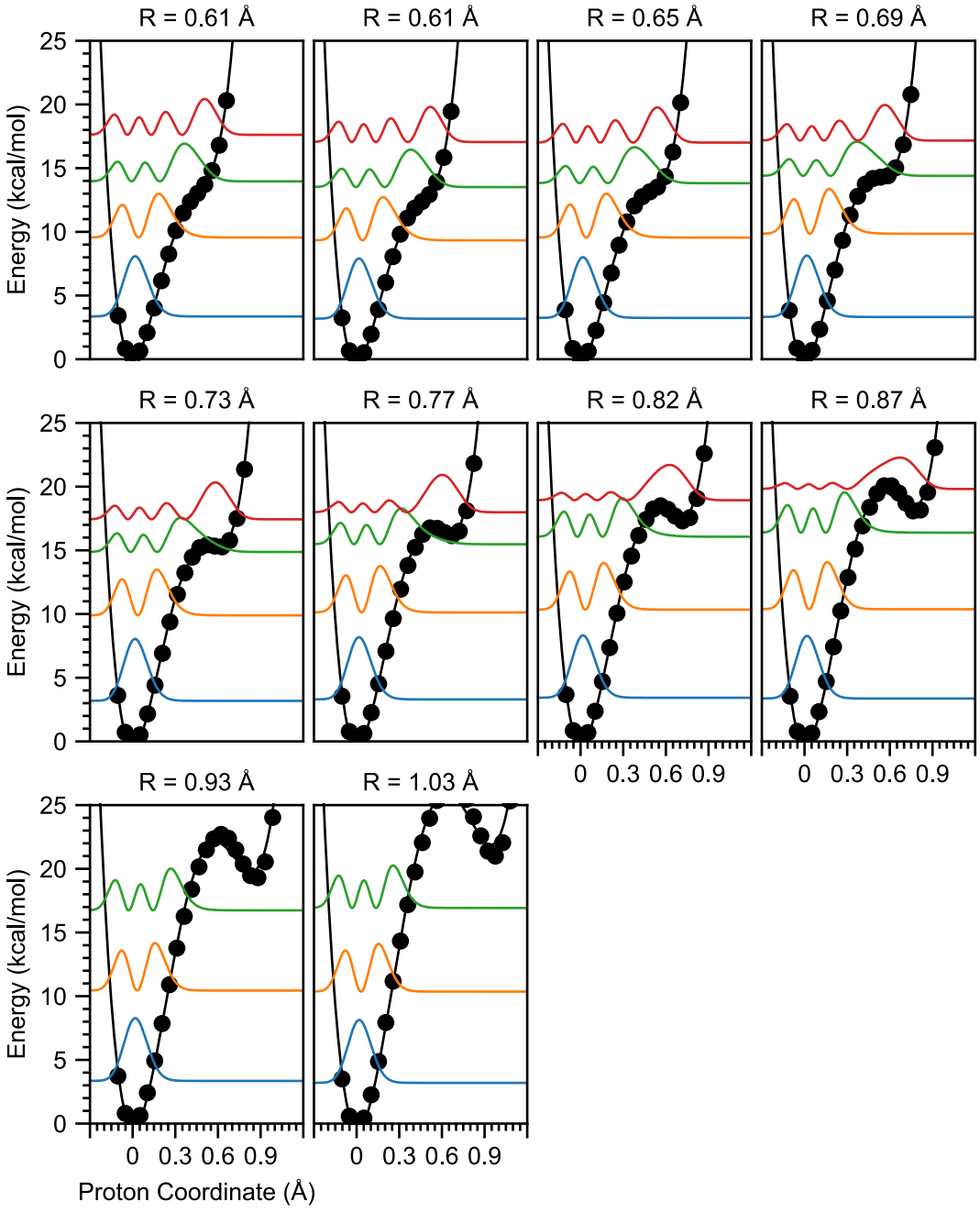

Figure A3.12 The calculated and fit reactant energy wells for diphenylmethane, with vibrational wavefunctions up to 20 kcal/mol in vibrational energy and labeled with the tunneling distance.

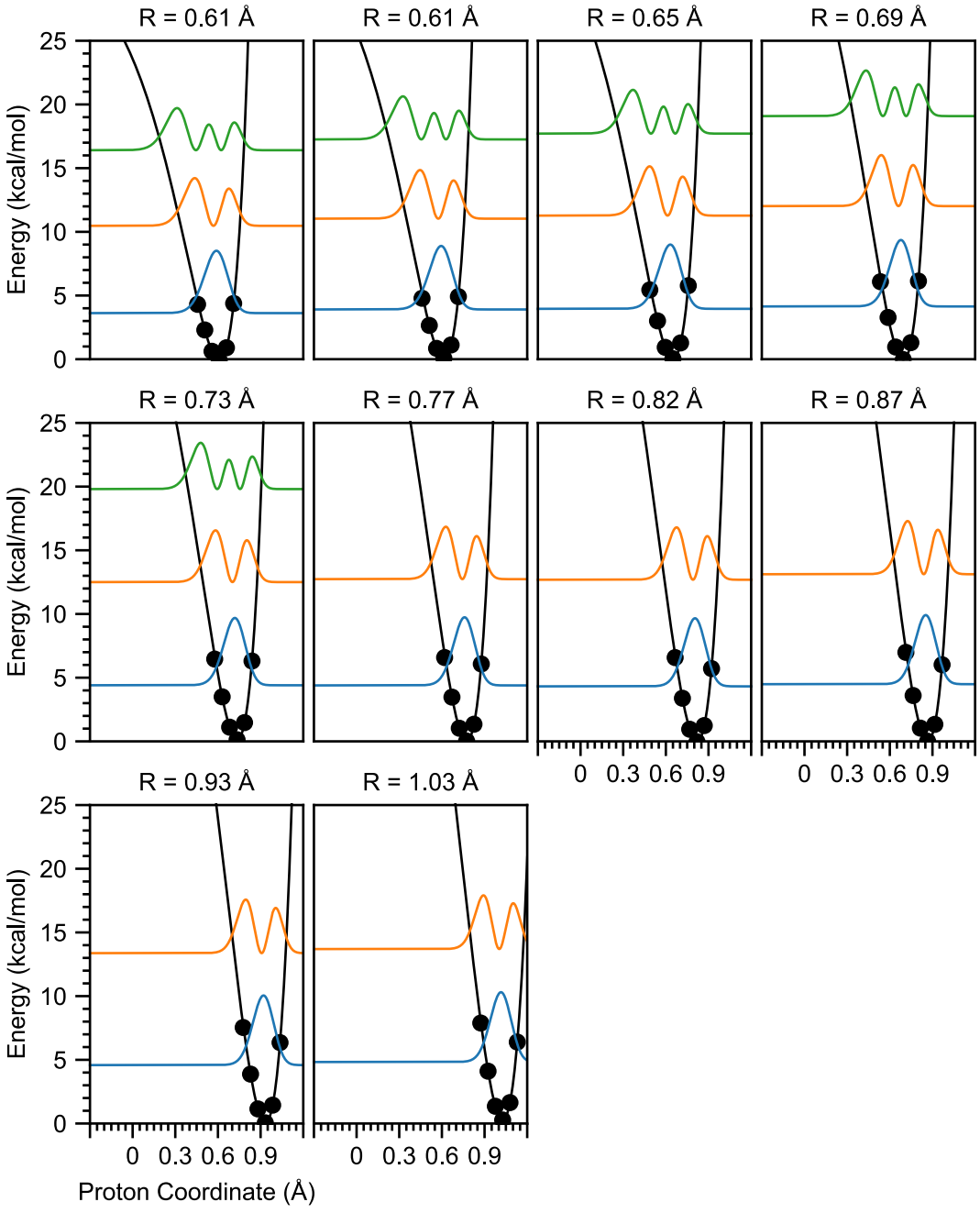

Figure A3.13 The calculated and fit product energy wells for diphenylmethane, with vibrational wavefunctions up to 20 kcal/mol in vibrational energy and labeled with the tunneling distance.

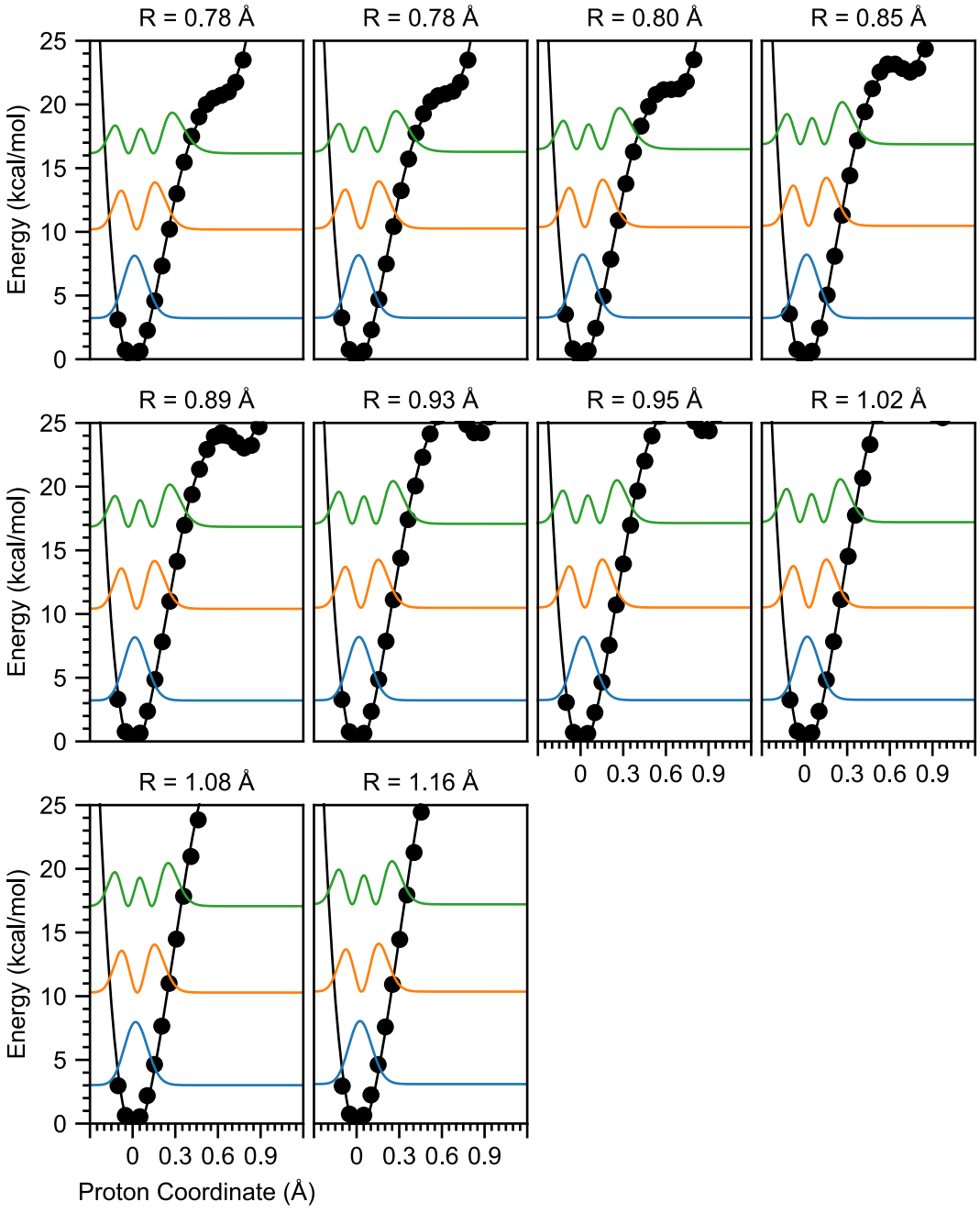

Figure A3.14 The calculated and fit reactant energy wells for 1,3-cyclohexadiene, with vibrational wavefunctions up to 20 kcal/mol in vibrational energy and labeled with the tunneling distance.

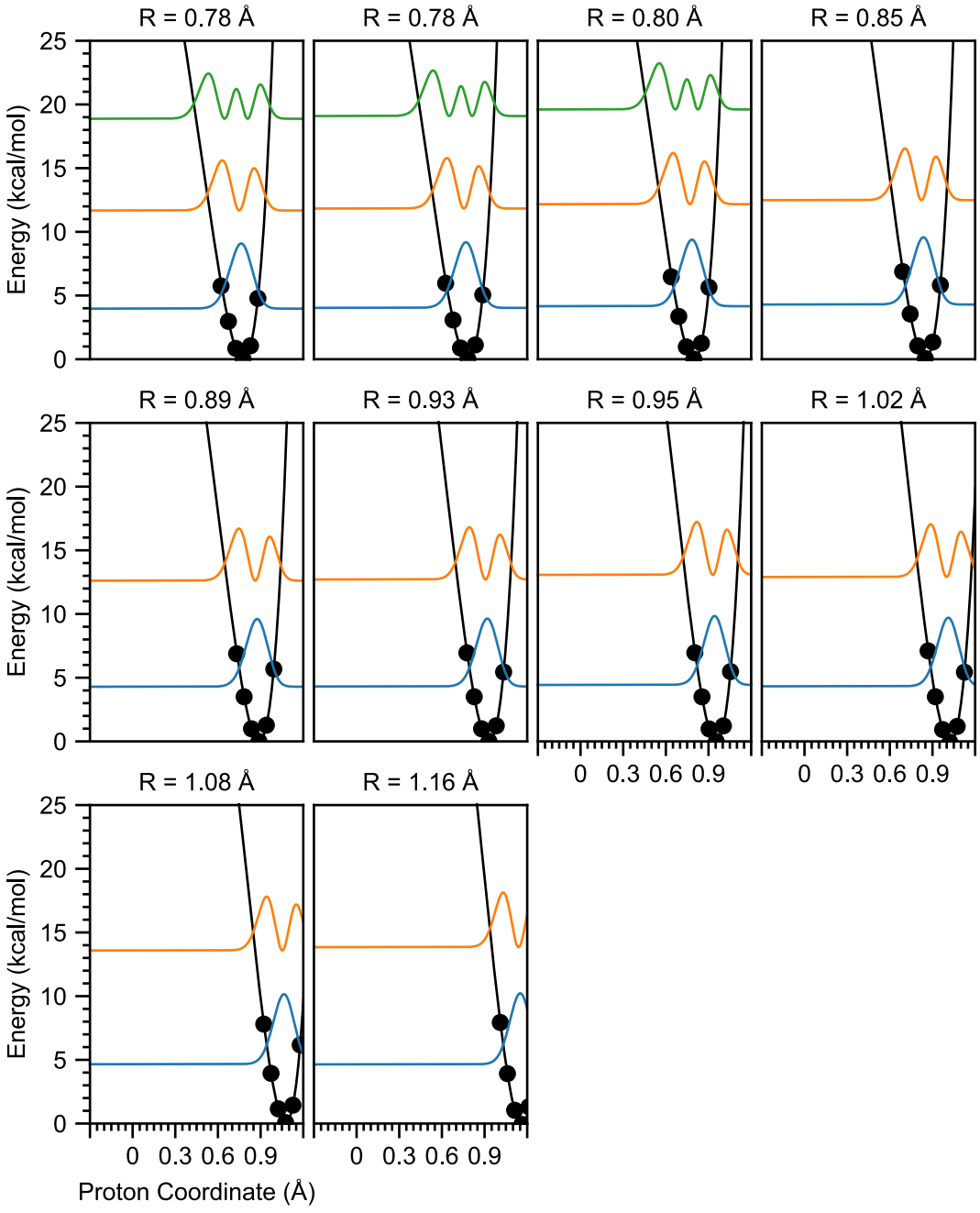

Figure A3.15 The calculated and fit product energy wells for 1,3-cyclohexadiene, with vibrational wavefunctions up to 20 kcal/mol in vibrational energy and labeled with the tunneling distance.

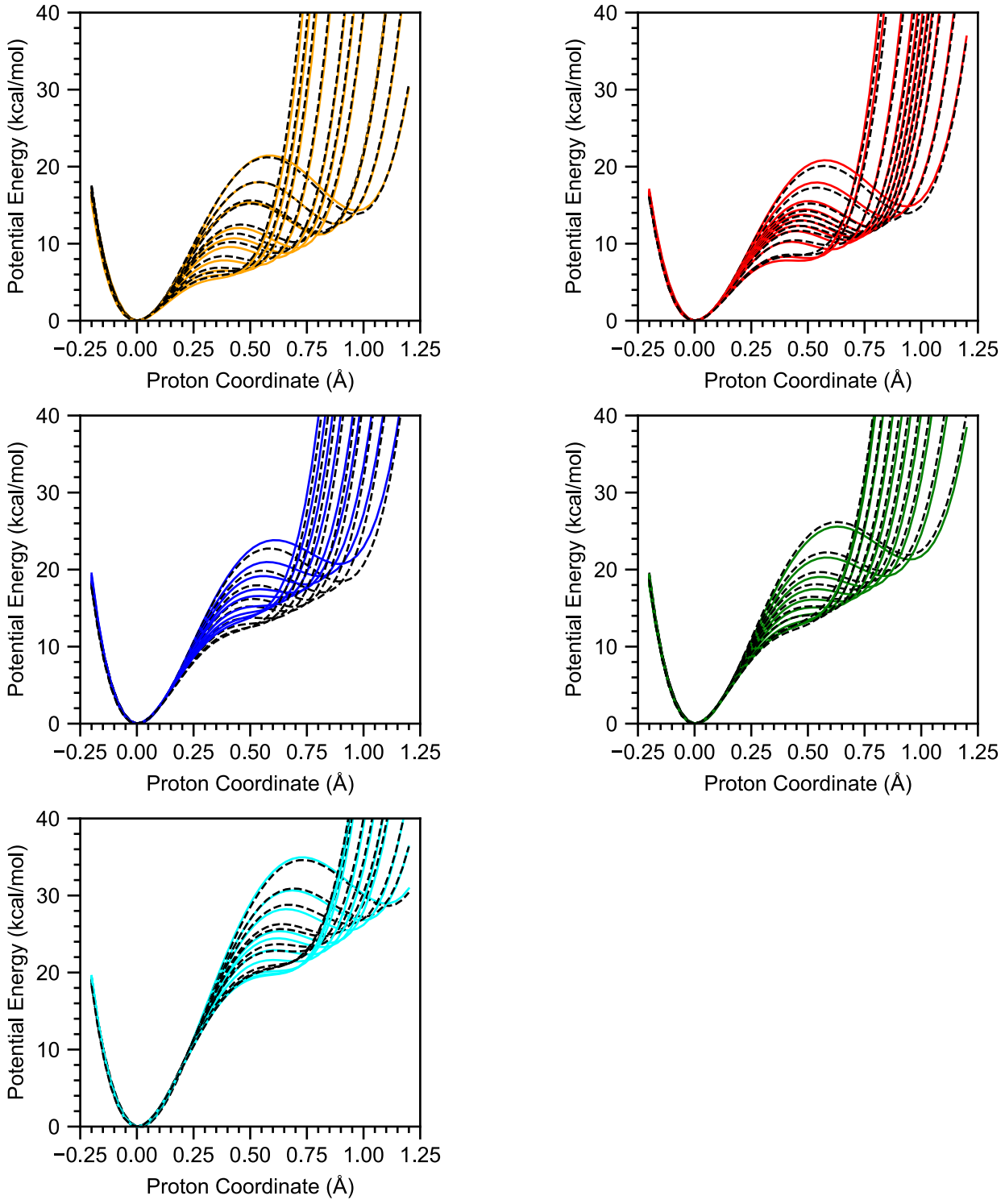

Figure A3.16 Quartic fits to DFT-calculated potential energy wells (black, dashed) and the predictions based on equation S12 (colored, solid) for 9-phenylfluorene (orange), fluorene (red), 9,10-dihydroanthracene (blue), diphenylmethane (green), and 1,3-cyclohexadiene (cyan).

In Equation 4.1 though Equation 4.6 the use of $(\Delta G^{\circ}_{PT} - 0.5\Delta G^{\circ}_{CPET})$ instead of ΔG°_{PT} ensures that the forward and reverse reaction have the same energy well, i.e. it satisfies microscopic reversibility. Using our parameterization of the square scheme (Figure 4.2A), the energy well that is parameterized in the forward direction with $(\Delta G^{\circ}_{PT} - 0.5\Delta G^{\circ}_{CPET})$ would be parametrized in the reverse direction as $\left((-\Delta G^{\circ\prime}_{ET}) - 0.5(-\Delta G^{\circ}_{CPET})\right)$. Substitution of $= -\Delta G^{\circ\prime}_{ET} = -\Delta G^{\circ}_{CPET} + \Delta G^{\circ}_{PT}$ demonstrates this results in the same energy well. The choice of $0.5\Delta G^{\circ}_{CPET}$ is not a unique solution to ensuring microscopic reversibility. We could add more of an admixture of ΔG°_{CPET} into ΔG°_{PT} and correspondingly less admixture into ΔG°_{ET} or *vice versa*. For instance, reactant wells would be parameterized with $(\Delta G^{\circ}_{PT} - 0.2\Delta G^{\circ}_{CPET})$ and product wells with $(\Delta G^{\circ}_{ET} - 0.8\Delta G^{\circ}_{CPET})$. This choice would also obey microscopic reversibility. Furthermore, because we are principally interested in the activation of C–H bonds to form an O–H bond, there is no reason that the parameterization has to be the same in the forward and backward direction. We could model H transferring from C to O (the forward direction) with ΔG°_{PT} and ΔG°_{ET}, but then model H transferring from O to C (the reverse direction) with $\Delta G^{\circ}_{PT} - \Delta G^{\circ}_{CPET}$ and $\Delta G^{\circ}_{ET} - \Delta G^{\circ}_{CPET}$. There is no chemical reason to do so, but it would not violate microscopic reversibility. *The only important detail in this parametrization is that for the reactant energy well is dependent on ΔG°_{PT}, and the product energy well is dependent on ΔG°_{ET}.*

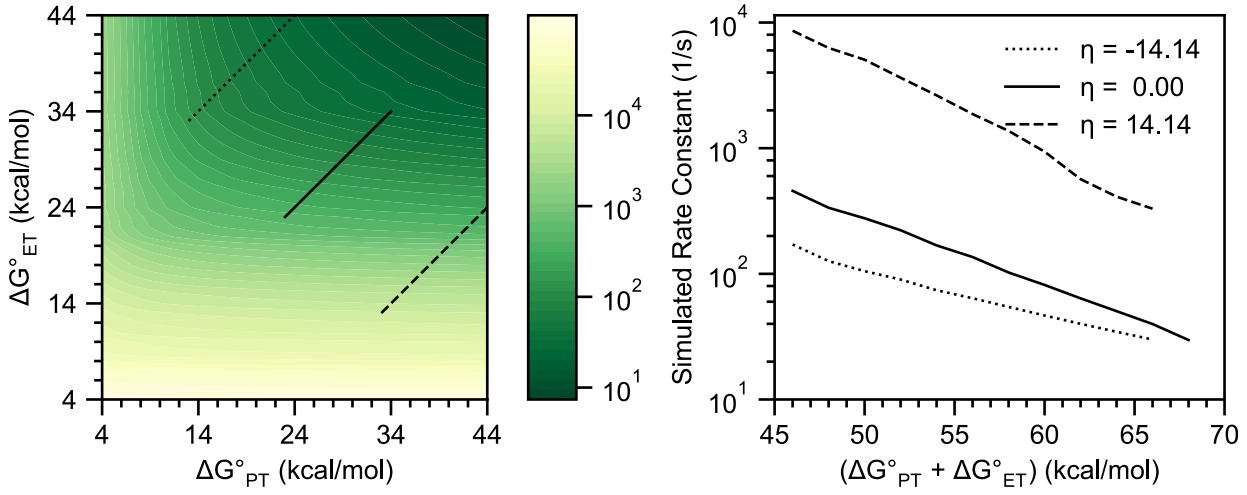

Figure A3.17 Simulated rate constants versus $\Delta G°_{PT}$ and $\Delta G°_{ET}$ with $\Delta G°_{CPET} = -12$ kcal/mol and $\lambda = 40$ kcal/mol.

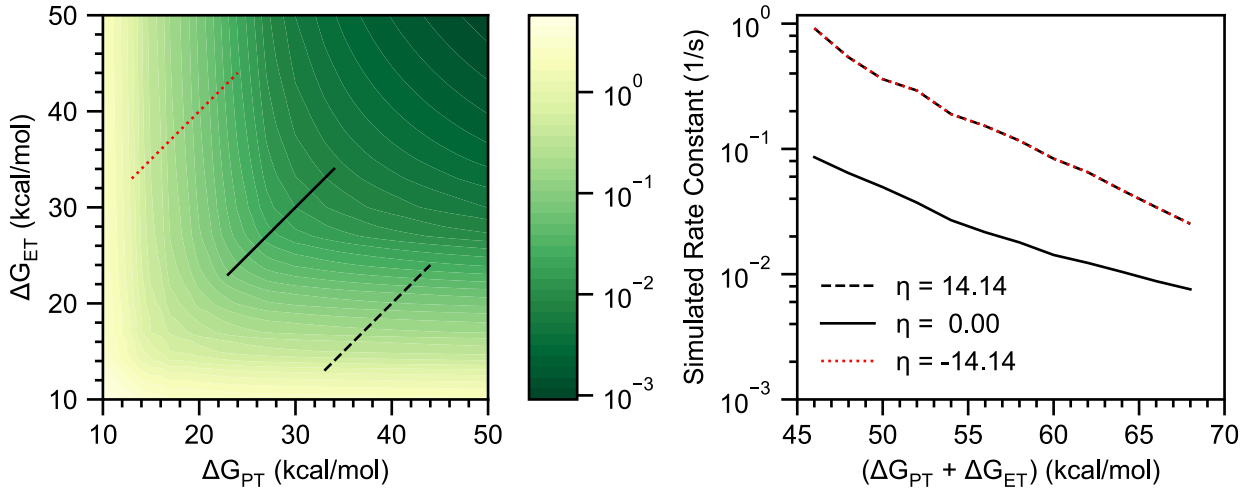

Figure A3.18 Simulated rate constants versus $\Delta G°_{PT}$ and $\Delta G°_{ET}$ with $\Delta G°_{CPET} = 0$ kcal/mol and $\lambda = 40$ kcal/mol.

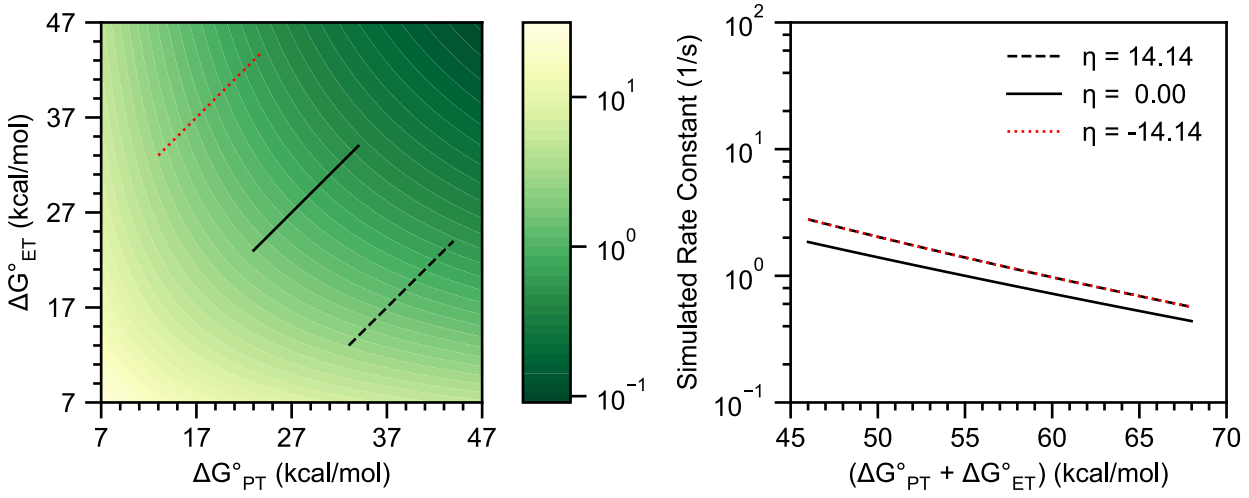

Figure A3.19 Simulated rate constants versus $\Delta G°_{PT}$ and $\Delta G°_{ET}$ with $\Delta G°_{CPET} = -6$ kcal/mol and $\lambda = 40$ kcal/mol with only reactivity from and into ground vibrational states.

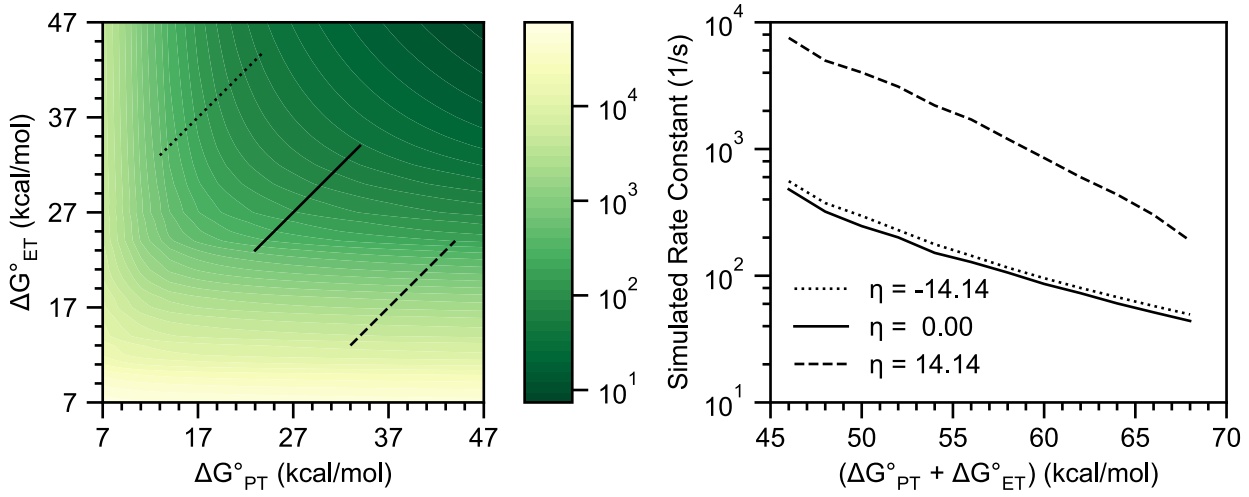

Figure A3.20 Simulated rate constants versus $\Delta G°_{PT}$ and $\Delta G°_{ET}$ with $\Delta G°_{CPET} = -6$ kcal/mol and $\lambda = 30$ kcal/mol.

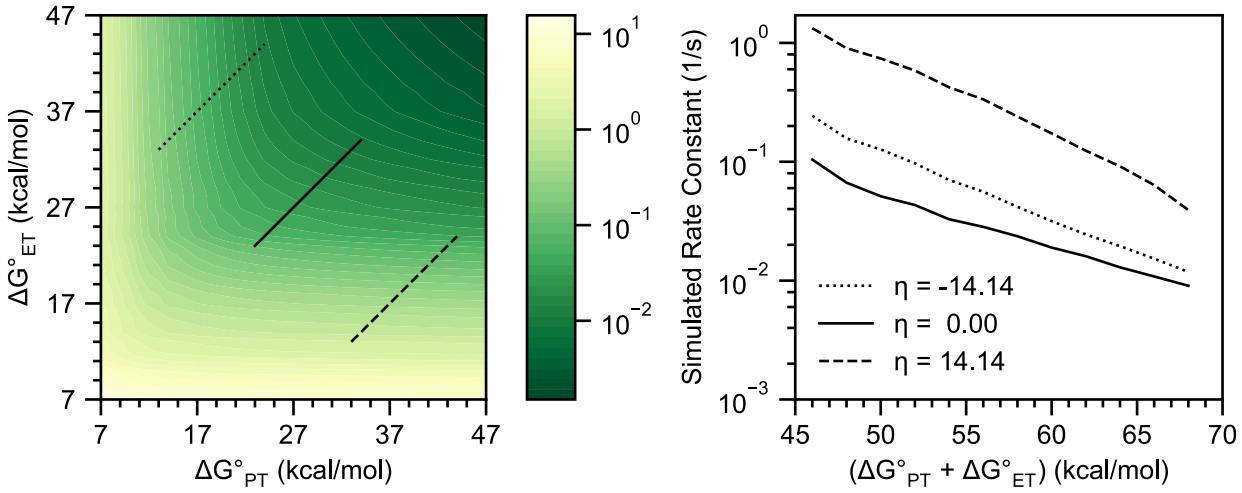

Figure A3.21 Simulated rate constants versus $\Delta G°_{PT}$ and $\Delta G°_{ET}$ with $\Delta G°_{CPET} = -6$ kcal/mol and $\lambda = 50$ kcal/mol.

Appendix A4: Supporting Information for Chapter 5

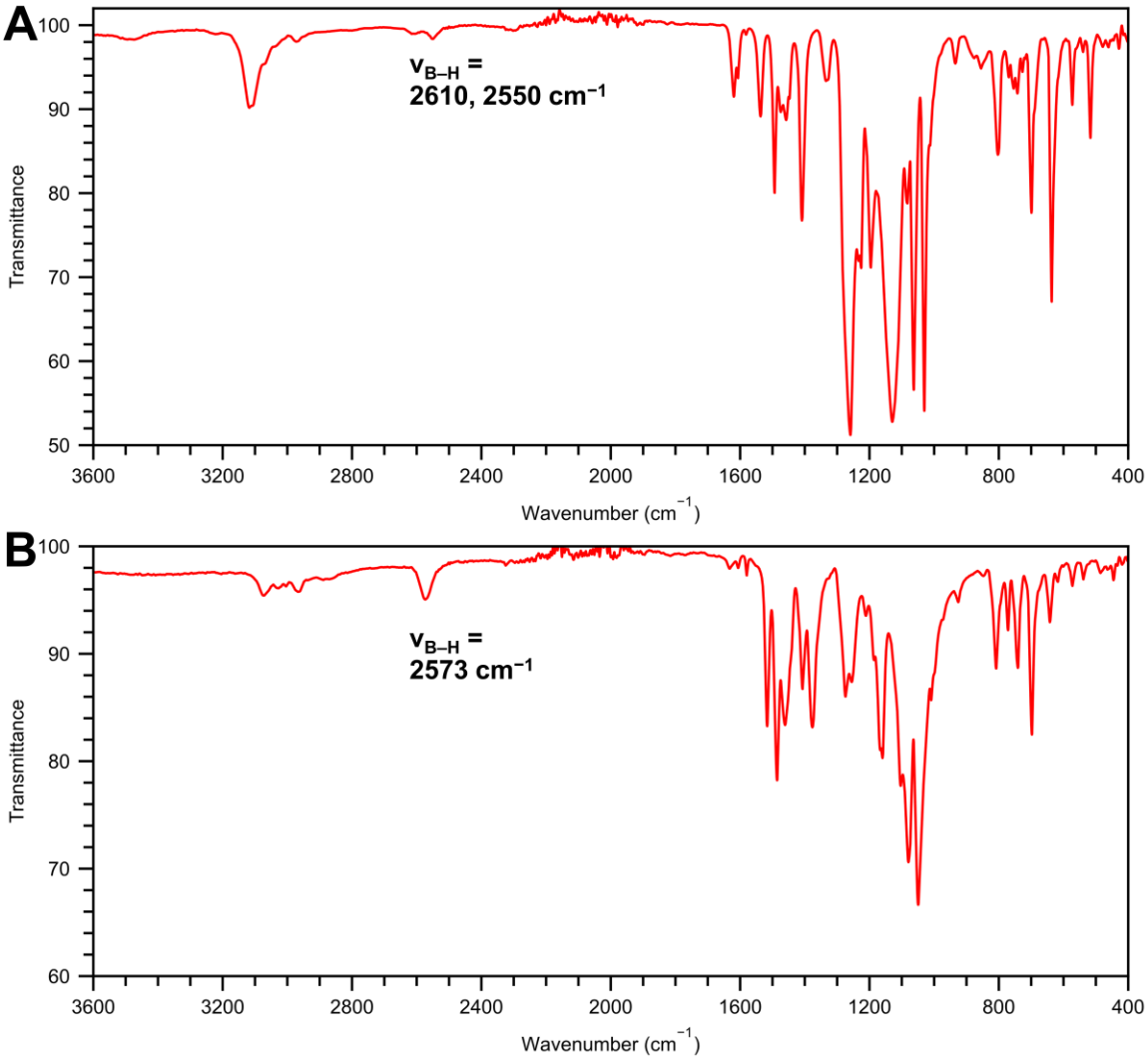

Figure A4.1 (A) ATR-IR spectrum of [(^{CF3,Ph}*m*Imid)$_3$PhB][OTf]$_2$ (B) ATR-IR spectrum of **1**.

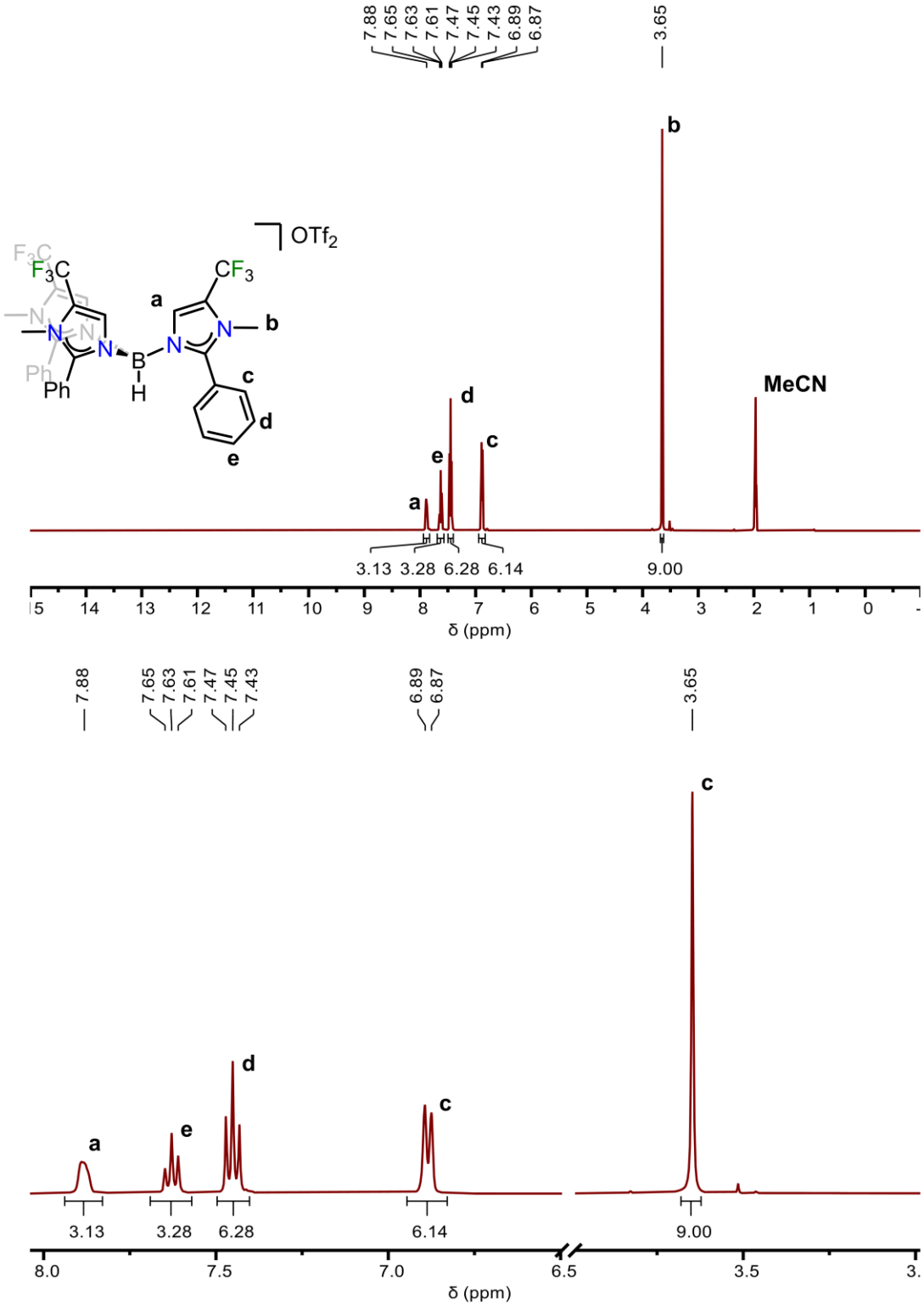

Figure A4.2 Full ^{1}H NMR spectrum (top) and zoom (bottom) for [($^{CF3,Ph)}$*m*Imid)$_3$PhB][OTf]$_2$.

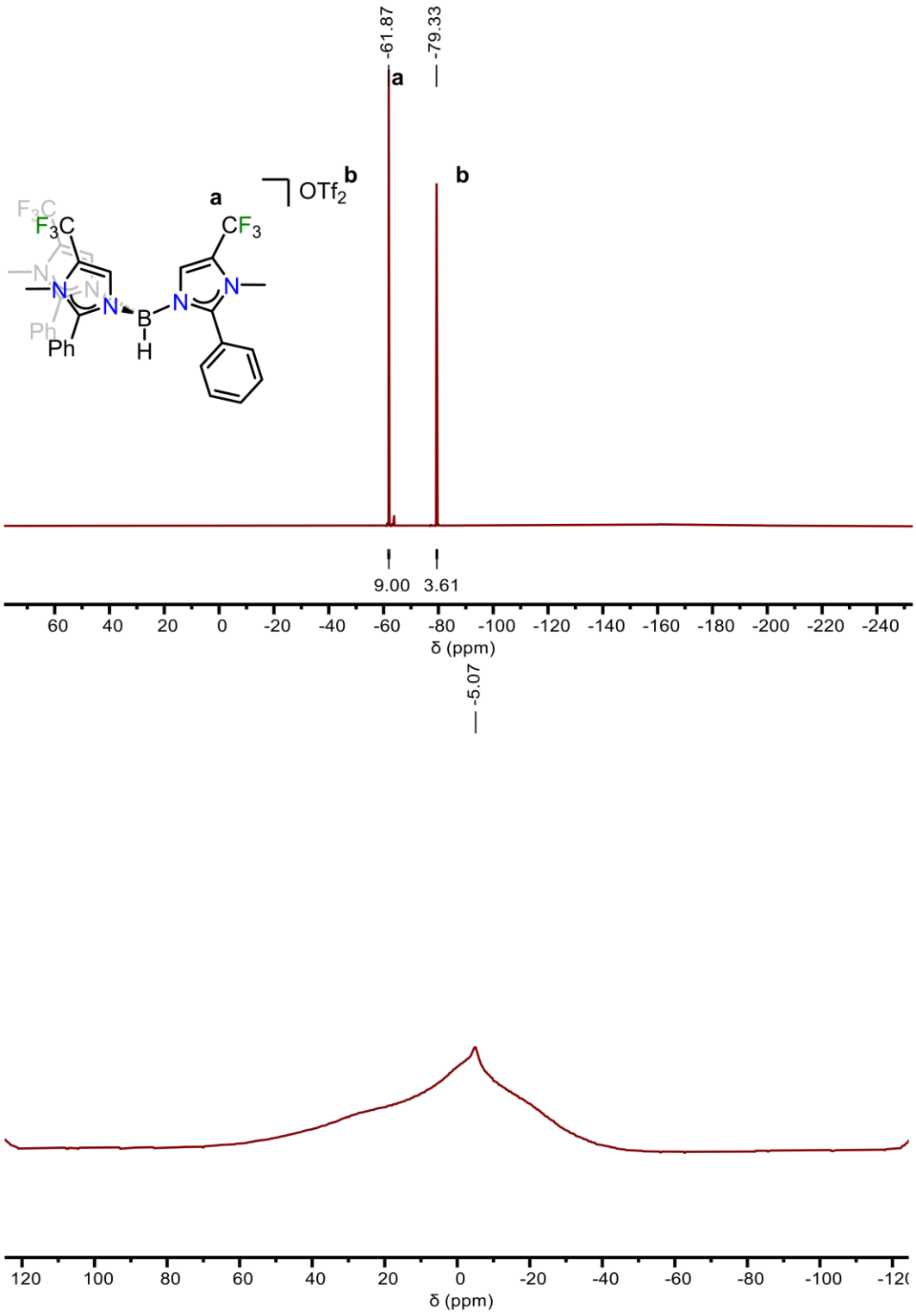

Figure A4.3 $^{19}F\{^{1}H\}$ (top) and $^{11}B\{^{19}F\}$ (bottom) NMR spectra $[(^{CF3,Ph)}m\text{Imid})_3\text{PhB}][\text{OTf}]_2$. The broad baseline for $^{11}B\{^{19}F\}$ is due to the borosilicate NMR tube.

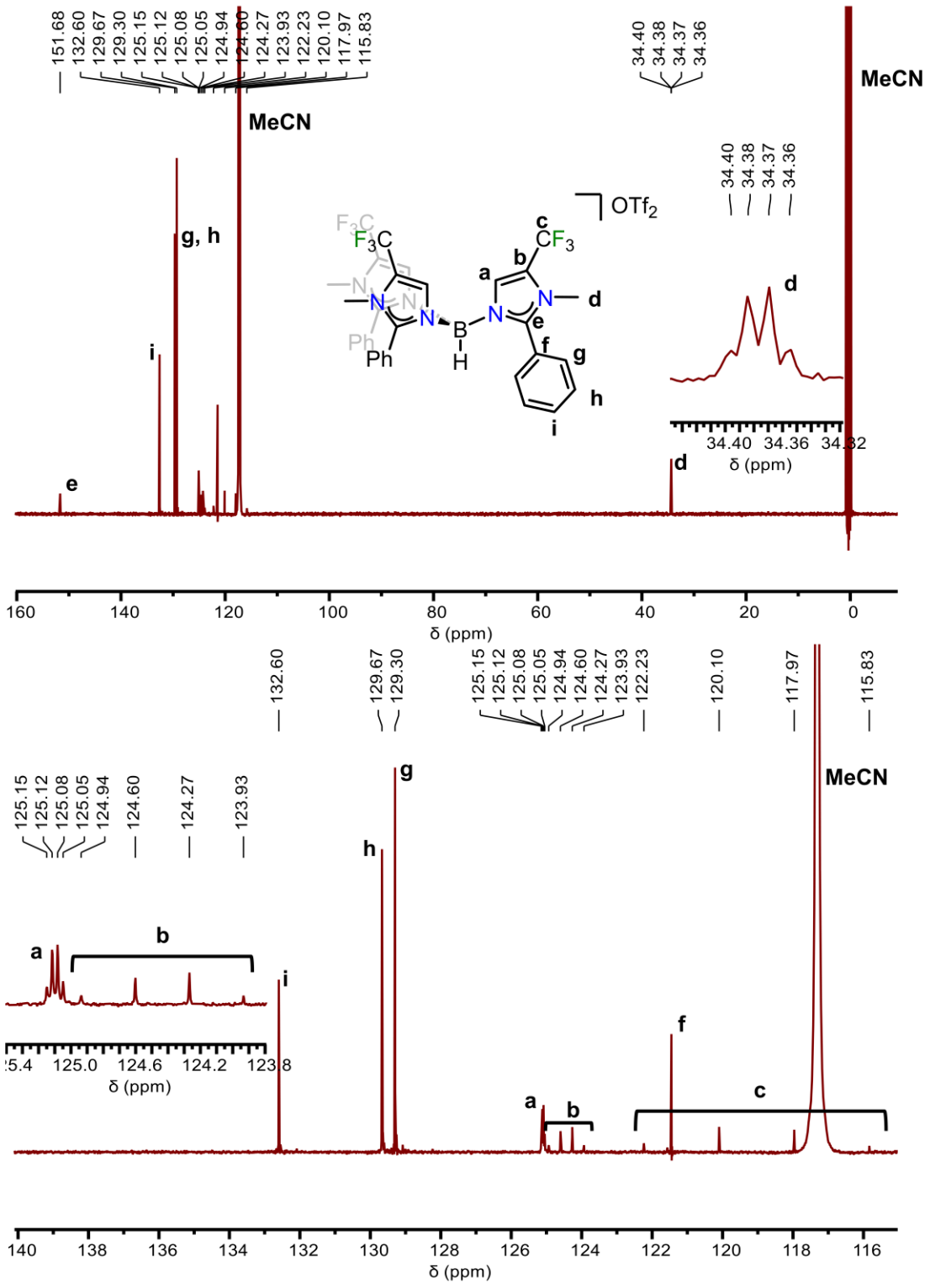

Figure A4.4 Full $^{13}C\{^{1}H\}$ NMR spectrum (top) and zoom (bottom) for $[(^{CF3,Ph)}m\text{Imid})_3\text{PhB}][\text{OTf}]_2$

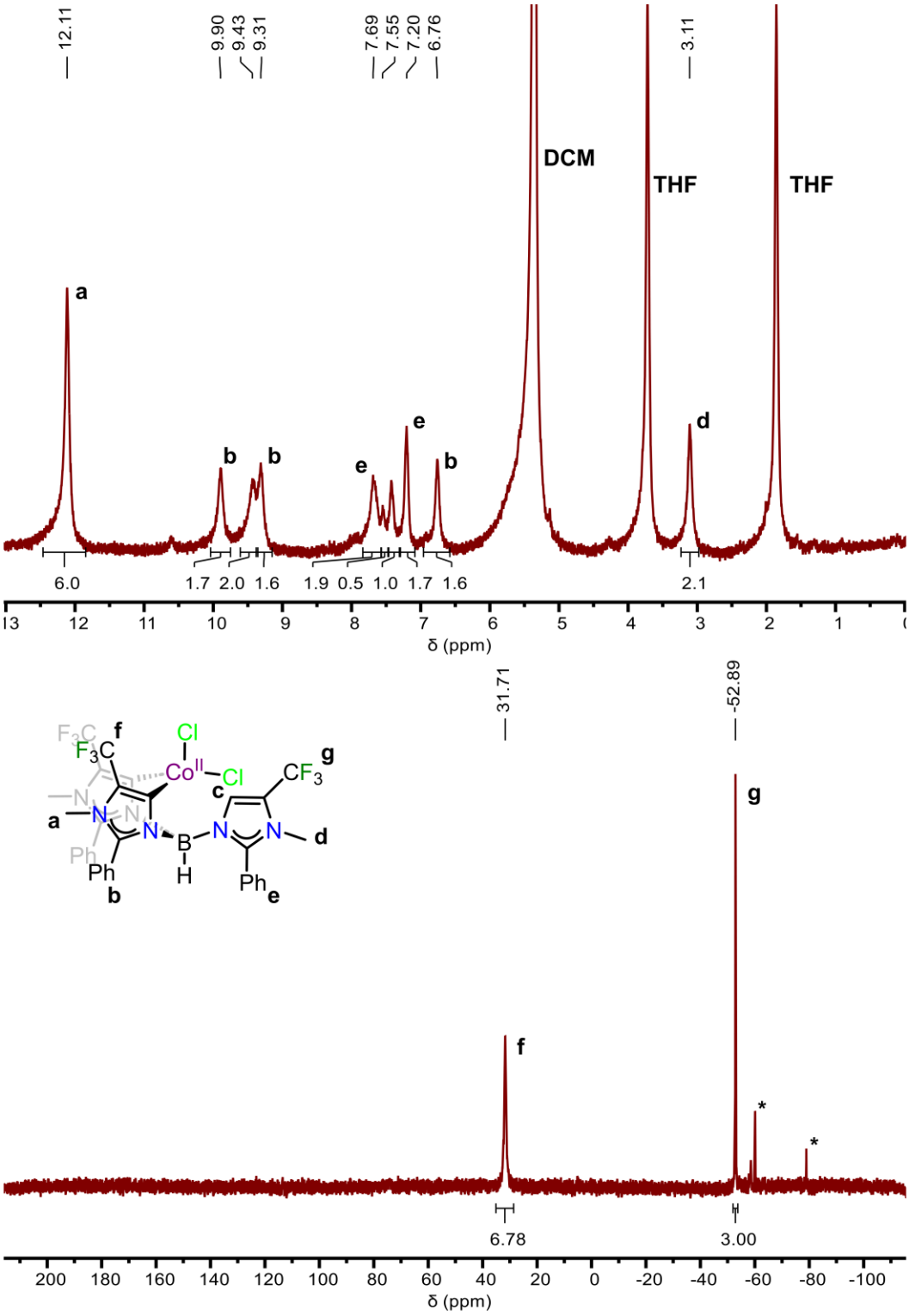

Figure A4.5 ^{1}H (top) and $^{19}F\{^{1}H\}$ (bottom) NMR spectra of the initial blue powder formed in the synthesis of **1** with the tentative assignments as a κ^2-complex shown.

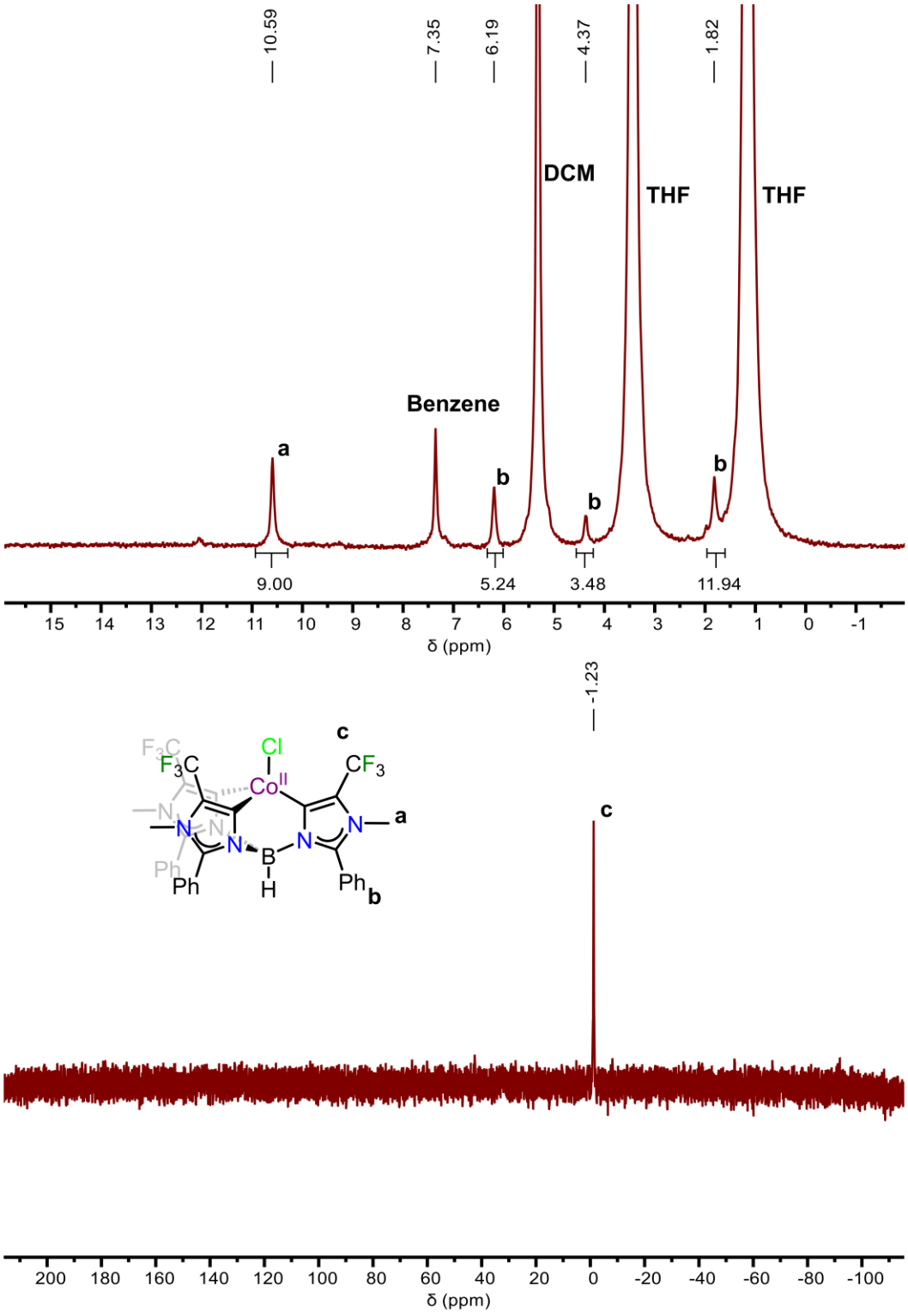

Figure A4.6 ^{1}H (top) and $^{19}F\{^{1}H\}$ (bottom) NMR spectra of **1**.

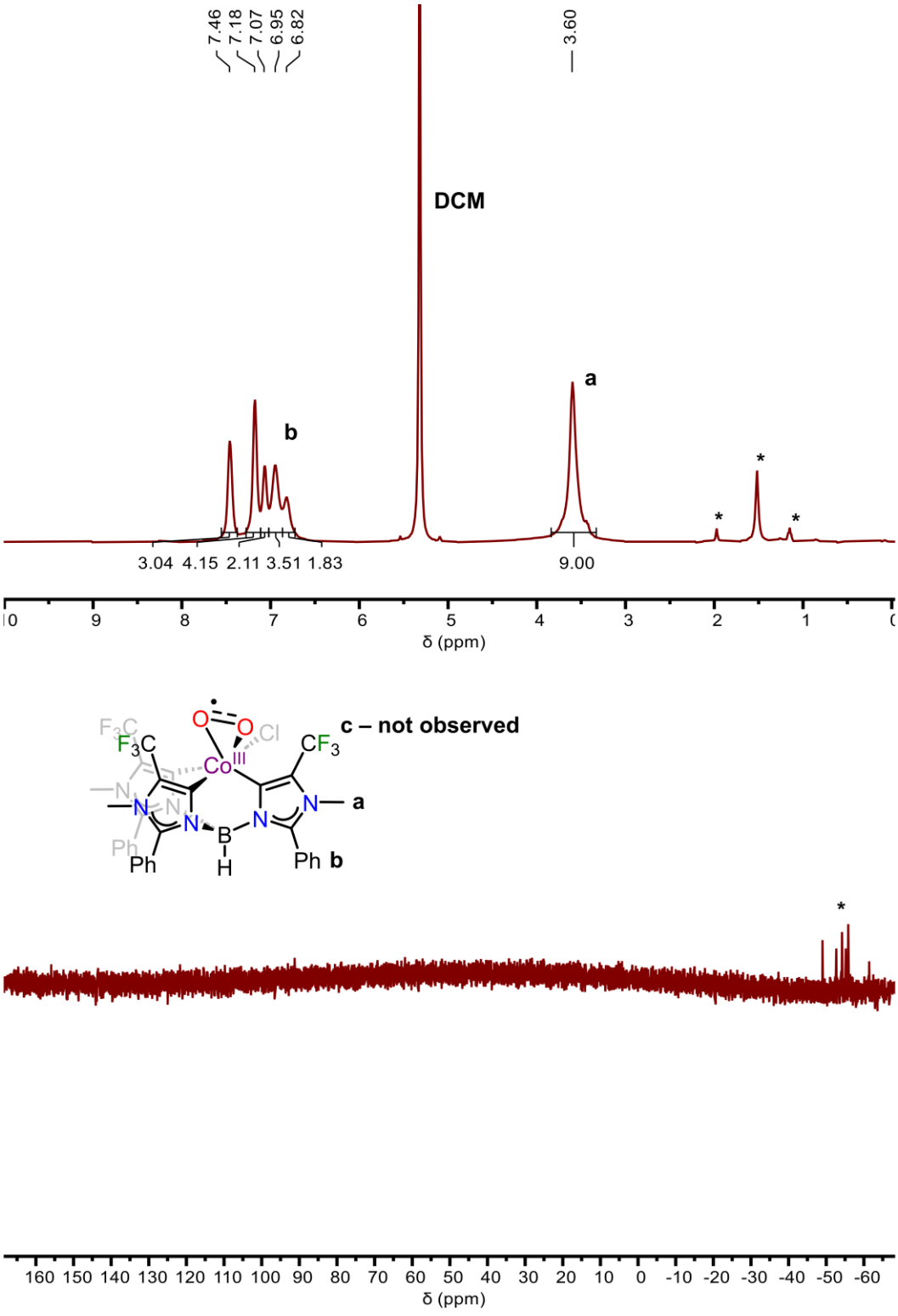

Figure A4.7 ^{1}H (top) and $^{19}F\{^{1}H\}$ (bottom) NMR spectra of **1-O$_2$**.

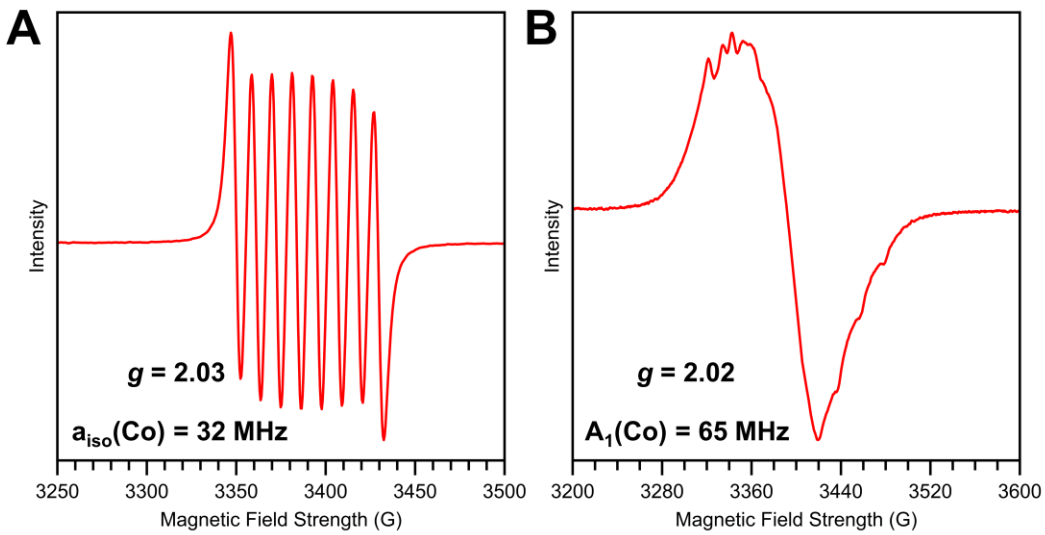

Figure A4.8 CW-EPR spectra of 1-O_2 in DCM at 9.6 GHz. (A) Room temperature (B) 140 K

Table A4.1 SXRD Parameters for reported crystal structures.

	1-O_2	**2**	**2-O_2**
Empirical formula	$C_{35}H_{29}BCl_5CoF_9N_6O_2$	$C_{66}H_{39}B_2Cl_2CoF_{33}N_6O$	$C_{77}H_{46}B_2CoF_{37}N_6O$
Formula weight	983.665	1818.70	1854.75
Temperature/K	99.9(6)	100.00	100(2)
Crystal system	triclinic	triclinic	triclinic
Space group	P-1	P-1	P-1
a/Å	11.2455(8)	12.0757(3)	13.6988(13)
b/Å	13.3750(7)	17.1630(4)	15.3207(15)
c/Å	13.5392(13)	20.2071(5)	20.166(2)
α/°	90.270(6)	65.7420(10)	106.958(2)
β/°	102.149(7)	78.6370(10)	104.506(2)
γ/°	97.748(5)	82.4740(10)	99.323(2)
Volume/$Å^3$	1971.5(3)	3737.53(16)	3790.8(6)
Z	2	2	2
$\rho_{calc}g/cm^3$	1.657	1.616	1.625
μ/mm^{-1}	7.298	0.434	0.369
F(000)	992.8	1832.0	1856.0
Crystal size/mm^3	0.24 × 0.05 × 0.04	0.266 × 0.082 × 0.07	0.733 × 0.154 × 0.08
Radiation	Cu Kα (λ = 1.54184)	MoKα (λ = 0.71073)	MoKα (λ = 0.71073)
2Θ range for data collection/°	6.68 to 117.86	3.8 to 50.72	4.318 to 51.808
Index ranges	$-12 \le h \le 12$, $-10 \le k \le 14$, $-15 \le l \le 15$	$-14 \le h \le 14$, $-20 \le k \le 20$, $-24 \le l \le 24$	$-16 \le h \le 16$, $-18 \le k \le 18$, $-24 \le l \le 24$
Reflections collected	17233	92227	63900
Independent reflections	5568 [R_{int} = 0.1297, R_{sigma} = 0.1128]	13680 [R_{int} = 0.0457, R_{sigma} = 0.0488]	14600 [R_{int} = 0.0704, R_{sigma} = 0.0704]
Data/restraints /parameters	5568/0/535	13680/1570/1099	14600/0/1160
Goodness-of-fit on F^2	1.085	1.080	1.042
Final R indexes [I>=2σ (I)]	R_1 = 0.1136, wR_2 = 0.2607	R_1 = 0.0525, wR_2 = 0.1441	R_1 = 0.0643, wR_2 = 0.1486
Final R indexes [all data]	R_1 = 0.1433, wR_2 = 0.2785	R_1 = 0.0801, wR_2 = 0.1536	R_1 = 0.1127, wR_2 = 0.1738
Largest diff. peak/hole (e $Å^{-3}$)	1.28/-1.06	0.91/-0.91	1.28/-0.63

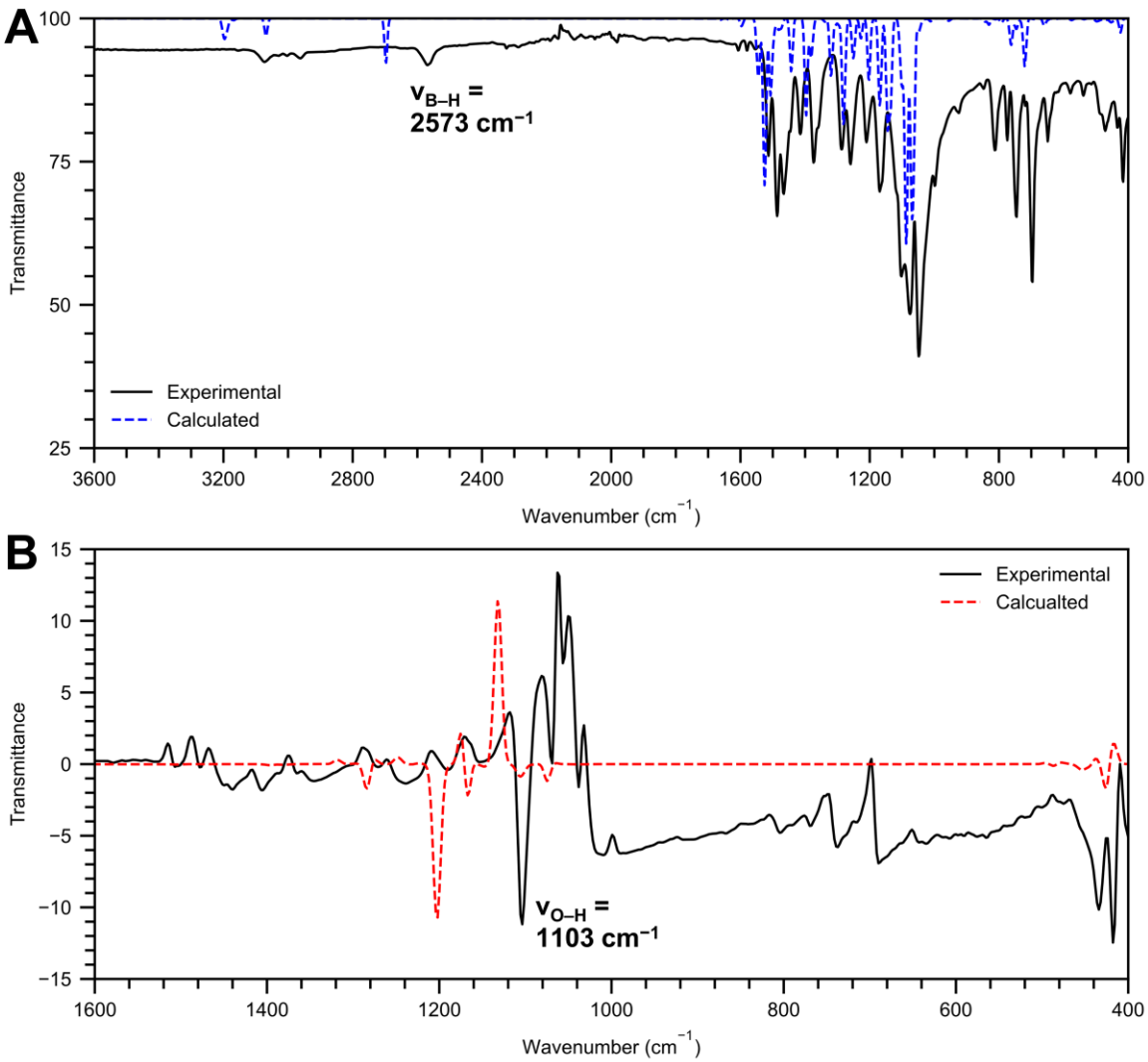

Figure A4.9 Experimental and calculated IR spectra of **1-O$_2$**. No correction factor has been applied to the calculated spectra. (A) Full experimental and calculated ATR-IR of **1-O$_2$**. (B) Experimental difference spectrum between **1-O$_2$** formed from $^{16}O_2$ vs from $^{18}O_2$ alongside the calculated spectrum.

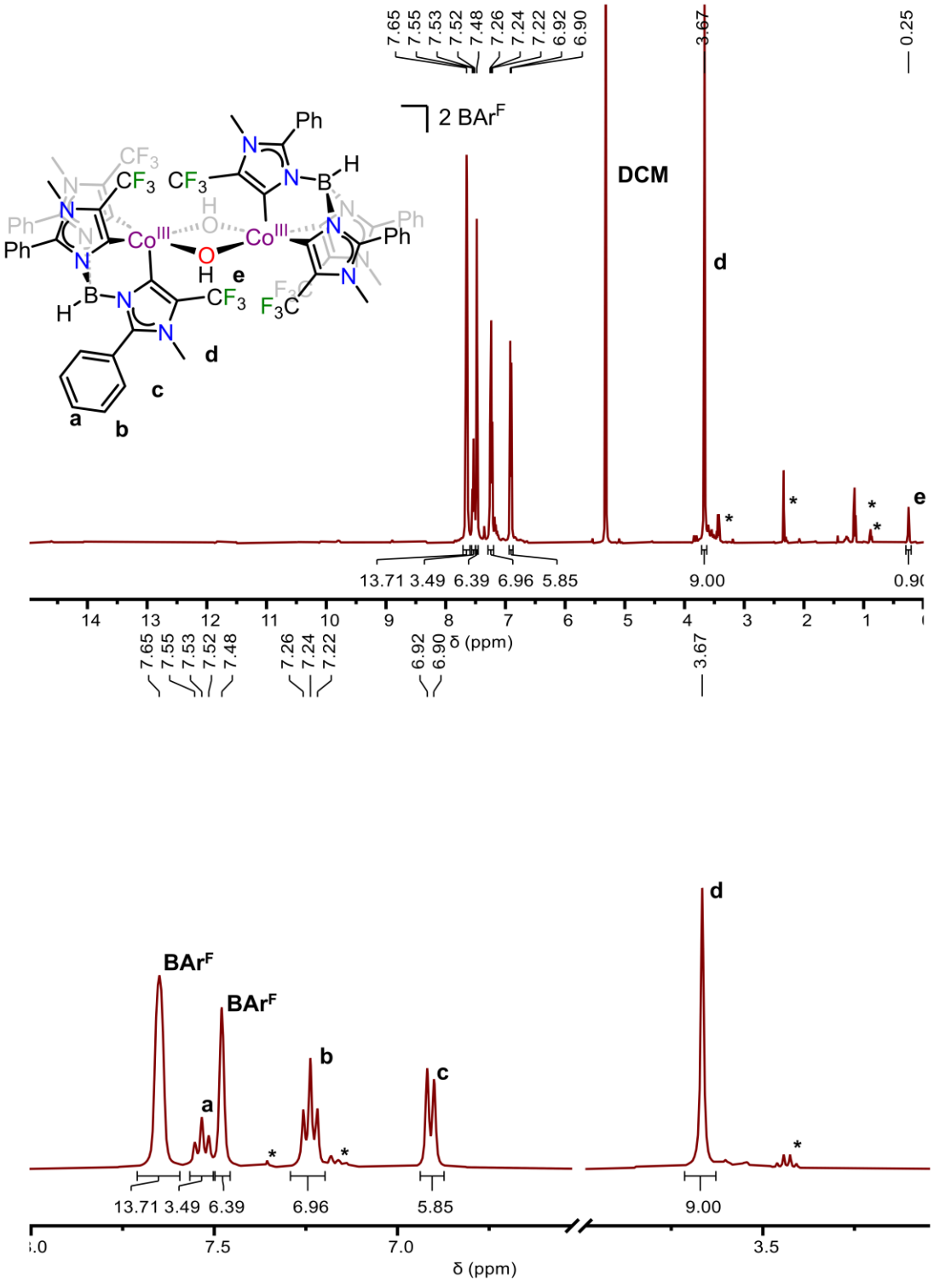

Figure A4.10 ^{1}H NMR spectrum of **2-H$_2$**.

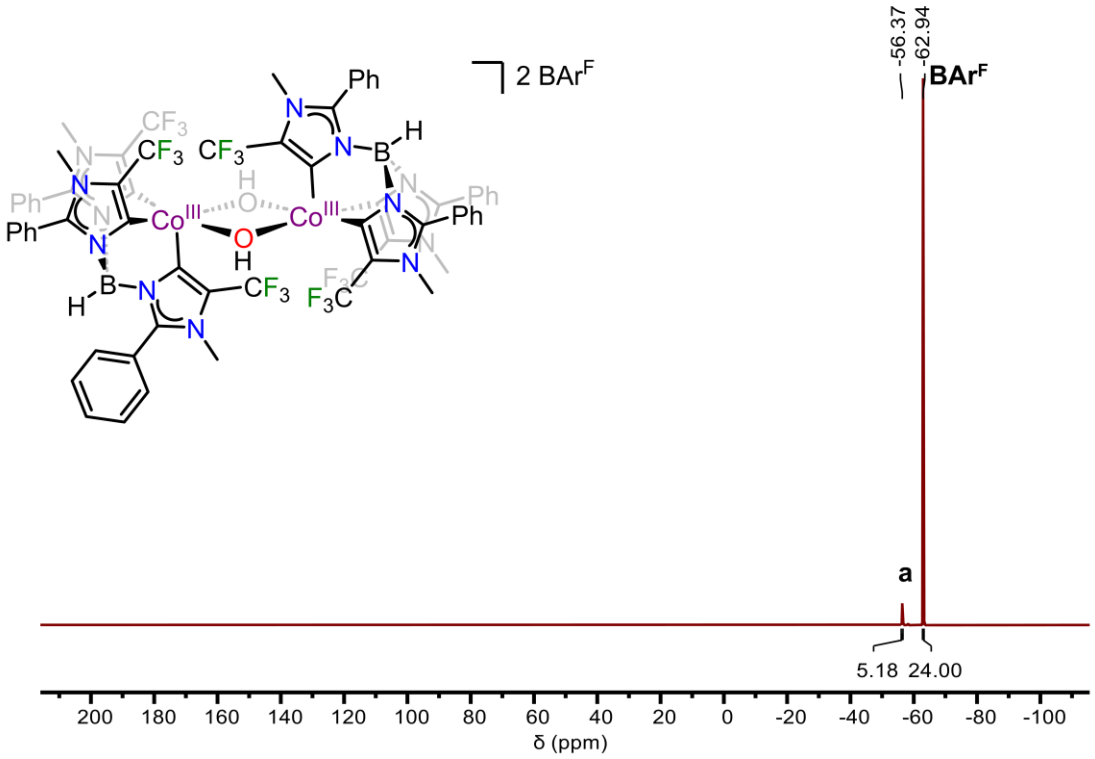

Figure A4.11 $^{19}F\{^{1}H\}$ NMR spectrum of **2-H2**.

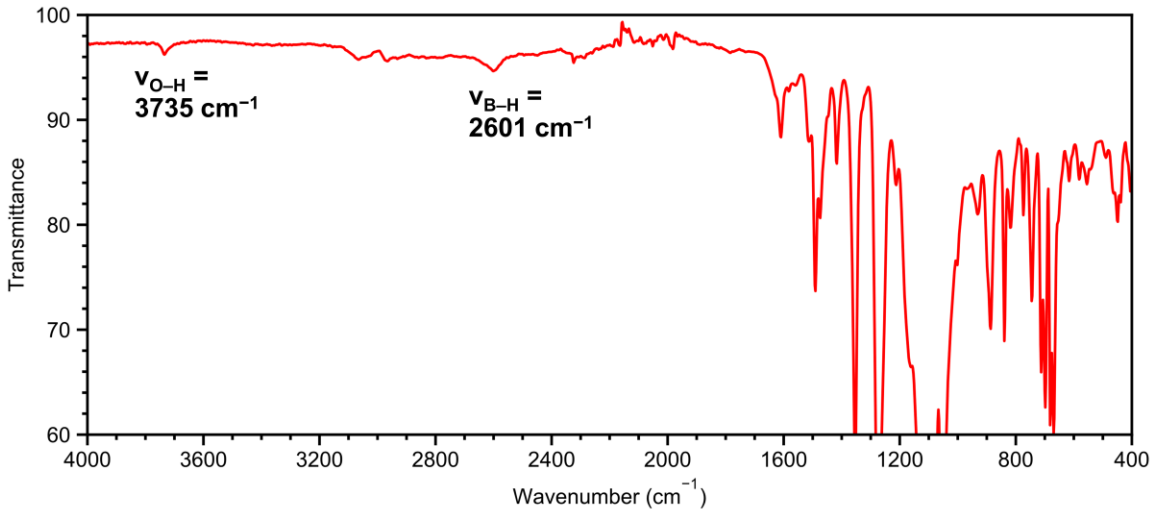

Figure A4.12 ATR-IR spectrum **2-H2**.

Table A4.2 Coordinates from the optimized structure of 1-O_2.

Co	-0.102662	0.035939	0.295874
Cl	-1.093217	1.932572	1.235946
O	0.894129	-0.232902	1.922194
O	-0.263323	-0.833113	1.992629
C	0.696143	-1.461582	-0.673837
C	1.377634	-2.648397	-0.447016
C	1.829710	-3.347602	0.791236
F	1.203010	-2.950393	1.897173
F	3.163021	-3.186113	1.009301
F	1.632847	-4.689205	0.694429
N	1.729191	-3.218007	-1.683651
C	2.537750	-4.417394	-1.917061
H	1.933963	-5.322874	-1.759768
H	3.395778	-4.415028	-1.230940
H	2.900876	-4.384591	-2.953108
C	1.253394	-2.418235	-2.652731
C	1.366880	-2.638852	-4.102999
C	0.846394	-3.806162	-4.689973
H	0.383665	-4.571826	-4.061016
C	0.895511	-3.972310	-6.077527
H	0.481352	-4.878338	-6.529099
C	1.459299	-2.976880	-6.885147
H	1.488662	-3.106017	-7.971143
C	1.986935	-1.816693	-6.303073
H	2.431875	-1.037687	-6.928724
C	1.945143	-1.648053	-4.917745
H	2.361857	-0.746356	-4.462607
N	0.637180	-1.379181	-2.069059
C	0.790136	1.209467	-0.939432
C	1.642708	2.291499	-0.858187
C	2.278610	2.935367	0.321698
F	3.597301	3.187482	0.092482
F	2.213262	2.170312	1.414122
F	1.730093	4.137724	0.634118
N	1.883385	2.780440	-2.150709
C	2.638881	3.984344	-2.502525
H	3.719125	3.776857	-2.485150
H	2.399202	4.779068	-1.782417
H	2.334098	4.301734	-3.509117
C	1.215642	1.993688	-3.016836
C	1.190733	2.100064	-4.480343
C	-0.044316	2.044191	-5.154668
H	-0.973034	1.996393	-4.581198

Table A4.2, continued.

C	-0.083446	2.054460	-6.550025
H	-1.047998	2.004900	-7.063151
C	1.106749	2.126992	-7.285669
H	1.074863	2.130922	-8.379251
C	2.337587	2.193731	-6.620987
H	3.269040	2.244953	-7.192076
C	2.383679	2.178011	-5.223838
H	3.348244	2.195259	-4.709415
N	0.568415	1.055525	-2.301025
C	-1.671428	-0.207779	-0.787428
C	-3.031388	-0.323848	-0.581250
C	-3.811911	-0.386709	0.684084
F	-3.038399	-0.639057	1.743026
F	-4.750013	-1.373275	0.639505
F	-4.500285	0.753260	0.943219
N	-3.675681	-0.393955	-1.825896
C	-5.111396	-0.550107	-2.064403
H	-5.657560	0.243308	-1.533606
H	-5.443332	-1.535584	-1.707995
H	-5.294033	-0.465065	-3.143290
C	-2.726783	-0.357210	-2.780379
C	-2.923443	-0.413414	-4.238803
C	-3.631997	0.601390	-4.907352
H	-4.074901	1.421813	-4.335719
C	-3.742824	0.574922	-6.301149
H	-4.288831	1.370494	-6.816202
C	-3.142588	-0.456068	-7.034303
H	-3.222639	-0.469012	-8.125336
C	-2.437568	-1.469239	-6.371896
H	-1.968025	-2.276889	-6.940719
C	-2.329650	-1.452250	-4.979423
H	-1.782088	-2.243710	-4.461467
N	-1.534500	-0.254616	-2.168764
B	-0.125352	-0.231140	-2.780026
H	-0.127240	-0.348073	-3.972696

Bibliography

1 M. Milan, M. Salamone, M. Costas and M. Bietti, *Acc. Chem. Res.*, 2018, **51**, 1984–1995.

2 H. B. Gray and J. R. Winkler, *Acc. Chem. Res.*, 2018, **51**, 1850–1857.

3 G. Yin, *Coord. Chem. Rev.*, 2010, **254**, 1826–1842.

4 V. A. Larson, B. Battistella, K. Ray, N. Lehnert and W. Nam, *Nat. Rev. Chem.*, 2020, **4**, 404–419.

5 D. Ostovic and T. C. Bruice, *Acc. Chem. Res.*, 1992, **25**, 314–320.

6 N. S. Lewis and D. G. Nocera, *Proc. Natl. Acad. Sci. U.S.A.*, 2006, **103**, 15729–15735.

7 J. Hohenberger, K. Ray and K. Meyer, *Nat Commun*, 2012, **3**, 720.

8 Z. Chen and G. Yin, *Chem. Soc. Rev.*, 2015, **44**, 1083–1100.

9 K. A. Joergensen, *Chem. Rev.*, 1989, **89**, 431–458.

10 J. P. McEvoy and G. W. Brudvig, *Chem. Rev.*, 2006, **106**, 4455–4483.

11 A. Gunay and K. H. Theopold, *Chem. Rev.*, 2010, **110**, 1060–1081.

12 J. R. Winkler and H. B. Gray, in *Molecular Electronic Structures of Transition Metal Complexes I*, eds. D. M. P. Mingos, P. Day and J. P. Dahl, Springer Berlin Heidelberg, Berlin, Heidelberg, 2012, pp. 17–28.

13 C. J. Ballhausen and H. B. Gray, *Inorg. Chem.*, 1962, **1**, 111–122.

14 M. K. Goetz, E. A. Hill, A. S. Filatov and J. S. Anderson, *J. Am. Chem. Soc.*, 2018, **140**, 13176–13180.

15 R. S. Hay-Motherwell, G. Wilkinson, B. Hussain-Bates and M. B. Hursthouse, *Polyhedron*, 1993, **12**, 2009–2012.

16 R. Gupta and A. S. Borovik, *J. Am. Chem. Soc.*, 2003, **125**, 13234–13242.

17 J. England, M. Martinho, E. R. Farquhar, J. R. Frisch, E. L. Bominaar, E. Münck and L. Que, *Angew. Chem. Int. Ed.*, 2009, **48**, 3622–3626.

18 J.-U. Rohde, J.-H. In, M. H. Lim, W. W. Brennessel, M. R. Bukowski, A. Stubna, E. Münck, W. Nam and L. Que, *Science*, 2003, **299**, 1037–1039.

19 J. T. Groves, G. A. McClusky, R. E. White and M. J. Coon, *Biochem. Biophys. Res. Commun.*, 1978, **81**, 154–160.

20 J. T. Groves, *J. Chem. Educ.*, 1985, **62**, 928.

21 M. Sono, M. P. Roach, E. D. Coulter and J. H. Dawson, *Chem. Rev.*, 1996, **96**, 2841–2888.

22 F. Ogliaro, N. Harris, S. Cohen, M. Filatov, S. P. de Visser and S. Shaik, *J. Am. Chem. Soc.*, 2000, **122**, 8977–8989.

23 J. J. Warren, T. A. Tronic and J. M. Mayer, *Chem. Rev.*, 2010, **110**, 6961–7001.

24 J. W. Darcy, B. Koronkiewicz, G. A. Parada and J. M. Mayer, *Acc. Chem. Res.*, 2018, **51**, 2391–2399.

25 J. H. Dawson and Masanori. Sono, *Chem. Rev.*, 1987, **87**, 1255–1276.

26 T. L. Poulos and E. F. Johnson, in *Cytochrome P450: Structure, Mechanism, and Biochemistry*, ed. P. R. Ortiz de Montellano, Springer International Publishing, Cham, 2015, pp. 3–32.

27 A. J. Mitchell, Q. Zhu, A. O. Maggiolo, N. R. Ananth, M. L. Hillwig, X. Liu and A. K. Boal, *Nat. Chem. Biol.*, 2016, **12**, 636–640.

28 J. Rittle and M. T. Green, *Science*, 2010, **330**, 933–937.

29 R. P. Hausinger, *Crit. Rev. Biochem. Mol. Biol.*, 2004, **39**, 21–68.

30 F. H. Vaillancourt, J. Yin and C. T. Walsh, *Proc. Natl. Acad. Sci. U.S.A.*, 2005, **102**, 10111–10116.

31 O. Planas, M. Clémancey, J.-M. Latour, A. Company and M. Costas, *Chem. Comm.*, 2014, **50**, 10887–10890.

32 M. S. Chen and M. C. White, *Science*, 2007, **318**, 783–787.

33 W. Liu, X. Huang, M.-J. Cheng, R. J. Nielsen, W. A. Goddard and J. T. Groves, *Science*, 2012, **337**, 1322–1325.

34 M. C. White and J. Zhao, *J. Am. Chem. Soc.*, 2018, **140**, 13988–14009.

35 W. Lai, C. Li, H. Chen and S. Shaik, *Angew. Chem. Int. Ed.*, 2012, **51**, 5556–5578.

36 J. M. Mayer, *J. Phys. Chem. Lett.*, 2011, **2**, 1481–1489.

37 J. M. Mayer, *Acc. Chem. Res.*, 2011, **44**, 36–46.

38 D. Dhar, G. M. Yee, A. D. Spaeth, D. W. Boyce, H. Zhang, B. Dereli, C. J. Cramer and W. B. Tolman, *J. Am. Chem. Soc.*, 2016, **138**, 356–368.

39 D. Schröder, S. Shaik and H. Schwarz, *Acc. Chem. Res.*, 2000, **33**, 139–145.

40 S. N. Dhuri, M. S. Seo, Y.-M. Lee, H. Hirao, Y. Wang, W. Nam and S. Shaik, *Angew. Chem. Int. Ed.*, 2008, **47**, 3356–3359.

41 D. Usharani, D. Janardanan, C. Li and S. Shaik, *Acc. Chem. Res.*, 2013, **46**, 471–482.

42 K.-B. Cho, E. J. Kim, M. S. Seo, S. Shaik and W. Nam, *Chem. Eur. J.*, 2012, **18**, 10444–10453.

43 C. T. Saouma and J. M. Mayer, *Chem. Sci.*, 2013, **5**, 21–31.

44 J. England, Y. Guo, K. M. Van Heuvelen, M. A. Cranswick, G. T. Rohde, E. L. Bominaar, E. Münck and L. Que, *J. Am. Chem. Soc.*, 2011, **133**, 11880–11883.

45 J. P. Bigi, W. H. Harman, B. Lassalle-Kaiser, D. M. Robles, T. A. Stich, J. Yano, R. D. Britt and C. J. Chang, *J. Am. Chem. Soc.*, 2012, **134**, 1536–1542.

46 N. Dietl, M. Schlangen and H. Schwarz, *Angew. Chem. Int. Ed.*, 2012, **51**, 5544–5555.

47 J. Amtawong, D. Balcells, J. Wilcoxen, R. C. Handford, N. Biggins, A. I. Nguyen, R. D. Britt and T. D. Tilley, *J. Am. Chem. Soc.*, 2019, **141**, 19859–19869.

48 G. K. Cook and J. M. Mayer, *J. Am. Chem. Soc.*, 1995, **117**, 7139–7156.

49 K. A. Gardner, L. L. Kuehnert and J. M. Mayer, *Inorg. Chem.*, 1997, **36**, 2069–2078.

50 M. K. Goetz and J. S. Anderson, *J. Am. Chem. Soc.*, 2019, **141**, 4051–4062.

51 J. M. Hodgkiss, J. Rosenthal and D. G. Nocera, in *Hydrogen-Transfer Reactions*, eds. Hynes, James T., Klinman, Judith P., Limbach, Hans-Heinrich, and Schowen, Richard L., John Wiley & Sons, Ltd, 2006, pp. 503–562.

52 T. H. Parsell, M.-Y. Yang and A. S. Borovik, *J. Am. Chem. Soc.*, 2009, **131**, 2762–2763.

53 D. Usharani, D. C. Lacy, A. S. Borovik and S. Shaik, *J. Am. Chem. Soc.*, 2013, **135**, 17090–17104.

54 S. K. Barman, J. R. Jones, C. Sun, E. A. Hill, J. W. Ziller and A. S. Borovik, *J. Am. Chem. Soc.*, 2019, **141**, 11142–11150.

55 D. Bím, M. Maldonado-Domínguez, L. Rulíšek and M. Srnec, *Proc. Natl. Acad. Sci. U.S.A.*, 2018, **115**, E10287–E10294.

56 T. Huang, E. S. Rountree, A. P. Traywick, M. Bayoumi and J. L. Dempsey, *J. Am. Chem. Soc.*, 2018, **140**, 14655–14669.

57 J. W. Darcy, S. S. Kolmar and J. M. Mayer, *J. Am. Chem. Soc.*, 2019, **141**, 10777–10787.

58 M. Mandal, C. E. Elwell, C. J. Bouchey, T. J. Zerk, W. B. Tolman and C. J. Cramer, *J. Am. Chem. Soc.*, 2019, **141**, 17236–17244.

59 C. E. Elwell, M. Mandal, C. J. Bouchey, L. Que, C. J. Cramer and W. B. Tolman, *Inorg. Chem.*, 2019, **58**, 15872–15879.

60 E. R. Sayfutyarova, Y.-C. Lam and S. Hammes-Schiffer, *J. Am. Chem. Soc.*, 2019, **141**, 15183–15189.

61 H. Kotani, H. Shimomura, K. Ikeda, T. Ishizuka, Y. Shiota, K. Yoshizawa and T. Kojima, *J. Am. Chem. Soc.*, 2020, **142**, 16982–16989.

62 M. Maldonado-Domínguez and M. Srnec, *J. Am. Chem. Soc.*, 2020, **142**, 3947–3958.

63 S. K. Barman, M.-Y. Yang, T. H. Parsell, M. T. Green and A. S. Borovik, *Proc. Natl. Acad. Sci. U.S.A.*, , DOI:10.1073/pnas.2108648118.

64 M. Maldonado-Domínguez and M. Srnec, *Inorg. Chem.*, 2022, **61**, 18811–18822.

65 J. K. Bower, M. S. Reese, I. M. Mazin, L. M. Zarnitsa, A. D. Cypcar, C. E. Moore, A. Y. Sokolov and S. Zhang, *Chem. Sci.*, 2023, **14**, 1301–1307.

66 R. G. Agarwal, S. C. Coste, B. D. Groff, A. M. Heuer, H. Noh, G. A. Parada, C. F. Wise, E. M. Nichols, J. J. Warren and J. M. Mayer, *Chem. Rev.*, 2022, **122**, 1–49.

67 R. Tyburski, T. Liu, S. D. Glover and L. Hammarström, *J. Am. Chem. Soc.*, 2021, **143**, 560–576.

68 T. H. Yosca, J. Rittle, C. M. Krest, E. L. Onderko, A. Silakov, J. C. Calixto, R. K. Behan and M. T. Green, *Science*, 2013, **342**, 825–829.

69 B. D. Groff, M. Cattaneo, S. C. Coste, C. A. Pressley, B. Q. Mercado and J. M. Mayer, *Inorg. Chem.*, 2023, **62**, 10031–10038.

70 J. M. Tedder, *Angew. Chem. Int. Ed.*, 1982, **21**, 401–410.

71 B. P. Roberts, *Chem. Soc. Rev.*, 1999, **28**, 25–35.

72 B. D. Groff, B. Koronkiewicz and J. M. Mayer, *J. Org. Chem.*, 2023, **88**, 16259–16269.

73 W. P. Jencks, *Chem. Rev.*, 1985, **85**, 511–527.

74 E. V. Anslyn and D. A. Dougherty, *Modern Physical Organic Chemistry*, University Science Books, Mill Valley, California, 2006.

75 J. N. Bronsted and C. E. Teeter, *J. Phys. Chem.*, 1924, **28**, 579–587.

76 R. P. Bell, *J. Chem. Soc.*, 1950, 409–419.

77 J. Horiuti and M. Polanyi, *J. Mol. Catal. A. Chem.*, 2003, **199**, 185–197.

78 M. G. Evans and M. Polanyi, *Trans. Faraday Soc.*, 1938, **34**, 11–24.

79 R. A. Ogg and M. Polanyi, *Trans. Faraday Soc.*, 1935, **31**, 604–620.

80 R. P. Bell, *Proc. R. Soc. Lond.*, 1936, **154**, 414–429.

81 Louis P. Hammett, *Physical Organic Chemistry*, 1940.

82 J. E. Leffler, *Science*, 1953, **117**, 340–341.

83 G. S. Hammond, *J. Am. Chem. Soc.*, 1955, **77**, 334–338.

84 R. A. Marcus, *J. Chem. Phys.*, 1956, **24**, 966–978.

85 R. A. Marcus and N. Sutin, *Biochim. Biophys. Acta, Rev. Bioenerg.*, 1985, **811**, 265–322.

86 R. A. M. O'Ferrall, *J. Chem. Soc. B*, 1970, 274–277.

87 E. D. Hughes, C. K. Ingold and U. G. Shapiro, *J. Chem. Soc.*, 1936, 225–236.

88 W. von E. Doering and H. H. Zeiss, *J. Am. Chem. Soc.*, 1953, **75**, 4733–4738.

89 J. F. Bunnett, *Angew. Chem. Int. Ed.*, 1962, **1**, 225–235.

90 E. R. Thornton, *J. Am. Chem. Soc.*, 1967, **89**, 2915–2927.

91 W. P. Jencks, *Chem. Rev.*, 1972, **72**, 705–718.

92 D. A. Jencks and W. P. Jencks, *J. Am. Chem. Soc.*, 1977, **99**, 7948–7960.

93 L. H. Funderburk and W. P. Jencks, *J. Am. Chem. Soc.*, 1978, **100**, 6708–6714.

94 C. F. Bernasconi and J. R. Gandler, *J. Am. Chem. Soc.*, 1978, **100**, 8117–8124.

95 T. Liu, R. Tyburski, S. Wang, R. Fernández-Terán, S. Ott and L. Hammarström, *J. Am. Chem. Soc.*, 2019, **141**, 17245–17259.

96 C. Costentin and J.-M. Savéant, *Chem. Sci.*, 2020, **11**, 1006–1010.

97 R. I. Cukier and D. G. Nocera, *Annu. Rev. Phys. Chem.*, 1998, **49**, 337–369.

98 A. Soudackov and S. Hammes-Schiffer, *J. Chem. Phys.*, 1999, **111**, 4672–4687.

99 S. Hammes-Schiffer and A. V. Soudackov, *J. Phys. Chem. B*, 2008, **112**, 14108–14123.

100 D. E. Lansky and D. P. Goldberg, *Inorg. Chem.*, 2006, **45**, 5119–5125.

101 R. A. Baglia, C. M. Krest, T. Yang, P. Leeladee and D. P. Goldberg, *Inorg. Chem.*, 2016, **55**, 10800–10809.

102 D. Bím, M. Maldonado-Domínguez, R. Fučík and M. Srnec, *J. Phys. Chem. C*, 2019, **123**, 21422–21428.

103 M. Maldonado-Domínguez, D. Bím, R. Fučík, R. Čurík and M. Srnec, *Phys. Chem. Chem. Phys.*, 2019, **21**, 24912–24918.

104 J. J. Warren and J. M. Mayer, *Proc. Natl. Acad. Sci. U.S.A.*, 2010, **107**, 5282–5287.

105 J. P. Reid and M. S. Sigman, *Nature*, 2019, **571**, 343–348.

106 C. B. Santiago, J.-Y. Guo and M. S. Sigman, *Chem. Sci.*, 2018, **9**, 2398–2412.

107 A. G. Maldonado and G. Rothenberg, *Chem. Soc. Rev.*, 2010, **39**, 1891–1902.

108 W. L. Williams, L. Zeng, T. Gensch, M. S. Sigman, A. G. Doyle and E. V. Anslyn, *ACS Cent. Sci.*, 2021, **7**, 1622–1637.

109 K. C. Harper, E. N. Bess and M. S. Sigman, *Nat. Chem.*, 2012, **4**, 366–374.

110 J. P. Reid and M. S. Sigman, *Nat. Rev. Chem.*, 2018, **2**, 290–305.

111 M. S. Sigman, K. C. Harper, E. N. Bess and A. Milo, *Acc. Chem. Res.*, 2016, **49**, 1292–1301.

112 D. Freedman, *Statistical models: theory and practice*, Cambridge University Press, Cambridge, 2005.

113 T. Hastie, J. Friedman and R. Tisbshirani, *The Elements of statistical learning: data mining, inference, and prediction*, Springer, New York, 2018.

114 R. Carter Hill, William E. Griffiths, and Guay C. Lim, *Principles of econometrics*, Wiley, Hoboken, NJ, 4th edn., 2011.

115 L. Buitinck, G. Louppe, M. Blondel, F. Pedregosa, A. Mueller, O. Grisel, V. Niculae, P. Prettenhofer, A. Gramfort, J. Grobler, R. Layton, J. Vanderplas, A. Joly, B. Holt and G. Varoquaux, *arXiv:1309.0238 [cs]*.

116 M. Sook Seo, N. Hee Kim, K.-B. Cho, J. Eun So, S. Kyung Park, M. Clémancey, R. Garcia-Serres, J.-M. Latour, S. Shaik and W. Nam, *Chem. Sci.*, 2011, **2**, 1039–1045.

117 S. Kundu, J. V. K. Thompson, L. Q. Shen, M. R. Mills, E. L. Bominaar, A. D. Ryabov and T. J. Collins, *Chem. Eur. J.*, 2015, **21**, 1803–1810.

118 C. V. Sastri, J. Lee, K. Oh, Y. J. Lee, J. Lee, T. A. Jackson, K. Ray, H. Hirao, W. Shin, J. A. Halfen, J. Kim, L. Que, S. Shaik and W. Nam, *Proc. Natl. Acad. Sci. U.S.A.*, 2007, **104**, 19181–19186.

119 C. Fertinger, N. Hessenauer-Ilicheva, A. Franke and R. van Eldik, *Chem. Eur. J.*, 2009, **15**, 13435–13440.

120 T. Kojima, K. Nakayama, K. Ikemura, T. Ogura and S. Fukuzumi, *J. Am. Chem. Soc.*, 2011, **133**, 11692–11700.

121 Y. J. Jeong, Y. Kang, A.-R. Han, Y.-M. Lee, H. Kotani, S. Fukuzumi and W. Nam, *Angew. Chem. Int. Ed.*, 2008, **47**, 7321–7324.

122 C. Arunkumar, Y.-M. Lee, J. Y. Lee, S. Fukuzumi and W. Nam, *Chem. Eur. J.*, 2009, **15**, 11482–11489.

123 K.-B. Cho, H. Kang, J. Woo, Y. J. Park, M. S. Seo, J. Cho and W. Nam, *Inorg. Chem.*, 2014, **53**, 645–652.

124 S. N. Dhuri, Y.-M. Lee, M. S. Seo, J. Cho, D. D. Narulkar, S. Fukuzumi and W. Nam, *Dalton Trans.*, 2015, **44**, 7634–7642.

125 D. Wang, K. Ray, M. J. Collins, E. R. Farquhar, J. R. Frisch, L. Gómez, T. A. Jackson, M. Kerscher, A. Waleska, P. Comba, M. Costas and L. Que, *Chem. Sci.*, 2013, **4**, 282–291.

126 J. R. Bryant and J. M. Mayer, *J. Am. Chem. Soc.*, 2003, **125**, 10351–10361.

127 G. Yin, A. M. Danby, D. Kitko, J. D. Carter, W. M. Scheper and D. H. Busch, *J. Am. Chem. Soc.*, 2008, **130**, 16245–16253.

128 S. Hong, H. So, H. Yoon, K.-B. Cho, Y.-M. Lee, S. Fukuzumi and W. Nam, *Dalton Trans.*, 2013, **42**, 7842–7845.

129 D. F. Leto, R. Ingram, V. W. Day and T. A. Jackson, *Chem. Commun.*, 2013, **49**, 5378–5380.

130 B. Wang, Y.-M. Lee, W.-Y. Tcho, S. Tussupbayev, S.-T. Kim, Y. Kim, M. S. Seo, K.-B. Cho, Y. Dede, B. C. Keegan, T. Ogura, S. H. Kim, T. Ohta, M.-H. Baik, K. Ray, J. Shearer and W. Nam, *Nat. Commun.*, 2017, **8**, 14839.

131 C.-M. Che, J.-L. Zhang, R. Zhang, J.-S. Huang, T.-S. Lai, W.-M. Tsui, X.-G. Zhou, Z.-Y. Zhou, N. Zhu and C. K. Chang, *Chem. Eur. J.*, 2005, **11**, 7040–7053.

132 W. W. Y. Lam, S.-M. Yiu, D. T. Y. Yiu, T.-C. Lau, W.-P. Yip and C.-M. Che, *Inorg. Chem.*, 2003, **42**, 8011–8018.

133 L. Falivene, Z. Cao, A. Petta, L. Serra, A. Poater, R. Oliva, V. Scarano and L. Cavallo, *Nat. Chem.*, 2019, **11**, 872–879.

134 G. Knizia, *J. Chem. Theory Comput.*, 2013, **9**, 4834–4843.

135 G. Knizia and J. E. M. N. Klein, *Angew. Chem. Int. Ed.*, 2015, **54**, 5518–5522.

136 F. Jensen, *Introduction to computational chemistry*, John Wiley & Sons, Chichester, 2007.

137 J. N. Harvey, *Annu. Rep. Prog. Chem., Sect. C: Phys. Chem.*, 2006, **102**, 203–226.

138 R. P. Bell, *The tunnel effect in chemistry*, Chapman and Hall, London; New York, 1980.

139 S. Hong, Y.-M. Lee, K.-B. Cho, K. Sundaravel, J. Cho, M. J. Kim, W. Shin and W. Nam, *J. Am. Chem. Soc.*, 2011, **133**, 11876–11879.

140 J. Yang, H. T. Dong, M. S. Seo, V. A. Larson, Y.-M. Lee, J. Shearer, N. Lehnert and W. Nam, *J. Am. Chem. Soc.*, 2021, **143**, 16943–16959.

141 D. W. Snelgrove, J. Lusztyk, J. T. Banks, P. Mulder and K. U. Ingold, *J. Am. Chem. Soc.*, 2001, **123**, 469–477.

142 A. Company, I. Prat, J. R. Frisch, D. R. Mas-Ballesté, M. Güell, G. Juhász, X. Ribas, D. E. Münck, J. M. Luis, L. Que and M. Costas, *Chem. Eur. J.*, 2011, **17**, 1622–1634.

143 A. T. Fiedler and L. Que, *Inorg. Chem.*, 2009, **48**, 11038–11047.

144 S. C. Sawant, X. Wu, J. Cho, K.-B. Cho, S. H. Kim, M. S. Seo, Y.-M. Lee, M. Kubo, T. Ogura, S. Shaik and W. Nam, *Angew. Chem. Int. Ed.*, 2010, **49**, 8190–8194.

145 C. R. Waidmann, X. Zhou, E. A. Tsai, W. Kaminsky, D. A. Hrovat, W. T. Borden and J. M. Mayer, *J. Am. Chem. Soc.*, 2009, **131**, 4729–4743.

146 K. A. Prokop, S. P. de Visser and D. P. Goldberg, *Angew. Chem. Int. Ed.*, 2010, **49**, 5091–5095.

147 Y. Liu, S.-M. Ng, W. W. Y. Lam, S.-M. Yiu and T.-C. Lau, *Angew. Chem. Int. Ed.*, 2016, **128**, 296–299.

148 K. Cho, P. Leeladee, A. J. McGown, S. DeBeer and D. P. Goldberg, *J. Am. Chem. Soc.*, 2012, **134**, 7392–7399.

149 J. P. T. Zaragoza, M. A. Siegler and D. P. Goldberg, *ChemComm.*, 2016, **52**, 167–170.

150 I. Garcia-Bosch, A. Company, C. W. Cady, S. Styring, W. R. Browne, X. Ribas and M. Costas, *Angew. Chem. Int. Ed.*, 2011, **50**, 5648–5653.

151 X. Wu, M. S. Seo, K. M. Davis, Y.-M. Lee, J. Chen, K.-B. Cho, Y. N. Pushkar and W. Nam, *J. Am. Chem. Soc.*, 2011, **133**, 20088–20091.

152 J. Chen, Y.-M. Lee, K. M. Davis, X. Wu, M. S. Seo, K.-B. Cho, H. Yoon, Y. J. Park, S. Fukuzumi, Y. N. Pushkar and W. Nam, *J. Am. Chem. Soc.*, 2013, **135**, 6388–6391.

153 J. England, J. O. Bigelow, K. M. V. Heuvelen, E. R. Farquhar, M. Martinho, K. K. Meier, J. R. Frisch, E. Münck and L. Que, *Chem. Sci.*, 2014, **5**, 1204–1215.

154 S. A. Wilson, J. Chen, S. Hong, Y.-M. Lee, M. Clémancey, R. Garcia-Serres, T. Nomura, T. Ogura, J.-M. Latour, B. Hedman, K. O. Hodgson, W. Nam and E. I. Solomon, *J. Am. Chem. Soc.*, 2012, **134**, 11791–11806.

155 W. Nam, S.-E. Park, I. K. Lim, M. H. Lim, J. Hong and J. Kim, *J. Am. Chem. Soc.*, 2003, **125**, 14674–14675.

156 M. Ghosh, K. K. Singh, C. Panda, A. Weitz, M. P. Hendrich, T. J. Collins, B. B. Dhar and S. Sen Gupta, *J. Am. Chem. Soc.*, 2014, **136**, 9524–9527.

157 A. N. Biswas, M. Puri, K. K. Meier, W. N. Oloo, G. T. Rohde, E. L. Bominaar, E. Münck and L. Que, *J. Am. Chem. Soc.*, 2015, **137**, 2428–2431.

158 M. Mitra, H. Nimir, S. Demeshko, S. S. Bhat, S. O. Malinkin, M. Haukka, J. Lloret-Fillol, G. C. Lisensky, F. Meyer, A. A. Shteinman, W. R. Browne, D. A. Hrovat, M. G. Richmond, M. Costas and E. Nordlander, *Inorg. Chem.*, 2015, **54**, 7152–7164.

159 J. Kaizer, E. J. Klinker, N. Y. Oh, J.-U. Rohde, W. J. Song, A. Stubna, J. Kim, E. Münck, W. Nam and L. Que, *J. Am. Chem. Soc.*, 2004, **126**, 472–473.

160 K. Nehru, M. S. Seo, J. Kim and W. Nam, *Inorg. Chem.*, 2007, **46**, 293–298.

161 J. Serrano-Plana, W. N. Oloo, L. Acosta-Rueda, K. K. Meier, B. Verdejo, E. García-España, M. G. Basallote, E. Münck, L. Que, A. Company and M. Costas, *J. Am. Chem. Soc.*, 2015, **137**, 15833–15842.

162 T. Kurahashi, A. Kikuchi, Y. Shiro, M. Hada and H. Fujii, *Inorg. Chem.*, 2010, **49**, 6664–6672.

163 X.-S. Xue, P. Ji, B. Zhou and J.-P. Cheng, *Chem. Rev.*, 2017, **117**, 8622–8648.

164 T. L. Hill, *An Introduction to Statistical Thermodynamics.*, Dover Publications, Newburyport, 2012.

165 F. Weigend, *Phys. Chem. Chem. Phys.*, 2006, **8**, 1057–1065.

166 F. Weigend and R. Ahlrichs, *Phys. Chem. Chem. Phys.*, 2005, **7**, 3297–3305.

167 N. C. HANDY and A. J. COHEN, *Mol. Phys.*, 2001, **99**, 403–412.

168 A. J. COHEN and N. C. HANDY, *Mol. Phys.*, 2001, **99**, 607–615.

169 A. D. Becke, *Phys. Rev. A*, 1988, **38**, 3098–3100.

170 F. Neese, *Wiley Interdiscip. Rev. Comput. Mol. Sci.*, 2018, **8**, e1327.

171 A. J. Johansson, M. R. A. Blomberg and P. E. M. Siegbahn, *J. Chem. Phys.*, 2008, **129**, 154301.

172 D. V. Avila, C. E. Brown, K. U. Ingold and J. Lusztyk, *J. Am. Chem. Soc.*, 1993, **115**, 466–470.

173 D. Andrae, U. Häußermann, M. Dolg, H. Stoll and H. Preuß, *Theoret. Chim. Acta*, 1990, **77**, 123–141.

174 S. Grimme, *Chem. Eur. J.*, 2012, **18**, 9955–9964.

175 S. van der Walt, S. C. Colbert and G. Varoquaux, *Comput. Sci. Eng.*, 2011, **13**, 22–30.

176 W. McKinney, *Proc. Python Sci. Conf.*, 2010, 56–61.

177 J. D. Hunter, *Comput. Sci. Eng.*, 2007, **9**, 90–95.

178 F. Pedregosa, G. Varoquaux, A. Gramfort, V. Michel, B. Thirion, O. Grisel, M. Blondel, P. Prettenhofer, R. Weiss, V. Dubourg, J. Vanderplas, A. Passos, D. Cournapeau, M. Brucher, M. Perrot and É. Duchesnay, *J. Mach. Learn. Res.*, 2011, **12**, 2825–2830.

179 P. Virtanen, R. Gommers, T. E. Oliphant, M. Haberland, T. Reddy, D. Cournapeau, E. Burovski, P. Peterson, W. Weckesser, J. Bright, S. J. van der Walt, M. Brett, J. Wilson, K. J. Millman, N. Mayorov, A. R. J. Nelson, E. Jones, R. Kern, E. Larson, C. J. Carey, İ. Polat, Y. Feng, E. W. Moore, J. VanderPlas, D. Laxalde, J. Perktold, R. Cimrman, I. Henriksen, E. A. Quintero, C. R. Harris, A. M. Archibald, A. H. Ribeiro, F. Pedregosa and P. van Mulbregt, *Nat. Methods*, 2020, **17**, 261–272.

180 A. Migliore, N. F. Polizzi, M. J. Therien and D. N. Beratan, *Chem. Rev.*, 2014, **114**, 3381–3465.

181 J. L. Dempsey, J. R. Winkler and H. B. Gray, *Chem. Rev.*, 2010, **110**, 7024–7039.

182 D. R. Weinberg, C. J. Gagliardi, J. F. Hull, C. F. Murphy, C. A. Kent, B. C. Westlake, A. Paul, D. H. Ess, D. G. McCafferty and T. J. Meyer, *Chem. Rev.*, 2012, **112**, 4016–4093.

183 S. Hammes-Schiffer, *J. Am. Chem. Soc.*, 2015, **137**, 8860–8871.

184 P. E. M. Siegbahn and M. R. A. Blomberg, *Chem. Rev.*, 2010, **110**, 7040–7061.

185 S. J. Edwards, A. V. Soudackov and S. Hammes-Schiffer, *J. Phys. Chem. A*, 2009, **113**, 2117–2126.

186 C. Costentin, *Chem. Rev.*, 2008, **108**, 2145–2179.

187 D. Mandal, R. Ramanan, D. Usharani, D. Janardanan, B. Wang and S. Shaik, *J. Am. Chem. Soc.*, 2015, **137**, 722–733.

188 H. Decornez and S. Hammes-Schiffer, *J. Phys. Chem. A*, 2000, **104**, 9370–9384.

189 A. S. Borovik, *Chem. Soc. Rev.*, 2011, **40**, 1870–1874.

190 R. P. Bell and C. N. Hinshelwood, *Proc. R. Soc. A.*, 1934, **143**, 377–399.

191 J. K. Bower, A. D. Cypcar, B. Henriquez, S. C. E. Stieber and S. Zhang, *J. Am. Chem. Soc.*, 2020, **142**, 8514–8521.

192 P. R. D. Murray, J. H. Cox, N. D. Chiappini, C. B. Roos, E. A. McLoughlin, B. G. Hejna, S. T. Nguyen, H. H. Ripberger, J. M. Ganley, E. Tsui, N. Y. Shin, B. Koronkiewicz, G. Qiu and R. R. Knowles, *Chem. Rev.*, 2022, **122**, 2017–2291.

193 E. C. Gentry and R. R. Knowles, *Acc. Chem. Res.*, 2016, **49**, 1546–1556.

194 T. F. Markle, J. W. Darcy and J. M. Mayer, *Sci. Adv.*, 2018, **4**, eaat5776.

195 R. S. J. Proctor and R. J. Phipps, *Angew. Chem. Int. Ed.*, 2019, **58**, 13666–13699.

196 H. E. Askey, J. D. Grayson, J. D. Tibbetts, J. C. Turner-Dore, J. M. Holmes, G. Kociok-Kohn, G. L. Wrigley and A. J. Cresswell, *J. Am. Chem. Soc.*, 2021, **143**, 15936–15945.

197 T. Wan, Z. Wen, G. Laudadio, L. Capaldo, R. Lammers, J. A. Rincón, P. García-Losada, C. Mateos, M. O. Frederick, R. Broersma and T. Noël, *ACS Cent. Sci.*, , DOI:10.1021/acscentsci.1c01109.

198 H. Hintz, J. Bower, J. Tang, M. LaLama, C. Sevov and S. Zhang, *Chem. Catal.*, 2023, 100491.

199 S. C. Coste, A. C. Brezny, B. Koronkiewicz and J. M. Mayer, *Chem. Sci.*, 2021, **12**, 13127–13136.

200 R. Tyburski and L. Hammarström, *Chem. Sci.*, 2021, **13**, 290–301.

201 C. F. Bernasconi, *Tetrahedron*, 1985, **41**, 3219–3234.

202 C. F. Bernasconi, in *Advances in Physical Organic Chemistry*, ed. J. P. Richard, Academic Press, 2010, vol. 44, pp. 223–324.

203 M. Salamone, M. Galeotti, E. Romero-Montalvo, J. A. van Santen, B. D. Groff, J. M. Mayer, G. A. DiLabio and M. Bietti, *J. Am. Chem. Soc.*, , DOI:10.1021/jacs.1c05566.

204 E. Grunwald, *J. Am. Chem. Soc.*, 1985, **107**, 125–133.

205 J. P. Klinman, *J. Phys. Org. Chem.*, 2010, **23**, 606–612.

206 J. P. Layfield and S. Hammes-Schiffer, *Chem. Rev.*, 2014, **114**, 3466–3494.

207 J. Meisner and J. Kästner, *Angew. Chem. Int. Ed.*, 2016, **55**, 5400–5413.

208 D. Mandal and S. Shaik, *J. Am. Chem. Soc.*, 2016, **138**, 2094–2097.

209 S. H. Bae, X.-X. Li, M. S. Seo, Y.-M. Lee, S. Fukuzumi and W. Nam, *J. Am. Chem. Soc.*, 2019, **141**, 7675–7679.

210 P. R. Schreiner, *J. Am. Chem. Soc.*, 2017, **139**, 15276–15283.

211 L. C. S. Melander and W. H. Saunders, *Reaction rates of isotopic molecules*, Wiley, New York, 1980.

212 P. T. Truong, S. G. Miller, E. J. McLaughlin Sta. Maria and M. A. Bowring, *Chem. Eur. J.*, 2021, **27**, 14800–14815.

213 R. Jaglan and D. Mandal, *Comput. Theor. Chem.*, 2020, **1187**, 112920.

214 P. M. Kiefer and J. T. Hynes, *J. Phys. Chem. A*, 2004, **108**, 11793–11808.

215 S. Hammes-Schiffer, *Energy Environ. Sci.*, 2012, **5**, 7696–7703.

216 E. R. Sayfutyarova, Z. K. Goldsmith and S. Hammes-Schiffer, *J. Am. Chem. Soc.*, 2018, **140**, 15641–15645.

217 J. P. Klinman and A. R. Offenbacher, *Acc. Chem. Res.*, 2018, **51**, 1966–1974.

218 S. Hammes-Schiffer and A. A. Stuchebrukhov, *Chem. Rev.*, 2010, **110**, 6939–6960.

219 Z. Pan, J. H. Horner and M. Newcomb, *J. Am. Chem. Soc.*, 2008, **130**, 7776–7777.

220 C. Kupper, B. Mondal, J. Serrano-Plana, I. Klawitter, F. Neese, M. Costas, S. Ye and F. Meyer, *J. Am. Chem. Soc.*, 2017, **139**, 8939–8949.

221 S. Mahapatra, J. A. Halfen, E. C. Wilkinson, L. Que and W. B. Tolman, *J. Am. Chem. Soc.*, 1994, **116**, 9785–9786.

222 S. Mahapatra, J. A. Halfen and W. B. Tolman, *J. Am. Chem. Soc.*, 1996, **118**, 11575–11586.

223 O. M. Reinaud and K. H. Theopold, *J. Am. Chem. Soc.*, 1994, **116**, 6979–6980.

224 J. Bonin, C. Costentin, C. Louault, M. Robert and J.-M. Savéant, *J. Am. Chem. Soc.*, 2011, **133**, 6668–6674.

225 A. Wu, E. A. Mader, A. Datta, D. A. Hrovat, W. T. Borden and J. M. Mayer, *J. Am. Chem. Soc.*, 2009, **131**, 11985–11997.

226 H. Kwart, M. W. Brechbiel, R. M. Acheson and D. C. Ward, *J. Am. Chem. Soc.*, 1982, **104**, 4671–4672.

227 M. P. Meyer, D. R. Tomchick and J. P. Klinman, *Proc. Natl. Acad. Sci. U.S.A.*, 2008, **105**, 1146–1151.

228 W. A. Francisco, M. J. Knapp, N. J. Blackburn and J. P. Klinman, *J. Am. Chem. Soc.*, 2002, **124**, 8194–8195.

229 S. Mahapatra, J. A. Halfen, E. C. Wilkinson, G. Pan, C. J. Cramer, L. Jr. Que and W. B. Tolman, *J. Am. Chem. Soc.*, 1995, **117**, 8865–8866.

230 J. E. M. N. Klein, D. Mandal, W.-M. Ching, D. Mallick, L. Jr. Que and S. Shaik, *J. Am. Chem. Soc.*, 2017, **139**, 18705–18713.

231 D. Mandal, D. Mallick and S. Shaik, *Acc. Chem. Res.*, 2018, **51**, 107–117.

232 J. H. Skone, A. V. Soudackov and S. Hammes-Schiffer, *J. Am. Chem. Soc.*, 2006, **128**, 16655–16663.

233 C. R. Goldsmith, R. T. Jonas and T. D. P. Stack, *J. Am. Chem. Soc.*, 2002, **124**, 83–96.

234 R. J. Bailey, P. Card and H. Shechter, *J. Am. Chem. Soc.*, 1983, **105**, 6096–6103.

235 Ch. Brevard, J. P. Kintzinger and J. M. Lehn, *Tetrahedron*, 1972, **28**, 2429–2445.

236 I. W. C. E. Arends, P. Mulder, K. B. Clark and D. D. M. Wayner, *J. Phys. Chem.*, 1995, **99**, 8182–8189.

237 M. H. V. Huynh and T. J. Meyer, *Chem. Rev.*, 2007, **107**, 5004–5064.

238 S. Hammes-Schiffer, *Acc. Chem. Res.*, 2009, **42**, 1881–1889.

239 M. Milan, M. Bietti and M. Costas, *Chem. Commun.*, 2018, **54**, 9559–9570.

240 Y. Georgievskii and A. A. Stuchebrukhov, *J. Chem. Phys.*, 2000, **113**, 10438–10450.

241 M. J. Knapp, K. Rickert and J. P. Klinman, *J. Am. Chem. Soc.*, 2002, **124**, 3865–3874.

242 T. F. Markle, M.-T. Zhang, M.-P. Santoni, L. O. Johannissen and L. Hammarström, *J. Phys. Chem. B*, 2016, **120**, 9308–9321.

243 T. F. Markle, A. L. Tenderholt and J. M. Mayer, *J. Phys. Chem. B*, 2012, **116**, 571–584.

244 Y. Liu, H. Liu, K. Song, Y. Xu and Q. Shi, *J. Phys. Chem. B*, 2015, **119**, 8104–8114.

245 A. A. Zavitsas, *J. Am. Chem. Soc.*, 1972, **94**, 2779–2789.

246 A. A. Zavitsas and A. A. Melikian, *J. Am. Chem. Soc.*, 1975, **97**, 2757–2763.

247 B. P. Roberts and A. J. Steel, *J. Chem. Soc., Perkin Trans. 2*, 1994, **0**, 2155–2162.

248 A. A. Zavitsas and C. Chatgilialoglu, *J. Am. Chem. Soc.*, 1995, **117**, 10645–10654.

249 B. P. Roberts, *J. Chem. Soc., Perkin trans. II*, 1996, **0**, 2719–2725.

250 M. T. Green, J. H. Dawson and H. B. Gray, *Science*, 2004, **304**, 1653–1656.

251 J. N. Harvey, M. Aschi, H. Schwarz and W. Koch, *Theor Chem Acc*, 1998, **99**, 95–99.

252 F. Neese, F. Wennmohs, U. Becker and C. Riplinger, *J. Chem. Phys.*, 2020, **152**, 224108.

253 S. Grimme, S. Ehrlich and L. Goerigk, *J. Comput. Chem.*, 2011, **32**, 1456–1465.

254 P. R. Ortiz de Montellano, *Chem. Rev.*, 2010, **110**, 932–948.

255 R. Banerjee, J. C. Jones and J. D. Lipscomb, *Annual Review of Biochemistry*, 2019, **88**, 409–431.

256 R. Balasubramanian, S. M. Smith, S. Rawat, L. A. Yatsunyk, T. L. Stemmler and A. C. Rosenzweig, *Nature*, 2010, **465**, 115–119.

257 M. O. Ross, F. MacMillan, J. Wang, A. Nisthal, T. J. Lawton, B. D. Olafson, S. L. Mayo, A. C. Rosenzweig and B. M. Hoffman, *Science*, 2019, **364**, 566–570.

258 J. England, Y. Guo, E. R. Farquhar, V. G. Young Jr., E. Münck and L. Que Jr., *J. Am. Chem. Soc.*, 2010, **132**, 8635–8644.

259 M. K. Goetz, J. E. Schneider, A. S. Filatov, K. A. Jesse and J. S. Anderson, *J. Am. Chem. Soc.*, 2021, **143**, 20849–20862.

260 A. E. Thorarinsdottir and D. G. Nocera, *Chem. Catal.*, 2021, **1**, 32–43.

261 K. Mittra and M. T. Green, *J. Am. Chem. Soc.*, 2019, **141**, 5504–5510.

262 H. V. R. Dias, H.-J. Kim, H.-L. Lu, K. Rajeshwar, N. R. de Tacconi, A. Derecskei-Kovacs and D. S. Marynick, *Organometallics*, 1996, **15**, 2994–3003.

263 H. V. R. Dias, H.-L. Lu, H.-J. Kim, S. A. Polach, T. K. H. H. Goh, R. G. Browning and C. J. Lovely, *Organometallics*, 2002, **21**, 1466–1473.

264 H. V. R. Dias and C. J. Lovely, *Chem. Rev.*, 2008, **108**, 3223–3238.

265 S. A. Cantalupo, J. S. Lum, M. C. Buzzeo, C. Moore, A. G. DiPasquale, A. L. Rheingold and L. H. Doerrer, *Dalton Trans.*, 2010, **39**, 374–383.

266 D. K. Dogutan, R. Jr. McGuire and D. G. Nocera, *J. Am. Chem. Soc.*, 2011, **133**, 9178–9180.

267 J. K. Elinburg and L. H. Doerrer, *Polyhedron*, 2020, **190**, 114765.

268 J. K. Elinburg, S. L. Carter, J. J. M. Nelson, D. G. Fraser, M. P. Crockett, A. B. Beeler, E. Nordlander, A. L. Rheingold and L. H. Doerrer, *Inorg. Chem.*, 2020, **59**, 16500–16513.

269 W.-T. Lee, D. A. Dickie, A. J. Metta-Magaña and J. M. Smith, *Inorg. Chem.*, 2013, **52**, 12842–12846.

270 J. Beerhues, H. Aberhan, T.-N. Streit and B. Sarkar, *Organometallics*, 2020, **39**, 4557–4564.

271 S. Han, X. Gao, Q. Wu, J. Li, D. Zou, Y. Wu and Y. Wu, *Advanced Synthesis & Catalysis*, 2019, **361**, 1559–1563.

272 S. B. Muñoz, W. K. Foster, H.-J. Lin, C. G. Margarit, D. A. Dickie and J. M. Smith, *Inorg. Chem.*, 2012, **51**, 12660–12668.

273 K. Verlinden, H. Buhl, W. Frank and C. Ganter, *Eur. J. Inorg. Chem.*, 2015, **2015**, 2416–2425.

274 R. E. Cowley, R. P. Bontchev, E. N. Duesler and J. M. Smith, *Inorg. Chem.*, 2006, **45**, 9771–9779.

275 I. Nieto, R. P. Bontchev, A. Ozarowski, D. Smirnov, J. Krzystek, J. Telser and J. M. Smith, *Inorganica Chimica Acta*, 2009, **362**, 4449–4460.

276 R. A. Juarez, W.-T. Lee, J. M. Smith and H. Wang, *Dalton Trans.*, 2014, **43**, 14689–14695.

277 J. W. Jr. Egan, B. S. Haggerty, A. L. Rheingold, S. C. Sendlinger and K. H. Theopold, *J. Am. Chem. Soc.*, 1990, **112**, 2445–2446.

278 R. D. Jones, D. A. Summerville and Fred. Basolo, *Chem. Rev.*, 1979, **79**, 139–179.

279 D. Diemente, B. M. Hoffman and F. Basolo, *J. Chem. Soc. D*, 1970, 467–468.

280 B. M. Hoffman, D. L. Diemente and F. Basolo, *J. Am. Chem. Soc.*, 1970, **92**, 61–65.

281 Y. M. Kwon, Y. Lee, G. E. Evenson, T. A. Jackson and D. Wang, *J. Am. Chem. Soc.*, 2020, **142**, 13435–13441.

282 X. Hu, I. Castro-Rodriguez and K. Meyer, *J. Am. Chem. Soc.*, 2004, **126**, 13464–13473.

283 H. Noh, D. Jeong, T. Ohta, T. Ogura, J. S. Valentine and J. Cho, *J. Am. Chem. Soc.*, 2017, **139**, 10960–10963.

284 D. E. DeRosha, B. Q. Mercado, G. Lukat-Rodgers, K. R. Rodgers and P. L. Holland, *Angew. Chem. Int. Ed.*, 2017, **56**, 3211–3215.

285 N. W. I. Terry, E. L. Amma and L. Vaska, *J. Am. Chem. Soc.*, 1972, **94**, 653–655.

286 J. Halpern, B. L. Goodall, G. P. Khare, H. S. Lim and J. J. Pluth, *J. Am. Chem. Soc.*, 1975, **97**, 2301–2303.

287 J. Cho, R. Sarangi, H. Y. Kang, J. Y. Lee, M. Kubo, T. Ogura, E. I. Solomon and W. Nam, *J. Am. Chem. Soc.*, 2010, **132**, 16977–16986.

288 A. F. M. M. Rahman, W. G. Jackson and A. C. Willis, *Inorg. Chem.*, 2004, **43**, 7558–7560.

289 C.-C. Wang, H.-C. Chang, Y.-C. Lai, H. Fang, C.-C. Li, H.-K. Hsu, Z.-Y. Li, T.-S. Lin, T.-S. Kuo, F. Neese, S. Ye, Y.-W. Chiang, M.-L. Tsai, W.-F. Liaw and W.-Z. Lee, *J. Am. Chem. Soc.*, 2016, **138**, 14186–14189.

290 F. Oddon, Y. Chiba, J. Nakazawa, T. Ohta, T. Ogura and S. Hikichi, *Angew. Chem. Int. Ed.*, 2015, **54**, 7336–7339.

291 M. W. Urban, Y. Nonaka and K. Nakamoto, *Inorg. Chem.*, 1982, **21**, 1046–1049.

292 K. Bajdor, K. Nakamoto, H. Kanatomi and I. Murase, *Inorg. Chim. Acta*, 1984, **82**, 207–210.

293 G. A. Rodley and W. T. Robinson, *Nature*, 1972, **235**, 438–439.

294 C. J. Cramer, W. B. Tolman, K. H. Theopold and A. L. Rheingold, *Proc. Natl. Acad. Sci. U.S.A.*, 2003, **100**, 3635–3640.

295 J. B. Gordon, A. C. Vilbert, M. A. Siegler, K. M. Lancaster, P. Moënne-Loccoz and D. P. Goldberg, *J. Am. Chem. Soc.*, 2019, **141**, 3641–3653.

296 T. Corona, S. K. Padamati, F. Acuña-Parés, C. Duboc, W. R. Browne and A. Company, *Chem. Commun.*, 2017, **53**, 11782–11785.

297 C.-W. Chiang, S. T. Kleespies, H. D. Stout, K. K. Meier, P.-Y. Li, E. L. Bominaar, L. Jr. Que, E. Münck and W.-Z. Lee, *J. Am. Chem. Soc.*, 2014, **136**, 10846–10849.

298 W. M. Haynes, Ed., *CRC Handbook of Chemistry and Physics*, CRC Press, Boca Raton, 97th edn., 2016.

299 G. Xue, R. De Hont, E. Münck and L. Que, *Nat. Chem.*, 2010, **2**, 400–405.

300 Y. Li, S. Handunneththige, J. Xiong, Y. Guo, M. R. Talipov and D. Wang, *J. Am. Chem. Soc.*, 2020, **142**, 21670–21678.

301 Y. Li, S. Handunneththige, E. R. Farquhar, Y. Guo, M. R. Talipov, F. Li and D. Wang, *J. Am. Chem. Soc.*, 2019, **141**, 20127–20136.

302 Y. Li, C. Abelson, L. Que and D. Wang, *Proc. Natl. Acad. Sci. U.S.A.*, 2023, **120**, e2307950120.

303 J. Amtawong, A. I. Nguyen and T. D. Tilley, *J. Am. Chem. Soc.*, 2022, **144**, 1475–1492.

304 A. S. Bhanu Prasad, T. M. Stevenson, J. R. Citineni, V. Nyzam and P. Knochel, *Tetrahedron*, 1997, **53**, 7237–7254.

305 M. Kawase, R. Saijo and K. Kurihara, *Heterocycles*, 2013, **87**, 2533.

306 G. M. Sheldrick, *Acta Cryst A*, 2008, **64**, 112–122.

307 O. V. Dolomanov, L. J. Bourhis, R. J. Gildea, J. a. K. Howard and H. Puschmann, *J Appl Cryst*, 2009, **42**, 339–341.

308 G. M. Sheldrick, *Acta Cryst C*, 2015, **71**, 3–8.

309 J. Tao, J. P. Perdew, V. N. Staroverov and G. E. Scuseria, *Phys. Rev. Lett.*, 2003, **91**, 146401.

310 F. Neese, *Wiley Interdiscip. Rev. Comput. Mol. Sci.*, 2022, **12**, e1606.

311 F. T. de Oliveira, A. Chanda, D. Banerjee, X. Shan, S. Mondal, L. Que, E. L. Bominaar, E. Münck and T. J. Collins, *Science*, 2007, **315**, 835–838.

312 M. R. Bukowski, K. D. Koehntop, A. Stubna, E. L. Bominaar, J. A. Halfen, E. Münck, W. Nam and L. Que, *Science*, 2005, **310**, 1000–1002.

313 T. H. Parsell, R. K. Behan, M. T. Green, M. P. Hendrich and A. S. Borovik, *J. Am. Chem. Soc.*, 2006, **128**, 8728–8729.

314 G. J. Palenik, *Inorg. Chem.*, 1967, **6**, 503–507.

315 J. Cho, J. Woo and W. Nam, *J. Am. Chem. Soc.*, 2012, **134**, 11112–11115.

316 D. Wang, M. Zhang, P. Bühlmann and L. Que, *J. Am. Chem. Soc.*, 2010, **132**, 7638–7644.

317 C. M. Che, W. T. Tang, W. T. Wong and T. F. Lai, *J. Am. Chem. Soc.*, 1989, **111**, 9048–9056.

318 C. J. Cramer and D. G. Truhlar, *Phys. Chem. Chem. Phys.*, 2009, **11**, 10757–10816.

319 F. Neese, *J Biol Inorg Chem*, 2006, **11**, 702–711.

320 M. H. Abraham, P. L. Grellier, D. V. Prior, P. P. Duce, J. J. Morris and P. J. Taylor, *J. Chem. Soc., Perkin Trans. 2*, 1989, 699–711.

321 M. H. Abraham, P. L. Grellier, D. V. Prior, J. J. Morris and P. J. Taylor, *Perkin Trans. 2*, 1990, 521–529.

322 A. Bondi, *J. Phys. Chem.*, 1964, **68**, 441–451.

323 R. S. Rowland and R. Taylor, *J. Phys. Chem.*, 1996, **100**, 7384–7391.

324 R. A. Marcus, *J. Phys. Chem.*, 1963, **67**, 853–857.

325 M. Radoń, *Phys. Chem. Chem. Phys.*, 2014, **16**, 14479–14488.

326 F. Neese, *Wiley Interdiscip. Rev. Comput. Mol. Sci.*, 2012, **2**, 73–78.

327 T. Matsuo and J. M. Mayer, *Inorg. Chem.*, 2005, **44**, 2150–2158.

328 A. Kohen and J. P. Klinman, *Acc. Chem. Res.*, 1998, **31**, 397–404.

329 H. S. Johnston and J. Heicklen, *J. Phys. Chem.*, 1962, **66**, 532–533.

330 M. J. Stern and R. E. Weston, *J. Chem. Phys.*, 1974, **60**, 2808–2814.